168
Advances in Polymer Science

Advances in Polymer Science

Recently Published and Forthcoming Volumes

Polymer Synthesis · Polymer Analysis
Vol. 171, 2004

NMR · Coordination Polymerization · Photopolymerization
Vol. 170, 2004

Long-Term Properties of Polyolefins
Volume Editor: Albertsson, A.-C.
Vol. 169, 2004

Polymers and Light
Volume Editor: Lippert, T. K.
Vol. 168, 2004

New Synthetic Methods
Vol. 167, 2004

Polyelectrolytes with Defined Molecular Architecture II
Volume Editor: Schmidt, M.
Vol. 166, 2004

Polyelectrolytes with Defined Molecular Architecture I
Volume Editor: Schmidt, M.
Vol. 165, 2004

Filler-Reinforced Elastomers · Scanning Force Microscopy
Vol. 164, 2003

Liquid Chromatography · FTIR Microspectroscopy · Microwave Assisted Synthesis
Vol. 163, 2003

Radiation Effects on Polymers for Biological Use
Volume Editor: Kausch, H.
Vol. 162, 2003

Polymers for Photonics Applications II
Nonlinear Optical, Photorefractive and Two-Photon Absorption Polymers
Volume Editor: Lee, K.-S.
Vol. 161, 2003

Filled Elastomers · Drug Delivery Systems
Vol. 160, 2002

Statistical, Gradient, Block and Graft Copolymers by Controlled/ Living Radical Polymerizations
Authors: Davis, K.A., Matyjaszewski, K.
Vol. 159, 2002

Polymers for Photonics Applications I
Nonlinear Optical and Electroluminescence Polymers
Volume Editor: Lee, K.-S.
Vol. 158, 2002

Degradable Aliphatic Polyesters
Volume Editor: Albertsson, A.-C.
Vol. 157, 2001

Molecular Simulation · Fracture · Gel Theory
Vol. 156, 2001

New Polymerization Techniques and Synthetic Methodologies
Vol. 155, 2001

Polymer Physics and Engineering
Vol. 154, 2001

Polymers and Light

With contributions by
S. Georgiou · W. Kautek · J. Krüger · T. K. Lippert
Y. Zhang

Springer

The series presents critical reviews of the present and future trends in polymer and biopolymer science including chemistry, physical chemistry, physics and material science. It is addressed to all scientists at universities and in industry who wish to keep abreast of advances in the topics covered.

As a rule, contributions are specially commissioned. The editors and publishers will, however, always be pleased to receive suggestions and supplementary information. Papers are accepted for "Advances in Polymer Science" in English.

In references Advances in Polymer Science is abbreviated Adv Polym Sci and is cited as a journal.

The electronic content of APS may be found at
http://www.springerLink.com

ISSN 0065-3195
ISBN 3-540-40471-6
DOI 10.1007/b12437
Springer-Verlag Berlin Heidelberg New York

Library of Congress Catalog Card Number 61642

Springer-Verlag is a part of Springer Science+Business Media

springeronline.com

Printed in Germany

Typesetting: Stürtz AG, Würzburg
Cover: Künkellopka GmbH, Heidelberg; design&production GmbH, Heidelberg

Printed on acid-free paper 02/3020/kk – 5 4 3 2 1 0

Volume Editor

Dr. Thomas K. Lippert
Paul Scherrer Institut
5232 Villigen-PSI
Switzerland
E-mail: thomas.lippert@psi.ch

Editorial Board

Prof. Dr. Martin Möller
Deutsches Wollforschungsinstitut
an der RWTH Aachen e.V.
Veltmanplatz 8
52062 Aachen, Germany
E-mail: moeller@dwi.rwth-aachen.de

Prof. Oskar Nuyken
Lehrstuhl für Makromolekulare Stoffe
TU München
Lichtenbergstr. 4
85747 Garching, Germany
E-mail: oskar.nuyken@ch.tum.de

Prof. Brigitte Voit
Institut für Polymerforschung Dresden
Hohe Straße 6
01069 Dresden, Germany
E-mail: voit@ipfdd.de

Prof. Gerhard Wegner
Max-Planck-Institut für Polymerforschung
Ackermannweg 10
Postfach 3148
55128 Mainz, Germany
E-mail: wegner@mpip-mainz.mpg.de

Preface

This special volume *Polymers and Light* deals with very recent developments of photon interactions with polymers, in areas outside the scope of the familiar photoresist technique and optical lithography. Recent developments in microlithography still apply the same processing steps (irradiation of the photoresist through a mask followed by a subsequent 'wet' chemical development step), but with new photoresist materials, and new irradiation sources, i.e. excimer lasers that emit in the UV, e.g. at 157, 193, and 248 nm. Excimer lasers are now the main photon sources for microlithography in many research laboratories and in industry.

This successful story started in 1977 when the first excimer laser became commercially available (Lambda Physik), which was only 7 years after the development of the first excimer (1970 by Basov et al.). In their first years, these lasers were used as unique, powerful photon sources for photochemical experiments. The first reports involving excimer laser induced structuring of polymers, were published in 1982, nearly simultaneously by Srinivasan et al. and Kawamura et al.. Excimer laser irradiation allowed high resolution structuring of polymers without any additional development steps, acting as a true dry etching technique, which was envisioned as a replacement or alternative technique to classical lithography with resists. In the following years, many problems were encountered for this application, such as low sensitivity of the polymers, contamination of optics and surface with the ablation products (debris), and chemical modification of the polymers which continuously changed the processing parameter. Nevertheless, there has been renewed interest in polymer ablation as a result of special niche applications found in an area that may be described as *microstructuring*. Examples of these applications include the via-hole drilling on multichip modules at IBM, or the drilling of the inkjet printer nozzles. Photon induced direct structuring of polymers has recently attracted more attention due to new applications, new instruments (photon sources), and new material developments. These new methods for polymer processing have the potential to create novel applications for polymers, and reveal the opportunity for polymer chemists to perform unique research at the interface of polymers and lasers. The utilization of high laser energies can result in truly new processes which are not possible to achieve with the classical low energy irradiation.

S. Georgiou summarizes the recent successes of laser cleaning of polymer substrates. The basic principles of the three most important cleaning processes, i.e. layer-by-layer removal, selective removal of impurities, and particle removal, are discussed in detail. Particular emphasis is given to the possible side effects of these procedures, which will determine the further success of these methods. Various experiments aimed at a better understanding of these processes using model or polymer systems are presented. Examples of its potential, especially to paintings, are shown together with the capabilities of various on-line monitoring tools.

The contribution of T. Lippert describes a different approach to polymer ablation, discussing the development of polymers that are designed for laser ablation at a specific wavelength (308 nm). These special polymers reveal properties that show the possibility of overcoming most problems associated with ablation of polymers: these polymers reveal a high sensitivity, show no-surface modification, and yield mainly gaseous products. These polymers are also used as probes for the mechanisms of polymer ablation that are still under discussion (photochemical vs. photothermal). Various experimental data on the designed polymers and a comparison with a reference polymer (polyimide) suggest the importance of a photochemical mechanism in the ablation process.

Two recent exciting developments in ablation are discussed by Krüger/Kautek and Zhang: the application of ultrashort pulses and the utilization of synchrotron radiation (x-rays).

These two contributions are the first reviews which summarize the recent results of ultrafast and x-ray structuring of polymers.

Femtosecond laser irradiation of polymers allows direct structuring of polymers that are transparent at most laser wavelengths (e.g. Teflon), and reveal structures with high quality and a very small heat affected zone (HAZ). Similarities and differences between the ablation of polymers and dielectrics are shown, together with the influence of the pulse duration and band-gap of the materials. Various potential applications in medicine and biosensoric are discussed.

Synchrotron structuring of polymers, using a 'small' synchrotron ring with 10 m circumference can be applied for directly structuring polymers with the high aspect ratios that are very difficult to obtain by other methods, e.g. laser irradiation. The fundamentals of X-ray lithography are discussed, followed by a comparison of synchrotron structuring with laser ablation and X-ray lithography (e.g. LIGA). The mechanism is different from laser ablation and an example of its potential application is also shown.

Villigen, January 2004 Thomas K. Lippert

Advances in Polymer Science
Also Available Electronically

For all customers who have a subscription to Advances in Polymer Science, we offer the electronic version via SpringerLink free of charge. Please contact your librarian who can receive a password for free access to the full articles by registering at:

http://www.springerlink.com

If you do not have a subscription, you can still view the tables of contents of the volumes and the abstract of each article by going to the SpringerLink Homepage, clicking on "Browse by Online Libraries", then "Chemical Sciences", and finally choose Advances in Polymer Science.

You will find information about the

– Editorial Board
– Aims and Scope
– Instructions for Authors
– Sample Contribution

at http://www.springeronline.com using the search function.

Contents

Adv Polym Sci (2004) 168:1–49
DOI: 10.1007/b12681

Laser Cleaning Methodologies of Polymer Substrates

Savas Georgiou

Institute of Electronic Structure and Laser,
Foundation for Research and Technology–Hellas, 71110 Heraklion, Crete, Greece
E-mail: sgeorgiu@iesl.forth.gr

Abstract Ever increasing technological and environmental needs pose significant demands on the removal of unwanted material from substrates. Laser irradiation has been shown to afford a highly effective method for addressing these problems. The three schemes examined include coating removal in a layer-by-layer approach, selective removal of surface impurities, and particle removal. The basic principles underlying these processes are presented. Particular emphasis is placed on the side effects of these procedures, since these will determine to a large extent the success and the wider acceptance of laser cleaning schemes. Elucidation of these effects is also of scientific interest, since they are intimately related with the nature of the processes underlying the interaction of intense laser pulses with molecular/polymeric materials. To this end, these effects are systematically addressed in experiments involving model and realistic systems and are exemplified in the particular case of laser-based restoration of painted artworks. It is shown that, with proper optimization of the irradiation parameters, the side effects of laser processing can be minimized and be inconsequential for substrate integrity. Thus, at least for certain cases, laser cleaning schemes may be a highly effective, accurate, and safe method providing specific advantages not only over conventional methods, but also over other emerging competing methods.

Keywords UV laser irradiation · UV ablation · Art conservation · Polymers · Photochemical processes · Structural modifications

Abbreviations

α	Absorption coefficient
a_{ac}	Acoustic wave damping coefficient
β	Thermal expansion coefficient at constant temperature
c_p	Heat capacity at constant pressure
c_v	Heat capacity at constant volume
c_s	Sound speed
Γ	Grüneisen coefficient
γ	Adiabatic ratio
δ	Ablation (etched) depth per pulse
$E_{binding}$	Binding energy to the substrate
D	Thermal diffusivity
E_a	Activation energy
E_{cr}	Critical energy density for ablation
E_{KIN}	Kinetic energy
F_{LASER}	Laser fluence
F_{thr}	Threshold fluence for material removal
ΔH_{vap}	Evaporation enthalpy
ΔH_{sub}	Sublimation enthalpy
η_c	Particle laser-induced removal efficiency
θ	Ratio τ_{pulse}/τ_{ac}
I	Laser intensity
k(T)	Reaction rate constant
κ_B	Boltzmann constant
κ_T	Isothermal compressibility
λ	Wavelength
M	Mass
N_{fringe}	Number of interference fringes
N_{pulse}	Number of laser pulses
n_R	Refractive index
n	Density of particles on surface after irradiation
n_0	Density of particles on surface before irradiation
ν_{ac}	Acoustic wave frequency
P	Pressure
PMMA	Poly(methyl methacrylate)
PS	Polystyrene
R	Reflectivity
R_B	Gas constant
ρ	Density
r_p	Particle radius
σ_p	Particle absorption coefficient
σ_{tens}	Surface tension coefficient
T	Temperature
t_{th}	Thermal diffusion time

τ_{pulse}	Laser pulse duration
τ_{ac}	Time for an acoustic wave to traverse the irradiated volume
υ	Expansion velocity
U	Wave amplitude in the hologram plane
ϕ	Phase of the optical wave

1 Introduction

Upon irradiation of condensed phases with laser pulses at high laser irradiances, material ejection is observed [1–6]. This efficient material removal has provided the basis for a wide spectrum of highly successful applications, ranging from analytical chemistry to microelectronics, to medicine, etc. In most of these applications, such as the etching of semiconductors and polymers [1–4] in microelectronics and other industrial sectors, photorefractive keratectomy, and laser-based excision of tissue in medicine [5–6], the aim is to effect the appropriate shaping of the substrates via the precise removal of material. As such, all these applications might be denoted as laser cleaning schemes. However, despite any arbitrariness, we are justified in restricting the use of the term to the removal of a relatively small amount of degraded or contaminated material from substrates. The present contribution focuses in particular on the use of laser techniques for the removal of unwanted/degraded coatings or particles from polymeric substrates. An overview of the development of laser techniques for other types of substrates is provided in the collection of articles in [7].

The need for the development of laser-based cleaning techniques derives largely from the inadequacy of conventional methods. The traditional methods of dealing with particle and coating removal rely on the use of mechanical or chemical means [8–9]. However, the use of mechanical means (e.g., abrasive methods, jet spraying, etc.) can lead to inadvertent material removal from the substrate and the destruction of its texture. On the other hand, chemical solvents (typical ones include methyl ethyl ketone, methylene chloride, phenol) may penetrate into the substrate and result in its irreversible damage. Furthermore, in many cases, the required chemicals are highly aggressive, thereby introducing serious environmental or even health hazards. Even in the case of benign solvents, their use introduces the risk of leakage of any toxic or hazardous contaminants (e.g., heavy metals, radioactive materials, chloroaromatics) that are often present in the substrates to be cleaned.

With increasing technological demands, traditional methods may, in fact, fail altogether. This is, for instance, the case for the removal of micron and submicron particles. Due to the ever-decreasing device size, cleaning of particles of such a size from surfaces has become a major need in lithography, microelectronics, telecommunications, and other industries. Because particulates of this size adhere with relatively strong forces [3, 8–9], conventional

removal techniques such as ultrasonics or jet spraying become ineffective, thereby necessitating the introduction of drastically new methods. As an indication of the technological and economic importance of the issue, it suffices to mention that at current 0.18 μm design rules, 80 out of the $\approx$400 total steps in integrated circuit manufacturing concern cleaning of components [8].

Demanding cleaning problems are also encountered in the field of artworks restoration (due to the specific interest of this issue, only the application to organic-based substrates, e.g., painted artworks, parchments, etc., will be considered) [10–13]. There are at least two major needs in the restoration of painted artworks: (a) cleaning of the surface (varnish) and/or of the support material (canvas, wood, etc.) from accumulated pollutants, photodegradation products, and dirt, and (b) removal of overpaintings in order to recover the original painting. Cleaning may be desirable for maintaining the aesthetics of artworks, but often it is absolutely imperative for prolonging their lifetime. However, because of the high complexity of these substrates, traditional methods have in many cases only partial success in meeting this objective. Thus, the recovery or restoration of the artwork may be performed at the expense of its authenticity and even of its integrity. Furthermore, the efficiency of these techniques depends critically on the expertise of the conservator. The need for highly efficient restoration techniques becomes even more pressing due to the ever-increasing environmental pollution effects on cultural heritage objects.

To overcome the limitations of conventional techniques, alternative methods are under examination both in industry and the area of the restoration of cultural objects. Since these techniques are at the developmental stage, their relative merits and limitations remain to be fully assessed. For instance, megasonic agitation is indicated to reach a critical effective limit at 0.1 μm particle size, plasma spraying requires reduced operating pressures that may not be easily implemented, and cryogenic (CO_2-based) cleaning is limited by the problem of thermal shock to the substrate. For a comparison of the status of development of these techniques, the reader is referred to comprehensive overviews [8–9]. Yet laser-based techniques are indicated to provide several specific advantages, so it appears safe to presume their final adoption in a number of cases. In particular, laser-based cleaning offers the advantages of automation, selectivity, versatility and, most importantly, a high degree of precision. Furthermore, it can be directly interfaced with a variety of in situ laser-based analytical techniques, thereby providing for a high degree of on-line control. This is a most crucial criterion to be met in the treatment of complex substrates. As illustrated in this review, there are now several examples demonstrating the potential of laser cleaning methods in dealing with highly demanding problems in microelectronics and, in particular, in the restoration of painted artworks.

However, the diversity of the problems that have to be dealt with, as well as the sensitive dependence of laser processing characteristics on the nature and specific properties of the substrates, requires that laser processing parameters are carefully optimized. In particular, given the complexity of the

laser/organic materials interaction, a number of issues must be carefully addressed. Besides the apparent issues of efficiency and effectiveness, the most important one concerns the nature and extent of any deleterious effects that may be induced to the substrate. This is crucial for organic/polymeric substrates, since minor chemical or structural modifications may result in their accelerated aging/deterioration in the long run.

In the following, the methodologies that have been developed for dealing with the various cleaning problems of organic substrates, as well as the principles underlying them, are presented first. The major emphasis is placed on the effects that are induced in the polymeric substrates. Addressing this question, in fact, touches upon fundamental aspects of the laser/material interaction. Furthermore, the attempt to address these issues has revealed new possibilities for material processing and analytical applications. For the purposes of illustrating these aspects, examples are mainly drawn from the laser-based restoration of painted artworks. This application exemplifies directly most problems and issues encountered in laser cleaning and laser–organic material processing schemes. Information on other related cases are included at appropriate places.

2
Cleaning Methodologies

2.1
Removal of Polymer Coatings

By far the most typical laser cleaning scheme applied to polymeric systems concerns the removal of unwanted coatings from a substrate. In the simplest case, the problem concerns the removal of polymeric coatings from a metallic or other substrate [14–15]. Other cases may be much more complex, entailing stratified media of varying composition, as for example in the situa-

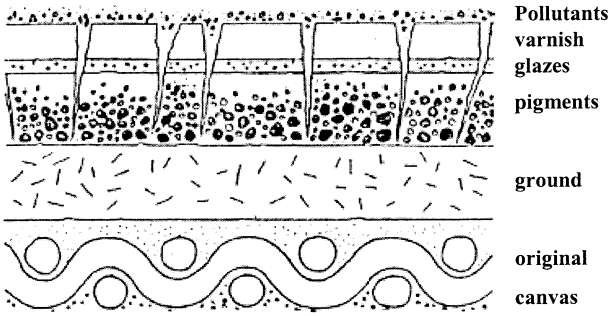

Fig. 1 Typical cross-sectional profile of a painting. In this case, the interest lies in removal of the indicated superficial pollutants or contaminations, as well as in the removal of the upper, degraded layers of the varnish, without affecting the highly sensitive pigments in the paint layer

tion of painted artworks. As indicated schematically in Fig. 1, a typical painting consists of several paint layers (each ≈20 to 50 μm thick) on a rather thick primer or ground layer that has been applied to the substrate (canvas, wood, etc.) [10–13]. On top of the paint (pigment) layer, varnish is applied (typically 50–80 μm thick) for aesthetic and protective purposes. Varnish is usually an ill-defined mixture of oligomers, deriving from a tetracyclic or pentacyclic organic compound with carbonyl or hydroxyl groups and, possibly, additional functional groups and/or double bonds in the side chains [10]. However, with time, it undergoes polymerization and photooxidation at its outer layers, with detrimental effects for the appearance and even for the integrity of the painting.

Removal of such coatings is based on ablation, i.e., the "macroscopic" material removal that is effected upon irradiation with intense laser pulses. Ablation has been reviewed in detail (e.g., [1–4]) so that only a brief outline of the phenomenon is given here. From a practical standpoint, the first aspect to consider concerns the efficiency and accuracy of material removal that can be attained with laser irradiation. This question is directly addressed by the examination of the so-called etching curves, which describe the dependence of the amount or of the depth of removed material (i.e., etching depth) on laser fluence, F_{LASER} (laser pulse energy per unit irradiated area) (Fig. 2a). The fluence at which the sharp increase in the etching depth is observed, or the F_{LASER} intercept of the extrapolation of the rising section of the curve, is considered to be the threshold for ablation (F_{thr}).

Various heuristic models have been developed for describing the features of the etching curves. The most usual one is the so-called blow-off model [1], based on the assumption that for an incident fluence, all material within a depth such as $F_{penetrated} \geq F_{thr}$ is removed. In this case, assuming Beer's law for the absorption process, the dependence of the etching depth on the incident laser fluence is given by:

$$\delta = \frac{1}{\alpha} \ln\left(\frac{F_{LASER}}{F_{thr}}\right) \quad \text{for} \quad F_{LASER} \geq F_{thr} \tag{1}$$

where α is the (effective) absorption coefficient. Strictly speaking, the formula holds for material ejection commencing after the end of the laser pulse. According to this model, what matters is the fluence that is absorbed at depth z, whereas the absorbed energy in the upper layers is essentially "wasted" (largely transformed into kinetic energy of the ejected material). On the other hand, it can be assumed that material removal occurs for a fixed absorbed energy density (per unit mass), once the threshold is exceeded. This assumption results in the so-called steady-state or stationary models [3, 6]. In this case:

$$\delta = \frac{F_{LASER} - F_{thr}}{\rho E_{cr}} \quad \text{for} \quad F_{LASER} \geq F_{thr} \tag{2}$$

where E_{cr} represents the required energy density (sometimes denoted as "ablation enthalpy" [6]) and ρ the density. The formula presumes that the rate

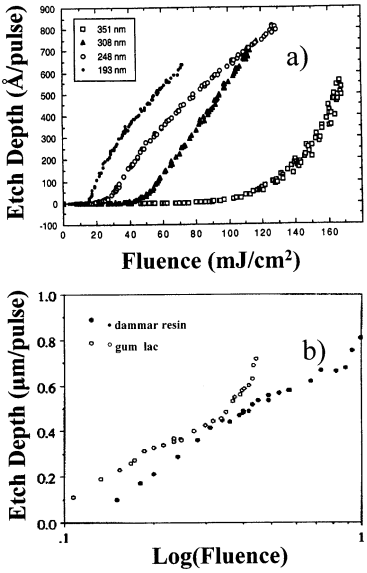

Fig. 2. a Etching curves typical of the ones determined in the UV ablation (ns pulses) of molecular systems (the particular ones concerning irradiation of polyimide at the indicated wavelengths: absorption coefficient α (193 nm)=4.25×10^5 cm^{-1}; α (248 nm)=3.1×10^5 cm^{-1}; α(308 nm)=10^5 cm^{-1}; α(351 nm)=0.32×10^5 cm^{-1}). The measurements rely on mass-loss measurements using a quartz crystal microbalance. Changes in the features of the curves depending on laser wavelength are clearly noted. Reprinted with permission from ref. [27]. **b** Etch rates for the ablation of dammar and gum lac aged varnish films with 248 nm irradiation

of energy deposition is balanced by the rate of energy removal due to material ejection. For this balance to be attained, a necessary condition is that material ejection starts early on during the laser pulse. Thus, strictly speaking, this model is applicable for μs or longer laser pulses. However, even for the ns laser pulses considered herein, a linear dependence on the incident laser fluence may be observed [3], though the interpretation may not be the one implicated by Eq. 2. At any rate, the values of the parameters in the above equations are usually chosen empirically, since in most cases they cannot be directly related to the known parameters of the materials. Furthermore, the exact shape of the curves may differ much according to the material and laser parameters, so that neither model describes satisfactorily the full etching curve. In addition, there may be other processes (in particular, absorption of the incident light by the ejected plume) that can result in similar dependences as the ones described above.

It has often been underlined [6, 26] that etching curves yield only limited physical insight into the underlying physical processes. In particular, it has proved to be very difficult to establish whether the full range of the curves represents a single process or if different sections are associated with physically distinct processes. Aside from its mechanistic implications, this issue is

Fig. 3. **a** An 18th century Flemish tempera painting on a wooden panel (size= 27×37 cm^2). Varnish in the painting had undergone extensive polymerization and was extremely hard. (a section that has been partially treated by laser is also evident). **b** The painting after laser processing and subsequent removal of any remaining loose varnish using a mild solvent. The varnish was removed by irradiation at 248 nm with ≈0.40 J/cm^2. LIBS was employed for monitoring the progress of the process

also most important for the optimization of laser processing schemes. Such examples are illustrated subsequently.

Despite any shortcomings, etching curves do provide a useful starting point. Based on Eq. 1, coating removal requires the use of wavelengths that are relatively strongly absorbed by the coating so as to achieve a good removal rate at moderate laser fluences (the importance of additional factors is considered later). Paint coating removal has been attempted [19–21, 28–32] by a variety of laser systems, the most notable being CO_2, Nd:YAG (1064 nm and its harmonics), excimer, and high-power diode lasers. However, the systematic comparison has been rather limited. Yet, excimer lasers have been the most popular, if not the most useful, since commercial paints and polymeric coatings generally absorb well in the UV.

For a specific example, in the case of painted artworks, varnish and its degradation products absorb strongly in the UV ($\alpha \approx 10^5$ cm^{-1} at 248 nm), thereby ensuring efficient and clean etching. Figure 2b illustrates etching rate curves (λ=248 nm) for model samples of oxidized varnish [17–18]. According to the determined ablation rates, contaminated surface layers of 20 to 300 μm thickness can be removed in a reasonable amount of time by excimer laser ablation with a resolution of 0.1 to 1 μm per pulse. Clearly, the accuracy of material removal by laser irradiation far surpasses that afforded by either mechanical or chemical techniques. Illustrative examples are depicted in Figs. 3 and 4. In the 18th century painting illustrated in Fig. 3, varnish had undergone extensive polymerization and was extremely hard for any conventional mechanical methods. The varnish has been removed by irradiation at 248 nm with ≈0.40 J/cm^2 (while laser-induced breakdown spec-

Fig. 4. a Image of a 17th century Byzantine icon. **b** The same icon after laser restoration with parameters comparable to those of Fig. 3

troscopy, LIBS, was used for the on-line monitoring of the process). Figure 3b illustrates the painting after laser processing and subsequent removal of any remaining loose varnish using a mild solvent. Figure 4 illustrates the processing of a painting that was in such a deteriorated condition that the use of even the "softest" mechanical or chemical means would result in its complete destruction. The painting has been restored via laser processing under similar conditions as in Fig. 3 with no apparent effect on its integrity. Cleaning of canvas, support material (wood, silk, etc.) has also been achieved [13, 16–17]. Besides KrF, an ArF laser (193 nm) has also been used for aged varnish removal with excellent results (i.e., very good surface morphology). However, because of the much higher absorptivity at 193 nm than at 248 nm [22–24], the etching depth is relatively low at 193 nm (note the inverse dependence of δ on α in Eq. 1). In combination with the relatively low output power of the ArF laser, this makes its use rather lengthy and expensive.

2.2 Selective Material Removal

In the previous examples, the etching depth is smaller than the film thickness that needs to be removed. Thus, the concept of layer-by-layer removal implied by Eq. 1 suffices for the purposes of the application. If, however, the impurity film is very thin (i.e., thickness comparable or smaller than the etching depth) or it consists of isolated pigments on the surface of the substrate, then a different approach has to be employed for effecting its removal without damage to the substrate. This objective may also be attained by laser irradiation, albeit only under certain conditions. The solution illustrates in the most direct way the need for a better understanding of the laser/organic substrate interaction.

At least for simple molecular systems, there is by now strong evidence that at low laser fluences, a thermal desorption/evaporation process operates, distinctly different from the unselective volume material ejection that is characteristic of ablation [34–35]. Specifically, both molecular dynamics simulations [34] and experimental work [35] strongly suggest that a fluence range can be delineated in which the ejection signals of compounds incorporated in a substrate correlate with their binding energy to the substrate (i.e., ejection signal proportional to $e^{-\frac{E_{binding}}{k_B T}}$). This fluence range differs distinctly from the ablative regime, which instead entails the massive (volume) ejection of material by other mechanisms (explosive boiling, stress-wave spallation, photochemical pressure generation etc.). In this latter case, ejection intensities cannot be correlated with specific binding energies. The extension of this delineation to more complex systems is far from established. Yet, at least for a number of different polymeric systems exhibiting so-called Arrhenius tails in the low-fluence portion of the etching rate vs fluence curves, this seems to be a valid statement [3, 33].

Within the previous delineation, impurities may be selectively removed via essentially a thermal evaporation process. In this case, for attaining a satisfactory removal rate, the fluence should be at least (under the assumption that the removal depth is equal to the penetration depth of light, α^{-1}) [36]:

$$F_{thr} = \rho\alpha^{-1}\Delta H_{sub}(1-R)^{-1} \tag{3}$$

For proper cleaning, the threshold for damage of substrate should be much higher than that of contaminants ($F_{s,thr}>F>F_{cont,thr}$). Assuming that heat conduction into the substrate can be neglected, the following condition must be satisfied (the second subscript, cont, refers to contaminants and the subscript, sub, to the substrate):

$$\frac{F_{cont,thr}}{F_{s,thr}} = \alpha_{sub}\Delta H_{sub,cont}(1-R_{sub})\rho_{cont}/(\alpha_{cont}\Delta H_{sub,sub}(1-R_{cont})\rho_{sub}) >> 1 \tag{4}$$

Therefore, for this approach to be effective, contaminants must have a higher absorption coefficient than the substrate and/or a much lower sublimation enthalpy. Alternatively, the substrate must exhibit a high reflectivity.

The efficiency of this approach has been examined [37] for parchments with carbonaceous contamination. For graphite, at λ=308 nm, R=0.35, $\alpha_{cont}\approx 2\times10^5$ cm^{-1}, $\Delta H_{sub,cont}=5.97\times10^4$ J g^{-1}. The experimentally determined threshold fluence for the contamination removal is found to be $F_{thr}\approx 0.4$ J cm^{-2}. On the other hand, for parchment, $\alpha_{sub}\leq 400$ cm^{-1}. Indeed, damage to the parchment is observed at much higher fluences (1.8 J cm^{-2} for 100 pulses). In agreement with Eq. 4, selective removal of dirt without any morphological changes of the parchment is demonstrated by irradiation with 308-nm laser light at 1.2 J/cm^2 [36]. However, since α_{sub} is nonnegligible, chemical alterations to the substrate may be induced. In fact, a ≈30% drop in the polymerization degree of cellulose is determined via size exclusion chromatography after a single shot at ≈1 J/cm^2 [37–38]. In contrast, di-

rect photon-induced photochemical modifications are not induced upon irradiation at 532 and 1064 nm of the low-absorptivity paper, silk, and cotton. However, natural cellulose materials containing colored components such as lignin do suffer degradation and yellowing even at 1064 nm. For this reason, recent work has focused on the exploitation of these wavelengths [38].

Irradiation at subthreshold fluences with pulsed laser irradiation has also been employed [39] for the removal of etch-induced polymer residues (indicated to be oxidized polytetrafluoroethylene derivatives) from underlying metallic films (e.g., Al-Cu film with TiN antireflective coating). Though the etch rate at these fluences is very low (<1 nm/pulse), the approach may still constitute a viable solution for cases where the polymer layer to be removed is quite thin (≈50 nm). In this case, again, absorption by the substrate may be the determining factor for the optimal laser processing parameters. Thus, though the 266 and 355 nm pulses of the Nd:YAG laser are found to result in a much greater etching rate than excimer laser pulses (248 nm), the metal film on the wafers is also more easily damaged as a result of the shorter pulse duration of the Nd:YAG laser (7 ns vs ≈25 ns for the excimer). Instead, the polymer residue is successfully removed by excimer laser irradiation at 248 nm at fluences well below the damage of the metal.

2.3 Particle Removal Techniques

In the last decade, there has been extensive work on the use of laser-based methods for the removal of submicron particles from silicon wafers. This work has been necessitated by the fact that for particles of this size, conventional cleaning techniques are highly ineffective. Particulates of this size adhere with relatively strong force, van der Waals force being the dominant one for submicron particles (whereas electrostatic force becomes important for $r_p \geq 20$–$25\ \mu m$) [3, 14]. For contact at a single point, the force is proportional to $Ar_p/8\pi z^2$ where z represents the separation between the particle and the surface, and A is a constant characteristic of the nature of particle/substrate material(s) (~0.5–1 eV for polymers). On the other hand, the cleaning force is proportional to the surface area (e.g., in gas/liquid jet spraying, the drag/cleaning force is proportional to the frontal surface area normal to the fluid flow [9]) or volume, and thus it decreases much faster than the adhesion force, which is proportional to the particle radius (i.e., the necessary acceleration for effecting ejection scales as r_p^{-2}) [3, 14]. As a result conventional removal techniques, such as ultrasonic or jet spraying, become ineffective for micron and submicron particles.

In contrast, laser irradiation has been shown to provide a potential solution to this problem. Laser-induced removal of the contaminants can be effected either via direct absorption of the laser light by the particles and/or the substrate ("dry laser cleaning") or via the prior application of a liquid film ("steam laser cleaning") [3]. The particle removal process can be evaluated either directly, by post-treatment optical or scanning electron microscopic examination of the sample, or indirectly via the scattering by the par-

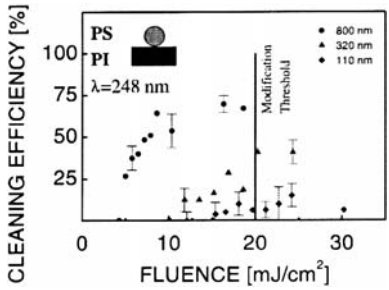

Fig. 5. a Experimental setup employed in the study of the laser cleaning of particles from surfaces. **b** Single-pulse cleaning efficiency of polystyrene particles from PMMA (λ=248 nm, τ_{pulse}=30 ns, relative humidity 28.4%, and average particle density $\approx 2\times10^5$ particles/cm^2) as a function of the incident laser fluence. The different symbols represent particles of different diameters

ticles of an incident probing laser beam. The direct and indirect methods have been compared by Mosbacher et al. [42] who showed that the intensity of the scattered light scales linearly with the density of the (scattering) particles on the surface. Thus, the use of the optical/scattering method is preferred, since it offers the additional advantages of direct online monitoring and high temporal resolution. A differential optical transmission technique has recently [46] been described for monitoring with very high sensitivity ($1/10^4$ transmission changes detected) particle removal from transparent polymer substrates.

The work on the laser-induced removal of particles from silicon wafers has recently been extended to polymer substrates. When both the particles and the substrate are transparent to the irradiation wavelength, e.g., irradiation of SiO_2 particles on PMMA at 248 nm, no cleaning is effected. In contrast, efficient cleaning is demonstrated for laser wavelengths that are absorbed either by the polymeric substrate or by the particulates. For instance, debris produced in the CO_2 laser (9.3 μm) via drilling of polyimide (PI) has been removed by subsequent irradiation at a much lower fluence (0.7 J/cm^2) [41]. The soot (<500 nm diameter) is removed with a much higher efficiency than the $\approx$5 μm fibrous debris (in five pulses vs ~50 pulses). It appears that the debris constituents are removed by different mechanisms [41]. SiO_2 particles of 400 and 800 nm, as well as PS particles with diameters down to 110 nm, can be removed from PI and PMMA upon irradiation at 193 and 248 nm [43]. The use of shorter laser pulses (30-ps pulses at 292 nm) for the removal of particles from polymeric substrates has also been examined with promising results [46].

The cleaning efficiency, defined as $(1-n/n_0)$ where n_0 and n represent respectively the density of the particles on the surface before and after irradiation, depends strongly on the incident laser fluence (Fig. 5). Most importantly, high cleaning efficiencies can be attained at fluences well below the damage threshold of the substrate. For instance, for SiO_2 particles on PMMA and PS, single-pulse efficiencies of even up to 69% are attained by irradia-

tion with 17.7 mJ/cm^2 at 248 nm. By contrast, surface modification of the PS substrate is observed at 22.5 mJ/cm^2 [43]. Similarly, PS particles on PMMA are removed with 80% efficiency by irradiation at fluences in the range 160–200 mJ/cm^2 (the upper value representing the surface damage of the substrate). However, the single-pulse efficiencies decrease strongly with particle size and they are only about 10% for the smallest examined (110 nm) particles [43]. Understandably, the range of fluences between the cleaning threshold and surface modification of the polymer substrate is narrower than that in the case of silicon wafers. Thus, considerably more caution has to be exercised in the use of the laser-based technique for the former. The dependence of the cleaning efficiency on the number of laser shots can be approximated as

$$\eta_c(N_{pulse}) \approx 1 - (1 - \eta_c)^{Npulse} \tag{5}$$

where η_c represents the cleaning efficiency for a single pulse. Thus, applying typically 10–20 pulses, efficiencies from 10–50% up to 40–90% are observed, until finally they saturate with a higher number of pulses. Equation 5 assumes that the probability of a particle to be removed is independent of the previously employed number of laser pulses. Furthermore, the particles are assumed to be identical and characterized by the same η. In practice, deviations from this simple law are usually observed and may be ascribed to the different cleaning threshold fluences for particles of different sizes, to the surface roughness of the substrate, etc.

The mechanisms of particle removal have been studied in detail in the case of silicon wafers [3, 44]. At present, particle removal from polymers has been analyzed along similar lines. The different cleaning mechanisms that seem to be relevant include:

- Direct ablation of the particles.
- Particle expansion. This is effective for strongly absorbing particles on transparent substrates.
- Evaporation of particles. This is essentially the same as described by Eq. 4 (with particle absorption cross-section being $\sigma_p \sim r_p^2$ for $r_p >> \lambda$ and $\sigma_P \sim r_p^3/\lambda$ for $r \leq \lambda$). Therefore, such a mechanism can be important for very small particles with low vaporization enthalpy.
- Rapid thermal expansion of absorbing substrate. This favors removal of larger particles. In fact, this is usually the most effective particle removal approach and thus it is treated in some detail.

Upon light absorption, the absorbing substrate expands (estimated surface acceleration of $\approx 10^8$ m/s^2 [47]), thus resulting in the particles gaining kinetic energy [45–47]:

$$E_{KIN} \approx mu^2 \approx \rho_p r_p^3 \left(\frac{\beta \alpha_s F_{LASER}}{\rho_s c_{p,s} \tau_{pulse}} \right)^2 \tag{6}$$

where the subscript s denotes substrate and p denotes particle. For cleaning to be attained, this energy must exceed the adhesion energy. Generally, the adhesion energy scales with the particle radius as $E_{ad} \approx \delta_n r_p^n$, where $1 \leq n \leq 2$ and δ_n is some proportionality coefficient. For example, n=1 corresponds to electrostatic double-layer adhesion and/or to Van der Waals (VdW) adhesion for a point contact. For capillary forces, $E_{ad} \sim \sigma_{tens} r_p^2$ where σ_{tens} is the surface tension coefficient. Thus, the condition $E_{KIN} > E_{ad}$ results in

$$\frac{\beta \alpha_s F_{LASER}}{\rho_s c_{p,s} \tau_{pulse}} \left(\frac{\rho_p r_p^{3-n}}{\delta_n} \right)^{1/2} > 1 \quad \text{or} \quad F_{LASER} \geqslant \frac{\rho_s c_{p,s} \tau_{pulse}}{\beta_s a_s} \left(\frac{\delta_n}{\rho_p} \right)^{1/2} \frac{1}{r_p^k} \tag{7}$$

where $1/2 < k \equiv (3-n)/2 < 1$. Accordingly, the cleaning threshold is predicted to increase with decreasing particle size, in good agreement with the experimental results (Fig. 5b).

Despite the indicated good agreement, the previous theoretical treatment is simplified. In fact, even for the simpler case of particles on silicon wafers, there have been a number of difficulties in the theoretical description of the process. For instance, depending on the parameters (e.g., pulse duration), the force balance may be more relevant than the energetic consideration. Changes in the shape of the particle due to the compression are also not considered in the previous analysis. Furthermore, a most important effect of the procedure has turned out to be the local field enhancement under the particles [45], which may lead to the local ablation of the substrate. This effect can be taken advantage of for the submicron structuring of polymeric substrates, but evidently it introduces a serious limitation of the dry laser cleaning schemes. Besides these problems, for polymeric substrates and particles, additional issues become important (e.g., photochemical modifications), but these have not been addressed in the literature.

For particle removal from wafers, considerable attention has been given to the liquid-mediated process ("steam laser cleaning") because of the high cleaning efficiencies obtained [3]. Typically, a wavelength that is strongly absorbed by the substrate is employed and liquid films a few tenths to several μm thick (consisting of water mixed with 10 to 20% alcohol) that are transparent at the incident laser wavelength are applied on the substrate. For sufficient deposited energy, the heat conduction ($2\sqrt{Dt}$) from the absorbing substrate results in the vaporization of the adjacent liquid [44, 49]. The high-amplitude pressure wave that is generated by the fast-growing bubbles results in large enough accelerations (10^8 to 10^9 m/s^2) of the particles to effect their detachment and their subsequent ejection by the induced high-speed jet stream. A wide range of different particulates, such as Au, Mo, and Si, are efficiently cleaned off wafers and membranes with KrF excimer laser radiation [3].

Because the exerted forces are about ten times higher than those developed by the thermal expansion of the substrate, laser steam cleaning efficiencies are much higher than those in dry cleaning. This permits the use of lower laser fluences, which is particularly important for heat-sensitive sub-

strates or particles that can melt. Furthermore, in contrast to dry laser cleaning, the cleaning efficiency is largely independent of the particle size [42], thereby permitting efficient cleaning even of collections of particles with a wide size distribution. For these reasons, it has been considered for polymer substrates. For instance, debris removal from polymer surfaces has been demonstrated using KrF laser radiation with transparent isopropanol films [50]. Organic coatings can also be removed from a variety of substrates, including painted artworks. In this case, however, the use of liquid on the highly sensitive organic/painted surfaces may have deleterious side effects and we have advocated the potential of the dry cleaning process instead.

3
Experimental Setups and Procedures

There are well-established designs from other (industrial) applications of lasers that can be directly adapted for the purposes of dry laser cleaning schemes (e.g., laser particle removal, laser restoration of painted artworks). The employed workstations generally comprise a substrate mounting stage, suitable optics for laser beam delivery and focusing, and diagnostic modules for the on-line monitoring and control of the cleaning process. The mounting stage can be a computer-controlled x-y-z mechanical translator or, alternatively, appropriate optical fiber or motorized "optical arms" can be employed for the accurate scanning of the laser beam over the substrate. On the other hand, experimental setups for steam laser cleaning are somewhat more involved. A laser cleaning setup specifically designed for industrial use is schematically shown in Fig. 6 and is described in further detail in [51]. Cleaning rates of up to 200 cm^2/min (for silicon wafers) are reported for this system.

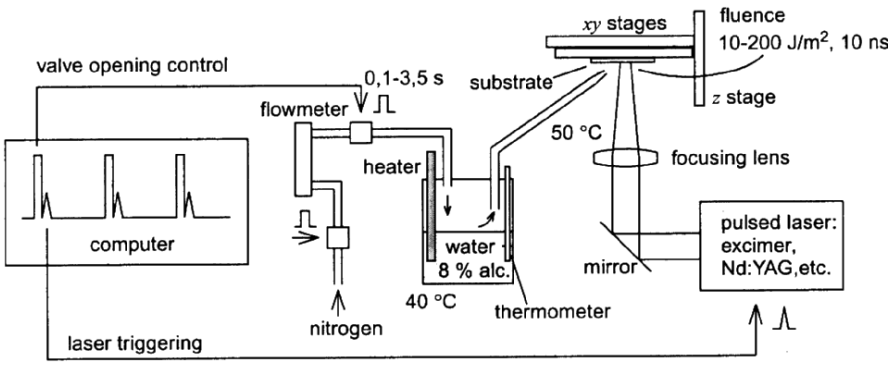

Fig. 6 Schematic diagram of a typical apparatus developed for industrial use of steam laser cleaning. The wafer is kept face down in order to avoid resettlement of the removed particles. Alcohol is commonly added to the water for improving wetting of the surface

Laser processing parameters (i.e., wavelength, fluence, repetition rate, pulse overlap) are defined according to the criteria and the studies described above. For more complex substrates (e.g. artworks), however, since there is a high variability in the nature of the substrates, the optimal laser parameters are best defined through a preliminary study of a representative sample of the object. Generally, the optimal fluences for cleaning paintings are in the range 200–600 mJ/cm^2, while the removal of overpaintings requires ≈2–3 times higher fluences. Furthermore, it is important that the pigment medium itself is not exposed to the laser irradiation. To this end, a thin layer of varnish is always left intact on the pigment medium. This layer (usually 5–10 μm thick) acts as a filter, preventing light from reaching the pigments and binding media.

In some applications, it is sufficient to define an operational range of laser parameters for attaining a successful treatment. This assumes invariability in the nature of the substrate and of the material to be removed. However, in more demanding applications, laser processing parameters may have to be appropriately adjusted during the procedure. Therefore, it is important to implement techniques for the in situ monitoring of the procedure, thereby enabling on-line control and safeguarding against damage. Monitoring can, in principle, be achieved by a variety of optical and laser-based spectroscopic techniques that have been developed previously in the framework of industrial, environmental or medical applications. For instance, in the case of particle removal, one of the reasons for developing optical scattering methods as a monitoring tool is that such methods are easily compatible with commercial systems employed extensively in industry for surface inspection. In the laser restoration of painted artworks, two techniques have proven most effective to this end, namely broadband reflectance spectroscopy and/or imaging and laser-induced breakdown spectroscopy (LIBS). These techniques are briefly discussed herein and in further detail elsewhere [16, 52–56].

Structural information about the painting can be derived from broadband reflectography [52]. This technique relies on the fact that the optical penetration depth differs greatly in the various spectral regions (e.g., varnish absorbs strongly in the UV–$\alpha \approx 10^5$ cm^{-1}, while it is practically transparent in the 760−2500 nm range). Thus, the specularly reflected or backscattered light in the corresponding spectral regions provides information about different layers of the substrate. In particular, the UV absorptivity of varnish increases strongly upon degradation/oxidation [23–24], and it is characterized by a much lower reflectivity than nondegraded/“clean” varnish. Thus, reflectography provides a powerful tool for optimizing the laser cleaning process (in fact, for any employed restoration method) by detecting the fresh layers that are exposed as dirt and debrisare removed (Fig. 7). Furthermore, multispectral imaging techniques can be used for mapping the composition and coloration of a painted artwork. To this end a specialized, single unit, multifunctional detection system appropriate for spectral imaging in the region of 0.35 to 1.6 μm has been developed [52].

Fig. 7 Image (*top*) and UV reflectography (*bottom*) of a laser-cleaned area on an 18th century oil painting. In the reflectance spectrum, the dark area represents the initial varnish in which the various photodegradation products absorb strongly the incident light (365 nm), whereas the laser-uncovered, "fresh" varnish is clearly characterized by higher UV reflectivity

On the other hand, direct analytical information can be obtained through the analysis of the emission spectrum radiated by the plasma (i.e., partially ionized material vapor) produced during ablation (LIBS). The spectrally and temporally resolved detection of atomic or small fragment emissions yields information about the elemental composition of the ablated volume [53–54]. The independence of the process from charging effects (thus, from substrate conductivity) in combination with the high sensitivity for pigment constituents makes LIBS a powerful tool for monitoring laser restoration of painted artworks. In the cleaning of varnish from realistic samples, the recorded spectra are found to be mainly due to excited dimers (neutral, ionic or radicals) that are produced abundantly during excimer laser ablation [18]. In particular, the spectra may exhibit strong bands ascribable to CO, which derives from the carbonyl and peroxo species/derivatives that are formed in the superficial layers of the varnish as a result of natural photooxidation [18]. In the removal of overpaintings, the spectra are dominated by the emission lines of the metal constituent(s) of the accumulated salts or of the paints (pigments) employed in the overpainting [18]. In either case, since the degree of photooxidation of the varnish and/or the extent of pollutant accumulation varies with increasing depth from the surface, analysis of the plasma emission enables monitoring of the laser cleaning progress on a

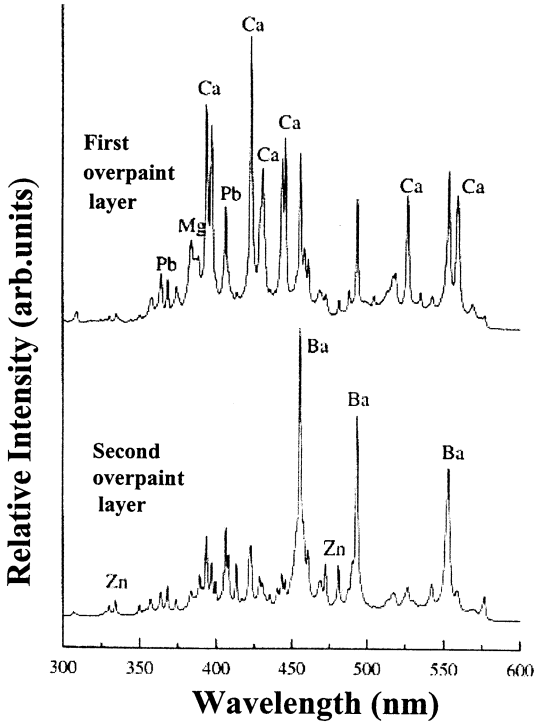

Fig. 8 LIBS spectra recorded with successive KrF pulses in the removal of an overpainting from a representative sample of a wall plaster, illustrating the changes observed in the detected elements for successive overpaint layers

pulse to pulse basis. An illustrative example of the variation observed in the LIBS spectra with successive laser pulses is shown in Fig. 8. LIBS has also been shown to be useful for monitoring laser cleaning of parchments [36].

Though outside the scope of this review, it is important to note that there is also great interest in the potential of adapting laser-based analytical techniques to art diagnostics. Several of the existing optical and laser spectroscopic techniques present significant advantages over the traditional analytical methods employed in the art conservation field, in particular as far as sensitivity, nondestructiveness, in situ capabilities, and ease of applicability are concerned. Thus, Raman spectroscopy has already found use in the characterization of pigments [55–56], while fluorescence is indicated [53–54] to hold significant merit for the identification of overpaintings etc. (Fig. 9). LIBS enables [53] virtually nondestructive elemental in-depth profiling of artworks. Figure 9 presents a case where the combined use of LIBS and laser-induced fluorescence (LIF) has been applied to the characterization of a painting and has established the presence of a secondary "retouching" of the original painting. The LIF spectrum (illustrated in the detail image) obtained under UV illumination reveals the presence of a painted area demon-

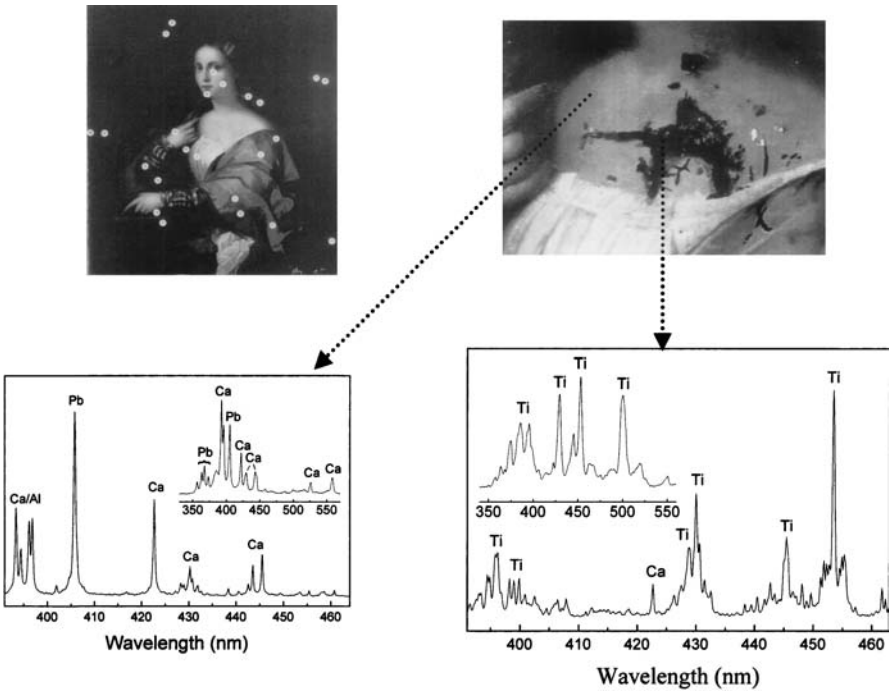

Fig. 9 Example of the combined use of LIBS and LIF for the examination of an oil painting (copy of Palma Vecchio's "La Bella"). The detail image demonstrating the retouching of part of the painting has been obtained under UV illumination. The LIBS spectra demonstrate that the original painting is rich in lead and calcium pigments, whereas titanium white has been mainly employed in the retouched area

strating where the retouching of part of the painting has been. The LIBS spectra demonstrate that in this section, titanium white has been mainly employed, which is not detected in the rest of the painting where instead, lead and calcium pigments have been used. Based on these chemical differences, the delineated area represents a restoration attempt of a much more recent vintage than the original painting. Such a combination of techniques can be directly implemented for laser cleaning purposes as well. Finally, the implementation of tunable lasers (i.e., optical parametric techniques) can enhance considerably the capabilities of IR reflectography for the layer-by-layer imaging and mapping of paintings. Other novel laser applications, such as the microetching of holograms for authentication and security purposes, have also been demonstrated [58].

4
Assessment of the Laser-Induced Effects

Besides the issue of efficiency, the most important consideration in the adoption of any cleaning technique concerns the nature and extent of side effects that may be induced in the substrate. In considering this issue, the subsequent discussion focuses on the side effects of coating removal via ablation, since this case has been examined in great detail and best illustrates the many fundamental questions that are involved in laser cleaning applications.

The interaction of intense laser pulses with molecular materials is, in general, quite complex. It is customary to delineate the induced processes in three types, namely thermal, photochemical, and photomechanical. Though this "formalistic" division provides a convenient basis for the discussion of the mechanisms and effects of UV ablation of polymers, the three phenomena are certainly closely interrelated. The inadequacies of this division will be most clearly illustrated in the examination of the chemical effects. The present review addresses all three types of side effects, but the major emphasis concentrates on the photochemical phenomena.

4.1
Photoexcitation Processes

The nature of the initial electronic excitation and subsequent deactivation step(s) is of direct relevance to the elucidation of the underlying processes of the laser cleaning procedure. In particular, the depth of affected material depends on the nature of radiation transport (propagation) during the laser pulse. This may deviate significantly from the simple Beer's law. Depending on the specific properties of the electronically excited states, saturation or multiphoton processes may dominate. In the former case, a larger portion of the incident light penetrates deeper into the material, thereby plausibly enhancing the etching process, but also the extent of photochemical modifications induced in the substrate. On the other hand, multiphoton processes (as well as plume attenuation) serve to limit light propagation into the substrate. Pettit et al. [60] have presented detailed modeling of the influence of multiphoton excitation and of chromophore saturation processes on the efficiency of material removal. Lazare et al. [59] considered the implications of the incident laser light absorption by the plume.

Systematic studies on the nature/dynamics of the excitation processes in the UV ablation of polymers have been reported by Masuhara and co-workers [61–63]. To this end, they have relied on the use of dopants dispersed within polymers. Given the relevance of their approach to the topic of the present article, their work will be presented in some detail. Time-resolved absorption and luminescence spectroscopies have been used to probe the dynamics of electronic excitation and deexcitation of the dopants. In the irradiation of fluorescing dopants (biphenyl or phenanthrene), the total emis-

sion intensity as a function of laser fluence saturates close to the ablation threshold, indicating that a new deactivation channel of the assessed S_1 state opens up. In particular, for some of the employed chromophores, the internal conversion from the excited S_1 state is noted to have a very low quantum yield to account for the heat generation necessary for the polymer decomposition and material ejection [63]. Furthermore, in the irradiation of these systems, the time-resolved absorbance is found to increase during the excitation pulse. A plausible explanation was advanced on the basis of a "cyclic multiphotonic absorption process". According to this, the absorbing dopants and/or the radicals produced by their photolysis absorb further photons to electronic states higher than S_1. Alternatively, higher electronic states may be formed via annihilation of the S_1 excited molecules. Deactivation of these states occurs extremely fast (~ ps) and provides a way for the rapid conversion of the absorbed energy into heat. Following deactivation, the recovered $A^*(S_1)$ can participate in subsequent excitation/deexcitation cycles (Scheme1). Excited triplet states, detected in temporally resolved absorption measurements, may also participate in the indicated cyclic process.

$$A + h\nu \rightarrow A^*(S_1)$$

$$A^*(S_1) + h\nu \rightarrow A^*(S_n) \rightarrow A^*(S_1) + heat$$
$$A^*(S_1) + A^*(S_1) \rightarrow A^*(S_n) \rightarrow A^*(S_1) + heat$$

Scheme 1 Cyclic multiphotonic scheme

Interestingly, variations of this cyclic multiphotonic scheme have been independently advanced in the study of the UV ablation of cryogenic films [65] as well as in the matrix-assisted laser desorption/ionization (MALDI) of biomolecules [66]. The reason for giving these results is to illustrate the emergence of common concepts/processes concerning UV ablation of molecular substrates.

Concerning applications, the important implication of the above studies is that the optical penetration depth, and thus the extent of damage, may be significantly reduced from that expected on the basis of the small signal absorption coefficient of the substrate. Unfortunately, thus far, there is no sufficiently established model to predict the relative importance of such processes for different polymers. In fact, even for the same system, dynamic changes of the absorption coefficient may differ significantly according to the employed wavelength [64]. Thus, the extent of the contribution must be evaluated experimentally in each individual case.

4.2 Thermal Effects

Following light absorption, given that deexcitation in condensed phases is very fast (ps for the rotovibrational states and usually ns for electronic

states), a good percentage of the absorbed energy–at least, for irradiation with typical nanosecond pulses–is expected to decay into thermal energy. Thus, thermal side effects are of major concern in the optimization of applications, since the processed substrates (e.g., painted artworks, parchment) tend to be thermally sensitive.

To a good approximation, the heat effects can be assessed by consideration of the diffusivity. However, understanding of the chemical processes calls for a detailed understanding of the temporal evolution of heat dissipation. To this end, a brief presentation of analytical approaches is useful in discussing ns ablation. Analytical approaches rely on the consideration of the heat conduction coupled with the thermal decomposition of the material (photofragmentation neglected). Usually, the enthalpy formulation of the heat equation is employed because of its convenience in dealing with phase changes including melting [3, 26]. Written in the frame of reference of the receding surface (assumed to be along the z-direction), this becomes:

$$\frac{\partial H}{\partial t} - \upsilon \frac{\partial H}{\partial z} = \frac{\partial}{\partial z}\left(\mathrm{k}\frac{\partial \mathrm{T}}{\partial z}\right) - \frac{\partial (\mathrm{I}e^{-\alpha z})}{\partial z}, H(\mathrm{T}) = \rho \int_{\mathrm{T0}}^{\mathrm{T}} \mathrm{C}(\mathrm{T}')d\mathrm{T}' \tag{8}$$

with the main boundary condition concerning the energy loss at the surface due to material removal, $\mathrm{k}\frac{\partial \mathrm{T}}{\partial z}\big|_{z=0} = \mathrm{D}\frac{\partial H}{\partial z}\big|_{z=0} = \upsilon_{\mathrm{int}}\left(\Delta H_{vap} - H_{\mathrm{s}} + H^{V}(\mathrm{T_s})\right)$. Here, υ_{int} represents the rate of material removal, and the term in the brackets the enthalpy difference between the vapor and the condensed phase (evaluated at the surface temperature $\mathrm{T_s}$). H_{s}, the enthalpy of the substrate at the interface, and $H^{V}{}_{\mathrm{s}}$, the vapor enthalpy–$H_{\mathrm{s}}^{\nu} = \rho \int_{\mathrm{To}}^{\mathrm{Ts}} c_P^{(\nu)}(\mathrm{T}')d\mathrm{T}'$–(all expressed per unit volume). Generally, this is a very difficult problem to treat analytically [26]. A fully satisfactory solution has been obtained only for ablation with long pulses, in which case a "stationary" condition is attained (i.e., rate of material removal during the laser pulse being constant, Eq. 2). However, this condition is hardly reached in the irradiation with ns pulses. The approximations necessary for solving the equation for the "nonstationary case" have been discussed amply in the literature [3, 26, 33].

Depending on the employed boundary condition, a distinction is made between the so-called surface and volume models. The difference between them is schematically illustrated in Fig. 10. In the surface model(s), the position of the receding interface is specified by the attainment of a specific temperature, whereas in the volume models, the interface is specified by the condition that the surface concentration of broken bonds reaches a specific/critical value. Bonds are assumed to be broken thermally via simple unimolecular reaction.

Thus, the extent of thermal decomposition up to time t is given by a time-integrated Arrhenius equation $\int_0^{\mathrm{t}} A \exp(-E_a/\mathrm{RT}(\mathrm{t}'))d\mathrm{t}'$ (where A and E_a are the corresponding preexponential factor and activation energy). This volume model succeeds in explaining various experimental results, in particu-

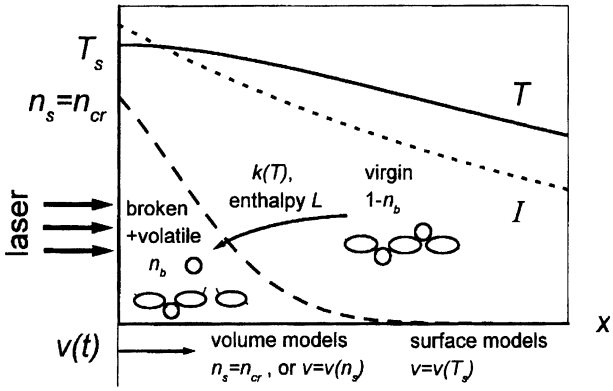

Fig. 10 Schematic of the laser intensity (I), temperature (T) distribution within the material. Thermal bond breaking (of the polymer) with the rate constant k(T) takes place within this volume, producing a distribution of broken bonds and plausibly of volatile species within the polymer matrix. The figure also illustrates the difference between the volume and surface models advanced for the theoretical description of ablation of polymers. The *subscript s* denotes the receding surface

lar that polymer ablation is observed above a well-defined fluence (threshold), and mass loss may nevertheless be observed at lower fluences. Yet the model does not take into account that reaction constants may be significantly affected by any changes in the physical state of the substrate. The importance of this factor is experimentally indicated later.

Neglecting the complexities of the issue, at least for high enough fluences, ablation can be considered to commence early during the laser pulse and to proceed at a constant interface velocity υ_{int}. In this case, minimization of heat effects can be attained if D/υ_{int} is small compared to α^{-1}. Typically, D for polymers and amorphous organic materials is $\approx 10^{-3}$ cm^2/s [1, 3]. Thus, the thermal diffusion length for typical ns pulses is estimated to be $\approx$100 nm, i.e., smaller or at most comparable to the typical optical penetration depth of polymers in the UV. Thus, the extent of "damage" is mainly specified by the substrate absorptivity at the irradiation wavelength. For instance, in the case of painted artworks, optical microscopic examination demonstrates "clean" etching for ablation at 248 nm, a strongly absorbed wavelength ($\alpha \sim 10^5$ cm^{-1}). In contrast, irradiation at 308 nm results in pronounced collateral damage and/or morphological changes. This difference is consistent with the lower absorption coefficient of varnish at 308 nm compared with that at 248 nm (at 308 nm, $\alpha \sim 10^2$ cm^{-1}) [22–24] resulting in absorption and destruction in the bulk. (The previous argument neglects the possibility that at 248 nm, two-photon or even higher order absorption processes are expected to be highly probable, thereby resulting in photochemical decompositions with further minimization of the energy dissipation to the surrounding medium.)

In contrast to the previous case, there are examples where thermal conduction clearly limits the efficiency of laser removal techniques. For in-

stance, in the irradiation of contaminated parchments, the separation between the absorbing units (impurities) and the substrate is comparable to the thermal diffusion length. Thus, IR irradiation of "neat" (uncolored) parchments does not result in any detectable chemical modifications. In contrast, in the presence of absorbing impurities, H_2O loss and ether cross-linking (resulting in an increase of the cellulose polymerization degree) are observed [37–38] as a result of the heat conducted from the absorbing units. Furthermore, for multicomponent systems with constituents of different binding energies to the matrix, segregation within the heat-affected zone may be significant, with deleterious effects [3–17] for the appearance or even the integrity of the substrate.

4.3 Photochemical Effects

Certainly, the most crucial question in laser processing of organic substrates (e.g., in laser restoration of painted artworks or in the pulsed laser ablation of tissues) concerns the nature and extent of chemical modifications to the substrate. The processed molecular substrates (polymers, tissues, etc.) generally include a wide variety of chromophores which, upon UV excitation, may dissociate into highly reactive fragments. Additional species may be formed by the thermal or stress-induced breakage of weak bonds. These species may form, in the short or long term, by-products (e.g., oxidation products) with detrimental effects for the integrity of the substrate. Thus, minimization of their accumulation in the substrate is crucial for the optimization of the laser applications.

The issue of chemical processes in the ablation of molecular substrates is also closely related to the question of the mechanism(s) of the phenomenon, since photochemical processes have been suggested to contribute to, or even dominate, the material ejection in the irradiation of photolabile systems [1, 4]. According to this "photochemical" model, the formation of a high number of photofragments of high translational energies and/or the formation of gaseous photoproducts that exert a high pressure may result in material ejection. This possibility was advanced in the first studies [1] in order to account for the observed "clean" etching effected with UV laser pulses as compared with the use of IR pulses. However, despite its importance, this issue has turned out very difficult to establish. In fact, the issue of photochemical vs thermal mechanisms has been the most hotly debated one in the field of ablation. Only for a few specifically designed polymers has the contribution of a photochemical mechanism presented well-defined evidence in its favor [4, 68–70]. Recently, molecular dynamics simulations [71] on the ablation of condensed molecular systems [35] have provided detailed information about the ways in which chemical processes may affect material ejection.

Aside from its importance for material ejection, the description of (photo)chemical processes and effects in the UV ablation of organic/polymer substrates has a wider scientific interest. Conventional photochemistry considers bond breaking and formation in a well-defined environment under

well-defined conditions. In contrast, UV ablation of polymers entails the parallel formation of a high number of electronically excited states, development of high temperatures, and generation of high-amplitude stress waves. All these occur within a time-varying framework. As a result of the combined influence of these factors, photophysical/chemical processes may deviate greatly from those described by conventional photochemistry. The importance of coupling of thermal and photochemical processes has been indicated in the irradiation of polymers doped with photolabile dopants [77–78]. Thus, the real challenge is the development of appropriate models with predictive power for describing chemical processes under the above conditions.

One of the major problems hindering investigation and elucidation of the chemical processes in the UV ablation of polymers derives from the chemical complexity of the substrates themselves. It is generally very difficult to identify and quantify the wide range of fragments and products that can form upon irradiation of the polymers with intense laser pulses. For the purpose of the systematic comparison of the induced chemical modifications with the ones observed at low laser fluences, our approach [83–88] relies on the use of simple, photosensitive organic compounds such as halonaphthalenes, dispersed within polymer films (dopants). The simplicity of the fragmentation/reactivity pattern of these compounds enables the systematic characterization of the induced modifications as a function of laser fluence. Furthermore, the doped systems constitute a good, even if idealized, model of the paint layer in artworks, which essentially consists of chromophores dissolved or dispersed within an organic medium [23–24].

Chemical processes and effects in the ablation of neat and doped polymers have been recently reviewed [4] in a comprehensive way. Studies on doped polymer systems have been specifically reviewed in [72]. This review has also underlined issues that must be carefully considered in the ablation of doped systems. In particular, it is noted that the incorporation of the dopants may affect various physical properties of the polymer, thereby affecting indirectly the induced processes. Only specific studies of direct relevance to the present purposes are discussed herein.

Masuhara and coworkers have studied [74] the decomposition of 5-diazo Meldrum's acid in the 248-nm ablation of PMMA films doped with this compound. The photodecomposition yield was determined to be somewhat smaller than unity. The major percentage of the ketene product of the dopant decomposition was detected during the laser pulse, with a minor percentage at later times (formed presumably through thermal decomposition). It was shown that, despite the high photodecomposition quantum yield of the precursor, ablation is governed by the amount of absorbed energy. This energy deposition was indicated to proceed via repeated photon absorption (cyclic multiphotonic excitation) by the ketene photoproduct. Lippert and Stoutland examined [75] the decomposition of the diazo Meldrum's acid within PMMA films during irradiation with 266-nm, 60-ps pulses. By using picosecond infrared spectroscopy, the intensity of the ketoketene intermediate was followed with ns time resolution both below and above the threshold. No significant change was found in the signal intensity over the exam-

ined fluence range, consistent with a one-photon process and a near unity quantum yield of decomposition. Finally, time-resolved absorption spectroscopy was employed [76] to follow the decomposition of the 1,1,3,5-tetraphenylacetone (TPA) dopant within a PMMA matrix upon excitation at 266 nm with nanosecond pulses. TPA was found to decompose into two diphenylmethyl radicals and CO. The first diphenylmethyl radical was shown to form within the nanosecond laser pulse, undergoing subsequently a rapid decarbonylation to give the second radical. At low fluences, the diphenylmethyl radical concentration grew linearly with fluence, while at higher fluences, excited radicals were also observed, suggested to form via a two-photon excitation process.

The previous studies seem to indicate that no significant change in the photoproduct formation/patterns occurs in the ablative regime. However, the employed dopants dissociate to stable compounds (CO or N_2). Their decomposition quantum yield is quite high, with a value close to unity. These features may account for the lack of any significant change as the fluence is raised above the threshold. Furthermore, the studies focused on the initial stages of the process ($\tau_{probing}$<30 ns). However, material ejection and its thermal influence on the substrate are known to last for much longer (μs to ms) [1–6]. Most reactions also take place on this longer time scale. Thus, it is conceivable that, though the initial photoexcitation/dissociation steps (depending on the nature of the dopant) do not differ much in the ablative vs subablative regime, considerable deviations may appear in the subsequent dopant reactivity.

This possibility is indicated in the study of the ablation of PMMA and PS doped with haloaromatic compounds (iodonaphthalene (NapI), iodophenanthrene (PhenI)). Experimentally these dopants offer the advantage that they exhibit negligible fluorescence, whereas their products are moderate or strong emitters. Thus, product formation can be conveniently monitored via laser-induced fluorescence (LIF). It is noted that the study has focused on the characterization of the species/products that remain in the substrate upon ablation. Thus, the experiment is of the "pump-probe" type, in which pump pulses at a particular wavelength (λ=308, 248 or 193 nm) are used to irradiate the films, and laser pulses of very low fluence are employed to induce photoproduct fluorescence ($F_{LASER} \leq 3$ mJ cm^{-2}, probing effected always at λ=248 nm). Detailed information on the experimental setup and procedures is provided elsewhere [83–85].

Figure 11 shows a LIF probe spectrum recorded from NapI/PMMA (1.2 wt%) samples after irradiation with a single "pump" pulse at 248 nm at fluences below and above the ablation threshold (~500 mJ cm^{-2}, as established by profilometric measurements). In recording these spectra, a relatively long delay ($\geq$1 min) between the pump and probe pulses is employed for ensuring quantitative reaction of the photoinduced radicals and formation of stable photoproducts. Since the iodo precursors and purified PMMA are characterized by negligible fluorescence, the observed spectra are due to emitting photoproducts formed by the fragments of the haloaromatic pho-

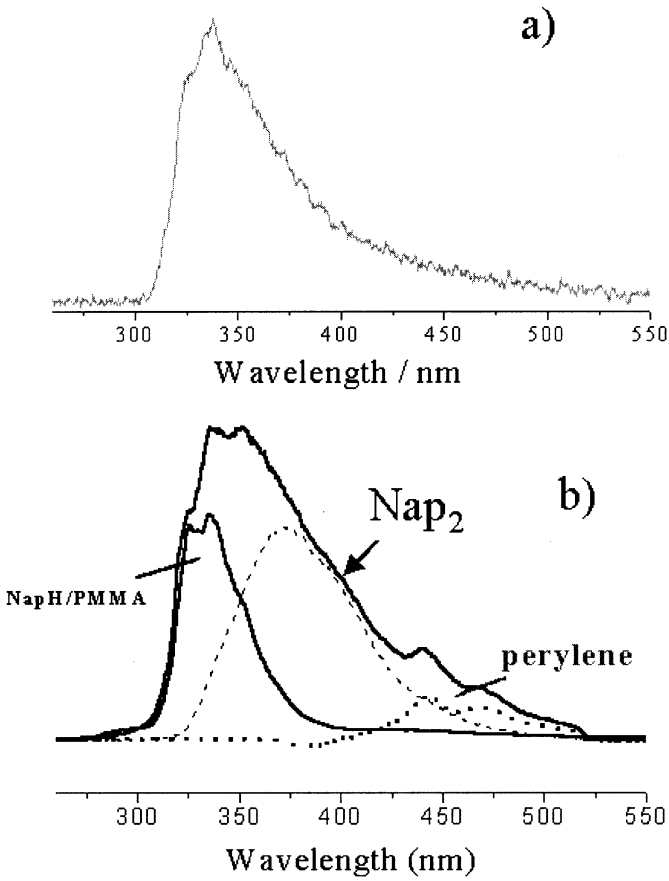

Fig. 11 Laser-induced fluorescence spectra recorded from NapI-doped PMMA samples (1.2 wt%) after their irradiation with a single "pump" pulse at 248 nm at laser fluences below **a**, and above **b** the corresponding ablation thresholds. For comparison purposes, the spectra have been scaled. The figure also illustrates the approximate deconvolution of the probe spectrum into the emission bands of the suggested species (the Nap_2 spectrum is recorded in the photolysis of high-concentration NapI solution, while the NapH/PMMA spectrum is recorded from PMMA doped with 0.08 wt% NapH)

todissociation (emission of PMMA photoproducts, such as reported in [73], being too weak).

For PMMA and PS films doped with low concentrations of NapI or PhenI (<1 wt%), the probe spectra (Fig. 11a) recorded after ablation are in all cases dominated by the aromatic $^1B_{3u} \rightarrow {}^1A_{1g}$ emission (at ≈330 nm for NapH and ≈375 nm for PhenH), as also established by comparison with fluorescence spectra recorded from NapH- and PhenH-doped samples [80]. Unfortunately, this emission band is not sensitive to the substitution of the aromatic skeleton [80]. Thus, it is not possible to ascertain the exact nature of the products from these spectra alone. Thus, as a precaution, we refer to these

products as NapH-like and PhenH-like. The products of the halogen fragment of the dopant are not evidenced in the fluorescence spectra and are not considered further.

The formation of the NapH- and PhenH-like products is ascribed to the aryl (naphthyl–Nap and phenanhthrenyl–Phen) radicals that are formed by the homolytic photodissociation of the precursors reacting with nearby polymer units (either by abstraction or addition reactions) (Scheme2).

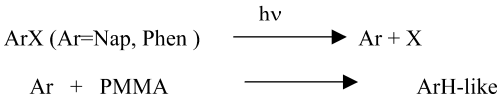

Scheme 2 Pathway for ArH-like photoproduct formation

Thermal decomposition is not considered in this scheme. Indeed, assuming the activation energy E_a for the C–I bond decomposition to be equal to the 2.6 eV bond energy (i.e., no activation barrier assumed) and a rather high preexponential factor of 10^{13} s^{-1}, the yield by thermal decomposition is estimated to be only 10^{-6} on a time scale of μs and $\approx 10^{-3}$ on ms time scales. The possibility of thermal decomposition is further discounted by the failure to detect any NapH-like photoproduct formation in the ablation of NapI/Rd/PMMA (0.4% and 0.1% by wt., respectively; Rd represents rhodamine 6G) at 532 nm. Nevertheless, it is reasonable to assume that comparable temperatures develop in the ablation of this system as in the 248-nm irradiation of NapI/PMMA. Therefore, thermal decomposition fails to account for the aromatic dopant decomposition.

Even in the case of simple aromatic dopants (naphthalene, anthracene, pyrene), fluorescence intensity is found to decrease with successive laser pulses and/or increasing laser fluence. The decrease may be ascribed to thermal desorption of the dopant, as indicated by Fukumura et al. [62], and/or to photooxidation/degradation of the dopants. In the present case, film transmission decreases in parallel with the dopant fluorescence, thus indicating the formation of photoproducts that absorb stronger than the precursor. (The photoproduct(s) are not detected in the fluorescence experiments, evidently because of its (their) low emission yield). NapH and related compounds are known to generate $^1O_2$ (Δ_g) efficiently [81]. This has a long lifetime within polymers and it can attack the aromatic to form the corresponding endoperoxide (Nap-O_2). Such processes have been shown to occur in related polymer systems.

Based on the study of the ArI/doped systems, three distinct differences have been delineated between the ablative regime and the very low fluences regime. Specifically, differences are observed concerning (a) efficient formation of biaryl-type products, (b) efficiency of ArH-like photoproduct formation, and (c) kinetics of product formation. These results demonstrate that dopant reactivity is both qualitatively and quantitatively modified from that at low laser fluences.

Concerning issues (b) and (c), the deviations observed in the ablative vs subablative regime depend on the wavelength and thus they will be considered in the section below. Concerning the efficient formation of new/additional products in the ablative regime, this is best illustrated in the examination of NapI/PMMA samples with a dopant concentration higher than 1 wt%. Following pump irradiation at low fluences, the probe spectra are indicative of NapH product exclusively (Fig. 11a). However, for pump irradiation at fluences at which polymer swelling is induced, the probe photoproduct spectra are observed to be much broader (Fig. 11b). The formation of Nap_2 and perylene is demonstrated, respectively, by the broad emission at $\approx$375 nm and the double peak structure around 450 nm. Figure 11b illustrates the deconvolution of the probe photoproduct spectrum into the emission bands of the suggested species. (In the case of the PhenI dopant, the evidence for formation of the corresponding recombination/fused products is not as conclusive as in the case of the NapX dopants.)

The biaryl species could be assumed to derive from the photolysis of preexisting NapI aggregates in the film. However, examination by a number of techniques indicates that dopant aggregation within the polymeric substrates becomes significant only at much higher concentrations [86]. Thus, the biaryl products are indicated to form mainly through the reaction of diffusing species (recombination of two Nap radicals). Assuming Fickian-like mobility of the radicals [82], the efficient biaryl formation for the examined dopant concentrations suggests polymer viscosity in the 10^1 to 10^3 Pa s^{-1} range. These values are comparable to the viscosity of polymer melts (10^2 and 10^6 Pa s^{-1}) [81–82]. Thus, a high degree of disruption of the polymer integrity during UV ablation is indicated. The high mobility has been implicitly assumed by Fukumura et al. [61–63] in their hypothesis for very efficient electronic energy transfer processes (Scheme 1). The present results demonstrate the implications of this high mobility for the chemical effects of UV ablation. In particular, the observation of biaryl species provides a direct experimental probe for evaluating the degree of substrate structure disruption during laser irradiation.

4.3.1
Wavelength Dependence

Wavelength is the most important parameter that needs specification in implementations of UV ablation [1–6]. Generally, irradiation at relatively strongly absorbed wavelengths is selected for ensuring efficient etching and good surface morphology. These are usually the only criteria employed for selection of the optimal wavelength. In addition, the operation of a photochemical mechanism may be dominant for irradiation at wavelengths absorbed mainly by photodissociable units [1, 4, 6, 68–70]. The operation of such a mechanism is considered to result in further decrease of the thermal "load" to the substrate.

For examining the importance of wavelength, a comparison of dopant-derived products is presented for irradiation of the NapX/PMMA (X=Br, I),

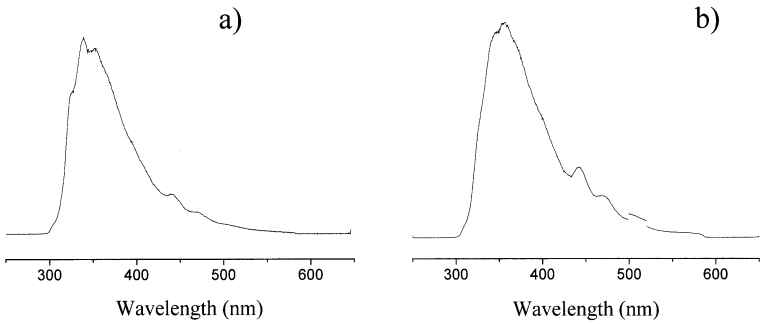

Fig. 12 Laser-induced fluorescence spectra recorded from NapI-doped PMMA samples (1.2 wt%) after their irradiation with a single "pump" pulse **a** at 248 nm and **b** at 308 nm at laser fluences about 1.5 times the corresponding ablation thresholds

PhenI/PMMA, and PhenI/PS systems at three typical excimer laser wavelengths (193, 248, and 308 nm) [85–86]. No difference in the type of photoproducts is detected for irradiation at the various wavelengths. However, there is clearly a tendency for reduced formation of the biaryl species with decreasing wavelength. For example, Fig. 12 shows that the relative emission intensity of the perylene and Nap_2 species vs that of the NapH-like product is higher following pump irradiation at 308 nm than at 248 nm. In the 193 nm irradiation of the same dopant concentration, hardly any biaryl species are detected. The observed difference appears to indicate a change in the degree of radical mobility (and thus the degree of polymer modification/melting) at the three wavelengths. However, the extent of biaryl formation should depend quadratically on the degree of NapI photolysis per unit volume which, as discussed below for a given fluence, decreases with increasing substrate absorptivity. This change in NapI photolysis yield accounts largely for the difference in the efficiency of biaryl species formation.

A strong dependence on wavelength is also observed in relationto the amount of ArH (Ar=Nap or Phen) photoproduct remaining in the substrate. To this end, the fluence dependence of the ArH photoproduct emission intensity following a single pump pulse on virgin polymer is plotted as a function of laser fluence (Fig. 13). This intensity should be proportional to the amount of the photoproduct that remains in the substrate after irradiation. However, a major limitation in the employed probing technique (in fact, of any spectroscopic study of the substrate) results from the highly modified film morphology upon ablation. This can greatly affect the propagation of the probing beam and thus the intensity of the induced fluorescence. Different approaches [83] have been employed to ensure that the changes in the F_{LASER}-dependence of the fluorescence intensity reliably represent the qualitative trends in photoproduct formation. On the other hand, caution should be used in extracting detailed quantitative information from such curves.

Figure 13 depicts the two limiting cases of F_{LASER}-dependences of the photoproduct intensity that have been determined in the UV irradiation of these

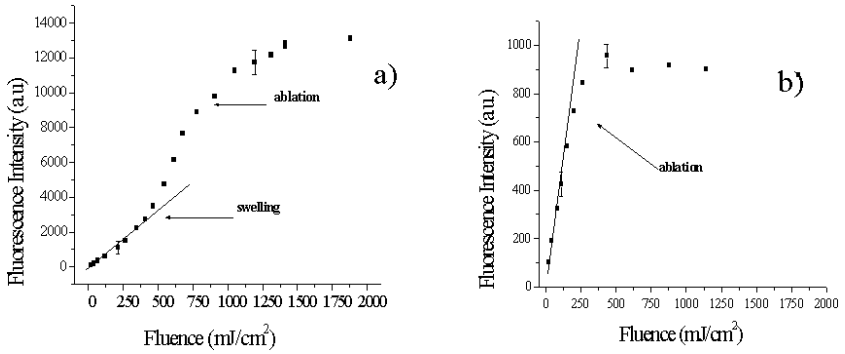

Fig. 13 The two limiting cases of F_{LASER}-dependence of aryl (NapH or PhenH) photoproduct emission that have been determined in the UV irradiation of doped PMMA and PS films. The indicated curves concern **a** NapI-doped PMMA (0.8 wt%) and **b** PhenI-doped PS (1 wt%) with a single"pump" pulse at 248 nm. The *error bars* represent 2σ. Qualitatively similar curves as that of **a** are observed for all systems irradiated at weakly absorbed wavelengths, while curve **b** is obtained for irradiation at strongly absorbed wavelengths

systems. For weakly absorbed wavelengths (e.g., 0.4 wt% NapI/PMMA samples at 248 and 308 nm), the linear increase of the photoproduct yield at low laser fluences is followed by a sharp rise above a specific laser fluence. It turns out that at this fluence, the polymer surface swells, as established by profilometric examination. Swelling on irradiation of weakly absorbing polymers, in particular of PMMA at 248 nm, is a well established observation [4]. The actual ablation threshold is at somewhat higher fluences (indicated by an arrow in Fig. 13). Thus, compared with irradiation at low fluences, photoproduct formation increases sharply above the swelling threshold. Since the enhancement is observed for all detected products, it is not due to the formation of a specific species at the expense of others. Most importantly, the increase is observed for films (<20 μm) much thinner than the optical penetration depth. Thus, the increase is not due to an increase of the depth over which photoproducts are formed, as would be the case if saturation of the absorption process were involved. Instead, there is enhancement in the photodegradation of the haloaromatic dopants per unit volume.

In contrast to the previous case, for irradiation at strongly absorbed wavelengths the product amount in the substrate is found to reach a limiting value near the ablation threshold (Fig. 13b). Clearly, any products formed in addition to those formed at lower fluences are removed by the etching process. Furthermore, the amount of dopant-derived photoproducts that remain in the substrate following ablation at strongly absorbed wavelengths is highly reduced from that in the irradiation at the other wavelengths.

For all systems that have been examined, i.e., independently of polymer or chromophore, there appears to be a close correlation between the absorption coefficient and the type of F_{LASER}-dependence of the photoproduct amount (Table 1). Of course, this conclusion does not imply that the chemi-

Table 1 Absorption coefficient of PMMA and PS at the examined wavelengths and type of observed F_{LASER}-dependence of the ArH-like photoproduct remaining in the substrate

	Wavelength (nm)	Penetration depth (cm)[a]	Type of observed F_{LASER}-dependence[b]
PS	193	1.3×10^{-6}[c,d]	B
	248	1.6×10^{-4}[c,e] 0.5×10^{-4}[f]	B
	308	$\approx10^{-3}$	A
PMMA	193	2.1×10^{-4}[d] 5×10^{-4}[g]	B
	248	7×10^{-3}[e]	A
	308	$>10^{-2}$	A

[a] Penetration depth based on reported absorption coefficients of the neat polymers at the indicated wavelengths

[b] Dependence observed for low concentrations of NapI or PhenI dopants (0.4 wt%) in the indicated polymers and wavelengths

[c] Lazare S, Granier V (1988) J Appl Phys 63: 2110

[d] Meyer J, Kutzner J, Feldmann D, Welge KH (1988) Appl Phys B 45:7

[e] Bolle M, Lazare S (1993) J Appl Phys 73:3516

[f] Frerichs H, Stricker J, Wesner DA, Kreutz EW (1995) Appl Surf Sci 86:405

[g] Cain SR, Burns FC, Otis CE, Braren B (1992) J Appl Phys 72: 5172; [43]

cal composition of the matrix is not significant, but that it is of secondary importance to the absorptivity, at least for the systems studied here. At present, this dependence can be understood by the fact that the absorption coefficient determines the relative ratio of etching depth vs optical penetration depth, and thus the depth over which photoproducts remain in the substrate. In parallel, with increasing substrate absorptivity, the ablation threshold also decreases, thereby resulting in a decrease of the photon flux. Both factors result in the reduction of the amount of dopant-derived photoproducts that remain in the substrate.

The previous findings directly indicate some shortcomings of the usual ablation models. As described by Eq. 1, i.e., by the standard "blow-off model", the material that is left behind should always be subject to the same F_{thr}. Thus, the amount of photoproduct in the remaining material should be constant, i.e., independent of the incident laser fluence. This expectation is largely borne out in the case of irradiation at strongly absorbed wavelengths. On the other hand, for irradiation at weakly absorbed wavelengths, the experimental results clearly deviate from this prediction.

An important indication about the involved factors comes from comparing the kinetics of photoproduct formation above vs below the threshold at the different wavelengths. Figure 14 illustrates the rate of NapH formation at two fluences above and below the threshold for different delay times of the probe beam after the ablating one (λ=248 nm). There is a distinct difference in the kinetics of product formation. Above the threshold, formation of

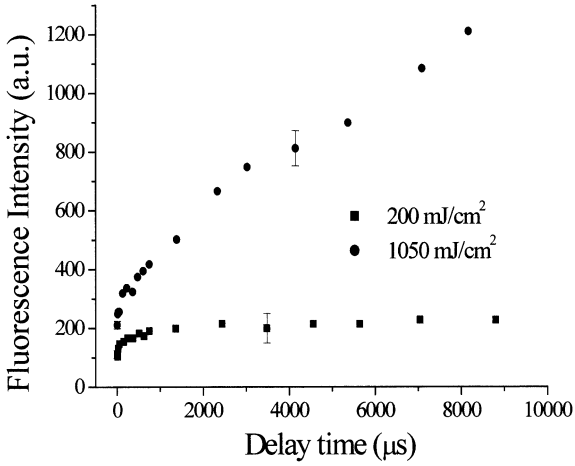

Fig.14 NapH-like photoproduct laser-induced fluorescence intensity as a function of the delay time between the pump and the probe beams in the 248 nm irradiation of NapI/PMMA films (0.8 wt%) (kinetics characteristic of irradiation at weakly absorbed wavelengths)

NapH photoproducts continues for well over ≈1 ms, whereas below the threshold, product formation is nearly complete after ≈100 μs. In contrast, for irradiation at strongly absorbed wavelengths, there is much less difference in the product formation kinetics above vs below the threshold. These differences in photoproduct formation kinetics appear to account largely for the different F_{LASER} dependences observed for the product amount remaining in the substrate upon irradiation at the corresponding wavelengths. Thus, for irradiation at weakly absorbed wavelengths, the prolonged product formation at high fluences as compared with that at low fluences accounts for the increase of product amount above the swelling threshold (Fig. 13a). In other words, the increase observed in Fig. 13a does not result from a difference in the (primary) photolysis efficiency of iodoaromatic dopant, but from the different kinetics of subsequent reactivity of the radicals.

A question is, then, raised concerning the observed "correlation" between product formation kinetics and the absorption coefficient of the substrate. A quantitative model accounting for this difference will be presented elsewhere. Briefly, the first factor affecting product kinetics relates to the fact that in ablation, temperatures remain high, thereby enabling activated processes, such as abstraction reactions by the aryl radicals, to proceed for longer. In contrast, at low fluences, because of the lower attained temperatures, reactivity may be "quenched" (i.e., the $-E_a$/RT factor in an Arrhenius equation becomes too small) already on μs scales. Furthermore, it is important to consider the effect of the "free volume" on reactivity within polymers [81]. Thus, below the swelling threshold, as the polymer structure is not disrupted, iodine and aryl radicals may be prevented from diffusing away, so that they recombine finally to reform the precursor ("cage effects"). The im-

portance of cage effects for reactivity within polymers is well documented [81]. In contrast, at higher fluences, at which the polymer structure is highly disrupted (due to melting, void formation due to gaseous production etc.), a high percentage of the radicals can diffuse away with a consequent reduction of the radical recombination efficiency. This process provides a source of reacting radicals and partly accounts for the prolonged ArH formation in the ablative vs nonablative regime, according to Scheme3. Based on a Noyes description [89] of the cage effects in combination with an approximate solution of Eq. 8, the observed kinetics have been qualitatively reproduced. Within this framework, the different kinetics at different wavelengths relate to the different extent of thermal load (heat conduction to the sublayers) and thus to the different degree of cage effect alleviation.

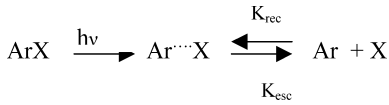

Scheme 3 Schematic of the ArX decomposition/recombination process

Independently of the responsible mechanisms, the present results clearly underline the importance of high substrate absorptivity for the success of laser processing schemes. It is generally assumed that the necessity for irradiation at strongly absorbed wavelengths is due to the need for attaining efficient etching and good morphology of the treated area. However, as shown above, with a high substrate absorptivity, the extent of induced photochemical modifications and of side product formation (in the substrate) is highly reduced, i.e., a high degree of "photochemical protection" is afforded to the remaining material.

The importance of high absorptivity of the processed molecular substrates has, for example, been demonstrated in the laser restoration of painted artworks. To this end, model samples of cinnabar red pigment (HgS) [17–18] in linseed oil covered with varnish were prepared and artificially aged. Then, varnish layers of various thickness were removed by KrF excimer laser irradiation and the remaining pigment/medium was analyzed by chromatographic techniques (GC/MS). No oxidation products are detected when at least a thin varnish layer is left intact. In contrast, when all varnish is removed and the laser has directly irradiated the pigment medium, oxidation products are observed in the remaining material. These results can be easily rationalized by the high absorptivity ($\alpha \approx 10^5$ cm^{-1}) of varnish, which ensures that photochemical effects are localized within d<1–5 μm, at most, from the surface.

There is another factor that may be involved and which has not been adequately addressed in the literature. As indicated above, Eq. 1 suggests the extent of photofragmentation and photoproduct formation in the remaining substrate to be constant with laser fluence (for $F \geq F_{thr}$). However, this neglects the possibility that fragments weakly bound to the matrix and/or photoproducts that are formed within the thermally affected zone below the

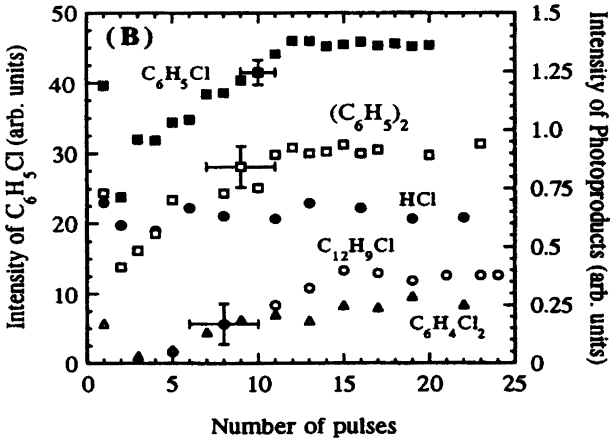

Fig. 15 Pulse evolution of the intensities of C_6H_5Cl and of the various photoproducts formed in the 248 nm irradiation of condensed films of C_6H_5Cl (F_{LASER}=150 mJ/cm^2, whereas the ablation threshold is 100 mJ/cm^2). It is clear that HCl is nearly constant with successive laser pulses, whereas for the other indicated species, accumulation with successive laser pulses is significant, until finally an equilibrium between amount of photoproduct formed and photoproduct ejected is attained. A more detailed description of the observed effects is given in [35]

ejected layer may diffuse to the surface and thermally desorb ("post-ablation" desorption). This possibility has been examined in the KrF laser ablation of C_6H_5Cl (chlorobenzene)-doped varnish. C_6H_5Cl is characterized by a high photodissociation quantum yield at 248 nm (0.4 in the gas phase) [93]. The ablation of liquid samples [94] and of condensed films of C_6H_5Cl [34] has been examined by a number of different techniques. Quadrupole mass spectrometry is employed to characterize the ejection photoproducts and their intensities are monitored on a pulse to pulse basis. The Cl and C_6H_5 fragments formed upon C_6H_5Cl photolysis are expected to produce, respectively, HCl (and also chloro adducts that are difficult to identify) and C_6H_5 adducts. For HCl, the ejection signal exhibits a weak pulse dependence. In contrast, a pronounced pulse dependence is observed for the C_6H_5-adduct species, with the dependence becoming less significant with increasing laser fluence. Since the relative intensity of the C_6H_5 adducts remains nearly constant, the pulse dependence cannot be ascribed to differences in chemistry with successive laser pulses. The different dependence shows that HCl, interacting relatively weakly with the matrix, desorbs even from the nonejected layers, whereas the stronger interacting C_6H_5 adducts accumulate in the underlying layers with successive laser pulses. For a more direct and conclusive demonstration of the involved factors, similar experiments have been performed on very simple (condensed) molecular films/mixtures of compounds, where binding energy to the substrate can be tailored via appropriate choice of dopants/matrix [95–96]. The results clearly show that a depth below the ejected layer attains a high degree of "fluidity" so that, for com-

pounds with weak interaction with the matrix, a significant percentage desorbs. In the case of the ablation of photolabile compounds, it is similarly demonstrated that photoproducts that interact weakly with the matrix and are formed below the ejected layers are efficiently removed [18, 97] (Fig. 15). In the case of polymers, recent theoretical work also supports the suggested delineation [33]. This effect may be an important factor for the success of the various laser–material processing schemes, since it indicates that small (usually the most reactive) species formed even below the etched depth may be efficiently removed. The importance of this contribution may depend on substrate absorptivity. With increasing substrate absorptivity, photoproducts remain "confined" closer to the surface and the probability of weakly bound species desorbing increases.

4.3.2
Dependence on Number of Laser Pulses

In most cases, a significant number of laser pulses may be required for the removal of the undesirable/contaminated surface layers. Thus, the dependence of the extent of photochemical modifications on the number of pulses is of direct relevance for the optimization of applications.

In the simplest case, with successive laser pulses, photoproduct accumulation in the substrate may be described by an exponential of the form $[1-\exp(-\sigma F_{LASER} N_{pulse})]$, where σ is the absorption cross-section and N_{pulse} is the number of pulses, until finally a plateau is reached. Indeed, this dependence is largely borne out in the experiments on the model, doped systems. Furthermore, examination of the probe spectra from samples that have been irradiated at various fluences but at approximately the same total photon dose (Fig. 16) indicates an interesting result. At all fluences, the photoproduct

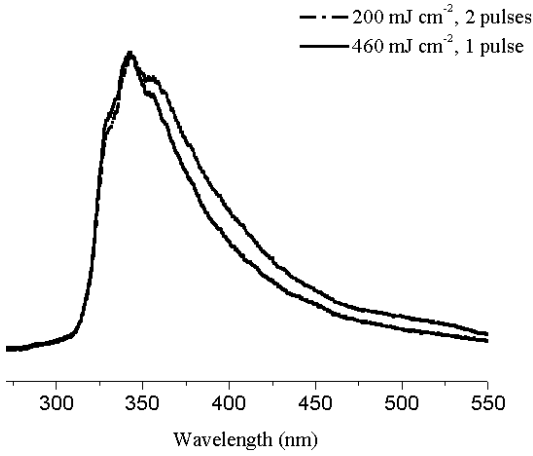

Fig. 16 Laser-induced fluorescence spectra recorded from NapI/PMMA (0.4 wt%) irradiated with the indicated number of pulses (at 248 nm) at the two indicated fluences

spectra following a single pump pulse are dominated by the ArH-type photoproduct emission, but with continuing irradiation, they get progressively broader and red-shifted. Consequently, for irradiation at the same total photon dose but at different fluences, accumulation of by-products is higher with increasing number of pulses that have irradiated a given spot (i.e., higher for irradiation at low fluences).

The previous result can be extrapolated to the case of chromophores which are part of the polymer chain, rather than dispersed within the polymeric matrix as dopants. For instance, this trend is observed in the irradiation of PS films (at 248 nm). The near-UV fluorescence spectrum of PS consists of an emission band at 320 nm [81]. This band is ascribed to excimer emission of the phenyl side groups (monomer fluorescence being mainly observed at ≈285 nm). Upon irradiation with successive laser pulses at low laser fluence values or the ablation threshold of PS at 248 nm, the PS fluorescence peak decreases gradually to very low values, with the decrease per pulse being more pronounced with increasing laser fluence. In parallel, a broad emission band at ≈440 nm is observed to grow. Based on previous studies [81], it is suggested that PS undergoes fragmentation to benzyl and/or phenyl radicals, thereby accounting for the decrease of the emission at ≈320 nm, and polyene structures (highly conjugated products derived from the PS chains), indicated by the emission at 440 nm. In contrast, in the irradiation above the threshold, the ratio of degradation/PS emissions never turns into the extreme one observed at low laser fluences. Thus, the results appear to be analogous to those observed for haloaromatic dopants, but further studies are needed to establish how these effects depend on other parameters (i.e., molecular weight, crystallinity, etc.).

The above differences may be accounted for by the operation of different material ejection mechanisms in the corresponding fluence ranges. As discussed previously, at low and moderate laser fluences an essentially thermal desorption mechanism may be operative so that removal of the "heavy" (i.e., strongly bound to the matrix) fragments is inefficient. Thus, with successive laser pulses, these species accumulate in the substrate and react to form a number of ill-defined side products. In contrast, in the ablative regime, formation of these side products is much reduced, due to the efficient removal of even the larger, strongly bound species. In this case, an equilibrium is established between new species produced and species removed. The deleterious effects of accumulating chemical modifications to the integrity of the substrate and/or efficiency of material ejection have been noted in MALDI [90] and in other polymers [91–92]. For a number of systems, upon irradiation close to the threshold, the desorbate signal monitored by mass spectrometry decreases with successive laser pulses becoming eventually minimal. The effect has been ascribed to the extensive chemical modification of the superficial substrate layers. Subsequent irradiation at higher fluences removes the modified layers, with restoration of the ejection signal.

In all, multipulse irradiation protocols are indicated to be detrimental for the chemical integrity of the substrates. Of course, in the various implementations of UV ablation, the number of required pulses is specified by the

etching efficiency as compared to the amount of material that must be removed. Thus, in practice, a compromise may have to be drawn between efficient material removal and minimization of photochemical effects.

Another issue that remains to be clarified concerns the relative importance of cross-linking and depolymerization processes that the macromolecular photoproduct radicals may undergo. It is highly plausible that the empirically found optimal fluence range in varnish removal corresponds to the first condition, i.e., of partial cross-linking, thereby regenerating the initial or a similar structure. Examination by other techniques (such as transient absorption spectroscopy) can address this aspect. Furthermore, such techniques can complement the fluorescence examination of the doped polymers and provide information on any nonfluorescing (dark) products. At any rate, as the experiments with these model systems strongly indicate, optimal irradiation conditions can be defined under which deleterious photochemical effects to the substrate are minimal.

4.3.3
Dependence on Laser Pulse Width–Femtosecond Ablation

Ablation with femtosecond pulses has attracted significant attention, because of the several advantages that it is considered to provide for material processing [3–4, 98, 99]. First, as implied by the discussion above, the heat-affected zone should be minimal; second, because of material ejection occurring well after the laser pulse, there is no plasma shielding (thus, maximum coupling of the incident laser energy into the substrate is effected); and third, due to the efficient energy use and the enhanced possibility of multiphoton processes, the ablation threshold is much reduced. It is generally demonstrated that quality of structuring with fs pulses far surpasses that attained in ns ablation.

Ablation with femtosecond pulses is comprehensively reviewed by Krüger and Kautek in this issue. The present discussion focuses exclusively on photoproduct formation in the irradiation of ArI-doped systems with fs pulses. This examination indicates several subtle mechanistic possibilities. Upon irradiation with 500-fs pulses at 248 nm, only ArH-like product formation is observed as the fluence is raised above the ablation threshold (Fig. 17). Recombination (e.g., Nap_2-type) or other by-products are not observed even for dopant concentrations as high as 4 wt% [83–84]. In contrast, at low fluences, a number of by-products are observed after irradiation with few laser pulses. In this case, the accumulating radicals evidently react with each other to produce ill-defined products. Most interestingly, ill-defined species are not observed above the threshold even after extensive irradiation (Fig. 17). It is clear that photochemical processes in the ablation with fs pulses must differ distinctly from those in ns ablation.

Plausibly, because of the limited thermal dissipation in the ablation with fs pulses, the integrity of the substrate is not compromised, and the mobility of the photoproduced radicals remains highly restricted. It is also tempting to argue that with the shorter pulses, material ejection occurs too fast for

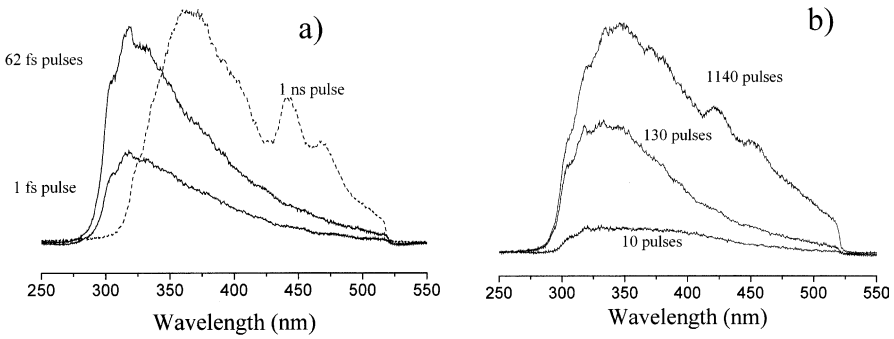

Fig. 17. a Illustration of the LIF photoproduct spectra recorded after the ablation of NapI/ PMMA (4.0 wt%) with the indicated number of laser pulses of 500 fs, in comparison with a spectrum recorded upon ablation with pulses of 30-ns duration (in both cases, λ=248 nm, F_{LASER}=1.2 J/cm^2). The spectra have been scaled for the purposes of the comparison. **b** LIF photoproduct spectra recorded in the irradiation of the same system with the indicated number of laser pulses of 500 fs at a low fluence (F_{LASER}=15 mJ/cm^2)

the formation of these species to compete. Indeed, it has been shown [98] that, in the irradiation with 500-fs pulses, material ejection from PMMA is already significant 10 ns after the pulse. Though these suggestions are reasonable, they do not seem sufficient to account for the extremely "clean" chemistry that is observed in irradiation at high fluences. Recently, Vogel et al. [100] advanced a model for the irradiation of biological tissues with ultrashort laser pulses based on the idea of a weak (low-density) plasma formation. As a consequence of the increasing importance of multiphoton processes, seed free electrons for avalanche ionization are produced efficiently in the irradiation with ultrashort laser pulses. As a result, a highly localized, weak-density plasma may be produced over a wide range of laser fluences well below the optical breakdown threshold (defined to correspond to a free electron density of 10^{21} cm^{-3}). The ejected free electrons may attach to functional units and initiate specific bond-breaking processes. Though several aspects of their modeling remain incomplete, there appear to be close relevancies between the present results and their suggestion. This will be the topic of future studies.

Concerning photoproduct formation efficiency, this is found to increase in the subthreshold range, reaching a limiting value at the threshold. The increase below the threshold may be ascribed to the enhanced contribution of multiphoton excitation processes in the irradiation with fs pulses. Indeed, film transmission is found to decrease significantly at low fluences (~10 mJ/cm^2 for 0.4 wt% NapI/PMMA). Multiphoton processes in the irradiation with shorter laser pulses have been indicated previously [98] for neat PMMA. They can, likewise, be expected to be important for the haloaromatic S_3 excited state (that is assessed at 248 nm) having a lifetime ($\approx$1 ps [80]) longer than the laser pulse width.

In conclusion, the photochemical effects in UV ablation with fs laser pulse widths are qualitatively and quantitatively highly defined and limited. Thus, besides the well-acknowledged advantages described above (i.e, limited heat load, highly efficient and localized energy deposition, etc.), fs ablation also affords a high degree of control over the induced photochemical modifications. Thus, processing with fs lasers may be highly potent in the treatment of molecular substrates. This potential has been recently demonstrated in the processing of biological substrates [101].

4.4 Photomechanical Effects

Several studies [102–108] have demonstrated the development of stress waves with amplitudes of several hundred bars in the excimer laser ablation of tissue and polymers. These stress waves may be generated in a number of different ways.

The first source of stress wave relates to the back-momentum exerted by the ejected material. This results in a compressive wave propagating through the substrate [1, 3]. The exact dependence of the peak stress amplitude on the incident fluence depends on the time scale of material removal, as well as the exact nature of the process (e.g., explosive vs surface vaporization). It can be estimated by assuming the ejected material to be an ideal gas expanding against the air and the substrate, resulting in the expression (for surface vaporization) [106]:

$$p_{max} \propto \left[\frac{(\gamma_{air}+1)\rho_{air}}{2}\right]^{\frac{1}{3}}\left[\frac{1}{f/2+1}\right]^{\frac{2}{3}}\left[\frac{(F_{LASER}-F_0)}{\tau_{pulse}}\right]^{\frac{2}{3}} \quad (9)$$

where $F_0 \approx F_{thr}$ is assumed to be the energy that remains as heat in the substrate, and $f=2c_v/R$, with c_v being the molar specific heat of ideal gas. The predicted scaling has been examined in the UV ablation of polyimide and of cornea [106]. At even higher fluences at which plasma formation becomes significant, the pressure relates to the expansion of the plasma, in which case p_{max} scales as $F_{LASER}{}^{3/4}$.

Second, the rapid laser-induced thermal expansion causes [103] a pressure rise, given by the product of the Grüneisen coefficient, Γ, and the absorbed energy density

$$\Delta P = \Gamma a F_{LASER}\left(\frac{1-e^{-\theta}}{\theta}\right) = \frac{\beta\alpha F_{LASER}}{\rho k_T c_V}\left(\frac{1-e^{-\theta}}{\theta}\right) \quad (10)$$

where β is the thermal expansion coefficient, c_v the heat capacity at constant volume, κ_T the isothermal compressibility, and $\theta=\tau_{pulse}/\tau_{ac}$ where τ_{ac} is the time required for an acoustic wave to traverse the irradiated volume. The factor in parentheses corrects for the reduction in the stress amplitude due to a wave propagating out of the irradiated volume during the laser pulse (assumed to have a rectangular time profile). The stress entails a radially

propagating cylindrical wave, which can usually be neglected for laser beam diameters substantially wider than the light penetration depth, and two plane waves counter-propagating along the laser beam axis (one toward the surface and the other into the sample). The wave that travels towards the free surface (polymer/air interface) suffers a change of its amplitude sign upon reflection from it, due to the higher acoustic impedance of the irradiated medium, ρc_s, than that of air. Physically, the thermal expansion directed into the medium generates a compression wave, whereas the outward expansion generates negative stress (rarefaction wave), i.e, the wave produced by this mechanism is bipolar. The faster the heating, the higher the magnitude of the generated thermoelastic stress in the medium, with the ultimate efficiency attained for heating times much faster than the times required for stress to propagate through the irradiated volume. This is usually expressed in terms of $\alpha c_S \tau_{\text{pulse}} << 1$.

A third source of stress waves derives from the expansion of any gases (CO, CN, N_2, CH_3 etc.) produced by thermal or photochemical decomposition within the substrate [104]. This factor, for instance, has been invoked to account for the transient stresses of about 0.1 MPa detected in the UV irradiation of polyimide below the ablation threshold [106]. In the case of doped PMMA, irradiation with 150-ps pulses at 1064 nm, Hare et al. [104] estimate that at the ablation threshold, the thermoelastic mechanism and the expansion of the decomposition products contribute about equally to the generated pressure. For specifically designed polymers that upon irradiation form a high enough concentration of volatile products, the generated pressure has been suggested to be the primary cause of material ejection [68–69].

Generally, peak pressure amplitudes range from a few MPa at the ablation threshold up to several hundred MPa at high laser fluences [104–108]. During propagation through the substrate, these high-amplitude waves may induce structural modifications at areas away from the ablation spot. Thus, in contrast to the photochemical effects which are confined to the laser-irradiated area, the photomechanical effects of UV ablation can be much more delocalized.

Measurement of the stress waves that are induced in the ablation of polymers has relied [102–108] on the use of piezoelectric transducers or on optical techniques. Though capable of high sensitivity and temporal resolution, these techniques yield information only about limited regions of the substrate. Furthermore, it is rather difficult to predict the type and extent of the induced structural modifications only through knowledge of the measured pressure amplitudes, since the nature of the modifications depends also on the substrate's mechanical properties, presence and type of interfaces, etc.

To overcome the above limitations, we employ double-exposure holographic interferometry [110]. Holographic techniques have the crucial advantage of storing the full field image of the sample before and after irradiation, thereby permitting spatially resolved characterization of the induced effects over the full sample. The technique is applied to the study of polymeric systems, either in the form of plates or mainly in the form of films cast on transparent substrates.

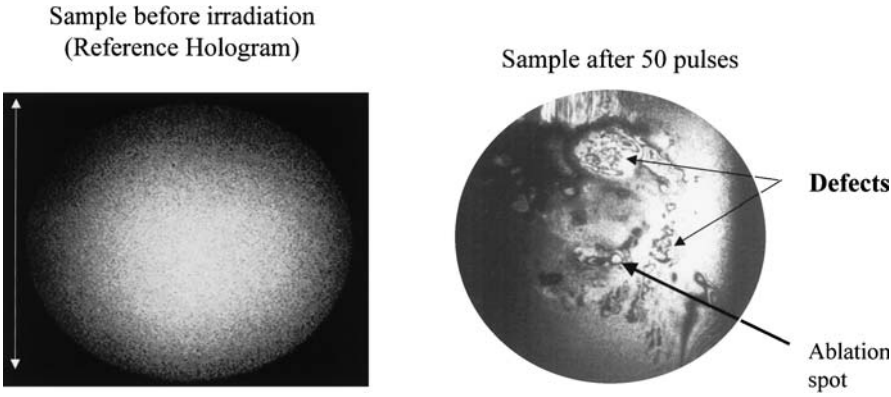

Fig.18 Interferograms recorded in the UV ablation of PMMA polymeric films on a Suprasil substrate at 193 nm ($F_{LASER}\approx 1$ J/cm^2) with ≈200 pulses. The interferogram clearly demonstrates defect formation at distances far away from the irradiation spot. For the purpose of enhancing defect formation, this particular film has not been annealed

The experimental setup is designed for the on-line holographic examination of the irradiated polymer substrates [111]. The holographic setup is aligned in an off-axis two-beam geometry for phase media (i.e., transmission mode). Two exposures (λ=632 nm) are made on the same hologram, one before and one after irradiation of the sample with a given number of excimer laser pulses. Any changes in the optical pathlength results in interference between the two successive holograms: $U(x,y)\propto U_0(x,y)$ $(1+\cos\{(2\pi/\lambda)\Delta\phi(x,y)\})$. The phase term $\Delta\phi$ is related to the induced refractive index changes. If the refractive index change is such that $\Delta\phi = \int [n_R(x,y,z) - n_{R0}]dz = N_{fringe}\lambda$, interference fringes are generated. Following this procedure for irradiation of the substrate with successive excimer laser pulses, the evolution of the induced modifications is characterized.

Figure 18 depicts holographic interferograms recorded upon ablation of nonannealed PMMA films cast on Suprasil substrate (250 pulses, λ=193 nm, $F_{LASER}\approx 1$ J/cm^2). Since the polymer films may undergo morphological changes/aging even in the absence of external disturbances, a strict protocol of comparing laser-treated samples vs untreated ones has been observed. The three-dimensional characteristics of the modifications are evaluated by examination of the recorded holographic images from different observation angles [110], indicating that fringe patterns correspond to local delaminations. This is further verified by optical and scanning electron examination of the samples. Most importantly, fringe patterns are resolved at several regions over the full extent of the substrate (radius of 2.5 cm). Given the large distance from the irradiation spot and the low laser repetition rate (1 Hz), thermal effects can be discounted, and the formation of these defects must be ascribed to the influence of propagating stress waves. Importantly, no such changes are detected in the irradiation below the ablation threshold,

even after extensive irradiation (≈1000 pulses). Thus, the ultrasound that develops by the thermoelastic phenomenon operative at low fluences is of insufficient amplitude to induce such defects.

Two types of deformations have been observed. For nonannealed samples, localized delaminations of the polymer films from the substrate are mainly observed, whereas for well-annealed samples, crack-type defects on the surface of the polymer dominate. For quantitative characterization, the extent of formation of the two defect types is plotted as a function of the number of laser pulses (the particular plot concerns irradiation at λ=193 nm, $F_{LASER} \approx 1$ J/cm^2, but similar dependences are also observed for irradiation at 248 nm) (Fig. 19). The delaminated area is expressed as a percentage of the total sample area, while the cracks are quantified by their number. Depending on the degree of sample annealing, an "initiation" phase (≈5–10 pulses) is observed, in which defects are not detectable. This initiation period must represent the laser-induced cyclic loading and unloading to the initially defect-free substrate, during which formation of "nuclei" (microscopic discontinuities acting as "stress raisers" [114]) occurs. Interestingly, "induction" periods where laser irradiation does not result in apparent structural effects/modifications have also been reported in the ablation of tissues [115]. Following, however, defect "nucleation", there is a gradual increase of both defect morphologies. The increase in the initial 10–30 pulses entails the appearance of new defects as well as the growth of previously formed ones, while after cumulative irradiation (>50 pulses), the defects start to fuse with each other. Finally, a plateau is generally reached, probably due to the prevention of the propagation (i.e., enhanced damping) of the stress waves by the developed delocalized defect network. At any rate, the use of multipulse irradiation protocols is indicated to be detrimental for the structural integrity of the substrates.

The propagation of the laser-induced stress waves in the polymer/substrate system has been modeled on the basis of a 3D finite element model (Fig. 20). The modeling successfully reproduces most experimental observations. For the present purpose, the following semiqualitative description suffices. Through the multiple reflections of the laser-induced waves back and forth between the polymer and the Suprasil substrate, a complex wave pattern propagates in the system. During propagation, the acoustic waveforms are attenuated by sound absorption, diffraction, and plausibly nonlinear acoustic effects. In contrast, waves refracted into the quartz substrate (based on the acoustic impedances of quartz and of the examined polymers, ≈0.25 of the incident wave intensity is refracted per reflection) do not represent losses, since upon reflection on the back, free surface of the Suprasil they propagate backwards into the system. Losses due to absorption are described by $P(z)=P_o\exp(-a_{ac}z)$ where z represents the propagation distance and P_o the pressure exerted by the removal process. Generally, the damping (attenuation) coefficient a_{ac} of polymers scales with ν_{ac}^2, where ν_{ac} is the frequency of the acoustic wave, with typical values ranging from 500 to 2×10^3 dB/m for longitudinal wave attenuation (for ν_{ac} from ≈6 MHz up to ≈30 MHz) and from 1.4×10^3 to 6.5×10^3 dB/m for shear wave attenuation

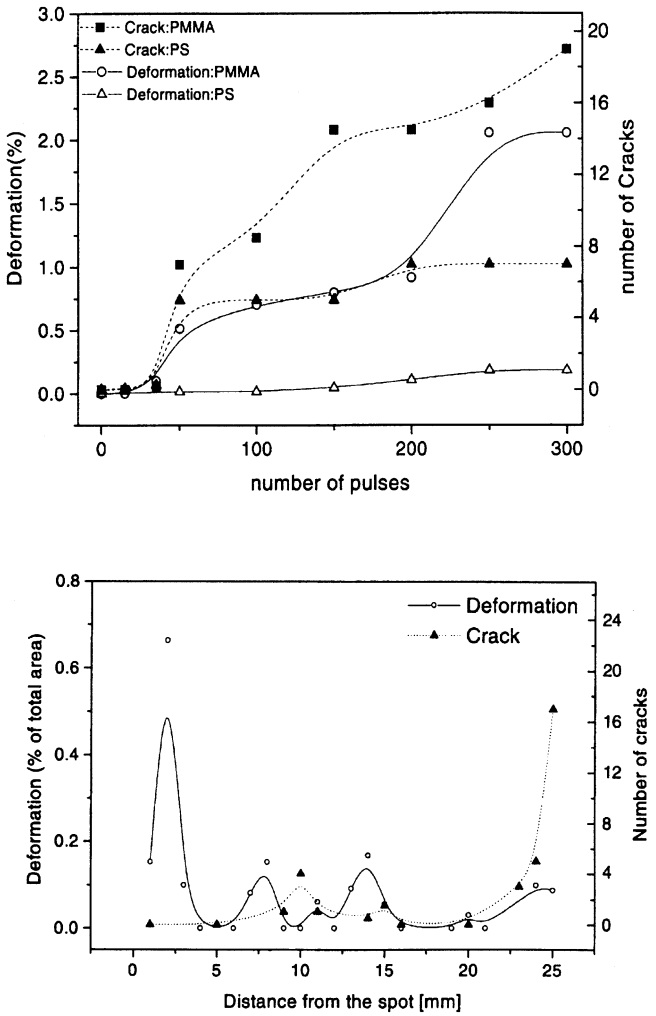

Fig. 19 *Top* Growth of defects in the irradiation of PMMA and PS films (M_w=1,900) on a Suprasil substrate at 193 nm as a function of successive laser pulses (F_{LASER} ≈1 J/cm^2). *Bottom* Spatial distribution of the defects following UV ablation of nonannealed PMMA films at 193 nm (F_{LASER} ≈1 J/cm^2, 200 pulses). The *lines* serve only as a guide to the eye. The ordinate values represent the average distance of the center of the defects, independently of their size, from the irradiation spot

[116] (attenuation factor of the sound intensity expressed in dB/m is equal to 8.686a_{ac}). Thus, 1/e loss of intensity is at 5–10 cm for low-frequency longitudinal waves and somewhat smaller for the shear ones. Polymer adhesion strength to substrates varies a lot [113]. For PS, adhesion strength to soda lime is reported to be ≈1 J/m^2 [112–113]. For nonannealed films, adhesion may be even weaker. Based on the previous studies [102–108] of the devel-

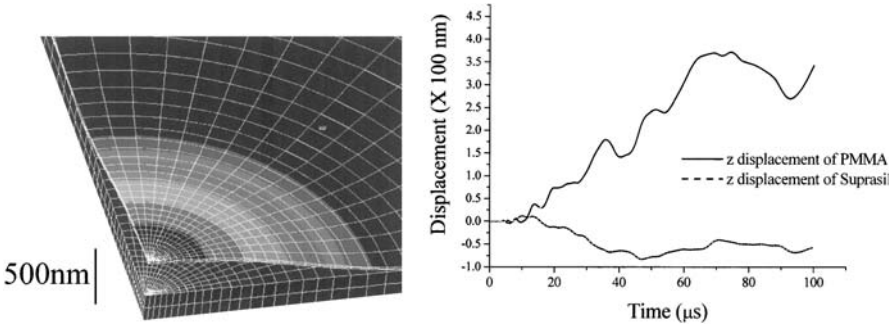

Fig. 20 Simulation of the propagation of the laser-induced stress wave as a function of distance from the irradiation spot. A three-dimensional finite element analysis program has been employed. The simulation shows that the highest probability for delamination is at the interface just behind the irradiation spot. This prediction is verified in the irradiation of nonannealed polymer samples on Suprasil

oped pressures in the ablation of polymers, the estimated energy deposited, on average, is estimated to be sufficient to result in the observed delaminations of $\approx 0.1-0.5$ mm^2. However, the observed diversity of structures indicates that different "deformation pathways" may be possible depending on the particular substrate properties.

The results clearly illustrate that structural effects at areas away from the ablation spot may be an issue of concern in the laser processing of mechanically fragile substrates. In the case of laser processing of tissues, structural changes deep below the irradiated area are often observed [115–118]. Holographic interferometry has been employed [18] to examine defect formation in the cleaning of realistic Byzantine icon models (i.e, samples composed of wooden support, pigment layer, and varnish). For these samples, defects in the form of delaminations develop mainly at the interfaces between the various layers, probably as a result of the different abilities of the two materials to accommodate the laser-induced stresses. Although the observation of defect formation is somewhat disturbing, the examination required the use of rather high laser fluences (≥ 1.5 J/cm^2) that in practice are avoided. Furthermore, after sufficient time, the laser-induced delaminations are indicated to gradually relax, i.e., their formation may be partly reversible. This issue of the degree of reversibility of the laser-induced defects is currently under investigation.

Aside from the mechanistic implications, the previous studies demonstrate that sequential holographic methodology is a powerful means for the examination of photomechanical effects over extended areas of the irradiated objects, and can be used for the on-line monitoring of UV laser processing schemes. Furthermore, the versatility of the technique allows its adaptation to the different detection requirements posed by the diverse types of processed objects. For instance, the technique can be directly employed in a reflection mode for the characterization of the effects in nontransparent

substrates. Real-time monitoring and/or pulsed lasers can be used for the study of the temporal evolution of the observed effects.

5 Conclusions

The present contribution has overviewed laser schemes for the cleaning of organic/molecular substrates. The three schemes examined include coating removal in a layer-by-layer approach, selective removal of surface impurities, and particle removal. The basic principles underlying these processes are presented. Laser irradiation is indicated and in a few cases well demonstrated to afford a highly effective method of removal of unwanted material from molecular solids/systems. Certainly, several experimental parameters must be carefully optimized in order to achieve proper cleaning. Furthermore, on-line monitoring may be essential for safeguarding against damage. With these precautions, laser cleaning can be a highly accurate and versatile method, surpassing by far the degree of selectivity and control afforded by traditional cleaning methods.

Particular emphasis is placed on the side effects of the procedures. The thermal, mechanical, and in particular the chemical effects are discussed from a fundamental/mechanistic standpoint and are exemplified in the case of the laser-based restoration of painted artworks. Certainly, the interaction of intense laser pulses with organic substrates is highly complex. In fact, in many respects, conventional photochemical concepts would suggest that the laser procedures would be particularly damaging for molecular/organic substrates. Yet these limitations or deleterious influences have been shown, at least empirically, to be avoidable to a large extent. This is best illustrated in the laser restoration of painted artworks. Despite their chemical and structural complexity, excimer lasers can be applied successfully to restoration, and irradiation conditions can be defined under which potentially damaging side effects to the substrate are minimal or at least inconsequential.

Studies on these model systems have also provided insight into the factors that are involved in these interactions. In particular, these studies have indicated significant deviations of processes from those of conventional photochemistry, thereby providing some indications for the success of laser cleaning schemes. Furthermore, these studies on model systems appear to be most useful for establishing criteria for the systematic optimization of laser processing techniques of molecular substrates. Thus, the absorptivity of the substrate at the irradiation wavelength is the major determinant for the extent of induced photochemical modifications. In contrast, irradiation with successive laser pulses is disadvantageous for the photochemical and structural integrity of the substrates. Besides their relevance to the optimization of various laser processing schemes, these results are of immediate mechanistic/scientific importance.

Acknowledgements The author would like to thank G. Bounos for his critical help in preparing this manuscript. The work was supported in part by the Ultraviolet Laser Facility oper-

ating at F.O.R.T.H. under the Improving Human Potential (IHP)-Access to Research Infrastructures program (contract No. HPRI-CT-1999-00074), the Training and Mobility of Researchers (TMR) program of the EU (project No. ERBFMRX-CT98-0188), and the PENED program (project No. 99E D 6) of the General Secretariat of Research and Technology–Ministry of Development (Greece).

References

1. Srinivasan R, Braren B (1989) Chem Rev 89:1303
2. Srinivasan R (1994) In: Miller JS (ed) Laser ablation principles and applications. Springer Ser Mater. Springer, Berlin Heidelberg New York
3. Bäuerle D (2000) Laser processing and chemistry, 3rd edn. Springer, Berlin Heidelberg New York
4. Lippert T, Dickinson TJ (2003) Chem Rev 103:453
5. Azema AG (1994) In: Laude LD (ed) Excimer lasers. Kluwer, Dordrecht
6. Vogel A, Venugopalan V (2003) Chem Rev 103:577
7. Luk'yanchuk BS (2002) Laser cleaning. World Scientific, Singapore
8. DeJule R (1998) Semicond Intern 8:65
9. Kern W (1993) Handbook of semiconductor wafer cleaning. Noyes, New York
10. Reed R (1970) Ancient skins, parchments, and leathers. Seminar, London New York
11. Wolbers R, Sterman RN, Stavroudis C (1990) Notes for workshop on new methods in the cleaning of paintings. The Getty Conservation Institute, Marina del Rey
12. Asmus JF (1986) IEEE Circuit Devic 2:6
13. Watkins KG, Larson JH, Emmony DC, Steen WM (1995) Proceedings of the NATO Advanced Study Institute on laser processing: surface treatment and film deposition. Kluwer, Dordrecht, p 907
14. Zapka W, Ziemlich W, Tam AC (1991) Appl Phys Lett 58:2217
15. Imen K, Lee SJ, Allen SD (1991) Appl Phys Lett, 58:203
16. Fotakis C, Anglos D, Balas C, Georgiou S, Vainos NA, Zergioti I, Zafiropulos V (1997) In: Tam AC (ed) OSA TOPS on lasers and optics for manufacturing, vol 9. Optical Society of America, Washington DC, pp 99–104
17. Zafiropulos V, Fotakis C (1997) In: Cooper M (ed) Laser cleaning in conservation: an introduction, chapter 6. Butterworth Heinemann, Oxford
18. Georgiou S, Zafiropulos V, Anglos D, Balas C, Tornari V, Fotakis C (1997) Appl Surf Sci 127–129:738
19. Brannon JH, Tam AC, Kurth RH (1991) J Appl Phys 70:3881
20. Manz C, Zafiropulos V (1997) Opto & Laser Europe (OLE) 45:27
21. Daurelio G, Chita G, Cinquepalmi (1999) Appl Phys A 69:S543
22. Mills JS (1956) J Chem Soc 2196
23. de la Rie ER (1988) Stud Conserv 33:53
24. de la Rie ER (1989) Anal Chem 61:1228A
25. Kakasaki T, Tsunemi A, Nagasaka K, Suda A, Tashiro H (1996) Appl Phys A 63:435
26. Bityurin N, Luk'yanchuk BS, Hong MH, Chong CT (2003) Chem Rev 103:519
27. Kuper S, Brannon J, Brannon K (1993) Appl Phys A 56:43
28. Schroeder K, Schuoecker D (1998) Laser Phys 8:38
29. Schmidt M, Li L, Spencer J, Key PH (1998) Appl Surf Sci 138/139:378
30. Galantucci LM, Gravina A, Chita G, Chinquepalmi M (1997) Polym Polym Compos 5:87
31. Liu K, Garmire E (1995) Appl Opt 34:4409
32. Schmidt MJJ, Li L, Spencer JT (2000) Appl Surf Sci 53:154
33. Bityurin N, Arnold N, Luk'yanchuk N, Bauerle D (1998) Appl Surf Sci 164:127
34. Zhigilei LV, Garrison BJ (2000) J Appl Phys 88:1281
35. Georgiou S, Koubenakis A, Lassithiotaki M, Labrakis J (1998) J Chem Phys 109:8591
36. Kautek W, Pentzien S, Rudolph P, Krüger J, König E (1991) Appl Surf Sci 127–129:746

37. Kolar J, Strlič M, Müller-Hess D, Gruber A, Troschke K, Pentzien S, Kautek W (2000) J Cult Heritage 1:S221
38. Kolar J, Strlič M, Marinček M (2002) Appl Phys A 75:673
39. Lu YF, Lee YP, Zhou MS (1998) J Appl Phys 83:1677
40. Koren G, Donelon JJ (1998) Appl Phys B 45:45
41. Coupland K, Herman PR, Gu B (1998) Appl Surf Sci 127–129:731
42. Mosbacher M, Dobler V, Boneberg J, Leiderer P (2000) Appl Phys A 70:669
43. Fourrier T, Schrems G, Mühlberger T, Heitz J, Arnold N, Bäuerle D, Mosbacher M, Boneberg M, Leiderer P (2001) Appl Phys A 72:1
44. Halfpenny DR, Kane DM (1999) J Appl Phys 86:6641
45. Mosbacher M, Mónzer H-J, Zimmermann J, Solis J, Boneberg J, Leiderer P (2001) Appl Phys A 72:41
46. Chaoui N, Solis J, Afonso CN, Fourrier T, Muehlberger T, Schrems G, Mosbacher M, Bäuerle D, Bertsch M, Leiderer P (2003) Appl Phys A 72:41
47. Dobler V, Oltra R, Boquillon JP, Mosbacher M, Boneberg J, Leiderer P (1999) Appl Phys A 69:335
48. Dongsik K, Park HK, Grigoropoulos CP (2001) Int J Heat Mass Trans 44:3843
49. Yavas OJ, Leiderer P, Park HK, Grigoropoulos CP, Poon CC, Tam AC (1994) Phys Rev Lett *72*:2021
50. Lee YP, Lu YF, Chan DSH, Low TS, Zhou MS (1998) Jpn J Appl Phys 37:2524
51. Tam AC, Park HK, Grigoropoulos CP (1998) Appl Surf Sci 127–129:721
52. Balas C (1997) IEEE Trans Biomed Eng 44:1
53. Anglos D (2001) Appl Spectrosc 55:186
54. Anglos D, Solomidou M, Zergioti I, Zafiropulos V, Papazoglou TG, Fotakis C (1996) Appl Spectrosc 50:1331
55. Clark RJH (1999) J Mol Struct 480/481:15
56. Castillejo M, Martin M, Silva D, Stratoudaki T, Anglos D, Burgio L, Clark RJH (2000) J Mol Struct 550/551:191
57. Lee JM, Watkins KG (2000) Opt Laser Eng 34:429
58. Vainos NA, Mailis S, Pissadakis S, Boutsikaris L, Dainty P, Parmiter PJM, Hall TJ (1996) Appl Optics 35:6304
59. Lazare S, Granier V (1990) Chem Phys Lett 168:593
60. Pettit GH, Ediger MN, Hahn DW, Brinson BE, Sauerbrey R (1994) Appl Phys A 58:573
61. Furutani H, Fukumura H, Masuhara H (1996) J Phys Chem 100:6871
62. Fukumura H, Mibuka N, Eura S, Masuhara H, Nishi N (1993) J Phys Chem 97:13761
63. Fujiwara H, Fukumura H, Masuhara H (1995) J Phys Chem 99:11844 and references therein
64. Lippert TK, Bennett LS, Nakamura T, Niino H, Yabe A (1996) Appl Surf Sci 96–98:601
65. Logan D, Wight CA, Apkarian VA (1997) Chem Phys 217:99
66. Ehring JH, Sundqvist BUR (1995) J Mass Spectr 30:1303
67. Venugopalan V, Nishioka NS, Mikic BB (1995) Biophys J 69:1259
68. Lippert T, Gerber T, Wokaun A, Funk DJ, Fukumura H, Goto M (1999) Appl Phys Lett 75:1018
69. Wei J, Hoogen N, Lippert T, Nuyken O, Wokaun A (2001) J Phys Chem 105:1267
70. Lippert T, Nakamura T, Niino H, Yabe A (1997) Appl Surf Sci 109–110:227
71. Yingling YG, Zhigilei LV, Garrison BJ (2001) Photochem Photobiol A 145:173
72. Lippert T, Yabe A, Wokaun A (1997) Adv Mater 9:105
73. Larciprete R, Stuke M (1987) Appl Phys B 42:181
74. Fujiwara H, Nakajima Y, Fukumura H, Masuhara H (1995) J Phys Chem 99:11481
75. Lippert T, Stoutland PO (1997) Appl Surf Sci 109/110:43
76. Arnold BR, Scaiano JC (1992) Macromolecules 25:1582
77. Webb RL, Langford SC, Dickinson JT, Lippert TK (1998) Appl Surf Sci 127–129:815
78. Lippert TK, Langford SC, Wokaun A, Georgiou S, Dickinson JT (1999) J Appl Phys 86:7116
79. Grivas C, Niino H, Yabe A (1999) Appl Phys A 69:S159

80. Haselbach E, Rohner Y, Suppan P (1990) Helv Chim Acta 73:1644
81. Rabek JF (1987) Mechanisms of photophysical processes and photochemical reactions in pPolymers: theory and applications. Wiley, Chichester
82. Haward RN, Young RJ (eds) (1997) The physics of glassy polymers, 2nd edn. Chapman & Hall, London
83. Lassithiotaki M, Athanassiou A, Anglos D, Georgiou S, Fotakis C (1999) Appl Phys A 69:363
84. Athanassiou A, Andreou E, Anglos D, Georgiou S, Fotakis C (1999) Appl Phys A 86:S285
85. Athanassiou A, Lassithiotaki M, Anglos D, Georgiou S, Fotakis C (2000) Appl Surf Sci 154/155:89
86. Andreou E, Athanassiou A, Fragouli D, Anglos D, Georgiou S (2002) Laser Chem 20:1
87. Athanassiou A, Andreou E, Bonarou A, Tornari V, Anglos A, Georgiou S, Fotakis C (2002) Appl Surf Sci 197–198:757
88. Athanassiou A, Andreou E, Fragouli D, Anglos D, Georgiou S, Fotakis C (2001) J Photochem Photobiol A 145:229
89. Noyes RM (1961) Prog React Kinet 1:29
90. Fournier I, Tabet JC, Bolbach G (2002) Int J Mass Spectrom 219:515
91. Krajnovich DJ (1997) J Appl Phys 82:427
92. Krajnovich DJ, Xazquez JE (1993) J Appl Phys 73:3001
93. Ichimura T, Mori Y, Shinohara H, Nishi Y (1994) Chem Phys 189:117 and references therein
94. Tsuboi Y, Hatanaka K, Fukumura H, Masuhara H (1994) J Phys Chem 98:11237
95. Koubenakis A, Elimioti T, Georgiou S (1999) Appl Phys A 69:637
96. Yingling YG, Zhigilei LV, Garrison BJ, Koubenakis A, Labrakis J, Georgiou S (2001) Appl Phys Lett 78:1631
97. Koubenakis A, Labrakis J, Georgiou S (2001) Chem Phys Lett 346:54
98. Preuss S, Spath M, Zhang Y and Stuke M (1993) Appl Phys Lett 62:3049
99. Baudach S, Krüger J, Kautek W (2001) Rev Laser Eng 29:705
100. Vogel A, Noack J, Hüttmann G, Paltauf G (2002) Proc SPIE 4633A:1
101. König K, Riemann I, Fritsche W (2001) Opt Lett 26:819
102. Mahan GD, Cole HS, Lin YS, Philipp HR (1988) Appl Phys Lett 53:2377
103. Gusev VE, Karabutov AA (1993) Laser optoacoustics. American Institute of Physics, New York
104. Hare DE, Franken J, Dlott DD (1995) J Appl Phys 77:5950
105. Lee I-YS, Wen X, Tolbert WA, Dlott DD, Doxtader D, Arnold DR (1992) J Appl Phys 72:2440
106. Zweig AD, Venugopalan V, Deutch TF (1993) J Appl Phys 74
107. Siano S, Pini R, Salimbeni R (1999) Appl Phys Lett 74:1233
108. Hopp B, Csete M, Révész K, Vinkó J, Bor Z (1996) Appl Surf Sci 96/98:611
109. Wagner F, Hoffmann P (1999) Appl Phys A 69:S841
110. Vest CH (1971) Holographic interferometry. Academic, New York
111. Bonarou A, Antonelli L, Tornari V, Georgiou S, Fotakis C (2001) Appl Phys A 73:647
112. Smith JW, Kramer EJ, Mills PJ (1994) J Polym Sci B: Polym Phys 32:1731
113. Wu S (1982) Polymer interface and adhesion. Marcel Dekker, New York
114. Callister WD (1997) Materials science and engineering: an introduction. Wiley, New York
115. Lokhandwalla M, Sturtevant B (2000) Phys Med Biol 45:1923
116. Blanchard D, Casalengo R, Pierre M, Trommsdorff HP (1988) J Appl Phys 65:3351
117. Watanabe S, Flotte TJ, McAuliffe DJ (1988) J Invest Dermatol 90:761
118. Doukas AG, McAuliffe DJ, Flotte TJ (1993) Ultrasound Med Biol 19:137

Adv Polym Sci (2004) 168: 51–246
DOI: 10.1007/b12682

Laser Application of Polymers

Thomas Lippert

Paul Scherrer Institut, 5232 Villigen-PSI, Switzerland
E-mail: Thomas.lippert@psi.ch

Abstract Laser ablation of polymers has been studied with designed materials to evaluate the mechanism of ablation and the role of photochemically active groups on the ablation process, and to test possible applications of laser ablation and designed polymers. The incorporation of photochemically active groups lowers the threshold of ablation and allows high-quality structuring without contamination and modification of the remaining surface. The decomposition of the active chromophore takes place during the excitation pulse of the laser and gaseous products are ejected with supersonic velocity. Time-of-flight mass spectrometry reveals that a metastable species is among the products, suggesting that excited electronic states are involved in the ablation process. Experiments with a reference material, i.e., polyimide, for which a photothermal ablation mechanism has been suggested, exhibited pronounced differences. These results strongly suggest that, in case of designed polymers which contain photochemically active groups, a photochemical part in the ablation mechanism cannot be neglected. Various potential applications for laser ablation and the special photopolymers were evaluated and it became clear that the potential of laser ablation and specially designed material is in the field of microstructuring. Laser ablation can be used to fabricate three-dimensional elements, e.g., microoptical elements.

Keywords Laser ablation · Ablation mechanism · Photopolymers · Polyimide · Spectroscopy

1 Introduction

1.1 Laser Ablation History

At the ripe age of 40 years old (the first laser, i.e., ruby laser, was reported in 1960 by T.H. Maiman [1]; in 1954 there were masers [2], the abbreviation also being used for “means of attaining support for expensive research” [3]), the laser has become a mature technological device with many applications.

This was not always true, of course. For many years, the laser was viewed as "an answer in search of a question". That is, it was seen as an elegant device, but one with no real useful application outside of fundamental scientific research. In the last two to three decades however, numerous laser applications have moved from the laboratory to the industrial workplace or the commercial market.

Lasers are unique energy sources characterized by their spectral purity, spatial and temporal coherence, and high average peak intensity. Each of these characteristics has led to applications that take advantage of these qualities:

- Spatial coherence: e.g., remote sensing, range finding and many holographic techniques.
- Spectral purity: e.g., atmospheric monitoring based on high-resolution spectroscopies.
- and of course the many other applications in communication and storage, e.g., CDs.

All of these high-tech applications have come to define everyday life in the late twentieth century. One property of lasers, however, that of high intensity, did not immediately lead to "delicate" applications but rather to those requiring "brute force". That is, the laser was used in applications for removing material or heating. The first realistic applications involved cutting, drilling, and welding, and the laser was little more advanced than a saw, a drill, or a torch. In a humorous vein A.L. Schawlow proposed and demonstrated the first "laser eraser" in 1965 [4], using the different absorptivities of paper and ink to remove the ink without damaging the underlying paper. Other early applications [5] used a laser to generate plasma at the surface of a solid, and the resulting spectral emission could be used for elemental analysis. Vastly more expensive than traditional tools, however, the laser only slowly found niche uses where its advantages made up for the added cost and complexity.

The early work by Brech and Cross [5] and the following work on energy of ions by time-of-flight [6] and of the emission of electrons and ions [7] led to the development of laser mass spectroscopies and the first commercial instrument in 1978 (Leybold-Heraeus). Other important papers appeared on laser photoemission [8], photography of ablation plumes [9], ablation of biological material [10], temperatures of plumes by rotationally and vibrationally resolved emission bands [11], clusters in ablation plumes [12], the first suggestion of laser fusion [13], vacuum ultraviolet generation [14], neutron- [15], and x-ray emission [16], multiply charged ions [17], and two- [18] and three-photon excited photoemission [19]. The first laser deposition of thin films was demonstrated by 1965 [20], but the films were of poor quality. During the 1970s and early 1980s the development and understanding of laser ablation was incremental and steady. In 1982, laser ablation of polymers was first reported nearly simultaneously by two groups (Y. Kawamura et al. [21] and R. Srinivasan et al. [22]). Srinivasan became

one of the leaders in the field of polymer ablation, while the Japanese group did not follow up on their discovery. Srinivasan probably also first used the term *laser ablation* which is now common language. The discovery of laser ablation of polymers sparked research in this field in many groups around the world. Nowadays, laser ablation of polymers is industrially used to prepare the via-holes in multichip modules through polyimide at IBM [23] and for the production of the nozzles for inkjet printers [24] (also polyimide).

Another important development of laser ablation started in 1983, when the first deposition of a superconducting film by laser ablation was reported [25], but became only well-known after reinvention in 1987 for thin films of high-temperature superconductors (Y-Ba-Cu-oxides) [26].

Several other laser ablation-based methods "came of age" in the late 1980s. Particularly spectacular has been the growth of laser-based medical procedures [27], such as laser-based ophthalmology (LASIK); in dermatology for the removal of birthmarks, tattoos, and smoothing of wrinkled skin; laser surgery for internal arthroscopic cutting and for arterial angioplasty; and in the future maybe for dental applications.

Laser ablation-based microanalysis techniques have also become very successful, e.g., matrix-assisted laser desorption/ionization (MALDI) has revolutionized the identification and study of large molecular weight biomolecules and polymers [28, 29].

Finally, extremely high-power laser ablation has paved the way to the generation of pulsed tabletop x-ray [30] and neutron sources [31].

As a paradigm for the evolving sophistication of laser ablation, the laser eraser described by Schawlow 30 years ago has now become a tool for graffiti removal, and more delicately for art restoration, e.g., paintings [32] and parchments [33].

Nowadays, the field of laser ablation may be divided as follows:

Micro-Structuring: lasers are used to remove material from various substrates to create (2- and) 3-dimensional structures.

Deposition: the ablated material is used to create thin films (from single crystalline to amorphous) of even complex stoichiometries on various substrates. The most common techniques are pulsed laser deposition (PLD) and laser ablation transfer (LAT). The applications of these films range from high Tc superconductors to films for improving surface properties.

Microanalysis: the removed material can be analyzed, either with optical methods, e.g., plasma emission, or other techniques, e.g., mass spectroscopy (MALDI, ICP-MS, TOF-MS).

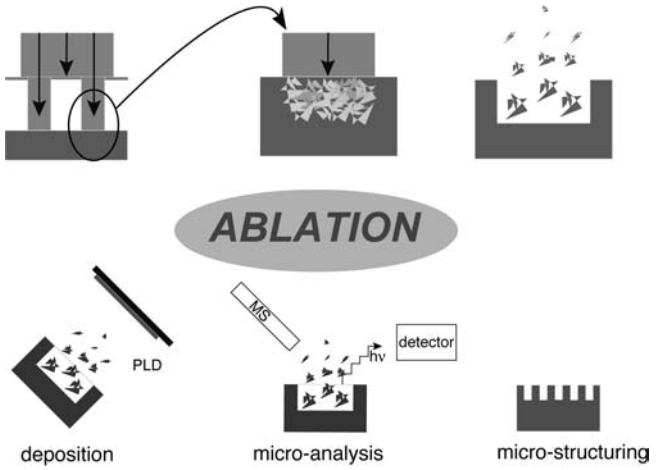

Fig. 1 Different applications of laser ablation

Various: creation of shock waves for high-pressure research; for laser plasma thrusters, and various other applications, e.g., pulsed X-ray generation. A scheme of the different fields of ablation is shown in Fig. 1.

Excellent summaries on various aspects of laser ablation can be found in various books [34–40] and recent reviews [41-47].

The vastly increasing research in laser ablation sparked many conference series (e.g., organized by SPIE, E-MRS) and even one biannual conference series focused solely on laser ablation (International Conference on Laser Ablation, COLA).

1.2 Laser Ablation of Polymers

During the last decade, processing of polymers has become an important field of applied and fundamental research [48]. One of the most important fields is laser ablation involving various techniques and applications. Laser ablation is used as an analytical tool for MALDI (matrix-assisted laser desorption/ionization) [28, 29] and LIBS (laser-induced breakdown spectroscopy) [49] or as a preparative tool for PLD (pulsed laser deposition) of inorganic materials [37] and of synthetic polymer films [50, 51]. Another application is surface modification of polymers [52]; if low fluences are applied, the polymer surface can be either chemically modified to improve adhesion [53], or it can be changed physically. This can be either a random increase [54] of the surface area or it can result in LIPMS (laser-induced periodic microstructures in the nm range) [54, 55], which have been suggested to be used for the alignment of liquid crystals. The application of high-energy UV

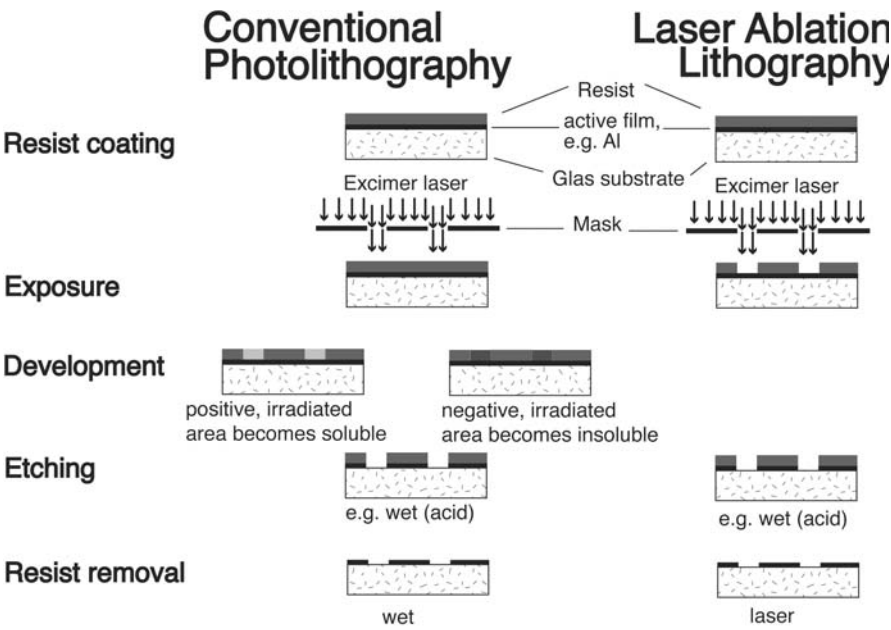

Fig. 2 Comparison between the process steps for conventional lithography and laser ablation lithography

lasers led to the discovery of a process termed ablative photodecomposition (APD) in 1982 [21, 22].

One of the most promising proposals for APD was for its application as a dry etching technique in photolithography. APD promised a higher resolution, due to the use of the shorter laser wavelength as compared to the traditional UV lamp (Hg-lamp) techniques, and a lower number of processing steps. The difference between standard photolithography and laser ablation is shown in Fig. 2. For a "real" dry etching technique there would be no need for a wet development. This would also eliminate a part of the liquid waste. Until now APD has mainly been used for producing via-holes in polyimide (PI) on MCM (multichip modules) [23] and not as a dry etching technique in photolithography. This is partly due to several disadvantages of APD compared to conventional photolithography. One reason is the comparison of lithography with APD using standard polymers such as PI, PET (polyethylene terephthalate) or PMMA [poly(methyl methacrylate)] [43, 54, 56, 57] which are designed for totally different applications, but are compared to the highly developed and specialized photoresists.

The other reason is the ongoing development and improvement of classical lithography, with methods such as chemical amplifying and phase shifting masks making it very difficult for laser ablation to compete with the standard methods. The microelectronics industry would only change a process if the new process were as least twice as good as the existing method

[58], and improvements on this scale can probably not be achieved by laser ablation.

1.2.1 *Mechanisms of Ablation*

One other important motivation of our research was the controversy over the mechanism of ablation. It has been suggested that the mechanism is either thermal, photothermal, or photochemical, or a mixture of these [54, 56, 57].

From an application standpoint, a photochemical mechanism would be most desirable. Photochemical decomposition would have an intrinsically higher resolution due to the lack of thermal damage to the surrounding area, and the polymer could be designed in a similar way to the photoresists, considering mainly the photochemical properties of various chromophores. In addition, it would be possible to design polymers which decompose mainly to gaseous products. This would delete the problem of redeposited material, the so-called debris. This incomplete removal of the polymer requires additional cleaning steps, thus losing one of the big advantages of APD—the lower number of processing steps.

The discussions about the mechanisms have gone on for more than two decades, but the original strict separation of the models (photochemical models by *chemists* and thermal/photothermal models by *physicists*) is slowly softening. It is generally agreed that in ns pulses the energy of the photons is transformed in a primary step into the energy of electronic excitation. However, subsequent steps in the ablation process may be very different. One problem for developing a complete model is the fact that the experimental data are measured by different techniques that yield nonequivalent results. Another problem is the application of different definitions, which results in additional problems. This is especially true for ablation near the threshold fluence for ablation. Some of the experimental facts that have to be explained by the models are:

- The ablation depths are measured by profilometry (optical interferometer, mechanical stylus [59], atomic force microscopy [60]) and starts sharply at the threshold fluence. Similar conclusions can be drawn from reflectivity [61] or acoustic measurements [62]. The problem with these measurements is that either single- or multi-pulse experiments are used to determine the ablation depths and threshold which might give different results.
- The ablation rates calculated from mass loss measurements using a quartz crystal microbalance (QCM) [63] or mass spectrometry [64] reveal a so-called Arrhenius tail [63] (linear increase of products at low fluences, followed by a much faster increase).
- The ablation is accompanied by chemical and/or physical (morphological) modifications of the polymer, e.g., for polyimide with an increase of electrical conductivity [65], change in optical transmission [66–68], and composition [69–71].

The different models and main features may be summarized as follows:

Photochemical models [56, 72–75]: Electronic excitation results in direct bond breaking.

Photothermal models [76–80]: Electronic excitations thermalize on a ps timescale, resulting in thermally broken bonds.

Photophysical models: Thermal and nonthermal features are important. The models consider two independent channels of bond breaking [81, 82], or imply different bond breaking energies for ground state and electronically excited chromophores [83, 84]. These models are mainly important for short pulse (ps and fs) lasers [85].

The models (photochemical and thermal) can be subdivided into *volume* and *surface* models. The processes responsible for ablation in surface models only take place within several monolayers of the surface. As a result, the velocity of the interface between the gaseous and condensed phase depends explicitly on the surface temperature or laser intensity. With volume models, the processes resulting in ablation take place within the bulk of the material.

The volume and surface models are:

Photochemical surface models [86], which normally require longer interaction times and/or higher laser fluences.

Photochemical volume models [56, 57, 72–74], reveal sharp ablation thresholds and lead to logarithmic dependence of the ablated depths per pulse. Such models may also result in a linear dependence if the movement of the ablation front is taken into account, and if the screening by ablation products is ignored. These models cannot explain the previously described Arrhenius tails observed in mass loss measurements.

Thermal surface models [79, 80, 82, 87], (developed mainly for metal ablation [88]) do reveal smooth Arrhenius tails, due to the Arrhenius dependence of the recession velocity on temperature. These models cannot describe the sharp ablation threshold of polymers.

Thermal volume models are quite often oversimplified [63, 78], because they ignore the influence of the moving boundary on the heat equation [77], which results in unrealistically high temperatures (and may also not report the Arrhenius tail).

In newer models, different models are combined, i.e., the volume features of the photochemical models and the features of the thermal surface models, resulting in a *volume photothermal* model [89]. In this model, ablation is described on the basis of photothermal bond breaking within the bulk material

(with a first-order chemical reaction), which can be described by an Arrhenius law. Ablation starts when the density of broken bonds at the surface reaches a certain critical value. With this model the sharp threshold and the Arrhenius tail can be modeled.

One comment is appropriate here. The modeling of ablation depths at high fluences is not sensitive to the underlying mechanisms of ablation itself. At such fluences ablation rates of most polymers are quite similar [90] and are determined by screening of the radiation by the ablated products [80, 82] or generated plasma [91].

This above described *volume photothermal* model was only applied for polyimide and does not take into account that photochemical decomposition is possible. This model, like all other thermal models, needs many material parameters for the calculations. Several of these parameters are obtained from fitting to data, or they use material parameters which might change upon heating (e.g., thermal conductivity or specific heat). For some of these parameters the temperature dependence is known, but only for a limited temperature range (up to a few hundred K) and for relatively slow heating rates (up to several K per second). For laser ablation conditions the temperature range is extrapolated to high temperatures (up to several thousand K), and for heating rates of up to 10^{10} K s^{-1}.

Another important feature of ablation, which is never discussed in the photothermal models was repeatedly emphasized by Srinivasan [92]: the products of pyrolysis or ablation with a CO_2 laser are very different to the products of excimer laser ablation in the UV. This suggests that different processes take place between pyrolysis (thermal decomposition) and UV laser ablation.

A different model describes one specific aspect of laser ablation, i.e., the thermalization of the laser energy in doped polymers. This model is based on spectroscopic data (time-resolved absorption/emission measurements [93, 94] and TOF-MS data [95]), but is mainly valid for irradiation with wavelengths $\geq$248 nm, and for polymers which contain polyaromatic compounds as dopants. The mechanism involves a *cyclic multiphotonic absorption* process with up to ten photons [96]. From the highly excited polyaromatic dopant molecules, the photon energy is transferred to the polymer matrix via rapid internal conversion. The associated temperature increase results in the thermal decomposition of the polymer. From the time-dependent absorption studies it was suggested that, in view of their longer lifetimes, excited triplet states should play a key role in this process.

The multiphoton absorption cycle was confirmed by a comparison of the temporal profile of the fluorescence of anthracene-doped polystyrene films with computational results based on the cyclic process [97]. In the computational studies, the ground state, first excited singlet state, and lowest triplet state have been included. The calculated temperature rise during the laser pulse depends nonlinearly on the laser intensity. Rapid internal conversion within the triplet manifold is the most effective mechanism for depositing heat at the irradiated surface.

The progress in computational methods (hardware and software) has led to the development of different types of models for laser ablation. These models are based on molecular dynamics (MD) calculations [98–100]. To gain a microscopic view of laser ablation the breathing sphere model was developed. In this model, each molecule (or an appropriate group of atoms) is represented by a single particle that has the true translational degrees of freedom but an approximate internal degree of freedom [101, 102]. This internal (breathing) mode allows one to reproduce a realistic rate of conversion of internal energy of the laser-excited molecules to translational motion. Since the molecules rather than the atoms are the particles of interest in the model, the system size can be large enough to model the collective dynamics leading to laser ablation and damage. Since the high-frequency atomic vibrations are not followed, it is possible to use longer time-steps in the numerical integration and therefore keep track of the process for longer [103]. This model yields a microscopic view of ablation [101–104] and the parameters of the ejected plume (velocity distribution of matrix and analyte for MALDI [105, 106], cluster ejection [103, 107, 108], and their dependence on the irradiation conditions, i.e., laser fluence [101, 102, 104, 107], pulse duration [103], and initial temperature of the sample [108]). One effect that cannot be directly simulated within the breathing sphere model is the propagation of the laser-induced pressure waves from the absorption region deeper into the bulk of the irradiated sample. Therefore, the MD model was combined with the continuum finite element method [109], which allows the study of the long-range propagation of waves and their interaction with other MD regions of a large system. One possible effect of such interaction is the reflection of the compressive (due to the ablation recoil) pressure wave from the free surface at the back of the irradiated sample which can cause the effect known as back spallation [110] (dynamic tensile strength of the material is exceeded by the reflected pressure wave) or extensive material removal on the front side [111].

The plume development in MD simulations can only be followed up to a few nanoseconds after the pulse, which is not enough to compare the data with various experimental techniques (such as MALDI, TOF-MS, shadowgraphy, interferometry, or for PLD). The long-term plume expansion is then modeled by the direct simulation Monte Carlo method, which was recently applied to systems relevant to MALDI [112].

Detailed comparisons of the model data with experimental results, or even better with time-resolved experimental data, are limited. Future studies could validate these models by the above-mentioned comparison with experimental data (especially for ablation, while for MALDI already more data exist).

1.2.2 *Why Special Polymers?*

The need for an ever-increasing resolution in photolithography has resulted in an ongoing improvement of laser systems which have replaced UV lamp systems for high-resolution applications. The decrease of the irradiation

wavelength resulted also in a need for new photoresist systems. For the traditional UV lamp system, diazoquinones in Novolac are employed [113], whereas for 248-nm irradiation, chemical amplification (CA) systems based on poly(hydroxystyrenes), where the hydroxy group is protected by an acid-labile functionality such as t-butoxycarbonyl, and a photochemical acid generator, e.g., an onium salt, are used [114]. To reach minimum feature sizes of 140 to 180 nm it is necessary to develop photolithography for 193-nm irradiation [115]. Due to the high absorption coefficient of styrene groups at 193 nm it is again necessary to develop new photoresist systems. At IBM, resists based on acrylic polymers are being developed [115], whereas at AT&T polymers based on cycloolefin–maleic anhydride copolymers are being tested [116]. Both of these systems are CA systems using a photochemical acid generator, plasma etching stabilizers, and some dissolution inhibitors.

An alternative approach to the complicated photoresist systems could be the application of APD (ablative photodecomposition), where a strong absorbance at the irradiation wavelength is one of the conditions for successful ablation. A logical approach to the use of APD as a dry etching technique in microlithography is the development of polymers designed for APD. This is especially true for photolithographic applications that do not require a submicron resolution, such as thin film transistor (TFT) fabrication for liquid crystal displays (LCD) which require a resolution around 1 μm.

We started to apply polymers designed for ablation in the early nineties. As an irradiation source we chose a XeCl excimer laser emitting at 308 nm. This laser wavelength has the following advantages: HCl as the halogen source is easier to handle than the F_2 required for the KrF lasers; high-power XeCl industrial lasers are the most advanced on the market, and the output level is sustained for more than 8 h of continuous operation; the 308 nm wavelength is also more forgiving than the deep-UV radiation; and typical optical materials and coatings have lower absorption and higher damage thresholds at 308 nm as compared to 248 nm or even 193 nm.

2
Ablation Mechanisms of Novel Photopolymers

2.1
Synthesis

The first step for the development of polymers sensitive to 308-nm irradiation was the designing of various photolabile compounds for physical doping (solvent mixing) of polymers [117, 118]. The best results have been achieved by using triazene (–N=N–N–) or pentazadiene compounds (–N=N–N(R)–N=N–). The π-π^* transition of the –N=N–X– chromophore is located around 300 nm [119].

The photochemical decomposition of these molecules yields N_2 and other gaseous products. Maximum ablation rates of up to 80 μm/pulse could be achieved which is the highest rate reported for a synthetic polymer [118].

The gaseous products act as a driving force of ablation and some indications were found suggesting that the photochemical properties of the dopants influence the ablation characteristics. Encouraged by these results the synthesis of polymers containing the –N=N–X– chromophore in the polymer main chain was started. The first polymer containing the –N=N–N– chromophore in the polymer chain is shown in Scheme 1, structure A.

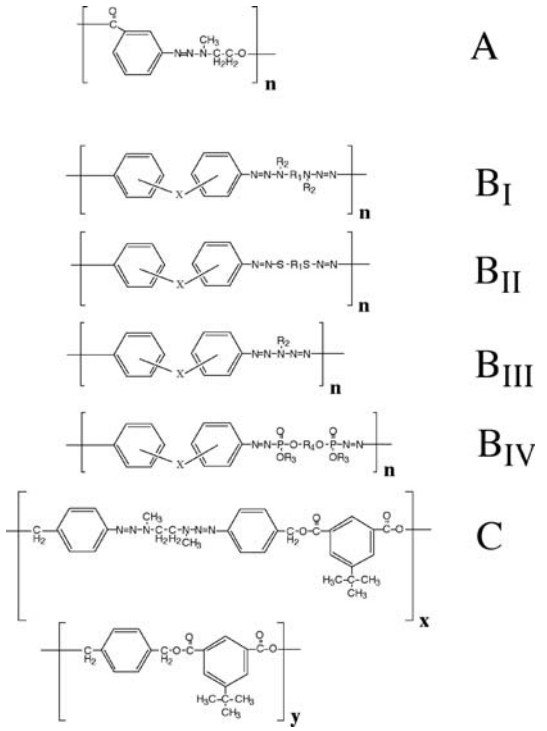

Scheme 1 Chemical structures of the different nitrogen-containing polymers, with X=CO, SO_2, O, HC=CH, and R=aliphatic groups

The polymer was synthesized by polycondensation of an aryl dialkyl triazene compound containing a meta-COOH group in the aryl part and an OH-group in the alkyl part of the compound. Both the ablation characteristics (e.g., quality of ablation structure) and the properties of the polymer (e.g., low molecular weight (M_w), glass transition temperature (T_g) below room temperature, and the long synthesis time (>48 h)) were not satisfactory [120]. Therefore, we modified our approach to a two-step synthesis, shown in Scheme 2 [121, 122], which results in polymers of the general structure B in Scheme 1.

The synthetic method is an interfacial polycondensation. An aromatic bis-amino compound is converted into a bis-diazonium salt. The next step, without further purification of the diazonium salt, is the reaction with an organic

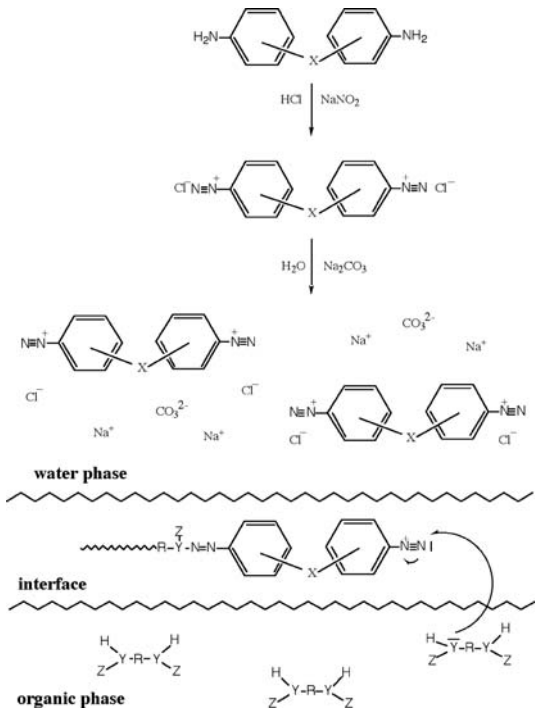

Scheme 2 Synthesis scheme of the interfacial polycondensation used for the preparation of the nitrogen-containing polymers. X and R are described in Scheme 1, Y and Z are aliphatic groups

compound at the interface of the vigorously stirred solution. The resulting polymers are precipitated out of the solution. The main difference between the various polymers is the organic compound. For the triazene polymer (TP), B_I, a bifunctional aliphatic secondary amine, for B_{II} (diazosulfide polymer, DASP), an aromatic 1,3-benzenedithiol, for B_{III} (pentazadiene polymer, PAP), a bifunctional aliphatic primary amine of 1:2 stoichiometry, and for B_{IV} (diazophosphonate polymer, DAPP), a bis-alkyl phosphite compound has been used [123]. The compound C in Scheme 1 was synthesized by polycondensation of a triazene group-containing polyester with "normal" polyesters. The polyesters were synthesized by polycondensation of diacyl chlorides and diols. This approach allowed a continuous variation of the triazene content in the polymer. Polymers with 0, 1, 5, 20, 35, 50, 60, 75, 90, and 100 percent of the triazene-containing polyester have been synthesized [123].

Designed polymers of the last generation are based on the triazene polymers (structure B_I in Scheme 1) but containing a second functional group, which enables selective photocross-linking without destruction of the triazene chromophore. For this purpose it is crucial that both steps, i.e., photocross-linking and laser ablation, can be separately performed using differ-

ent irradiation wavelengths and intensities. Since the triazene chromophore shows a strong absorption between 300 and 350 nm and weak absorption at shorter wavelengths, the photocross-linkable groups should absorb at longer wavelengths (e.g., >395 nm). For this purpose monomers based on cinnamylidene malonic acids, which are known to photodimerize via [2+2] π-cycloaddition [124], were used as photocross-linkable groups. The substituted cinnamylidene malonic acids were synthesized by a Doebner condensation of cinnamoyl aldehyde with malonic acid using pyridine as a catalyst. The dichlorides were obtained by reacting the acids with thionyl chloride in the presence of potassium carbonate. The dichlorides were then reacted with diol compounds to give the triazene-containing polyesters and triazene-free polyesters [125], which were tested for ablation. The latter polyesters reveal a higher chemical stability than the triazene polymers [126].

2.2
Ablation Characteristics–Mechanism of Ablation

The following chapters summarize several studies on the evaluation of the ablation characteristics and the ablation mechanisms.

2.2.1
Etch Rates and Qualities

2.2.1.1
Introduction

The most common parameters to characterize the ablation of polymers are the ablation rates at various fluences, the threshold fluence, and the effective absorption coefficient. These values and the quality of the achieved structures can give first indications about the mechanism of ablation. For this study various designed polymers (described in more detail below) and one reference polymer were selected.

From the standpoint of ablation properties, triazene group (–N=N–N<)-containing laser resists have been identified as the most promising candidates. The triazene polymers reveal high etch rates, a good stability upon storage, and a high absorption coefficient at laser irradiation wavelengths of 308 and 351 nm. Unfortunately problems are encountered with the stability with respect to the following steps during a complete processing cycle, e.g., oxidation of the substrate [126]. Selected polyesters (PE) and polyester carbonates (PEC) have also been found to exhibit good ablation behavior [127]. The sensitivities of the PEs and PECs are lower as compared to the triazene-based polymers, but they exhibit a higher chemical stability. These polymers also produce small gaseous products (CO_2, CO) upon decomposition.

Introducing a functional ester group that enables selective photocross-linking without destruction of the polymer backbone can improve the stability of the polymers without changing the sensitivity to direct laser structur-

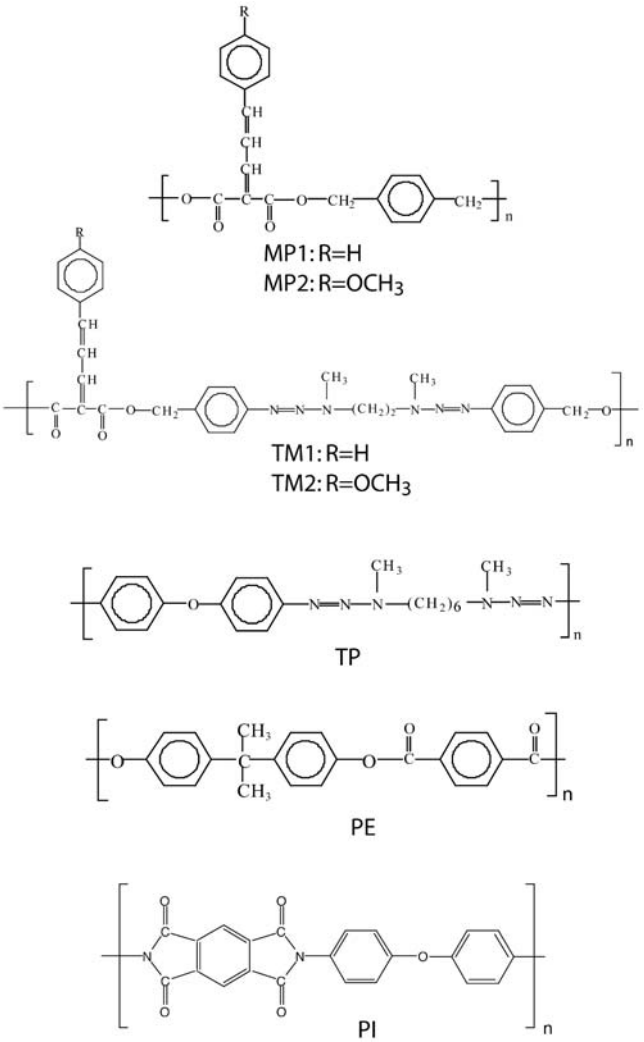

Scheme 3 Chemical structures of the polymers. REPRINTED WITH PERMISSION OF [Ref. 82], COPYRIGHT (2001) American Chemical Society

ing [128]. These polymers can function as positive (laser ablation) as well as conventional negative resists. An application could be envisioned where first a large-scale structuring, using standard negative resist methods, is followed by a positive (i.e., laser ablation) step to structure the remaining areas in more detail. The order of processing can be reversed without altering the quality of the structures [129].

The chemical structures of the tested polymers TM1, TM2, MP1, and MP2 are shown in Scheme 3. TM1 and TM2 contain triazene functional groups,

whereas MP1 and MP2 are the polyesters without the triazene groups. To compare the ablation properties of these polymers several other polymers were included as references in this study, i.e., polyimide (PI, Kapton from Goodfellow) as representative of a highly absorbing "standard "polymer, a commercial polyester (PE, Bayer AG) as representative of standard ester polymers, and TP, as representative of the original triazene polymers, without the photocross-linkable ester group.

The polymers, TM1, TM2, MP1, and MP2, were synthesized using a standard polycondensation reaction. The synthesis is described in detail elsewhere [125]. Photocross-linking of the polymers was realized by irradiation at λ>395 nm for 20–40 min at an irradiance of 100 mW cm^{-2}, resulting in cross-linking yields greater than 50%. After cross-linking, the polymers are named TM2C, MP1C, and MP2C.

2.2.1.2
Results

Physical Properties of the Polymers. All polymers in this study can be classified as highly absorbing polymers ($\alpha_{lin} \geq 8000$ cm^{-1} at the irradiation wavelength of 308 nm), as shown in Table 1. Cross-linking reduced the absorption coefficient only slightly for the triazene-containing polymer, while for

Table 1 Chemical properties and ablation parameters of the polymers

	α_{308}[a] (cm^{-1})	ε_{308}[c] (M^{-1} cm^{-1})	α_{eff}LF[d] (cm^{-1})	F_{th}LF[e] (mJ cm^{-2})	α_{eff}HF[f] (cm^{-1})	F_{th}HF[g] (mJ cm^{-2})
MP1	102,000	27,400	50,700±2,100	63±3	16,200±700	343±42
MP1C	39,000[b)]	n.m.	49,000±2,700	66±4	17,200±800	323±43
MP2	32,000	7,100	57,000±2,000	48±3	20,600±1,800	269±59
MP2C	17,000[b)]	n.m.	57,600±3,200	53±3	22,800±1,600	229±40
TM1	69,000	57,000	56,100±3,400	27±2	14,400±900	410±46
TP	100,000	27,700	49,800±2,900	27±2	16,700±1,100	317±63
TM2	92,000	35,600	53,300±2,500	28±2	18,500±1,200	225±40
TM2C	81,000[b)]	n.m.	49,700±2,300	31±3	18,600±1,300	236±36
PI	95,000	n.m.	83,300±3,400	60±3	17,400±1,500	508±65
PE	8,000	1,000	51,500±3,200	73±4	19,200±1,600	340±60

[a] Linear absorption coefficient at 308 nm determined by UV spectroscopy and profilometry

[b] Linear absorption coefficient at 308 nm calculated from UV spectroscopic data after photocross-linking

[c] Molar extinction coefficient measured in solution

[d] Effective absorption coefficient calculated from Eq. 1 at low fluences

[e] Threshold fluence calculated from Eq. 1 at low fluences

[f] Effective absorption coefficient calculated from Eq. 1 at high fluences

[g] Threshold fluence calculated from Eq. 1 at high fluences

n.m.: not measured (insoluble)

MP1 a very pronounced reduction was observed. The novel polymers were especially selected according to the criterion of similar α_{lin}, which would allow a direct comparison of the polymers. This could be accomplished for the high end of absorptivity for four different polymers, i.e., TP, TM2, MP1, and PI. The glass transition temperatures, T_G, are very similar for all designed polymers, i.e., 63 °C for TP, 73 °C for TM1, 79 °C for TM2, 64 °C for MP1, and 74 °C for MP2. The cross-linked polymers reveal no T_G. The decomposition temperatures range from 227 °C for TP, 245 °C for TM1, and 248 °C for TM2 to 321 °C for MP1, 327 °C for MP2 to around 500 °C for PI. This shows that the decomposition temperatures of the bifunctional polymers (triazene + ester group) are governed by the triazene group.

Ablation at High Fluences (0.5–10 J cm^{-2}). The etch rates (etch depth/pulse) at high fluences were calculated from linear plots of the etch depths vs pulse number at a given fluence. All plots were linear, showing no incubation behavior as expected for highly absorbing polymers.

The etch rates versus the natural logarithm of the fluence are shown for all polymers in Fig. 3a. The etch rates increase approximately linearly at lower fluences (0.5–6 J cm^{-2}). The highest etch rate of ≈2.3 μm/pulse at a fluence of 10 J/cm^2 was measured for TCP1, but the difference to the etch rates of the other polymers is quite small (shown in Fig. 3b). The triazene-containing polymers exhibit slightly higher etch rates than the nontriazene-containing polymers. Photocross-linking has only minor effects on the etch rates at high fluences as shown by the very similar etch rates determined before and after photocross-linking.

The ablation parameters, α_{eff} (effective absorption coefficient) and F_{th} (threshold fluence) were calculated according to Eq. 1 [73, 130],

$$d(F) = \frac{1}{\alpha_{eff}} \ln\left(\frac{F}{F_{th}}\right) \quad (1)$$

where d(F) is the etch rate (etch depth per pulse). The calculated values for α_{eff} and F_{th} are summarized in Table 1, and are quite different from the values obtained at low fluences (see below and Table 1). The effective absorption coefficient, which is a measure of the penetration depth of the laser, depends strongly on the applied laser fluence. Several factors can account for this fact, i.e., the incoming photons are absorbed by ablation products in the gas phase and polymer film. These products can be either neutrals or, more likely, radicals. At higher fluences and therefore greater ablation depths, more products are formed. The absorption is also dependent on the lifetime of the products [92]. The lifetime is strongly dependent on the complexity of the molecules. The more complex the molecule, the longer the lifetime. In the condensed phase, as in the case of PI, such radical intermediates can persist for time periods of the order of nanoseconds (laser pulse ≈20 ns). The importance of this fact to the UV laser decomposition of, e.g., PI, lies in the UV absorption characteristics of free-radical intermediates. Their strongly delocalized electrons will result in a more intense absorption of the incom-

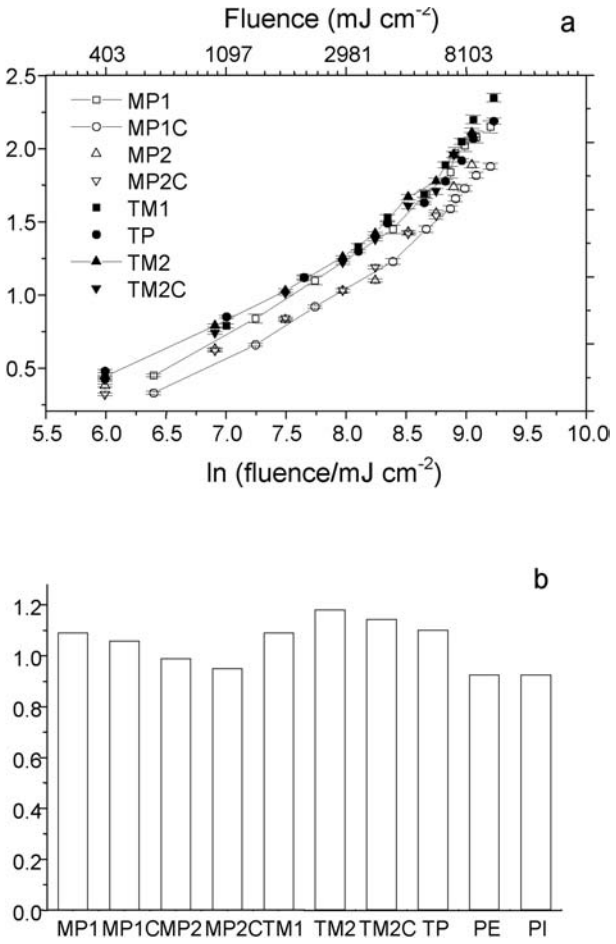

Fig. 3. a Measured etch rates as a function of natural logarithm fluence at high fluences (0.5 to 10 J cm^{-2}). **b** Calculated etch rates of all polymers at 2,000 mJ cm^{-2}. REPRINTED WITH PERMISSION OF [Ref. 82], COPYRIGHT (2001) American Chemical Society

ing radiation than PI itself. Their contribution to the absorption will be determined by their stationary concentration, i.e., the ratio of their rate of formation to their rate of disappearance. The other important factor is the absorption of the incoming photons by the laser-created plasma, which is observed at high fluences. The absorption of the incident laser radiation is quantitatively described in the model of the moving interface by Lazare et al. [91, 131]. In general, lower effective absorption coefficients are obtained compared to the linear absorption coefficients, which suggests that bleaching [68, 132] and/or decomposition of the absorbing chromophore takes place during irradiation [133].

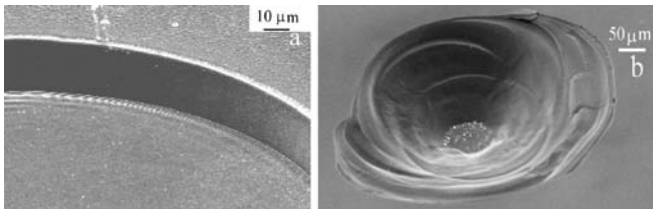

Fig. 4 SEM micrographs of craters ablated with high fluences. **a** TM2 irradiated at 8.5 J cm^{-2} with 10 pulses. **b** MP2C irradiated at 7.3 J cm^{-2} with 11 pulses. REPRINTED WITH PERMISSION OF [Ref. 82], COPYRIGHT (2001) American Chemical Society

The calculated etch rates (Eq. 1) at 2000 mJ/cm^2 of polymers are shown in Fig. 3b. The ablation rates were calculated from ablation plots, such as Fig. 3a, for identical fluences to allow a direct comparison of different polymers.

The etch rates of the triazene-containing polymers, TM1, TM2, and TP, are around 1100 nm/pulse, which is slightly higher than for the nontriazene-containing polymers, MP1 and MP2. The polyester (PE) and polyimide (PI) exhibited slightly lower etch rates (≈900 nm).

The morphology of the polymer films after laser ablation was examined using a scanning electron microscope (SEM). In Fig. 4 the SEM micrographs of the structures in TM2 and MP2C are shown as examples. Generally, well-defined circular craters are created on all polymers with the exception of MP2C. Sharp edges and smooth bottoms are obtained, as shown in Fig. 4a, indicating no pronounced thermal damage. Almost no ejected material is deposited around the craters. A clean surface is important for the application of laser ablation in lithography. In the case of MP2C, craters with lower structural quality are obtained for fluences above 7 J cm^{-2}. The resulting craters are very irregular as shown in Fig. 4b. The diameter is about 600 μm, which is much larger than the 280 μm diameter of the beam and of the craters in the other polymers. A similar phenomenon was observed for TP in a previous study [111]. It has been suggested that the larger crater is due to a shock wave, which was created by the ablation process. The shock wave is reflected from the substrate, causing the spallation of a larger area of the polymer film. Shock waves in the polymer film of TP were also detected previously [133]. However, no such irregular craters are observed for TM1, probably due to a different thickness of the polymer film. Regular craters are obtained in MP2C for fluences lower than 7 J cm^{-2}, indicating a threshold fluence for the creation of these large areas of damage.

Ablation at low fluences (up to 400 mJ cm^{-2}). The high fluence range is mainly interesting for applications where high ablation rates in small areas are important, e.g., drilling or cutting. The low fluence range offers the opportunity to study the influence of structural parameters on the ablation rates. The low fluence range is also important for lithographic applications, where the cost of producing the photons is important. Low fluences are de-

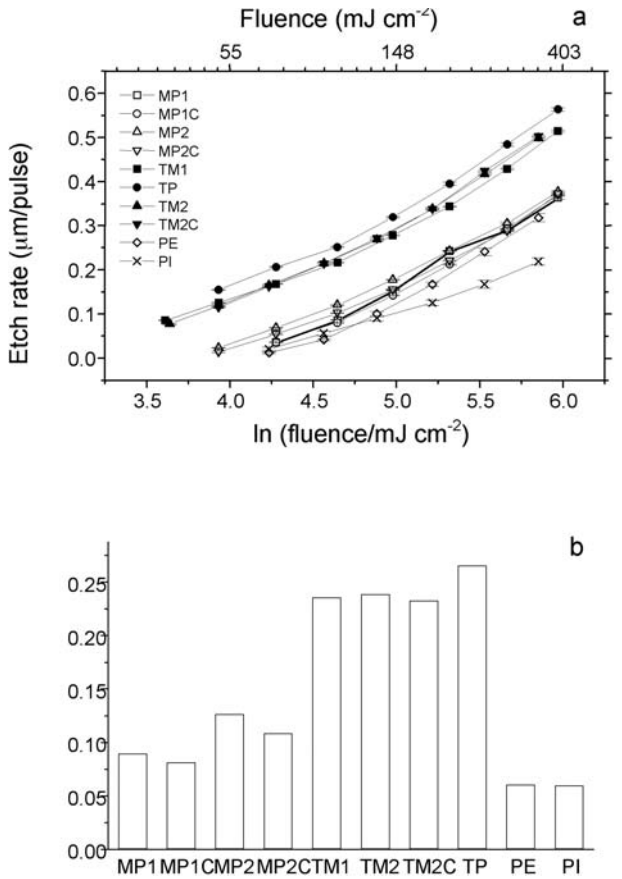

Fig. 5. a Etch rates at low fluences (up to 400 mJ cm^{-2}) as a function of the natural logarithm of the laser fluence. **b** Calculated etch rates at 100 mJ cm^{-2} for all polymers. REPRINTED WITH PERMISSION OF [Ref. 82], COPYRIGHT (2001) American Chemical Society

fined in this study from 10 to 400 mJ cm^{-2}. The etch rates were determined according to the procedure described for the high fluence. Linear plots of the etch depths vs the pulse number were also obtained. A plot of the etch rates versus the natural logarithm of the fluences is shown in Fig. 5a. A satisfactory linearity between etch rates and the logarithm of fluence is obtained. The designed polymers (MPs, TMs and TP) can be divided into two groups with respect to the etch rates (shown in Fig. 5a). All triazene-containing polymers have significantly higher etch rates than the other polymers. The designed polyesters (MPs), as well as PE, reveal a higher etch rate than PI. The etch rate is independent from α_{lin} (see Table 1) and determined by the chemical structure. In Fig. 5b a comparison of the calculated etch rates at 100 mJ cm^{-2} is shown for all polymers. The etch rates of nontriazene-con-

taining polymers, MP1 and MP2, are approximately 100 nm/pulse, which is about half the value of the triazene-containing polymers, TM1, TM2, and TP. A slightly higher etch rate is obtained for TP, which has the highest triazene density per polymer chain. The etch rates of the PE and PI are about 60 nm/pulse, which is again about half of the value of the designed polyesters. This is remarkable because the linear absorption coefficients of the designed polyesters (including the cross-linked) cover the same broad range as PE and PI.

The effective absorption coefficient, α_{eff}, and threshold fluence, F_{th}, were calculated according to Eq. 1 and are summarized in Table 1. The α_{eff} values calculated at low fluences are much larger than those obtained at high fluences. The effective absorption coefficients do not correlate with the linear absorption coefficients (Table 1), maybe with the exception of PI. A difference between the values of α_{eff} and α_{lin} is observed for most polymers. An important feature is the similarity of α_{eff} for all designed polymers, including PE ($\approx$54,000$\pm$5000 cm^{-1}), while PI reveals a much higher value (Table 1).

From an economic point of view, a polymer with a threshold fluence as low as possible is most desirable. The threshold fluences of the triazene-containing polymers, TM1, TM2, and TP, are about 30 mJ/cm^2, which is much lower than those for the nontriazene-containing polymers, MP1 and MP2 ($\approx$60 mJ cm^{-2}). These values are, to our knowledge, the lowest threshold fluences reported for laser ablation of polymers at 308 nm. The threshold fluence of TP obtained from this study is in good agreement with the value determined previously by UV spectroscopy [134]. The calculated threshold fluences (from Eq. 1), shown in Table 1), also agree very well with the experimentally observed threshold fluences (i.e., from the onset of ablation measured by the profilometer). The threshold fluences of the cross-linked polymers are slightly higher than for noncross-linked polymers (see Table 1), suggesting that cross-linking has a minor influence on the ablation properties of the polymers.

The appearance of the craters obtained at low fluences varies partly from the morphologies of the craters formed at high fluences. Figure 6 shows the craters created on TM2 at fluences of 69 and 51 mJ cm^{-2}, respectively. Conical structures were observed in both cases at the bottom of the circular cra-

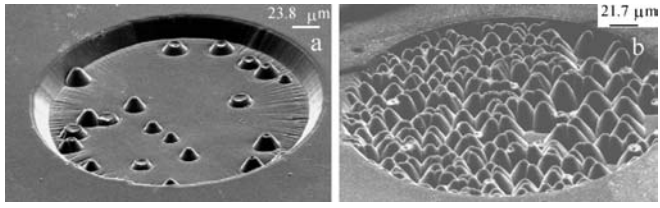

Fig. 6 SEM micrographs of ablated craters at low fluences. **a** Crater in TM2, irradiated at 69 mJ cm^{-2} with 88 pulses. **b** Crater in MP2C irradiated at 51 mJ cm^{-2} with 200 pulses. REPRINTED WITH PERMISSION OF [Ref. 82], COPYRIGHT (2001) American Chemical Society

ters. The number of cones decreases dramatically on increasing the fluence, indicating a fluence range for obtaining these cone structures. The number of cones increases also with the number of laser pulses at a fluence within the range described above. No cones are observed after laser irradiation, in case of TM2, if the fluences are higher than 80 mJ cm^{-2}. The formation of cone-like structures within a certain fluence range was observed previously for other polymers, e.g., PI [135]. The formation of the cones has been assigned to impurities in the polymer [136, 137]. These impurities have a higher ablation threshold than the polymer, which results in shading of the underlying polymer by the impurity particles, causing the formation of the cone structures. If the fluence is increased above a certain value, which corresponds to the threshold fluence of the impurity material, smooth ablation surfaces are obtained again. In case of PI, calcium was detected as an impurity by energy-dispersive X-ray analysis (EDX). Graphitic carbon was found by Raman microscopy on top of the calcium, at the tip of the cones [138]. For TM2C, carbon was neither detected on top of the cones nor in the surroundings of the ablated craters, using Raman microscopy. This indicates that carbonization during laser ablation of the polymer is not the reason for the creation of the cones and that "clean" ablation can be achieved with the triazene-containing polymers. This was also confirmed previously for TP by analyzing the surface after ablation with X-ray photoelectron spectroscopy (XPS). The clean ablation is an important feature for practical applications, because carbonization of the polymer surface will alter the ablation characteristics and therefore reduce the reproducibility of ablation. The elemental composition on top of the cones was determined with EDX for TM2, and Si, O, and Cl were identified as impurities. The formation of the cones in TM2 is therefore most probably also due to impurities in the polymer. Cone structures were also observed after ablation of the other polymers, but at slightly different fluences and in smaller numbers. This can be explained by different quantities of impurities within different polymers.

Microstructuring of Polymers. A microstructure with broad (ca. 8 μm) and narrow (ca. 4 μm) channels was created in the polymers to demonstrate the possibility of structuring the polymers with a resolution in the micron range. High quality microstructures can be created on all designed polymers as shown for MP2C and TM2C in Fig. 7. The SEM micrograph with the higher magnification (Fig. 7b) reveals nearly no debris in the areas surrounding the structure. The structures have flat bottoms and the remaining ridges are well defined. The depths of channels can be controlled by fluence and/or pulse number. The experimental results show that the designed polymers are suitable for microstructuring and exhibit structures with similar qualities. With an improvement of the experimental setup, it should be possible to create various microstructures with an even higher resolution.

Measurement of Gaseous Products During Laser Ablation. It is very important, as discussed above, that the ablation products or debris are not contaminating the polymer surface and optics. It has been suggested that a large

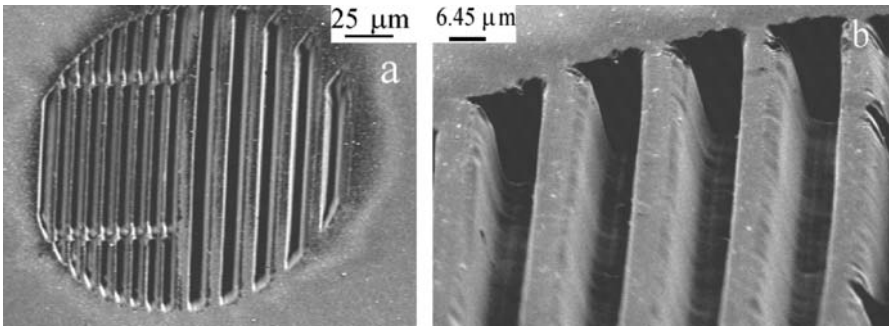

Fig. 7 SEM micrographs of microstructures. **a** Structure in MP2C irradiated at 4.6 J cm^{-2} with 9 pulses. **b** Structure in TM2C irradiated at 4.6 J cm^{-2} with 11 pulses. REPRINTED WITH PERMISSION OF [Ref. 82], COPYRIGHT (2001) American Chemical Society

amount of gaseous products is necessary to achieve this goal. The neutral gaseous products and fragments of laser ablation were analyzed with quadrupole mass spectroscopy as described in the experimental section. The ablation experiments were performed with TM1 and MP1 in the low and high fluence ranges, i.e., at 130 and 540 mJ cm^{-2}. The detected masses (after electron impact ionization at 70 eV), their relative intensities, and suggested elemental compositions are shown for a fluence of 130 mJ cm^{-2} in Table 2.

Table 2 Gaseous products determined with a modified quadrupole mass spectrometer. The ablation experiment was performed at a fluence of 130 mJ cm^{-2}

m/z	Fragment	Relative intensity of peaks in % MP1	Relative intensity of peaks in % TM1
12	C	11	6
14	N	5	10
	CH_2		
15	CH_3	15	35
16	CH_4	24	19
	O		
25	C_2H	29	9
26	C_2H_2	100	43
27	C_2H_3	20	51
28	C_2H_4	56	100
	CO		
	N_2		
39	C_3H_3	26	6
44	CO_2	100	10
50	C_4H_2	30	2
51	C_4H_3	18	1

The detected masses are of course a mixture of primary or direct ablation products, and secondary products resulting from reactions in the ablation plume as well as from fragmentation induced by the electron impact ionization. The C_xH_y structures, e.g., C_2H_x, C_3H_x, and C_4H_x, are typical products of the fragmentation of aromatic compounds. With the given data it is impossible to determine whether these are primary or secondary products. In case of the triazene-containing polymer, TM1, the main product has a mass of m/z=28, corresponding either to N_2, CO, or C_2H_4. All these species might be produced during laser ablation. Our experimental setup does not have the resolution to distinguish between these isotopic variants. However, a time-of-flight mass spectrometry study of TP shows that the main ablation product is N_2. This suggests that, in case of TM1, N_2 may also be the main product. Nitrogen as main product is consistent with a laser-induced decomposition mechanism of the triazene molecules. The primary decomposition step is the homolytic bond breaking between the nitrogen atoms N^2 and N^3 of the triazene group, forming a very reactive azo radical from which N_2 is eliminated. For MP1, the main products, with identical intensity, are CO_2 and C_2H_2. This is consistent with quantum chemical calculations showing that absorption at the irradiation wavelength occurs within the whole cinnamylidene malonyl group, causing the decomposition of this structure into the above described fragments. The same fragments are also detected for TM1, but with lower intensities. It is noteworthy to mention that the overall intensity of all fragments is ten times higher for the triazene-containing polymers. This is consistent with the higher ablation rates of the triazene polymers and the suggested role of gaseous products as driving/carrier gas of ablation.

Photochemical Properties. A simple experiment was performed to compare the photochemical activity of the MP with the TM polymers. Solutions of TM1 and MP1 in quartz cuvettes with the same absorptivity were irradiated with 60 mJ cm^{-2}. The UV-Vis spectra before and after irradiation are shown in Fig. 8. A comparison of the absorption bands after 100 pulses shows that about 50% of TM1 and only 20% of MP1 are decomposed. This confirms clearly that the triazene-containing polymers decompose photochemically much more easily than the polymers without this group. It is important to point out that TM1 contains the same structural unit as MP1 (Scheme 3), but with the additional triazene unit in the repetition unit of the polymer. Irradiation of low concentrations of the polymer in solution can be interpreted as pure photochemical decomposition with nearly no thermal influences.

2.2.1.3 Discussion

The experiments at high fluences reveal that under these conditions the material properties of the polymers are only of minor importance. All polymers have very similar ablation rates which indicates that, with the excess of laser energy and photons, similar processes govern the ablation behavior. It is

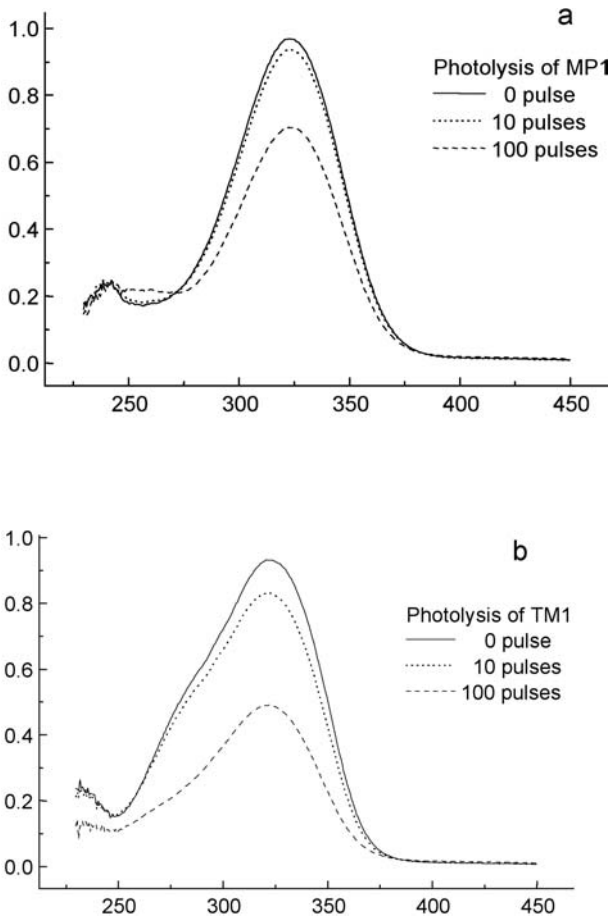

Fig. 8 UV spectra recorded after irradiation of MP1 and TM1 in THF. 1.2 ml of solution (ca. 10^{-5} M) was irradiated by laser pulses with energy of 110 mJ REPRINTED WITH PERMISSION OF [Ref. 82], COPYRIGHT (2001) American Chemical Society

most probable that the polymers decompose into similar small products, and that the created plasma is also comparable. This was also suggested by emission spectroscopy, confirming that the main species in the plasma are CN, C_2, and CH species for all polymers. The plasma and the products of ablation shield the incoming laser radiation, which limits the etch rates. This is observed for the triazene polymers at fluences >12 J cm^{-2} (not shown in Fig. 3). At these high fluences the etch rates are more or less constant. Therefore, similar ablation parameters are derived for all polymers including the two reference polymers PI and PE. The only important difference between the ablation characteristics is the deposition of debris in the area surrounding the ablation contours. In the case of PI, carbon deposits are detected in the surroundings of the contours. The thickness of the deposits increases

with pulse number, while the area of deposition increases with fluence and only slightly with pulse number [138]. Inside the ablation feature, carbonization is also detected. As mentioned above, this carbonization will alter the ablation characteristics, thus making the whole ablation process less predictable. The deposition of the carbon debris is, of course, also of concern for optical components which are in the vicinity of the ablation sites. Contrary to PI, no deposits in the areas surrounding or inside the ablation crater are detected for the triazene-containing polymers. This reveals the superior properties of the designed polymers. Two explanations might be offered for this behavior. The content of aromatic systems is lower in the triazene polymers as compared to PI. The small decomposition fragments of aromatic systems, such as C_2, are thought to be the "building blocks" of carbonization. Another, maybe more important, feature is the high amount of gaseous fragments obtained by laser ablation of the designed polymers. These gaseous fragments act as the driving gas of ablation and carry away the carbon fragments. It has been shown with TOF-MS for TP that N_2 is the major product (factor 15 higher intensity than for other products) of ablation. This inert product is entraining other products, proving the carrier gas concept. The carbon fragments are carried away in the nitrogen, which might even act as a diluent, rendering the recombination of the carbon fragments more difficult. At low fluences a pronounced difference between the polymers can be detected. The tested polymers can be roughly divided into three groups: the polymers containing the triazene group, the polyesters (maybe with inclusion of PE into this group), and PI. The triazene-containing polymers have by far the highest activity (highest etch rate and lowest threshold fluence) to laser ablation, followed by the polyesters and then PI. A comparison of all polymers is shown in Fig. 9. The linear absorption coefficients of the polymers are plotted against the etch rate at a fluence of 100 mJ cm^{-2} (Fig. 9a) and against the threshold fluence (Fig. 9b).

Among the triazene-containing polymers, TP reveals the highest activity, probably due to the highest density of triazene groups in the polymer chain, resulting in larger amounts of nitrogen as ablation product. The same order of activity is also confirmed by other experimental techniques, i.e., irradiation of the polymer in solution (Fig. 8) and mass spectrometry. The triazene-containing polymers decompose much faster during irradiation in solution, where thermal effects should be of only minor importance. In the mass spectroscopy studies a much higher amount of gaseous products is detected for the triazene-containing polymers, confirming of course the higher etch rates, but also the role and importance of the gaseous species. These very pronounced differences are even more remarkable if we consider that the polymers were selected for similar absorption properties. At least one polymer out of each group has a comparable, linear absorption coefficient (97,000±5,000 cm^{-1}), i.e., TP and TM1 for the triazene-containing polymers, MP1 for the designed polyesters, and PI for the reference polymers (see Fig. 9). This ensures that a direct comparison of these polymers is possible, due to the deposition of the laser energy within the same volume of the polymer. If the effective absorption coefficient is considered, then the triazene polymers can still be compared to the polye-

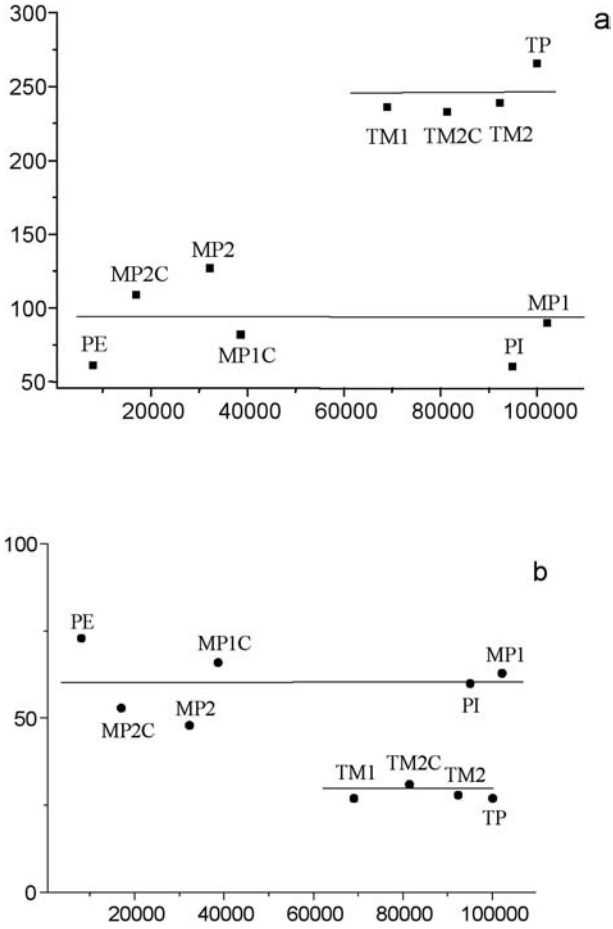

Fig. 9 Influence of the linear absorption coefficients at the laser wavelength on **a** the etch rates at 100 mJ cm^{-2} and on **b** the threshold fluences. The *lines* in the figure are just for guiding the eyes. REPRINTED WITH PERMISSION OF [Ref. 82], COPYRIGHT (2001) American Chemical Society

sters because their values are again quite similar (54,000±5,000 cm^{-1}). Only PI reveals a quite different effective absorption coefficient, similar to the value of the linear absorption coefficient. Whereas the effective absorption coefficients are comparable, very pronounced differences between the triazene-containing polymers and the polyesters are obtained for the ablation activity. This suggests that α_{eff} is of only minor importance for the ablation performance. The same is true for the linear absorption coefficients, because a variation of α_{lin} within one group of polymers has again no pronounced influence as seen when comparing, e.g., MP1 and MP2 (see Fig. 9). It is probably more important for its value to lie above a certain threshold (approx. 10,000 cm^{-1}), where direct

ablation without incubation is observed. Of course one might argue that the same order of activity is also obtained if only the decomposition temperatures (T_{dec}) are considered, i.e., lowest T_{dec} for the triazene polymers, followed by the polyesters and then PI. However, a comparison reveals that the largest difference in thermal stability (170 °C) between polymers of different groups, i.e., PI and MP1, corresponds to the smallest difference in ablation activity, while the smallest difference in thermal stability (70 °C), between TM2 and MP1, corresponds to the largest difference in ablation activity. This is even more remarkable when recalling that this inequality is valid in a broad fluence range (from 10 to at least 400 mJ cm^{-2}), which covers a quite broad thermal range. This suggests that thermal considerations are less important for the laser ablation of these polymers. Just using the decomposition temperatures is of course a simplification, because other parameters such as thermal conductivity, specific heat, thermal diffusivity etc. are also important. Looking at the chemical structure of the polymers shows that all polymers have at least common parts, suggesting that they might have comparable values for these constants, and hence justifying the simplification. Together with the experiments in solution, where concentrations in the 10^{-5} molar range of the polymers are used, this suggests an only minor part of a thermal mechanism.

Now we would like to take a step back and look in more detail at some fundamental, photochemical aspects of laser ablation. The photon energy of the XeCl excimer laser is 4.02 eV, which is just above the binding energy of C–C (3.6 eV), C–N (3.2 eV), and C–O (3.7 eV) bonds, but clearly above the value of the N–N bond (1.7 eV) [139]. This suggests that direct photochemical breaking of these bonds is at least possible. Quantum chemical calculations have shown that the triazene chromophore is responsible for the absorption at 308 nm [119], and photochemical studies of monomeric triazene identified the N–N bond as initial photodecomposition site [140]. The fragments found in the MS analysis of the triazene polymers are also compatible with the mechanism in Scheme 4. The differences between PI and the polyesters can be explained in two ways. Quantum chemical calculations have shown that the absorption at 308 nm in the designed polyesters is due to the entire cinnamylidene malonyl group, which is, according to the fragments, also the preferential decomposition site, yielding CO_2 and C_2H_2 as main fragments. (A possible decomposition scheme is shown in Scheme 4). The absorption at 308 nm is less localized for polyimide, and the imide system as well as the oxygen of the biphenylether groups have been identified as primary decomposition sites [141]. This, together with the lower amount of gaseous products, might be responsible for the lower ablation activity. The amount of gaseous products follows the same order as the ablation activity, i.e., triazene polymers>polyesters>PI. The second, more probable reason for the low ablation activity of PI, is that decomposition of PI proceeds according to a purely photothermal mechanism [63], as suggested by a theoretical model [89]. For the designed polymers, a mechanism might be active which combines the photochemical activity with the resulting pressure/volume increase of the gaseous fragments inside the polymers.

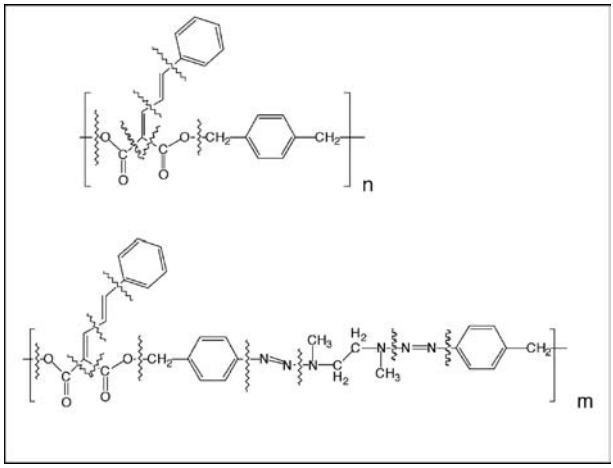

Scheme 4 Possible decomposition mechanism of the polymers TM1 and MP1. Resulting fragments are identified in the mass spectra. REPRINTED WITH PERMISSION OF [Ref. 82], COPYRIGHT (2001) American Chemical Society

One interesting point worth analyzing in more detail is the quite similar effective absorption coefficients for all designed polymers, which are independent of the linear absorption coefficients. The effective absorption coefficient of PI is different to the more or less constant values of the designed polymers and is similar to the linear absorption coefficient. This might also be an indication for different ablation mechanisms acting for PI and the designed polymers. All designed polymers are supposed to decompose according to a similar mechanism, i.e., direct photolysis, during which homolytic bond breaking occurs. Radicals are formed as intermediates, such as phenyl radicals, which might be present for all designed polymers. These radical intermediates would limit the effective absorption coefficient for all polymers to a similar value. In case of PI, different intermediates might be formed, e.g., ionic species, which should have quite different absorptivities, resulting in the different effective absorption coefficients. Another possible explanation invokes the thermal route of decomposition of PI, which would take place immediately after the laser pulse. In this case, the modifications of the ablated polymer surface, e.g., the carbonization, or the higher temperature of the remaining polymer might be responsible for the difference between the linear and effective absorption coefficient.

A detailed analysis of the ablation characteristics of cross-linked vs not cross-linked polymers reveals that for the cross-linked polymers, consistently lower ablation activities are obtained. This is probably due to the higher mechanical stability and larger viscosity of the cross-linked polymers. The latter observation is consistent with data showing that polymers with higher molecular weight reveal lower ablation rates [118, 142].

2.2.1.4
Summary

The ablation characteristics of various polymers were studied at low and high fluences. The polymers can be divided into three groups: polymers containing triazene groups and a cinnamylidene malonyl group, the same polymers without the triazene group, and polyimide as reference polymer. At high fluences a very similar behavior, i.e., etch rates and effective absorption coefficients, was obtained for all polymers. The main difference is the absence of carbon deposits for all designed polymers. At low fluences very pronounced differences are detected. The polymers containing the most photochemically active group (triazene) are also the polymers with the lowest threshold of ablation and the highest etch rates, followed by the designed polyesters and then polyimide. No pronounced influences of the absorption coefficients, neither α_{lin} nor α_{eff}, on the ablation characteristics are detected. The thermal properties of the designed polymers are only of minor importance. The amount of detected gaseous products follows the same trend as the ablation activity, suggesting a combined mechanism of photochemical decomposition and associated volume increase (volume explosion) of the designed polymers. The clear difference between PI and the designed polymers might be explained by a pronounced thermal part in the ablation mechanism of PI.

2.2.2
Analysis after Irradiation

The logical next step after studying the ablation properties is the application of analytical methods to the polymer surface after irradiation. Changes in the chemical composition and morphology can give first indications about possible decomposition mechanisms. In this study, surface and standard analytical techniques were used to study one selected polymer (shown in Scheme 5) after laser irradiation with 248 and 308 nm to get more information about the acting mechanism. One reason for selecting this polymer is visible in the UV-Vis spectrum (Fig. 10). The absorption maximum at 330 nm corresponds to the triazene group, while an absorption minimum is located at 248 nm. In addition the potential of UV laser irradiation for selective polymer surface modification was probed.

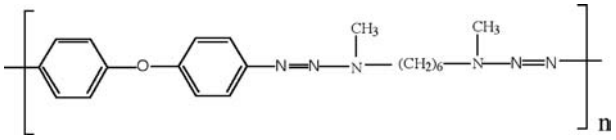

Scheme 5 Structural unit of the triazene polymer. REPRINTED WITH PERMISSION OF [Ref. 60], COPYRIGHT (1996) Springer Verlag

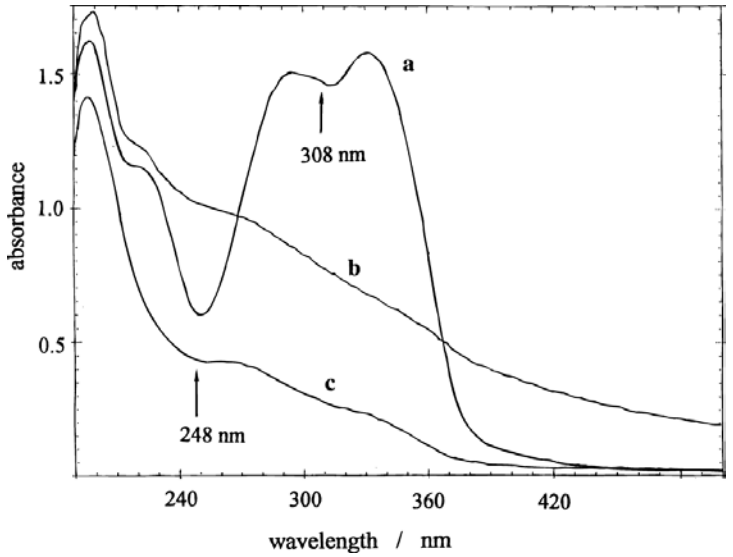

Fig. 10. a UV spectrum of the untreated polymer film on a quartz wafer. Thickness about 200 nm. **b** After irradiation with 10 mJ cm^{-2} (2000 pulses) at 308 nm. **c** After irradiation with 9 mJ cm^{-2} (500 pulses) at 248 nm. REPRINTED WITH PERMISSION OF [Ref. 62], COPYRIGHT (1996) American Chemical Society

2.2.2.1
Results

UV Spectroscopy. Thin films of the polymer (100 to 350 nm) were cast on quartz wafers. It was not possible to use thicker polymer films due to the high absorption coefficient of the polymer (166,000 cm^{-1} at 308 nm and 66,000 cm^{-1} at 248 nm). For fluences above the threshold of ablation (32 mJ cm^{-2} at 248 nm and 22 mJ cm^{-2} at 308 nm) [120] the film was ablated nearly completely after a few pulses and no absorption was detected in the range 230 to 500 nm, whereas below 230 nm some absorption remained. An optical inspection of thicker films cast on quartz, which could not be used in the UV spectrometer, revealed a pronounced difference between irradiation with 248 and 308 nm. After irradiation with 308 nm only a slight loss of transparency could be seen, whereas after irradiation at 248 nm the films turned black. This behavior was found at various repetition rates (1–40 Hz) and for different substrates (glass and quartz). This shows that the appearance of the polymer film after irradiation is not due solely to thermal effects of the substrate or cumulative heating effects of the laser pulses. The blackening of the surface after irradiation with 248 nm was never found for 308-nm irradiation, even with high repetition rates and glass as substrate, showing that for each wavelength a different mechanism is acting. The term *surface blackening* is used because, during contact angle measurements, the water droplets turned black, showing that at least a part of the *black* appearance is located at the

surface. For the fluences below the threshold of ablation a different behavior after irradiation with the two wavelengths was found also. With 248-nm irradiation the absorption decreased continuously, as shown for 500 pulses in Fig. 10c. In the case of the 308-nm irradiation, first the absorption decreased to a similar curve as shown for 248-nm irradiation in Fig. 10c. After more than 250 pulses an overall increase of the absorption is detected (shown in Fig. 10b for 2000 pulses). An optical inspection of the sample revealed a loss of transparency and an opaque appearance. The broad appearance of the absorptivity suggests that the increase of the absorption is due to a scattering process. The films were examined with scanning electron microscopy (SEM) to decide whether this is due to an increase of surface roughness

SEM. SEM pictures were taken after irradiation at both wavelengths with fluences below and above the threshold of ablation after various numbers of pulses. After irradiation at both wavelengths with fluences below the threshold of ablation, no changes of the surface morphology could be detected. A totally different behavior was observed for the higher energies. After 308-nm irradiation with 30 mJ cm^{-2} roughening of the surface was detected. The microstructures reached a maximum intensity after about ten pulses (Fig. 11a) and got less pronounced with successive pulses, as shown for 60 pulses in Fig. 11b.

The microstructures which appear as holes in the pictures have a diameter of about 1 μm. In the case of 248-nm irradiation the surface appeared different. A well-pronounced "nap" structure is detected (Fig. 12 a) with growing nap sizes. After 250 pulses (shown in Fig. 12b) the naps reach a size of about 5 μm. On the top of the naps additional material is detected, which grows in some cases to "tree-like" structures (shown in Fig. 12c). It can also be seen that this material did not cover the surface completely.

Contact Angle. To study whether chemical modifications take place in addition to the physical changes of the surface, contact angle measurements were used. For both irradiation wavelengths, again, fluences below and above the threshold of ablation were used, and the contact angle of water was measured directly after the irradiation. For the fluences below the threshold of ablation a similar behavior for both irradiation wavelengths was observed. The contact angle decreased from 57.5 to about 20 degrees (Fig. 13). The SEM pictures have shown that no surface roughening took place which could cause a decrease of contact angle [143]. Therefore the change of the contact angle is due to chemical alteration of the surface.

In the case of the higher irradiation fluence different behavior is observed (Fig. 14). For 308-nm irradiation the contact angle decreased only slightly. This is in agreement with the SEM pictures (Fig. 11) which show a slight roughening of the surface. With 248-nm irradiation more complex behavior is observed. First the contact angle decreased, due to the observed formation or growth of the microstructures.

After more than five pulses the trend changes and the contact angle increases drastically, although the SEM pictures show the development of more

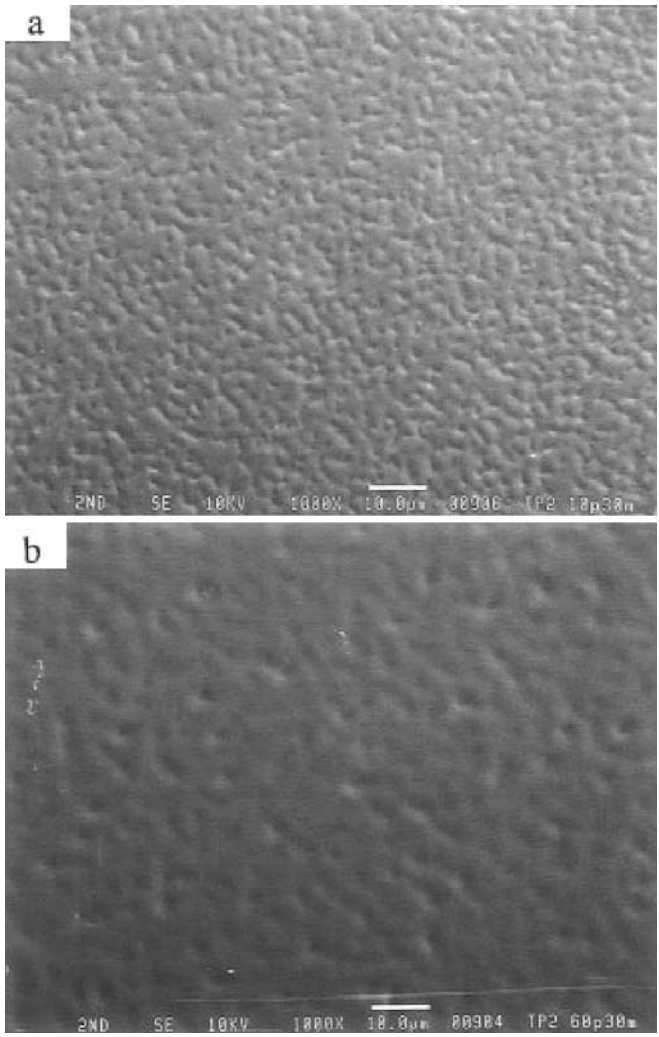

Fig. 11 Scanning electron micrographs of surface changes. **a** after 10 pulses with 30 mJ cm^{-2} at 308 nm and **b** after 60 pulses with 30 mJ cm^{-2} at 308 nm. REPRINTED WITH PERMISSION OF [Ref. 62], COPYRIGHT (1996) American Chemical Society

Fig. 12 Scanning electron micrographs of surface changes. **a** after 10 pulses with 36 mJ cm^{-2} at 248 nm, **b** after 250 pulses with 36 mJ cm^{-2} at 248 nm, and **c** enlarged view of b at 45°. REPRINTED WITH PERMISSION OF [Ref. 62], COPYRIGHT (1996) American Chemical Society

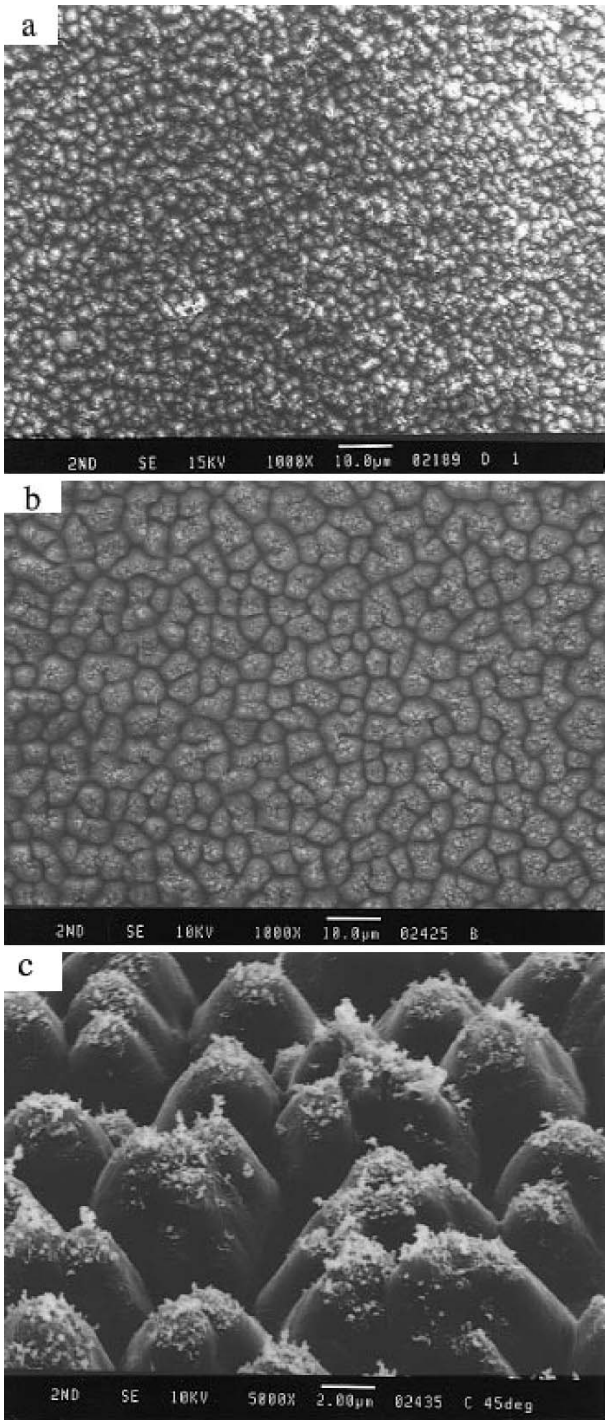
a
2ND SE 15KV 1000X 10.0µm 02109 D 1
b
2ND SE 10KV 1000X 10.0µm 02425 B
c
2ND SE 10KV 5000X 2.00µm 02435 C 45deg

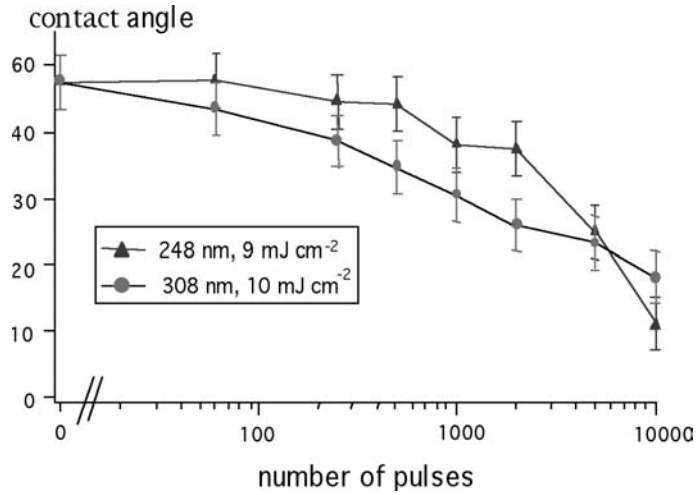

Fig. 13 Changes of the water contact angle after irradiation with fluences below the threshold energy of ablation. Irradiation with various pulse numbers at 248 and 308 nm. REPRINTED WITH PERMISSION OF [Ref. 62], COPYRIGHT (1996) American Chemical Society

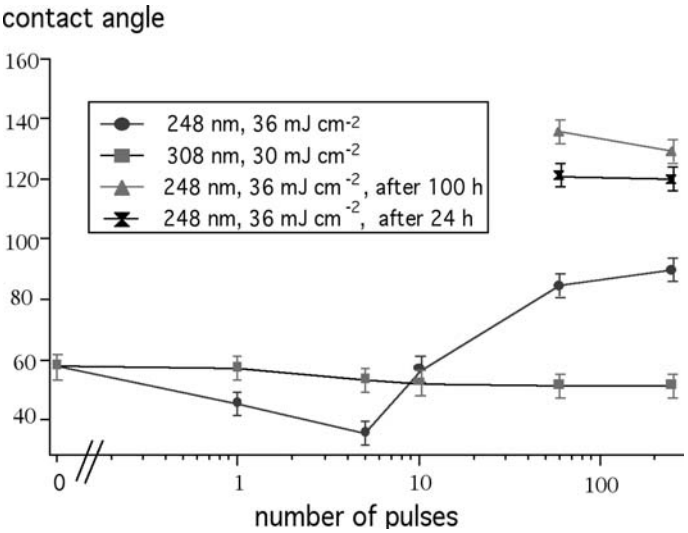

Fig. 14 Changes of the water contact angle after irradiation with fluences above the threshold energy of ablation. Irradiation with various pulse numbers at 248 and 308 nm. REPRINTED WITH PERMISSION OF [Ref. 62], COPYRIGHT (1996) American Chemical Society

pronounced microstructures. Therefore, a large change in the surface polarity must be the reason for this behavior. For more than 60 pulses the surface appears black and the contact angle becomes time dependent. If the contact angle is measured immediately after the irradiation, values of about 80° result, but also fast darkening of the water droplet and a decreasing angle are observed. If the contact angle is measured after 24 h or more the values are constant at about 140° and the water droplet does not turn black.

FT-Raman Spectroscopy. In order to get information about the observed chemical changes of the surface, FT-Raman spectroscopy was used to examine the surface after laser irradiation. Due to the high penetration depth of the Nd:YAG laser beam of the spectrometer we were well aware that possible information would mainly consist of bulk properties. But nevertheless the spectra are valuable because there is also a large possibility of decomposition, especially of the triazene chromophore in the bulk. Raman spectroscopy was used, as compared to IR spectroscopy, because of the less complex band structure of the polymer and the larger Raman cross section of the N=N–N chromophore. Measurements with normal Raman spectroscopy were not possible, due to a high fluorescence background with the use of visible excitation light.

In Fig. 15 the Raman spectra of the polymer are shown: (a) before irradiation, (b) after 10,000 pulses at 308 nm with 10 mJ cm^{-2}, (c) after 1,000 pulses at 248 nm with 9 mJ cm^{-2} (both are below the threshold of ablation), (d) with 250 pulses at 308 nm with 30 mJ cm^{-2}, and (e) with 60 pulses at 248 nm with 36 mJ cm^{-2}. Spectra (a) to (d) are all measured under the same conditions, using films of about 3-μm thickness on glass. Additionally a silver plate was used under the glass to increase the intensity. The laser for this measurement was used in the "spot" (100 mW) mode of the instrument, giving higher intensities. For each of these spectra 56 scans were accumulated. In the case of spectrum (e) it was necessary to change to the "defocused mode" (10 mW) of the spectrometer, because in the focused mode the "black" surface disappeared after a few scans, due to the high thermal load. Therefore, the defocused mode was used and 1,000 scans were accumulated. The peaks marked with an asterisk are due to the laser (plasma lines) and the glass substrate on silver (background). The peak with the highest intensity of the polymer at 1392 cm^{-1} was assigned to the triazene chromophore, according to comparison with data for monomeric triazene compounds [144] and the expected high Raman cross section of the N=N bond.

After irradiation with 10,000 pulses with 10 mJ cm^{-2} at 308 nm (b), an increase of the bands corresponding to the polymer is detected, whereas the "background" decreases slightly. No new bands could be detected and the peak ratios remain constant.

Irradiation with 9 mJ cm^{-2} at 248 nm (1,000 pulses) revealed different behavior, showing that the slight loss of optical transparency is due to a different reason. The increase of the baseline (c) is a typical feature for a thermal load of the sample caused by absorption of the near infrared (NIR) excita-

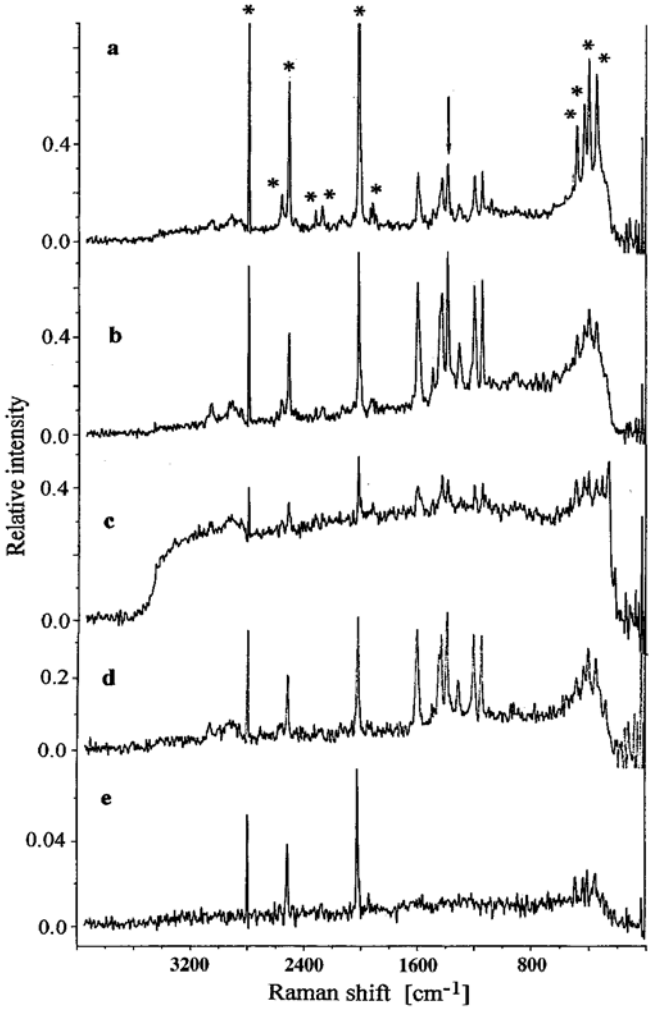

Fig. 15 FT Raman spectra of **a** the untreated polymer, **b** after 10,000 pulses with 10 mJ cm^{-2} at 308 nm, **c** after 1,000 pulses with 9 mJ cm^{-2} at 248 nm, **d** after 250 pulses with 30 mJ cm^{-2} at 308 nm, and **e** after 60 pulses with 36 mJ cm^{-2} at 248 nm. The *asterisks* indicate the background (see description in the text) and the *arrow* marks the N=N–N band. REPRINTED WITH PERMISSION OF [Ref. 62], COPYRIGHT (1996) American Chemical Society

tion laser [145]. It also appears that the intensity of the band assigned to the triazene chromophore decreased more than the other bands.

After irradiation with 30 mJ cm^{-2} at 308 nm a behavior similar to that for the low-energy irradiation is detected. The band ratios remain constant and the intensity of the polymer bands increases. The difference is in the overall intensity of the spectrum which decreased by a factor of about two.

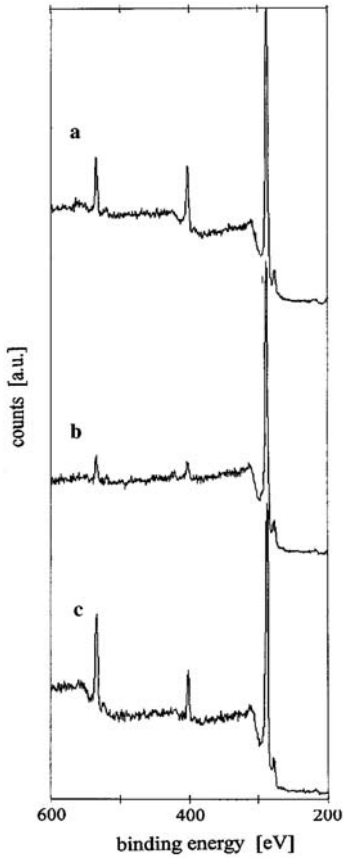

Fig. 16 X-ray photoelectron core level spectra of the triazene polymer. **a** untreated, **b** after 60 pulses with 36 mJ cm^{-2} at 248 nm, and **c** after 2,500 pulses with 9 mJ cm^{-2} at 248 nm. The peaks at 285 eV correspond to the C 1 s, at 400 eV to the N 1 s, and at 532 eV to the O 1 s band. REPRINTED WITH PERMISSION OF [Ref. 62], COPYRIGHT (1996) American Chemical Society

For the irradiation with the high energy at 248 nm (e), where a surface blackening is observed, no polymer could be detected, partially due to the low signal to noise ratio in the defocused mode, which is ten times less than for the focused mode. It was also not possible to detect bands which are specific for graphite species, even with the use of standard Raman experiments with the excitation wavelength of an Ar^+ (or Kr^+) laser.

X-Ray Photoelectron Spectroscopy (XPS). In order to get more information about the chemical changes of the polymer surface, high vacuum surface spectroscopic techniques were used. For XPS measurements the analytical depth is in the order of 5 nm and should therefore be more sensitive to surface modifications than FT-Raman spectroscopy. The XPS spectra before and after irradiation at 248 nm are shown in Fig. 16.

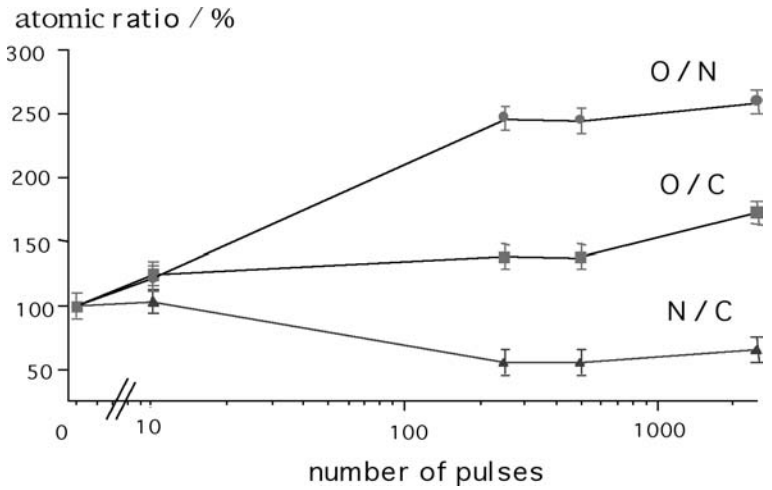

Fig. 17 Atomic ratios in % of the triazene polymer after irradiation with various pulse numbers with 9 mJ cm^{-2} at 248 nm. REPRINTED WITH PERMISSION OF [Ref. 62], COPYRIGHT (1996) American Chemical Society

The experimental values derived from the peak area of the different atoms were different from the stoichiometric values, a quite common feature for polymers due to surface contamination, additives or differences between surface and bulk composition [146, 147]. In this first study of the triazene polymers it was not the aim to resolve the XPS spectra in detail. The aim was to study relative changes of the surface composition after laser treatment. For this reason the changes are shown in percent relative to the untreated polymer, for which the atomic ratios are set to 100%. As a result we did not try to fit the peaks according to the different oxidation states of the atoms. Additionally there is a lack of reference data for polymers with N=N bonds. It is known for nitrogen compounds that the shake up satellites can account for up to 30% of the peak intensity and are difficult to observe because they are masked by the inelastic loss structure [148, 149]. Nevertheless the N 1 s peak is still a function of the single and double bonded nitrogen and therefore an excellent probe for changes of the nitrogen content. The relative changes of the O/N, O/C and N/C atomic ratios after laser treatment were used to analyze the surface modifications.

The irradiation with fluences below the threshold of ablation revealed similar behavior for both irradiation wavelengths. In the case of 248-nm irradiation (Fig. 17) an increase of O/N and O/C is detected, whereas the N/C ratio decreases. The main changes of the ratio take place during the first 250 pulses and stay then constant up to 2500 pulses.

The increases of the two oxygen ratios show clearly that the surface has a higher O content than before the irradiation. It is also determined that the N-functionalities are preferentially removed. In the case of the 308-nm irra-

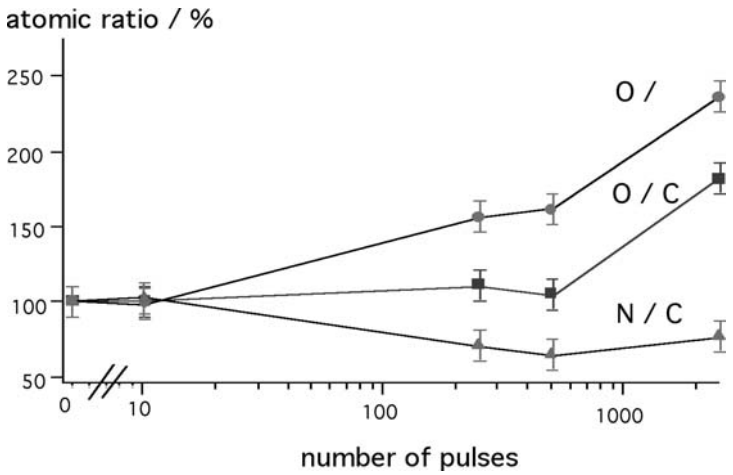

Fig. 18 Atomic ratios in % of the triazene polymer after irradiation with various pulse numbers with 10 mJ cm^{-2} at 308 nm. REPRINTED WITH PERMISSION OF [Ref. 62], COPYRIGHT (1996) American Chemical Society

diation (Fig. 18) the same kind of changes of the ratios are found, in detail the increase of the O/N and O/C ratios. The main difference is that constant values are not reached. After 2500 pulses all ratios reach values similar to those for 248-nm irradiation.

For irradiation with fluences above the threshold of ablation a totally different behavior is detected. For 248-nm (KrF laser) irradiation only the O/N increases, whereas the O/C and N/C ratios decrease (Fig. 19). In particular, the decrease of the O/C ratio shows that no surface oxidation takes place but

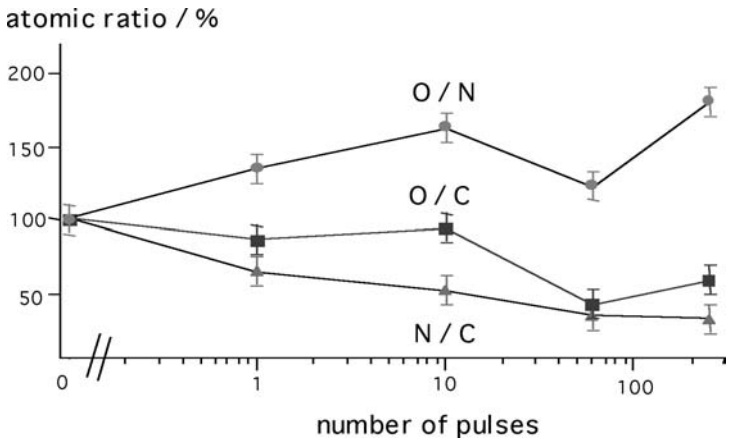

Fig. 19 Atomic ratios in % of the triazene polymer after irradiation with various pulse numbers with 36 mJ cm^{-2} at 248 nm. REPRINTED WITH PERMISSION OF [Ref. 62], COPYRIGHT (1996) American Chemical Society

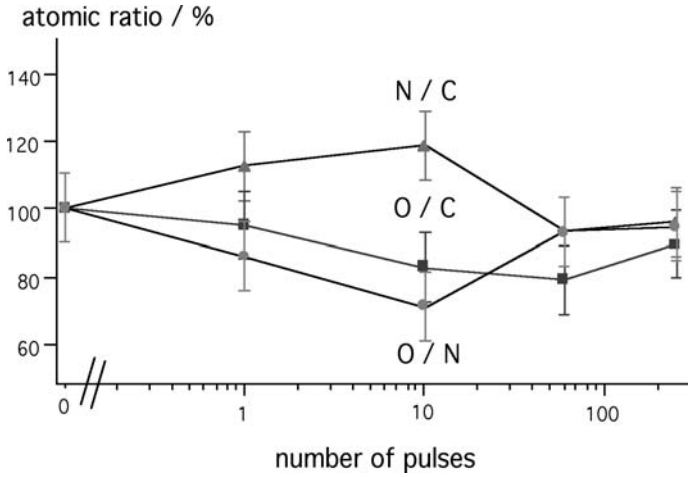

Fig. 20 Atomic ratios in % of the triazene polymer after irradiation with various pulse numbers with 30 mJ cm^{-2} at 308 nm. REPRINTED WITH PERMISSION OF [Ref. 62], COPYRIGHT (1996) American Chemical Society

rather a carbonization. Surface carbonization was also found with XPS for the irradiation of polyimide with 193 nm [150]. The two other ratios indicate again the release of nitrogen. This is in agreement with the nonpolar surface measured with the contact angle and the black appearance of the polymer films after irradiation.

In the case of 308-nm irradiation with fluences above the threshold of ablation, the most complex behavior is found (Fig. 20). Only minor changes took place between 1 and 10 pulses. These changes can be attributed to removal of oxygen and carbon surface contaminations. In addition, the largest roughening of the surface (Fig. 11a) is detected for 10 pulses, which can also influence the relative atomic ratios. After more than 10 pulses the atomic ratios approach, within the error of the experiment, the starting values. This indicates that no surface modification took place and the polymer is ablated layer by layer.

In addition to XPS we tried static SIMS to get more information about the nature of the surface modifications. SIMS has the advantages of a smaller sampling depth (1 nm as compared to the 5 nm of XPS) and direct chemical information in the spectra. The problems are the quantification of spectra and the complex data acquisition [151, 152]. In the positive as well as in the negative SIMS spectra no new peaks appeared after laser irradiation. In the positive SIMS spectra, the peaks could be assigned to the typical aliphatic CH and some aromatic CH fragments [152]. After irradiation the higher molecular weight fragments (>70) could not be detected. The overall intensities of the spectra were reduced after laser irradiation. For both wavelengths the reduction was higher for irradiation with fluences above the threshold, and for 248 nm higher than for 308-nm irradiation. In the case of 308-nm irradi-

ation with fluences above the threshold of ablation the reduction was only about one third. This indicates that either the small changes of the atomic ratios have a pronounced influence on the SIMS spectra or that changes at the surface take place without changing the atomic ratios. An example for this would be cross-linking of the polymer chains, resulting in an overall decrease of the SIMS intensities. Due to the reduced intensities it is not possible to detect higher molecular weight fragments. Nevertheless there are no new peaks, indicating a surface modification, and the reduction of the intensity is only minor and close to the instrumental error.

For the 248-nm irradiation above the threshold of ablation the intensity of the spectra were reduced drastically (1/30). This can be assigned to a shielding effect of the carbon species at the surface of the polymer, as detected with the other spectroscopic techniques.

The negative SIMS spectra showed only low molecular weight fragments, like CH^-, CH_2^-, C_2H^- and CN^- before irradiation. After irradiation the overall intensity was only reduced slightly (10 to 30%). These values are close to the instrumental error, but might be due to a fragmentation of the polymer at the surface, which would have only a minor influence on the intensity of the low molecular weight fragments.

2.2.2.2 Discussion

A mechanism for the laser irradiation of the triazene polymer is outlined in Scheme 6.

Fluences Below the Threshold of Ablation. First we discuss the changes of the polymer after irradiation with laser fluences below the threshold of ablation. The SEM pictures have shown that no changes of the surface morphology after irradiation took place. From the UV measurements decomposition of the triazene chromophore can be seen, as demonstrated by the decrease of the absorption maximum at 330 nm. The UV spectra for 248- and 308-nm irradiation revealed a difference in the curves (shown in Fig. 10). For 248-nm irradiation the absorption decreased continuously to a curve which remained nearly constant after 500 pulses (Fig. 10c). In the case of 308-nm irradiation, the absorption first decreased, similar to 248-nm irradiation, but then after more than 250 pulses an overall increase (from 190 to 1000 nm, partly shown in Fig. 10b) of the absorption is detected. The broad appearance of the absorption over the whole UV-Vis range suggests that this is not due to the formation of new absorption bands, but to a "scattering" effect. The SEM pictures have shown that there is no surface roughening; therefore it must caused by an "internal" roughening from gaseous bubbles, trapped in the polymer matrix and probably filled with nitrogen (Scheme 6, step 5). The nitrogen is a product of the photolytic decomposition of the triazene bond, creating an unstable radical, which decomposes on a very fast time scale [140] (shown in steps 1 and 2 in Scheme 6). Even with ESR spin trap experiments it was not possible to detect a diazo radical, resulting

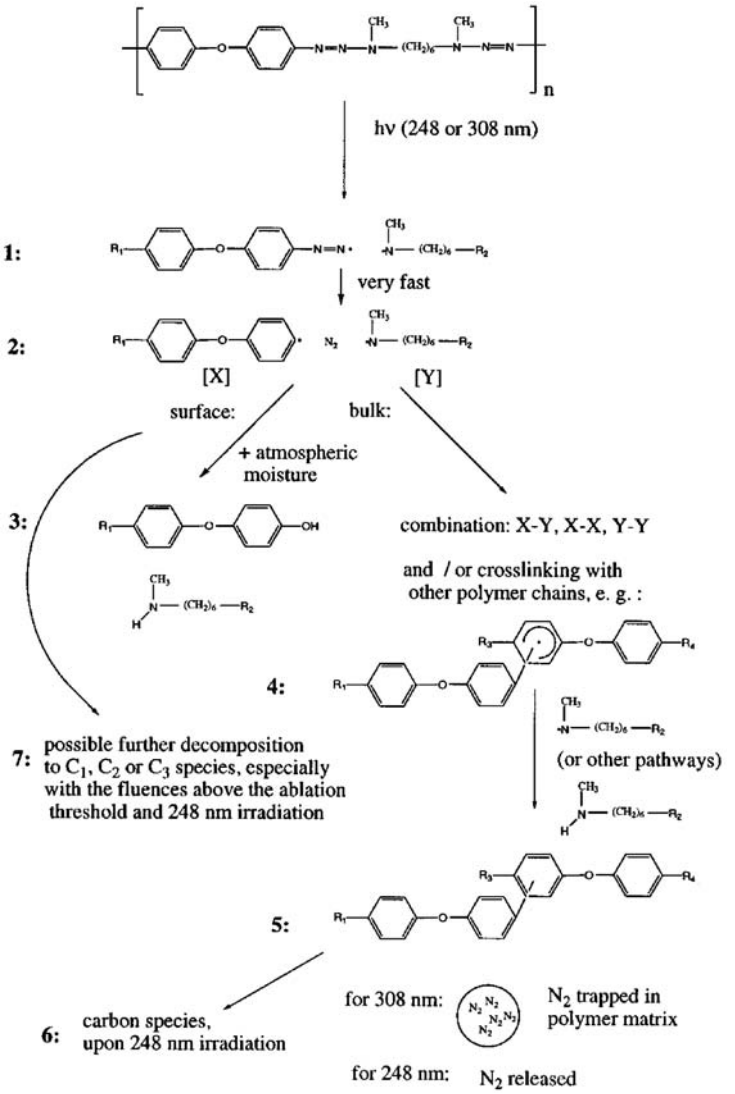

Scheme 6 Proposed mechanism for the decomposition of the triazene polymer after laser irradiation with 248 and 308 nm. REPRINTED WITH PERMISSION OF [Ref. 62], COPYRIGHT (1996) American Chemical Society

from the photolysis of aryl dialkyl triazenes [153]. The increase of the absorption over the whole range from 190 to 1000 nm also suggests a size distribution of the bubbles inside the polymer matrix in the same range. In the FT-Raman spectra of the polymer after irradiation with 10,000 pulses at 308 nm with 10 mJ cm^{-2} (Fig. 15b), an increase of all polymer bands was de-

tected. This behavior could also be due to an increase of the scattering of the laser light. The extended Kubelka-Munk theory for Raman scattering shows that the relative intensity of the Raman spectra is a function of the absorption coefficient and the scattering coefficient [145]. Under certain conditions an increase of the scattering can lead to an increase of the relative intensity of the Raman spectra [154]. The SEM pictures have shown that there is no roughening of the surface and the UV spectra have indicated that "internal" scattering is present. Therefore it can be assumed that this could be the reason for the increased intensity of the polymer bands and the decrease of the background in the FT-Raman spectra (also). The irradiation is thought to create "microbubbles" of trapped nitrogen, released from the photolytic decomposition of the triazene chromophore. The bubbles reach sizes up to one micron causing the scattering of the laser excitation light (1064 nm). For 248-nm irradiation no internal scattering was detected in the UV and FT-Raman spectra. The Raman spectra (Fig. 15c) showed a decomposition of the triazene chromophore, as derived from the decrease of the intensity of this band and an increase of the baseline. A baseline increase is a typical feature for a thermal load of the sample during the FT-Raman measurement. This is caused by the absorption of the laser light (1064 nm).

To explain the difference between the 248- and 308-nm irradiation some properties of the polymer and laser at the two irradiation wavelengths must be discussed. At 248 nm the penetration depth of the laser is about 150 nm, whereas for 308 nm the penetration depth is only 60 nm. In addition, the photon energy at 248 nm is 5 eV as compared to the 4 eV at 308 nm. This is one of the reasons why the quantum yield (QY) of photolysis in solution for 248 nm is higher (1.5%) than for 308 nm (0.22%) [120]. A closer inspection of the UV spectra (Fig. 10) reveals that 248 nm is at a minimum of the absorption curve. Assuming a Lorentzian profile for the different absorption bands, it is obvious that an irradiation with 248 nm can lead to a direct excitation of the absorption bands below and above 248 nm.

The higher QY results in a faster decomposition of the polymer and therefore a higher partial pressure of the nitrogen inside the polymer matrix. The pressure is released and no gaseous bubbles are developed. In addition, 248-nm irradiation is capable of exciting the aromatic system and has sufficient energy to decompose C–C bonds.

Therefore we suggest the following steps for the bulk decomposition of the polymer after irradiation with fluences below the threshold of ablation. First the photolabile triazene group is decomposed, with nitrogen as the first product (Scheme 6, steps 1 and 2). This is confirmed with the decreasing N content in the XPS spectra (Figs. 17 and 18). Then the phenyl and aminyl radicals created inside the polymer matrix can combine or lead to cross-linking or branching of the polymer, as shown for cross-linking in steps 4 and 5 of Scheme 6. It was suggested that cross-linking will lead to a peak broadening in the XPS spectra [155]. We also detected some broadening of the peaks after irradiation and found some insoluble residues for thick films, indicating a polymer network. The decreased intensity of the SIMS spectra also indicated a polymer network. In addition, it was demonstrated

that the structurally related monomeric bis-triazene compounds can be used as thermal cross-linkers for polyimides and aromatic polymers [156]. Therefore only cross-linking is shown in Scheme 6.

The cross-linked polymer still has an absorption at 248 nm. Excessive irradiation with 248 nm can therefore result in some further decomposition of the cross-linked polymer or other possible products, like branched systems or amines (Scheme 6, step 4). The main products of such a process are carbon species, which will absorb at 1064 nm, as revealed by the thermal load in the FT-Raman spectra.

At the polymer surface the radical species (Scheme 6, steps 1 and 2) can react with atmospheric moisture to form surface hydroxyl groups (shown in step 3). The existence of polar groups, like –OH, at the surface is clearly shown in the contact angle measurements where a decrease of the water contact angle is detected (Fig. 13). In the XPS measurements an increase of the oxygen content is revealed (Figs. 17, 18), which confirms a surface oxidation of the polymer.

Fluences Above the Threshold of Ablation. The main difference between the irradiation of the triazene polymer with low and high fluences is a clear change in the polymer response. There is no simple photochemical mechanism acting alone but, in addition, material is removed (ablation) corresponding to a much higher QY than for the normal photolysis [68]. The UV spectra of the films could not give any valuable information because the films were totally removed during ablation. Therefore thicker films were used, revealing a pronounced difference between the two irradiation wavelengths. Optical inspection of the films after multiple pulses at 248 nm showed a black appearance, whereas no darkening took place after 308-nm irradiation. The SEM pictures also revealed a different appearance of the polymer surface after irradiation with the two lasers. For 308-nm irradiation, microstructures with an increasing intensity were found, but after more than 10 pulses the trend was reversed and the microstructures became less pronounced (Fig. 11). After 248-nm irradiation the microstructures were also observed. There was no decrease of their intensity and some "tree-like" structures were found on the top of the microstructures (Fig. 12). Microstructures of polymers were reported previously for subthreshold irradiation of polymers with polarized laser beams for controlled roughening of the surface with various laser irradiation wavelengths [55, 157]. With fluences above the threshold of ablation it is also possible to create microstructures [158]. These features are found for films and fibers and are attributed to different mechanisms like Marangoni convection [159], surface scattered waves [160], recombination of microcracks [135], and a mixture of several mechanisms [161]. It is also known that the irradiation of stretched polymers results in the creation of microstructures due to the release of the stress fields [52] upon laser irradiation and surface melting, which leads to a crystalline-to-amorphous transition of the polymers [162].

Pronounced differences between the microstructures created with different irradiation wavelengths above the threshold of ablation with similar fluences

have not been reported to our knowledge. Assuming that the decomposition mechanism of the triazene polymer does not change totally in the case of ablation, but results mainly in material removal at a higher rate and some possible variations to the mechanism, we suggest a different mechanism for the microstructures. As for the low-irradiation fluence, the XPS spectra and the nonsoluble residues after irradiation suggest a cross-linking mechanism (step 5 in Scheme 6). In addition, parts of the polymer and low molecular weight fragments are removed during ablation. Thus a polymer network, with lower volume, remains with the appearance of the nap structures. The tree-like structures on the top of the nap are the result of a further polymer decomposition. There are two possibilities for this: a decomposition of the cross-linked polymer or a complete decomposition of the ablated fragments, which are redeposited. It was shown that, in the case of polyimide ablation, carbon clusters remained. These clusters can have a molecular weight of up to 5,000 and sometimes have included heteroatoms, like nitrogen [163–166]. With time-of-flight measurements, fullerenes have been found in the ablation plume [163–166]. The fullerenes can only be formed from a complete fragmentation to C_1, C_2, and C_3 fragments [167], which have been found with laser-induced fluorescence measurements [168]. Whether the tree-like structures are formed by the redeposition of plume particles or by remaining carbon clusters is not clear. Graphite and amorphous carbon were identified on polyimide (PI) after laser irradiation (308 nm) with Raman spectroscopy of single black particles [169]. The carbonized PI surface showed increased conductivity [65] and is suggested to be the result of a thermal mechanism leading to fused ring structures (248-nm irradiation) [170]. For laser irradiation (248 nm) of poly(vinyl chloride), no graphitization was found but polyene and polyyne structures were detected with Raman spectroscopy [171].

Attempts have been made to assign the carbon species to one of the above mentioned forms, but due to the low intensities of these bands and the tree-like structures (SEM picture), which cover the surface only partly, we were not able to assign the carbon in detail. Nevertheless we believe that a carbonization of the surface took place. The contact angle measurements have shown a drastic increase of the contact angle (Fig. 14), as expected for a very nonpolar surface like, e.g., graphite. The XPS spectra have also confirmed carbonization of the surface for 248-nm irradiation (Fig. 19).

For 308-nm irradiation a different behavior is found. The XPS spectra and contact angle measurements showed nearly no changes of the surface after irradiation. The small variation can be explained by the initial development of the microstructures, which became less pronounced after several pulses. The XPS spectra showed that the surface has nearly the same chemical composition as the starting material. This suggests that the polymer is removed completely layer by layer without altering the remaining material. The FT-Raman spectra have shown only an overall decrease of all polymer bands, indicating a decrease of the polymer thickness. A possible explanation is again the different penetration depth of the laser. In the case of 308-nm irradiation, the whole laser energy is concentrated in a thin layer and mainly the photolabile triazene group is excited and decomposed. The ini-

tial microstructures could be the result of some cross-linking in the early stages of ablation. A possible reason for this is shielding effects of surface contaminants which must be removed first. After several pulses these contaminants are removed and the polymer is ablated completely. The lack of debris [111, 120] after ablation and the absence of any solid or liquid fragments in the ablation plume [172], as revealed by ns-photography, suggests further fragmentation of the ablation products (Scheme 6, step 7). In conclusion we suggest that for 308-nm irradiation the polymer is ablated layer by layer with no modification of the polymer bulk.

2.2.2.3 Summary

It was demonstrated with surface analysis techniques that the polymer surface is modified selectively with different laser irradiation wavelengths. The two laser energy regimes, above and below the threshold for laser ablation, reveal pronounced differences. For both irradiation wavelengths (248 and 308 nm) the polymer surface modification is solely chemical after treatment with fluences below the threshold. Each irradiation wavelength leads to a surface oxidation, as shown with the contact angle and XPS measurements. The oxidation is a result of the radical pathway of photodecomposition of the triazene chromophore.

At fluences above the threshold of ablation, a different behavior is observed for each wavelength. After irradiation with 248 nm, growing nap-like structures are detected, possibly as a result of cross-linking of the polymer. The surface appeared black and carbonized, suggesting a variation of the mechanism of the low fluence irradiation. The polymer is only partly removed, due to the higher penetration depths. The remaining cross-linked polymer can be decomposed to carbon species, especially with the higher-photon energy of the 248-nm laser.

In the case of 308-nm irradiation some microstructures are created first, but the ablated surface becomes smooth again after some pulses. The chemical composition also remains unchanged after several pulses, suggesting a photochemical mechanism, removing the polymer completely layer by layer without any redeposition of ablation products.

2.2.3 *Nanosecond Transmission Studies*

2.2.3.1 Introduction

One weakness of postirradiation methods, i.e., analysis of the ablation properties and surface analysis, as tools for studying the ablation mechanisms of polymers is the possibility that reactions after irradiation cause the observed effect. These results are therefore only indirectly related to the abla-

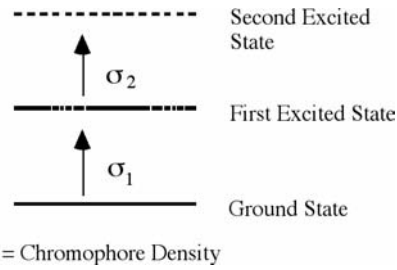

Fig. 21 Theoretical chromophore absorption model to analyze the dynamic absorption of the triazene polymer. Initially the polymer chromphores are in the ground state with the chromophore density ρ. Absorption of photons from the laser pulse promotes some chromophores to the first and second excited states. The absorption cross section of both are indicated with σ_1 and σ_2. REPRINTED WITH PERMISSION OF [Ref. 60], COPYRIGHT (1996) Springer Verlag

tion process. Time-resolved measurements, on the other hand, can give information about the reaction during irradiation and hence direct insight into the ablation mechanism. These data can also be used to evaluate some models suggested for laser ablation. Various models have been developed to describe the influence of thermal aspects on the ablation characteristics. Arrhenius-type rate expressions [76], thermal diffusion [173], and a model assuming one-dimensional heat transfer after the two-level chromophore absorption show good agreement with experimental data [78].

In recent studies of a photochemical model, attention was drawn to the absorption properties of the polymer during the laser pulse [132, 174]. These results were analyzed theoretically using a "two-level" model of chromophore absorption [175]. In this model, excited states of the chromophore are capable of photon absorption. The model is shown in Fig. 21. In Eqs. 2 and 3 the single photon absorption for ablation depth and transmission ratio is described,

$$d = \frac{1}{\rho}(S_0 - S_{th}) + \frac{1}{\rho\sigma_1}\ln\left(\frac{1 - e^{-\sigma_1 S_0}}{1 - e^{-\sigma_1 S_{th}}}\right) \tag{2}$$

where d=the etch rate, S_0=photon density striking the surface target, S_{th}=photon density at the threshold fluence, ρ=chromophore density, and σ=absorption cross section.

$$\frac{T_H}{T_L} = \frac{e^{(\rho\sigma_1 d)}}{\sigma_1 S_0}\ln\left(1 + \frac{e^{(\sigma_1 S_0)} - 1}{e^{(\rho\sigma_1 d)}}\right) \tag{3}$$

In Eq. 3 T_H is the transmission of the laser pulse at various fluences and T_L is the transmission of the sample measured with low energy, e.g., a UV-Vis spectrometer.

The model can be extended to two levels of excited states (Fig. 21), as described in Eq. 4

$$\frac{dS}{dx} = -\rho\sigma_2 S - \rho\frac{\sigma_1 - \sigma_2}{\sigma_1}\left[1 - e^{(-\sigma_1 S)}\right] \quad (4)$$

where S=photon density in the laser pulse (F/h), x=depth in the target, σ_1=absorption cross section of the first excited state, and σ_2=absorption cross section of the second excited state.

The absorption cross sections can be calculated according to Eq. 5,

$$\alpha_{\text{lin}} = \rho * \sigma \quad (5)$$

where ρ=chromophore density and σ=absorption cross section.

The chromophore density can be calculated according to Eq. 6

$$\rho = n * \rho_{\text{m}} \quad (6)$$

where ρ=chromophore density, n=number of chromophores, and ρ_{m}=the monomer density.

The photochemical model was probed by using one triazene polymer (structure shown in Scheme 5). Semiempirical calculations for a model compound, i.e., a bis-triazene (shown in Scheme 7) were applied to determine a realistic number of chromophores, which results in a decreasing number of "free" fitting parameters.

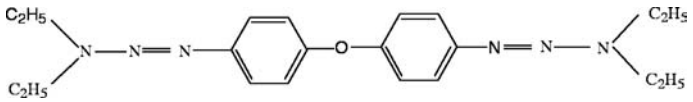

Scheme 7 Structural unit of the bis-triazene model compound. REPRINTED WITH PERMISSION OF [Ref. 60], COPYRIGHT (1996) Springer Verlag

2.2.3.2 Results and Discussion

The change in absorbance △A after irradiation was obtained from the spectra recorded by UV spectroscopy for films with a thickness of 0.21 μm. The single-shot transmission of the laser pulse (T_H) was measured at various fluences by using an experimental setup shown in Fig. 22. The low intensity

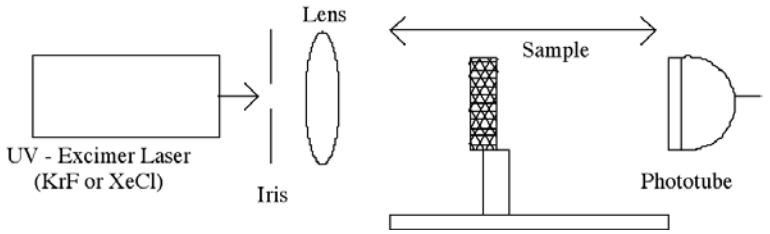

Fig. 22 Experimental setup for the transmission studies. REPRINTED WITH PERMISSION OF [Ref. 60], COPYRIGHT (1996) Springer Verlag

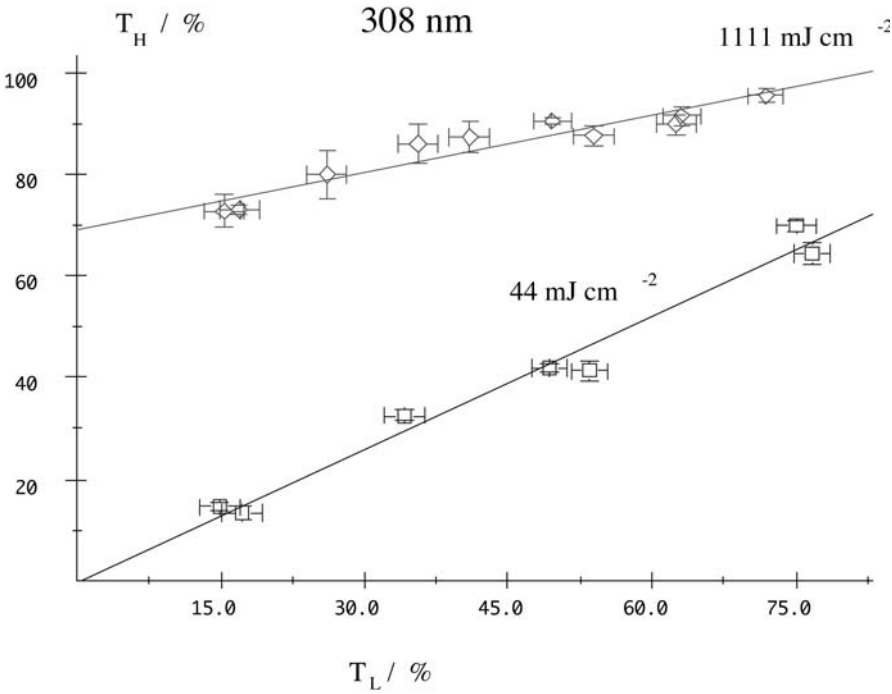

Fig. 23 Linear plot of the transmission value at low energy (T_L) derived from a UV spectrometer, vs the values measured with the laser experiment (T_H). Two different fluences (1.11 J cm^{-2} and 44 mJ cm^{-2}) are shown. The higher fluence represents the case of chromophore saturation, whereas the lower fluence shows the linear transmission behavior (see Fig. 28). REPRINTED WITH PERMISSION OF [Ref. 60], COPYRIGHT (1996) Springer Verlag

value of transmission was measured for all films using a conventional UV spectrometer. This value is called T_L in agreement with ref [170]. Plots of T_H vs T_L are linear as shown in Fig. 23. For each fluence the value of T_H for a fixed film thickness of 0.21 μm was calculated and used for the plot of the ratio T_H/T_L vs the applied fluence F. For 248-nm irradiation, linear plots of T_H vs T_L are also obtained.

The following material constants were determined to apply the above described model: linear absorption coefficient, α_{lin}, of 166,000 cm^{-1} at 308 nm and 66,000 cm^{-1} at 248 nm; polymer density of about 1.16 g cm^{-3}. Using these values a monomer density of 1.9×10^{21} cm^{-3} can be calculated ($\phi=\rho/MW*N_A$).

The threshold fluence (F_{Th}) was specifically determined for thin films, because for the transmission measurements thin films were used. The threshold fluence is normally determined from a linear plot of the etch depth d(F) vs ln F according to Eq. 1.

With this method, the etch depth and energy are normally averaged over many pulses due to the pulse energy deviation of the laser (up to 20%) and

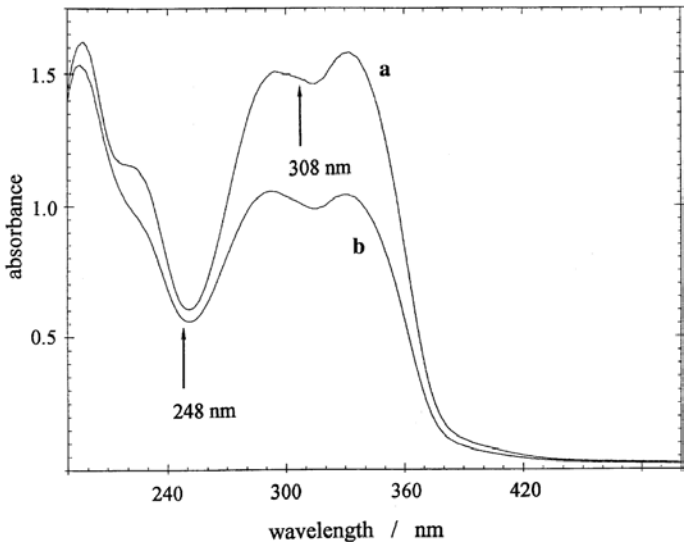

Fig. 24 UV absorption spectra of a thin polymer film (about 0.2 μm) on a quartz wafer **a** before and **b** after irradiation with a single pulse of 30 mJ cm^{-2} at 308 nm. This value represents a fluence above the threshold of ablation and the change of the absorbance corresponds to ablation. As evident from the figure, 248 nm corresponds to an absorption minimum, whereas 308 nm is close to the absorption maximum. REPRINTED WITH PERMISSION OF [Ref. 60], COPYRIGHT (1996) Springer Verlag

the relatively high energies applied. The use of the higher fluences results in ablation depths which can be measured more accurately, but small variations of the slope result in quite large uncertainties in the threshold fluence.

This variation is one of the reasons why other investigations have applied a quartz microbalance (QMB) [63, 176] technique to measure the threshold with a much higher precision. As an alternative technique, conventional UV spectroscopy is used in this study to determine the ablation threshold with single pulses. The absorbances of thin polymer films cast on quartz wafers were measured before and after irradiation with various fluences, as shown in Fig. 24.

For all of the measurements, only single pulses on fresh areas of film were used, in order to exclude the influence of chemical (incubation) or physical (microstructures) changes due to successive pulses. The change of the ab-sorbance, $\triangle$A, after irradiation was normalized for the different fluences, $\triangle$A/F. Figures 25 and 26 show the change of the absorbance, $\triangle$A/F, as a function of laser fluence for 248- and 308-nm irradiation respectively. The data were acquired for a film thickness of 0.21 μm. Linear rather than logarithmic axes are chosen for a more detailed view of the absorbance changes. The reason for choosing this particular film thickness will be discussed later.

The threshold fluence is defined as the fluence where a sudden increase of $\triangle$A/F is observed. A comparison of the $\triangle$A/F values calculated from these experiments using thin films with those calculated from experiments done

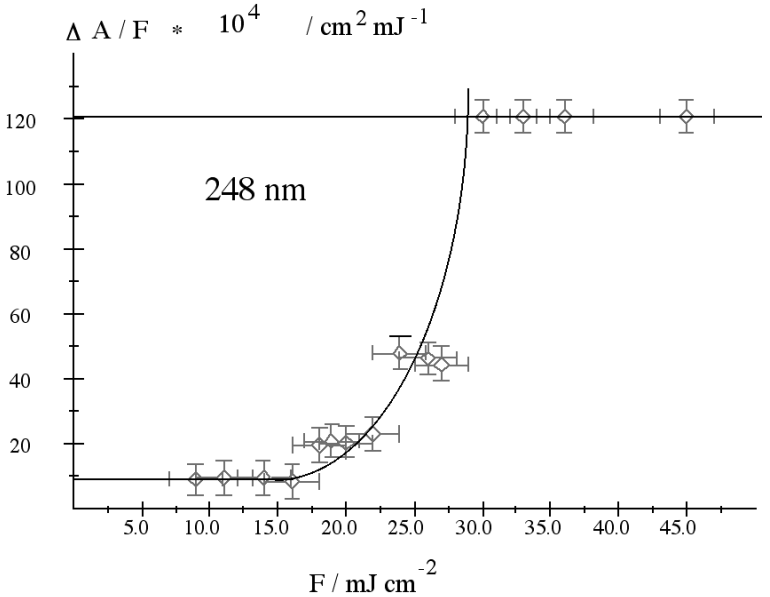

Fig. 25 Plots of the change of absorbance △A of thin polymer films (0.21 μm), recorded before and after single pulse irradiation with 248 nm. The values are normalized with the applied fluence and plotted vs the fluence. A nearly exponential increase is detected between 16 and 28 mJ cm^{-2}. REPRINTED WITH PERMISSION OF [Ref. 60], COPYRIGHT (1996) Springer Verlag

in solution reveals different behaviors. In solution the change of the absorbance in the applied fluence range is smaller than those in the films, and no sudden increase was observed. For the solution experiments, approximately the same beam size and same absorption was used as for the thin films. The only difference is the path length of the beam through the film (100 to 350 nm) as compared to the solution (1 cm). Values for △A/F of 1.3 with 10 mJ cm^{-2} and of 1.2 with 30 mJ cm^{-2} result for 308-nm irradiation (the values for 248 nm are about the same). The slightly larger (about 10) change of △A/F for 10 mJ cm^{-2} in the films is rationalized by an additional thermal decomposition of the polymer, which is caused by the exothermic photodecomposition due to the higher density of the chromophores in the condensed phase.

The absence of the sudden increase of △A/F in the solutions at higher fluence indicates that such an increase is a result of a solid-state process due to the ablation. To prove that ablation really occurred, the samples were inspected optically after irradiation. The clean surface of the quartz wafer was detected after several pulses, showing that the polymer was completely removed during the laser irradiation.

For both irradiation wavelengths (248 and 308 nm) *new values* of F_{th}^{new} are determined from the experiments with the thin films at low laser fluences. The *old values*, F_{th}^{old}, which were derived from the linear regression

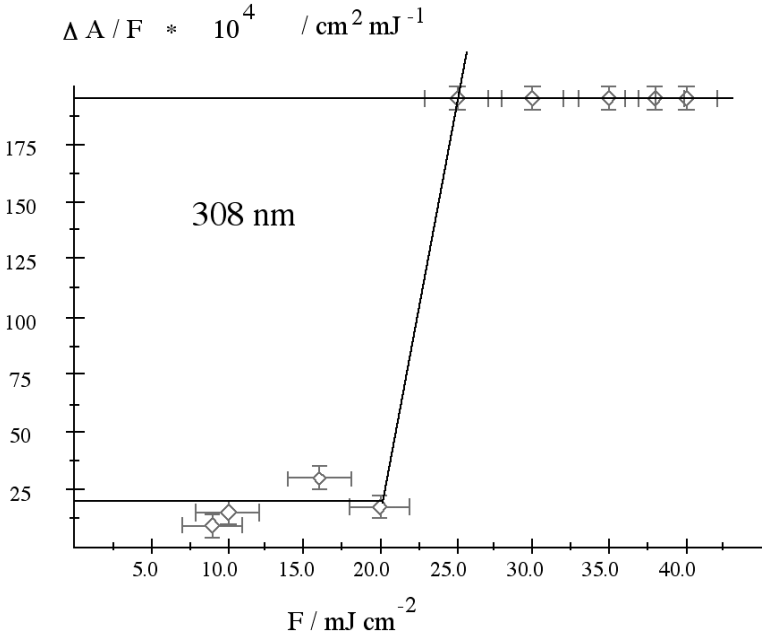

Fig. 26 Plots of the change of absorbance △A of thin polymer films (0.21 μm), recorded before and after single pulse irradiation with 308 nm. The values are normalized with the applied fluence and plotted vs the fluence. A sudden increase is detected between 20 and 25 mJ cm^{-2}. REPRINTED WITH PERMISSION OF [Ref. 60], COPYRIGHT (1996) Springer Verlag

according to Eq. 1 had given higher values [120]. Possible reasons for the quite large deviations are the aforementioned errors in the linear regression analysis and changes (physical and chemical) of the polymer for consecutive pulses. Another possibility for the different values is a change of the mechanism between thick films and thin films cast on quartz. The films cast on quartz have an additional interface between the polymer and quartz. An influence of internal reflection did not appear in the data. For all applied fluences linear relations between the film thickness and the transmission value were found (Fig. 23). Whether adhesion between the polymer and quartz has an influence on the ablation characteristics is not totally clear. Considering that adhesion will have the most influence on the first layer between the polymer and quartz, and the fact that for our measurements polymer always remained (Fig. 24) on the quartz, suggests that adhesion has only a minor influence. Other possibilities are shock waves, reflected from the substrate, and thermal heating due to absorption of the substrate. Therefore it is necessary to keep in mind that thin films might alter the ablation mechanism.

The new values derived for the thin films are compiled together with old values and other optical and ablation parameters in Table 3.

Table 3 Optical and ablation parameters of the triazene polymer

	248-nm irradiation	308-nm irradiation
d_{max} [μm][1]	1.3	3.2
α_{lin} [cm^{-1}]	66,000	166,000
α_{eff} [cm^{-1}][1]	41,000	18,000
F_{th}^{new} [mJ cm^{-2}]	16–32	22.5
F_{th}^{old} [mJ cm^{-2}][1]	91	114
monomer density, ρ_0	1.9×10^{21} cm^{-3}	1.9×10^{21} cm^{-3}

[1] Ref. [112]

Threshold Behavior. A closer inspection of the Figs. 25 and 26 shows that a different behavior is observed for 248- and 308-nm irradiation. The ablation at 308 nm, where the polymer has a higher absorption coefficient (Fig. 24), shows a very clear and well-defined threshold fluence. This type of sharp threshold was previously found only for irradiation of polyimide with an ArF excimer laser (193 nm). In a study of polyimide laser ablation at various wavelengths, this behavior was assigned to a "photochemical process" [63]. In this study only single-pulse data were employed and the thresholds of ablation were analyzed by using the QMB technique.

The threshold at 248-nm irradiation is not clearly defined as compared to the 308-nm threshold. A description as a "threshold fluence region" [177] is more appropriate. In the fluence range from 16 to 32 mJ cm^{-2} an increase of $\triangle$A/F is detected. The increase is exponential, followed by a constant area as shown in Fig. 25. This was also seen by Küper et al. [63] and ascribed to a "photothermal mechanism". The threshold behavior indicates that a photochemical model can be applied, at least for an irradiation at 308 nm.

Another significant characteristic of the triazene polymer is the difference between α_{lin} and α_{eff}, especially at 308 nm. These values differ by one order of magnitude which is unusual. Generally, only slight changes, similar values [178], or changes in the opposite direction [73] have been reported. In the case of a higher value of α_{eff} [73] this behavior was assigned to a "significant increase of the temperature" during ablation.

One explanation for the decrease of α is chromophore saturation, which is similar to those reported for the ablation of collagen at 193 nm [179] and PI at 193 and 248 nm [132, 174, 175]. In these studies, the transmission of the laser pulse through thin polymer films was used as a probe for the dynamic target optics, which is also described with the same theoretical model we are using in this study.

Thickness Dependence. Before describing the transmission behavior, the influence of the film thickness must be discussed. During the determination of the threshold fluence, an unexpected feature was detected. For both irradiation wavelengths, a dependence of ΔA/F on the film thickness was detected. At 308-nm irradiation, this is observed above the threshold fluence, and for 248 nm at the upper level of the threshold fluence range (32 mJ cm^{-2}). At

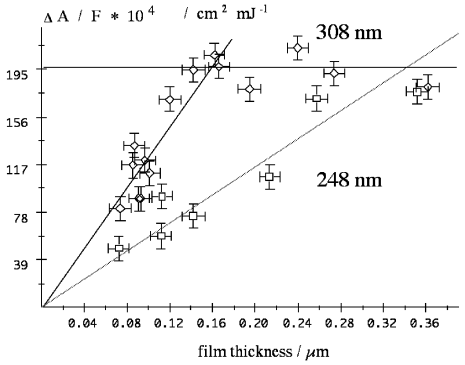

Fig. 27 Plots of the normalized change of the absorbance (△A/F) vs the used film thickness. At 308-nm irradiation (◇) a maximum value is reached. In the case of 248-nm irradiation (❑) a maximum value is reached within the applied film thickness. REPRINTED WITH PERMISSION OF [Ref. 60], COPYRIGHT (1996) Springer Verlag

fluence values of 22.5 mJ cm^{-2} at 308 nm and 32 mJ cm^{-2} at 248 nm, △A/F increases with increasing film thickness, whereas for the fluences below the threshold △A/F is independent of the film thickness.

In the case of the XeCl laser irradiation, the △A/F values increase with increasing film thickness to reach a maximum value as shown in Fig. 27. For 248-nm irradiation, an increase of the ratio can also be detected, but with a shallower slope, as seen in Fig. 27.

In the case of KrF laser irradiation, no clear maximum was observed within the applied range of film thickness. Thicker films could not be used because the high absorption coefficient at the maximum resulted in optical densities too large to measure.

From the UV spectra [a final curve (b) is shown in Fig. 24], it can be deduced that the film is not completely ablated at the applied fluence. The UV spectrum after the irradiation still shows the same absorption only with lower absorbance values.

Since α_{lin} is not valid during ablation it must be considered that nonlinear effects, chromophore saturation, or decomposition of the polymer occur during the time scale of the pulse.

Thermal and photochemical decomposition release energy and accelerate the polymer decomposition. This additional energy can lead to a higher decomposition rate than expected from the laser energy alone. Thermogravimetric analysis (TG) of the polymer showed that the exothermic decomposition starts at about 500 K [121, 156]. In the case of the photochemical decomposition, no experimental data, whether of an exo- or endothermic process, are available. However, semiempirical MO [180] calculations were conducted for a model compound (shown in Scheme 5) and its fragments; the heats of formation were calculated using the PM 3 Hamiltonian [181, 182], and the UV transitions were calculated by ZINDO [183] using the INDO/1 Hamiltonian. The calculations, assuming a homolytic bond cleavage be-

tween the N–N single bond with a subsequent release of nitrogen, also showed an exothermic decomposition with a similar decomposition enthalpy as that measured with differential scanning calorimetry (DSC) for the thermal decomposition. The result that both decomposition pathways are exothermic gives some indication that a photothermal part might be involved in the ablation mechanism.

Calculation of the Number of Chromophores. One important parameter in the model is the number of chromophores. In previous studies [132, 175] this number was always used as an adjustable parameter in the model. In our opinion it seemed to be more correct to calculate the chromophore number independently. This would result in a better use and evaluation of the model. The most important property of the triazene polymer is the absorption maximum around 330 nm which was assigned to the triazene chromophore in structurally similar compounds [119, 140].

For a more detailed analysis of the absorption properties, the UV spectrum of the model compound (Scheme 7), which was also synthesized, was calculated using semiempirical methods (MOPAC/ZINDO). The experimental UV spectrum of the model compound is nearly identical to the spectrum of the polymer. From the calculation it was derived that four UV transitions contributed to the absorption maximum at 330 nm. In detail, these are the HOMO→LUMO, the HOMO→LUMO+1, the HOMO→LUMO+2, and the HOMO→LUMO+3 transitions. The first two orbital excitations showed a large involvement of the triazene group, whereas the other two are mainly localized at the phenyl moieties. Similar results were previously reported for aryl dialkyl triazenes [119, 184] which have the same structural unit. Starting from simple chemical considerations, it could be thought that the number of chromophores responsible for the absorbance at around 300 nm is a low value, for example 2 or 4 per unit. On the other hand, the semiempirical calculations indicated the involvement of the phenyl moieties in the absorption properties; therefore, the chromophore number in the calculation was not restricted to low values. As a starting point for the calculation, numbers close to the expected value were chosen.

In the case of the 248-nm irradiation, it is more complicated to predict a chromophore number because the absorption spectrum (Fig. 24) showed an absorption minimum around these wavelengths. Assuming a Lorentzian profile of the UV transitions, the KrF excimer laser can excite both absorption bands, below and above 248 nm. Therefore, no indication is given whether the phenyl system (below 248 nm) or the triazene group (above 248 nm) will be excited.

A simple consideration of typical values for N–N bond energies shows that they are in the range 1.5 to 3.0 eV (taken from hydrazine derivatives) [184]. Therefore, both the 248-nm (5 eV) and the 308-nm (4 eV) excimer lasers are capable of breaking this bond directly. For aryl dialkyl triazene compounds, which exhibit a similar structural unit, a radical pathway of decomposition was reported [119, 140, 153]. The first step in this pathway is the homolytic bond cleavage between the N–N bond, creating a labile diazo

radical which decomposes at an extremely fast rate. The fact that both applied lasers are capable of direct bond breaking in the polymer creates the possibility of applying a photochemical model.

2.2.3.3 Application of the Model

Transmission Studies. To determine the influence of the optical dynamic properties on the high etch rate at 308 nm, the transmission of the laser pulse through thin polymer films was measured.

The ratio of T_H/T_L, as suggested by Pettit et al. [175], was plotted against the laser fluence. For 248-nm irradiation, only fluence values up to about 800 mJ cm^{-2} could be used because at higher fluences (e.g., 1.1 J cm^{-2}) ablation of the quartz occurs. For the same reason, the upper fluence limit for 308-nm irradiation is about 2.5 J cm^{-2}. These values are in rough agreement with studies of the ablation of silica [185, 186], which also showed a strong dependence of the ablation on the surface quality [186].

For the 308-nm irradiation, a clear increase of the transmission ratio starting at about 120 mJ cm^{-2} is derived (shown in Fig. 28). For 248 nm, only a slight increase is found (shown in Fig. 29) although this could be due to the limited fluence range. The dynamic optical behavior of the polymer can provide a preliminary explanation of the difference between the experimental etch rates compared with the expectation from the linear absorption coefficient and the prediction from Eq. 2.

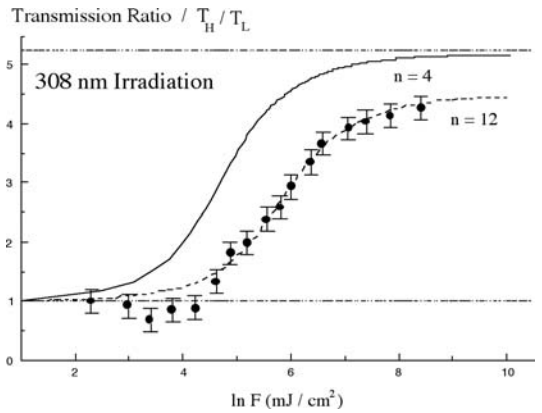

Fig. 28 Transmission ratio (high fluence transmission/low fluence transmission) vs laser fluence at 308 nm. The discrete data points indicate the experimental results. The linear behavior is indicated with the *line* at T_H/T_L=1, whereas the *line* at T_H/T_L=5.26 indicates the theoretical maximum value for the transmission ratio according to Eq. 1. The *solid* curve is the result of applying the fit parameter of Fig. 29, which gives a satisfying result for the ablation rate. The *dashed line* shows the result of a fit which gives better results for T_H/T_L. REPRINTED WITH PERMISSION OF [Ref. 60], COPYRIGHT (1996) Springer Verlag

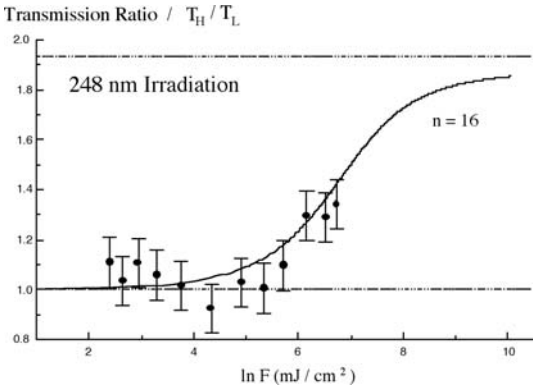

Fig. 29 Transmission ratio (high fluence transmission/low fluence transmission) vs laser fluence at 248 nm. The discrete data points indicate the experimental results. The linear behavior is indicated with the *line* at T_H/T_L=1, whereas the *line* at T_H/T_L=1.95 indicates the theoretical maximum value for the transmission ratio according to Eq. 1. The *solid* curve is the result of applying the fit parameter of Fig. 30, which gives a satisfying result for the ablation rate. REPRINTED WITH PERMISSION OF [Ref. 60], COPYRIGHT (1996) Springer Verlag

The etch rates of the polymer together with the predicted values (from Eq. 2, dash-dot line) are shown in Figs. 30 and 31 for both irradiation wavelengths.

In the case of 308-nm irradiation, the difference between the experimental data and values predicted by Beer's law is much higher than in the case of 248 nm. Also, the increase of the transmission ratio T_H/T_L vs fluence at 308 nm exceeds that at 248 nm, showing that the target's dynamic optical properties could explain the experimental etch rates.

To obtain a more detailed understanding of the dynamic process, the theoretical model of Pettit et al. [175] was applied to the experimental data of the triazene polymer. It was not possible to obtain satisfying fits to the experimental data using the single-photon treatment and Eqs. 2 and 3 [132, 175], therefore the two-level absorption model was used. Equation 4 may be solved numerically using a fourth-order Runge-Kutta method. The results of numerically integrating Eq. 4 were compared to the exact solution for the single-photon absorption, σ_2=0, Eqs. 2 and 3 to benchmark the solution method. The two calculated transmission ratios agreed to within <0.1%, but the ablation depths varied by as much as about 10%. This is not surprising since Eq. 4 is a direct function of S but not of *x*.

308-nm Irradiation. For both data sets, etch rate and transmission ratio T_H/T_L, the two-level model must be applied. With this model, it was possible to obtain a good fit of the ablation rate up to a fluence range of about 20 J cm^{-2} as shown in Fig. 30 for the polymer films with a thickness of about 200 μm. For this fit, values for ρ=7.60×10^{21} cm^{-3}, σ_1=2.184×10^{-17} cm^2, and σ_2=1.420×10^{-19} cm^2 were used which correspond to a chromophore number (*n*) of 4.

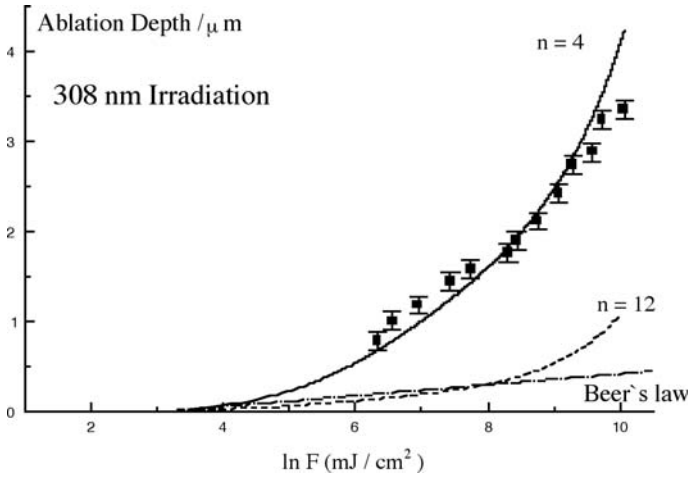

Fig. 30 Ablation depth vs pulse fluence relationship for the 308-nm XeCl excimer laser irradiation of a 200-μm-thick polymer film. The experimental data are taken from [11]. The *dash-dot* curve indicates the predicted relationship based on Beer's law. The *continuous* curve uses n=4 to reach a satisfying fit. The *dash* curve shows the result of a different fit parameter, n=12, which must be used to reach a satisfying fit of the transmission ratio in Fig. 27. REPRINTED WITH PERMISSION OF [Ref. 60], COPYRIGHT (1996) Springer Verlag

These values are consistent with the values discussed previously. The result of this fit is shown as the solid curve in Fig. 30, where the etch rate based on Beer's law is also included. This line is obviously much lower than the experimental values.

Unfortunately, it was not possible to use the same set of fitting parameters for the transmission ratio. The fit with n= 4, shown in Fig. figciteplus>28 by the solid line, increases much earlier (close to 10 mJ cm^{-2}) than the measured values, and nearly reaches the theoretical maximum value. This value is calculated from Eq. 7

$$\frac{T_H}{T_L}|_{max} = \frac{1}{e^{-\alpha_{lin} d}} = e^{\alpha_{lin} d} \tag{7}$$

and is indicated in Fig. 28 with the dash-dot-dot line at 5.26. The discrepancy, especially at the point where the curve increases, is not due to a bleaching of the film during the measurement of T_L. This would lead to lower values of the transmission ratio as compared to the true film transmission. This is stated as one possible reason for deviations in Ref [170]. The energy of the UV spectrometer which is used to determine T_L is clearly much lower (around 0.2 μJ cm^{-2}) [187] than the value used in Ref [170] (2 mJ cm^{-2}). It is very unlikely that such a low value would bleach the film. To achieve a satisfying fit (dashed line) of the transmission ratio, it was necessary to change the parameters to ρ=2.28×10^{22} cm^{-3}, σ_1= 7.281×10^{-18} cm^2, and σ_2=6.917×10^{-19} cm^2 which correspond to 12 chromophores. This value

would also be consistent with the possible number of chromophores, as discussed previously. Unfortunately, the etch rate with these values results in a curve (dashed line in Fig. 28) close to the curve predicted by Beer's law, which is also much too low.

Further attempts at fitting both experimental curves showed that the necessary parameters always follow opposite trends.

A multiphoton absorption process as described by Pettit et al. [132, 174], which was successfully applied to the ablation of Teflon with femtosecond pulses at 248 nm [132] and 798 nm [188], was not considered in this case. The two reasons are the high absorption coefficient and the detected bleaching of the absorption in the transmission ratio, whereas a multiphoton process would increase the absorption. Whether a cyclic multiphoton process [97] described for anthracene-doped PMMA can be responsible for this different behavior will be the subject of further studies. During this process, the excited triplet states play the key role; therefore, transient absorption spectra will give valuable information. For a similar polymer where only the bridging atom between the phenyl ring is changed, time-dependent measurements have already given valuable information [133]. According to these results the bleaching detected in the transmission studies can also be ascribed to the polymer decomposition during the time scale of the pulse (in this case 351-nm irradiation is used) [133]. In further studies, the influence of thermal aspects must be included in the mechanism of ablation at 308 nm.

248-nm Irradiation. Contrary to the results at 308 nm, it was possible to fit the etch depth (Fig. 31) as well as the transmission ratio (Fig. 29) with one set of parameters.

As for 308-nm irradiation it was not possible to use the one-photon absorption model, therefore the two-level model was applied again. The parameters for the fit are $\rho=3.04\times10^{22}$ cm^{-3}, $\sigma_1=2.171\times10^{-18}$ cm^2, and $\sigma_2=1.085\times10^{-18}$ cm^2. This is equal to 16 chromophores. The value of chromophores is again in the expected and reasonable range for the involvement of the phenyl moieties in the absorption. The result is shown as the solid curve in Fig. 29. Again, the maximum theoretical value is included as a dash-dot-dot line. Additionally, it should be stated that the data set for the transmission ratio is very limited, and that the Beer's law absorption (dash-dot line in Fig. 31) gave at least a similar result as the fit. For the linear fit, the deviation is mainly in the higher fluence range, whereas for the transmission study a slight increase in the transmission is found.

Nevertheless in the case of 248-nm irradiation, the fit with one set of parameters shows agreement with both sets of experimental data. This may be an indication, together with the different threshold behavior as compared to 308-nm irradiation, that there are different mechanisms acting at the different laser wavelengths, and that the concept of designing polymers for special laser wavelengths is working.

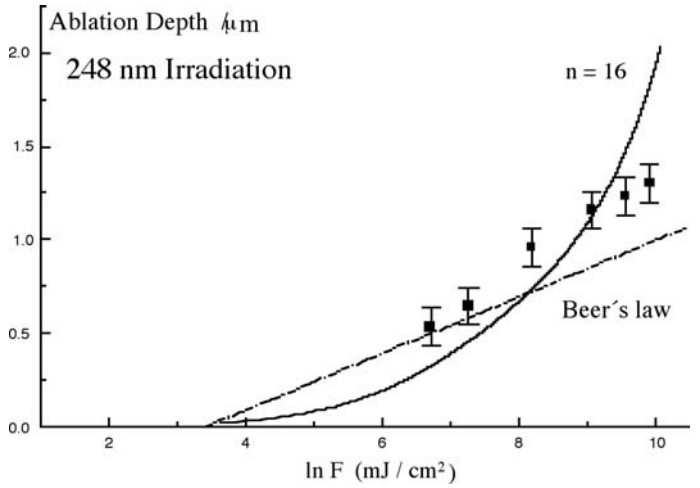

Fig 31. Ablation depth vs pulse fluence relationship for irradiation of a 200-µm-thick polymer film with the KrF excimer laser (248 nm). The experimental data are taken from [11]. The two curves are plotted over a large fluence range. The *dash-dot* curve indicates the predicted relationship based on Beer's law. The *continuous* curve is the result of the two-level absorption model, using the same fit parameter (*n*) as in Fig. 29. The parameter is described in the text. REPRINTED WITH PERMISSION OF [Ref. 60], COPYRIGHT (1996) Springer Verlag

2.2.3.4
Summary

The study of the triazene polymer showed a clearly defined threshold fluence at 308 nm, whereas with 248-nm irradiation a "threshold fluence region" is determined. Films with different thicknesses exhibit a dependence of the change of the absorbance on the film thickness. The fluence-normalized change of the absorbance, $\Delta A/F$, increases with increasing film thickness to reach, in the case of 308 nm, a constant value. For 248-nm irradiation, a maximum value cannot be reached because of the limited range of film thickness which can be studied. The lack of correlation between the thickness where the value becomes constant and the linear absorption coefficient shows that, even at such low fluences, α_{lin} is not valid during ablation or that thermal decomposition takes place.

The transmission for ns UV pulses is clearly dependent on the fluence in a range of a few mJ cm^{-2} to several J $cm^{-2.}$ With 248-nm irradiation, only a slight increase of the transmission ratio, $T_H/T_{L,}$ could be detected, whereas with the XeCl excimer laser irradiation much higher transmission ratio values are reached which are close to the theoretical limit.

Again there is a significant difference between the irradiation at 248 and 308 nm. The two-level model of Pettit et al. [175] can only describe the behavior with both sets of data for 248-nm irradiation but not for the 308-nm irradiation. In the latter case, it is possible to reach a satisfactory fit to either

the etch rate or the transmission ratio but unfortunately not to both sets of data. Taken together, this demonstrates that it was not possible to apply the photochemical model to a triazene polymer which is known to be photolabile. This suggests that additional parameters, such as decomposition enthalpy, should be considered. Therefore it is probably impossible to separate the ablation mechanism into photochemical or photothermal. The mechanism will always be a mixture of both, with a variable contribution of the photochemical and photothermal part, depending on the polymer.

2.2.4
Nanosecond Interferometry

2.2.4.1
Introduction

The analysis of the transmission of the film during irradiation suggests that decomposition of the triazene chromophore occurs during irradiation. The decomposition of the chromophore in the film should result in changes of the surface topography. Therefore another time-resolved method was applied that can give this information. This technique is nanosecond interferometry, which allows the observation of the surface morphology with nanosecond resolution.

Intense pulse laser irradiation results in high-density excitation of organic chromophores, leading to morphological changes of the films [94, 189]. The coupling between molecular processes and morphological changes is one of the most unique and important characteristics of laser ablation. However, both have been studied rather separately and discussed independently. Excitation energy relaxation dynamics and primary chemical processes of organic molecules in laser ablation have been investigated by using various time-resolved spectroscopies, such as fluorescence [93, 94, 190, 191], absorption [93, 94, 190], Raman [192], and IR [193] spectroscopies. Under the ablation conditions, normal photophysical and photochemical processes are modified and new relaxation channels are opened. For example, it has been revealed that cyclic multiphoton absorption and mutual interactions between excited states were brought about, causing rapid temperature elevation of the polymer matrix [93, 95, 96] and thermal decomposition of the polymer [95, 192]. On the other hand, morphological dynamics has been studied mainly with respect to ejection behavior of fragments or plume [94, 172, 194–197]. Of course the ejection dynamics is a reflection of the molecular process, but direct information is not clearly contained in the ejection behavior, since the primary molecular processes are already completed when fragments or plume ejection are brought about. Therefore, it is most desirable to correlate the molecular process with morphological changes during or just after the excitation laser pulse, from which new aspects of the laser ablation mechanism will be clarified. Nanosecond interferometry allows one to measure 20–30-nm expansion and contraction of irradiated films with a time resolution

of ≈10 ns [198, 199]. Such nanosecond morphological changes of biphenyl- or pyrene-doped poly(methyl methacrylate) (PMMA) and poly(methyl acrylate) (PMA) films were successfully measured above and below the ablation threshold [200]. It was demonstrated that, even below the ablation threshold, transient expansion of the polymer films emerged during the excitation pulse, which was confirmed to be thermal expansion due to the nanosecond photothermal heating by doped aromatic molecules [198, 199]. The expansion dynamics was well interpreted to be consistent with the glass-rubber transition of the polymer films [199]. It was shown that, above the ablation threshold, expansion already started during the excitation pulse and then ejection of ablated polymer followed explosively [198].

One of the designed photolabile triazene polymers (Scheme 8) was selected to test whether a different behavior can be detected for these materials. In this report, decomposition dynamics of the photosensitive triazene polymer film upon intense XeF excimer laser irradiation is studied by applying the nanosecond interferometric technique with a newly improved optical setup. On the basis of the revealed morphological dynamics as well as the obtained time-resolved transmission and reflectance, the ablation mechanism and the dynamics of the triazene polymer film are discussed in detail.

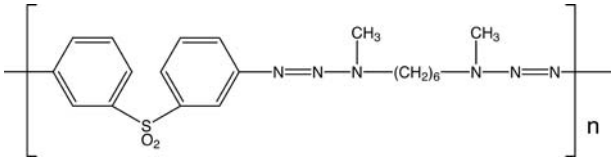

Scheme 8 Structural unit of the triazene polymer

The experimental setup for the nanosecond interferometry experiments has been described previously [198, 199], except for a novel improved optical configuration. The optical configurations are illustrated in Figs. 32a and b, which are called *surface* and *internal* configurations, respectively. The surface configuration is the same as that in the previous works [198, 199], while the internal configuration is a novel design.

In the case of the surface configuration, the interference pattern results from the interference between the reference light and the light reflected at the polymer surface. In order to avoid a disturbing interference due to light reflected at the back surface of the plate, a quartz plate whose two surfaces are not parallel is applied. The interference pattern represents the surface profile of expansion or etching of the irradiated polymer film, as long as the optical properties in the pathway of the probe beam are not changed appreciably. However, fragments or gaseous products are sometimes ejected from the surface of the sample film upon laser ablation, which may vary the effective optical path length of the reflected light. The disturbance by the ejected products will lead to an overestimation of the surface displacement of the irradiated polymer film, since the ejected products have a higher refractive index than air. To overcome this problem, the internal configuration has been

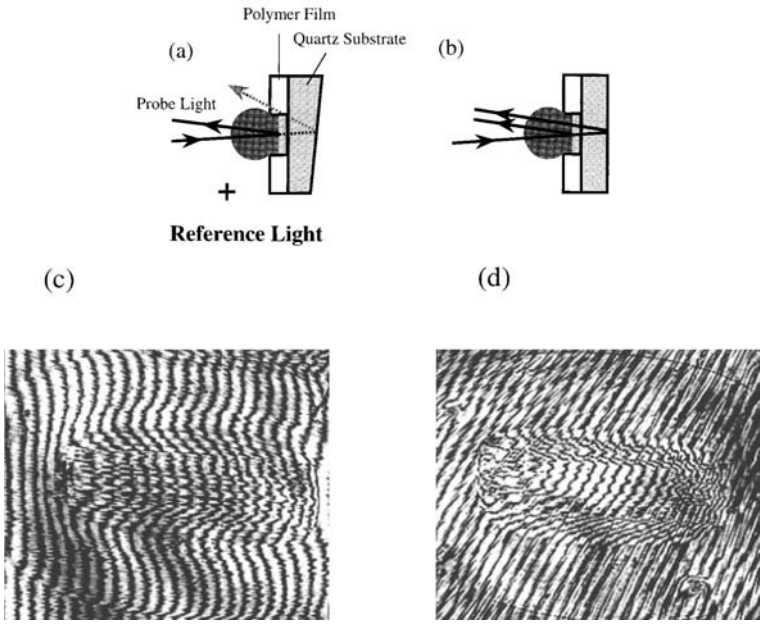

Fig. 32 Optical setups of (**a**) the surface configuration and (**b**) the internal configuration. Typical interference images of the triazene polymer film obtained with (**c**) the surface configuration and (**d**) the internal configuration. Both images were acquired under the same conditions at 4.0μs after excitation with a fluence of 250 mJ cm^{-2}, and fringe movement to the right represents an etching for both configurations. REPRINTED WITH PERMISSION OF [Ref. 125], COPYRIGHT (1997) American Chemical Society

developed. In this case, a quartz plate whose two surfaces are slightly tilted are used while the reference mirror is masked. Thereby, two beams reflected at the polymer surface and at the back surface of the quartz substrate interfere with each other. As both reflected light beams pass through the ejected ablation products similarly, the optical disturbance due to the ablated products is eliminated. Only the change of thickness and/or refractive index of the polymer film may be included in the shift of the interference patterns because the quartz substrate is not excited by the laser irradiation. Figures 32c and d show the superior performance of the internal configuration, by comparing interference patterns at +4.0 μs after irradiation with the same fluence (250 mJ/cm^2) obtained by both optical configurations. Here fringe movement to the right represents etching for both configurations. In the case of the internal configuration (Fig. 32d), the fringe shift was observed only in the border of the irradiated area, while additional fringe deformations inside and around the irradiated area are clearly visible for the surface configuration (Fig. 32c). A probable reason is the inhomogeneous distribution of the ejected gas molecules. The central fringe shift and the surrounding fringe deformation in Fig. 32d are due to etching of the film and the expanding shock wave, respectively.

Effective Change of Optical Path Length in Sample Film. The change of the optical path length induced by excimer laser irradiation can be extracted from the fringe shifts in the interference patterns. As the optical path length is a product of refractive index and the real distance in the path of a probe light (in the case of the internal configuration), not only the thickness change but also the refractive index change of the polymer film cause variation of the optical path length. The refractive index change is most probably due to the temperature elevation and formation of photochemical reaction products. Initially the change should occur only at a thin surface layer of the film (~90 nm) since the sample film has a high absorbance of about 4.6 at the excitation wavelength in a film of 1-μm thickness. The contribution of the refractive index change is not so large, due the small change of refractive index in the thin layer. Therefore it can be assumed that the index change of the film is negligible in the calculation of the thickness change during excimer laser irradiation.

2.2.4.2
Results and Discussion

In Fig. 33 the interference patterns at a fluence of 250 mJ cm^{-2} with the surface configuration are shown as a function of the delay time. It should be

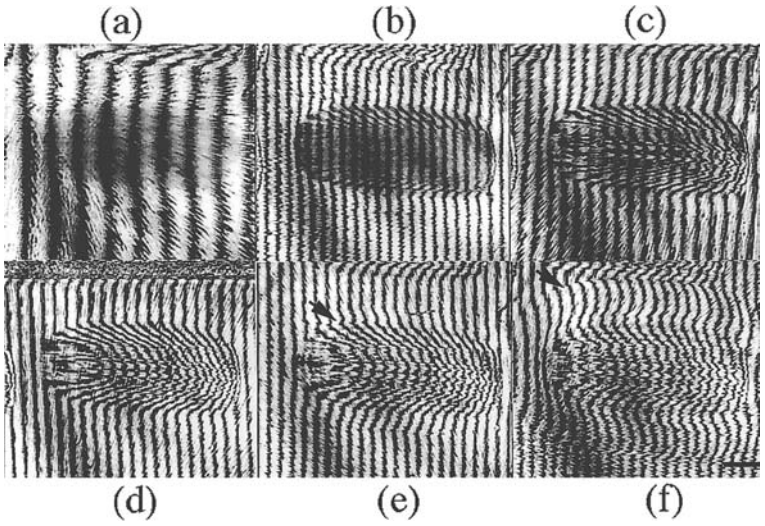

Fig. 33 A series of nanosecond time-resolved interferometric images of the triazene polymer film at a fluence of 250 mJ cm^{-2}, which were obtained with the surface configuration. In this case, fringe shift to the right represents an etching. Delay time (Δt):(**a**) −9 ns, (**b**) +10 ns, (**c**) +57 ns, (**d**) +260 ns, (**e**) +1μs, and (**f**) +3 μs. The *black bar* in (**f**) indicates 1 mm in the image. *Arrows* in (**e**) and (**f**) point to the propagation front of the shock wave. REPRINTED WITH PERMISSION OF [Ref. 125], COPYRIGHT (1997) American Chemical Society

noted that the interference fringe patterns vary slightly, due to the application of a fresh surface for each experiment.

In this experiment a movement of the fringe to the right side represents an etching of the polymer film, which was attained by adjusting the optical condition. Slight fringe shifts to the left side, expressing a swelling of the film, and darkening in the irradiated area were observed even at the onset of the excimer laser pulse ($\Delta t=-9$ ns). Then increasing fringe movement to the right side, expressing an etching of the polymer film, was detected after about a $\Delta t=+10$ ns. The shift increased with time until, after a few tens of nanoseconds, the pattern in the irradiated area became inhomogeneous, which is ascribed to effects caused by ejected products (inevitably involved in the *surface* configuration). From $\Delta t=+1.0$ μs distortions of the fringe pattern outside the irradiated area expanded (arrows in the figure), which is considered to correspond to shock waves.

Their propagation velocity is ~1000 m s^{-1}, which is consistent with that observed by nanosecond photography of the same triazene polymer film [172]. It is noteworthy that interference patterns in the irradiated area were always visible at all delay times. This is a new case, since laser ablation of PMMA films doped with biphenyl or pyrene results in dense ejection of fragmented debris leading to shielding of probe light [198]. The present results suggest that only gaseous products are generated and ejected by the excimer laser irradiation, which is also consistent with the fact that no debris and no contamination were observed around the etched areas [200]. The expansion and etching behavior can be obtained by analyzing the interference patterns at each delay time, because a shift of one fringe spacing to the right corresponds to etching of 266 nm, i.e., the half wavelength of the probe laser. The results obtained with two different optical setups are summarized and shown for the fluence of 250 and 60 mJ cm^{-2} in Figs. 34 and 35, respectively. The apparent etching obtained by the surface configuration is always deeper than that by the internal configuration. The permanent etch depth at 250 and 60 mJ cm^{-2} is 600 and 140 nm, respectively. These values are in agreement with the etch depth determined by a profilometer.

Darkening and Small Expansion at the Early Part of the Excimer Laser Pulse. Prior to etching, darkening and slight expansion of the film were observed from ~−10 ns for 60 and 250 mJ cm^{-2} irradiation as shown in Fig. 33a. Such darkening upon laser ablation was reported for PMMA and poly(ethylene terephthalate) (PET) by other researchers and assigned to scattering by ejected materials or bubble formation in the irradiated surface upon laser ablation [194, 195]. In this time region, the expansion dynamics measured with both internal and surface configurations were quite similar to each other, as shown in Figs. 34 and 35, which means that the disturbance by the ejected products is negligible. It is most probable that etching and ejection of ablation products starts with the beginning of the excimer laser pulse, although irradiation of the excimer laser should induce decomposition of the triazene polymer. Formation of small bubbles in the irradiated surface, leading to light scattering, also seems to be unlikely, since the fringe pattern dur-

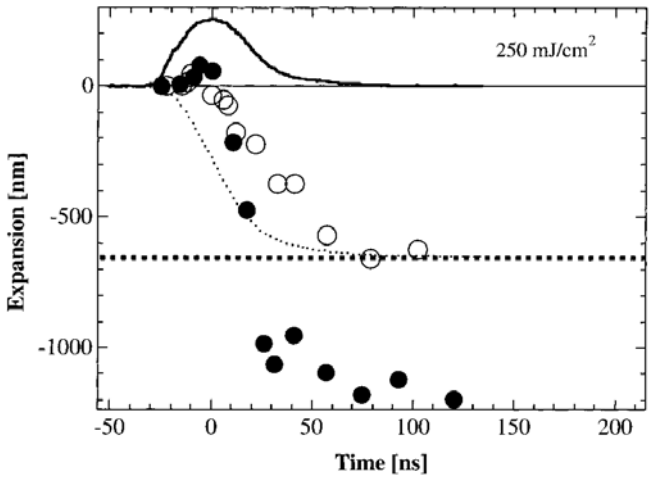

Fig. 34 Etching evolution of the triazene polymer film at the fluence of 250 mJ/cm^{-2} with the surface configuration (●) and with the internal configuration (◯). The *thick dashed line* represents the permanent etched depth (~660 nm). The *thick solid curve* is a profile of the excimer laser pulse, and the *dotted curve* is an inverse of its integration. The latter is normalized to the permanent etched depth. REPRINTED WITH PERMISSION OF [Ref. 125], COPYRIGHT (1997) American Chemical Society

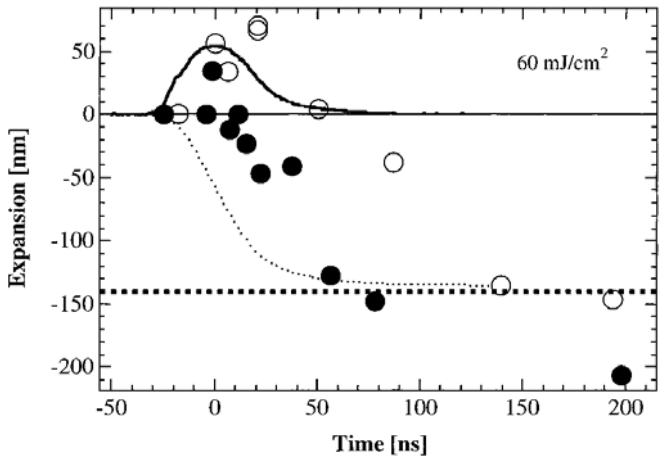

Fig. 35 Etching evolution of the triazene polymer film at the fluence of 60 mJ cm^{-2} with the surface configuration (●) and with the internal configuration (◯). The *thick dashed line* represents the permanent etched depth (~140 nm). The *thick solid curve* is a profile of the excimer laser pulse, and the *dotted curve* is an inverse of its integration. The latter is normalized to the permanent etched depth. REPRINTED WITH PERMISSION OF [Ref. 125], COPYRIGHT (1997) American Chemical Society

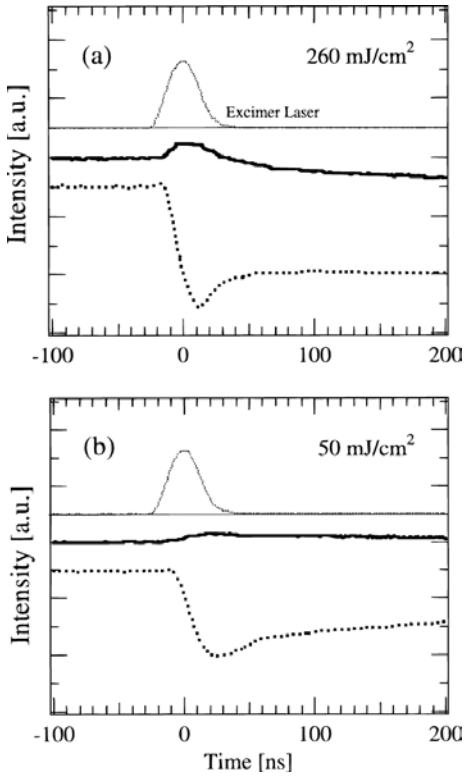

Fig. 36 Time-resolved transmission and reflectance of the triazene polymer film at (**a**) 250 mJ cm^{-2} and (**b**) 50 mJ cm^{-2}. The *thick solid* and *dashed curves* represent transmission and reflectance changes, respectively, while the *dotted* one is the time profile of the excimer laser pulse. REPRINTED WITH PERMISSION OF [Ref. 125], COPYRIGHT (1997) American Chemical Society

ing darkening was not distorted but defined clearly. It is therefore quite possible that the previously suggested mechanisms for the darkening are not active in this case. The small swelling of a few tens of nanometers around 0 ns can be explained by two theories. One is a simple expansion of the triazene polymer film, while the other assumes that photodecomposed products such as monomers and oligomers start to expand. The latter may be more probable, although further experiments are needed to be conclusive. The time-resolved transmission and reflectance of the irradiated triazene polymer film above 580 nm was measured to analyze the temporal evolution of the darkening,

In Fig. 36, time-resolved transmission and reflectance are shown for a fluence of 250 mJ cm^{-2}. The reflectance starts to decrease and recovers to some extent from the onset of the excimer laser pulse, whereas the transmission slightly increases initially, followed by a gradual decrease. If the darkening was caused by light deflection or scattering by ejected gas or bubbles formed

upon excimer laser irradiation, both transmission and reflectance should be attenuated. The increase of the transmission indicates that the sudden drop of the reflectance is not due to light deflection or scattering, but due to the decrease of reflectivity of the film. It is reasonable to assume that a change of the reflectivity was induced by the decrease of the refractive index at the irradiated polymer surface, and photodecomposition of the triazene polymer may cause this decrease of the refractive index. The triazene chromophores in the main chain decompose rapidly upon excimer laser irradiation. As a result, the absorption spectrum of the triazene chromophore in the ultraviolet region should change (decrease of the band assigned to the triazene chromophore), and the spectral change should cause a slight decrease of the refractive index in the visible region. As the triazene polymer has a high absorption coefficient at the excitation wavelength, the refractive index change is estimated to take place at a surface layer of about 90 nm as mentioned above. It is therefore quite probable that the photodecomposition of the triazene polymer at the thin surface layer causes the decrease of the refractive index, resulting in the decrease of the reflectivity, even if the photodecomposition in this time region does not cause a pronounced change of the optical path length in the film. A slight permanent increase in transmission, and a decrease followed by a slight recovery were observed at 60 mJ cm^{-2} (shown in Fig. 36b).

Etching Dynamics During and After the Excimer Laser Irradiation. Ablation of the film was initiated around the peak time of the excitation laser pulse; however, different time evolutions of etch depth were observed with the two different experimental configurations. The difference is more pronounced after the initial slight expansion. The time-resolved ablation depth, estimated with the *surface* configuration is larger than the depth obtained by the *internal* configuration. The former ablation depths exceed temporally the permanent depth (the thick dashed line in the figure), which is obtained after a delay of a few microseconds. The behavior can be assigned to the disturbances by the products ejected from the film in the measurement with surface configuration. The apparent depth emerging from $\Delta t \sim +10$ ns means that explosive ejection of the decomposed polymer from the film surface started from this delay time. Qualitatively the behaviors at 250 and 60 mJ cm^{-2} were similar to each other. In the case of 250 mJ cm^{-2}, the increase of the absolute ablation depth and of the difference between both profiles obtained by the two different configurations ceased almost at the end of the excimer laser pulse ($\Delta t \sim +80$ ns). The exothermic thermal degradation is expected to sustain the temperature, resulting in a continuation of ablation after the end of the excimer laser irradiation. However, the ablation process was not clearly observed after the end of the excimer laser pulse, suggesting that the polymer is instantaneously decomposed mainly via the photochemical pathway as reported before [111, 120]. On the other hand, for a fluence of 60 mJ cm^{-2}, the etching process continued until +140 ns, as shown in Fig. 35. The time-dependent etching behavior differed from that for the fluence of 250 mJ cm^{-2}, and the etching ceased about 60 ns after the end of the

excimer laser irradiation (Δt~+140 ns). The prolonged etching after the excimer laser irradiation implies that not only the photochemical pathway of the decomposition of triazene polymer but also some delayed decomposition are involved for the lower fluence of 60 mJ cm^{-2}. When the laser fluence is high enough only photodecomposition is observed. In the case of irradiation with 60 mJ cm^{-2} it is possible that the thermal process is observed. It is noteworthy to mention, that the decomposition of the triazene polymer is an exothermic reaction [111]. Photodecomposition of the polymer also results in a temperature rise, causing thermal degradation. It is critical to determine the relative contribution of photochemical and photothermal processes upon laser ablation, and the direct measurement of the fluence-dependent etching behavior makes it possible to discuss these features.

Refractive Index Change in the Surface Layer. An increase of the transmission was initially observed followed by a decrease after Δt~+10 ns (shown in Fig. 36). The decrease of transmission and increase of reflectance (in the range of +10 to +100 ns) is observed on a time scale which exceeds that of ablation. The permanent ablation depth of 600 nm was already attained at the end of the excitation pulse for a fluence of 250 mJ cm^{-2}. The change of effective refractive index at the surface layer (decrease followed by an increase), suggests that ejected gaseous products are responsible for the observed optical behavior. The time evolution of transmission and reflectance is shown in Fig. 36b, for a fluence of 50 mJ cm^{-2}. An increase of transmission was also observed, although the dynamics is clearly different to the behavior detected for irradiation with 260 mJ cm^{-2}. The transmission and reflectance begin to change from Δt~−10 ns, which is slower than in the case of 260 mJ cm^{-2}. The transmission decreases and slight gradual recovery of the attenuated reflectance continues until 200 ns, while the permanent etching is complete after 140 ns. This again suggests the contribution of gaseous products to the effective refractive index change, although the detailed mechanism is not yet known.

2.2.4.3 Summary

It is quite interesting that the ablation of the film did not start from the beginning of the excimer laser pulse for both fluences, although the photodecomposition of the triazene polymer probably starts with the observed darkening of the film that starts almost from the onset of the excimer laser pulse. The starting time of the ablation for the fluence of 250 mJ cm^{-2} was about Δt +10 ns, while for a fluence of 60 mJ cm^{-2} the ablation starts at Δt +30 ns. The time-dependent ablation depth should follow the integration curve of the excimer laser pulse (thin dashed lines in the Figs. 34 and 35), if the decomposed products are ejected instantaneously. The delay of the ablation profile for the excimer laser suggests that ablation of the film cannot be initiated unless the triazene polymer is decomposed to some extent. It has been shown that only gaseous products without any large debris were ejected

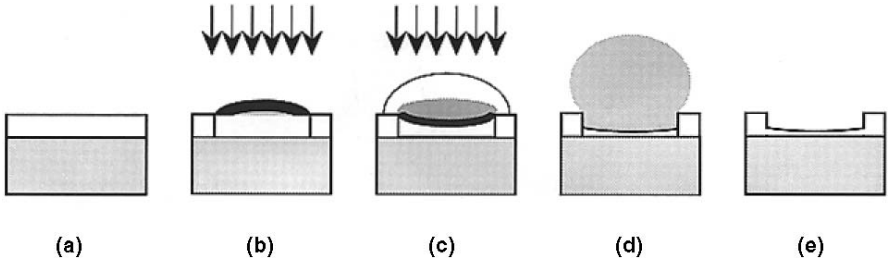

Fig. 37 Schematic diagram of laser-induced decomposition and ablation dynamics of the photosensitive triazene polymer film (**a**) before excimer laser irradiation, (**b**) slight expansion of the film and darkening of the irradiated surface at the beginning of the excimer laser pulse, (**c**) initiation of etching of the film and ejection of gaseous fragments decomposed from the polymer, (**d**) completion of the etching and expansion of ejected plume, and (**e**) after the ablation. REPRINTED WITH PERMISSION OF [Ref. 125], COPYRIGHT (1997) American Chemical Society

upon ablation [172, 200], which suggests that the polymer is decomposed successively in the solid film until the initiation of the detectable ablation process. The explosive ejection of the ablated polymer will be initiated and ablation of the polymer film starts after the triazene polymer is decomposed by a certain amount into gaseous low molecular weight products. The present results on laser-induced decomposition and ablation dynamics of the triazene polymer film are schematically summarized in Fig. 37.

A slight initial expansion of the film and darkening of the irradiated film surface are observed prior to ablation for both fluences (250 and 60 mJ cm^{-2}, shown in Fig. 37b). Ablation of the film starts, depending on the fluence, at a later time. The ending of the ablation process is also affected by the applied laser fluence. Ablation stops at +80 ns, which coincides almost with the end of the excitation laser pulse for 250 mJ cm^{-2}, while it continues until +140 ns for 60 mJ cm^{-2} (Fig. 37d). The fluence-dependent ablation dynamics indicates that not only photochemical reactions but also photoinitiated thermal reactions are involved in the ablation process of the triazene polymer film.

2.2.5 *Nanosecond Shadowgraphy*

2.2.5.1 Introduction

Another method that can give complementary information to interferometry is nanosecond shadowgraphy. Shadowgraphy directly shows the speed of ablated fragments and yields information about the size of the ejected fragments. Solid fragments can result in contamination of the optics and remaining polymer surface. This is probably due to the incomplete decomposition of the polymer. To avoid this kind of contamination in microfabrica-

tion, an understanding of how materials are decomposed and ejected is necessary.

The ejected plume has been compared to a microexplosion that produces shock waves in the surrounding gaseous media which have been used to classify the explosion and discuss the released energy [201–203]. The observed shock waves resemble explosively formed blast waves, which can be analyzed with point blast theory or may necessitate the use of a theory that includes the source mass of the explosion close to the polymer surface.

Blast Waves. In a spherical explosion that forms a blast wave, the reaction is assumed to occur instantaneously, and the energy released by the explosion, E_0, is mainly deposited in the gaseous product. This high-pressure gas expands at a velocity greater than the speed of sound in the surrounding atmosphere, and acts as a piston pushing this atmosphere outward in a compressive wave referred to as a blast wave. This wave travels faster than the product front and encompasses an ever-increasing spherical volume of the surrounding atmosphere. Because the energy supplied by the explosion is finite, the blast wave strength decays polynomially with radial propagation distance. The rate of the blast wave propagation is used to classify it as either a weak, intermediate or strong blast wave. A weak blast wave travels near to the speed of sound in the surrounding atmosphere [203]. The propagation of a strong blast wave may be analyzed with a few simplifying assumptions concerning the explosive, such as its energy being instantaneously released into the gaseous product, a negligible point mass source of this energy, and a spherical shock occurring in the surrounding atmosphere. With these assumptions, the propagation radius, R, and time, t, may be related for a strong blast wave [203–205],

$$R = \zeta_0 \left(\frac{E_0}{\rho_0}\right)^{1/5} t^{1/5} \tag{8}$$

where ρ_0 is the undisturbed atmospheric density and the constant, ζ_0, may be found from strong shock theory [205]. The negligible explosive mass assumption leads to this being referred to as a "point blast theory" and imposes limitations on the propagation radius to which Eq. 8 applies. A minimum radius limitation, R_1, is determined by the mass of the atmosphere encompassed by the spherical blast wave being significantly greater than the original explosive mass, M_0. In the case of excimer laser-induced reactions on a polymer plate, the plate and its backing will act as a boundary, so the mass encompassed by the blast wave is only a hemisphere, $2/3\pi 3\rho_0 R^3$, thus R_1 should be expressed as [202],

$$R_1 = \left(\frac{3M_0}{2\pi\rho_0}\right)^{1/3} \tag{9}$$

The propagation distance must be about an order of magnitude greater than R_1 for Eq. 8 to apply, but it may suffice to use only a multiple of five

[202]. The maximum radius limitation, R_2, occurs when the peak pressure within the blast wave, P_1, is no longer significantly greater than that ahead of it in the ambient atmosphere, P_0. When $P_1 \cong P_0$, strong shock relations no longer apply. This limit has been estimated to occur at the radius where a sphere containing ambient atmosphere has an equal internal energy to the energy of the explosion [202],

$$R_2 \cong \left(\frac{E_0}{P_0}\right)^{1/3} \tag{10}$$

For a blast wave propagation radius less than the minimum radius, models that do not neglect the mass of the explosion product should be applied. Two analytical solutions that include the source mass are readily available in the strong shock regime. In formulating both of these, the effects of shock waves in the relatively thin polymer and quartz backing are ignored. Since the shock speeds in the solid materials are significantly faster than those in the surrounding air, the effects of the shock waves through these materials will terminate within the first few nanoseconds. The first analytical solution applies to planar blast waves, which will be the case at the center of the laser irradiation area for a limited propagation radius until the edge effects converge on the center axis [206]. Several assumptions are necessary in this theory, such as one-dimensional, instantaneous transfer of the explosive energy into the product gases, uniform distribution of the compressed atmosphere behind the blast front, and averaging of the explosive product velocity and pressure [206]. Applying hydrodynamic conservation laws along with these assumptions allows a solution for the propagation radius with respect to the propagation time,

$$R = \frac{\left\{\left[1.5\,C_5\,(E_0)^{1/2}t + C_4^{3/2}\right]^{2/3} - C_4\right\}}{C_5} \tag{11}$$

where

$$C_4 = \frac{A\delta}{8}\left(\frac{2}{\gamma+1}\right)^2 \rho_s \quad C_5 = \frac{\rho_0 A}{\gamma+1}\left(\frac{1}{\gamma-1} + \frac{4}{\gamma+1}\right) \tag{a}$$

Here, γ is the specific heat ratio of the atmosphere, A is the planar area, ρ_s is the initial explosive density, and δ is the axial thickness of the explosive prior to detonation. In the laser-induced ablation case, these will be the laser-ablated area, the solid polymer density, and the ablation depth, respectively. The second analytical solution that includes the explosive mass applies to a spherical blast wave [205]. Again, several assumptions are used, such as instantaneous transfer of the explosive energy to a spherical mass of expanding product gases, averaging the mass of the product gases over its radius, and uniform distribution of the compressed atmosphere into an isotropic spherical shell [205]. These assumptions, along with flow conservation laws, allow a solution for the propagation radius in the form of a differential equation,

$$\frac{dR}{dt} = \left[\frac{E_0}{C_1 + C_2 R^3}\right]^{1/2} \tag{12}$$

where

$$C_1 = \frac{4\pi}{3(\gamma + 1)^2}\rho_s R_s^3 \qquad C_2 = \frac{4\pi\rho_0}{3}\left[\frac{2}{(\gamma + 1)^2} + \frac{1}{(\gamma^2 - 1)}\right] \tag{b}$$

Here, R_4 is the initial radius of the hemispherical explosive charge and the constants C_1 and C_2 reflect the volumes encompassed by a hemispherical blast wave instead of the spherical blasts for which the solution was initially designed. Although the original authors of this formula choose to evaluate Eq. 12 in terms of an elliptic integral [205], a simple computational solution utilizing a fourth-order Runge-Kutta method was employed here.

2.2.5.2 Experimental

A photosensitive triazene polymer with the structure shown in Scheme 8 was applied and a XeF excimer laser (351 nm) was used as irradiation source. Ejected plumes and blast waves were illuminated by fluorescence from a methanol solution of Rhodamine 101 which was excited by the second harmonic of a Q-switched Nd^{3+}:YAG laser. The principles of this imaging method are the same as those reported previously for poly(methyl methacrylate) (PMMA) [94, 195, 199, 207] and liquid benzene [208].

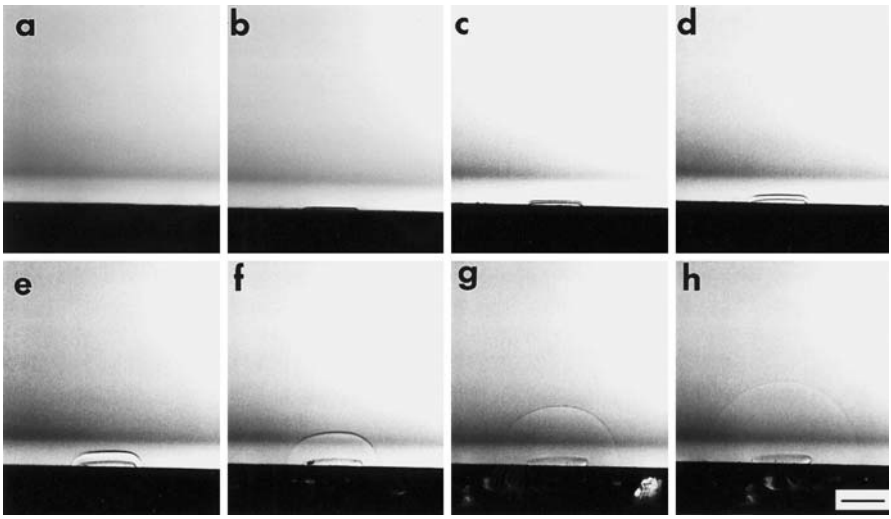

Fig. 38 A series of nanosecond shadowgraphs showing the shock fronts formed in the 50 mJ cm^{-2} fluence case. Delay time: **a** 4.8 ns; **b** 51.2 ns; **c** 106 ns, **d** 200 ns; **e** 420 ns; **f** 1,000 ns; **g** 2,000 ns; **h** 3,000 ns. The *bar* indicates 1 mm on this scale. REPRINTED WITH PERMISSION OF [Ref. 167], COPYRIGHT (1996) Springer Verlag

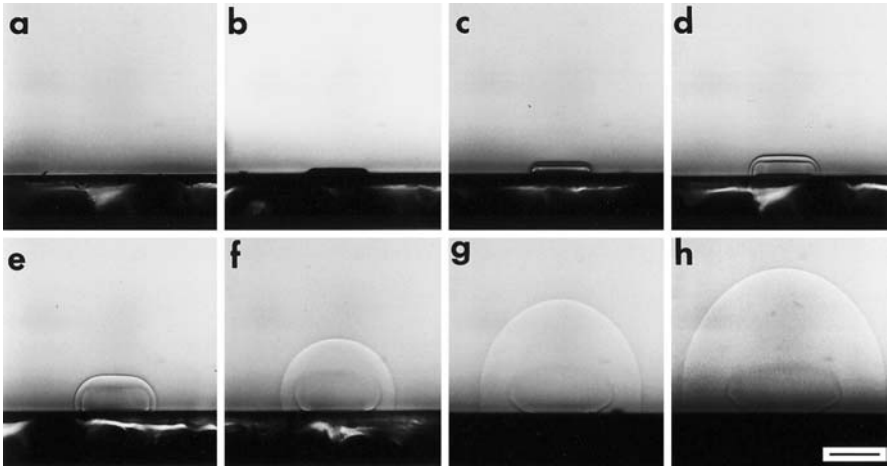

Fig. 39 A series of nanosecond shadowgraphs showing the shock fronts formed in the 250 mJ cm^{-2} fluence case. Delay time:**a** 7.2 ns; **b** 44.8 ns; **c** 111 ns; **d** 204 ns; **e** 407 ns; **f** 1,000 ns; **g** 2,000 ns, **h** 3,000 ns. The *bar* indicates 1 mm on this scale. REPRINTED WITH PERMISSION OF [Ref. 167], COPYRIGHT (1996) Springer Verlag

The majority of a series of shadowgraphs recorded at a laser fluence of 50 mJ cm^{-2} are displayed in Fig. 38 and most of those from a series of experiments with a 250 mJ cm^{-2} fluence laser are shown in Fig. 39. The time zero chosen for these photographs was at the peak of the excimer laser irradiation [209]. In this time zero reference, a photo was also taken at time=-4.8 ns for the 50 mJ cm^{-2} fluence laser and at time=-7.2 ns for the 250 mJ cm^{-2} fluence laser. Although both of these "negative" time photos were well after the beginning of the laser irradiation, neither showed any indication of shock wave formation or material expansion [94]. A depth profiler was used to measure a final ablation depth of 50 nm in one of the 50 mJ cm^{-2} fluence case experiments and 650 nm in one of the 250 mJ cm^{-2} fluence case experiments.

2.2.5.3 Results

To analyze these experiments, the blast wave was first classified by plotting the measured blast wave propagation distance in each photo vs time on a log-log plot. The slope of this log-log plot will simply be the time dependency constant and thus determine the blast wave strength. A weak blast wave will have a slope of 1.0 and a strong blast wave will have a slope of 0.4 on this type of plot. The propagation distances were measured in reference to the initial surface at the center of the ablated area in each photo. As will be further discussed, the photos showing shock waves before 100 ns in each fluence strength series should be treated separately from this blast wave portion of the analysis. For the 50 mJ cm^{-2} fluence laser case, the remaining photos from Fig. 38 were divided into sequential sets to show that the time dependency

constant develops from an initial value of 0.87 to a final value of 0.80. For the 250 mJ cm^{-2} fluence laser, the later series of photos from Fig. 39 show that the time dependency constant develops from an initial value of 0.83 to a final value of 0.64. The minimum radius, R_1, for which a point source solution applies was calculated from Eq. 9, where the mass of the "exploded" polymer was found from the volume ablated and the density of the polymer, ρ_s=1.2 g cm^{-3}. These measured volumes, V, the mass they represent, M_0, and the calculated values of the minimum radius are listed in Table 4 for both fluence cases. Since the ablation depth was measured for only one of the series of experiments in each fluence case, the ablated volume and mass may be a source of error when comparing these calculations to the measured values. The majority of the measurements in Figs. 38 and 39 are within an order of magnitude of the minimum radii, so the theories including explosive mass should be applied. Thus, the log-log slopes of greater than 0.4 do not necessarily indicate that the blast waves are below the strong shock regime, but that they may simply still be influenced by the mass of the microexplosion product. For laser-induced ablation of polymers, the energy released by the chemical reaction and the volumetric expansion does not seem sufficient to produce a self-propagating detonation in the polymer. As a result, the energy released by the reaction in Eqs. 8–12 is often neglected and just the laser irradiation energy, E_{is}, or some fraction of this is substituted for E_0 [201, 202, 209, 210]. Experiments in which metallic plates were ablated with a pulse laser displayed good agreement with Eq. 8 given this substitution [209, 210]. Ben-Eliahan et al. [203] included the energy released by the thermal decomposition, E_{th}, of their glycidyl azido polymer in addition to the laser irradiation energy. These energy values will be influenced by the area irradiated and the volume of polymer ablated, which are listed in Table 4. The decomposition enthalpy of the polymer has previously been measured as −258 kJ mol^{-1} and the molecular weight as 413.8 g mol^{-1} [111]. Thus, the decomposition-specific enthalpy is −623.5 J g^{-1}. A common assumption in models of energetic reactions is that the decomposition-specific energy is equal to the decomposition-specific enthalpy at atmospheric pressure [211]. Assuming all of the decomposition energy is released by the ablated mass allows the decomposition energy, E_{th}, to be found by multiplying this specific energy by the ablated mass. The decomposition energy and the total laser energy, E_{is}, i.e., the fluence multiplied by the irradiated area, are also listed in Table 4. The shocks will be propagating through air initially at about ambient pressure and temperature, which has a density of 1.1844×10^{-3} g cm^{-3} and a specific heat ratio, γ, of 1.4.

Utilizing the values given in Table 4, a study of the energy deposited into the product gases was conducted with the planar and spherical models, Eq. 11 and Eq. 12, for the blast wave propagation distance. The amount of laser energy deposited in the polymer should decay exponentially with the penetration depth. The absorption coefficient for this polymer with a 351-nm excimer laser has been measured as 4.566 gm^{-1}. From this coefficient it is calculated that only 5.1% of the energy should be absorbed by the first 50 nm of material, as in the 50 mJ cm^{-2} fluence case, and 99.8% should be absorbed by the 650 nm ablated in the 250 mJ cm^{-2} case. However, the best

Table 4 Values used to calculate the blast wave propagation distance

	50 mJ cm^{-2}	250 mJ cm^{-2}
Ablated volume, V (mm^3)	1.011×10^{-4}	1.314×10^{-3}
Ablated mass, M_0 (g)	1.213×10^{-7}	1.577×10^{-6}
Irradiated area, A (mm^2)	2.021	2.012
Minimum radius, R_1 (mm)	0.366	0.860
Maximum radius, R_2 (mm)	2.205	3.906
Laser energy, E_{is} (mJ)	1.011	5.053
Thermal decomposition energy, E_{th} (mJ)	0.076	0.983
Equilivent hemispherical radius, R_s (mm)	0.036	0.086

fits to the measured blast wave propagation distances were obtained when the maximum available energy was employed, i.e., 100% of the laser irradiation energy and the thermal decomposition energy, for both fluence cases. This may be reasonable since the absorbance increases beyond the ablation threshold fluence [93, 96, 97, 212]. A comparison of the measured blast wave propagation distances to those calculated by Eqs. 11 and 12, using either just the laser energy, E_{is}, or the maximum available energy, $E_{is}+E_{th}$, is shown in Fig. 40. For both fluence cases the planar model with the maximum available energy produces the best agreement with the measured data. This agreement is not surprising within the first few hundred nanoseconds since the edge effects should not have interfered with the planar region in this time, but this is not expected after the edge effects have converged on the center axis. The encroachment of the edge effects is apparent in Figs. 38 and 39 which show the flat tops of the blast waves decreasing with time.

For the spherical model, it was necessary to calculate the radius of an initially hemispherical polymer mass, R_s, based on the volume of the ablated slab, $V=A\delta$, as a starting point for the numerical integration of Eq. 5. These radii are given in Table 4.

The failure of the spherical model to sufficiently fit the measured data is not surprising, because the minimum width of the ablated area is of the same order of magnitude as the propagation distance. The blast wave and product front velocities, U_i, may be found by measuring the distance traveled between each sequential set of photographs, $\Delta R_i=R_i-R_{1-i}$, based on the distance from the initial polymer surface and dividing this by the time elapsed between each photo, Δt_i, i.e., $U_i=\Delta R_i/\Delta t_i$. This method yields only the average velocity between each sequential set of photographs and not the instantaneous velocity of each. These calculated velocities are plotted vs time for both the 50 mJ cm^{-2} and the 250 mJ cm^{-2} fluence cases in Fig. 41. Since each photo was taken from an independent experiment, these measured velocities may contain significant error. However, the general trends discussed below seem to be the same and indicate similar phenomena in both fluence cases.

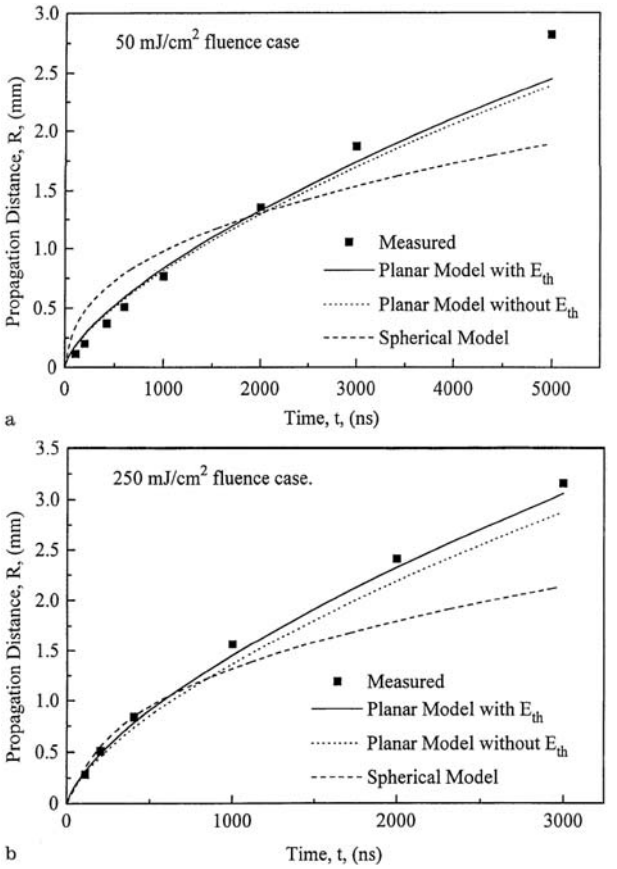

Fig. 40 Measured and calculated blast wave propagation distances by planar and spherical models including the source mass. REPRINTED WITH PERMISSION OF [Ref. 167], COPYRIGHT (1996) Springer Verlag

For both fluences, only one front was visible until about 100 ns, after which two fronts became distinguishable. As can be seen in Figs. 41a and b, the velocity of this initial shock wave rapidly decays well below the velocity at which the blast wave next appears. This leads to the conclusion that this initial shock is separate from the blast wave or product front. Therefore, the first velocities calculated for both the blast wave and product front in both the 50 and 250 $mJcm^{-2}$ fluence laser can be questioned, since they are based on the final position of the initial shock. Because of this doubt, these points have been left open in contrast to the filled points used for the remainder of the blast wave and product front points. The apparently separate initial shock is of particular interest, because it appears in both fluence cases and persists for a similar duration even though the propagation distance is quite different. This indicates that a relatively strong material ejection occurs near the peak of the laser pulse and then abruptly stops. In both fluence

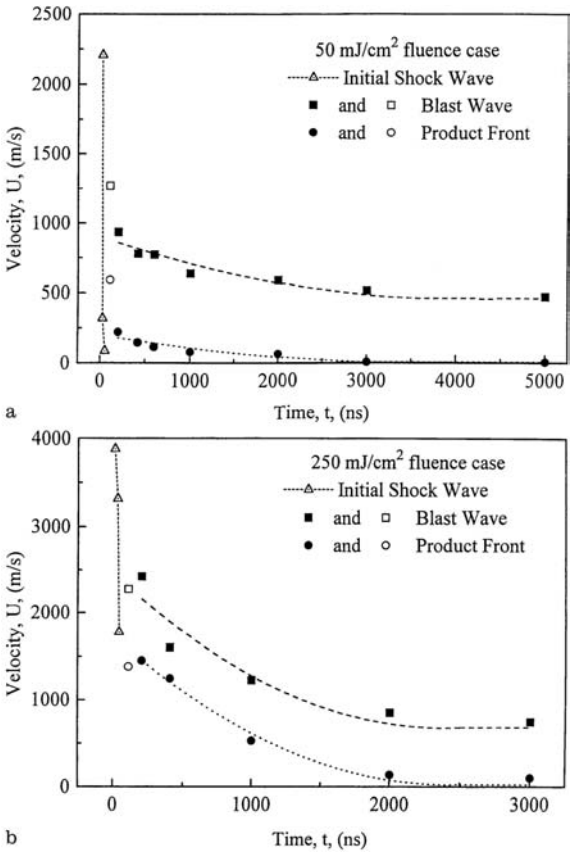

Fig. 41 Initial shock and blast wave velocities and product front velocities. REPRINTED WITH PERMISSION OF [Ref. 167], COPYRIGHT (1996) Springer Verlag

cases this initial ejection is followed by the later product front and blast wave structure. The initiation time of the second plume is difficult to specify because it is masked by the first plume, but it seems to be delayed by approximately 100 ns after the first ejection. It is possible that these material ejections are the result of either two separate, sequential or independent chemical reactions or the same unstable reaction of the polymer that initiates and quenches and then again reinitiates.

2.2.5.4
Summary

For both the 50 and 250 mJ cm^{-2} laser fluence cases, the blast wave propagation distances observed are within an order of magnitude of the minimum propagation radius for a point blast theory. Thus, the blast waves are still developing during these observations so any calculations of the

blast wave propagation distance must include the mass of the ablated polymer. Of the two source mass theories applied, the one-dimensional approach including all of the laser and thermal decomposition energy fits the experimental data best for both fluence cases. The front velocity measurements indicate that both cases display an initial shock which seems separate from the later blast wave and product front structure. This dual shock structure may indicate either instabilities in the chemical reaction that forms the ejected product material, or two sequential or independent reactions.

2.2.6
Time-of-Flight Mass Spectrometry (TOF-MS)

2.2.6.1
Introduction

The shadowgraphy data in the previous chapter allow the analysis of the products and the shock wave created by the ablation process in air. The shadowgraphy images suggest that only "small" gaseous products are formed, but no information about the chemical composition of the fragments is obtained by this method. To obtain this information mass spectroscopic methods, such as TOF-MS, must be applied.

Srinivasan [92] has repeatedly emphasized the importance of looking at the product distribution in order to establish and/or test ablation mechanisms. Mass spectrometric studies have been performed on various polymers under various conditions, e.g., as a function of irradiation wavelength and laser fluence [213]. Analysis of the ejected material has revealed ionic and neutral species with masses ranging from small degradation fragments [214, 215], to the monomer (from unzipping reactions) [216, 217], to carbon clusters [218], and finally to polymer fragments with molecular weights of up to 2,500 [168, 219]. Time-of-flight (TOF) distributions (in reality, these are "time-of-arrival" curves) of neutral fragments have been analyzed to determine the energy distributions of the fragments. For several polymers such as polystyrene, Teflon, and poly(methyl methacrylate) (PMMA), Maxwell-Boltzmann distributions were obtained, yielding temperatures compatible with photothermal decomposition [220–222]. In the case of polystyrene irradiated at 193 nm, an adiabatic expansion model inferred temperatures of ~2,350 K [223]. When absorbing chromophores were purposefully added to PMMA, a combined photochemical/photothermal mechanism was evident [224].

In general, most TOF-MS studies have given strong indications for photothermal ablation mechanisms. To test whether a photochemical mechanism could be identified with TOF-MS, we chose a polymer considered photolabile, which also has excellent properties as a resist for high-resolution microlithography [111, 225–228]. Here we show that the principal products (chiefly N_2) from this triazene polymer have components that are much

more energetic than expected for thermal products. Further, the fluence dependence of the emissions is a strongly nonlinear function of fluence, again suggestive of a nonthermal decomposition mechanism. Nevertheless, an Arrhenius description (used previously for the UV laser-induced products from PTFE [216]), assuming an activation energy equal to the thermal decomposition energy of the polymer, yields a good description of the emission intensities.

2.2.6.2 Experiment and Curve Fitting

The chemical structure of the polymer is diagramed in Scheme 9. The average molecular weight is about 71,000 g/mole, corresponding to about 190 monomer units (*n* in Scheme 9). It should be noted that the decomposition of the monomer is exothermic with a decomposition enthalpy of −624 J/g [122]. The absorption coefficient at 248 nm is ~66,000 cm^{-1}, which is quite high; nevertheless, it is not at the maximum (typically at wavelengths in the 310–350 nm region).

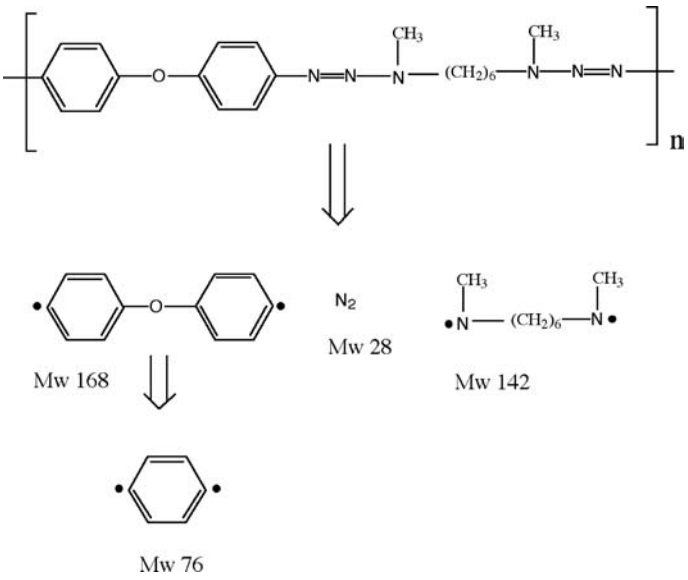

Scheme 9 Chemical structure and a possible decomposition scheme for the triazene polymer. REPRINTED WITH PERMISSION OF [Ref. 324], COPYRIGHT (1999) American Institute of Physics

The experimental arrangement has been described previously [229]. The polymer films were irradiated at 248 nm at a pulse repetition rate of 1 Hz to avoid accumulative heating. Emissions were detected with a quadrupole mass spectrometer mounted with the ionizer 30 cm from the sample. Time-

resolved quadrupole mass spectroscopy was used to simultaneously measure both the charge to mass ratio (m/z) and the time-of-flight distributions of the emitted species. Curve fitting techniques were employed to test various models of the emission process.

Nitrogen molecules emitted from the polymer showed both highly energetic components (short TOF) and very slow components consistent with emission long after the laser pulse. The overlap between the fast and slow components, and the fact that a large majority of the total counts reside in the slow component, make it particularly important to describe the leading edge of the slow component accurately in order to characterize the fast component. To carry this out a number of models were tested by curve fitting the acquired TOF curves.

The model employed below assumed that the emission intensity of the slow component was controlled by a thermally activated process (which we assume is decomposition rate but could be diffusion limited) which continued after the laser pulse. That is, the emission rate, $S(t')$ is given by:

$$S(t') = S_0 \exp\left(\frac{-E_a}{kT}\right) \tag{13}$$

where E_a is an activation energy, k is Boltzmann's constant, and T is the surface temperature. The laser will heat the surface to some temperature $T_{RT}+\Delta T$ (where T_{RT}=room temperature) and the surface subsequently cools. The emission rate is a strong function of how the sample cools, which in turn depends on the initial temperature distribution. We assume that laser heating is initially confined to a surface layer of depth a. This initial temperature distribution is consistent with the highly absorbing nature of the polymer. At the fluences employed in this work, the absorbing centers should be "saturated" to a significant depth. If the saturated material lacks the ability to absorb additional photons (which may require the absorption of more than one photon), the depth of the heated region should be a strong function of laser fluence, while the temperature of the heated material remains roughly constant (determined by the chromophore concentration and the number of photons required to saturate the chromophores). Under these conditions, the surface temperature after the laser pulse varies as:

$$T = T_{RT} + \Delta T\, erf\left(\frac{a}{2\sqrt{\kappa t}}\right) = T_{RT} + \Delta T\, erf\left(\frac{\alpha}{\sqrt{t}}\right) \tag{14}$$

where κ is the thermal diffusivity, t is the time since the laser pulse, and $\alpha=1/2\sqrt{\kappa}$, the actual fit parameter employed in modeling. Although the physical model (and the number of parameters) may seem to be unnecessarily complex, the resulting equations displayed good behavior when fits to the slow tail were extrapolated back into the fast/slow overlap region. This is not the case with several simpler models, including those based on linear, Beer's law absorption.

To predict the actual detected signal, $I(t)$, at the detector position relative to the sample (x,y,z), the emitted rate was convoluted with the Maxwell-Boltzmann velocity distribution, $MB(t-t')$,

$$I(t) \quad = \quad \int_0^t S(t')MB(t-t')\,dt' \tag{15}$$

where $MB(t-t')$ is given by:

$$MB(t-t') = \frac{x}{2\pi(t-t')_4}\left(\frac{m}{kT}\right)^2 \exp\left(\frac{--m(x^2+y^2+z^2)}{2kT(t-t')^2}\right) \tag{16}$$

S_o, E_a, ΔT, and α were determined by least squares fitting techniques [230].

Extrapolating this model to short times produced a physically plausible leading edge to the slow emission component, allowing for a reasonable description of the fast component. The fast component was described by assuming that the emitted N_2 had a Gaussian energy distribution with amplitude A, most probable energy E_o, and standard deviation σ, where all particles are emitted during the laser pulse (a delta function in time). This distribution is readily transformed to yield a particle density at the ionizer vs time.

Experimentally, the analysis of the fast component is complicated by the delay between particle ionization (with the rate given by Eq. 16) and particle detection at the exit aperture of the quadrupole mass filter. Ionized particles entering the mass filter gain a kinetic energy of 15 eV, which is much greater than the kinetic energies of typical particles with effective temperatures below a few thousand K. Thus for thermal distributions, the travel time through the mass filter is essentially constant and can be simply subtracted from the arrival time at the detector. However, particle velocities (before ionization) in the fast component are much higher and significantly affect the travel time through the quadrupole mass filter. The travel time through the mass filter for these particles was determined by solving the appropriate fourth order equation by iteration for each data point.

2.2.6.3 Results and Discussion

Photodecomposition of the polymer is expected to yield significant amounts of volatile N_2 (28 amu) and phenyl radicals (76 amu) via the proposed reaction pathways shown in Scheme 9. Other low molecular weight species are also expected (e.g., various CH fragments), but in most cases it is not clear whether these other fragments were created during ablation or are cracking fractions created by electron impact ionization. Therefore we focus our attention on N_2 and the phenyl radical. No intact repetition units were found among the ablation fragments, presumably due to the photolabile character of the triazene units ($R–N^1=N^2–N^3<$), of which two are found in each repetition unit. The photochemistry of the triazene group in monomeric com-

pounds has been previously studied in detail. The first step of UV photodecomposition involves homolytic bond breakage between the N^2 and N^3 (R–N^1=N^2–N^3<) nitrogen atoms, creating two radicals [140, 153]. The diazo radical is quite unstable and would be expected to decompose by elimination of N_2, creating R· species which have been detected by ESR [140, 153].

The neutral fragments observed during UV laser ablation of the polymer are in fact compatible with this decomposition mechanism. The two fragments with the highest intensities are N_2 (m/z=28 amu/e) and the phenyl fragment (m/z=76 amu/e). Two molecules of each species can be liberated by the decomposition of each repetition unit. N_2 is chemically inert and relatively stable during electron impact ionization. Similarly, the phenyl fragment, as most aromatic compounds, shows a very stable parent molecular ion. In contrast, aliphatic compounds like the aliphatic amino fragment (m/z=142) undergo extensive fragmentation in the ionizer. Phenyl fragments can also be formed by fragmentation of intact diphenyl ether fragments (m/z 168) during electron impact ionization or during laser-induced decomposition. The diphenyl ether fragment (M_w 168) absorbs strongly at 248 nm, which would promote dissociation into phenyl fragments.

By far the most intense neutral signal is due to N_2. Figure 42 compares the time-of-flight curves for N_2 at three fluences. Only the first 500 μs of data is shown. Over this time interval, the great majority of the detected signal can be attributed to N_2 emitted directly from the sample, as opposed to molecules bouncing off the chamber walls. (This was verified by performing identical TOF measurements after blocking the direct path between the sample and the ionizer.)

All three TOF curves in Fig. 42 show a distinctive shoulder on the fast leading edge, followed by a broad peak and long tail. The particles in the shoulder are moving extremely fast; the position of the shoulder corresponds to a kinetic energy above 0.7 eV. The Gaussian energy distributions used to model these fast peaks are also shown in Fig. 42. At the lower fluences, where the effect of gas-phase collisions on the energy distributions can be neglected, the center (mean) energy of the Gaussian distributions corresponds to 1.1±0.1 eV. These energies are well above those expected for typical thermal processes, and are presumably due to the concerted motion of decomposition fragments. That is, the reaction fragments depart from the parent molecule without colliding with other particles; these particles are not "thermalized" and display kinetic energies comparable to the loss of potential energy in the exothermic decomposition reaction. Similar TOF curves have been observed in reaction fragments following the IR-induced, exothermic decomposition of molecular cyclotrimethylene-trinitramine (RDX), an energetic compound used in explosives and rocket propellants [231]. UV laser irradiation (248 nm) of solid RDX single crystals yielded a number of product species exhibiting both a "hot" and "cold" component [232].

The broad peak and tail in the N_2 TOF distribution are much broader than Maxwell-Boltzmann distributions with similar peak TOFs. Nevertheless, the peak TOF does shift to shorter times with increasing fluence. This shift is often associated with thermal emission, where higher fluences produce higher

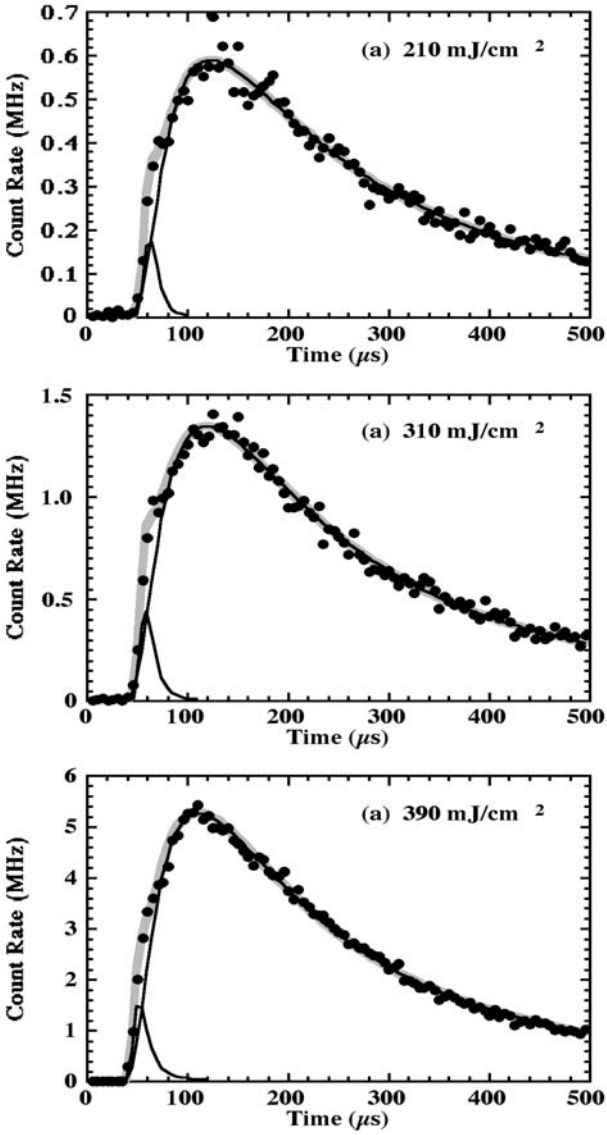

Fig. 42 Time-of-flight signals for N_2 at three laser fluences. A curve fit to the data using a Gaussian energy distribution for the shoulder and Eq. 16 for the slow peak is shown in the *light, broad line*; the individual fast and slow components are shown in *dark lines*. REPRINTED WITH PERMISSION OF [Ref. 324], COPYRIGHT (1999) American Institute of Physics

surface temperatures and thus faster particles. In such cases, long emission tails are often associated with emission *after* the laser pulse [233, 234]. For instance, either a thermal decomposition rate decreasing in time due to cooling or the diffusion of volatile species (produced in the bulk of the polymer) to the surface could explain a slowly decaying component of emission that persists long after the laser pulse. Estimates of the total yield of N_2 per laser pulse exceed 10^{15} molecules/cm^2 as the fluence is increased to 310 mJ/cm^2. At this particle density, collisions among the emitted N_2 molecules are expected to modify the original (as emitted) velocity distribution [235].

Weaker emissions at 76 amu (the phenyl radical) are also observed. Typical TOF distributions are shown in Fig. 43. Note that higher fluences are employed in these measurements to provide measurable signals for analysis. Again, the leading edge of the TOF distribution is fast. The maximum particle velocities at this mass are only slightly less than the maximum N_2 particle velocities at the same fluence. The higher mass of the phenyl radical ensures that the energies of the fastest phenyl radicals are much higher than the energies of the fastest N_2 molecules. We attribute the high velocities of the fastest phenyl radicals to collisions with fast N_2 molecules, leading to entrainment of the heavier molecules.

In the limit of large numbers of collisions, the fast N_2 and fast phenyl radicals will move with very nearly the same velocities, as observed. (This process is exploited to accelerate massive molecules to high kinetic energies, by entraining them in a supersonic molecular beam formed by free adiabatic expansion of a light gas such as helium.) As noted above, the N_2 densities at the lowest fluence displayed in Fig. 42 (310 mJ/cm^2) are adequate to account for such a collisional acceleration of the phenyl radicals. Like the N_2, the phenyl radicals also display a long tail, consistent with slowly decaying emission intensities, long after the laser pulse. The phenyl intensities were typically less than 1% of the N_2 intensities at the same fluence.

The intensities of both N_2 and phenyl radicals depend strongly on fluence. Their fluence dependence is displayed as log-log plots in Fig. 44. As discussed above, N_2 is much more intense than the phenyl radical (by almost two orders of magnitude) and is first detected at considerably lower fluences. Much of this intensity difference can be attributed to differences in the survival and ionization probabilities of the two species.

Thus it is not clear how much of the apparent difference in emission threshold for N_2 and phenyl radicals in Fig. 44 is due to different emission intensities versus different detection probabilities. Since two N_2 molecules must be emitted to release one phenyl radical, some difference in fluence dependence is expected. For both species, the intensity rises above the background in approximately power law fashion. Finally, at still higher fluences, the intensity rolls over, growing more slowly with increasing fluence. The slopes of the "power-law" portions of the two plots are 8 for N_2 and ~12 for the phenyl radical, respectively. Although we could suggest that this corresponds to an eight- and 12-photon process (either multiphoton or multiple photon) this seems totally unacceptable and unreasonable. Furthermore, it is inconsistent with a simple photodecomposition mechanism, where we

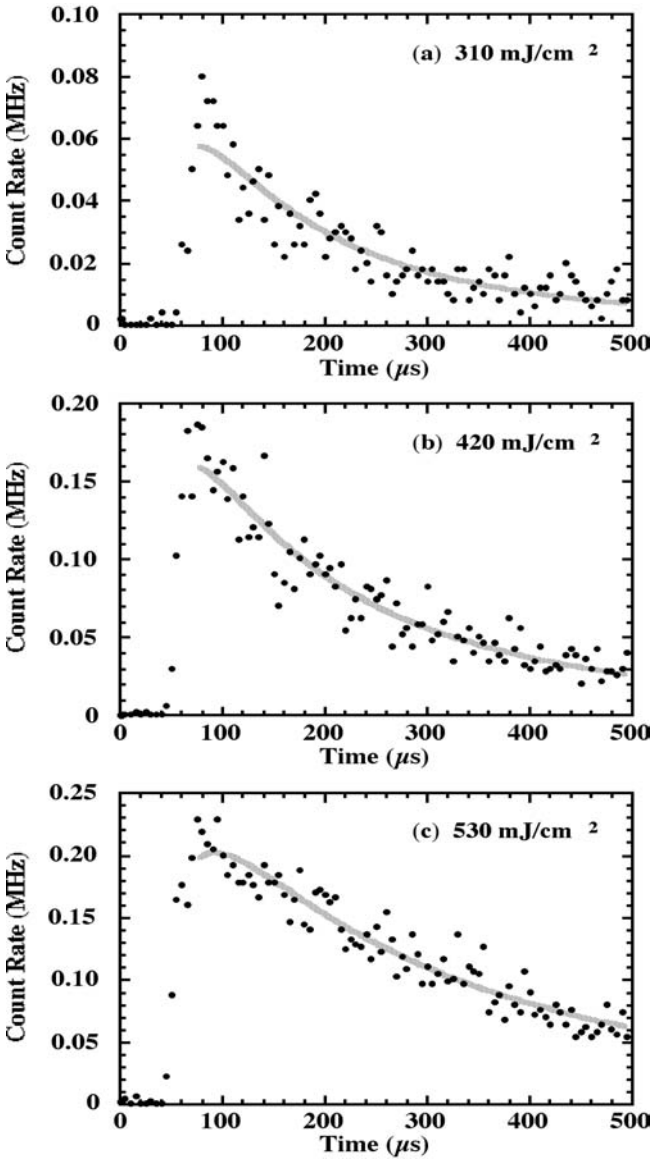

Fig. 43 Time-of-flight signals for the phenyl radical at three laser fluences. A curve fit to the data using Eq. 16 is shown in the *light, broad line*. REPRINTED WITH PERMISSION OF [Ref. 324], COPYRIGHT (1999) American Institute of Physics

would expect the number of product molecules (broken bonds) to be first order in the laser fluence.

An alternative mechanism to explore in terms of this fluence dependence is a photothermal mechanism which we propose would fit an Arrhenius

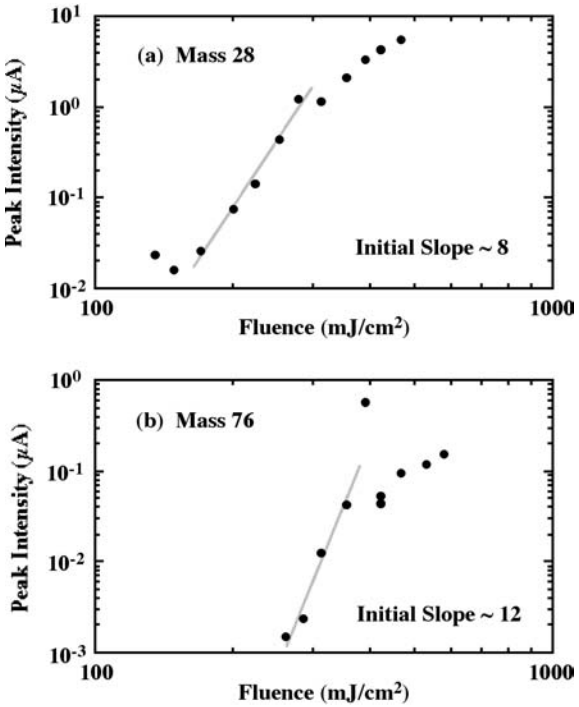

Fig. 44 Log-log plots of the signal intensities for the two principal fragments (**a**) N_2 (28 amu) and (**b**) the phenyl radical (76 amu), as a function of laser fluence. REPRINTED WITH PERMISSION OF [Ref. 324], COPYRIGHT (1999) American Institute of Physics

equation [216]. For a single-photon photothermal process, where all absorbed light goes into heat, and neglecting thermal diffusion, the temperature rise can be expressed in terms of the absorption coefficient, α:

$$\Delta T = \frac{F_o(1-R)\alpha}{\rho C_v} \tag{17}$$

where F_o is the laser fluence at the sample surface, R is the surface reflectivity at the laser wavelength, ρ is the sample density, and C_v=heat capacity of the sample. Thermal diffusion can be neglected if the conduction during the laser pulse is less than the laser spot size or the thickness of the heated layer. This is ensured if the characteristic thermal diffusion length, $(2\kappa\tau)^{1/2}$, (where κ is the thermal diffusivity of the polymer and τ is the laser pulse width–30 ns), is much less than the radius of the laser spot (500 μm) and the thickness of the heated layer ($\sim\alpha^{-1}\sim$170 nm). Assuming that the thermal properties of this polymer are similar to polycarbonate or polyethylene, the characteristic diffusion length is in the order of 60 nm during the laser pulse. This

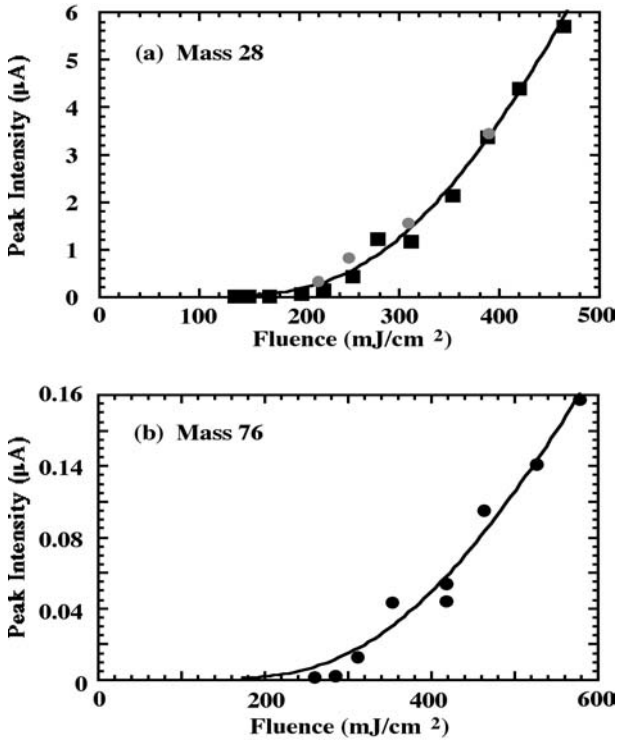

Fig. 45 Linear plots of the signal intensities for the two principal fragments (**a**) N_2 (28 amu) and (**b**) the phenyl radical (76 amu), as a function of laser fluence. The *dark line* shows a least-squares fit of the data to a thermal model for emission, assuming an activation energy of 2.1 eV (the polymer thermal activation energy). The *gray dots* in (**a**) indicate the area of the N_2 fast peak determined from curve fits to the TOF data. REPRINTED WITH PERMISSION OF [Ref. 324], COPYRIGHT (1999) American Institute of Physics

is indeed much smaller than the laser spot size and significantly smaller than the expected thickness of the heated layer.

Using this temperature, an Arrhenius-like description of the emission intensity yields:

$$I(t) = A \exp\left[\frac{-E_a}{k(T_{RT} + \Delta T)}\right] \tag{18}$$

where E_a is the activation energy. In principle, one can determine E_a by fitting Eq. 18 to the data, but a more stringent test of the thermal decomposition hypothesis is obtained if we fix E_a to the known activation energy of thermal decomposition for this material (E_a~2.1 eV). Equation 18 was then fitted to the intensity vs fluence data (with the omission of an outlier data point in Fig. 44b) and the results are shown in Fig. 45. Although one might argue that the data systematically depart from the model at the lower flu-

ences, the fluence range adequately treated by Eq. 18 is significantly greater than the "power law" region of Fig. 44. Furthermore, we can plot the intensities of the mass 28 fast component at the lower laser fluences. These data points are shown in Fig. 45a and are seen to fall directly on the Arrhenius equation fit. Our conclusion is that a thermal-activation model describes the intensity vs fluence data quite adequately.

The predicted temperature rise from Eq. 18 provides a check on the physical reasonableness of a thermal activation description. At a fluence of 400 mJ/cm^2, both curve fits in Fig. 45 indicate a temperature change of about 6000 K. This is on the high end of what one might consider to be physical temperature values. However, it is consistent with temperatures predicted by curve fits to individual TOF curves at this fluence using Eq. 15. We also note that decomposition measurements on second to minute time scales (as in differential scanning calorimetry) yield much lower decomposition temperatures (500–550 K). Due to the short time scales for heating during laser ablation, much higher temperatures are required for observable decomposition. Improved thermal models would better predict the duration of heating, which depends on the depth of the heated layer (as in Eq. 14).

The slow decay of the N_2 and phenyl intensities after the laser pulse requires that molecules are ejected from the surface after the laser pulse. (Although collisions can slow particles as well as speed them up, the net effect in TOF measurements is to shift the peak TOF to shorter times [235]. Collisions cannot explain the long tails.) The duration of this emission can be estimated from the source function used to describe the slow tails (Eq. 13). The fast molecules were excluded from the analysis by considering only those particles arriving at least 80 μs after the laser pulse. The source functions corresponding to the data of Figs. 42 and 43 are shown in Fig. 46, all normalized to unit intensity at time t=0.

The source functions for N_2 are all very similar to each other and to the low-fluence source functions for the phenyl radical. (The low-fluence N_2 source function is displayed for comparison with the phenyl source functions as the light, broad line in Fig. 46). At higher fluences, the phenyl radical source functions extend to slightly longer times. At low fluences, the emission of N_2 and phenyl radicals is very likely controlled by the same process.

This tail is in fact entirely consistent with the proposed thermal decomposition rate (Eq. 18) decaying due to cooling of the surface given by Eq. 14.

2.2.6.4 Summary

In summary, mass-selected TOF measurements during the UV laser (248 nm)-induced decomposition of a photolabile polymer show fast neutral particles which are most likely due to particles emitted directly from the surface by a concerted, exothermal chemical reaction. At this point, time-of-flight measurements cannot distinguish whether this reaction is initiated directly by photon absorption (photochemical dissociation) or exothermic de-

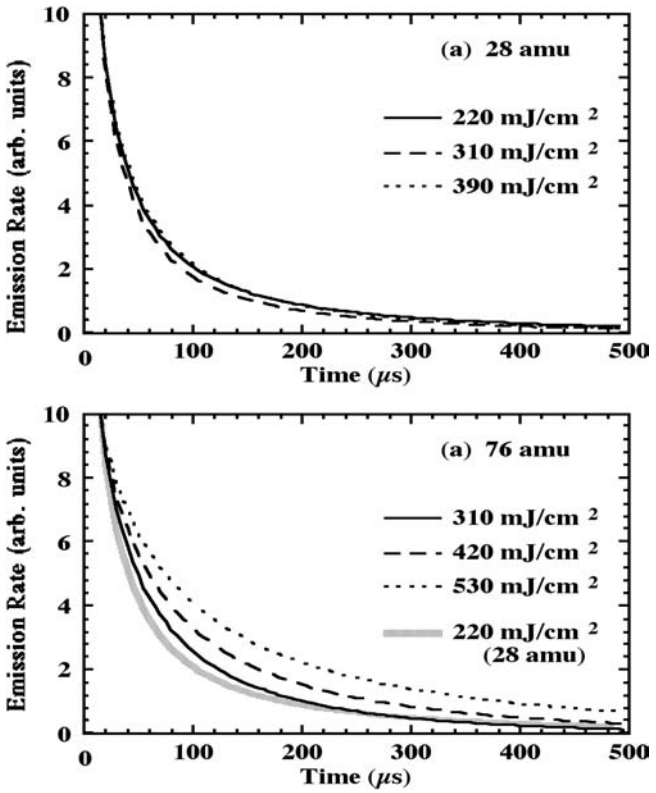

Fig. 46 Plots of the source functions determined from fitting Eq. 16 to the TOF data of (**a**) Fig. 42 (N_2) and (**b**) Fig. 43 (phenyl radical), all normalized to the same initial intensity. The N_2 source function at 220 mJ/cm^2 is also plotted as the *light line* in (**b**) to facilitate comparison of the N_2 and phenyl radical source functions. REPRINTED WITH PERMISSION OF [Ref. 324], COPYRIGHT (1999) American Institute of Physics

composition induced by thermal excitation. Importantly, the fast mass 28 (N_2) component, the total mass 28 (N_2) emission, *and* the total mass 76 (phenyl radical) emission all follow an Arrhenius relation where the temperature is predicted from the total laser energy deposited. We therefore propose that photothermal processes are dominating the rates of formation of these products. The fast component of N_2 emission may then be attributed to a thermally induced exothermic decomposition where the products come off prior to equilibrating with the surface. The cooling of the surface (Eq. 1515) explains the slow tail in the emission that follows the laser pulse {(by as much as a hundred microseconds), e.g., seen in Fig. 46.

We are currently exploring the use of low temperatures (i.e., 77 K) and using low fluences to attempt to suppress the thermal processes. Furthermore, in the case of triazene polymers, we also expect stronger signals due to irradiation at 308 nm, near a maximum in the photodissociation cross section.

These experiments may also provide us with more information on the significance of gas-dynamic processes among the emitted fragments, where a substantial population of phenyl radicals appears to have been accelerated by entrainment, perhaps by reducing the density of the emitted N_2 to where we might be able to see the direct phenyl radical time-of-flight. It is possible, as proposed in an earlier laser–polymer study [224], that *both* photochemical and photothermal mechanisms are occurring.

2.2.6.5
Additional Time-of-Flight Mass Spectrometry Experiments

The previously described results were obtained with 248-nm irradiation which is close to an absorption minimum, while 308 nm (351 nm) which was used for most other studies is close to an absorption maximum. A comparison of these two irradiation wavelengths, one corresponding to the absorption of the photochemically active triazene group (308 nm), the other to the photochemically more stable aromatic system (248 nm), could give valuable information about the influence of these structural units on the ablation mechanism.

For a direct comparison between the two irradiation wavelengths, the relative maximum peak intensities of different fragments are compared. In Fig. 47 the response of the most intense mass (i.e., 28 amu from N_2) at the two different irradiation wavelengths is shown. The data taken after irradiation at 308 nm exhibit a linear increase of the signal intensities at low fluences (<40 mJ cm^{-2}), as shown in the insert in Fig. 47. At higher fluences a fast increase is observed. This is an indication that at fluences above

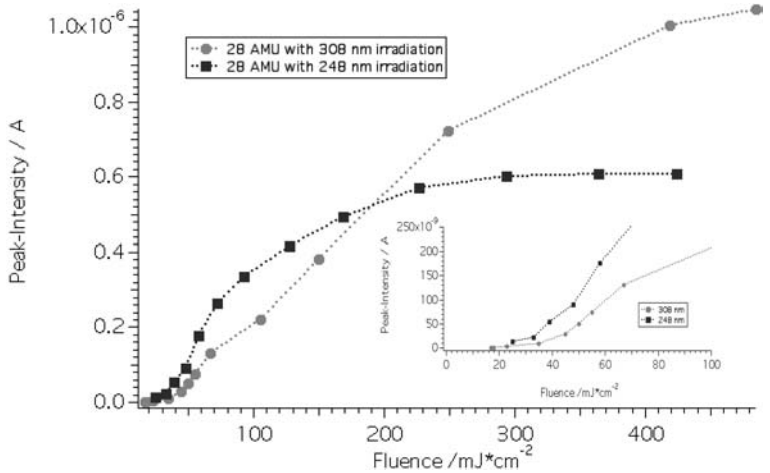

Fig. 47 Intensity of the 28 amu signal from decomposition of TC at various fluences with 248- and 308-nm irradiation. REPRINTED WITH PERMISSION OF [Ref. 56], COPYRIGHT (2001) Elsevier Science

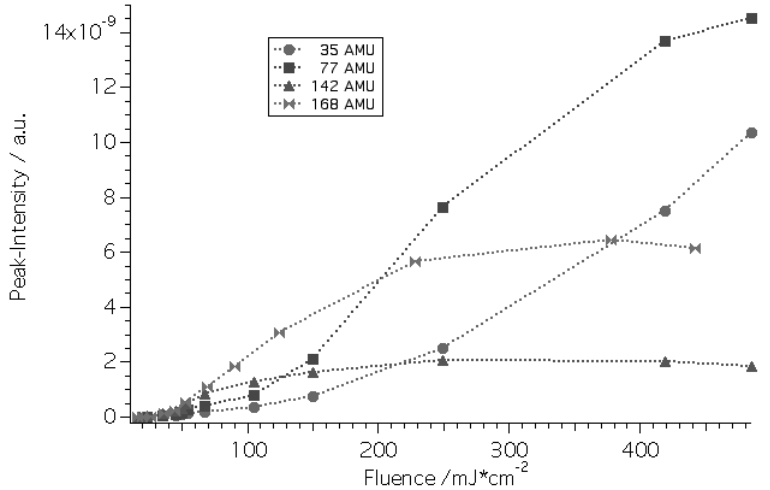

Fig. 48 Intensity of the other fragments from decomposition of TC at various fluences with 308-nm irradiation. REPRINTED WITH PERMISSION OF [Ref. 56], COPYRIGHT (2001) Elsevier Science

≈40 mJ cm^{-2}, the process changes from a linear photochemical reaction to the nonlinear ablation process. This value agrees very well with the ablation threshold of ≈25–30 mJ cm^{-2}, which was determined with other techniques [68, 134].

After irradiation at 248 nm a much faster increase of the signal was detected and no linear range can be observed (see insert in Fig. 47). At higher fluences the signal intensity reaches a maximum. This is probably due to absorption of the incoming photons by aromatic fragments (e.g., radicals, which are produced during ablation). In Fig. 48 the observations for other analyzed masses after irradiation at 308 nm are summarized.

Only signals which can be assigned to direct laser ablation products were analyzed (see Scheme 9), maybe with the exception of mass 76/77, which could be a primary product of laser ablation but also a fragment of the electron impact or of reactions in the ablation plume. The resolution of our experimental setup does not allow us to distinguish between these two masses.

A tentative interpretation of the signal is as follows. The fragment with mass 35 (fragment of the solvent chlorobenzene that cannot be removed totally from the films) is nonlinearly increasing over the whole fluence range; chlorobenzene probably contributes also to the 77/76-amu signal. At low fluences the signal is quite low and increases significantly at fluences above 150 mJ cm^{-2}. This can be explained by a surface region which contains less solvent than the deeper layers [224]. As the fluence increases, the depth of the ablated crater increases and more solvent is removed. The fragment with mass 76/77 results from the fragmentation of the solvent and from the decomposition of the 168-amu fragment (cf. Scheme 9). At lower fluences, the 76/77 amu signal seems to be correlated with the 35 amu signal, while it

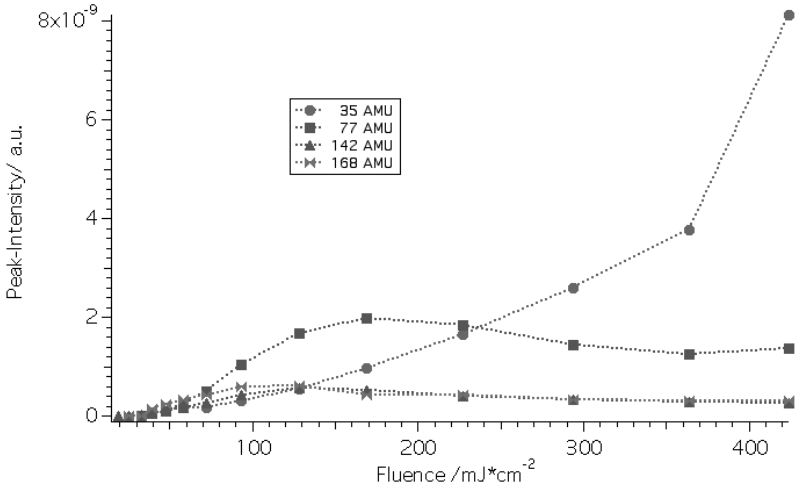

Fig. 49 Intensity of the other fragments from decomposition of TC at various fluences with 248-nm irradiation. REPRINTED WITH PERMISSION OF [Ref. 56], COPYRIGHT (2001) Elsevier Science

starts to increase more rapidly in the fluence range where the 168 amu signal levels off. The 168-amu fragment decreases at higher fluences and an increase of the 76/77-amu signal is detected. The 142-amu fragment intensity increases initially, similar to the 28-amu signal, suggesting that both are products of the same process. At higher fluences the signal intensity stays constant, probably due to the decomposition of this fragment. The 168-amu signal reveals a similar behavior as the 142-amu signal.

In Fig. 49 the signal intensities of the same masses are shown for 248-nm irradiation. The 35-amu signal intensity increases slowly at the beginning and much faster at the high fluence end. This can again be due to a dense surface region with a lower amount of solvent, which has been previously found for PMMA cast from chlorobenzene [224]. Other possibilities are the higher ablation rates at higher fluences, which result in higher Cl signals, or a more effective decomposition of the chlorobenzene at higher fluences. The 76/77-amu signal increases slowly at the beginning, but when the fluence reaches the value where the 168-amu signal decreases, a fast increase is observed. At still higher fluences, the phenyl fragment signal decreases again, most probably due to decomposition. This is only observed for 248-nm irradiation. The higher photon energy at 248 nm is sufficient to decompose the aromatic system, causing a decrease of the signals related to the aromatic fragment. The 142-amu signal increases at low fluences, until it reaches a certain maximum. Then it decreases slowly to reach a constant value. This behavior can again be explained by a decomposition of this fragment at higher fluences (similar to 308-nm irradiation).

In comparison, pronounced differences between the signal intensities at 248- and 308-nm irradiation are observed. The fragments with masses high-

er than 35 reveal clearly higher intensities for 308-nm irradiation. This is due to the higher etch rates at 308 nm at higher fluences, but also to further decomposition of the larger fragments with the higher photon energy of the 248-nm irradiation. At lower fluences, especially in the case of N_2, higher intensities are detected for 248 nm. For 308-nm irradiation a linear behavior of the signal with the laser fluence can be observed. Around the threshold of ablation this linear behavior changes, i.e., faster increase of the signal intensity. As argued above, we observe the photochemical decomposition of the triazene polymer with 308-nm irradiation at low fluences. The triazene group (N^1=N^2–N^3<) decomposes photochemically between the N^2 and N^3 nitrogen atoms, and N_2 is released (shown in Scheme 9). The other radical fragments of this homolytic decomposition of the N–N bond are combining to form an insoluble cross-linked polymer network, as described in the next paragraph in more detail. The available experimental data do not really show this linear relation for 248-nm irradiation at low fluences, maybe due to the low intensities of the N_2 fragment.

2.2.7
Excimer Lamp Irradiation

2.2.7.1
Introduction

Excimer lamps were selected to study the low fluence irradiation region, where linear (no ablation) photochemistry is taking place. This is the fluence range (e.g., insert in Fig. 47 of the previous chapter), where a linear relation between reaction products and laser fluence is observed. This may correspond to the range of "linear" photochemistry, i.e., below the threshold of ablation (see, e.g., Figs. 25 and 26), or the so-called Arrhenius tail. The excimer lamps emit at the same wavelengths as the excimer lasers, but with incoherent radiation, and in quasi-CW mode. The peak photon fluxes of the lamps are low compared to the excimer laser, suggesting that multiphoton processes are not important. Thin films of the triazene polymer on quartz substrates were irradiated with the excimer lamps under different conditions, i.e., in Ar, air, and O_2.

2.2.7.2
Experimental

The incoherent excimer radiation from a dielectric barrier discharge (silent discharge), operating in pure xenon, gas mixtures of krypton/chlorine, and xenon/chlorine, provides intense narrow-band radiation. More details about the excimer UV sources can be found in the literature [236, 237]. As irradiation sources a XeCl (308 nm), a KrCl (222 nm), and a Xe_2 (172 nm) excimer lamp were selected. Excimer lamps based on fluorine-containing excimers are difficult to operate, due to etching of the quartz housing by the F_2.

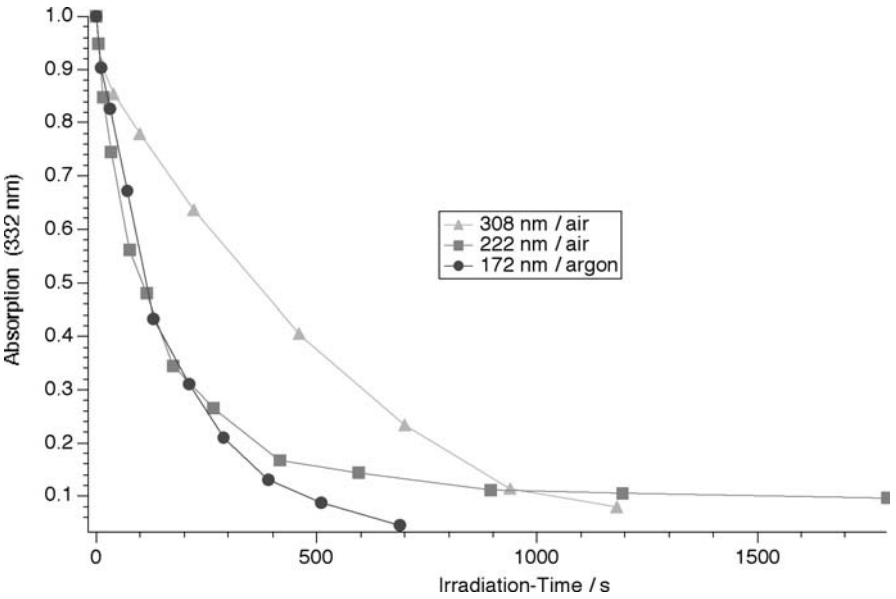

Fig. 50 Change of the absorption at 332 nm at various irradiation times with 172, 222, and 308 nm. The irradiation was performed in air for 308 and 222 nm wavelengths, and in Ar for 172 nm. The absorption was normalized to 1 for all experiments. REPRINTED WITH PERMISSION OF [Ref. 56], COPYRIGHT (2001) Elsevier Science

Therefore the KrCl excimer lamp was used instead of the KrF 248-nm irradiation, and additionally the Xe_2 excimer lamp. Different atmospheres were used for the 172-nm irradiation, because oxygen has a strong absorption band around 172 nm and ozone, oxygen-radicals, and excited molecular oxygen species are formed upon irradiation [238]. These reactive oxygen species cause photooxidation, in addition to the direct photolytic decomposition of the polymer. The irradiance of the XeCl and KrCl excimer lamps was measured by chemical actinometry. The intensity of the excimer lamps is $\approx$24 mW cm^{-2} while KrCl excimer lamps have an intensity of $\approx$50 mW cm^{-2}.

The irradiations at 308 and 222 nm were carried out in air. Effective direct etching of polymers by excimer lamps can only be observed at reduced pressures (between 0.1 to 100 mbar) [239], which was not examined in this study where only atmospheric pressure was applied. The decomposition of the polymer was analyzed at the two maxima, i.e., 196 and 330 nm. The former corresponds mainly to the absorption of the aromatic groups, the latter to the triazene groups [68].

With 308-nm irradiation, decomposition of the triazene group (330 nm) is observed almost exclusively. Only very minor changes are observed for the band at 196 nm. This is shown in Figs. 50 and 51, where the changes of the two absorption maxima are plotted as a function of the irradiation time for all irradiation wavelengths. A detailed analysis of the changes of the band

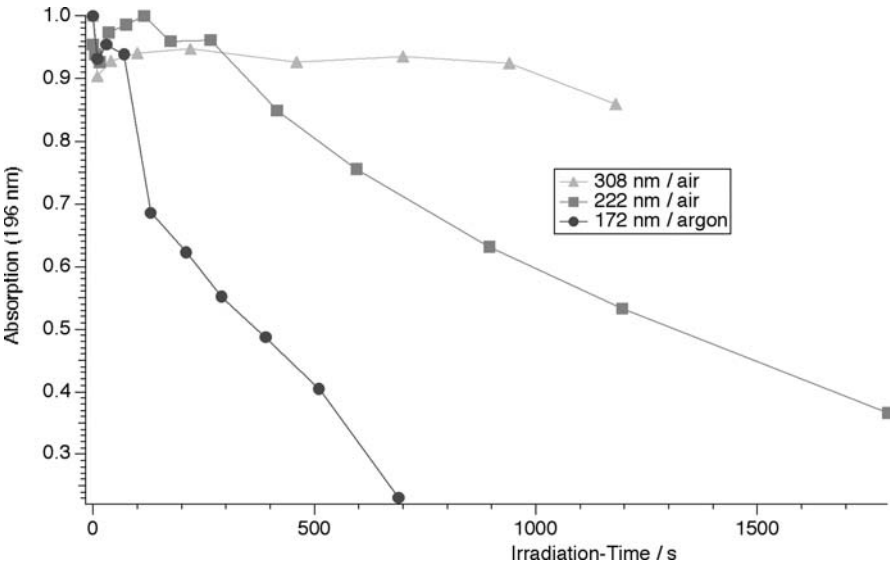

Fig. 51 Change of the absorption at 196 nm at various irradiation times with 172, 222 and 308 nm. The irradiation was performed in air for 308 and 222 nm wavelengths and in Ar for 172 nm. The absorption was normalized to 1 for all experiments. REPRINTED WITH PERMISSION OF [Ref. 56], COPYRIGHT (2001) Elsevier Science

at 196 nm (Fig. 49) reveals an instant drop of intensity for all irradiation wavelengths. The reasons for this behavior are not clear, but it might be due to desorption of adsorbed species or most probably to the temperature increase of the polymer surface upon irradiation with the hot lamp. After this initial decrease of intensity an increase can be observed. This increase is clearly visible for all irradiation wavelengths, but is most pronounced for irradiation at 222 nm. It might be caused by an increase of the molecular weight of the polymer (cross-linking), which has also been detected after thermolysis of the polymer in bulk [240]. The cross-linking can be explained by the photochemical decomposition mechanism of the polymer (see Scheme 9). Radical species are created upon the homolytic bond scission of the N–N bond. In the next step, nitrogen is eliminated and the radicals combine to form a cross-linked polymer. This cross-linked polymer is insoluble and the whole process is comparable to the processing of a negative photoresist. The photon energy (4.02 eV) of the 308-nm excime -lamp has enough energy to break the N–N bond (1.7 eV), but the energy is only slightly above the binding energy of C–C bonds (3.6 eV) and clearly below the energy of a C=C bond (6.36 eV). The binding energies of the bonds in the aromatic systems, which are probed at 196 nm, should be somewhere between these values. This explains why only small changes of the band at 196 nm are detected for 308-nm irradiation.

In the case of 222-nm irradiation both bands are decreasing. As expected, a faster decrease of the 330-nm band is observed compared to 308-nm irra-

diation (see Fig. 50). The excitation of electronic transitions is *not* localized, and a fast redistribution of the energy takes place, resulting not just in the decomposition of groups that are directly related to the irradiation wavelength. In other words, it is expected that with irradiation at 222 nm (or 172 nm) the most labile bond, i.e., the triazene group is broken first. The higher photon energy of the 222-nm photons (5.58 eV) is more effective for the decomposition of the N–N bond, resulting in the faster decomposition of the triazene group, i.e., band at 330 nm (Fig. 50). Contrary to 308-nm irradiation, the band at 196 nm is also decreasing with 222-nm irradiation (Fig. 51). This can only be observed after an initial increase and a period of nearly constant absorption. The increase of absorption and the constant range can be explained by the above described cross-linking of the polymer. These cross-linked structures could have a higher absorption coefficient at 196 nm than the starting material. The energy of the 222-nm photons is high enough to decompose the aromatic system, and therefore to destroy the newly created cross-linked structures. As long as a many new radicals are formed upon the decomposition of the triazene group and cross-linking takes place, a quasi-steady state between decomposition and creation of cross-linked structures exists. This is the range of nearly constant absorption of the band at 196 nm. After about 250 s of irradiation, when around 80% of the triazene groups are decomposed, more cross-linked groups are decomposed than formed and the absorption decreases.

The irradiation at 172 nm results in the fastest decomposition of both bands. In Figs. 50 and 51 the changes upon irradiation in Ar are shown, because under these conditions additional effects of oxygen, as described below, are omitted. Again, an initial increase of the band at 196 nm (Fig. 51) is observed, but is followed by a quite fast decrease. This can be explained by the high photon energy (7.2 eV) of the 172-nm radiation, which can directly break all bonds in a polymer. The decomposition of the polymer upon 172-nm irradiation is, in addition, dependent on the atmosphere in the irradiation chamber. The fastest decomposition is observed in air, followed by oxygen and argon. The 172-nm radiation is absorbed by the oxygen in the reaction chamber, and ozone, oxygen radicals, and excited molecular oxygen species are formed [239]. These species are very reactive and decompose the polymer. This process was described previously as photooxidative decomposition [241], which can also result in etching at atmospheric pressure. We observed etch rates of $\approx$5.5 nm min^{-1} in air, which is comparable to etch rates reported for other polymers (1–5 nm min^{-1}) [239, 241]. This additional decomposition path is absent in Ar, resulting in the slowest decomposition rates. In pure oxygen, on the other hand, the radiation is absorbed close to the lamp, where the reactive species are formed. Therefore, less reactive species and photons are reaching the polymer surface in O_2. As a result, the fastest decomposition of the polymer is observed in air.

The excimer lamp irradiation experiments show clearly that photochemical decomposition of the triazene polymer takes place, even at low fluences and quasi-CW irradiation (the excimer lamps emit bursts of UV pulses with ns duration, but with repetition frequencies in the kHz range).

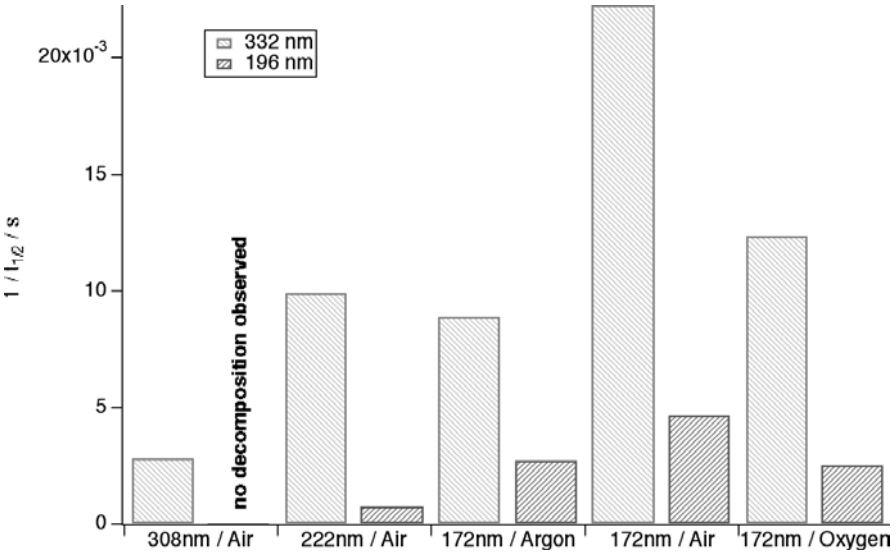

Fig. 52 The inverse half-life times of the 196 and 332 nm absorptions with all irradiation wavelengths and under all conditions. REPRINTED WITH PERMISSION OF [Ref. 56], COPYRIGHT (2001) Elsevier Science

The results are summarized in Fig. 52, where the inverse half-life periods of the two bands at the different irradiation wavelengths are shown. It is clearly visible that with 308-nm irradiation only the triazene band at 330 nm decreases, while for all other irradiation wavelengths both bands are decreasing. The irradiation wavelength with the highest photon energy results in the fastest decomposition of both bands. For irradiation at 172 nm a pronounced influence of the atmosphere can be observed. Irradiation in air results in the fastest decomposition of the band at 196 and 330 nm, due to oxidative decomposition of the polymer by the above described reactive oxygen species. Upon irradiation with 308 nm and in the early stages of the irradiation at 222 nm, an insoluble polymer network is formed. A quantitative comparison of the half-life periods between the different irradiation wavelengths is not possible, due to the different irradiation doses. It is also noteworthy to mention that the irradiation is accompanied by a temperature increase (<100 °C), due to the temperature of the excimer lamps.

2.2.8 *Picosecond Infrared Spectroscopy*

2.2.8.1 Introduction

The time-resolved measurements in the previous chapters have shown that the decomposition of the polymer starts during the nanosecond irradiation pulse.

Therefore we have developed an experimental setup which provides mid-IR spectroscopy on timescales from pico- to milliseconds. For the proof-of-principle experiments an azo compound, i.e., diazo Meldrum's acid, was selected. This compound was used as dopant in a polymer matrix, allowing variation of the absorption strength of selected mid-infrared bands over of a wide range. The IR absorption bands of azo functional groups are additionally in a range where nearly no other IR bands are located (~2200 cm^{-1}). Azo compounds are also structurally closely related to the triazene groups in our designed polymers and are classical representatives of photoactive compounds.

In the course of a chemical reaction, reactants are converted through various transition states and intermediates that occur on the reaction pathway. The properties of these reactive intermediates and/or transition-state species are central to determining the reaction rate and selectivity. Recent developments in laser techniques have made pico- and femtosecond timescales available (on a routine basis) for the observation of short-lived intermediates and even the transition state [242]. The study of reactions on ultrafast time scales helps in understanding the details of the reaction pathway and reaction coordinates. In addition, ultrafast measurements are necessary for determining the kinetics of fast reactions. For example, most investigations of ultrafast dynamics have been performed by observation of the changes in the visible region of the spectra. Unfortunately, for larger and more complex systems, the visible absorption spectrum consists typically of broad, overlapping features from which one can extract little structural information. This difficulty has led to the development of structurally sensitive, ultrafast vibrational spectroscopies that now allow one to gather correlated structural and temporal information on these large and complex systems. Use of time-resolved Raman techniques, such as CARS [243], also gives detailed structural information, but CARS measurements are restricted to only a few strong Raman bands. In this chapter, we describe our experimental setup, which was developed to study the thermal decomposition of crystalline energetic materials embedded in polymer matrices using time-resolved infrared absorption spectroscopy, which allows the observation of far more bands than Raman techniques. We will discuss first the results for a model compound in a polymer matrix.

2.2.8.2 Experimental

The experimental setup is shown in Fig. 53. A ps Nd:YAG laser is used to drive a regenerative amplifier, which acts as pump laser, while the doubled Nd:YAG laser is used to pump a dye jet laser.

Short pulse mid-IR was generated using two different setups. For IR generation between 1800 and 2900 cm^{-1}, the outputs of the amplified dye laser and the frequency-doubled regenerative amplifier are overlapped in time and then passed through a $LiIO_3$ crystal in a type I difference frequency mixing configuration.

To generate mid-IR pulses of longer wavelength a different setup was used. In this case, a two-crystal mixing scheme is used with minor modifica-

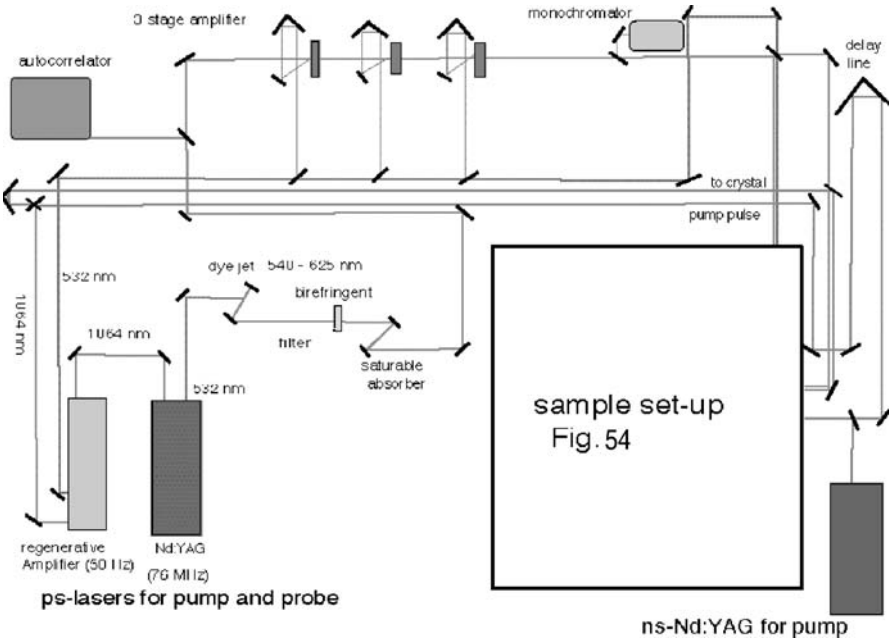

Fig. 53 General experimental setup

tions to the laser setup. In the first stage of the two-crystal setup, a KD*P crystal is used for difference frequency mixing of the dye beam with 1064 nm. In the second stage, the tunable near-IR and the leftover 1064 nm are difference frequency mixed in an $AgGaS_2$ crystal resulting in mid-IR pulses. With this configuration it is possible to reach mid-IR wavelengths between 770 and 1905 cm^{-1}.

The temporal resolution of the two different crystal setups is determined by the pulse length of the pump pulse: the remaining fundamental of the regenerative amplifier. The pulse length of the 1064-nm fundamental is about 100 ps; for the harmonics the pulse lengths are about 70 and 60 ps for 532 and 355/266 nm, respectively. Thus, our temporal resolution is about 20 ps by applying standard deconvolution methods. The optical delay line (computer controlled) of the pump beam determines the maximum time scale of the experiment, about 8 ns, but it can be doubled to 16 ns by implementing a double-pass setup.

A second mid-IR and pump source was integrated into the setup to reach longer delays (which are important to follow reactions further than their initial steps). A ns Nd:YAG laser is now used as the pump. The laser runs at a maximum repetition rate of 10 Hz and is equipped with doubling crystals to yield the harmonics of the laser. At 1064 nm, the pulse length is about 7 ns with a maximum energy of 225 mJ, at 532 nm it is 6 ns with 100 mJ, at 355 nm it is about 6 ns with 55 mJ, and at 266 nm it is also about 6 ns with 35 mJ The pump beam is aligned onto the same optical path as the ps pump

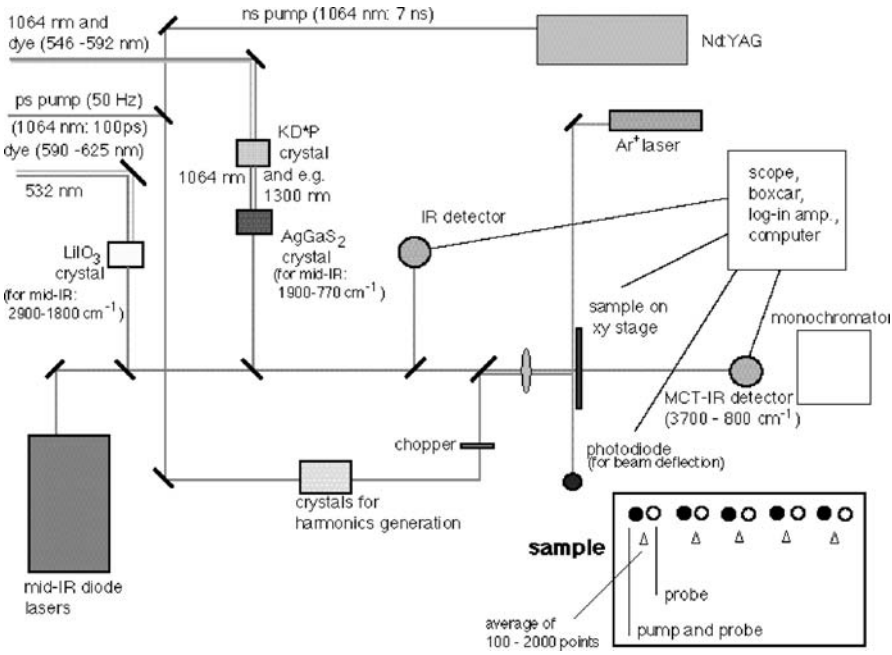

Fig. 54 Detailed scheme of the setup in the sample area

beam as shown in Figs. 53 and 54. To probe the longer time scale CW mid-IR diodes are used (shown in Fig. 54). These laser diodes can be tuned over a range of about 100 cm^{-1} by changing the temperature and current of the diode. The details of the sample area are shown in Fig. 54. Due the nature of our samples, i.e., crystalline energetic material in a solid matrix, only single-shot experiments of each irradiated area are possible; with each laser pulse the material is decomposed or ablated at the high pump energies.

Therefore, a typical sample consists of a thin coating of our probe molecules in a polymer matrix [poly(methyl methacrylate), PMMA, or poly(vinyl chloride), PVC] either as freestanding film or on a polymer substrate (polypropylene, PP).

Sample Preparation and Selected Materials. To test the experimental setup a diazoketone was selected, which is structurally related to the triazene polymers. Diazoketones are widely used for imaging applications [244]. These compounds undergo a photoinduced Wolff rearrangement to form a ketene intermediate which subsequently hydrolyses to a base-soluble carboxylic acid (shown in Scheme 10, together with other suggested intermediates) [245–247]. This particular diazoketone (5-diazo-2,2-dimethyl-1,3-dioxane-4,6-dione or 5-diazo Meldrum's acid, DM) is sensitive to deep UV (200–260 nm) making it suitable for high-resolution lithographic applications [248–250].

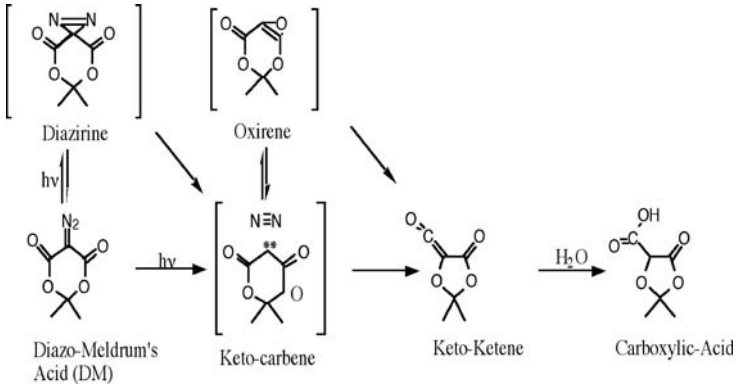

Scheme 10 Mechanism of the photodecomposition of diazo Meldrum's acid. REPRINTED WITH PERMISSION OF [Ref. 188], COPYRIGHT (1996) American Chemical Society

Thermally induced reactions in polymers are also of increasing interest for fundamental and applied research. In particular, various imaging systems are based on putting energy into a thin polymer film with a laser. The energy is put into a dye (shown in Scheme 11) that converts the energy into heat within a few picoseconds. Subsequently, the films start to decompose, break up, and eventually ablate [251]. Additional energetic materials are thought to increase the efficiency of this process.

One possible candidate is again DM, which is also known to undergo a thermally induced Wolff rearrangement [252]. Two types of films were used, i.e., one prepared for irradiation in the UV (266 nm) and one prepared for irradiation at 1064 nm, to allow a comparison of the photochemical reaction with the thermal reaction. For the photochemically induced reaction, we used a mixture of PMMA and DMA. This diazo compound has two features which make it a perfect test molecule. It has the strong azo absorption band in the mid-IR (2176 cm^{-1}) and has one known reaction product (keto-ketene), shown in Scheme 11, which also has a strong absorption band in the mid-IR (reported between 2000 and 2200 cm^{-1}) [253]. For the thermal reaction of the diazo compound we used 1064-nm irradiation to excite a "heater"

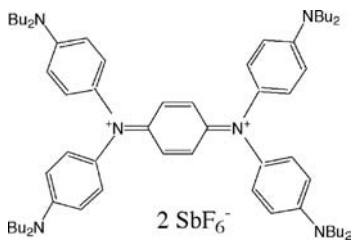

Scheme 11 Structural formula of IR-165

dye (IR-165, shown in Scheme 11) which dumps its energy into the matrix within a few picoseconds [189], raising the matrix "temperature" to one to two thousand Kelvin.

2.2.8.3
Results and Discussion

266-nm Excitation. The change of the IR absorbance was monitored following 266-nm excitation with 30–130 μJ per pulse in the diazo/ketene region from 2120 to 2210 cm^{-1} at intervals of 10 cm^{-1}. Maximum changes in absorption occurred at 2190 cm^{-1} (shown in Fig. 55) where a decrease in absorbance was observed, and at 2150 cm^{-1} where an increase in absorbance was observed.

The 2190 cm^{-1} change was assigned to the bleaching of the diazo Meldrum's acid, and the 2150 cm^{-1} change to the appearance of the keto-ketene intermediate. Figure 55 shows the bleaching of the azo band monitored at 2190 cm^{-1}. The decrease in absorbance at 2190 cm^{-1} occurs within our instrument response and is constant for 6 ns as expected for the photodissociation. Similarly, the rise time of the 2150 cm^{-1} feature we assign to the keto-ketene can also be described by our instrument response. Using deconvolution techniques it is possible to assign an upper limit on the appearance of the keto-ketene of τ<20 ps; no change was seen out to 6 ns. In Fig. 56 is shown the difference spectra observed at 300–500 ps, generated by averaging the 300–500 ps data in each of the kinetic traces. As the bands due to the starting diazo compound and the keto-ketene overlap significantly, it is nec-

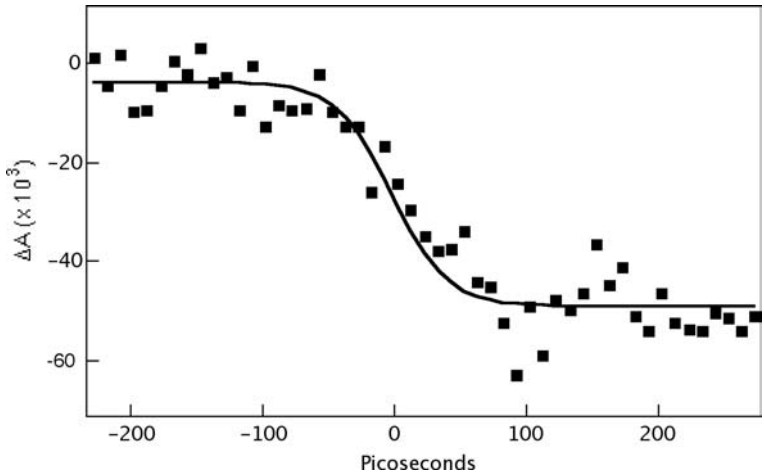

Fig. 55 Change of absorbance as a function of time from −200 to 300 ps at 2190 cm^{-1}. The *solid line* is the instrument response. REPRINTED WITH PERMISSION OF [Ref. 188], COPYRIGHT (1996) American Chemical Society

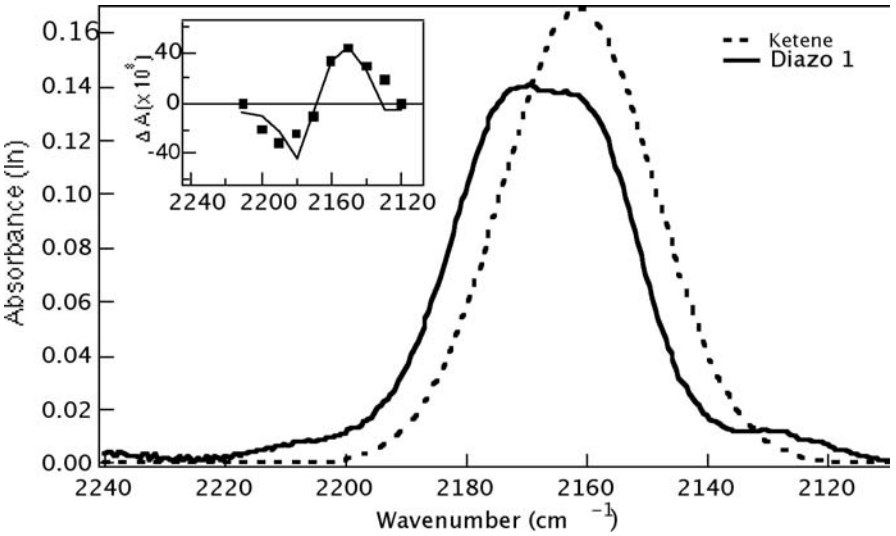

Fig. 56 Spectra of DM (*solid line*), and the keto-ketene (*dashed line*) at 300–500 ps calculated by fitting the difference spectrum (*inset*) to the difference of the DM spectra and a Gaussian function which best represents the ketene spectrum. The fit which results from the difference of the two spectra is shown in the *inset*. The fourth harmonic (266 nm) of a Nd:YAG laser with an energy of about 120 μJ has been applied. The diameter of the UV pulse was typically 400 μm, corresponding to a fluence of about 95 mJ cm^{-2}. REPRINTED WITH PERMISSION OF [Ref. 251], COPYRIGHT (1997) Elsevier Science

essary to fit the difference spectra to the difference of the DM infrared spectra and a Gaussian function representing the keto-ketene.

The best fit yields a spectrum for the keto-ketene centered at 2161 cm^{-1} and with a width (FWHM) of 29 cm^{-1}. Deviation from the experimental data at some wavelengths suggests that the spectrum is more complex than a single Gaussian, as expected for dopants dispersed in polymeric matrices. The energy dependence of the signal intensities at 2150 cm^{-1} for 1 ns is shown in Fig. 57. The key point is that there is no dramatic change above the ablation threshold (≈70 μJ), suggesting that ablation occurs on a longer time scale (i.e., >6 ns). The ejection of material would be expected to increase the observed signal (ΔA at 2150 cm^{-1}) drastically due to light scattering. In addition, within experimental error, the signal size is linear over the entire range in laser energy, consistent with a one-photon event and a quantum yield of decomposition of 0.6 [212] and 1 [254]. The quantum yield for the ketene appearance is about the same, suggesting that side reactions are not significant.

1064-nm Excitation. The resulting difference spectra (Fig. 58) are similar to that seen with 266-nm excitation. Here pump pulses at 1064 nm with 0.2–1.0 mJ are used. The product bands are red shifted slightly and are less in-

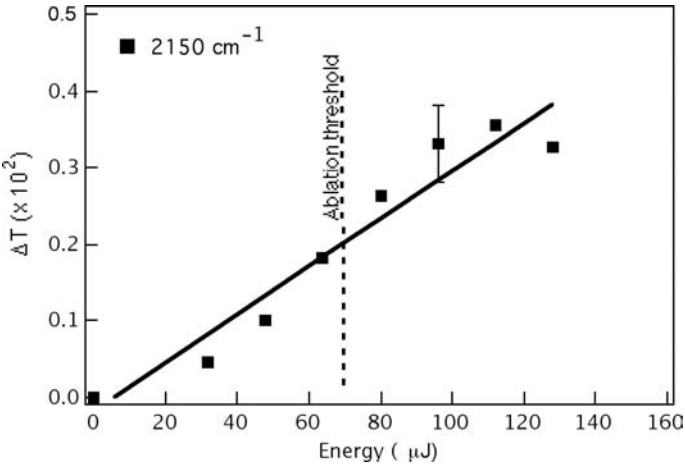

Fig. 57 Dependence of the signal intensity on the laser energy (266 nm). The irradiated area is about 1.25×10^{-3} cm^2. A typical *error bar* is shown in the graph. The bandwidth of the IR probe is ~8 cm^{-1}. REPRINTED WITH PERMISSION OF [Ref. 251], COPYRIGHT (1997) Elsevier Science

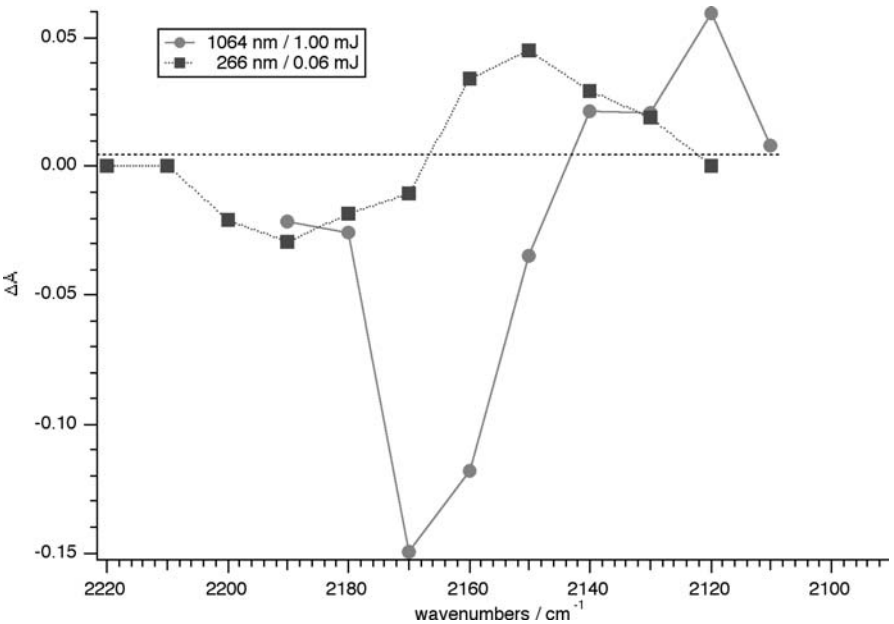

Fig. 58 IR difference spectra between 2220 and 2100 cm^{-1} after irradiation at 266 and 1064 nm. Spectra averaged over 1 ns

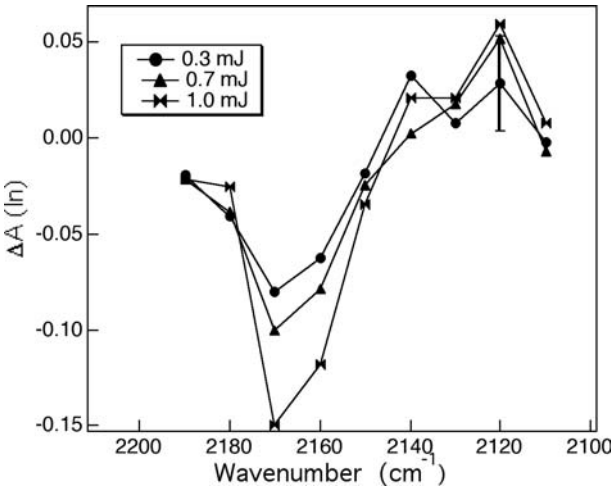

Fig. 59 Change of the absorbance as a function of irradiation energy (1064 nm) for a time of 1 ns. The irradiated area is about 0.49×10^{-3} cm^2. A typical *error bar* is shown in the graph. The bandwidth of the IR probe is ~8 cm^{-1}. REPRINTED WITH PERMISSION F [Ref. 251], COPYRIGHT (1997) Elsevier Science

tense than those seen for 266 nm. Varying the laser energy resulted in changes in the intensities of the bands, but not the band positions (Fig. 59). This suggests that bands are observed from a reaction product (ketene) and not exclusively from thermal effects that would result in an energy-dependent red shift at increasing laser energies, but only minor intensity changes. The product band is centered at 2120–2145 cm^{-1}, and is less intense than seen in the photochemical experiments. The red shift of the observed product band is probably due to a red shift of IR bands with increasing temperature (change of density and anharmonicity) [255]. A typical shift [256] for similar IR bands (from static measurements) yields a shift of about 4 cm^{-1}/100 °C. The observed red shift would then account for a temperature jump of about 1,000 °C, which is well within the range of the estimated (laser energy, heat capacity etc.) temperature increase [257].

2.2.8.4 Summary

A novel setup was developed to study laser-driven reactions in solid matrices (e.g., polymers) using time-resolved IR spectroscopy. The first experiments have provided one of the first examples of how ultrafast infrared spectroscopy may be used to examine laser-driven reactions in polymeric matrices. The photochemically as well as the thermally initiated reaction of a model compound has been studied in a PMMA matrix. It is remarkable that both initial reactions happen on a time scale faster than our experimental limit of 20 ps. While the initial reaction products are probably the same, the

band position and intensity of difference spectra of the UV and thermally initiated reaction are different. These variations are probably due to additional side reactions, temperature effects, and different matrix interactions at elevated temperatures.

The data show clearly that ultrafast IR spectroscopy is a very promising tool to study laser ablation of polymers, because time-resolved data about specific chemical groups can be obtained. Unfortunately it was not possible to resolve the decomposition kinetics of the studied azo group and to clearly distinguish between thermally and photochemically induced decomposition. This was due to the unexpected fast thermal decomposition of the azo group. Future developments should be aimed at the application of mid-IR pump-probe experiments based on solid-state laser technology which will give a better stability of the laser system, and which will extend the time resolution into the femtosecond range (e.g., with Ti–sapphire-based systems).

2.3
Comparison with a Reference Polymer (Polyimide)

In the previous chapters experimental data on ablation of the designed polymers have been shown. Polyimide was applied as reference polymer to compare the ablation behavior of the designed polymers versus a commercial polymer which exhibits similar absorption properties. Polyimide is most probably also the most studied polymer in ablation, and numerous reference data about ablation, but also about the chemical properties, exist (e.g., thermal diffusivity, heat capacity, reflectivity, lifetime of exited states etc.). This is also the reason why many models are benchmarked against ablation data of polyimide.

Therefore we decided to gather new data about the laser-induced decomposition of polyimide and contrast them with results from pyrolysis using the same experimental technique, i.e., diffuse reflectance infrared Fourier-transform (DRIFT) spectroscopy.

2.3.1
DRIFT Analysis of Polyimide After UV Laser Irradiation

2.3.1.1
Introduction

During the past three decades, since the commercialization of Kapton polyimide, an impressive variety of polyimides have been synthesized [258, 259]. Polyimides possess outstanding key properties, such as thermooxidative stability [260], high mechanical strength [261], high modules, excellent electrical [262] and optical properties [263, 264], and superior chemical resistance [265]. Recently polyimides have also been applied as membranes for gas separation [266, 267]. Approximately 15 years ago the direct structuring or laser ablation of polyimides by excimer lasers was first described [73, 130].

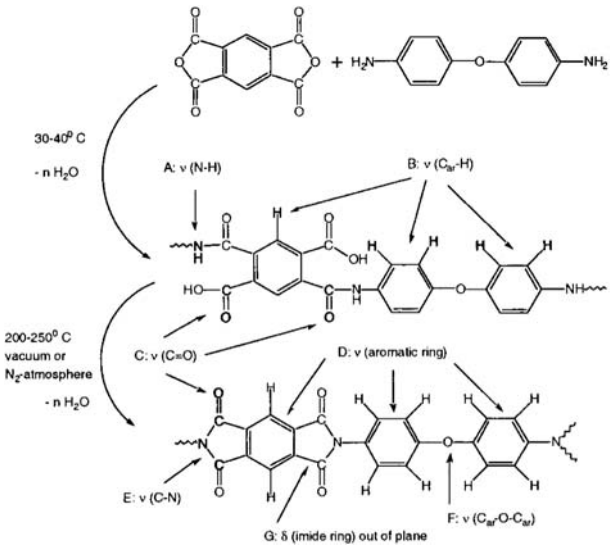

Scheme 12 Scheme of the synthesis of Kapton. Some bands relevant for the discussion are marked (*bold*) and assigned. REPRINTED WITH PERMISSION OF [Ref. 135], COPYRIGHT (2000) American Chemical Society

These studies showed clearly that ablation caused clean etching of the material with micron-size precision. Because of the importance of polyimides in numerous applications and the difficulty in etching these polymers by other means, such findings prompted intensive further research [268]. At the present time laser ablation of polyimide is a routine part of microelectronic packaging [269, 270] and the fabrication of nozzles for inkjet printer heads [24]. In addition, laser irradiation is being explored as a means of generating uniform thin polymer films, which may also prove to be useful in electronic packaging as well as in other applications such as polyimide film coating of various materials [271]. As discussed above, the term polyimides refers to a group of polymers. Most ablation studies, including this, have been conducted on one specific polyimide known as Kapton. Kapton is produced commercially by DuPont, using a condensation reaction of pyromellitic dianhydride (PMDA) and oxydianiline (ODA), with polyamic acid as intermediate, as shown in Scheme 12. During laser ablation the incident radiation is absorbed within some finite volume of the material, unless the material is completely transparent at the laser wavelength. Kapton shows a broad UV absorption band in the region between 180 and 400 nm, allowing the effective absorption of all common excimer laser wavelengths (193, 248, 308, and 351 nm) [178]. It is generally agreed that the mechanism is mainly photothermal, with additional photochemical features, especially at 193-nm irradiation [63]. Prominent features of Kapton ablation are the sharp ablation threshold (measured with atomic force microscopy, AFM), Arrhenius tails

(smooth Arrhenius-type ablation onset, measured with mass spectrometry or quartz microbalance, QMB), and differences in the ablation rate near the threshold between two very sensitive methods, i.e., AFM and QMB [89]. The lower threshold fluences are obtained by QMB, suggesting the additional or exclusive ejection of gaseous molecules at low fluences (maybe even below the threshold of ablation). Ablation products have been studied by a variety of techniques. Infrared spectroscopy [69], gas chromatography [166], and mass spectrometry [272] have been used to identify the principal gaseous products of Kapton ablation: CO_2, CO, H_2O, HCN, and various light hydrocarbons (up to four carbon atoms). Laser-induced fluorescence measurements indicate that diatomic fragments C_2 and CN are also formed, at least transiently, during ablation [273]. Larger molecules (e.g., C_{60}) up to visible carbon particles are also formed [274]. The soot is partly redeposited around the ablation crater and consists of amorphous carbon with some crystalline features. The ablated area of Kapton was also analyzed and carbonization in a certain fluence range was detected [170]. This carbonization results in an increase of the conductivity of up to 12 orders of magnitude [275]. The carbonized material consists of amorphous carbon, but also graphitic material [276]. Other surface species, intermediates, and products in the polymer film, which could be indicative of a mechanistic scheme, are not reported to our knowledge. The analysis of the surface of polymers is quite difficult. The laser radiation is absorbed within a layer of 100 nm (at 308 nm) of the polymer film, thus resulting in changes within a very thin layer.

The analytical method of choice should be sensitive enough to analyze the surface and should also be capable of identifying changes of specific groups in the polymer chains. One promising candidate is infrared (IR) spectroscopy, which is an important method for the characterization of polymer conformation [277], orientation [278], and solvent effects [279]. Newer developments in IR spectroscopy include time-resolved [280, 281] and two-dimensional techniques [282, 283] for dynamic processes in polymers, such as conformational changes, diffusion, and polymerization. The standard technique for IR spectroscopy is transmission spectroscopy, which is not suitable for our purpose, because the polymer films are too thick and the method is not sensitive enough for surface species. A surface-sensitive technique such as attenuated total reflection (ATR) [284, 285] or diffuse reflectance infrared Fourier-transform (DRIFT) spectroscopy should be suitable for the investigation of the polymer films after laser irradiation. ATR spectroscopy is suited to the analysis of samples with flat surfaces, e.g., polymer films, but it is well known that surface structures and roughening of the polymer films takes place during ablation. In one study, ATR was used to examine polymer films after irradiation in a relatively small fluence range [286]. The DRIFT spectroscopy is specifically designed to study powdered samples, and is well known for its high sensitivity. A wide variety of materials can be analyzed using DRIFT spectroscopy. Some of these materials can be analyzed in substance, without any sample preparation. In previous works diffuse reflectance spectra of

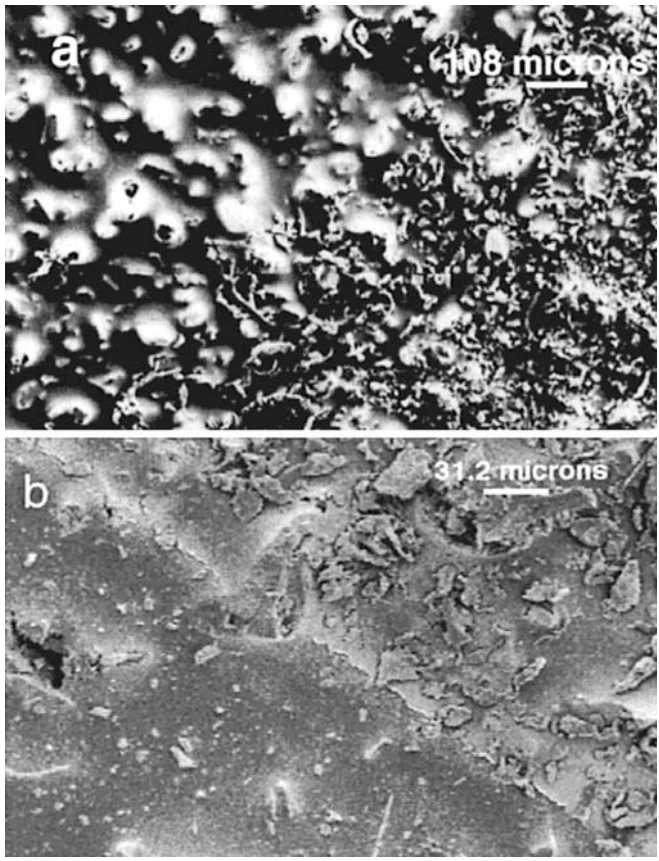

Fig. 60 Scanning electron microscopy (SEM) pictures of a SiC disk. **a** In the *lower right* part of the picture the abraded Kapton is visible as scrapes. **b** The border between laser-treated and untreated area is shown. The *lower left* side corresponds to the laser-treated area (20 pulses at 155 mJ cm^{-2}). REPRINTED WITH PERMISSION OF [Ref. 135], COPYRIGHT (2000) American Chemical Society

polymer films were collected by placing KBr powder over the sample [287]. Unfortunately the quality, the amount, the size of the particles used, and how they are packed in the sample holder significantly affect the scattering characteristics of the overlayer material and therefore the quality of the spectra [288]. This problem can be overcome by the use of a silicon carbide (SiC) sampling kit and using polymer scrapes, as shown in Fig. 60 a.

The XeCl laser (308 nm)-induced decomposition of Kapton is studied to identify reaction steps leading to the previously mentioned gaseous products, and to identify the intermediate steps of the surface carbonization of Kapton. The XeCl laser is applied in the industrial processing of polyimide due to the reliability of its optical and laser components at the emission

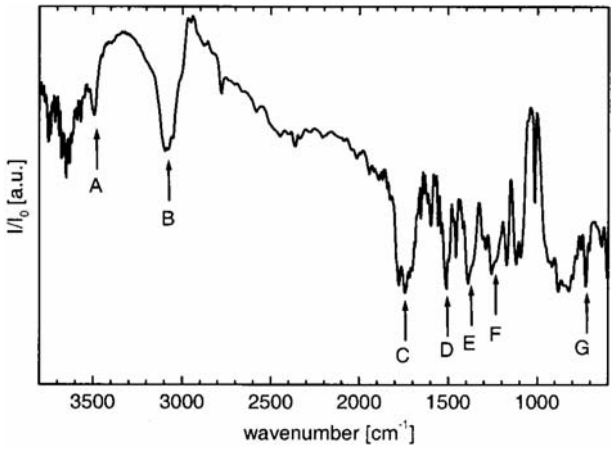

Fig. 61 DRIFT spectrum of Kapton; 1,024 scans with a resolution of 4 cm^{-1} and using SiC as background. The following bands are assigned:(A) 3490 cm^{-1}: N–H stretching; (B) 3060 cm^{-1}: C–H stretching; (C) 1740 cm^{-1}: C=O stretching; (D) 1500 cm^{-1}: aromatic ring stretching; (E) 1390 cm^{-1}: C–N stretching; (F) 1260 cm^{-1}: C_{ar}–O–C_{ar} stretching of aryl ether; (G) 725 cm^{-1}: out-of-plane bending of the imide ring. REPRINTED WITH PERMISSION OF [Ref. 135], COPYRIGHT (2000) American Chemical Society

wavelength (308 nm). The Kapton samples are studied after irradiation at various laser fluences and laser repetition rates.

DRIFT spectra are usually presented in Kubelka–Munk units. In this work the spectra are presented as relative reflectance units (I/I_0). The reflectance of the abraded polymer changes upon irradiation. The SiC substrate is grayish-black and absorbs strongly throughout the whole mid-IR region. These properties violate one of the basic assumptions of the Kubelka–Munk theory, i.e., the presence of a non- or weakly absorbing substrate [289], therefore reflectance units are used. The spectra shown in the figures (with exception of the reference spectrum of polyimide in Fig. 61) are difference spectra between the material before and after laser treatment. An increase of surface species corresponds to an increase of the absorption and therefore to negative peaks (going down) and peak areas. The peaks that are going up denote a decreasing band, due to the reduced absorption of disappearing species. For the analysis of the laser-induced decomposition mechanism of Kapton, several relevant vibrational frequencies are chosen which are important for the decomposition mechanism. A detailed assignment of all bands can be found in the literature [290–295]. The assignment of the polyimide bands is mainly based on model compounds; see, e.g., the thorough study by Ishida et al. [291] which could also be used for many products identified in this study.

2.3.1.2
Results

Reference Spectra and Assignment of Bands. The reference spectrum (Fig. 61) of Kapton obtained with the SiC sampling method agrees well with previously published data. Several bands in the reference spectrum (Fig. 61) and also in the corresponding scheme of the synthesis of Kapton (Scheme 12) are marked with letters (A to G). These bands are used in the discussion about the decomposition mechanism.

In the high wavenumber regions two bands are prominent, a sharp band at 3490 cm^{-1} (denoted A in Fig. 61) and a broad absorption at 3080 cm^{-1} (denoted B). The first band is assigned to the N–H stretching vibration of polymer chain end groups and NH groups of polyamic acid, due to an incomplete imidization during the synthesis. Band B belongs to the C–H stretching vibrations of the aromatic rings. The broad band around 1740 cm^{-1} (denoted C) is due the C=O stretching vibration of the imide ring. The sharp peaks at 1600 and 1500 cm^{-1} (band D) are assigned to the stretching vibrations of the aromatic systems, i.e., the 1,2,4,5-tetra-substituted and the 1,4-disubstituted rings. The broad absorption at 1390 cm^{-1} (band E) is assigned to the C–N stretching in the imide ring while the band at 1260 cm^{-1} (band F) is assigned to the asymmetric C_{ar}–O–C_{ar} stretching vibration of the diaryl ether group. The sharp band at 725 cm^{-1} (band G) corresponds to the out-of-plane bending vibration of the imide ring.

Laser Ablation of Kapton with 308-nm Irradiation. The laser ablation of Kapton at 308 nm has been studied previously in detail [276]. An ablation threshold of 40 mJ cm^{-2} has been determined for the same Kapton samples and the same experimental setup as in this study. The term ablation threshold is defined in this study as the laser fluence necessary to remove polymer material in the irradiated area, measured by a profilometer. For this study we used laser fluences below, at, and above the threshold of ablation of Kapton films.

Irradiation of the SiC Substrate. The stability of the SiC disks under laser ablation conditions was tested first. A spectrum of a SiC disk was used as background. The difference spectra of the SiC disk after irradiation with the highest fluence applied in this study (155 mJ cm^{-2}) were measured after various pulse numbers (50, 100, 500, and 5,000) and at the highest repetition rate (10 Hz). No changes in the spectra were observed, suggesting that SiC is stable under the applied conditions.

Kapton Irradiated with 80 mJ cm^{-2}. For the first experiments a fluence (80 mJ cm^{-2}) well above the threshold fluence of ablation (40 mJ cm^{-2}) was applied. To test the general feasibility of our approach a variation of the general procedure was used. The sample used for the reference spectrum was irradiated with 50, 150, 500, and 5,000 pulses at a repetition rate of 10 Hz.

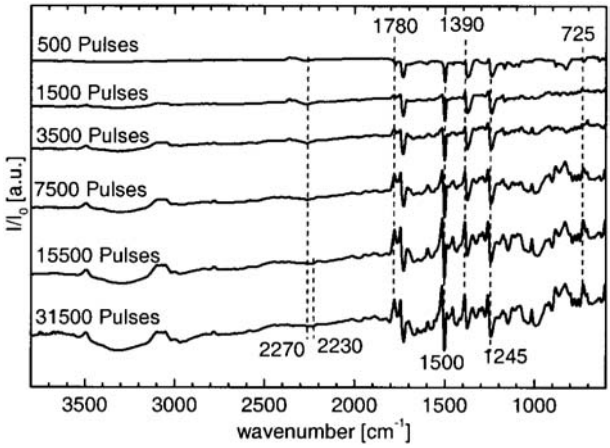

Fig. 62 DRIFT difference spectra of Kapton obtained with an accumulation of 1,024 scans. The untreated SiC-supported Kapton was used as background. The sample was irradiated at 10 Hz with 40 mJ cm^{-2} with various pulse numbers. The relevant bands are marked with their exact location. REPRINTED WITH PERMISSION OF [Ref. 135], COPYRIGHT (2000) American Chemical Society

After each irradiation a DRIFT spectrum was measured. As expected, all bands are decreasing in intensity, indicating a continuous decomposition of the polymer. This shows that it is possible to follow the decomposition of polyimide using difference spectra up to several thousands of pulses, with no artifacts, e.g., carbonization, interfering with the measurements.

In the following experiments the SiC disk with abraded Kapton was used as background spectrum. The disk was irradiated with various pulse numbers and spectra were taken after each irradiation.

Irradiation at the Threshold of Ablation: 40 mJ cm^{-2}. To identify possible intermediates of the laser-induced decomposition of Kapton the threshold fluence of ablation was chosen. At this fluence ablation is just starting and changes in the material should be slow, giving the best chance to monitor intermediates.

The freshly prepared sample was irradiated with various pulse numbers (500, 1,500, 3,500, 7,500, 15,500, and 31,500) at a repetition rate of 10 Hz. After each irradiation the DRIFT spectra were measured. The spectra are shown in Fig. 62. After 500 pulses several bands are growing in intensity, i.e., 1730, 1500, 1375, 1245, 830, and 725 cm^{-1}, whereas only two bands are decreasing, i.e., 1390 and 1260 cm^{-1}.

An absorption increase is also observed over the whole mid-IR region, denoted by the rising baseline. This increase of the baseline has already been reported previously and was assigned to an accumulation of carbonaceous species in and surrounding the irradiated area [287, 294]. With increasing pulse numbers only few bands are increasing further (1730, 1500, 1375, and

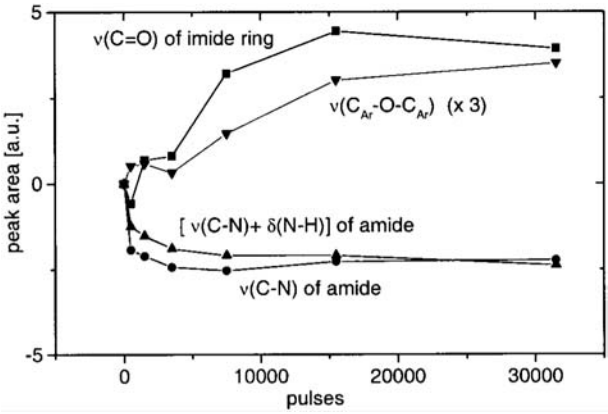

Fig. 63 Changes of the peak areas as a function of the pulse number for the following bands: at 1780 cm^{-1} the C=O stretching vibration of the imide ring (■); at 1375 cm^{-1} the C–N stretching vibration of the amide (●); at 1500 cm^{-1} the combination band C–N stretching vibration and N–H deformation of the amide (▲); and at 1260 cm^{-1} the C_{ar}–O–C_{ar} stretching vibration (▼). Positive values correspond to decreasing absorption, and vice versa. REPRINTED WITH PERMISSION OF [Ref. 135], COPYRIGHT (2000) American Chemical Society

1245 cm^{-1}) but additionally bands are decreasing now (1780, 1745, 1515, 1390, 1260, 830, 725 cm^{-1}). To analyze the changes in the DRIFT spectra in more detail a semi-quantitative analysis was performed. The peak areas of several bands are plotted versus the pulse numbers, as shown in Figs. 63 and 64.

The two bands at 1780 and 1745 cm^{-1} reveal a very similar behavior. Both are decreasing in a very similar fashion (as shown for the 1780 cm^{-1} band in Fig. 63, ■ as symbol). Therefore we assign them to the doublet of the C=O stretching vibration of the imide ring, whereas the increasing band at 1730 cm^{-1} is assigned to a carbonyl functional group of an open ring species. This could be either the amide structure (called also amide I band) and/or the aryl–C=O structure (both are shown in Scheme 13). The changes of the peak areas of the C–N stretching vibration of the imide ring at 1390 cm^{-1} and of the out-of-plane bending of the imide ring at 725 cm^{-1} are very similar to the one shown for the imide carbonyl peak (shown in Fig. 63).

The increasing bands at 1730, 1500, 1375, and 1245 cm^{-1} follow very similar trends. The band at 1500 cm^{-1} is assigned to the combination band of the N–H deformation and the C–N stretching vibration (also named amide II band, shown as ▲ in Fig. 63). The band at 1375 cm^{-1} is assigned to the C–N stretching band of an amide (also named amide III band, shown as ● in Fig. 63), while the band at 1245 cm^{-1} is assigned to the C_{ar}–O stretching vibration (see Scheme 13) from the decomposed diaryl ether group.

Amide bands are not present in cyclic imides, but are typical for the intermediate of the Kapton synthesis, the polyamic acid. All of the above mentioned increasing bands reveal changes of the peak areas very similar to the

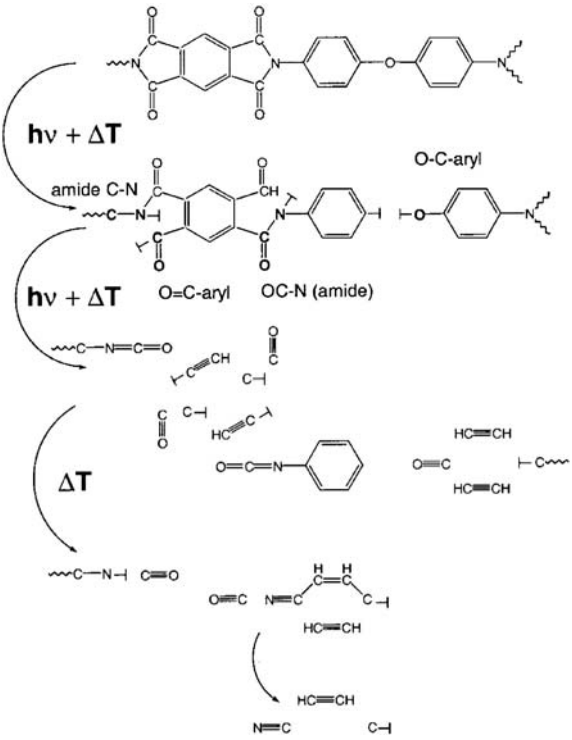

Scheme 13 Suggested decomposition scheme. Several bands are marked (*bold*) and assigned. ⊥ indicates a broken bond; information on the character (radical, ionic, terminated) is not available from the present experiments. REPRINTED WITH PERMISSION OF [Ref. 135], COPYRIGHT (2000) American Chemical Society

two representations shown in Fig. 63. The decomposition of the imide system is characterized by the decrease of the carbonyl bands, of the C–N stretching vibration, and of the out-of-plane bending vibration of the imide system.

Upon further irradiation other increasing bands are detected. A broad absorption around 3320 cm^{-1} with a shoulder at higher wavenumbers is developed. This is assigned to the C–H stretching vibration of acetylenes and to the N–H stretching vibration of amides, which are typically between 3200–3400 cm^{-1}. All of these bands show, as discussed above, a similar behavior and reveal more or less the exact mirror image of the previously described decreasing bands.

Three bands distinguish the aromatic system: the broad C–H stretching band around 3080 cm^{-1} (a magnification is shown in Fig. 65 a, and ● in Fig. 64) and the ring stretching vibrations at 1600 and 1515 cm^{-1} (▲ in Fig. 64). All of these bands decrease upon laser irradiation, as shown in Fig. 64, revealing the decomposition of the aromatic systems. Another sig-

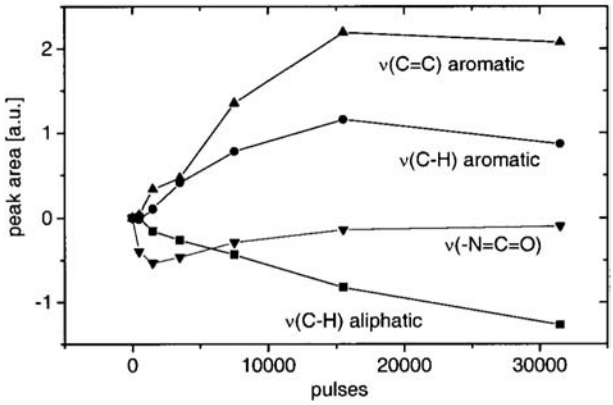

Fig. 64 Changes of the peak areas as a function of the pulse number for the following bands: at 2950 cm^{-1} the C–H stretching vibration of aliphatic hydrocarbons (■); at 3080 cm^{-1} the C–H stretching vibration of aromatic hydrocarbons (●); at 1515 cm^{-1} the aromatic ring stretching vibration (▲); at 2270 cm^{-1} the –N=C=O stretching vibration (▼). REPRINTED WITH PERMISSION OF [Ref. 135], COPYRIGHT (2000) American Chemical Society

nificant band in the IR spectra of Kapton is the C_{ar}–O–C_{ar} stretching vibration at 1260 cm^{-1} of the aromatic ether. The decrease of the peak area suggests that this group is also one of the primary decomposition sites.

Growing bands are detected around 2950 cm^{-1}, and can be assigned to C–H stretching vibrations of aliphatic groups (magnification shown in Fig. 65). There are no aliphatic C–H groups present in Kapton; therefore we can assign these groups to reaction products. The increase of the peak area is different from the previously described changes. The peak area increases nearly linearly with laser pulses, as shown in Fig. 64 (■ as symbol). Further identification of the aliphatic chains is very difficult because of the complex band structure in the region where e.g. C–C (1260–700 cm^{-1}), C=C (1680–1620 cm^{-1}), C–O (1270–1060 cm^{-1}), and C–N bonds (1420–1400 cm^{-1}) are absorbing. A very interesting region in the mid-IR spectra is between 2300 and 2100 cm^{-1}. There are only a few groups absorbing in this region. Most of these groups are characterized by strong and sharp absorption. In Fig. 65b magnification of this region is shown. The broad absorption around 2350 cm^{-1} is the typical doublet of gas-phase CO_2. Carbon dioxide is a very IR-active molecule and slight changes in the concentration, e.g., due to variations in the compressed air purge or slightly different purge times, will cause continuous changes in the intensity of the CO_2 band. Around 2270 cm^{-1} a growing band can be observed. With increasing pulse numbers the band starts to decrease (shown with▼ as symbol in Fig. 64), while new bands at 2255 and 2230 cm^{-1} are getting more pronounced with increasing pulse numbers. The peak at 2270 cm^{-1} can be assigned to the asymmetric –N=C=O stretching vibration of an isocyanate species and the two bands at the low-

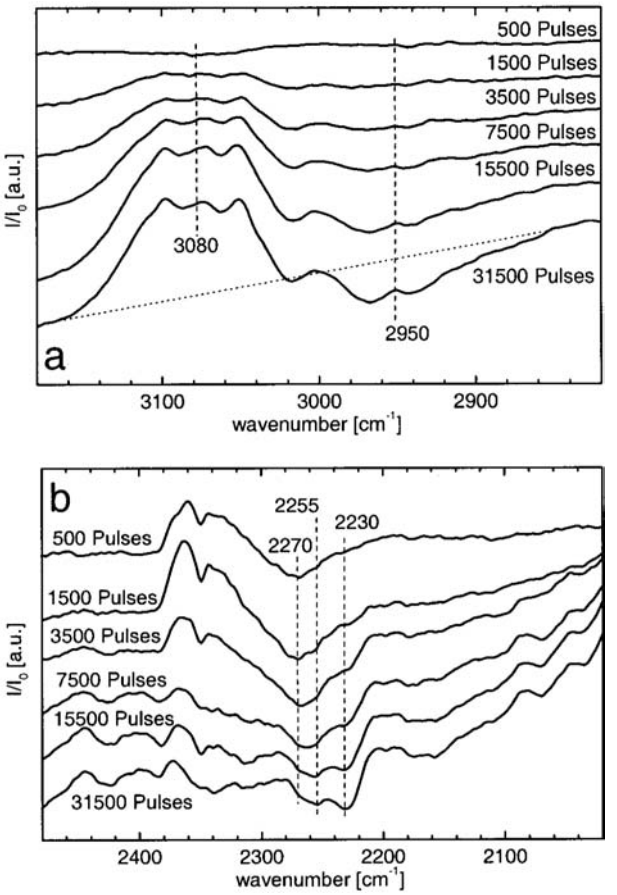

Fig. 65 Magnification of two regions in the DRIFT spectra of Kapton presented in Fig. 62. **a** Region of C–H stretching vibrations: at 3080 cm^{-1} aromatic hydrocarbons; at 2950 cm^{-1} aliphatic hydrocarbons. The baseline applied for the peak area calculation is shown as a *dotted line* in the spectrum for 31,500 pulses. **b** Region of conjugated double bonds and triple bonds: at 2270 cm^{-1} the –N=C=O stretching vibration; at 2255 cm^{-1} the –C≡C– stretching vibration; and at 2230 cm^{-1} the –C≡N stretching vibration. Around 2350 cm^{-1} the typical doublet of gas-phase CO_2 is present. REPRINTED WITH PERMISSION OF [Ref. 135], COPYRIGHT (2000) American Chemical Society

er wavenumbers to the stretching vibration of alkynes (–C≡C–) and nitrile (–C≡N) groups.

Irradiation Above the Threshold of Ablation. The applied fluences were increased to a level well above the threshold of ablation to test whether the previously described changes in the DRIFT spectra are really due to ablation.

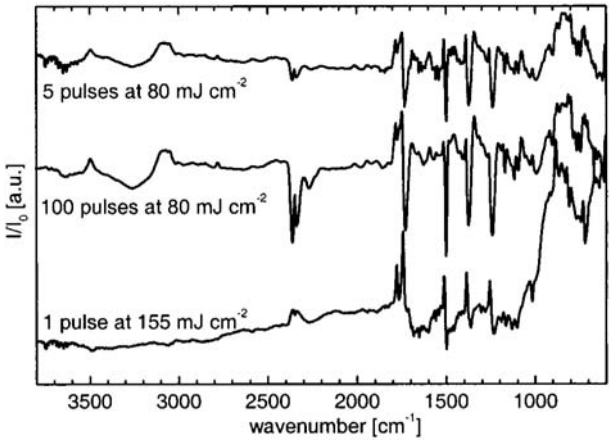

Fig. 66 DRIFT difference spectra of Kapton irradiated with fluences above the threshold of ablation (80 and 155 mJ cm^{-2}). REPRINTED WITH PERMISSION OF [Ref. 135], COPYRIGHT (2000) American Chemical Society

80 mJ cm^{-2}. The freshly prepared sample was irradiated with 1, 2, 5, 10, 20, 50, and 100 pulses at a repetition rate of 10 Hz. In Fig. 66 the spectra recorded after 5 and 100 pulses are shown. After the first pulse several bands are growing in intensity (going down: at 1730, 1500, 1370, 1245 cm^{-1}) while others are decreasing (1780, 1745, 1600, 1515, 1390, 830, and 725 cm^{-1}). All bands assigned to the imide ring are decreasing (1780, 1745, 1390, and 725 cm^{-1}) whereas the bands assigned to the amide and aryl carbonyl groups are increasing. After 100 pulses the bands assigned to the isocyanate and nitrile groups (2270 and 2230 cm^{-1}) are clearly present. The bands at lower wavenumbers (< 1100 cm^{-1}) are more difficult to observe, due to the steeply increasing background. This is most probably due to accumulation of carbon species in the irradiated area [287, 294]. The changes in the spectra are very similar to the data described previously for irradiation with 40 mJ cm^{-2}. Only 100 pulses are needed to reach a similar state of decomposition as compared to the 31,500 pulses at 40 mJ cm^{-2}. This shows clearly that for the present flux, we are observing the ablative decomposition of Kapton, for which a sharp threshold of ablation is observed.

To study the influence of the laser repetition rate on the decomposition of Kapton, a SiC disk with abraded Kapton was irradiated with 80 mJ cm^{-2} at a repetition rate of 0.086 Hz. This is well below the frequency where accumulative heating from the laser is important [296]. The spectra match very well the spectra from the experiments using 10 Hz. The only difference is an enhanced absorption of the band at 2270 cm^{-1}, suggesting that in the experiments with higher repetition rates additional thermal decomposition of the isocyanate group takes place.

155 mJ cm^{-2}. At still higher fluences (155 mJ cm^{-2}) very pronounced changes in the IR spectra are detected even after 1 pulse (shown in Fig. 66). Below 1100 cm^{-1} the background is rising extremely steeply, thus not allowing an analysis of bands in this region. This is, as discussed above, most probably due to carbonization of the irradiated surface, which leads to an overall increase of the IR absorption in this region [287, 294]. This is supported by the black optical appearance of the SiC disk in the irradiated area. With increasing pulse numbers the shift of the baseline is even more pronounced, therefore only the spectrum after one pulse can be analyzed. Similar features as for the lower fluence irradiations are observed. The bands of the imide system, aromatic ring, and the diaryl ether group are decreasing, while the bands connected with the amide and the isocyanate group are increasing. One observed difference is the absence of the increasing band at 1730 cm^{-1}. This band was assigned to the stretching vibration of a carbonyl group attached to an aromatic system. In Fig. 60b the SEM picture of a SiC disk after irradiation with 20 pulses at 155 mJ cm^{-2} is shown. The difference between the irradiated and unirradiated areas is clearly visible (top right area is not irradiated). In the irradiated area the Kapton scrapes (see Fig. 60a) are not observed any more, although the IR spectra still suggest the presence of Kapton.

Products of Laser Ablation. The volatile products of laser ablation of a Kapton film were measured with quadrupole mass spectrometry and with emission spectroscopy using the same Kapton samples and experimental setup as for the DRIFT measurements. In the mass spectra C_2H_2, HCN, CO, CO_2, C_4H_2, and C_6H_2 could be detected, while the emission spectra showed the C_2 and CN emission lines. The chemical species in the mass spectra were assigned according to the Refs [61] and [162], which used gas-phase FTIR and GC–MS for the assignment of the decomposition products.

Irradiation Below the Threshold of Ablation: with 10 mJ cm^{-2}. A Kapton sample was irradiated at 1 Hz repetition rate (to exclude thermal effects) to test whether even below the threshold of ablation any signs of degradation can be observed. After 7,500 pulses small changes in the spectrum are detected. Our mass spectrometry setup is not sensitive enough to detect this small amount of ablation product, but in studies using a quartz microbalance (e.g., [81]) a reduction of the polymer mass at this low fluence was detected. Therefore it can be assumed that (if at all) only portions of the ablation products are trapped within the polymer. The spectra match the previously described changes after irradiation with higher fluences and much lower pulse numbers.

2.3.1.3 Discussion

Laser irradiation with a fluence equal to the threshold fluence of ablation results in a slow decomposition of the polymer. The changes in the peak areas of several selected bands suggest a decomposition pathway as follows.

The bands corresponding to the imide system (1780, 1745, 1390, 725 cm^{-1}) are decreasing. The changes in the peak area (shown in Fig. 63 for the C=O band) are very similar for all of these bands. Corresponding to the decrease of these bands is an increase of the bands at 1730, 1500, and 1375 cm^{-1} (shown in Fig. 63). These bands are assigned to species resulting from the breakage of the –N–(CO)– bond in the imide system. The resulting structure is an amide system, with a C–N bond (1375 cm^{-1}), an aryl –C=O (1730 cm^{-1}), and an amide –(CO)–N– group (1780 cm^{-1}), shown in Scheme 13. The band at 1260 cm^{-1}, assigned to the C_{ar}–O–C_{ar} group, decreases in a very similar manner (shown in Fig. 63) to the bands assigned to the imide system. Corresponding to this decrease is an increase of a band at 1245 cm^{-1}, assigned to a C_{ar}–O stretching vibration. Therefore the following reaction pathway has been suggested (shown in Scheme 13). The imide system breaks between the imide N and carbonyl carbon with a simultaneous decomposition of the diaryl ether group, either in the same repetition unit or at some other place along the polymer chain. Upon further laser irradiation a constant concentration of these species is maintained, suggesting that creation and decomposition of these groups reach a quasi-steady state.

This first step is probably photon induced, but we cannot rule out that the temperature rise, which will take place during irradiation, is also important. A temperature rise can also increase the efficiency of photochemical reactions [297]. It would be very difficult to calculate a temperature rise, because it is closely related to the absorption depth of the laser irradiation and depends on the lifetime and absorption of reaction intermediates. The lifetime is strongly dependent on the complexity of the molecules. The more complex the molecule, the longer the lifetime. In the condensed phase, as in the case of PI, such intermediates can last for time periods of the order of nanoseconds (laser pulse τ~20 ns). The importance of this to the UV laser decomposition of PI lies in the UV absorption characteristics of free-radical intermediates. Their strongly delocalized electrons will result in a more intense absorption of the incoming radiation than that of PI itself. However, their contribution to the absorption will be determined by their stationary concentration, i.e., their rate of formation less their rate of disappearance. We do not have these data; therefore we cannot calculate the temperature rise.

In the next steps which could also be thermally induced, the aromatic systems (3080, 1600, and 1515 cm^{-1}) decompose, while acetylenes (3320 and 2255 cm^{-1}) are formed. At the same time isocyanate species are detected (2270 cm^{-1}), which decompose upon further irradiation, or by reaction with other species (e.g., water to form amines). This decomposition is at least partially thermal, because at low repetition rates (0.086 Hz as compared to 10 Hz) the decrease of the isocyanate band is less pronounced. In the following steps nitrile (2230 cm^{-1}) and aliphatic hydrocarbons (CH) are formed (2950 cm^{-1}), as shown in Fig. 65. The increase of the peak area of the aliphatic CH compounds is slower and nearly linear with pulse numbers, suggesting that these species are formed continuously, probably through combination reactions. The volatile products detected by mass spectrometry and

emission spectra are compatible with the mechanism described in Scheme 13. The laser fluence or the corresponding temperature increase is most probably high enough to eliminate the CO group simultaneously from the amide system.

To clarify whether the overall decomposition reaction is purely thermal, additional experiments were performed. First we compared our data and reference mass spectra with mass spectra obtained during pyrolysis of Kapton [298, 299]. The main products from pyrolysis are derived from a single benzene ring such as C_6H_5CN, C_6H_5OH, $C_6H_5NH_2$, $C_6H_4(CN)_2$, p-aminophenol, and C_6H_5NC. Benzene and its derivatives are only minor products during laser ablation. CN, also seen in the emission spectra, and HCN are important products of laser ablation, while they are not detected during pyrolysis. During pyrolysis neither small (C_1, C_2, or C_3) fragments nor carbon clusters ($>C_{38}$) are seen while they are abundant during UV laser ablation. Then additional DRIFT experiments were performed: DRIFT spectra were recorded at different temperatures in an air stream. The spectra were analyzed analogous to the laser experiments. The difference spectra only showed a continuous decomposition of the complete polymer without pronounced intermediates. This is completely different to the laser experiments and clearly suggests that the laser photons and therefore the photochemical step play an important role. The temperature DRIFT experiments could be used to develop a decomposition model and to calculate even kinetic parameters of the polymer decomposition at localized sites (functional groups) in the polymers. The SEM pictures (Fig. 60b) show the SiC disk after irradiation with 20 pulses at 155 mJ cm^{-2}. The irradiated area is clearly visible (lower left area). No distinct polymer scrapes are visible, while the IR spectra still reveal the typical bands of Kapton. A possible explanation could be the degradation of the polymer to lower molecular weight species, which soften/flow to build a homogenous layer on the SiC disk.

Upon irradiation with fluences below the threshold of ablation (10 mJ cm^{-2}) changes in the DRIFT spectra are observed. These in principle unexpected changes could be due either to imperfections in the laser beam profile, resulting in partial higher fluences, or to a slow photolytic decomposition of Kapton not resulting in ablation of the polymer. The latter could also account for the difference in the threshold fluences measured by mass-sensitive techniques (QMB) and surface morphology-sensitive techniques (AFM). Gaseous decomposition products, such as CO, CO_2, HCN, and C_2H_2, could be ejected without changing the surface morphology. This would be detected by QMB, which indeed suggests a lower ablation threshold than AFM.

2.3.1.4 Summary

Silicon carbide (SiC) is a suitable substrate for studies of laser-induced processes in polymers. The SiC substrate is stable under the applied conditions, i.e., fluences up to 155 mJ cm^{-2}, and well-resolved DRIFT spectra of poly-

mers can be obtained. The surface-sensitive DRIFT technique allows detection of reaction intermediates and products of the laser treated *solid* polymer. The first step of the UV laser (308 nm)-induced decomposition of the polyimide (Kapton) is the simultaneous breakage of the nitrogen–(carbonyl carbon) bond of the imide system and of the diaryl ether group. The resulting species, belonging to the amide system, and aromatic carbonyl groups are detected. Decomposition of the aromatic system is also detected, and an isocyanate-rich surface is formed. In the next steps aliphatic hydrocarbons, nitriles, and alkynes are created. Volatile species compatible with this decomposition mechanism (CO, CO_2, HCN, and C_2H_2) are identified by mass spectrometry. Even below the threshold of ablation a decomposition of the polymer is detected. This could be due to either inhomogeneities in the beam profile or real decomposition of the polymer at this fluence. The latter could also explain the differences in the threshold fluence measured with QMB and AFM. The QMB would detect the removal of gaseous species which could happen without structuring of the polymer.

2.3.2
DRIFT of Kapton After Thermal Decomposition

2.3.2.1
Introduction

In the previous chapter polyimide was analyzed after UV laser irradiation using DRIFT spectroscopy. Various intermediates and products of the laser-induced decomposition could be identified. Experiments with the same material were performed to test whether it is possible to distinguish between UV laser-induced decomposition and thermally induced decomposition, i.e., pyrolysis.

Pyrolysis of polyimide is used for the preparation of carbon materials, i.e., high-quality graphite films. Complete pyrolysis and carbonization of polyimide foils has the advantage that the films are carbonized without any change in shape and that it is possible to convert the carbonized material into graphite [300]. Pyrolysis and thermolysis of polymers are usually studied using thermal analysis methods, such as thermogravimetry, thermomechanical analysis, differential thermal analysis (DTA), and differential scanning calorimetry. These methods can be used to characterize bulk polymer properties, but no information regarding specific chemical functionalities is provided. Volatile decomposition products evolve during heating of polymeric samples, which can be identified by coupling a mass analyzer or IR spectroscopy to the purge of the thermal analysis instruments. However, gas compositions do not provide information about changes in polymer structure, and are not helpful at all when polymers undergo structural changes without evident volatile products. IR spectroscopy provides a substantial quantity of information about the molecular structures of materials. Unfortunately, IR transmission measurements are not suitable for studies of sur-

face species, because the infrared beam passes through the entire sample. The absorption bands of the bulk material largely cover the bands of the surface species.

In contrast, diffuse reflectance infrared Fourier-transform (DRIFT) spectroscopy allows one to monitor solid-state structural changes. It is specifically designed to study powder samples, and is well known for its high sensitivity. A wide variety of materials can be analyzed using DRIFT spectroscopy. Some materials can be analyzed neat, without any sample preparation, but polymers have to be diluted normally by embedding them into a matrix.

The quantitative interpretation of diffuse reflectance spectra is based on the theory developed by Kubelka and Munk [289, 301, 302] and extended by Kortum and coworkers [303–305] about the scattering of light in samples diluted in nonabsorbing matrices. In the developed model, mathematical simplification is achieved by assuming that the sample is comprised of a single absorbing material contained in a nonabsorbing matrix. Typically, nonabsorbing compounds such as KCl, KBr or diamond powders are employed as diluent. The Kubelka-Munk model predicts a linearity with a zero y-intercept between concentration and IR absorption.

The aim of this work is to investigate the reaction scheme of the thermally induced decomposition of Kapton in air and compare it to the UV laser-induced decomposition. This should help to decide whether the laser-induced decomposition (ablation) of Kapton is comparable to pyrolysis. Using DRIFT spectroscopy the changes in the concentration of different functional groups of the polymer are monitored during the thermal decomposition process. This information is used to develop a kinetic reaction scheme and to calculate kinetic parameters.

2.3.2.2 Experimental

The experimental setup consists of a gas dosing system and the DRIFT spectroscopy apparatus. For the pyrolysis experiments KBr was selected as matrix, different to the laser-induced decomposition experiments [141], where SiC was used. KBr was chosen because the emissivity did not increase drastically, as in the case of SiC, where it interfered with the measurements. The Kapton–KBr mixtures are placed in the sample holder of the DRIFT cell and packed using a pressure of 1 MPa as described elsewhere [288, 306]. The sample is heated in an inert gas atmosphere to the desired temperature using a heating rate of 10 K min^{-1}. The spectrum of the Kapton–KBr mixture at a given temperature is collected and used as background spectrum. The following experiments were carried out.

1. Thermal decomposition in inert gas. The sample is heated to 841 K and flushed with 50 ml_N min^{-1} argon.
2. Thermal decomposition in air. The sample is heated in nitrogen to the desired temperature, then the feed gas is changed to air (compressed air). The

applied total flow is 50 $ml_N\ min^{-1}$. The experiment is carried out at several temperatures, i.e., 727, 755, 783, 794, 812, and 841 K.

3. Influence of the oxygen concentration on the pyrolysis. The sample is heated in nitrogen to the desired temperature, then the feed gas is changed to a mix consisting of 25% compressed air and 75% nitrogen. The applied total flow is 50 $ml_N\ min^{-1}$. The experiment is repeated at 772 and 823 K.
4. Influence of the total flow on the thermal decomposition in air. The Kapton–KBr mixture is heated in nitrogen to 841 K, then the feed gas is changed to air. The applied total flow is 12.5 $ml_N\ min^{-1}$, which is only 1/4 of the flow in the other experiments.

2.3.2.3 Results and Discussion

Qualitative and Quantitative Analysis of the DRIFT Spectra. DRIFT spectra are usually presented in Kubelka–Munk units. DRIFT spectra with small baseline errors can be obtained when measurements are made at ambient temperature. However, if measurements are performed at higher temperatures, IR radiation emitted from the heated sample can affect the collected spectra, especially if MCT detectors are employed. This is even more pronounced when the refractivity of the sample changes with time. The baseline artifacts are added to the collected spectra.

To remove these artifacts the procedure proposed by White [307, 308] was used. Each collected spectrum is referred to a suitable background spectrum. The collected reflectance spectra are converted to apparent absorbance format, the baseline is adjusted, and the spectra reconverted to reflectance. The corrected reflectance spectra are then used to evaluate the concentration of the desired compounds quantitatively. The use of relative reflectance units (I/I_0) to present the spectra is more appropriate, due to the change of reflectance of the sample during decomposition. An increase of surface species corresponds to an increase of absorption and therefore to negative peaks (going down) and peak areas. The peaks that are going up denote a decreasing band, due to the reduced absorption of disappearing species.

In Fig. 66, a spectrum of Kapton in KBr with KBr as background is shown. The broad band around 1740 cm^{-1} is due to the C=O stretching vibration (see band B). The sharp peak at 1600 cm^{-1} and the band at 1500 cm^{-1} (see band C) are assigned to the stretching vibration of both aromatic rings (1,2,4,5-tetrasubstituited and 1,4-disubstituited). The broad absorption at 1390 cm^{-1} (see band D in Fig. 67) and at 1250 cm^{-1} (see band E in Fig. 67) are assigned to the C–N stretching vibration in the imide ring and to the asymmetric C_{Ar}–O–C_{Ar} stretching vibration of the aryl ether, respectively. C_{Ar} indicates the carbon atom of the aromatic ring. The C–H in-plane bending vibrations of the aromatic rings are located between 1070 and 1015 cm^{-1}.

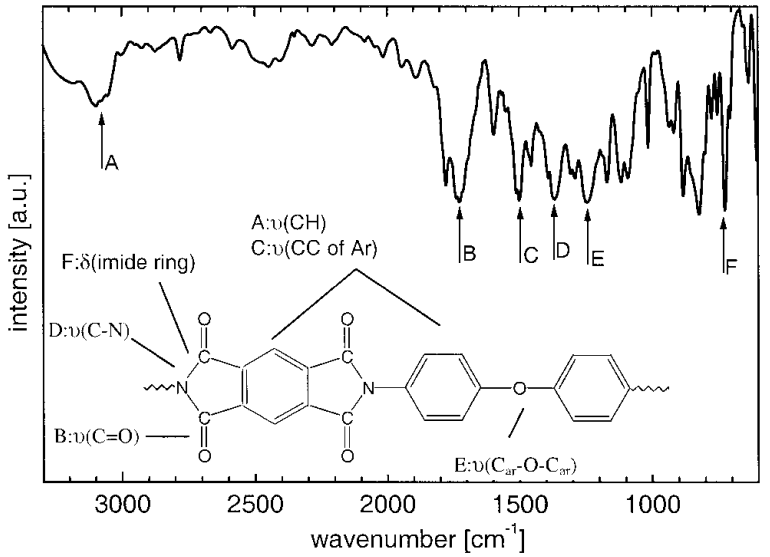

Fig. 67 DRIFT spectrum of Kapton; 1,024 scans with a resolution of 4 cm^{-1} using KBr as the background and matrix. The following bands are assigned: (A) 3060 cm^{-1}: C–H stretching of hydrogen at the aromatic rings; (B) 1740 cm^{-1}: C=O stretching; (C) 1500 cm^{-1}: aromatic ring stretching; (D) 1390 cm^{-1}: C–N stretching of the imide rings; (E)1260 cm^{-1}: C_{ar}–O–C_{ar} stretching of aryl ether; (F) 725 cm^{-1}: out-of-plane bending of the imide ring. The assigned vibrational bands are marked in the inserted molecular scheme. Applied Spectroscopy by T. Lippert [Ref. 281], COPYRIGHT (2001) by SOC FOR APPLIED SPECTROSCOPY. Reproduced with permission of SOC FOR APPLIED SPECTROSCOPY in the format Textbook via Copyright Clearance Center

The broad absorption around 880 cm^{-1} consists of several contributions, the most important being the C–H out-of-plane bending vibrations of aromatic rings. The sharp band at 725 cm^{-1} (see band F) is assigned to the out-of-plane bending vibration of the imide ring. At higher wavenumbers a broad absorption around 3060 cm^{-1} (see band A) is assigned to the C_{Ar}–H stretching vibrations of hydrogen located at the aromatic ring.

An exhaustive investigation and discussion of the band assignments can be found in the literature [290–295, 309–315].

Thermal Decomposition in Inert Gas. An experiment was carried out to investigate the thermal decomposition of Kapton. The sample is heated to 841 K and kept at this temperature in argon. After 12 h only a small reduction of the Kapton bands is observed (data not shown), indicating that Kapton in a KBr matrix is stable up to this temperature. It was not possible to reach higher temperatures with the applied experimental setup. Therefore, it was impossible to study the carbonization decomposition of Kapton in an inert gas atmosphere at very high temperatures.

White and coworkers [316] reported an influence of alkali halides on the thermal decomposition of polymers (PMMA and PHEMA). In case of Kapton

no influence of the KBr matrix on the decomposition process could be identified during TGA (data not shown). This result is consistent with data reported in the literature about the resistivity of polyimides towards chemical agents. Concentrated H_2SO_4 or fuming HNO_3 are the only solvents [317]. Therefore, KBr can be applied as matrix for the thermal decomposition experiments.

Thermal Decomposition in Air. In Fig. 68, DRIFT spectra of the pyrolysis of Kapton in air at 783 K are shown. These are difference spectra, with Kapton in KBr as background at the given temperature. In all further experiments the difference spectra are used. As expected, with increasing time all bands are going up indicating a continuous decomposition of the polymer. New bands are formed around 2220 cm^{-1} (see Fig. 68, bottom) and with increasing time at 2240 cm^{-1}. These groups are intermediates, which decompose completely at the end of the process, shown with ● in Fig. 69 and by the spectrum named *Residual* (see below) in Fig. 68. The high-frequency band can be assigned to the stretching vibration of alkynes (–C≡C–), while the band at 2220 cm^{-1} is assigned to the stretching vibration of conjugated nitriles (–C≡N). The red shift of its maximum, compared to reference data [293], suggests that alkyne groups in a central position (–C–C≡C–C–) might also be involved. Nitriles and alkynes were already identified as intermediates during the UV laser-induced decomposition of Kapton [141]. It is also noteworthy that most reference data are recorded at room temperature, while our spectra are recorded at high temperatures. It is well known that IR bands can shift with temperature changes. This shift is dependent on the vibrational mode, typically red shifts of 3 cm^{-1}/100 K are observed, but sometimes only broadening or even blue shifts are detected [255, 257, 318]. This effect is a manifestation of the anharmonicity of a given vibrational band and the volume changes as a function of temperature. Therefore, it is quite difficult to assign new bands at elevated temperatures.

The spectrum (in Fig. 68) marked with *Residual* was collected at the end of the process (15 h), and pure KBr was used as background. In this spectrum Kapton signals cannot be observed, suggesting a complete pyrolysis of the polymer. Noteworthy is the absence of carbon–carbon bands, indicating a total pyrolysis of the investigated compound. The band at 1640 cm^{-1} reveals a decrease of the water content, typically present in KBr. The two bands located at 2160 and 1400 cm^{-1} can be assigned to CO in a KBr matrix [319, 320] and to cyano groups bound to an aliphatic group (–CH_2–CN) [292]. Black residue particles were observed optically after the pyrolysis experiments. These particles consist mainly of carbon, as suggested by energy dispersive X-ray (EDX) analysis. This proves that a weak carbonization process is also active.

The peak areas of all relevant bands are evaluated as a function of the time to analyze the kinetics of the pyrolysis process. In Fig. 69 the normalized changes of peak areas of several bands are shown for a temperature of 812 K. Four different behaviors can be identified. The bands assigned to the imide system (bands D and F in Fig. 67) decrease rapidly (see▲ in Fig. 69; the out-of-plane bending vibration of the imide ring is shown). The bands

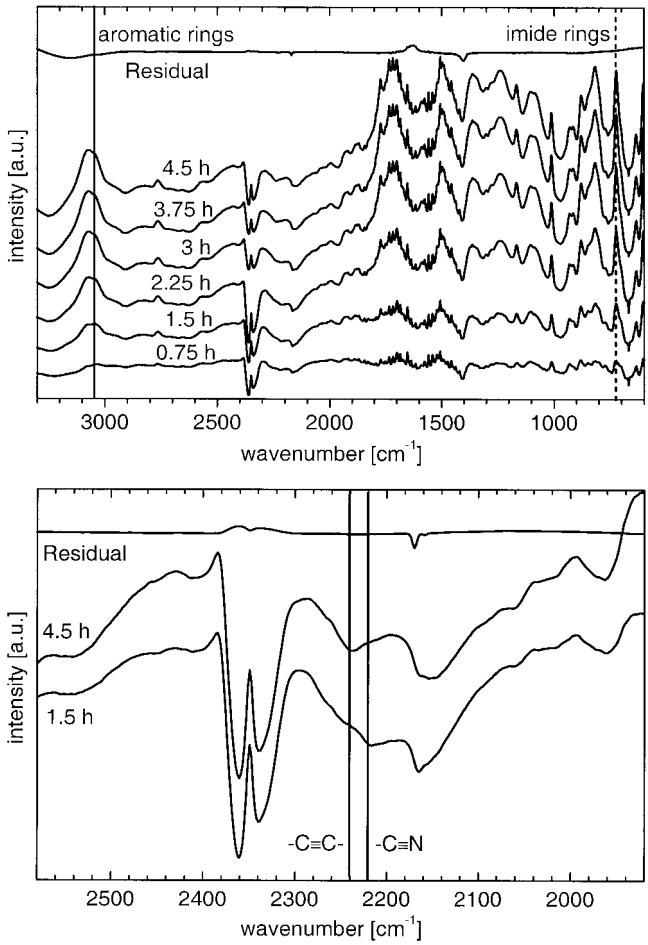

Fig. 68 (*Top*) DRIFT difference spectra of Kapton obtained with 1,024 scans. The untreated KBr–Kapton mixture was used as the background. The sample was heated to 812 K in nitrogen and then kept at this temperature in air with a total flow of 50 mL_N min^{-1}. The spectrum marked as "Residual" was collected after completion of the reaction (15 h) and measured with KBr as the background. The marked bands correspond to the C_{ar}–H stretching vibration of the aromatic rings (3060 cm^{-1}) and to the out-of-plane bending vibration of the imide ring (725 cm^{-1}). (*Bottom*) Magnification of the 1920–2580 cm^{-1} region. The marked bands are the –C≡C– stretching (2240 cm^{-1}) and the –C≡N stretching (2220 cm^{-1}) vibrations. Applied Spectroscopy by T. Lippert [Ref. 281], COPYRIGHT (2001) by SOC FOR APPLIED SPECTROSCOPY. Reproduced with permission of SOC FOR APPLIED SPECTROSCOPY in the format Textbook via Copyright Clearance Center

related to the aromatic rings (A, C, and E in Fig. 67) reveal a two-step curve (see▼ in Fig. 69), with an initial slow decomposition followed by a more rapid decomposition. The bands assigned to the carbonyl stretching vibration of the amide and imide (B in Fig. 67) groups, which are marked with ■ in

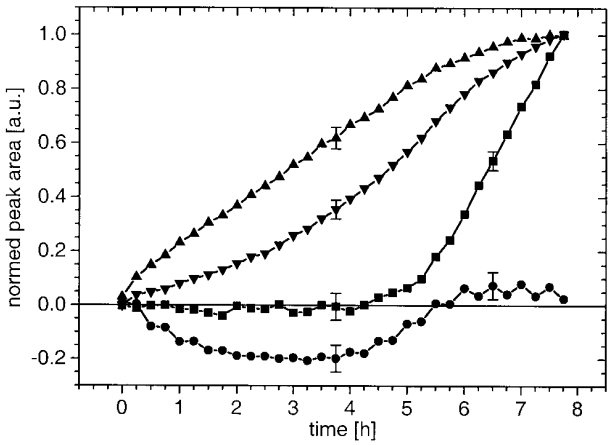

Fig. 69 Changes of the normalized peak area of the bands at 725 cm^{-1} [(▲) the out-of-plane bending of the imide ring], at 3060 cm^{-1} [(▼) C–H stretching vibrations of the aromatic ring], at 1750 cm^{-1} [(■) imide and amide C=O stretching vibration], and at 2220 cm^{-1} [(●) –C=N stretching vibration]. The experiment was performed at 812 K using a total flow of 50 mL_N min^{-1} of compressed air. Applied Spectroscopy by T. Lippert [Ref. 281], COPYRIGHT (2001) by SOC FOR APPLIED SPECTROSCOPY. Reproduced with permission of SOC FOR APPLIED SPECTROSCOPY in the format Textbook via Copyright Clearance Center

Fig. 69, remain quasi-constant, until a fast decrease at the end of the pyrolysis. The curve marked with ● represents an intermediate, i.e., the –C≡N stretching bands at 2220 cm^{-1}, which decomposes again completely. The alkynes (–C≡C-) show the same behavior as the nitrile band. It is noteworthy, that the carbonyl bands of the amide and imide decrease only at a very late stage of the pyrolysis, when the intermediates are already more or less decomposed.

The weak presence of bands, in the region of the aliphatic C–H stretching vibrations (2980–2780 cm^{-1}), indicates that only a very small amount of aliphatic structures are formed. This is also consistent with the band at 1400 cm^{-1} that was assigned to a $–CH_2–CN$ group.

Figure 69 shows (filled triangles and filled squares) that different structural parts of Kapton decompose at different times. Intermediates are formed at the same time (filled circles in Fig. 69) and subsequently pyrolysed again. This suggests that Kapton decomposes completely in air via a multistep process, without the formation of polymers with low molecular weight.

The bands representing the out-of-plane bending vibrations of the imide ring (see band at 725 cm^{-1} in Fig. 68) and the C–H stretching vibrations of the aromatic rings (see band at 3060 cm^{-1} in Fig. 68) were examined in more detail for a quantitative analysis. These two bands were chosen because they are directly related to a specific part of the polymer and they are at an isolated position in the IR spectrum, avoiding the interference of neighboring bands. In other regions of the IR spectrum the qualitative and quantitative analysis is

very difficult due to the complex band structure in the region where, e.g., C–C (1260–800 cm^{-1}), C=C (1680–1620 cm^{-1}), C–O (1270–1060 cm^{-1}), C=O (1800–1700 cm^{-1}), and C–N (1420–1400 cm^{-1}) groups absorb.

The C–N bonds of the imide rings were identified as primary decomposition sites during the pyrolysis of Kapton. The resulting structures can be described best as amide groups. The next step is the decomposition of the aromatic systems. Simultaneously –C≡N and –C≡C– groups are formed as intermediates. The last step of the decomposition is the elimination of the carbonyl groups. A carbon- and nitrogen-rich residue remains.

A scheme suggesting a possible decomposition mechanism is shown in Scheme 14. This scheme includes the detected intermediates and assumes a

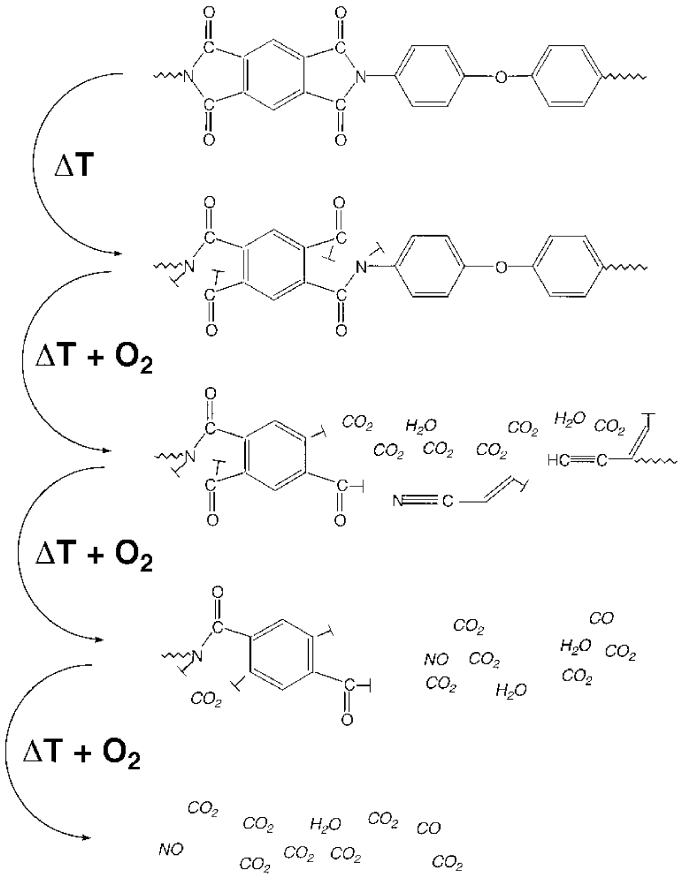

Scheme 14 Suggested scheme of the thermal decomposition of Kapton, including various intermediates, assuming a total oxidation of the carbon. ⊥ indicates a broken bond; information on the nature (radical, ionic, terminated) is not available from the present experiments. Applied Spectroscopy by T. Lippert [Ref. 281], COPYRIGHT (2001) by SOC FOR APPLIED SPECTROSCOPY, Reproduced with permission of SOC FOR APPLIED SPECTROSCOPY in the format Textbook via Copyright Clearance Center

total oxidation of the carbon. It is difficult to quantify the oxidation product, CO_2, in the DRIFT spectra, because it is a trace impurity in the feed gas. A clear difference between pyrolysis and UV laser (308 nm)-induced decomposition of Kapton is detected. During laser-induced decomposition the diaryl ether group decomposes simultaneously with the imide system, while the decomposition of the ether bridge is not clearly observed during pyrolysis. The decomposition of the imide system during photolysis results in the formation of an amide system which decomposes again quite fast under elimination of the carbonyl groups, which is one of the last steps of decomposition during pyrolysis. In both cases, i.e., photolysis and pyrolysis, the formation of aliphatic hydrocarbons, nitriles, and alkynes is observed, but isocyanate groups are only observed during photolysis. These results clearly show that the mechanism of UV laser-induced decomposition is not identical to pyrolysis as suggested previously.

Modeling of Time Dependence. Simple Topological Description of the Overall Reaction. A better understanding of the reaction can be achieved by plotting the conversion of a specific structural unit. The conversion is proportional to the normalized peak area, and is plotted vs the normalized time necessary for the complete reaction [289, 301–305]. Similar plots are used in heterogeneous catalysis to study the rate-controlling step of a process [321]. In Fig. 70 top, a plot for the aromatic rings (3060 cm^{-1}) at temperatures of 783 K (▽), 812 K (+) and 841 K (▼) is presented. In Fig. 70 bottom, the imide system (725 cm^{-1}) is plotted at the same temperatures (783 K: Δ; 812 K: ×; and 841 K:▲).

A) High temperatures—reaction control

At the highest applied temperature (841 K: solid symbols in Fig. 70) the plots decrease rapidly to ≈20% of the initial concentration, followed by a slow decrease to zero. This evolution is typical for a chemical reaction control process. The rate velocity of such a process can be described using Eq. 19 [321]

$$S_{ex}^{-1}\frac{dN_{Kapton}}{dt} = -k_s C_{O_2} \tag{19}$$

The sample is represented by a constant number of similar particles. S_{ex} is the external surface of the particle, which can be approximately described as a sphere ($S_{ex}=4\pi r^2$). N_{Kapton} is the mole number of Kapton, C_{O2} is the molar concentration of oxygen in the gas flow, and k_s is the reaction velocity on the surface of the particle. By solving Eq. 20, the time t necessary to oxidize a particle is obtained as function of the radius (R_0 and R_t) of the particle [Eq. (20)].

$$t = \frac{\rho_{Kapton}}{k_s C_{O_2}}(R_0 - R_t) \tag{20}$$

ρ_{Kapton} is the molar density of Kapton. R_0 is the radius of the starting particles, while R_t denotes the radius of the particles at the time t. The time τ required for complete conversion is given for R_t=0. The decrease in the radius, or increase in fractional conversion of the particle X_{Kapton} as function of the normalized time (t/τ) is given in Eq. 21.

$$\left(\frac{R_t}{R_0}\right)^3 = 1 - X_{Kapton} = \left(1 - \frac{t}{\tau}\right)^3 \tag{21}$$

For the exponent in Eq. 21 a variable is used to fit the data points for the aromatic and imide system in Fig. 70. At the highest temperature (solid symbols), a value of 3.0±0.1 is obtained for the exponent. This shows that this step is a chemical reaction control process.

B) Low temperatures—shrinking particle

At the lower temperature (783 K: open symbols in Fig. 70) a substantially different behavior is observed. The imide band (Δ in Fig. 69 bottom) decreases quasi-linearly with the elapsed time (see Eq. 24). The aromatic band (∇ in Fig. 70 top) is complex, revealing two distinct decomposition patterns. At the beginning (first half) of the normalized time a slow linear decrease is observed, followed by a fast decrease. The decrease of the imide band and the change of the aromatic band in the second part of the curve are typical for a film diffusion-controlled reaction of shrinking particles in a gas flow in the Stokes regime. To confirm this observation a new mathematical model is used to fit the curves [321]. Starting from Eq. 20, the reaction velocity k_s is substituted with k_g=D R_t^{-1} [321]. D is the diffusion velocity and k_g the mass transfer coefficient between fluid and particle. The differential equation is solved and the time necessary to reduce a particle from a starting radius R_0 to R_t is obtained [see Eq. (22)] [321].

$$t = \frac{\rho_{Kapton} R_0}{2DC_{O_2}} \left(1 - \left(\frac{R_t}{R_0}\right)^2\right) \tag{22}$$

The fractional conversion of the particle X_{Kapton} as function of the normalized time (t/τ) is shown in Eq. 23.

$$1 - X_{Kapton} = \left(1 - \frac{t}{\tau}\right)^{\frac{3}{2}} \tag{23}$$

The data points (open symbols) in Fig. 70 were fitted using Eq. 24 with the exponent as variable. The obtained values, around 1.5 ±0.1, confirm the hypothesis of the film diffusion-controlled reaction of shrinking particles in the Stokes regime.

C) Refinement at low temperature—differences for imide/aromatics

The aromatic band (∇ in Fig. 70 top) decreases slow and linearly in the first part of the plot. Fitting of this part of the data, considering a shrinking

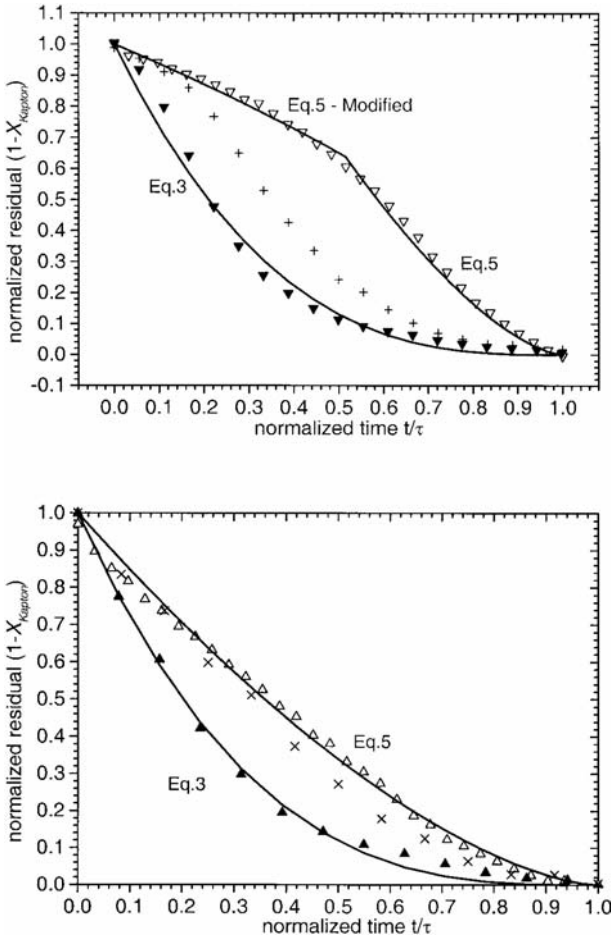

Fig. 70 Normalized residual ($1-X_{Kapton}$) as a function of the normalized time for a complete conversion (t/τ) at 783 K (*open symbols*), 812 K (+ and x), and 841 K (*solid symbols*). The equations applied for fitting the data points are included in the plot (see text). (*Top*) The band at 3060 cm^{-1} (▼,, and +) representing the aromatic rings. (*Bottom*) The band at 725 cm^{-1} (▲, △, and x) representing the imide rings. Applied Spectroscopy by T. Lippert [Ref. 281], COPYRIGHT (2001) by SOC FOR APPLIED SPECTROSCOPY, Reproduced with permission of SOC FOR APPLIED SPECTROSCOPY in the format Textbook via Copyright Clearance Center

particle, did not give satisfactory results. The first part of the plot (open symbols in Fig. 70 top) is fitted using Eq. 23, with the exponent as variable. The obtained value of $n \approx 0.6$ suggests that the model for Eq. 23 is not really valid in this case. A mathematical analysis of the exponent in Eq. 23 reveals that this value is dependent on the particle radius (see Eq. 24). The left side in Eq. 23 is substituted by a volume ratio of the particles at the start (R_0')

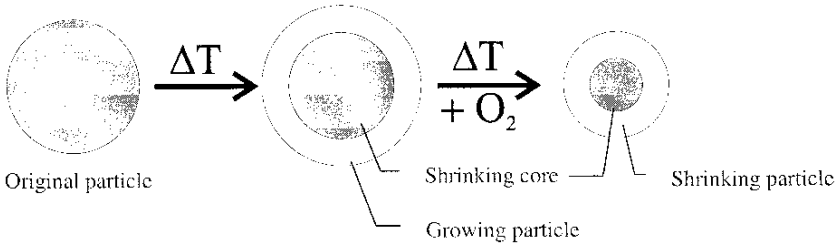

Fig. 71 Suggested decomposition scheme:shrinking particle with a shrinking core. The pyrolysis of the core has an Arrhenius activation energy of E_A=162±19 kJ mol^{-1} (imide rings), and the pyrolysis of the residual particle one of E_A=212±37 kJ mol^{-1} (aromatic rings). Applied Spectroscopy by T. Lippert [Ref. 281], COPYRIGHT (2001) by SOC FOR APPLIED SPECTROSCOPY, Reproduced with permission of SOC FOR APPLIED SPECTROSCOPY in the format Textbook via Copyright Clearance Center

and a given time (R_t). The exponent on the right side is substituted with the variable *x*.

$$\left(\frac{R_t}{R_0'}\right)^3 = \left(1 - \frac{t}{\tau}\right)^x \tag{24}$$

Equalizing (1-t/τ) from Eqs. 23 and 24 and solving for the volume ratio yields a relation between the actual starting radius R_0' (Eq. 24) and the theoretical starting radius of R_0 (as in Eq. 23).

$$\left[\left(\frac{R_t}{R_0'}\right)^3\right]^{\frac{1}{x}} = \left[\left(\frac{R_t}{R_0}\right)^3\right]^{\frac{2}{3}} \tag{25}$$

Solving Eq. 25 for R_0 gives the relation

$$R_0 = \left(R_t^{2x-3}\, R_0'^{\,3}\right)^{\frac{1}{2x}} \tag{26}$$

The analysis of Eq. 26 shows that, for values of x<1.5, the theoretical radius R_0 is larger than the actual starting radius R_0'. This implies that the particles expand temporarily, followed by shrinking. A tentative representation of the decomposition mechanism is shown in Fig. 71. An increase of the polymer surface is a well-known effect during polymer decomposition [322]. An accumulation of gaseous products will also result in surface swelling [224]. This observation is consistent with an immediate decomposition of the imide ring, causing an increase of the surface area of the particle, and the delayed decomposition of the aromatic rings. This behavior explains the unsatisfactory results obtained for other decomposition mechanism models (see above), and the observation of a multistep process for the pyrolysis of Kapton.

Estimation of Activation Energies of Consecutive Steps. The activation energies for the two distinct processes visible in Figs. 69 and 70 were extracted to obtain quantitative kinetic data on the thermal decomposition of Kapton. For this purpose, reaction rate constants are calculated for the imide signal

(first step in Fig. 71) and from the aromatic signal at high turnovers (second step in Fig. 71). The reaction rate constants were calculated (in Fig. 69) with the assumption that the pyrolysis process starts as a first order reaction. In case of the imide system a linear regression of the short-time turnover with zero-x/y intercept (initial rate) is used for the analysis. For the aromatic ring the slope at t$\geq$ 4.5 h in Fig. 69 is used to calculate the reaction rate. This corresponds to the faster second reaction step visible in Fig. 70 (top), corresponding to the second step in Fig. 71 (shrinking particle). This reaction step reaches the maximum velocity only after an incubation period. Therefore, a linear regression without zero-x/y intercept is used. The Arrhenius plot for the decomposition of the imide rings (▲ in Fig. 72, bottom) and of the aromatic ring (▼ in Fig. 72, top) is shown in Fig. 72. From this plot the Arrhenius activation energy E_A is calculated according to Eq. 27.

$$\ln k = \ln A - \frac{E_A}{R} T^{-1} \tag{27}$$

The obtained values are:

E_A (imide rings, early time)=162±19 kJ mol^{-1}
E_A (aromatic ring decomposition, late phase)=212±37 kJ mol^{-1}

This result is consistent with the observation of a rapid decomposition of the imide rings, followed by the decomposition of the aromatic systems. The obtained values agree quite well with values reported in the literature. Traeger and Salazar [323] reported an activation energy of 163±20 kJ mol^{-1} for the pyrolysis of Kapton in air, while Heacock and Berr [324] published values between 162 and 165 kJ mol^{-1}. The same authors reported a two-step process with an activation energy of 232 kJ mol^{-1} for the thermal degradation of polyimide in helium. All of these experiments were performed at temperatures between 523 and 723 K using TGA.

This result confirms that DRIFT spectroscopy can be used to analyze *simultaneously* the decomposition mechanism *and* kinetics of polymers (at least Kapton).

Reflections on Refined Topological Models. As there are at least two reactions, the actual situation would correspond to a shrinking core (undecomposed polymer) with an initially expanding then shrinking shell of aromatics. To analyze the rate constants and activation energies for this situation, it would be required to develop a new mathematical model and to perform the experiments at low temperatures where this behavior could be observed.

Additionally, another quite plausible model, i.e., an ash diffusion reaction control model, was tested (see Eq. 28) [321] for the imide pyrolysis.

$$\left(1 - \frac{t}{\tau}\right) = 3\left(1 - X_{Kapton}\right)^{2/3} - 2\left(1 - X_{Kapton}\right) \tag{28}$$

No satisfactory results were obtained with this model. This is probably due to the fact that this model is not really valid for shrinking particles [321]. The ash diffusion model was also applied for the high-temperature ex-

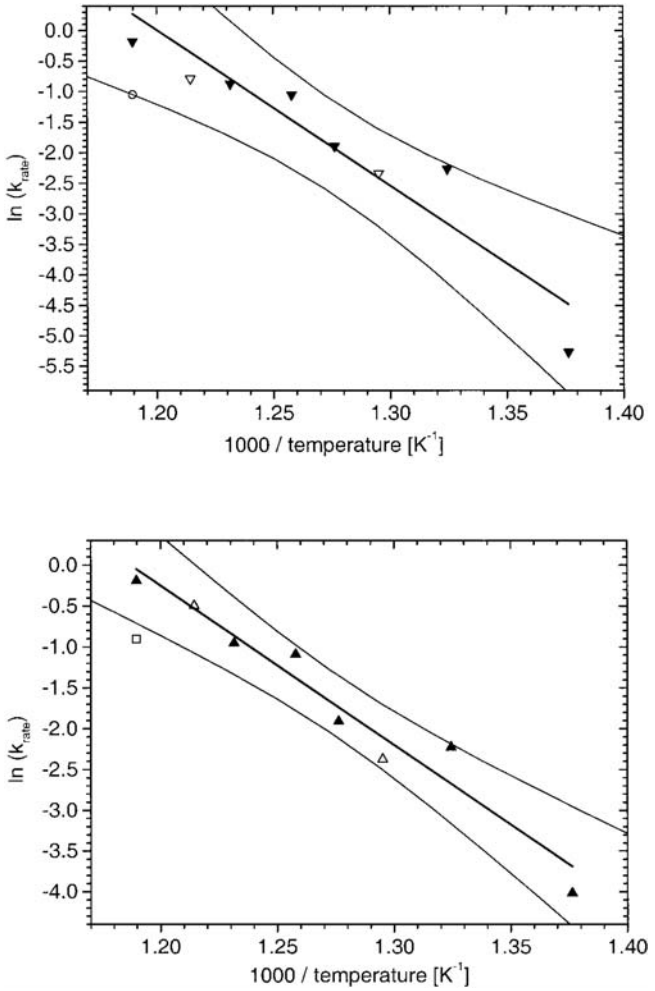

Fig. 72 Arrhenius plots and confidence range (2σ) for the decomposition of the aromatic systems (*top*) and imide rings (*bottom*). Only solid symbols (▲ and ▼) are used for the calculation of the Arrhenius activation energies. (*Top*) Band at 3080 cm^{-1} for the following conditions: 50 mL_N min^{-1} air (▼); 12.5 mL_N min^{-1} air and 37.5 mL_N min^{-1} N_2 (); and 12.5 mL_N min^{-1} air (O). (*Bottom*) Band at 725 cm^{-1} for the following conditions: 50 mL_N min^{-1} air (▲); 12.5 mL_N min^{-1} air and 37.5 mL_N min^{-1} N_2 (Δ); and 12.5 mL_N min^{-1} air (□). Applied Spectroscopy by T. Lippert [Ref. 281], COPYRIGHT (2001) by SOC FOR APPLIED SPECTROSCOPY, Reproduced with permission of SOC FOR APPLIED SPECTROSCOPY in the format Textbook via Copyright Clearance Center

periments. The model agrees quite well with the experimental data at the end of the reaction, where the accumulation of carbon species might play a role. This is also in agreement with the EDX data and optical detection of small amounts of carbon materials after the pyrolysis (data not shown).

Influence of the Oxygen Concentration. The O_2 concentration in the feed gas was reduced to 25% of the concentration in air. The experiment was repeated at two different temperatures, i.e., 772 and 823 K. The changes of the concentration of the different functional groups are very similar (data not shown) to those obtained in air. The reaction rate was calculated as described previously. The obtained values are included in the Arrhenius plots (Fig. 72; aromatic rings: Δ in upper graph; and imide rings: ∇ in lower graph). The calculated parameters are close to the fit, indicating that the reaction rate constants are not influenced by the applied O_2 concentration in the gas phase (at least within the tested range). This result suggests that the process is, depending on the applied temperature and gas flow, either chemical reaction controlled or product desorption/diffusion controlled.

Influence of the Total Flow. A simple test to assess the influence of the total gas flow was carried out. The feed gas of compressed air was reduced to 12.5 $ml_N\ min^{-1}$, which is only a quarter of the flow in the previous experiments. The experiment was performed only at the highest temperature (841 K). The change of the concentrations assigned to the different functional groups differs from those obtained with the higher flow, and lies between the data obtained at 783 and 812 K (data not shown). The reaction rate was calculated as described above. The obtained values are included in the Arrhenius plots (Fig. 72: aromatic rings: ❍ in the upper graph; and imide rings: ❒ in the lower graph). The calculated values are consistently below the values obtained in the previous experiments, indicating a reduced reaction rate velocity. This might be due to a reduction of the overall diffusion, caused by the increased thickness of the gas film.

The same variation of the rate constant can be obtained by changing the temperature. A relatively small increase of the temperature is equivalent to a large increase of the gas flow, probably reducing the film diffusion resistance significantly. This result is consistent with the previously described observations of a film diffusion-control process at low temperatures and chemical reaction control at high temperatures.

2.3.2.4 Summary

The experimental data show that KBr can be used for pyrolysis experiments of Kapton by DRIFT spectroscopy. No artifacts are observed with and without the sample upon heating to 841 K. The spectra, i.e., difference spectra, are obtained rapidly, the position of a given band is related to a specific functional group, and the peak area can be used for quantitative analysis. The pyrolysis of Kapton shows pronounced differences from laser-induced (UV) decomposition. The polyimide system decomposes thermally in distinct steps, i.e., first the imide ring, without elimination of the carbonyl groups, followed by the aromatic system and then the carbonyl groups. Several intermediates, such as nitriles and alkynes, are identified. The quantitative analysis of the spectra suggests that Kapton decomposes in two steps, i.e., as a growing par-

ticle with shrinking core followed by a shrinking particle. The growing particle with shrinking core is the nonreacted polymer as core and a polyamic structure as growing part, while the shrinking particle is the complete pyrolysis of the polymer. The activation energies for these two steps are 162±19 and 212±37 kJ mol^{-1}, respectively. The reaction rate appears to be diffusion controlled at low temperatures and surface reaction controlled at higher temperatures. The oxygen concentration has no pronounced influence within the tested range. DRIFT spectroscopy has the potential as an important analytical tool for the decomposition of polymers. Information on the mechanism, thermal properties, and kinetic data can be obtained simultaneously.

2.4 Discussion of the Ablation Mechanisms

In the previous chapters we have described the ablation properties of polymers designed for ablation and of reference polymers, i.e., mainly polyimide.

2.4.1 *Designed Polymers*

The specially developed photopolymers, particularly the triazene polymers, reveal the following unique features:

- Absorption maximum around 300 nm, corresponding to the λ_{irr} of a XeCl excimer laser (308 nm). This absorption maximum is mainly due to the photochemically active triazene chromophore, and is relatively decoupled from the absorption of other parts of the chemical structure (e.g., the aromatic groups around 190 nm).
- The thresholds of ablation for 308-nm irradiation are around 25 mJ cm^{-2}, corresponding to the lowest thresholds of ablation reported for 308-nm irradiation.
- The etch rates, e.g., 260 nm per pulse at 100 mJ cm^{-2}, at low fluences (defined here as <400 mJ cm^{-2}) are the highest reported values.
- The ablation contours are well defined and clean, with no signs of a heat-affected zone or deposited debris in the ablation craters or in the surroundings [325].
- The etching of the polymer takes place within the time frame of the laser pulse, with no signs of surface swelling. The triazene chromophore decomposes during the laser pulse.
- No ejection of solid products, which might contaminate the surface of the polymer (or the optics). The resulting shock wave (into air) is supported by the energy of the exothermic decomposition of the triazene polymer.
- The surface of the ablated polymer reveals a composition very similar to the starting material.

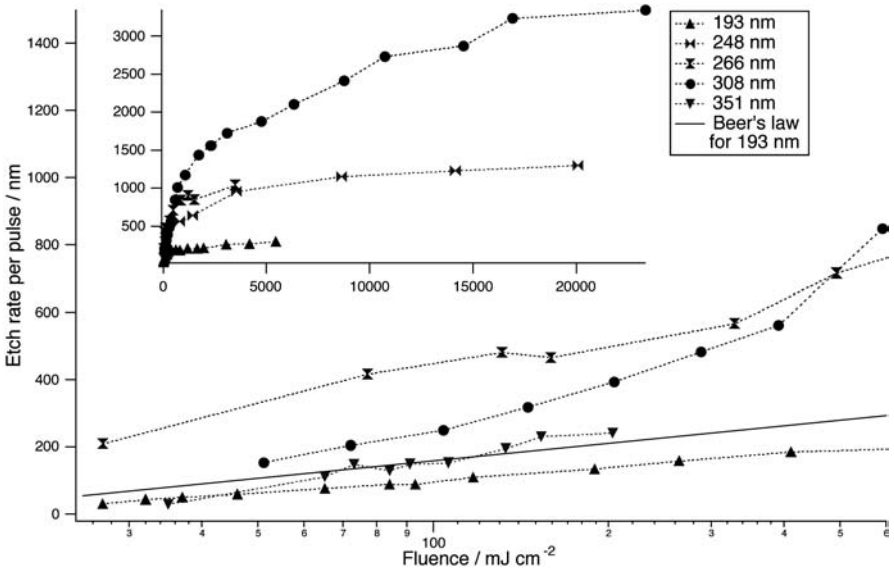

Fig. 73 Measured etch rates of TP vs the logarithm of the fluence (up to 600 mJ cm^{-2}) for different irradiation wavelengths. *Insert* shows the same plot for the complete linear fluence range. REPRINTED WITH PERMISSION OF [Ref. 221], COPYRIGHT (2002) Elsevier Science

Other designed polymers (e.g., the cinnamylidenemalonyl esters) also reveal low ablation thresholds and high etch rates, but the ablation characteristics are still better for the triazene polymers. The ranking of ablation properties (i.e., low threshold, high etch rates) follows the trends of photochemical activity and is independent of the linear absorption coefficient. Another very interesting characteristic is the similar effective absorption coefficient obtained for all designed polymers. All designed polymers are probably decomposing according to similar mechanisms (at least the initial steps), i.e., direct photolysis, during which homolytic bond breaking occurs [140, 153]. Radicals are formed as intermediates, especially aromatic radicals, which should be present for all designed polymers. These common products/intermediates could be the reason for the very similar values of α_{eff}.

The importance of the photoactive group (i.e., triazene group) is also exemplified in etch rates obtained for different irradiation wavelengths (shown in Fig. 73). For 248-nm irradiation only data points for high fluence are available. The data points seem to fit quite well to the 266-nm irradiation data. The different irradiation wavelengths correspond to different features of the UV-Vis spectrum.

The spectrum reveals two strong bands around 196 nm, corresponding mainly to the aromatic parts of the polymer, and 332 nm, corresponding mainly to the triazene chromophore [68]. The etch rates can more or less be divided into two groups (shown in Fig. 73), i.e., the wavelengths which directly excite the triazene system (266, 308, and maybe 351 nm) and 193 nm

that is in resonance with the aromatic system. Irradiation with 193 nm results in the lowest ablation rates, which are even below the etch rates described by Eq. 1 using the linear absorption coefficient α_{lin} from Beer's law (included in Fig. 73).

This behavior is very different from that observed with the other irradiation wavelengths, where much higher etch rates result than predicted by Beer's law. This is most probably due to decomposition (ablation) of the polymer during the pulse. The difference between 308 and 193 nm is even more remarkable when we consider that the absorption coefficients are quite similar. The etch rates of the three wavelengths which are in resonance with the triazene chromophore follow, at low fluences, the values of photon energy (highest photon energy=highest etch rate). At higher fluences, lower etch rates are obtained for 266- as compared to 308-nm irradiation (see insert Fig. 73). This can be explained by absorption of the laser photons by the ablation products in the gas phase (shielding), especially by aromatic radicals. It is also noteworthy that the etch rates obtained for 193- and 266-nm irradiation follow a linear relation (on the logarithmic fluence scale) over the whole fluence range. For all irradiation wavelengths similar low-threshold fluences result, i.e., 12±2 mJ cm^{-2} for 193 nm, 8±2 mJ cm^{-2} for 266 nm, 27±3 mJ cm^{-2} for 308 nm, and 25±3 mJ cm^{-2} for 351-nm irradiation. This suggests that with all irradiation wavelengths the same reactions are induced. This is most probably the decomposition of the triazene system, where homolytic bond breakage of the N–N single bond can be achieved with the energy of a single photon at all irradiation wavelengths.

2.4.1.1 Polyimide

Many of the above described features are quite different to published and our own data for polyimide. Polyimide (PI) has a linear absorption coefficient at 308 nm similar to the designed polymers (around 95,000 cm^{-1}). The first pronounced differences between the ablation characteristics between PI and our polymers are the higher threshold of ablation (three times), lower etch rates, and an effective absorption coefficient which is similar to the linear absorption coefficient. A comparison of the ablation quality between a designed polymer (TP) and the standard polymer (PI) is shown in Fig. 74.

The structures were created by imaging a diffractive gray tone mask onto the polymer surfaces. The experimental details are described in detail elsewhere [326]. The structure in TP (left) is well defined with no debris contaminating the polymer surface, while in the case of PI pronounced contamination in the surroundings of the structure is visible. A closer inspection (not shown) reveals that contaminants are also present inside the structure and that the structure exhibits a lower resolution. Raman microscopy has been used to analyze the deposited debris in the surroundings of the ablation crater. The debris consists mainly of amorphous carbon with some crystalline features.

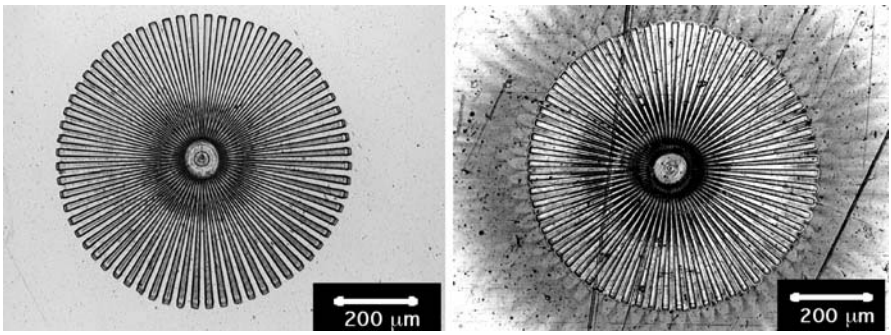

Fig. 74 SEM images of Siemens stars fabricated by laser ablation. Siemens stars in the triazene polymer (*left*) and in polyimide (*right*) using 5 pulses. REPRINTED WITH PERMISSION OF [Ref. 221], COPYRIGHT (2002) Elsevier Science

The thickness of the deposit increases with pulse number while the area increases with fluence. A transmission electron microscopy (TEM) picture (Fig. 75) shows that the carbon is loosely packed and that the thickness decreases from the edge of the crater (left in the TEM pictures). PI was chosen as reference polymer mainly for two reasons. The above described absorption properties, and the fact that the newest photothermal model could until now describe all experimental data (see above). Therefore, we thought that PI can be used as a typical example for a polymer which follows a photothermal model [89], while the triazene polymers reveal several features which might be considered photochemical (e.g., wavelength dependence, products and decomposition at low fluences, and etching during the pulse).

2.4.1.2 Additional Experiments

To validate the photothermal model some additional experiments were performed. Infrared spectroscopy was applied to study the excimer laser- and thermal (heating)-induced decomposition of PI. Pronounced differences were detected, giving first doubts about the purely photothermal model. One problem of this comparison is, of course, the very different time scale of the reactions. The laser-induced photothermal decomposition, suggested in the model, has heating rates of up to 10^9 K s^{-1}, while the pyrolysis experiments are performed with heating rates of 0.17 K s^{-1}. Whether these vastly different heating rates may change the product/intermediate distribution in the postreaction analysis is not clear. Our ultrafast, in situ IR experiments have shown that the primary decomposition step for the photochemically *as well as* thermally induced reaction of a structurally related azo compound takes place on a time scale faster than the temporal resolution of this setup (<20 ps). These experiments only show the initial reaction and give no indication whether differences exist for following reactions or, more importantly, ablation itself, because ablation was not observed within the maximum

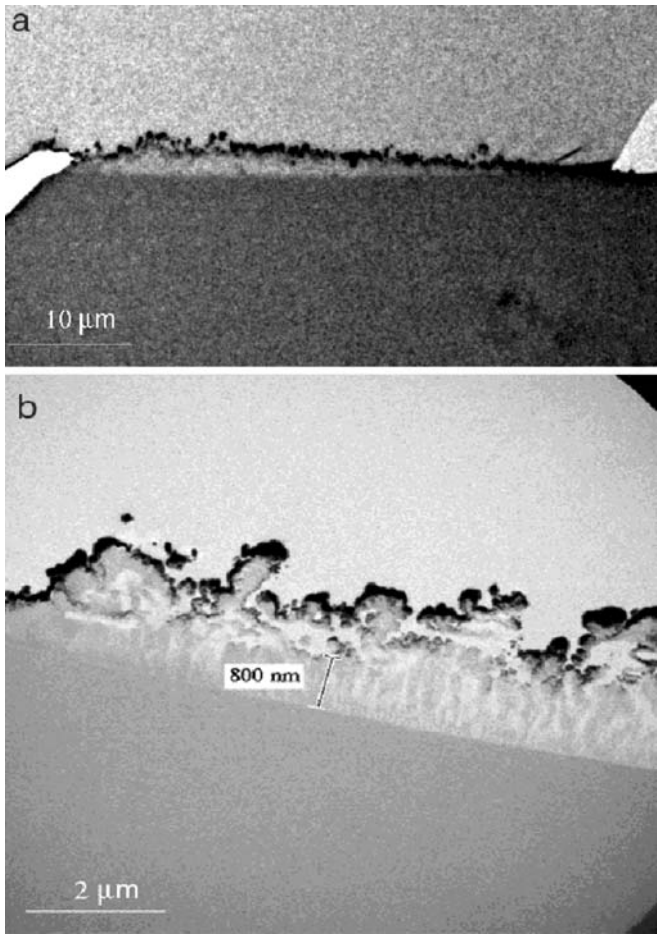

Fig. 75 TEM micrographs of the transverse section of the line structure obtained with 800 pulses at 80 mJ cm^{-2}, showing the edge of the crater (at the *far left* of the micrographs). **a** Overall view of the profile of the deposited material. The width of the region is 36 μm. **b** The section near the edge of the crater, showing the details of the deposited material. REPRINTED WITH PERMISSION OF [Ref. 132], COPYRIGHT (2000) American Institute of Physics

time limit of the setup (8 ns). The late occurrence of ablation is probably due to the fact that doped polymers were used with a relatively low concentration of the absorbing species (3–5 wt%). In neat, high-absorbing polymers faster ablation will most probably be observed. These ultrafast measurements showed nevertheless that laser-induced thermal reaction can occur on a pico- to subpicosecond time scale, suggesting that a simple comparison of time scales of initial reactions is not sufficient for distinguishing between photochemical and photothermal reactions.

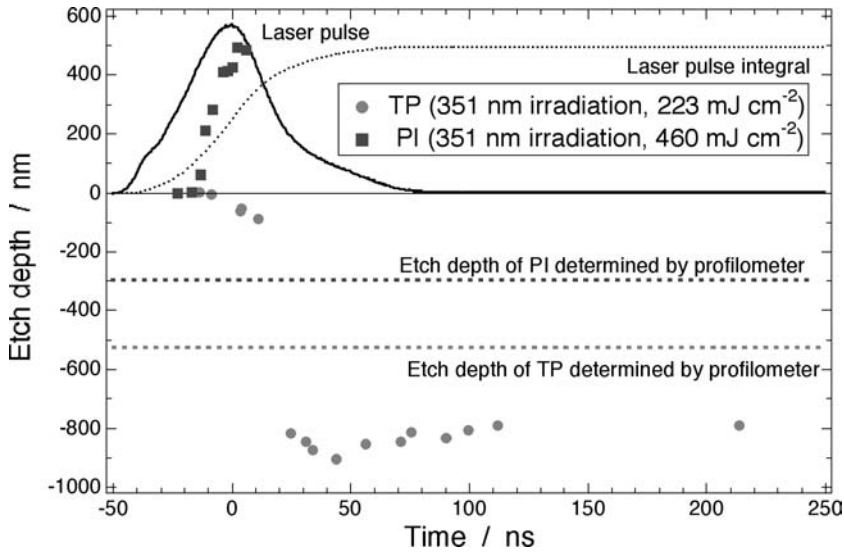

Fig. 76 Nanosecond expansion/etching behavior of the triazene polymer and polyimide after 351-nm irradiation. REPRINTED WITH PERMISSION OF [Ref. 221], COPYRIGHT (2002) Elsevier Science

Interferometry. To compare the ablation behavior and the ablation mechanism of PI and TP in more detail, additional experiments were performed on an identical time scale with interferometry. Interferometry has the potential to give simultaneously information on the time scale of ablation (and reactions) and ablation itself. A comparison of data between TP and PI is shown in Fig. 76. TP and PI were studied with an irradiation wavelength of 351 nm. The ablation threshold for TP at 351 nm is also 25 mJ cm^{-2}, while PI exhibits a threshold of 210 mJ cm^{-2}. The experiments were performed with fluences above the threshold of ablation, i.e., 225 mJ cm^{-2} for TP and 460 mJ cm^{-2} for PI. The etching of the triazene polymer starts and ends within the excitation pulse of the excimer laser. Prior to etching, darkening of the surface is observed, which is probably due to the creation of the first products, i.e., N_2, inside the polymer [133]. The overestimation of the etch depths is due to the experimental configuration, described in detail elsewhere [133]. In the case of PI a very different behavior is observed. It was only possible to observe swelling of the polymer surface (up to several hundred nm), but time-resolved etching or swelling after several ns could not be observed, probably due to the ejection of fragments which shield the probe light. The differences between TP and PI in the dynamic interferometric studies suggest that different mechanisms are active for TP and PI.

For further evaluation of the photothermal model for the ablation of PI, additional measurements were performed with different irradiation wavelengths (248 and 351 nm). The data are shown in Fig. 77. Both irradiations

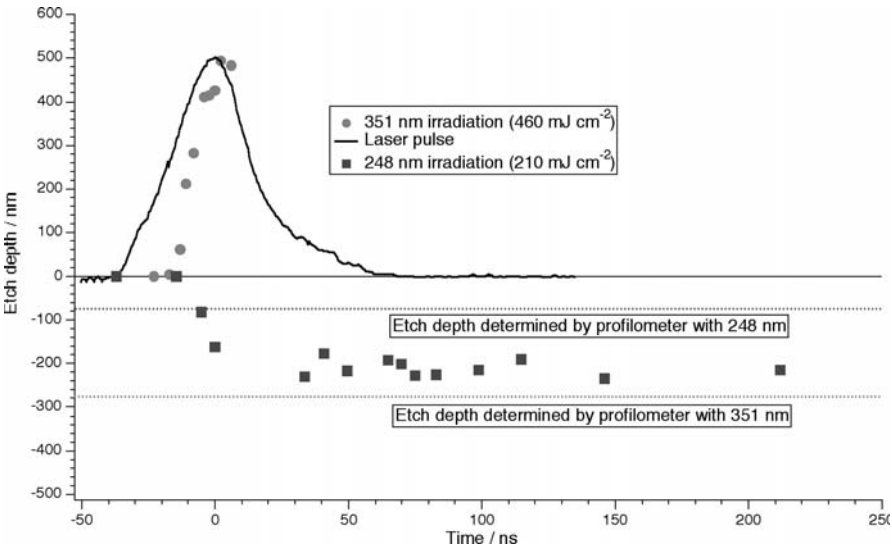

Fig. 77 Nanosecond expansion/etching behavior of polyimide after 248- and 351-nm irradiation. REPRINTED WITH PERMISSION OF [Ref. 223], COPYRIGHT (2002) Elsevier Science

were performed with fluences above the threshold of ablation (F_0 for 248 nm is 40 mJ cm^{-2}). Pronounced differences are detected between the two irradiation wavelengths. After 351-nm irradiation a very pronounced swelling of the surface and very delayed etching is observed, while for 248-nm irradiation etching takes place within the laser pulse (similar to the behavior of TP). These differences cannot be explained by the published model, where a comparable behavior for 248- and 351-nm irradiation is predicted. It is noteworthy to mention that the absorption coefficients at 248 and 351 nm are quite different ($\alpha_{248\ nm}$=31.1 μm^{-1} and $\alpha_{351\ nm}$=1.21 μm^{-1}) and that the film thickness is quite low (1.5 μm). This results in laser penetration depths of ≈50% of the film thickness in the case of 351-nm irradiation and of ≈1% in the case of 248-nm irradiation. These very different laser-affected layers could be the reason for the observed differences.

These additional data show clearly that even the most advanced photothermal model that was developed over several years and that could explain all the data up to now is still not complete, or that additional experiments are necessary to explain the new data.

Time-of-Flight Mass Spectroscopy. The last set of data that strongly suggests that at least some photochemical features should be considered in models of laser ablation results from very recent TOF-MS measurements of the triazene polymer. When the quadrupole mass spectrometer is tuned to detect particles with a charge to mass ratio of 28 amu/e, the resulting signal shows highly energetic components (short TOF, curve (b) in Fig. 78), very slow

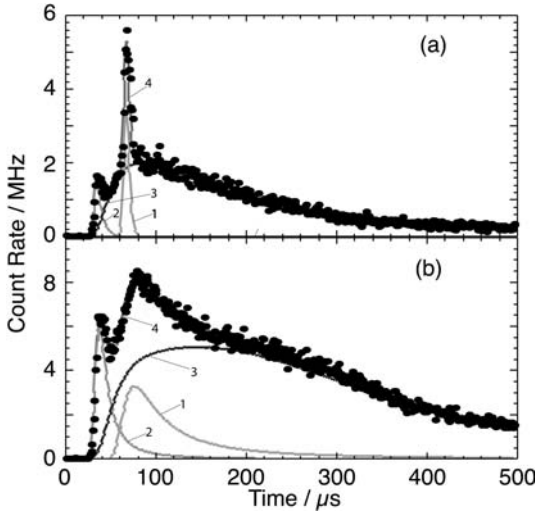

Fig. 78 Time-of-arrival curves of the 28 amu fragment; **a** irradiation with 308 nm and 260 mJ cm^{-2} and **b** irradiation with 248 nm and 260 mJ cm^{-2}. The curves (1) and (2) represent Gaussian distribution, the curve (3) is fitted by a decaying Maxwell–Boltzmann distribution, while the curve (4) is the sum of the three fitted curves. REPRINTED WITH PERMISSION OF [Ref. 223], COPYRIGHT (2002) Elsevier Science

components consistent with emission long after the laser pulse, and a sharply peaked component of intermediate energies (curve (a) in Fig. 78). The fast and slow components have been described in previous work at 248 nm [327, 328]. The peak at intermediate energies was only observed when the quadrupole was aligned perfectly along a straight line from the sample. This was most probably not the case in our previous experiments. A possible explanation for this peak could be a metastable species, because metastable particles are not focused by the electric fields of the quadrupole.

Experimentally, the fast component was identified as a ground state neutral. As the physical TOF distribution of these particles is not known, the data were fitted with an empirical TOF distribution based on a Gaussian energy distribution in one dimension, with central energy and standard deviation E_0 and σ, respectively. The TOF of the fast component (arriving <50 μs after the laser pulse) is unusually short for a neutral molecule. Kinetic energy estimates, assuming that these molecules were emitted with a Gaussian energy distribution and experienced no subsequent collisions, range from 3–6 eV [327, 328].

The broad peak, attributed again to ground state neutrals, could not be simply described by a simple Maxwell–Boltzmann distribution of particles emitted during the laser pulse. The leading edge of the particle distribution was far too fast to be consistent with any Maxwell–Boltzmann distribution that could account for the very long tail in the detected emissions. Thus emission appears to continue for some time after the laser pulse. Although

the physical validity of the model chosen to describe this emission is open to debate, it accounts for the emission intensity vs time well. To account for emission after the laser pulse, we assumed that the emission intensity is controlled by a thermally activated process (which we assume is decomposition related but could refer to particle transport in the bulk).

The narrow peak 50–100 μs after the laser pulse was most remarkable in that it was only weakly affected by the mass filter setting and was surprisingly resistant to modification by modest electric fields. In previous work, signals have been frequently found that are not mass resolved and that can be attributed to nonequilibrium plasmas, which are also called ±charge clouds [329–331]. The substantial electron component of these charge clouds can screen the accompanying ions from applied electric fields. In the presence of the electron component, these ions can then pass through the ionizer optics despite the positive potential applied to the inner grid (+15 V) as well as the combined AC/DC electric fields of the mass filter. Since charge clouds incorporate charges of both signs, one expects to observe charges of both signs with similar arrival times if one biases the quadrupole detector for the detection of positive and negative charge in turn.

TOF measurements made with the ionizer and mass filter optics grounded, and with the quadrupole detector biased to detect positive charge, produced a strong signal and peaks at about 70 μs. When the quadrupole detector is biased to detect negative charge, a somewhat weaker signal is observed with a virtually identical time-of-flight distribution. These results are consistent with the detection of a cloud of co-moving positive and negative charge. Most charge clouds, however, fail to show such consistent positive and negative charge arrival times, due to the high mobility of the electron component of the charge cloud relative to the positive ion component.

To examine the possibility that the positive and negative charge signals might indeed be due to a single metastable particle, attempts were made to modify the time-of-flight signals of the positive charge signal by applying high electrostatic potentials to the ionizer optics at the entrance aperture of the mass filter. To further confirm that the observed particles were passing unhindered through the mass filter, these measurements were made with the mass filter tuned to 8 amu, where no positive ion signal is expected. The time-of-flight of the metastable peak at 248 and 308 nm becomes shorter as the fluence is increased. With the ionizer optics grounded, two positive charge peaks are observed, one roughly 37 μs and the other about 100 μs after the laser pulse. The slower peak is virtually eliminated when +200 V is applied to the ionizer optics. However, the height and arrival time of the 37-μs peak are hardly affected as the voltage on the ionizer optics is raised from 0 to +1,000 V. We therefore attribute the slower peak (at 100 μs) to a ±charge cloud which has degraded the resolution of the mass filter for these particles. However, it appears that the particles responsible for the fast 37-μs peak are indeed neutral. Since ground state neutrals are not capable of producing a signal in the quadrupole detector, these particles must be in an excited, metastable state. A most likely candidate for the metastable peaks is molecular nitrogen. In its lowest vibrational level, the first excited electronic

state of N_2 ($A^3\Sigma_u^+$) has 6.17 eV of internal energy [332], more than enough to produce a secondary electron at the front cone of the quadrupole particle detector. Further, radiative transitions to the ground state are spin forbidden, resulting in a relatively long lifetime (in the order of 2 s). Although atomic N has long-lived metastable states, their internal energy (2–3 eV) is marginal at best for detection with the particle detector employed in this work. Although atomic O has suitable metastable excited states, the internal energy of the triazene group in this polymer is ideally situated for the production of excited species containing nitrogen. Therefore, we tentatively attribute the intermediate peak in Fig. 78 to metastable N_2 produced by the photodecomposition of the triazene moiety. Because both charge clouds and energetic metastable particles are difficult to perturb with electric fields, distinguishing them can be difficult in many cases. Charge clouds in particular are frequently observed from ionic materials [329–331], even at laser fluences insufficient to produce visible luminescence [229]. The difficulty in producing ion emission from most polymeric substances is consistent with the weakness of charge clouds observed in this work. Because charge clouds are observed from a wide range of materials and over a wide range of irradiation parameters, caution is advised in identifying observed species as metastable.

Other observations support the identification of the narrow peak with metastables as opposed to charge clouds. The width of the narrow peak from the triazene polymer is roughly ten percent of the mean kinetic energy—much more narrow that the energy distributions of typical charge clouds. Because most charge clouds carry a net positive charge, they tend to broaden as they travel away from the sample. It has been found that charge clouds from ionic crystals become extremely broad as the fluence is raised, even to the point of "turning around" substantial fractions of the charge cloud material so that they travel back toward the sample [333]. The detection of the narrow peak was also quite sensitive to the alignment of the laser spot with the long axis of the quadrupole detector; by way of contrast, the fluid-like properties of charge clouds render them relatively insensitive to the alignment of the laser spot with the long axis of the quadrupole detector—the component particles can "turn corners" to some degree. Taken together, these observations provide strong supporting evidence for the identification of the particles comprising this peak as metastable neutrals.

The photon energies employed in this work (4–5 eV) are insufficient to excite ground state N_2 into its lowest lying metastable state (6.17 eV) via single photon excitations alone [332]. Thus the creation of metastable N_2 may involve multiple-photon excitations or strong contributions from internal energy of the triazene group. However, the gradual decrease in the peak time-of-flight with increasing fluence suggests that energy transfer to these neutral units involves a process with much smaller quanta than single photons or high-lying metastable states. Thermal excitations, for instance, would be spaced closely enough to provide for an apparently continuous shift in peak time-of-flight. Another quite likely possibility is the energy released upon the exothermic decomposition of the triazene polymer. It was

shown above that this energy contributes to the shock wave created upon ablation in air. It is therefore possible that the decomposition energy is also important for the energy of the metastable species, and the increase of the energy with increasing fluence can be explained by an increasing amount of the decomposing polymer.

2.4.1.3 Summary

To summarize the arguments given in this chapter, it is most probably best not to paint the usual black and white picture, i.e., photothermal vs photochemical, but a more or less gray picture with different shades of gray. In the case of our designed polymers we are sure that photochemistry plays an important role, as shown by the different analytical methods. For example, the TOF-MS data about the metastable species suggest strongly the importance of electronic states, but also a possible involvement of photon thermalization or involvement of the decomposition enthalpy (ΔH) of the polymer. Many of the other data, e.g., etching during the laser pulse, low-threshold etching without modification, and etch rates of different polymers following the order of the photochemical activity, support the importance of photochemical properties. In the case of PI the picture will be more or less dark gray. Thermal processes are very important, but the pure thermal models, i.e., the interferometry data, cannot explain everything. Our DRIFT data also suggest that there are differences between the laser- and temperature-induced decomposition of PI, and that decomposition of PI takes place at very low fluences and repetition rates. This suggests that photochemical reactions are also occurring during ablation/irradiation of PI.

3 Applications

In the following chapters various applications or better possible applications for laser ablation and the designed polymers are described and discussed. The applications are either closely related to the field of microstructuring with lasers, where laser ablation might be a candidate as a dry etching technique, or utilize one of the special properties of the designed polymers, such as the exothermic decomposition, clean etching, and high etch rates.

3.1 Laser Ablation Resists (Dry Etching)

3.1.1 *Introduction*

During the last decade laser processing of polymers has become an important field of applied and fundamental research. One of the most promising

proposals, to use laser ablation as a dry etching technique in photolithography, has not yet been developed into an industrial application [334]. Many disadvantages of laser ablation, compared to conventional photolithography, are the result of the use of standard polymers. These polymers are designed for totally different applications, but have to compete with the highly specialized photoresists. Here, our new approach to laser polymer ablation is summarized, i.e., the development of polymers specially designed for high-resolution laser ablation [111]. These polymers (TC polymers) contain photolabile groups (–N=N–X–) in the polymer backbone, which decompose upon laser irradiation. Various functional groups, such as X=–N<, –S–, –N–N=N–, or phosphate, have been tested as shown and described earlier [225]. The triazene polymers with –N=N–N< as structural unit revealed the most desirable properties, e.g., formation of high-quality films, stability to storing, and one-step synthesis. The requirements for the application of laser ablation as an alternative technique to classical photolithography are: *sensitivity* (etch rate/pulse at 100 mJ $cm^{-2} \geq 100$ nm [335]); *stability* to "wet" acid etching; production of high-*quality* films by spin coating; and *resolution* of the ablation structures of ≤ 1 μm. The TC polymers, novel polymers based on cinnamylidene malonic acid ester groups (CM polymers), and polyimide (PI) were tested for the previously described requirements.

The chemical structure of the polymers is shown in Scheme 15.

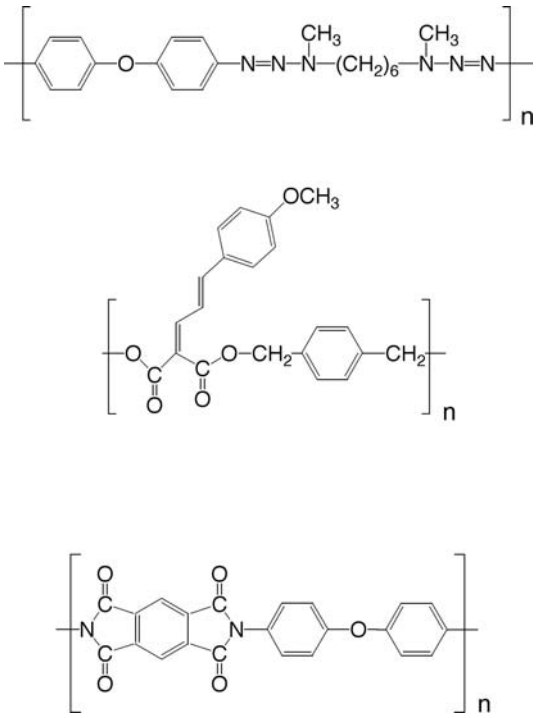

Scheme 15 Chemical structures of the polymers; from *left to right*: TC, CM, PI

3.1.2 *Results*

The laser ablation characteristics of the polymers, i.e., TC polymer, CM polymer, and PI, were studied at high (>0.5 J cm^{-2}) and low fluences (at 308 nm). All polymers can be characterized as highly absorbing polymers (α_{lin}>100,000 cm^{-1}). The relevant physical data are summarized in Table 5. PI was chosen as a benchmark to compare our designed specialty polymers with a well-studied, commercial polymer, which was not designed for laser ablation. At high fluences no pronounced differences between the polymers are detected. This is not unexpected, because the ablation characteristics at high fluences are governed, for strongly absorbing polymers, by effects such as plasma absorption and other shielding effects [56]. At low laser fluences pronounced differences between the different polymers are detected. The data were analyzed according Eq. 1. The parameters calculated from the fits are listed in Table 5.

The etch rates at a given fluence are obtained from the slope of linear plots of the etch depth vs the number of pulses delivered at a given fluence. For all polymers linear relations were obtained. A comparison of the etch rates/pulse at low fluences for the different polymers is shown in Fig. 79.

The TC polymer reveals the highest etch rates and lowest threshold fluence, followed by the CP polymer, and PI. The detailed analysis of the data in Table 5 confirms that the designed polymers (TC and CM polymers) pass the *sensitivity* criterion, while PI fails. The difference in the etch rates between the TC and CM polymers can be explained in a first estimate by the higher photochemical activity of the TC polymers (in solution more than a factor of 2). The *resolution* of the ablation structures for all polymers is within the desired limits, but in the case of PI carbonization inside the ablation structures and in the surroundings of the structures, due to redeposition of ablation products, was detected [276]. The designed polymers decompose mainly into gaseous products, which do not contaminate the surface after ablation [225]. The *quality* of the films is also sufficient. For solvent-cast films, an average roughness from 8 to 10 nm was detected with a profilometer (scan length 100 μm), while for a spin-coated TC film a roughness of 1.5–2.0 nm was detected by atomic force microscopy (scan length 10 μm) [325]. As a last test the *stability* of the tailored polymers to wet "acid" etching is examined. A thin polymer film was immersed in a HNO_3 (42 wt%)/HCl (3.6 wt%)/H_2O (54.4 wt%) mixture (standard mixture for etching Al wafers) for 1 min, and

Table 5 Physical and ablation data of the various polymers

	TC polymer	CM polymer	Polyimide
α_{lin}/cm^{-1}	116,000	32,000	95,000
α_{eff}/cm^{-1}	50,000	57,000	83,000
F_0/mJ cm^{-2}	27	48	60
d (100 mJ cm^{-2})/nm	267	128	61
d (10 J cm^{-2})/μm	2.1	1.88	1.89

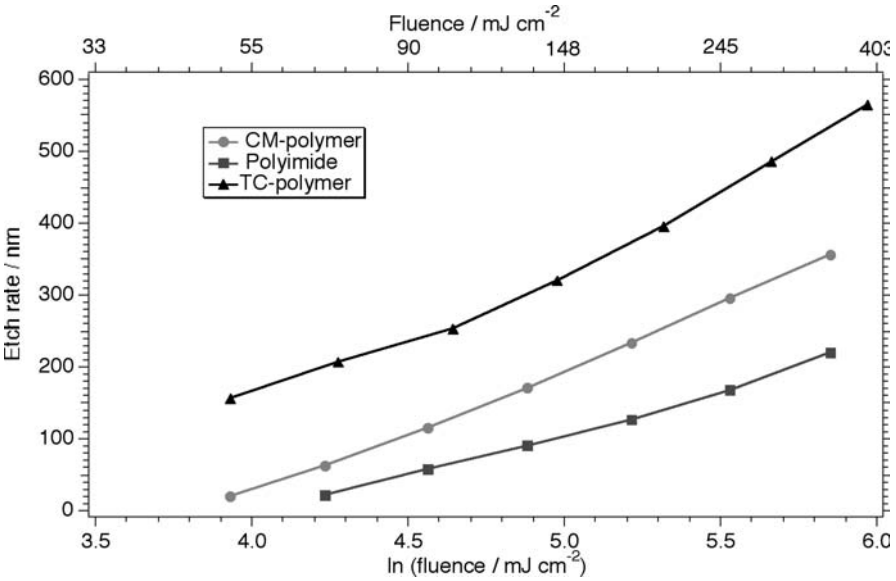

Fig. 79 Etch rates vs laser fluence of the various polymers. REPRINTED WITH PERMISSION OF [Ref. 118], COPYRIGHT (2000) Elsevier Science

UV-Vis spectra were recorded before and after immersion. The TC films decomposed totally, while the CM polymer films revealed nearly no changes in the spectra. This shows that the CM polymers are stable under wet acid conditions, and therefore pass the *stability* criterion.

3.1.3 *Summary*

Several polymers were tested for application of laser ablation as an alternative to a photolithographic process. The polymers, which were especially designed for laser ablation, revealed a higher sensitivity than a commercial polymer with a similar absorptivity. The most sensitive polymers are based on the triazene chromophore (–N=N–N<), which is unfortunately also sensitive to subsequent processing steps, i.e., wet etching. The polymers based on the cinnamylidene malonic acid ester group did not only show a sufficiently high sensitivity, but also stability to wet etching, high film forming and ablation quality. This proves that it is possible to apply laser ablation as an alternative photolithographic technique, if the polymers are especially designed for this application.

3.2
New Stable Resists–Combined Positive-Negative Resists

3.2.1
Introduction

The development of the designed ultrasensitive polymers now allows fast and efficient structuring of polymers using 308-nm irradiation [111, 336]. With this approach high-resolution structuring of the polymer is possible, but the irradiation area is limited by the laser beam size. In a production environment many structures must be fabricated in the shortest possible time and with a minimal use of expensive techniques, e.g., laser photons. A "pure" laser process would be slow and tedious for the creation of arrays of structures, e.g., microlens arrays, on a large substrate. To overcome this limitation, novel photopolymers have been developed which can be used as classical negative (cross-linking) resists, but still exhibit very high sensitivity towards laser direct structuring. These polymers are based on polyesters containing cinnamylidene malonic acid groups (CM polymers) which undergo photocross-linking upon irradiation at λ>395 nm and laser direct structuring at λ=308 nm [128]. The CM polymers are also specially designed for excimer laser lithography using the XeCl excimer laser (308 nm) and pass the fundamental test for laser resists described in the previous chapter [126]. The order of processing, i.e., first negative then positive (−/+) structuring or vice versa (+/−) does not affect the quality of the structures on a micrometer scale. Such a combined process was to our knowledge only reported once, but for a different and even more complex technique, i.e., ion-beam irradiation [337].

3.2.2
Results and Discussion

The structure and cross-linked structure of the CM polymers is shown in Scheme 16. The photodimerization, i.e., 2+2 cycloaddition, of cinnamate side chains [338] is a classical method of polymer photocross-linking, e.g., used

Scheme 16 Structure of the cinnamylidene malonic ester polymer (CM) before and after cross-linking with λ>395 nm for 20 min and 100 mW cm^{-2}. REPRINTED WITH PERMISSION OF [Ref. 120], COPYRIGHT (2000) Wiley-VCH Verlag GmbH

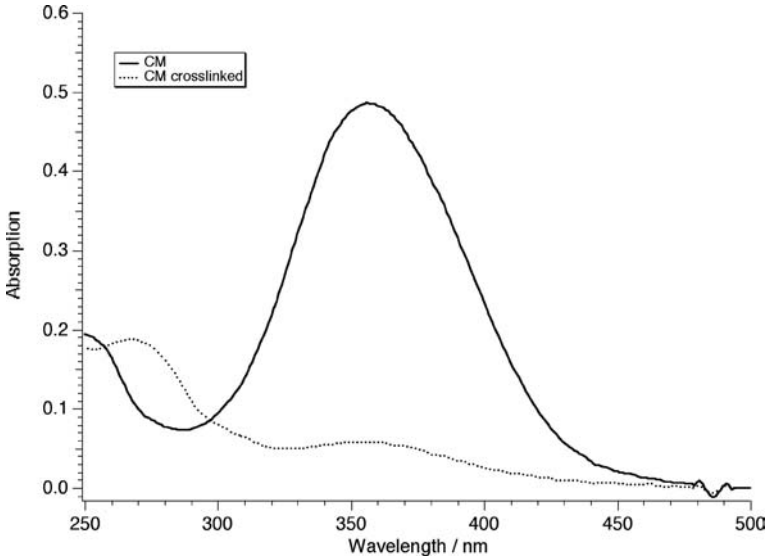

Fig. 80 UV-Vis spectra of the CM polymer (R=*p*-OCH_3) before and after cross-linking. The *insert* shows the result of a ZINDO calculation of the UV-Vis spectra of a model repetition unit. REPRINTED WITH PERMISSION OF [Ref. 120], COPYRIGHT (2000) Wiley-VCH Verlag GmbH

in the KPR Eastman Kodak resist which has otherwise a very different chemical structure. During cross-linking a cyclobutane system is created, which has a shorter wavelength absorption maximum than the cinnamate group.

The UV spectra (R=*p*-OCH_3) before and after cross-linking are shown in Fig. 80. Semiempirical methods (MOPAC/ZINDO) were used to calculate the absorption spectrum of a repetition unit of the CM polymer. It was derived from the calculations that the absorption maximum in the UV spectrum (at 357 nm) is mainly due to transitions which involve the whole cinnamylidene malonyl system. The calculated spectrum (ZINDO) is shown as an insert in Fig. 80. The shape of the spectrum is quite similar to the experimental spectrum, but the calculated absorption maximum is shifted to longer wavelengths (by ~80 nm). Several factors will lead to differences between calculated and experimental spectra. The calculated spectra are for gas-phase molecules, while the experimental spectra are taken from thin films. This leads to modification of the molecule's electronic states due to intermolecular interactions. Additionally, model compounds are used for the calculations due to the limited number of atoms allowed in ZINDO. The absorption maximum of the CM polymers can be shifted between 328 and 357 nm by varying the substituent R of the phenyl ring [125]. The synthesis of the CM polymers is described in detail elsewhere [125]. In all following experiments the CM polymer with R=*p*-OCH_3 is used which allows fast and selective photocross-linking of the polymer at $\lambda_{irr} \geq 395$ nm. This results in the development of an insoluble polymer network, but also a reduction of the absorp-

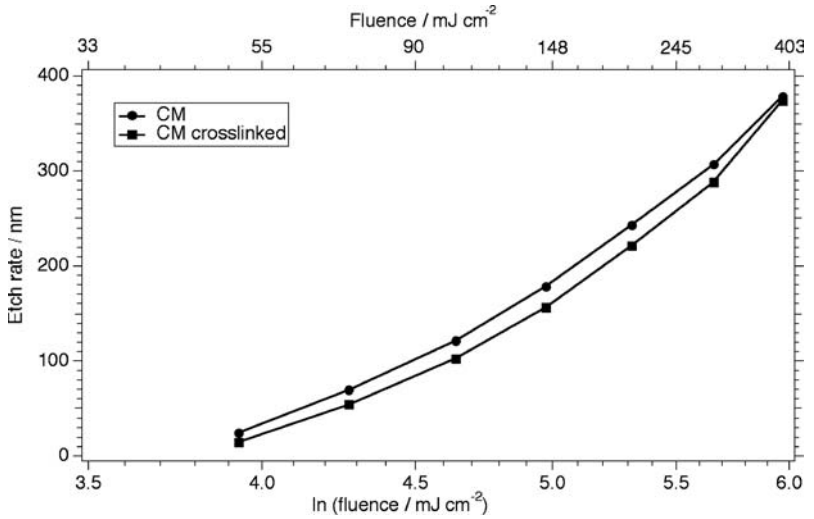

Fig. 81 Ablation rates per pulse, d, as a function of the laser fluence, F, for the CM and CM_{cross} polymer. REPRINTED WITH PERMISSION OF [Ref. 120], COPYRIGHT (2000) Wiley-VCH Verlag GmbH

tion coefficient, i.e., from 32,000 to 17,000 cm^{-1} at the irradiation wavelength of the XeCl laser (308 nm). The cross-linking rate was not determined in detail but infrared spectroscopic data suggest rates higher than 50%.

The etch rates of the polymer before (CM) and after cross-linking (CM_{cr}) are determined at moderate laser fluences (<500 mJ cm^{-2}) to test whether crosslinking has a pronounced influence on laser ablation. The comparison of the two etch rates is shown in Fig. 81. A slightly lower etch rate is obtained for the cross-linked polymer. This is probably due to the lower absorption coefficient at the irradiation wavelength, or less likely to an improved mechanical stability of the cross-linked polymer. One of the most important features of polymer laser ablation is the existence of a sharp threshold fluence for material removal [57]. Below this material-dependent laser fluence *no* laser ablation can be observed, while photochemical decomposition/reactions can take place within the polymer film. The threshold fluence, F_0, can be calculated according to Eq. 1. The calculated threshold fluences are 48 and 53 mJ cm^{-2} for CM and CM_{cr}, respectively, showing that only slightly higher laser fluences are necessary for the cross-linked polymer. The effective absorption coefficients are more or less the same for both polymers, i.e., 57,000 cm^{-1} for CM and 58,000 cm^{-1} for CM_{cr}. Maximum etch rates of 1.54 μm for CM and 1.54 μm for CM_{cr} can be obtained at high laser fluences, i.e., here 6.3 J cm^{-2}.

To prove that the concept of combining the characteristics of positive and negative resists (with laser ablation as positive etching) is applicable, a complete combined process was carried out. We would like to emphasize that for this proof of principle, a very simple experimental setup was used

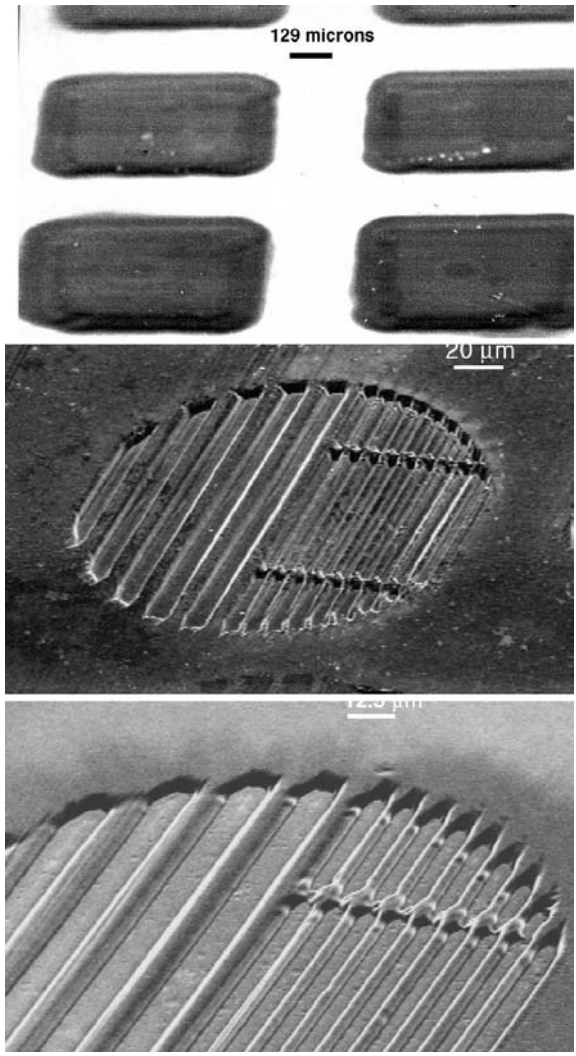

Fig. 82 SEM pictures of the CM polymer after cross-linking. *Top*: after wet development in $CHCl_3$; *middle*: structuring of the cross-linked and wet developed polymer (from top SEM) (1 pulse with 7.9 J cm^{-2} at 308 nm); *bottom*: inverse processing, i.e., first laser structuring, then cross-linking and wet development. REPRINTED WITH PERMISSION OF [Ref. 120], COPYRIGHT (2000) Wiley-VCH Verlag GmbH

and neither the solvent system for the negative development nor the cross-linking parameters were optimized. A brass mask (100-μm thick) with a rectangular pattern was placed on a thin (3 to 5 μm) polymer film on a quartz wafer, cast from $CHCl_3$ as the solvent. This setup is roughly representative of proximity illumination. Then the film was irradiated through the mask pattern with a Xe lamp equipped with a filter (λ_{Irr}>395 nm) for

20 min at a power of 100 mW cm^{-2}. The irradiated film was developed by immersing CM_{cr} into chloroform for 10 s, which is a good solvent for CM. A scanning electron microscope (SEM) picture of the developed, negatively structured film is shown in Fig. 82 (top). The size of the remaining polymer squares is slightly larger than for the mask pattern (520 μm) and also exhibits sloping walls. This is most probably due to the nonoptimized experimental conditions, i.e., proximity illumination, illumination time, solvent system, and development time. An excessively long illumination time, for example, will cause cross-linking under the mask edges, i.e., widen the cross-linked area, due to multiple reflections between the mask and the polymer surface. The cross-linked polymer squares were subsequently irradiated with a XeCl excimer laser, through a copper mask with a varying slit pattern, which was demagnified with a reflective objective. The SEM picture in Fig. 82 (middle) shows the microstructures obtained with a single pulse at 7.9 J cm^{-2}. Our experimental setup does not allow a precise alignment of the structuring beam. Therefore, multiple structures within the polymer squares are created. In the upper part of the SEM picture an additional structure is visible. The microstructures, obtained with single pulses at 7.9 J cm^{-2}, are well resolved and show a resolution close to the limits of our setup (~1 μm). This proves our concept to combine classical negative resist properties with laser ablation.

To test whether there is a preferential order of processing steps, i.e., first negative development and then positive laser structuring or vice versa, a polymer film was first structured with the laser, then cross-linked and developed in $CHCl_3$. The microstructure (Fig. 82, bottom) reveals the same quality (as far as we can judge from SEM pictures) as the structures obtained for the experiments with the opposite sequence. Of course volume shrinkage upon cross-linking is expected, but was not determined in this study, where only the feasibility of the +/− concept was the aim.

3.2.3 *Summary*

In summary, novel polymers, based on cinnamylidene malonic acid groups, were designed which combine two key properties for polymer processing: they are highly sensitive to laser ablation at a specific irradiation wavelength, and they can act as a classical, negative photoresist. The laser ablation step is used to fabricate microstructures, while the classical wet processing is used for large area structuring. After cross-linking the photopolymers exhibit nearly the same high sensitivity to laser ablation. Combined processes of cross-linking–wet development, laser microstructuring, but also vice versa were carried out. No preferential order of processing was found, which clearly proves the feasibility of our concept, which allows us to combine the strengths of both methods.

3.3
Laser Ablation–Implantation

3.3.1
Introduction

Laser ablation studies of polymers sensitized with aromatic molecules [75] have recently led to the report of a new process called Laser Molecular Implantation (LMI) [339]. This involves the transfer of aromatic molecules from a doped polymer film source to a neat target film firmly in contact, using low-intensity pulsed UV laser radiation. Careful examination of the target surface fails to show polymer ablation traces if the number of laser pulses is kept low, and since the transferred molecules show no apparent evidence of decomposition, this process has attracted some interest. Useful medical and technological applications could emerge by further developing LMI. At present, the aim is to gain a more concrete understanding of that process and to resolve the mechanism behind it. A thermally activated molecular diffusion mechanism has been suggested [340] to support the experimental evidence so far, distinguishing LMI in this fashion from the already established laser ablation transfer (LAT) process [341]. The low-intensity laser radiation below the ablation threshold will be absorbed only by the dopant molecules in the source film via a cyclic multiphotonic absorption scheme according to this mechanism [97]. This repetitive molecular excitation and rapid relaxation via an internal conversion process will efficiently convert most of the absorbed photon energy during each pulse into heat, and result in the temperature rise of the surrounding polymer. In this manner, the mobility of the dopant molecules will suddenly increase and diffusion will be allowed between the solid polymers at high rates resulting in molecular implantation at shallow depths in the neat polymer surface. Here, we investigate the laser-induced transfer of aromatic molecules under ablation conditions. A triazene polymer, Scheme 5, characterized for its explosive decomposition upon exposure to UV laser wavelengths [342] is doped at low concentration with pyrene which shows negligible absorption at the irradiating wavelength. The aim is to investigate the influence of the laser-induced exothermic triazene polymer photodecomposition on the efficiency of molecular transfer at the source–target polymer interface. The choice of a fluorescent molecule as a dopant was mainly for the convenience of visualization during the detection phase. It is shown for the first time that intact molecular transfer between solid polymer films is possible under laser ablation conditions, maintaining the smooth surface character of the receiving polymer without signs of particle contamination. The process becomes more efficient as the laser pulse number increases while keeping the intensity at a low level.

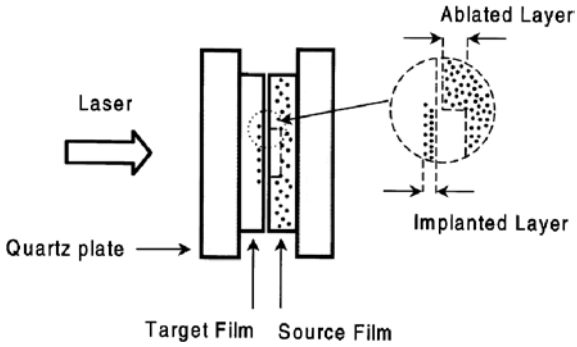

Fig. 83 Schematic diagram of the laser-induced molecular transfer process. REPRINTED WITH PERMISSION OF [Ref. 360], COPYRIGHT (1998) Elsevier Science

3.3.2 *Experimental*

A scheme of the experimental setup is shown in Fig. 83, where a laser beam (355 nm, 3 ns) is directed from the rear of the target film onto the triazene polymer film (doped with pyrene) as shown in Fig. 82. The laser fluence was estimated by averaging the total energy of the incident beam over the irradiated area. The target films [poly(butyl methacrylate), PBMA, T_g=293 K and poly(ethyl methacrylate), PEMA, T_g=338 K] were characterized with a fluorescence microscope and a conventional spectrofluorometer.

3.3.3 *Results and Discussion*

Figure 84 shows a sequence of fluorescent (a and b) and optical microscopic images (c and d), comparing laser molecular transfer into PBMA or PEMA target polymers. Five laser pulses of fluence 200 mJ cm^{-2} were used to ablate the pyrene-containing triazene polymer, almost ten times greater compared to the ablation threshold value of 20–25 mJ cm^{-2}. The laser spot size was restricted to a circle of 200-μm diameter. Blue emission was observed in both cases from a circular pattern of similar dimensions at the center of the fluorescent images and specifically, in the PEMA case, some additional yellowish emission was also visible. Presumably the emission emanated from the transferred molecules excited with probe light from a continuous UV source between 330–380 nm, and was observed beyond 420 nm.

It is interesting that the fluorescing region of the PBMA surface looks smooth and uncontaminated in a conventional micrograph (Fig. 84c) without any material deposition, implying that most of the transferred molecules are fully embedded beneath the surface layer. In contrast, scattered aggregate-like structures are clearly visible in both optical and fluorescent images

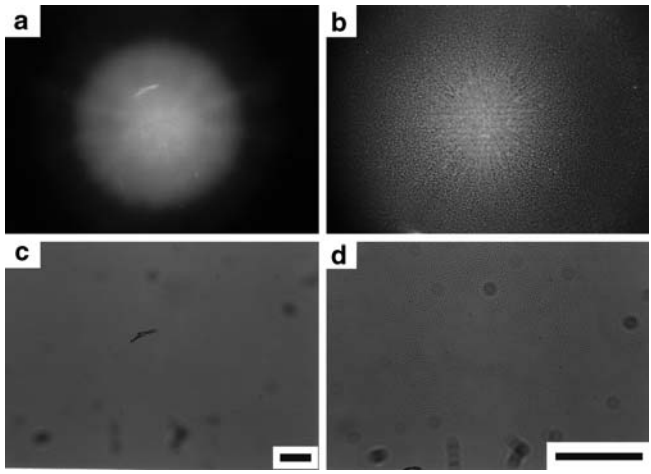

Fig. 84 Comparison of fluorescence and optical microscopic images of poly(butyl methacrylate) PBMA (**a**) and (**c**), and poly(ethyl methacrylate) PEMA (**b**) and (**d**) target polymer surface following 355-nm laser-induced molecular transfer of pyrene contained in triazene polymer. Irradiation dose: 5 pulses, 200 mJ cm^{-2}. The *bar* denotes 100 μm in each case. REPRINTED WITH PERMISSION OF [Ref. 360], COPYRIGHT (1998) Elsevier Science

of the PEMA surface around and inside the irradiated area (Fig. 84b and d). These could presumably relate to condensed partially decomposed triazene polymer ablation products. The exact origin of the observed emission is clarified by the pyrene fluorescence spectra shown in Fig. 85. They were

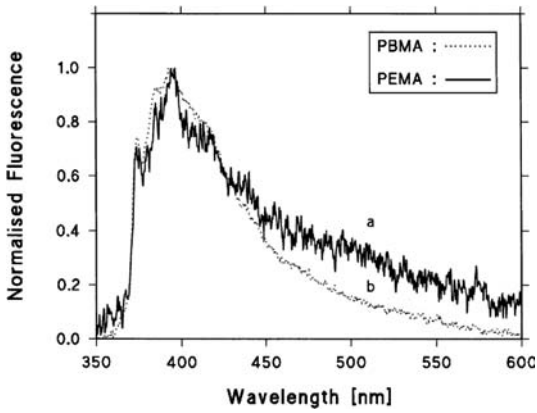

Fig. 85 Fluorescence spectra from the target polymer surface of (**a**) poly(ethyl methacrylate) PEMA and (**b**) poly(butyl methacrylate) PBMA, following 355-nm laser-induced pyrene transfer using ablation of a triazene polymer. Irradiation dose: 10 pulses, 100 mJ cm^{-2}. REPRINTED WITH PERMISSION OF [Ref. 360], COPYRIGHT (1998) Elsevier Science

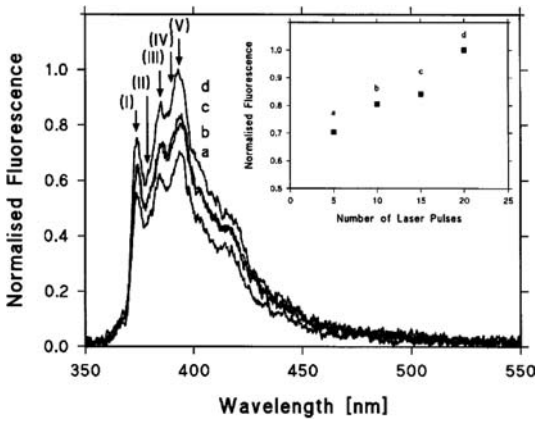

Fig. 86 Fluorescence spectra of a pyrene-implanted PBMA surface as a function of laser pulse number. Pyrene was transferred using ablation of a triazene polymer. Laser fluence: 100 mJ cm^{-2}, (**a**) 5 pulses, (**b**) 10 pulses, (**c**) 15 pulses, (**d**) 20 pulses. The vibrational pyrene emission peaks are denoted (I–V). *Inset*: Normalized fluorescence intensity of the V pyrene peak at 393 nm vs laser pulse number. Data are taken from the spectra in the main figure. REPRINTED WITH PERMISSION OF [Ref. 360], COPYRIGHT (1998) Elsevier Science

recorded from the center of the emitting spot for both PBMA and PEMA target polymers using light excitation at 335 nm and were corrected for scattering.

Ten laser pulses with a fluence of 100 mJ cm^{-2} were used to ablate the pyrene-containing source film. For the PBMA case, the fluorescence emission clearly originated from implanted pyrene existing in monomer form. This was also verified by UV absorption spectroscopy of the implanted surface, exhibiting a strong absorption band around 300–340 nm in good agreement with the S_2–S_0 absorption band of pyrene. Additionally gas chromatographic–mass spectrometric analysis (GC–MS) of a methanol extract, produced by rinsing the implanted surface, exhibited only one peak in the chromatogram related to the pyrene molecule. These results clearly indicated that intact pyrene molecules were transferred by laser irradiation. In comparison, the fluorescence spectrum recorded from the pyrene-implanted PEMA surface exhibits a wide tail towards longer wavelengths (430–600 nm) which is a characteristic of excimer-like structures, suggesting that pyrene aggregates may be formed on the higher T_g polymer surface, which justifies the yellow emission observed. A similar tendency is observed with PEMA irradiation at higher fluence. In order to avoid the complexities of pyrene aggregation in our qualitative analysis, we used only PBMA to study the effect of laser intensity and pulse number on the efficiency of laser molecular transfer. It was observed (Fig. 86) that by increasing the laser pulse number, taking care to avoid a complete etch through of the thin TP film, the fluorescence intensity emitted from the target film was enhanced. The vibrational peak of the pyrene emission at 393 nm (peak V) was used as probe. As this signal is less

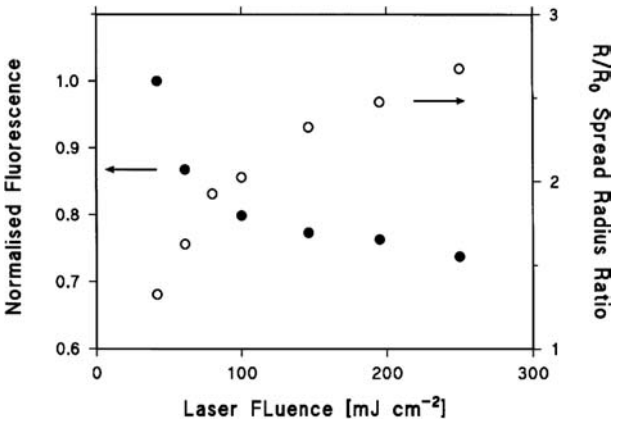

Fig. 87 Normalized fluorescence intensity of the V pyrene peak at 393 nm from an implanted PBMA surface and ratio of pyrene spread radius R to laser spot size radius R_0 as a function of laser fluence. Number of laser pulses: 10. REPRINTED WITH PERMISSION OF [Ref. 360], COPYRIGHT (1998) Elsevier Science

dependent on dielectric properties of the medium [343], it is a more reliable measure for comparing the amount of pyrene molecules transferred. The mentioned increase is in obvious agreement with expectations, since more pyrene molecules become available for transfer with repetitive etching of the source film.

In contrast, Fig. 87 shows a slow decline in the (V) peak fluorescence intensity accompanying the growth of laser fluence. This effect was confirmed regardless of the laser spot size varied between 200 μm and 1 cm diameter, and was partly attributed to a uniform spreading of pyrene around the irradiated area on the target surface. This is illustrated in Fig. 87 by plotting the ratio of the pyrene spread radius R to the laser spot radius R_0 as a function of laser fluence. For the higher fluence range pyrene was found to stretch nearly as far as three times the irradiated spot size, suggesting that the hydrodynamic expansion of the TP decomposed products between the two films plays a key role in this process. Nevertheless a measure of the peak fluorescence intensity ratio (I/V) showed a slight decline with increasing laser fluence, suggesting that the polarity of the receiving polymer decreased [343]. This could be the result of either an increase in density of the embedded pyrene in the target polymer or a contribution from TP photoproducts on the target surface increasing with laser fluence. A fluorescence quenching mechanism due to TP ablation products embedded together with pyrene in the target film could be involved in the observed decline of fluorescence intensity in Fig. 87.

Although laser ablation of neat TP in air results in efficient decomposition to low molecular weight products [111], it was found in the current study to produce small amounts of biphenyl derivatives condensed at the target surface, presumably produced by partial TP photodecomposition. These prod-

ucts exhibit a broad absorption band peaking at substantially shorter wavelengths (~260–270 nm) compared with the pyrene fluorescence emission peak (~400 nm), and therefore their production during the ablation of pyrene-containing triazen -polymer is not expected to quench the pyrene fluorescence by energy transfer. Nevertheless a charge-transfer mechanism between these molecules and implanted pyrene cannot be totally excluded, which would contribute to a fluorescence quenching process [344]. The low molecular weight photoproducts, such as nitrogen [111] obtained from the TP explosive photodecomposition, will expand their volume rapidly away from the irradiated area due to a high local pressure. Since the process follows a photochemical decomposition route [172], the surface temperature is not expected to rise to high levels. Assuming a condition at the very early stage of decomposition where the polymer properties are still unchanged and energy is released only by the ablated products, i.e., hot gases, small fragments etc., an estimate for the lowest limit of their temperature rise can be made from the measured specific enthalpy of decomposition ($\Delta H = -255.1$ kJ mol^{-1}) [111], and is found to vary between 400 and 500 K for the average fluence range of this experiment. Although this temperature is not considered high enough to cause significant pyrene thermal decomposition [345], it can affect the surface properties of the target polymers in contact. These polymers exhibit relatively low T_g values, and it is reasonable to assume that pyrene molecules will be enabled to diffuse into inner layers below their surface if a free volume expansion is maintained for a sufficient time by the temperature rise. This process competes with the supersonic propagation of the ablated products [172]. The high pressure exerted from their fast-traveling leading front will violently repel the target polymer, transiently creating a thin channel between them and suspending the film contact around the irradiated area. One might expect that the subsequent gas expansion in the generated free space would result in the multiple reflections between the two polymer films, thereby reducing the temperature of the ablation products at the same time. In this manner, the pyrene molecules contained in the expanding cloud might be horizontally propagated along the surface of the target polymer, spreading uniformly to a wider range as compared to the laser spot size. This effect will be enhanced as laser fluence increases. As the higher T_g target polymer shows a limited elastic behavior to the pressurized gas propagation, pyrene molecules will be hampered from penetrating into the inside and will eventually accumulate on the surface. For PEMA, this effect could be manifested by the observation of pyrene excimer formation due to the high local concentration on its surface. Hence, it is expected that pyrene is located both beneath and above the target surface. The low-T_g polymer will enable dopant diffusion more easily, and therefore increase the implantation efficiency under the same irradiation conditions. Although a measure of the implanted depth is not given here, it is typically expected to be in the range of a few tens of nm [339]. Significant dopant photodecomposition is not believed to take place in either source or implanted target polymer during the laser molecular transfer, since pyrene shows negligible absorption at the irradiating wavelength

(α_{pyrene}=109 cm^{-1}). In general it is considered that condensed aromatic molecules are more stable at high temperatures in comparison with other structures [345], and so it can be assumed that only a minimum amount of the dopant might be thermally decomposed which would not affect seriously the main character of the process. The lack of pyrene derivatives in the target polymer (from the GC–MS analysis) is surprising though, since they would be expected to be formed by reactions with radicals produced by the exothermic TP photodecomposition. In conclusion, it is found that intact pyrene molecular transfer between solid polymers in contact can be achieved by using laser ablation of an explosively decomposing triazene polymer. The efficiency of the process is enhanced by increasing the laser pulse number and reducing the glass transition temperature of the receiving film. The spatial resolution of the transferred image becomes poorer, though, with increasing laser fluence due to a horizontal molecular spreading.

3.3.4
Conclusion

The LMI method allows mixing of otherwise incompatible materials in thin layers (nm) of solid materials. It has been shown that implantation with a lateral resolution in the nm range is possible and that even reactions can be carried out (by implanting different molecules) on a nm scale.

3.4
From Micro- to Nanostructuring

3.4.1
Introduction

In the following chapters some examples of micro- and nanostructuring are presented. Below, a short general introduction to micro- and nanotechnology are given, because they are used as keywords in many aspects of life and science (especially for funding). Microtechnology and microstructuring are already well-known terms and techniques, and therefore only a few facts are given in this introduction. Nanotechnology, on the other hand, is a relatively new field and more information is given below.

3.4.1.1
Microtechnology

A few years ago, the microtechnology industry was science's "poor relation", but in recent years it has enjoyed an almost meteoric rise in public profile, mainly thanks to successes in the fields of analysis, biotechnology, and medical engineering. Its uses also extend to automotive engineering, print technology, and electronics. The industry's sales for the year 2000 are >$50 billion and the next few years should see phenomenal growth. The integration

of MEMS, micromachines, and microsystems into machinery and equipment is changing how we live, work, and play. These devices are making manufacturing processes more efficient, cars and workplaces safer, computers faster, our homes more comfortable, and surgical procedures less invasive. Although once measured only in microns, research and commercialization have expanded the range from submicrons to millimeters. These devices, primarily microsensors, microactuators, and microsystems (a combination of the first two), are tiny, and generally manufactured in mass quantities using one of three fabrication techniques. In the vast majority of applications, only a small percentage of manufacturers are currently including micromachined parts in their equipment, but that percentage is slowly and steadily growing. The manufacture of these devices for a growing number of applications has been climbing at a rate of 20% to 30% per year since 1990, and this strong growth is likely to continue due to the fact that many devices currently being developed will not hit the market for at least ten years.

3.4.1.2 Nanotechnology

With the discovery of manipulation techniques of the individual constituents of matter, as well as the increasing insights into self-organization principles of these entities, a worldwide industrial conquest of nanoscale dimensions began. Purely geometrically, the prefix “nano” (Greek: dwarf) describes a scale 1,000 times smaller than that of present construction elements of the micrometer-scale (1 nm corresponds to a millionth part of a mm). The nm scale has become accessible both by application of new physical instruments and procedures and by further diminution of present microsystems. Also, structures of an animated and nonanimated nature were used as models for self-organizing matter. If the mastery of this atomic and molecular dimension succeeds, the prerequisites for the optimization of product properties within the areas of energy engineering (gas cells, batteries, solar cells, etc.) and environmental technology (material cycles, disposal, cleaning, etc.), as well as in information technology (high-density memories, efficient processors, etc.), health, and aging can be further enhanced. The primary aim of nanotechnology is the utilization of new functions, which are based either on geometrical size or on material-specific peculiarities of nanostructures. With the conquest of this nanometer dimension, the speed of innovation achieved in the meantime led to the situation that physical fundamentals are still being investigated while first product groups are already entering the world markets. So far two ways in the generation of nanosystems have been taken and pursued in research and development within the respective fields.

On the one hand, we tried to understand and utilize processes running in animated nature. With the growing understanding of the principles of self-organizing structures and functional units, the knowledge was applied particularly within the areas of life-scientific research and for the development of new materials.

On the other hand, the technology of nonanimated structures was making headway into the nanometer dimension by constantly manufacturing smaller structures and basic elements of new materials. Realizations derived by these experiences supplied contributions especially to the fields of electronics, optoelectronics, and sensor technology. The most promising nanotechnological lines of development can be divided into five groups:

1. Ultrathin layers (e.g., transparent dirt deflectors, energy-saving reflector layers, implants with greater longevity).
2. Lateral nanostructures (e.g., Fresnel optics, diffraction gratings, lithography masks, memories/terabit chips, quantum-, molecular-, opto-, vacuum, and nanoelectronics, e.g., diode lasers with pyramid-shaped nanoquantum points, and quantum wires).
3. Ultraprecise surface figuring (e.g., optics with accuracy in the nm scale, i.e., stepper optics, x-ray-optics, infrared optics, diffractive optics, laser mirrors).
4. Analysis of nanostructures (e.g., instrument technique [i.e., profilometers/interferometers, microscopes, scanning probes, positioning items], nanolaboratory analysis and structuring, nanoparticle catalysis research, single-molecule analysis).
5. Nanomaterials and molecular architectures (e.g., zeolite reactors, nanocomposite ceramic process technique, resists, NLO elements, catalysts with increased surface, systems of compact nanomaterials, i.e., membranes, polymers, light-absorbing material, aerogels, light emitters).

The prerequisites for a technological change leading to new product generations are the availability and usage of production and structuring technologies up to manipulations in the atomic scale. The driving strength is thereby the advancement from microelectronics to nanoelectronics. In this way it is necessary to make use of new physical interaction mechanisms, whose causes are based on the transition from continuum physics to quantum physics. For more than ten years now, intensive efforts have been made in order to produce geometrically limited structures for the elucidation of quantification effects in mesoscopic systems. For the future production of sub-100-nm-scale structures, most diverse ideas are being discussed. These refer usually to projecting, but also to serial writing techniques with light and particle beams.

The actual production of structures deals with particles smaller than 100 nm. Up to this day, it has remained a domain of electron-beam lithography. But this follow-up technology of optical exposure is too slow for mass production, too. Therefore, diverse writing techniques are specified in view of their field of deployment.

1. Nanoimprint: stamping with precision.
2. Lithography with light forces (e.g., SNOM).
3. Manipulation of atoms and molecules (e.g., AFM, STM).
4. Dusty plasmas (plasma-assisted growth of nanoparticles and clusters).

In the following chapters both worlds (the present micro- and the future nano-world) are shown, from the perspective of lateral structures using laser ablation and/or the specially designed polymers. Selected examples/applications of microstructures (diffractive gratings, Fresnel lenses) and possible future writing techniques (AFM and SNOM) are presented.

3.4.2 *Interference Gratings*

3.4.2.1 Introduction

Gratings, especially diffraction gratings, are fabricated using two different processes. Mechanically ruled gratings are fabricated with diamond tools, whereas interference (sometimes called holographic) gratings are fabricated with light. Interference gratings have the advantage that there exist no errors in ruling compared to mechanically fabricated grooves. In addition, interference gratings are entirely free of small periodic or random groove placement errors, found on even the best mechanically ruled gratings [346]. This gives significant advantages for spectroscopic systems in which light is performance limiting (e.g., Raman spectroscopy of solids).

Gratings having micron to submicron periodicity have other important applications in optoelectronic devices (e.g., Bragg-type filters) [347] and for alignment of liquid crystals [348]. The standard technique for the fabrication of these gratings is the irradiation of a photoresist followed by various development and dry etching processes [349]. These are relatively complicated, time-consuming technologies. Many different approaches for the direct writing of gratings in polymers and glasses have been developed. For example, using polarized UV laser beams and fluences *below* the threshold of polymer ablation, laser-induced periodic surface structures are formed (LIPSS) [350, 351]. Gratings with spacings in the submicron range can be produced in this way. The process has some difficulty in reproducing gratings with exactly the same spacing [352] and it is still a relatively time consuming process, needing several hundreds of laser pulses. Laser ablation, on the other hand, offers an alternative, simple technique for grating generation. Grating-like structures can be produced under ablation conditions (laser fluences above the ablation threshold) from stretched polymer films [52, 353, 354]. A completely different approach uses a photocurable monomer and a contact mask (using the volume contraction of the polymer and diffusion of the monomer into the polymerization area) [355]. Faster techniques for highly reproducible gratings use phase masks [356, 357], Talbot interferometers [358, 359], transmission gratings with imaging optics [360], and Michelson interferometers [361]. All of these techniques use laser fluences above a certain material-dependent threshold. The resulting gratings range in size from micron to sub-100-nm-size spacing, and are highly reproducible. Single pulse grating formation has been reported only recently [347].

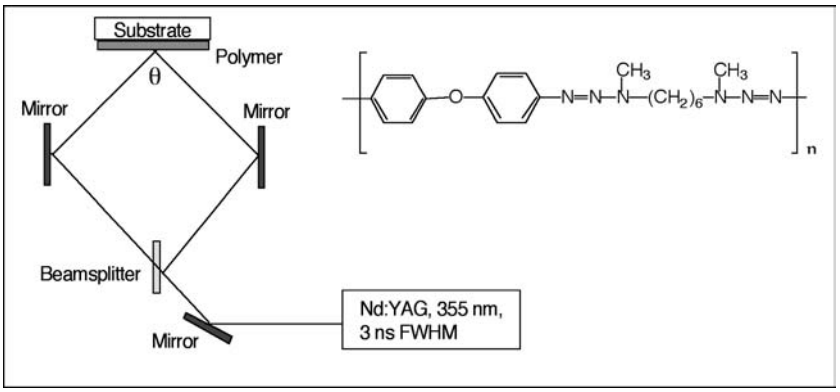

Fig. 88 Experimental setup with inserts of the chemical structure of the polymer. REPRINTED WITH PERMISSION OF [Ref. 326], COPYRIGHT (1999) American Institute of Physics

The single- and multiple ($\leq$10 pulses)-pulse grating formation in a photodecomposable polymer at 355 nm using a Michelson setup is shown in Fig. 88. The polymer was chosen because of its high sensitivity [68, 111], the possibility of a photochemical ablation mechanism [133], and the absence of solid ablation products [172] which could contaminate the surface, lowering the grating quality or necessitating additional cleaning steps. The linear absorption coefficient of the polymer at 355 nm is $\approx 1.15 \times 10^5$ cm^{-1}. The spacing of the grating, s, can be varied according the equation

$$s = \frac{\lambda}{2 \sin\left(\frac{\theta}{2}\right)} \tag{29}$$

by changing the intersection angle θ (λ is the laser wavelength, here fixed at 355 nm). The grating formation (depth and spacing) was determined by AFM. Two different spacings, s, of $\approx$1.09 μm and $\approx$180 nm, respectively, were created at two different laser fluences and with single and multiple laser pulses. The grating spacing of 180 nm was chosen because it is close to the theoretical limit of $\lambda/2$.

3.4.2.2 Results and Discussion

Well-defined interference gratings with spacings corresponding to the expected values were found for single-pulse experiments. The quality of the gratings is at least as good as the best previously reported gratings formed in polymers by direct writing methods. The gratings formed here are much deeper than the gratings described in Refs [356–361] or for single-pulse gratings in PI. Gratings with a spacing of 1 μm and a depth of about 80 nm could be achieved. However, scanning electron microscope results suggested that some ablation products (debris) were contaminating the grating surface

[347]. The specially designed polymer used in our experiment results in a debris-free ablation, promising a one-step process, i.e., no postprocessing is necessary. This arises from the fact that the polymer produces gaseous products, which do not condense on the surface. In other studies, multiple pulses (four to several hundreds) have been used, but the grating depths were still quite limited (20–100 nm) [355–360]. In addition, multipulse techniques seem to have problems with the quality of the gratings. Sometimes, substructures on top of the remaining ridges are detected [357, 358], or the grooves are wider than the remaining ridges [359].

Using laser ablation as a fabrication technique provides the unique advantage that the grating depth can be varied continuously by adjusting the laser power. Realistic depths, for specially designed polymers and not too shallow angles θ, are in the range of several hundred nm for a single pulse. Moreover, reference data for etch rate vs laser fluence allows the depths of the grooves to be predetermined. In addition, the spacing of the grating is also easily accessed by varying the angle θ. Thus, spacings of $\approx\lambda/2$ to ≈ 10 μm for our setup are readily achievable.

While ruled gratings are separated into different families according to their blaze angle, interference gratings are categorized by using the modulation frequency, α, defined as:

$$\alpha = \frac{\mathrm{d}}{\mathrm{s}} \tag{30}$$

where d=depth and s=spacing of the grating [346].

In general, five different ranges are used to categorize an interference grating:

- $\alpha \leq 0.05$, with a peak reflectivity wavelength at $3.4\mathrm{d}=3.4\alpha\mathrm{s}$ (a blazed grating with an equivalent peak wavelength will require a groove depth 1.7 times greater).
- $0.05 \leq \alpha < 0.15$, with a flat efficiency for the first order of λ/s from 0.35 to 1.4.
- $0.15 \leq \alpha < 0.25$, with a reasonable efficiency for $\lambda/\mathrm{s} > 0.45$.
- $0.25 \leq \alpha < 0.40$, with the maximum efficiency of all interference gratings for $0.65 < \lambda/\mathrm{s}$.
- $\alpha > 0.4$, with few applications, except sometimes for grazing incidence applications.

Gratings with Micron Spacings (1.09 μm). Two different laser fluences (80 and 240 mJ cm^{-2}) and therefore two different depths were achieved when creating the gratings. Figure 89 shows AFM data for the experiment with a single pulse and a fluence of 80 mJ cm^{-2}. The insert in Fig. 88 shows the X-Z plot of the data. As seen in the figures, the grating is of high quality, with no debris contaminating the surface, nor is there any evidence of substructures. The grooves and ridges are equidistant and the tops of the ridges are relatively flat and not rounded. The depth of the grating is $\approx$135 nm, corresponding to a modulation frequency, α, of 0.12.

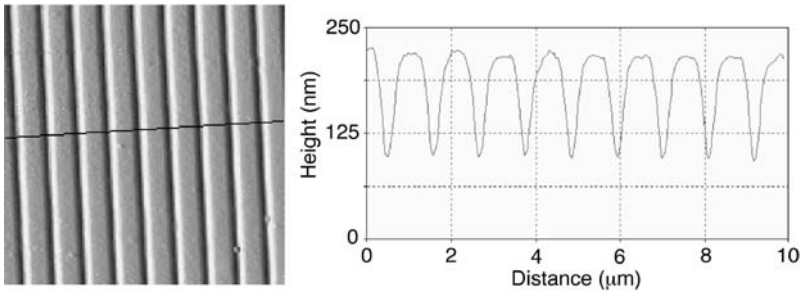

Fig. 89 AFM image of grating of 1090-nm spacing. 1 pulse with 80 mJ cm^{-2} with the X-Z plot as *insert*. REPRINTED WITH PERMISSION OF [Ref. 326], COPYRIGHT (1999) American Institute of Physics

Higher laser fluences yielded deeper gratings as expected, but we observed slight differences in the width of the grooves. Specifically, at 80 mJ cm^{-2}, 0.7-μm-wide grooves are found, while 0.85-μm-wide grooves are observed at 240 mJ cm^{-2}. This has been previously reported and attributed to the ablation threshold [357, 358], which will cause wider areas to be ablated at the higher fluences. Assuming a Gaussian laser intensity profile, the diameter of the beam with intensities above a constant threshold increases with increasing energy. For the 240 mJ cm^{-2} irradiation a grating depth of around 450 nm results, corresponding to a modulation frequency of 0.41. This demonstrates how easily modulation frequencies are accessed with the laser ablation approach and through the use of specially designed polymers.

Gratings with nm Spacings (180 nm). The 180-nm-spaced gratings reveal much shallower depths at the same given laser fluence than the micron-sized gratings. For example, applying 80 mJ cm^{-2} results in a groove depth of 30 nm, while for the micron-sized gratings a depth of 125 nm was found. The nm-grating experiments are conducted close to the theoretical spacing limit, and therefore require an angle θ close to 180°. We modeled the interference pattern of two overlapping plane waves at the angle (θ) corresponding to the 1-μm and 180-nm gratings. Adding up the fields and attenuating the fields for the penetration into the material, using the linear absorption coefficient, revealed differences in the etch depth between the two gratings. The experimental results could be reproduced very well with an additional scaling factor for the etch depth. This shows that the difference in the grating depths for the 180-nm and 1-μm- gratings at the same laser fluence is caused by the longer path within the material, and hence less deep penetration of the interference field into the material for the shallow angles.

Nevertheless, gratings with nm-sized spacing were fabricated. Figure 90 shows the AFM data and X-Y plot for a single pulse grating with an irradiation fluence of 155 mJ cm^{-2}.

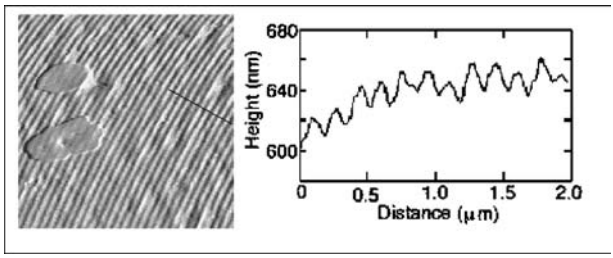

Fig. 90 AFM image of grating of 180-nm spacing. 1 pulse with 155 mJ cm^{-2} with the X-Z plot as *insert*. The curvature of the grating lines is an experimental artifact. REPRINTED WITH PERMISSION OF [Ref. 326], COPYRIGHT (1999) American Institute of Physics

The unstructured patches in Fig. 90 are most probably due to impurities or decomposed polymer that exhibit no absorption at the irradiation wavelength. The structure shows quite a lot of irregularities. This is due to the mentioned mechanism for irradiation at very shallow angles. The surface roughness (2 nm) and surface contaminants will cause substantial shading at grazing incidence irradiation.

The grating depths of 30 and 60 nm for irradiation with 80 mJ cm^{-2} and 155 mJ cm^{-2} correspond to modulation frequencies of 0.17 and 0.33, respectively.

Multiple Pulse Experiments. In an attempt to improve the modulation frequency by increasing the grating depths, experiments with multiple pulses (two to ten) have been performed.

After multiple pulses a pronounced deterioration of the grating was detected, as shown in Fig. 91. For the 1-μm grating the depth increased slightly with the second pulse, but the structure showed recognizable deterioration of the grating quality. Upon further irradiation the depth and the quality of

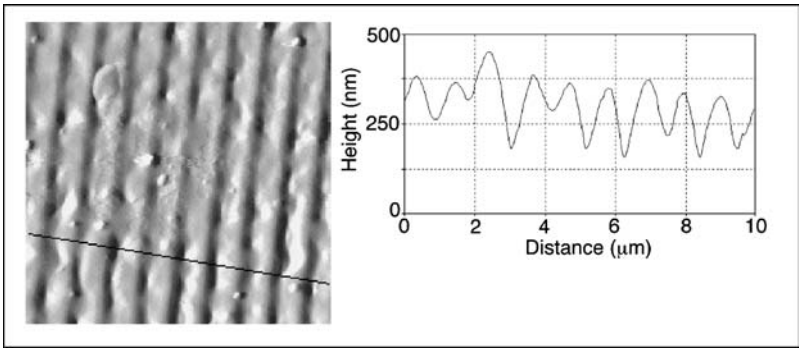

Fig. 91 AFM image of grating of 1090-nm spacing. 5 pulses with 80 mJcm^{-2} with the X-Z plot as *insert*. REPRINTED WITH PERMISSION OF [Ref. 326], COPYRIGHT (1999) American Institute of Physics

the gratings were reduced. This effect is even more pronounced for the 180-nm gratings.

The deterioration of the grating (shown in Fig. 91) with successive pulses cannot be attributed to thermal effects, since in an experiment using a mask and projection technique (1 μm slit pattern and multiple pulses with 200 mJ cm^{-2}) sharp contours remained. Additionally, the thermal diffusion length for the laser pulse corresponds only to 30–40 nm for commercial polymers such as poly(ethylene terephthalate).

At the present stage of our research program we can only offer tentative explanations for these observations. Laser instabilities, such as thermal lensing, can definitely change the beam path between successive pulses, which will laterally shift the grating from pulse to pulse. A shadowing effect of the already existing grating on successive pulses is most probably not responsible, especially in the case of the micron-sized grating, where θ is only 18°. Diffracted light from the grating formed in the first pulse may not reach the ablation threshold, as the diffraction efficiency for orders n>1 amounts to less than 5%. Another possible reason could be the fact that the film thickness is only 1–2 μm, and the absorption coefficient is 115,000 cm^{-1}. Therefore, some light will penetrate the film and be partially reflected from the substrate. Light below the threshold of ablation will decompose the chromophores and thereby bleach the material, but not cause ablation. So polymer areas with different absorption at the laser wavelength or partially cross-linked polymers, with different properties, are formed. These material properties will also influence the possible application of the gratings. UV light causes decomposition of the polymer and will thus damage the grating and reduce its durability. Therefore an application as reflective grating would be desirable, where metallization would act as UV protection to increase the durability.

3.4.2.3 Conclusions

The formation of two beam interference gratings in a specially designed polymer using a "direct" writing method (laser ablation) have been demonstrated. Well-defined gratings with variable spacings and depths (and therefore modulation) can be achieved with single pulses. No further cleaning steps are necessary, because the products of ablation are gaseous. Additional pulses deteriorate the gratings, demonstrating the importance of the single pulse approach.

3.4.3
Phase Masks for the Fabrication of Microstructures

3.4.3.1
Introduction

The ablation properties of the specially designed polymers led to the development of special phase masks for laser ablation. These masks were fabricated into quartz mask blanks using electron-beam lithography [326, 362]. The phase masks were designed for 308 nm as irradiation wavelength using an 80-mm focal length projection lens at demagnification factors between 2 and 4. The grating pitch was kept constant at 3 μm, which provides a sufficiently high deflection angle of the diffracted light. Only the 0th order was used for the structuring (higher orders were blocked by an aperture) as shown in Fig. 92. The zero-order efficiency of the phase mask can be calculated by simple scalar diffraction theory and depends on the duty cycle. The duty cycle is defined as the ratio between the spacing of the grating line widths and the grating period. At a duty cycle of 0.5, the zero-order diffraction efficiency is 0 when the depth of the grating structures is matched to give a phase shift of π.

The ablation depths were measured after ablation using phase masks with various duty cycles. The ablation depths follow the theory quite well. The deviations can be explained by the nonlinear ablation behavior and the existence of a fluence threshold for ablation. Including these parameters into the design of the phase masks improves the efficiency of the ablated structures, e.g., gratings, by a factor of 2. An example of the improved quality of blazed gratings in polyimide fabricated by laser ablation is shown in Fig. 93. The profilometer traces of the uncorrected structure resemble more an interference grating than a blazed grating. After correction for the threshold and nonlinear etch rate, profiles are obtained which resemble blazed gratings quite well. Further improvements should be possible by a more sophisticated correction for the phase masks and the application of our designed photopolymers.

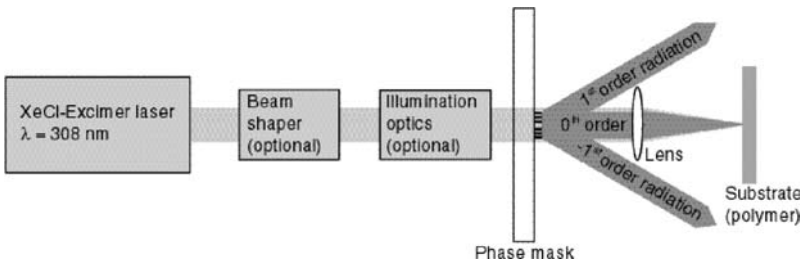

Fig. 92 Setup for the patterning of polymer surfaces by laser ablation using diffractive masks. REPRINTED WITH PERMISSION OF [Ref. 322], COPYRIGHT (2001) Elsevier Science

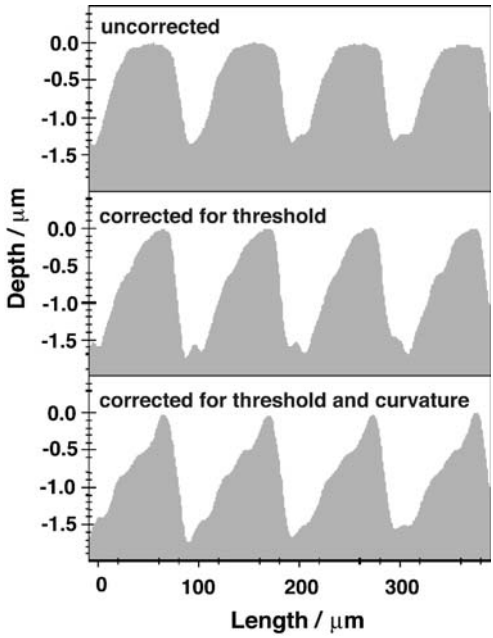

Fig. 93 Profilometer scans of blazed grating structures ablated into polyimide. The profile shape depends on the corrections for the polymer response, i.e., etch rate per pulse at a given fluence. REPRINTED WITH PERMISSION OF [Ref. 322], COPYRIGHT (2001) Elsevier Science

Various structures were ablated into the triazene polymer (TP) and polyimide (PI). PI was again selected as reference polymer, because the absorption coefficient (100,000 cm^{-1}) is comparable to TP, but with a higher threshold (60 mJ cm^{-2}) and lower etch rates (e.g., of 61 nm $pulse^{-1}$ with 100 mJ cm^{-2}). For PI a photothermal ablation mechanism is generally accepted at longer wavelengths, while it has been suggested that that the triazene polymer ablation is mainly photochemical. It has been shown that the decomposition products of the triazene polymer are mainly gaseous, which do not contaminate the surface, without modification of the remaining polymer surface. In the case of PI and most commercial polymers, solid ablation products (debris) and carbonization of the polymer surface has been detected. An example of Siemens stars etched into a triazene polymer (right) and PI (left) is shown in Fig. 94. The modified and redeposited material is clearly visible around the ablated structure of the PI, but is absent for TP. The magnifications of the Siemens stars are shown in Fig. 94 (bottom). It is clearly visible that the deposited material originates from ablation structures and that the quality of the structures is higher for the triazene polymer. A closer microscopic examination and studies using Raman microscopy [138] and imaging X-ray photoelectron spectroscopy [276] have shown that carbonization also takes place inside the ablated structures. Any surface contamina-

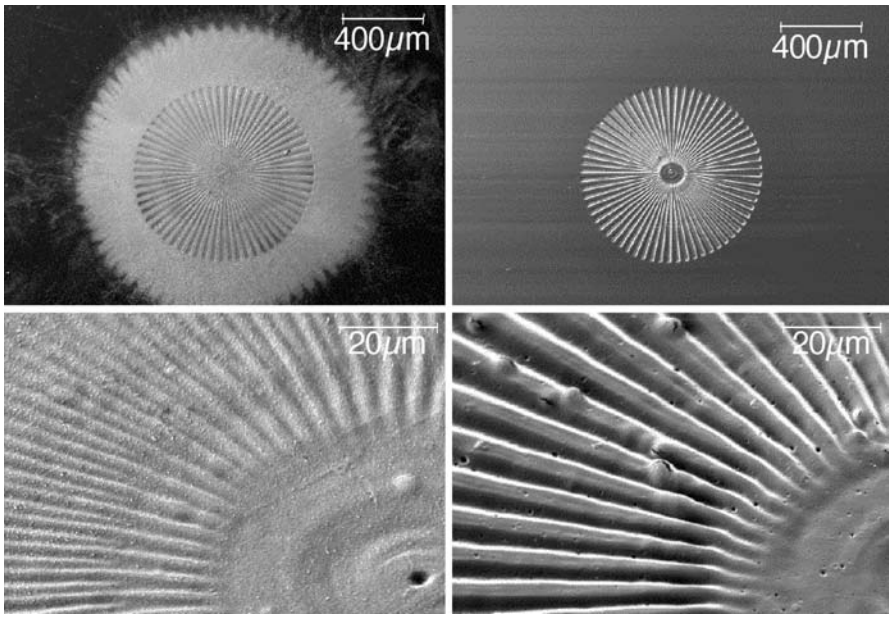

Fig. 94 SEM images of Siemens stars fabricated by laser ablation. *Top*: Siemens stars in polyimide (*left*) and in the triazene polymer (*right*) using 5 pulses. *Bottom*: magnification of the Siemens stars in the top row. REPRINTED WITH PERMISSION OF [Ref. 322], COPYRIGHT (2001) Elsevier Science

tion or modification will deteriorate the performance of the microoptical elements and render the ablation rates unpredictable.

An example of Fresnel lenses etched into the triazene polymer is shown in Fig. 95. The ablation structures are well defined (shown in Fig. 95, left),

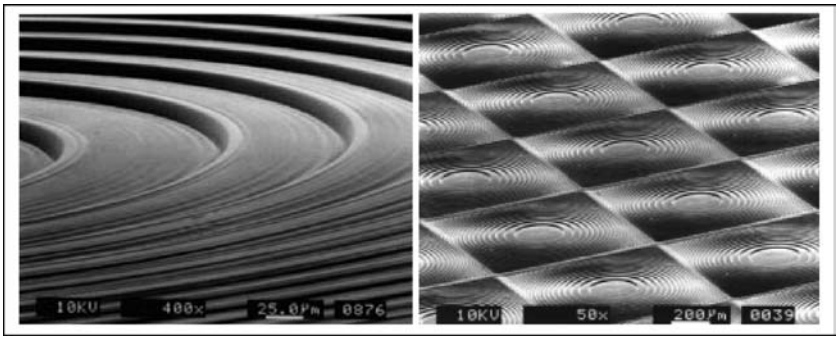

Fig. 95 SEM micrograph of diffractive lens structures ablated into polyimide (*left*, lens diameter 2.5 mm) and array of lens structures (using a step and repeat mode, lens dimensions 900×900 μm). REPRINTED WITH PERMISSION OF [Ref. 322], COPYRIGHT (2001) Elsevier Science

and even arrays of structures (Fig. 95, right) can be created fast and easily. The higher sensitivity and etch rates of the triazene polymer allows the application of larger phase masks. Alternatively, fewer pulses are necessary to fabricate an optical element with a given depth of the structures.

3.4.3.2 Conclusion

The combination of gray-tone phase masks with the highly sensitive photopolymers is suitable for the fast fabrication of three-dimensional topographies. Single laser pulses can create complex structures, such as Fresnel lenses. A pattern transfer into glass or quartz, e.g., by proportional etching techniques, would open an even larger spectrum of applications.

3.4.4 *Structuring with AFM and SNOM*

3.4.4.1 Introduction

The search for fabrication techniques to produce sub-50-nm structures with other methods [363] than electron-beam lithography (EBL) has culminated in the direct manipulation of atoms [364, 365] and molecules [366]. Most of these techniques take advantage of the spatial resolution of the electronic emission from a tip to locally expose ultrathin electron resists [367–370], such as self-assembled monolayers [371, 372] or Langmuir–Blodgett films [373], or to directly modify the structure of the superficial layer [374–377], such as the oxygenation of hydrogenated silicon [378, 379]. A few methods based on mechanically engraving a soft layer with the sharp atomic microscope tip have also been proposed [380]. In particular the PMMA resist bilayer process, commonly used in EBL, has been directly adapted [381]. These techniques have been named *lift-off lithography with AFM* [382] or *ploughing with AFM* [383–385]. Another method is based on scanning near-field optical microscopy (SNOM), or better, laser ablation (irradiation) through a near-field optical probe [386, 387]. If the tip is held very close to the sample surface, within a few nanometers, the illuminated area is essentially defined by the size of the aperture [388, 389]. This permits material ablation (irradiation) from an area smaller than the Abbe-barrier, the limit of resolution if diffractive optics is used (1/2 of the irradiation wavelength). Specially designed tips [389] with a high optical transmission and high damage thresholds allow one to couple up to 300 μJ of laser pulse energy into the fiber. The resulting power density under the tip is high enough to ablate the material placed in the optical near-field of the tip [387]. Lateral resolution of less than 100 nm has been achieved in this way [387].

In the following paragraphs, experiments are shown which utilize a specially designed polymer (or its model compound) for nanostructuring with AFM and SNOM.

3.4.4.2
AFM Structuring

The structure of the triazene polymer used for the following experiments is shown in Scheme 5 (same material as in most other chapters). Thin films of the polymer were spin-coated onto quartz wafers, and structuring was performed in the contact mode of the AFM.

Consistent structuring of the polymer was not possible, if films were used as produced. This is most probably due to the fact that the films were not soft enough for mechanical structuring. One way to soften a polymer is a reduction of the molecular weight. The triazene polymer, or better, the triazene chromophore is photochemically active and decomposes upon UV irradiation as shown in previous chapters. After decomposition of the triazene chromophore nitrogen is released and a polymer with lower molecular weight results. After extensive irradiation insoluble polymer networks are formed. In Fig. 96 the reduction of the molecular weight upon irradiation with 308 nm and fluences well below the threshold of ablation are shown. The molecular weight was analyzed by gel permeation chromatography (GPC). After "laser softening" of the polymer it was possible to structure the polymer film by AFM.

In Fig. 97, the nanostructures in the polymer are shown. Three lines are visible, which have a width of approximately 25 nm and a length of 200–300 nm. The mechanical nature of the structuring is clearly visible by the walls at the end of the structured line (lower part of the line, green color).

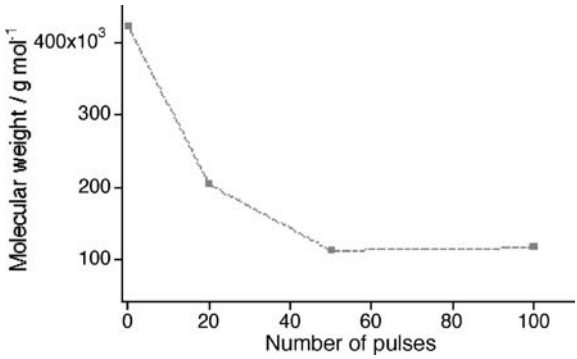

Fig. 96 Reduction of the molecular weight as a function of the laser pulses after irradiation at 308 nm with ≈5m J cm^{-2}. The molecular weight was determined by GPC analysis

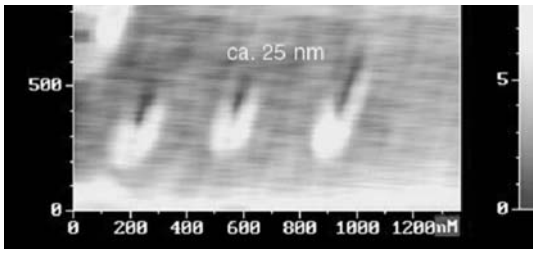

Fig. 97 Nanostructures in the laser-softened triazene polymer. The structuring was performed by moving the AFM tip from the upper part downwards. The image was taken in the noncontact mode of the same AFM instrument

This combined method has the advantage that the surface of the AFM resist is not too sensitive to storage or handling, because the polymer only gets activated by laser irradiation just prior to its application.

3.4.4.3 SNOM Structuring

The nanostructuring is achieved by directing a pulse from a frequency-tripled Nd:YAG laser with a pulse width of 35 ps, a wavelength of 355 nm, and up to 250 μJ pulse energy through a near-field optical tip. The tip had a diameter aperture of around 170 nm, creating ablation craters with about the same diameter (see below). Molecular crystals (the same bis-triazene that was used as model compound for the triazene polymers in other studies, shown in Scheme 7) were applied as substrates, because the main goal of this study was the development of *nanoscale atmospheric-pressure laser ablation–mass spectrometry* [390].

Here, mainly the structuring is presented, but it was possible to detect the main product of the photochemical decomposition of the triazene group, N_2, by mass spectrometry [390]. An array of ablation craters in the bis-triazene is shown in Fig. 98. The craters have a diameter of around 200 nm, corresponding quite well to the aperture size of the tip, and are around 20 nm deep.

An estimate of the quantum yield for a photochemical decomposition of the bis-triazene suggests also that the mentioned photochemical decomposition causes these craters. The estimation gives a quantum yield of 2.8×10^{-4}, assuming an energy of 2 nJ, a hole radius of 100 nm with a depth of 20 nm, and a density of 1 g cm^{-3}. The value of the quantum yield is quite comparable to the quantum yield of the photodecomposition of crystalline diphenyltriazene (DPT), i.e., 6×10^{-4} [391] which has the same active chromophore. Further supporting the validity of this comparison, the quantum yield of decomposition of DPT in solution, 10^{-3}–2×10^{-2} depending on the solvent [392], matches the range of 1.8×10^{-3}–1.33×10^{-2} reported for various aryl dialkyl triazenes [140]. Finally, detection of products by the mass spectrometer strongly supports that material ablation is responsible for the observed

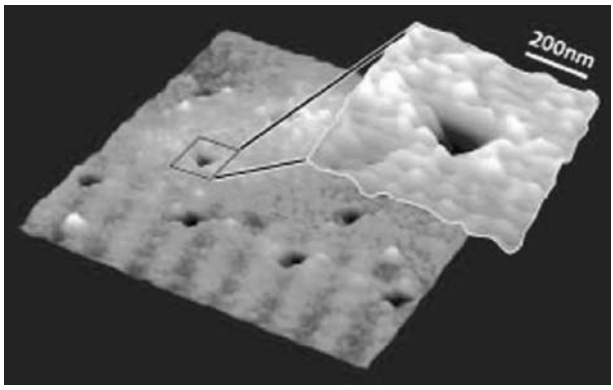

Fig. 98 Topographic image of the surface of the bis-triazene following the ablation experiment. Irradiation at 355 nm, with a pulse width of 35 ps and an energy of 2 nJ

craters, as opposed to indentations "written" into the sample surface thermomechanically, by transient elongation of the SNOM tip [393, 394].

3.4.5 *Conclusion*

Nanostructuring of designed polymers and of a model compound was achieved by light force (SNOM) and mechanical manipulation (AFM). The latter process was carried out in combination with low-fluence laser irradiation to activate (soften) the polymer for mechanical structuring.

3.5 As Fuel for Micro/Nanosatellites Using Laser Plasma Thrusters

3.5.1 *Introduction*

A very different application of laser ablation of polymers can be found in aerospace science. With the advent of microsatellites (>10 kg), nanosatellites (1–10 kg), and even picosatellites (<1 kg) it is necessary to develop steering engines which have a small mass ($\leq$200 g) and size, produce a high specific impulse, and are inexpensive. One promising candidate for this application are laser plasma thrusters (LPTs) [395], which have some advantages over more common candidates for microthrusters, such as pulsed plasma thrusters or resistojets. One quite serious problem with existing nozzle thrusters is that unpredictable physical regimes are entered when the dimensions of the nozzles are so small that the gas flow can no longer be described by the theory of viscous flow, which is the case for a 1-μm nozzle at a pressure of 10 bar. Nozzles are not necessary for LPTs, because the plasma expansion is already similar to a nozzle expansion. One other advantage of a LPT is the

possible higher maximum specific impulse and the high efficiency of ≈50%. For chemical rockets the maximum impulse is about 500 s, limited by the available temperatures, while a specific impulse of 8,000 s was reported for laser ablation of Al [396]. Due to the specific demands, i.e., weight and power, of small satellites, small powerful (≥1 W) diode lasers must be used. These lasers emit in the near-IR (930–980 nm), with an available power of around 1–5 W and pulse lengths from 100 μs to the ms range. Fluences of several hundred J cm^{-2} can be achieved with standard optical components (laser spot diameter around 5 μm). The long pulse lengths of the diode lasers restrict the applicable materials to polymers, which have low thermal conductivities. It was, for example, not possible to create a plasma with the previously mentioned diode lasers on Al. The performance of the LPTs is to a large extent dependent on the properties of the polymers used in these devices. The well-defined exothermic decomposition of the above mentioned photopolymers was an attractive feature to test these polymers also for an application with near-IR irradiation.

3.5.2 *Results*

To analyze the performance of the polymer films for LPTs, the target momentum was measured by the torsion balance and used to calculate the momentum coupling coefficient, C_m. This quantity is defined as

$$C_m = \frac{m\Delta v}{W} \tag{31}$$

with $m\Delta v$ as the target momentum produced during the ejection of laser-ablated material. W is the incident laser pulse energy. Another important parameter for thrusters is the specific impulse, I_{sp}, which is defined as

$$C_m\, Q* = v_E = I_{sp}\, g \tag{32}$$

Q^* is the specific ablation energy (incident power/mass ablation rate), v_E is the exhaust velocity, and g is the acceleration due to gravity. In other words, I_{sp} is the time for which an acceleration of g would have to act to bring the exhaust mass up to the velocity v_E.

A scheme of an envisioned design for the LPTs is shown in Fig. 99. Two geometries are possible, i.e., reflection mode, which has the advantage of two times higher C_m, but the disadvantage of an awkward geometry which requires additional shielding for the optical components. The transmission mode has the better geometry and the protected optics, but the disadvantage of a two times lower C_m (partial absorbing of the substrate, reflection and different "burn-through mode").

The measurements were performed in the transmission mode, which is the most probable candidate for LPTs. PET was chosen as substrate with a thickness of >25 μm. With thinner substrates a negative momentum was observed due to a burn-through of the substrates. This was not observed for

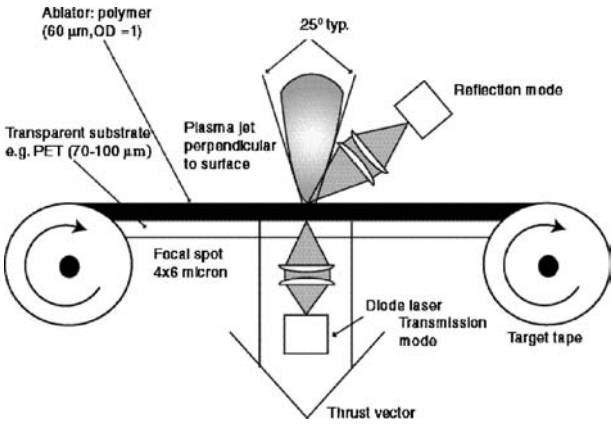

Fig. 99 Scheme of the possible design for LPTs. REPRINTED WITH PERMISSION OF [Ref. 222], COPYRIGHT (2001) Elsevier Science

uncoated PET, even at higher fluences. Therefore it can be assumed that the carbon-doped polymer starts to decompose at the interface to the PET, causing also the decomposition of the PET. If the substrate burns through faster than the coated polymer, a negative momentum will be detected. This was confirmed by holes in the PET after these experiments. Therefore thicker PET substrates (≈100 µm) were applied. Two polymers were selected for the tests, i.e., a polymer designed for laser ablation (triazene polymer) in the UV and a commercial polymer [poly(vinyl alcohol), PVA]. Both polymers pass the fundamental requirements for LPTs: the polymers give homogenous films with a good adhesion on PET; they do not stick to each other; they are elastic over a broad temperature range (−50 to + 60 °C); and have an optical density (OD) of about 1. The latter requires that it is possible to dope the films homogeneously with carbon. Most polymers have to be doped to accomplish an effective absorption in the near-IR. Carbon was chosen as dopant due to the broad homogeneous absorption over the whole near-IR range. The films of both polymers were prepared with an optical density of ≈0.9 and a thickness of around 60 µm. The film thickness is the upper limit which can be accomplished for these polymers by our preparation method and tools.

In Fig. 100 the momentum coupling coefficients at various laser fluences of the carbon-doped triazene polymer and of a carbon-doped PVA are shown. The triazene polymer reveals higher coupling coefficients and, more importantly, a quite well defined threshold for a maximum C_m. In Fig. 101 the specific impulses, I_{sp}, at various laser fluences are shown.

The carbon-doped triazene polymer clearly reveals a higher specific impulse than the PVA. The fewer data points for the triazene polymer are due to the very irregular shape of the craters, which did not allow measurements of the ablated volume at all laser fluences. The I_{sp} values are clearly higher

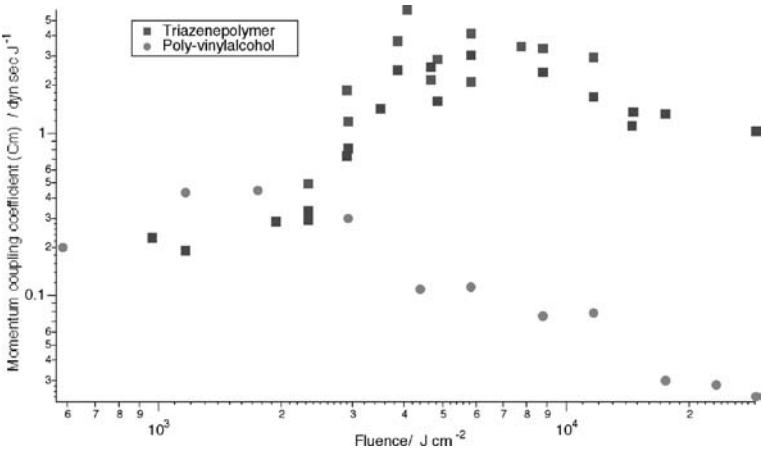

Fig. 100 Momentum coupling coefficients (impulse/laser energy) at various fluences for the carbon-doped polymers. Optical density at 935 nm ≈0.9, film thickness ≈65 μm, PET substrates. REPRINTED WITH PERMISSION OF [Ref. 222], COPYRIGHT (2001) Elsevier Science

for the triazene polymer, and probably reveal a threshold at a similar fluence range as for C_m.

The well-defined threshold and higher C_m of the triazene polymer is an important feature for the design of a plasma thruster with tape-like polymer fuel, because the optimum incident laser fluence and tape speed are clearly defined. The decreasing values of C_m after the maximum are due to the in-

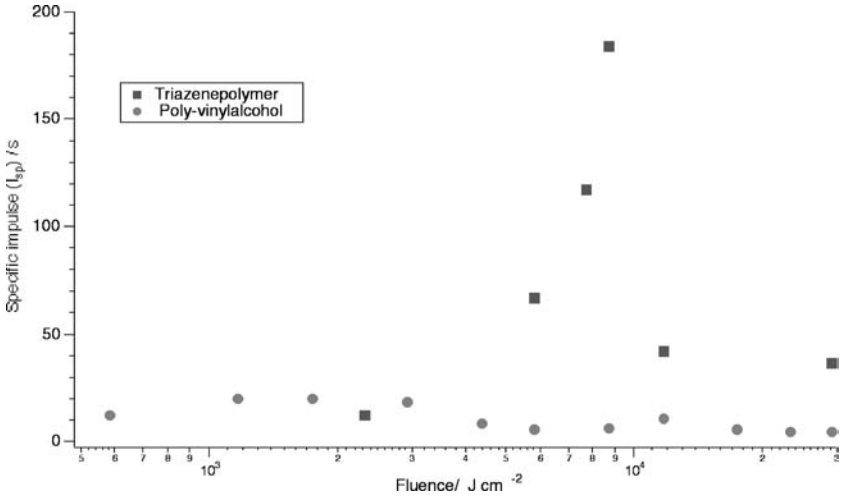

Fig 101 Specific impulse at various fluences for the carbon-doped polymers. Same materials as in Fig. 100. REPRINTED WITH PERMISSION OF [Ref. 222], COPYRIGHT (2001) Elsevier Science

creasing fraction of incident laser energy devoted to accelerating vapor, then creating plasma, and to absorption of the laser energy by the created plasma [397]. The well-defined threshold and higher values are probably due to the decomposition properties of the triazene polymer. The thermal decomposition, initiated by absorption of the laser energy by the carbon, follows most probably the same pathway as the UV laser-induced decomposition. The N_3-group is the photolabile group in the polymer, but also the primary decomposition site of thermolysis, as suggested by product analysis by mass spectrometry [240]. In thermolysis, the triazene polymer exhibits a well-defined, quite sharp (FWHM≈60 °C) decomposition temperature (≈227 °C) and an exothermic decomposition enthalpy (≈−0.7 kJ g^{-1}) while the PVA exhibits a very broad (FWHM≈200 °C) decomposition peak centered around 260 °C. The decomposition is also exothermic (<−0.5 kJ g^{-1}), but the enthalpy could not be determined exactly due to the sloping, ill-defined baseline of the DSC scans. Whether the amount of released energy, the maximum temperature or the width of the decomposition process are more important for creating a threshold for a maximum C_m is not clear at the moment.

If the thermally induced decomposition follows the same pathway as the UV laser-induced decomposition, then it could be possible to select the polymers for LPTs according to similar principles as for UV laser ablation. The most important design features for polymers designed for UV laser ablation are: an exothermic decomposition into gaseous products; well-defined primary decomposition sites in the polymer main chain; and a high absorptivity at the irradiation wavelengths. In future experiments these assumptions will be tested.

3.5.3 *Conclusion*

The combination of phase masks and specially designed, highly sensitive photopolymers can be used to fabricate fast, three-dimensional topographies using laser ablation. The improvements of the phase mask, by incorporating the ablation behavior of the polymer into the mask design, and the application of photopolymers which decompose without contamination of the surface, allows a fast fabrication of microoptical elements.

The designed polymers also have superior properties for applications in the near-IR. The carbon-doped triazene polymer shows higher values of C_m and I_{sp} as compared to a commercial polymer (PVA). The well-defined threshold for the momentum coupling coefficient is an important aspect for the application of polymers in laser plasma thrusters.

3.6 Discussion of Possible Applications

After the first reports about laser ablation of polymers in 1982, various applications have been suggested. One of the most important applications of

laser ablation, i.e., dry etching for microlithography, was never realized. The reasons for this "failure" were the lack of polymers designed for laser ablation in the early days of ablation (1980s). Laser ablation was performed with standard commercial polymers, which revealed several severe drawbacks, such as low sensitivity and carbonization upon structuring. To overcome these limitations it is necessary to apply polymers which are optimized for laser ablation.

When we started the development and exploration of polymers designed for ablation in the early 1990s it was nearly impossible to compete with the existing lithography techniques. The state-of-the-art systems for microlithography were developed from feature sizes of ≥ 1 μm in the mid-eighties to $\approx$350 nm in the mid-nineties, and most of the "big" advantages of laser ablation were diminished (e.g., structure size, footprint in clean room, resist costs, and availability). The technique of microlithography had advanced from the application of mercury lamps to excimer lasers (248 and 193 nm), which are identical to the lasers used in laser ablation.

To evaluate the limits of laser ablation it is necessary to optimize the complete ablation process. This includes the development of polymers for ablation.

The concept for the design of these polymers is based on the following criteria:

- Incorporation of photochemically active groups in the polymer. This results in the high sensitivity of the polymers for laser ablation, which is a condition for nearly all applications (laser photons are relatively expensive; 1 Einstein=19 CHF for $\lambda \geq 193$ nm, the prize for 157 nm photons is higher by a factor of 6 [398]).
- The absorption band of the photochemically active chromophore is separated from the aromatic groups in the polymer (aromatic systems are most probably the reason for carbonization upon laser irradiation).
- The photochemically active chromophore has a high absorption coefficient at the laser wavelength, and is part of the polymer main chain. This results in small polymer fragments upon decomposition of the chromophore.
- A large amount of gaseous product is created upon decomposition. These small fragments can act as carrier gas for larger fragments which could cause contamination of the surface.
- Exothermic decomposition of the photochemically active chromophore, supporting the decomposition of the polymer.

These criteria resulted in the design of laser ablation polymers for 308 nm as irradiation wavelength, where it is possible to separate the absorption bands of the photochemically active chromophore from the aromatic groups in the polymer. The importance of this concept was discussed previously. Irradiation of the polymers with 248 nm caused carbonization of the polymer surface, while irradiation with 308 nm did not yield carbonization. These results prove that our concept of separating the absorption bands is valid, but

also reveal the limitation of this concept. The separation of the absorption bands limits the applicable wavelengths to $\lambda_{irr} \geq 308$ nm. These wavelengths are already longer than the irradiation wavelengths used in high-resolution microlithography (and the resulting feature sizes scale directly with irradiation wavelength). This suggests that laser ablation cannot be used in high-resolution microlithography, because carbonization can only be avoided if longer wavelengths are applied, and carbonization will always deteriorate the resulting structures (Figs. 74 and 75), including cone formation (see Fig. 12c).

Therefore the only remaining applications in microlithography are where the size of the necessary features is in the range of 0.5 to 1 μm. We had the opportunity to test our polymers against benchmarks given by Hitachi for one specific application, i.e., thin-film transistor production for liquid crystal displays, where the necessary feature size is about 1 μm. All criteria (for a process having the same costs as the conventional microlithography process) given by Hitachi could be fulfilled, but we were only better by a factor of two (with respect to the process costs [58]) compared to the standard method. Meanwhile, since 1999, it is only a factor of 1.5, which is not enough for industry to consider a change of an existing technique (a factor of 5–10 would be necessary). Our designed polymers are still the most advanced materials for laser ablation (Hitachi tried independently to develop their own laser ablation polymers, but was never better than the existing technique), but they are still not a real alternative for industry. Therefore we have to conclude that laser ablation, even with designed polymers, will probably never replace processes in microlithography.

There may be some niche application for laser ablation and designed polymers, e.g., for arrays of structures which could be accomplished by novel systems, such as the combined resists. The application of this combined positive-negative resist is still under discussion.

Other very important applications of laser ablation are in the field of microstructuring. In this work, microlithography is defined as the processes used in the miniaturization of electronic devices (i.e., integrated circuits), while microstructuring aims at the fabrication of 3D structures. These applications range from:

– Complex 3D microstructures for microsystems:

1. Lasers are used as fabrication tool (e.g., for microtweezers, microcables, microholes, and microfluidic devices, i.e., lab-on-a-chip).
2. Lasers are used to produce the "master" which is used for mass production, e.g., in Laser LIGA [399] (**Li**thographie**G**alvanoformung**A**bformung/lithography-electroplating-molding).

– Rapid prototyping of small quantities.

The number of applications in microtechnology which are laser based will increase in the coming years and special polymers may be the key for many applications. The applications range from parts in micromechanical, microfluidic, and microelectronic components to microoptical elements and

medicine. Related applications are laser (micro) welding and soldering of polymers and tissue and laser marking. In previous chapters, examples of microoptical elements are shown. The resulting structures show clearly the potential of laser ablation in this field. The application of the designed polymers improves the quality of the resulting structures (see, e.g., Fig. 93). Whether the properties of the designed polymers are applicable or adjustable for the desired applications has to be tested in the near future.

The application of laser ablation in nanotechnology may be limited to SNOM-based processes, where the diffraction limit can be overcome. Whether this technique will and can be developed to an industrial process is not clear. More important could be the development and application of special materials and polymers for nanotechnology. One possible example could the development of materials for X-ray lithography. Possible strategies could be:

- Increased amount of the active chromophore in the resist (the concentration of the chromophore is limited in UV resists, due to the short penetration depths of UV light compared to X-rays in polymers). The application of "labile" groups may improve the sensitivity of X-ray resists.
- Application of conducting polymers, which may also be of advantage for electron-beam lithography.
- Incorporation of heavy atoms in the resist, e.g., Br, which have a larger absorption cross section in the X-ray region than the lighter elements in polymers.

Another more exotic application of the designed polymers is as fuel for laser plasma thrusters. The good performance of the laser polymers is probably due to the exothermic decomposition and the high density of "labile" triazene groups. This suggests the great potential of material design, even for quite different laser-based applications.

Laser ablation has grown to be an important technique for the fabrication of microelements. The role of microtechnology will increase in the coming years and laser-based fabrication processes are one of the key technologies for the future. The application of designed materials, especially polymers, will further improve the performance of laser-based methods. Already companies are specialized and offer polymers designed for laser structuring.

4 Summary

Laser ablation of polymers has been studied with designed materials under two aspects:

- The mechanism of ablation and the role of photochemically active groups on the ablation process.
- Applications of laser ablation and designed polymers.

The incorporation of photochemically active groups lowers the threshold of ablation and allows high-quality structuring without contamination and modification of the remaining surface. This can only be observed at laser wavelengths which excite directly the active chromophore and *not* the aromatic groups in the polymer. The decomposition of the active chromophore takes place during the excitation pulse of the laser, without pronounced swelling of the polymer surface during the laser pulse. Delayed swelling of the surface has previously been assigned to thermal decomposition of the polymer. The decomposition products are mainly gaseous (or at least smaller than 600 nm) and are ejected with supersonic velocity. The resulting shock wave in air is supported by the decomposition energy of the polymer. Analysis of the ablation products by time-of-flight mass spectrometry reveals that the main product is nitrogen, which is ejected with very high kinetic energies (1–3 eV). The detection of a metastable species, which is most probably excited N_2, shows that excited electronic states are involved in the ablation process. Decomposition of the triazene chromophore was also detected with laser fluences below the ablation threshold and low-intensity excimer lamps, confirming the photochemical sensitivity of the designed materials.

Experiments with a reference material, i.e., polyimide, for which a photothermal ablation mechanism has been suggested, exhibited pronounced differences, e.g., swelling of the surface prior to ablation, modifications of the surface after irradiation, and higher threshold (at an irradiation wavelength where polyimide has the same absorption coefficient as the designed materials).

These results strongly suggest that, in case of the designed polymers which contain photochemically active groups, a photochemical part in the ablation mechanism cannot be neglected. The additional data for polyimide also suggest that photochemical reaction may be important.

The data discussed above suggest that the mechanisms of ablation are not just photothermal, but contain photothermal and photochemical features. The latter has been neglected in recent models and studies about the ablation mechanism.

Various potential applications for laser ablation and the special photopolymers were tested. The materials were tested as possible resists for a laser ablation-based microlithography process, but it became quite clear that laser ablation cannot be used as an alternative for microlithography. The potential of laser ablation and specially designed material are in the field of microstructuring. Laser ablation can be used to fabricate 3D elements, e.g., microoptical elements. The quality of these structures is higher if the designed polymers are used. These materials may even have possible applications in nanotechnology and in totally different applications, such as laser plasma thrusters.

Acknowledgements This work was supported by the Swiss National Science Foundation. I thank Macarena Montenegro, PSI, for help with the literature database and Katharina Meissner for help with the figures.

References

1. Maiman TH (1960) Nature 187:493
2. Gordon JP, Zeiger HJ, Townes CH (1954) Phys Rev 95:282
3. Kneubühl FW, Sigrist MW (1999) Laser. Teubner Studienbücher Physik, Stuttgart
4. Schawlow AL (1965) Science 149:13
5. Brech F, Cross L (1962) Appl Spectrosc 16:59
6. Linlor WI (1965) Bull Am Phys Soc 7:440
7. Honig RE, Woolston JR (1963) Appl Phys Lett 2:138
8. Murray JJ (1963) Bull Am Phys Soc 8:77
9. Ready JF (1963) Appl Phys Lett 3:11
10. Rosan RC, Healy MK, McNary J, W.F. (1963) Science 142:236
11. Howe JA (1963) J Chem Phys 39:1362
12. Berkowitz J, Chupka WA (1964) J Chem Phys 40:2735
13. Basov NG, Krokhin ON (1964) Sov Phys JETP 19:123
14. Ehlers AW, Weissler GL (1966) Appl Phys Lett 8:89
15. Basov NG, Kruikov PG, Zakharov SD, Senatskii YV, Tchekalin SV (1968) IEEE J Quant Electron Q40:864
16. Langer P, Tonon G, Floux F, Ducauze A (1966) IEEE QE2:499
17. Archibold E, Hughes TP (1964) Nature 204:670
18. Sonneburg H, Heffner H, Spicer W (1964) Appl Phys Lett 5:95
19. Logothetis EM, Hartman PL (1967) Phys Rev Lett 18:581
20. Smith AH, Turner AF (1965) Appl Opt 4:147
21. Kawamura Y, Toyoda K, Namba S (1982) Appl Phys Lett 40:374
22. Srinivasan R, Mayne-Banton V (1982) Appl Phys Lett 41:576
23. Patel RS, Wassick TA (1997) Proc SPIE-Int Soc Opt Eng 2991:217
24. Aoki H (04/1998). 5736999, US
25. Zaitsev-Zotov SV, Martynyuk AN, Protasov NE (1983) Sov Phys Solid State 25:100
26. Dijkamp D, Venkatesan T, Wu XD, Shaheen SA, Jiswari N, Min-Lee YH, McLean WL, Croft M (1987) Appl Phys Lett 51:619
27. Longo L
28. Karas M, Bachmann D, Hillekamp F (1985) Anal Chem 57:2953
29. Zenobi R, Knochenmuss R (1999) Mass Spectrom Rev 17:337
30. Rose-Petruck C, Jiminez R, Guo T, Cavalleri A, Siders CW, Raksi F, Squire JA, Walker BC, Wilson KR, Barty CJP (1999) Nature 398:310
31. Perkins LJ, Logan BG, Rosen MD, Perry MD, de la Rubia TD, Ghoniem NM, Ditmire T, Springer PT, Wilks SC (2000) Nuclear Fusion 40:1
32. Zafiropulos V, Fotakis C (1998) Laser cleaning in conservation. Butterworth Heinemann, Oxford
33. Rudolph P, Pentzien S, Krüger J, Kautek W, König E (1998) Restauro 6:396
34. Ready JF (1971) Effects of high power laser radiation. Academic, New York
35. (1989) Laser-induced plasmas and applications. Marcel Dekker, New York
36. Vertes A, Gijbels R, Adams F (1993) Laser ionization mass analysis. Wiley, New York
37. Chrisey DB, Hubler GK (1994) Pulsed laser deposition of thin films. Wiley, New York
38. (1994) Laser ablation principles and applications. Springer, Berlin Heidelberg New York
39. (1998) Laser ablation and desorption. Academic, San Diego
40. Bäuerle D (2000) Laser processing and chemistry. Springer, Berlin Heidelberg New York
41. Zhigilei LV, Leveugle E, Garrison BJ, Yingling YG, Zeifman M (2003) Chem Rev 103:321
42. Georgiou S, Koubenakis A (2003) Chem Rev 103:349

43. Lippert T, Dickinson JT (2003) Chem Rev 103:453
44. Paltauf G, Dyer PE (2003) Chem Rev 103:487
45. Bityurin N, Luk'yanchuk B, Hong MH, Chong TC (2003) Chem Rev 103:519
46. Chrisey DB, Pique A, McGrill RA, Horwitz JS, Ringeisen BR, Bubb DM, Wu PK (2003) Chem Rev 103:553
47. Vogel A, Venugopalan V (2003) Chem Rev 103:577
48. (1990) Lasers in polymer science and technology: applications, vol I-IV. CRC, Boca Raton
49. Dekker M (1989) Laser-induced plasmas and applications, New York
50. Blanchet GB (1996) Chemtech June:31
51. Jiang W, Norton MG, Tsung L, Dickinson JT (1995) J Mater Res 10:1038
52. Lippert T, Zimmermann F, Wokaun A (1993) Appl Spectrosc 47:1931
53. Watanabe H, Takata T (1996) Angew Makromol Chem 235:95
54. Dyer PE (1992) Photochemical processing of materials. Academic, London
55. Bolle M, Lazare S (1993) Appl Surf Sci 69:31
56. Lazare S, Granier V (1989) Laser Chem 10:25
57. Srinivasan R, Braren B (1989) Chem Rev 89:1303
58. Suzuki K (1998), Hitachi Ltd, Mobara, Japan
59. Babu SV, D'Couto GC, Egitto FD (1992) J Appl Phys:692
60. Himmelbauer M, Arenholz E, Bäuerle D (1996) Appl Phys A 63:87
61. Paraskevopoulos G, Singleton DL, Irwin RS, Taylor RS (1987) J Appl Phys 70:1938
62. Taylor RS, Singleton DL, Paraskevopoulos G (1987) Appl Phys Lett 50:1779
63. Küper S, Brannon J, Brannon K (1993) Appl Phys A 56:43
64. Lippert T, David C, Dickinson JT, Hauer M, Kogelschatz U, Langford SC, Nuyken O, Phipps C, Robert J, Wokaun A (2001) J Photochem Photobiol. A Chem 145:145
65. Schumann M, Sauerbrey R, Smayling M (1991) Appl Phys Lett 58:428
66. Ball Z, Hopp B, Csete M, Ignacz F, Racz B, Sauerbrey R, Szabo G (1995) Appl Phys A 61:547
67. Ball Z, Hopp B, Csete M, Ignacz F, Racz B, Szabo G, Sauerbrey R (1995) Appl Phys A 61:575
68. Lippert T, Bennett LS, Nakamura T, Niino H, Ouchi A, Yabe A (1996) Appl Phys A 63:257
69. Srinivasan R, Hall RR, Loehle WD, Wilson WD, Allbee DC (1995) J Appl Phys 78:4881
70. Lippert T, Nakamura T, Niino H, Yabe A (1996) Macromolecules 29:6301
71. Lu J, Deshpande SV, Gulari E, Kanicki J, Warren WL (1996) J Appl Phys 80:5028
72. Deutsch TF, Geis MW (1983) J Appl Phys 54:7201
73. Andrew JE, Dyer PE, Foster D, Key PH (1983) Appl Phys Lett 43:717
74. Sutcliffe E, Srinivasan R (1986) J Appl Phys 60:3315
75. Mahan GD, Cole HS, Liu YS, Philipp HR (1988) Appl Phys Lett 53:2377
76. Cain SR, Burns FC, Otis CE (1992) J Appl Phys 71:4107
77. Cain S (1993) J Phys Chem 97:7572
78. D'Couto GC, Babu SV (1994) J Appl Phys 76:3052
79. Luk'yanchuk B, Bityurin N, Himmelbauer M, Arnold N (1997) Nucl Instrum Met B 122:347
80. Arnold N, Luk'yanchuk B, Bityurin N (1998) Appl Surf Sci 127:184
81. Srinivasan V, Smrtic MA, Babu SV (1986) A Appl Phys 59:3861
82. Schmidt H, Ihlemann J, Wolff-Rottke B, Luther K, Troe J (1998) J Appl Phys 83:5458
83. Luk'yanchuk B, Bityurin N, Anisimov S, Bäuerle D (1993) Appl Phys A 57:367
84. Luk'yanchuk B, Bityurin N, Anisimov S, Arnold N, Bäuerle D (1996) Appl Phys A 62:397
85. Bityurin N, Malyshev A, Luk'yanchuk B, Anisimov S, Bäuerle D (1996) Proc SPIE-Int Soc Opt Eng 2802:103
86. Bityurin N (1999) Appl Surf Sci 138-139:354
87. Treyz GV, Scarmozzoni R, Osgood J, R. M. (1989) Appl Phys Lett 55:346

88. Anisimov SI, Khokhlov VA (1995) Instabilities in laser–matter interaction. CRC, Boca Raton
89. Arnold N, Bityurin N (1999) Appl Phys A 68:615
90. Wei J, Hoogen N, Lippert T, Nuyken O, Wokaun A (2001) J Phys Chem B 105:1267
91. Lazare S, Granier V (1990) Chem Phys Lett 168:593
92. Srinivasan R (1993) Appl Phys A 56:417
93. Fujiwara H, Fukumura H, Masuhara H (1995) J Phys Chem 99:11844
94. Fukumura H, Takahashi E-i, Masuhara H (1995) J Phys Chem 99:750
95. Fukumura H, Mibuka N, Eura S, Masuhara H, Nishi N (1993) J Phys Chem 97:13761
96. Fujiwara H, Hayashi T, Fukumura H, Masuhara H (1994) Appl Phys Lett 64:2451
97. Fukumura H, Masuhara H (1994) Chem Phys Lett 221:373
98. Wu X, Sadeghi M, Vertes A (1998) J Phys Chem B 102:4770
99. Dutkiewicz L, Johnson RE, Vertes A, Pedrys R (1999) J Phys Chem A 103:2925
100. Chang T-C, Dlott D (1989) J Phys Chem 90:3590
101. Zhigilei LV, Kodali PBS, Garrison BJ (1997) J Phys Chem B 101:2028
102. Zhigilei LV, Kodali PBS, Garrison BJ (1998) J Phys Chem B 102:2845
103. Zhigilei LV, Garrison BJ (2000) J Appl Phys 88:1281
104. Zhigilei LV, Kodali PBS, Garrison BJ (1997) Chem Phys Lett 276:269
105. Zhigilei LV, Garrison BJ (1997) Appl Phys Lett 71:551
106. Zhigilei LV, Garrison BJ (1998) Rapid Commun Mass Spectrom 12:1273
107. Zhigilei LV, Garrison BJ (1999) Appl Phys Lett 74:1341
108. Zhigilei LV, Garrison BJ (1999) Appl Phys A 69:S75
109. Smirnova JA, Zhigilei LV, Garrison BJ (1999) Comput Phys Commun 118:11
110. Dekel E, Eliezer S, Henis Z, Moshe E, Ludmirsky A, Goldberg IB (1998) J Appl Phys 84:4851
111. Lippert T, Wokaun A, Stebani J, Nuyken O, Ihlemann J (1993) J Phys Chem 97:12297
112. Zeifman M, Zhigilei LV, Garrison BJ (2001) 6th international conference on laser ablation, Tsukuba
113. Reichmanis E, Wilkins Jr. CW (1989) Microelectronic polymers. Dekker, New York
114. Ito H (1997) IBM J Res Develop 41:69
115. Allen RD, Wallraff GM, Hofer DC, Kunz RR (1997) IBM J Res Develop 41:95
116. Nalamasu O, Wallow TI, Reichmanis E, Novembre AE, Houlihan F, Dabbagh G, Mixon DA, Hutton RS, Timko AG, Wood OR, Cirelli RA (1997) Microelect Engin 35:133
117. Lippert T, Yabe A, Wokaun A (1997) Adv Mat 9:105
118. Lippert T, Stebani J, Ihlemann J, Nuyken O, Wokaun A (1993) Angew Makromol Chem 213:127
119. Panitz J-C, Lippert T, Stebani J, Nuyken O, Wokaun A (1993) J Phys Chem 97:5246
120. Lippert T, Stebani J, Ihlemann J, Nuyken O, Wokaun A (1993) Angew Makromol Chem 206:97
121. Stebani J, Nuyken O, Lippert T, Wokaun A (1993) Makromol Chem Rapid Commun 14:365
122. Stebani J, Nuyken O, Lippert T, Wokaun A, Stasko A (1995) Makromol Chem Phys 196:739
123. Nuyken O, Dahn U, Hoogen N, Marquis D, Nobis MN, Scherer C, Stebani J, Wokaun A, Hahn C, Kunz T, Lippert T (1999) Polym News 24:257
124. Sadafule DS, Panda SP (1979) J Appl Polym Sci 24:511
125. Hoogen N, Nuyken O (2000) J Polym Sci Polym Chem 38:1903
126. Lippert T, Wei J, Wokaun A, Hoogen N, Nuyken O (2000) Appl Surf Sci 168:270
127. Kunz T, Stebani J, Ihlemann J, Wokaun A (1998) Appl Phys A 67:347
128. Wei J, Hoogen N, Lippert T, Hahn C, Nuyken O, Wokaun A (1999) Appl Phys A 69:S849
129. Lippert T, Wei J, Wokaun A, Hoogen N, Nuyken O (2000) Macromol Mat Eng 283:140
130. Srinivasan R, Braren B (1984) J Polym Sci 22:2601
131. Lazare S, Granier V (1989) Appl Phys Lett 54:862
132. Pettit GH, Sauerbrey R (1993) Appl Phys A 56:51

133. Furutani H, Fukumura H, Masuhara H, Lippert T, Yabe A (1997) J Phys Chem A 101:5742
134. Lippert T, Bennett LS, Nakamura T, Niino H, Yabe A (1996) Appl Surf Sci 96-98:601
135. Tonyali K, Jensen LC, Dickinson JT (1988) J Vac Sci Technol A 6:941
136. Dyer PE, Jenkins SD, Sidhu J (1986) Appl Phys Lett 49:453
137. Hopp B, Bor Z, Homolya E, Mihalik E (1998) SPIE Proc, vol 3423 p 389
138. Raimondi F, Abolhassani S, Brütsch R, Geiger F, Lippert T, Wambach J, Wei J, Wokaun A (2000) J Appl Phys 88:1
139. Atkins PW (1994) Physical chemistry. Oxford University Press, Oxford
140. Lippert T, Stebani J, Stasko A, Nuyken O, Wokaun A (1994) J Photochem Photobiol 78:139
141. Ortelli EE, Geiger F, Lippert T, Wei J, Wokaun A (2000) Macromolecules 33:5090
142. Van Saarloos PP, Constable JJ (1990) J Appl Phys 68:377
143. Lazare S, Granier V, Lutgen F, Feyder G (1988) Revue Phys Appl 23:1065
144. Zimmermann F, Lippert T, Beyer C, Stebani J, Nuyken O, Wokaun A (1993) Appl Spectrosc 47:931
145. Schrader B, Moore DS (1995) vol 12
146. Beamson G, Briggs D (1992) High resolution XPS of organic polymers. Wiley, Chichester
147. Clark DT (1985) Pure Appl Chem 57:941
148. Gelius U (1974) J Electron Spectrosc Relat Phenom 5:985
149. Beamson G, Briggs D (1992) Mol Phys 76:919
150. Brezini A, Zekri N (1994) J Appl Phys 75:2015
151. Briggs D (1989) Br Polym J 21:3
152. Briggs D, Brown A, Vickermann JC (1989) Handbook of static secondary ion mass spectrometry. Wiley, Chichester
153. Stasko A, Adamcik V, Lippert T, Wokaun A, Dauth J, Nuyken O (1993) Makromol Chem 194:3385
154. Schrader B, Bergmann G (1967) Fres Z Anal Chem 225:230
155. Novis Y, De Meulemeester R, Chtaïb M, Pireaux J-J, Caudano R (1989) Br Polym J 21:147
156. Lau ANK, Vo LP (1992) Macromolecules 25:7294
157. Bolle M, Lazare S, Leblanc M, Wilmes A (1992) Appl Phys Lett 60:674
158. Dyer PE, Farley RJ (1990) Appl Phys Lett 66:1884
159. Bahners T, Schollmeyer E (1989) J Appl Phys 66:1884
160. Dyer PE, Farley RJ (1993) J Appl Phys 74:1442
161. Arenholz E, Wahner M, Heitz J, Bäuerle D (1992) Appl Phys A 55:119
162. Dunn DS, Ouderkirk AJ (1990) Macromolecules 23:770
163. Creasy WR, Brenna JT (1990) J Chem Phys 92:2269
164. Otis CE (1989) Appl Phys B 49:455
165. Campbell EEB, Ulmer G, Hasselberger B, Hertel IV (1989) Appl Surf Sci 43:346
166. Campbell EEB, Ulmer G, Hasselberger B, Busmann H-G, Hertel IV (1990) J Chem Phys 93:6900
167. Singleton DL, Paraskevopoulos G, Irwin RS (1989) J Appl Phys 66:3324
168. Srinivasan R, Braren B, Seeger DE, Dreyfus RW (1986) Macromolecules 19:916
169. Gu XJ (1993) Appl Phys Lett 62:1568
170. Feurer T, Sauerbrey R, Smayling MC, Story BJ (1993) Appl Phys A 56:275
171. Shimoyama M, Niino H, Yabe A (1992) Makromol Chem 193:569
172. Bennett LS, Lippert T, Furutani H, Fukumura H, Masuhara H (1996) Appl Phys A 63:327
173. Furzikov NP (1990) Appl Phys Lett 56:1638
174. Pettit GH, Sauerbrey R (1991) Appl Phys Lett 58:793
175. Pettit GH, Ediger MN, Hahn DW, Brinson BE, Sauerbrey R (1994) Appl Phys A 58:573
176. Lazare S, Soulignac JC, Fragnaud P (1987) Appl Phys Lett 50:624
177. Reyna LG, Sobehart JR (1994) J Appl Phys 76:4367

178. Brannon JH, Lankard JR, Baise AI, Burns F, Kaufmann J (1985) J Appl Phys 58:2036
179. Pettit GH, Ediger MN, Weiblinger RP (1993) Appl Opt 32:488
180. Stewart JJP, Bloomington
181. Stewart JJP (1989) J Comput Chem 209:221
182. Stewart JJP (1990) J Comput Aided Mol Design 4:1
183. ZINDO
184. Shaw R (1975) The chemistry of the hydrazo, azo and azoxy groups. Wiley, New York
185. Braren B, Srinivasan R (1988) J Vac Sci Technol B 6:537
186. Ihlemann J, Wolff B, Simon P (1992) Appl Phys A 54:363
187. Corporation S (1995)
188. Kunagai H, Midorikawa K, Toyoda K, Nakamura S, Okamoto T, Obara M (1994) Appl Phys Lett 65:1850
189. Chen S, Lee I-Y, Tolbert SWA, Wen X, Dlott DD (1992) J Phys Chem 96:7178
190. Tsuboi Y, Fukumura H, Masuhara H (1995) J Phys Chem 99:10305
191. Tsuboi Y, Hatanaka K, Fukumura H, Masuhara H (1994) J Phys Chem 98:11237
192. Hare DE, Dlott DD (1994) Appl Phys Lett 64:715
193. Lippert T, Koskelo A, Stoutland PO (1996) J Am Chem Soc 118:1151
194. Srinivasan R, Braren B, Casey KG, Yeh M (1989) Appl Phys Lett 55:2790
195. Srinivasan R, Braren B, Casey KG, Yeh M (1990) J Appl Phys 67:1604
196. Gilgenbach RM, Ventzek PLG (1991) Appl Phys Lett 58:1597
197. Srinivasan RJ (1993) J Appl Phys 73:2743
198. Furutani H, Fukumura H, Masuhara H (1994) Appl Phys Lett 65:3413
199. Furutani H, Fukumura H, Masuhara H (1996) J Phys Chem 100:6871
200. Furutani H (1997), Ph.D. thesis, Osaka University
201. Gupta A, Braren B, Casey KG, Hussey BW, Kelly R (1991) Appl Phys Lett 59:1302
202. Dyer PE, Sidhu J (1988) J Appl Phys 64:4657
203. Ben-Eliahu Y, Haas Y, Welner S (1995) J Phys Chem 99:6010
204. Korobeinikov VP (1991) Problems of point blast theory. Institute of Physics, New York
205. Freiwald DA, Axford RA (1975) J Appl Phys 46:1171
206. Freiwald DA (1972) J Appl Phys 43:2224
207. Kim H, Postlewaite JC, Zyung T, Dlott DD (1988) J Appl Phys 64:2955
208. Tsuboi Y, Fukumura H, Masuhara H (1994) Appl Phys Lett 64:2745
209. Bobin JL, Durand YA, Langer PP, Tonon G (1968) J Appl Phys 39:4184
210. Hall RB (1969) J Appl Phys 40:1941
211. Bennett LS, Horie Y (1994) Shock Waves 4:127
212. Fujiwara H, Nakajima Y, Fukumura H, Masuhara H (1995) J Phys Chem 99:11481
213. Kokai F, Koga Y, Kakudate Y, Kawaguchi M, Fujiwara S, Kubota M, Fukuda M (1994) Appl Phys A 59:299
214. Estler RC, Nogar NS (1986) Appl Phys Lett 49:1175
215. Krajnovich DJ (1997) J Phys Chem A 101:2033
216. Dickinson JT, Shin J-J, Jiang W, Norton MG (1993) J Appl Phys 74:4729
217. Blanchet GB, Fincher JCR (1996) Appl Phys Lett 68:929
218. Hansen SG (1989) J Appl Phys 66:1411
219. Larciprete R, Stuke M (1987) Appl Phys B 42:181
220. Tsunekawa M, Nishio S, Sato H (1994) J Appl Phys 76:5598
221. Tsunekawa M, Nishio S, Sato H (1995) Jpn J Appl Phys 34:218
222. Danielzik B, Fabricius N, Röwekamp M, Linde D (1986) Appl Phys Lett 48:212
223. Feldmann D, Kutzner J, Laukemper J, MacRobert S, Welge KH (1987) Appl Phys B 44:81
224. Lippert T, Webb RL, Langford SC, Dickinson JT (1999) J Appl Phys 85:1838
225. Lippert T, Kunz T, Hahn C, Wokaun A (1997) Recent Res Develop Macromol Res 2:121
226. Lippert T, Dickinson JT, Hauer M, Kopitkovas G, Langford SC, Masuhara H, Nuyken O, Robert J, Salmio H, Tada T, Tomita K, Wokaun A (2002) Appl Surf Sci 197–198c:611
227. Lippert T, David C, Hauer M, Wokaun A, Robert J, Nuyken O, Phipps C (2001) J Photochem Photobiol A:Chem 145:87

228. Lippert T, David C, Hauer M, Masuhara H, Nuyken O, Phipps C, Robert J, Tada T, Tomita K, Wokaun A (2002) Appl Surf Sci 186:14
229. Shin JJ, Ermer DR, Langford SC, Dickinson JT (1997) Appl Phys A 64:7
230. Press WH, Flannery BP, Teukolsky SA, Vetterling WT (1989) Numerical recipes in Pascal:the art of scientific computing. Cambridge University, Cambridge
231. Zhao X, Hintsa EJ, Lee YT (1988) J Chem Phys 88:801
232. Dickinson JT, Jensen LC, Doering DL, Yee R (1990) J Appl Phys 67:3641
233. Webb RL, Langford SC, Dickinson JT (1995) Nucl Instrum Meth Phys Res B 103:29
234. Dickinson JT, Shin J-J, Langford SC (1996) Appl Surf Sci 96-98:326
235. Kelly R, Dreyfus RW (1988) Nucl Instr Methods Phys Res B 32:341
236. Eliasson B, Kogelschatz U (1988) Appl Phys B 46:299
237. Kogelschatz U (1990) Pure Appl Chem 62:1667
238. Eliasson B, Kogelschatz U (1991) OZONE Sci Eng. 13:356
239. Zhang JY, Esrom H, Kogelschatz U, Emig G (1993) Appl Surf Sci 69:299
240. Nuyken O, Stebani J, Lippert T, Wokaun A, Stasko A (1995) Macromol Chem Phys 196:751
241. Srinivasan R, Lazare S (1985) Polymer 26:1297
242. Zewail AH (1996) J Phys Chem 100:12701
243. Tas G, Hambir SA, Franken J, Hare DE, Dlott DD (1997) J Appl Phys 82:1080
244. Rabek JF (1987) Mechanism of photophysical processes and photochemical reactions in polymers. Wiley, New York
245. Delaire JA, Faure J, Hassine-Renou F, Soreau M, Mayeaux A (1987) Nouv J Chim 1:15
246. Vleggaar JJM, Huizer AH, Kraakman PA, Nijssen WPM, Visser RJ, Varma CAGO (1994) J Am Chem Soc 116:11754
247. Tanigaki K, Ebbesen TW (1989) J Phys Chem 93:4531
248. Willson CG, Clecak NJ, Grant BD, Twieg RJ (1980) Electrochem Soc Preprints:696
249. Grant BD, Clecak NJ, Twieg RJ, Willson CG (1981) IEEE Trans Electron Devices 28:1300
250. Willson CG, Miller RD, McKean DR (1987) Proc SPIE-Int Soc Opt Eng:771
251. Wen X, Hare DE, Dlott DD (1994) Appl Phys Lett 64:184
252. Tidwell TT (1995) Ketenes. Wiley, New York
253. Ulbricht M, Thurner J-U, Siegmund M, Tomaschewski G (1988) Z Chem 28:102
254. Winnik MA, Wang F, Nivaggioi T, Hruska Z, Fukumura H, Masuhara H (1991) J Am Chem Soc 113:7655
255. Gillet P, Goyot F, Malezieux J-M (1989) Phys Earth Planet Interiors 58:141
256. Fishbine B, Lippert T, Dick JJ (1997) Los Alamos National Laboratory
257. Lippert T, Stoutland PO (1997) Appl Surf Sci 109-110:43
258. Sroog CE (1996) Polyimides—fundamentals and applications. Marcel Dekker, New York
259. Dimitrakopoulos CD, Machlin ES, Kowalczyk SP (1996) Macromolecules 29:5818
260. Matsumoto T (1999) Macromolecules 32:4933
261. Hasegawa M, Sensui N, Shindo Y, Yokota R (1999) Macromolecules 32:387
262. Chern YT (1998) Macromolecules 31:5837
263. Pyo SM, Kim SI, Shin TJ, Park HK, Ree M, Park KH, Kang JS (1998) Macromolecules 31:4777
264. Chen JP, Labarthet FL, Natansohn A, Rochon P (1999) Macromolecules 32:8579
265. Wilson A (1984) Polyimides. Plenum, New York
266. Kawakami H, Mikawa M, Nagaoka S (1998) Macromolecules 31:6636
267. Coleman MR, Koros WJ (1999) Macromolecules 32:3106
268. Pettit GH (1996) Polyimides—fundamentals and applications. Marcel Dekker, New York
269. Bachman F (1989) Chemtronics
270. Lankard JR, Wolbold G (1992) Appl Phys A 54:355
271. Hansen SG, Robitaille TE (1988) Appl Phys Lett 52:81
272. Ulmer G, Hasselberger B, Busman H-G, Campbell EEB (1990) Appl Surf Sci 46:272
273. Koren J, Yeh YTC (1984) J Appl Phys 56:2120

274. Srinivasan R, Braren B, Dreyfus R (1987) J Appl Phys 61:372
275. Ball Z, Sauerbrey R (1994) Appl Phys Lett 65:391
276. Lippert T, Ortelli E, Panitz J-C, Raimondi F, Wambach J, Wei J, Wokaun A (1999) Appl Phys A 69:S651
277. Moyses S, Spells SJ (1999) Macromolecules 32:2684
278. Shimomura M, Okumoto H, Kaito A, Ueno K, Shen JS, Ito K (1998) Macromolecules 31:7843
279. Minagawa M, Yoshida W, Kurita S, Takada S, Yoshii F (1997) Macromolecules 30:1782
280. Snively CM, Koenig JL (1998) Macromolecules 31:3753
281. Buback M, Kowollik C (1998) Macromolecules 31:3211
282. Ozaki Y, Liu YL, Noda I (1997) Macromolecules 30:2391
283. Ren YZ, Murakami T, Nishioka T, Nakashima K, Noda I, Ozaki Y (1999) Macromolecules 32:6307
284. Storey RF, Donnalley AB (1999) Macromolecules 32:7003
285. Ortelli E, Geiger F, Lippert T, Wokaun A (2001) Appl Spectrosc
286. Kokai F, Saito H, Fujioka T (1990) Macromolecules 23:674
287. Mihailov S, Duley W (1988) Proc SPIE-Int Soc Opt Eng 957:111
288. Yeboah SA, Wang S-H, Griffiths PR (1984) Appl Spectrosc 38:259
289. Kubelka P, Munk F (1931) Z Tech Phys 11:593
290. Ehlers GFL, Fisch KR, Powell WR (1970) J Polym Sci 8:3511
291. Ishida H, Wellinghoff ST, Baer E, Koenig JL (1980) Macromolecules 13:826
292. Brekner MJ, Geger C (1987) J Polym Sci 25:2005
293. Socrates G (1994) Infrared characteristic group frequencies. Wiley, New York.
294. Borisevich NA, Khovratovich NN (1961) Optics Spectrosc 10:309
295. Molis S (1987)
296. Ball Z, Feurer T, Callahan DL, Sauerbrey R (1996) Appl Phys A 62:203
297. Graham JL, Berham JM, Dellinger B (1993) J Photochem Photobiol A 71:65
298. Sroog CE (1976) Polym Sci Macromol Rev 11:176
299. Dussel JJ, Rosen H, Hummel DO (1976) Makromol Chem 177:2343
300. Inagaki M, Takichi T, Hishiyama Y, Obslei A (1999) Chemistry and physics of carbon. Marcel Dekker, New York
301. Kubelka P (1948) J Opt Soc Am 38:1067
302. Kubelka P (1954) J Opt Soc Am 44:330
303. Kortum G (1957) Spectrochim Acta 6:534
304. Kortum G (1962) Trans Faraday Soc 58:1624
305. Kortum G, Braun W, Herzog G (1963) Angew Chem Intern Ed 2:333
306. Weigel JM, Fröhlich C, Baiker A, Wokaun A (1996) Appl Catal 140:29
307. White RL (1992) Appl Spectrosc 46:1508
308. White RL (1992) Anal Chem 64:2010
309. Snyder RW, Wade Sheen C, Painter PC (1988) Appl Spectrosc 42:503
310. Sakuma T, Ogitani S, Ikeda A (1995) J Photopolym Sci Technol 8:277
311. Buncick MC, Denton DD (1991) J Vacuum Sci Technol A9:350
312. Snyder RW, Sheen CW (1988) Appl Spectrosc 42:296
313. Digiulio C, Gautier M, Jasse B (1984) J Appl Polym Sci 29:1771
314. Mayer GW, Glass TE, Grubbs HJ, McGrath JE (1994) Polym Prepr. 35:549
315. Deshpande JSV, Gulari E, Kanicki J, Warren WL (1996) J Appl Phys 80:5028
316. Chandrasekhar TM, White RL (1996) J Appl Polym Sci 60:1209
317. Sroog CE, Endrey AL, Abramo SV, Berr CE, Edwards WM, Olivier KL (1965) J Polym Sci A 3:1373
318. Anderson OL, Susuki J (1983) J Geophys. Res 88:3549
319. Peri JB (1968) J Phys Chem 72:2917
320. Peri JB (1982) J Phys Chem 86:1615
321. Levenspiel O (1972) Chemical reaction engineering. Wiley, New York
322. Elias HG (1975) Makromoleküle. Hütig & Wepf, Basel, Heidelberg
323. Traeger RK, Salazar EA (1971) Polym Preprints 12:292

324. Heacock JF, Berr CE (1965) SPE Trans 5:105
325. Lippert T, Gerber T, Wokaun A, Funk DJ, Fukumura H, Gorto M (1999) Appl Phys Lett 75:1018
326. David C, Wei J, Lippert T, Wokaun A (2001) Microlectr Eng 57-58:453
327. Lippert T, Wokaun A, Langford SC, Dickinson JT (1999) Appl Phys A 69:S655
328. Lippert T, Langford SC, Wokaun A, Georgiou S, Dickinson JT (1999) J Appl Phys 86:7116
329. Webb RL, Jensen LC, Langford SC, Dickinson JT (1993) J Appl Phys 74:2323
330. Webb RL, Jensen LC, Langford SC, Dickinson JT (1993) J Appl Phys 74:2338
331. Ermer DR, Langford SC, Dickinson JT (1997) J Appl Phys 81:1495
332. Wright AN, Winkler CA (1968) Active nitrogen. Academic, New York
333. Ermer DR, Langford SC, Dickinson JT (1998) Surf Sci 127–129:977
334. Suzuki K, Matsuda M, Ogino T, Hayashi N, Terabayashi T, Amemiya K (1997) Proc SPIE-Int Soc Opt Eng 2992:98
335. Suzuki K, Matsuda M, Hayashi N (1998) Appl Surf Sci 127–129:905
336. Kunz T, Hahn C, Wokaun A (1998) Adv Mater 10:786
337. Seki S, Kanzaki K, Yoshida Y, Tagawa S, Shibata H, Asai K, Ishigure K (1997) Jpn J Appl Phys 36:5361
338. Schue F, Giral L (1998) Makromol Chem, Makromol Symp 24:21
339. Fukumura H, Kohji Y, Nagasawa K, Masuhara H (1994) J Am Chem Soc 116:10304
340. Gery G, Fukumura H, Masuhara H (1997) J Phys Chem B 101:3698
341. Tolbert WA, Lee I-YS, Doxtader MM, Ellis EW, Dlott DD (1993) J Imag Sci Technol 37:411
342. Lippert T, Bennett L, Kunz T, Hahn C, Wokaun A, Furutani H, Fukumura H, Masuhara H, Nakamura T, Yabe A (1997) Proc SPIE-Int Soc Opt Eng 2992:135
343. Kalyanasundaram K, Thomas JK (1977) J Am Chem Soc 99:2039
344. Guillet J (1985) Polymer photophysics and photochemistry. Cambridge Univ Press, Cambridge
345. Stein SE, Fahr A (1985) J Phys Chem 89:3714
346. (1996) Diffraction grating handbook, Rochester
347. Hill KO, Fujii Y, Johnson DC, Kawasaki BS (1978) Appl Phys Lett 32:847
348. Newsome CJ, O'Neill M, Farley RJ, Bryan-Brown GP (1998) Appl Phys Lett 72:2078
349. Söchtig J, Schütz H, Widmer R, Lehmann R, Grosse R (1994) Proc SPIE-Int Soc Opt Eng 2213:98
350. Lazare S, Bolle M, Cros A, Bellard L (1995) Nucl Instrum Methods Phys Res B 105:159
351. Lazare S, Drillhole D (1997) J Photochem Photobiol A:Chem 106:15
352. Sendova M, Hiraoka H (1993) Jpn J Appl Phys 32:6182
353. Niino H, Kawabata Y, Yabe A (1989) Jpn J Appl Phys 28:L2225
354. Knittel D, Kesting W, Schollmeyer E (1997) Polym Int 43:231
355. Okamoto T, Ohmori R, Hayakawa S, Seo I, Sato H (1997) Opt Rev 4:516
356. Dyer PE, Farley RJ, Giedl R (1996) Opt Commun 129:98
357. Dyer PE, Farley RJ, Giedl R, Karnakis DM (1996) Appl Surf Sci 96-98:537
358. Phillips HM, Callahan DL, Sauerbrey R, Szabò G, Bor Z (1991) Appl Phys Lett 58:2761
359. Phillips HM, Callahan DL, Sauerbrey R, Szabò G, Bor Z (1992) Appl Phys A 54:158
360. Chen K, Ihlemann J, Simon P, Baumann I, Sohler W (1997) Appl Phys A 65:517
361. Ilcisin KJ, Fedosejevs R (1987) Appl Opt 26:396
362. David C, Hambach D (1999) Microelectron Eng 46:219
363. Marrian CRK (1993) Technology of proximal probe lithography. SPIE, Bellingham
364. Eigler DM, Schweizer LK (1990) Nature 344:524
365. Lebreton C, Wang ZZ (1994) Scanning Microsc J 8:441
366. Beton PH, Dunn AW, Moriarty P (1995) Appl Phys Lett 67:1075
367. Marrian CRK, Dobisz EA (1992) J Vac Sci Technol B 10:2877
368. Majumdar A, Oden PI, Carrejo JP, Nagahara LA, Graham JJ, Alexander J (1992) Appl Phys Lett 61:2293
369. Park SW, Soh HT, Quate CF, Park SI (1995) Appl Phys Lett 67:2415

370. Kragler F, Günther LE, Leuschner R, Falk G, Hammerschmidt A, von Seggern H, Saeman-Ischenko G (1995) Appl Phys Lett 67:1163
371. Marrian CRK, Perkins FK, Brandow SL, Koloski TL, Dobisz EA, Calvert JM (1994) Appl Phys Lett 64:390
372. Kumar A, Biebuyck HA, Abbott NL, Whitesides GM (1992) J Am Chem Soc 114:9188
373. Stockman L, Neuttiens G, Van Haesendonck C, Bruynseraede Y (1993) Appl Phys Lett 62:2935
374. Thundat T, Nagahara LA, Oden PI, Lindsay SM, George MA, Glausinger WS (1990) J Vac Sci Technol A 8:3537
375. Thibaudau F, Roche JR, Salvan F (1994) Appl Phys Lett 64:523
376. Minne SC, Soh HT, Flueckiger P, Quate CF (1995) Appl Phys Lett 66:703
377. Hattori T, Ejiri Y, Saito K, Yasutake M (1994) J Vac Sci Technol A 12:2586
378. Dagata JA, Schnier J, Harary HH, Evans CJ, Postek MT, Bennet J (1990) Appl Phys Lett 56:2001
379. Kramer N, Birk H, Joritsm J, Schöneberger C (1995) Appl Phys Lett 66:1325
380. Larsen NB, Bjornholm T, Ganaes J, Larsen J, Schaumburg K (1995) Ultimate limits of fabrication and measurements. Kluwer, Dordrecht
381. Sohn LL, Willet RL (1995) Appl Phys Lett 67:1552
382. Bouchiat V, Esteve D (1996) Appl Phys Lett 69:3098
383. Jung TA, Moser A, Hug HJ, Brodbeck D, Hofer R, Hidber HR, Schwarz UD (1992) Ultramicroscopy 42-44:1446
384. Jin X, Unertl WN (1992) Appl Phys Lett 61:657
385. Boschung E, Heuberger M, Dietler G (1994) Appl Phys Lett 64:3565
386. Krausch G, Mynek J (1996) Microelectron Eng 32:219
387. Dutoit B, Zeisel D, Deckert V, Zenobi R (1997) J Phys Chem B 101:6955
388. Synge EH (1928) Phil Mag 6:356
389. Hecht B, Sick B, Wild U, Deckert V, Zenobi R, Martin OJF, Pohl DW (2000) J Chem Phys 112:7761
390. Stöckle R, Setz P, Deckert V, Lippert T, Wokaun A, Zenobi R (2001) Anal Chem 73:1399
391. Baro J, Dudek D, Luther K, Troe J (1983) Ber Bunsenges Phys Chem 87:1161
392. Baro J, Dudek D, Luther K, Troe J (1983) Ber Bunsenges Phys Chem 87:1155
393. Hoen S, Mamin HJ, Rugar D (1993) Appl Phys Lett 64:267
394. La Rosa AH, Yakobson BI, Hallen HD (1995) Appl Phys Lett 67:2597
395. Phipps CR, Luke J (2000) Proc SPIE-Int Soc Opt Eng 4065:801
396. Phipps CR, Michaelis MM (1994) Laser Part Beams 12:23
397. Phipps CR, Turner TP, Harrison RF, York GW, Osborne WZ, Anderson GK, Corlis XF, Haynes LC, Steele HS, Spicochi KC, King TR (1988) J Appl Phys 64:1083
398. Kokorakis A (2001)
399. Hsieh YS, Yang CR, Hwang GY, Lee YD (2001) Macromol Chem Phys 202:2394

Adv Polym Sci (2004) 168:247–289
DOI: 10.1007/b12683

Ultrashort Pulse Laser Interaction with Dielectrics and Polymers

Jörg Krüger · Wolfgang Kautek

Laboratory for Thin Film Technology, Federal Institute for Materials Research and Testing, Unter den Eichen 87, 12205 Berlin, Germany
E-mail: joerg.krueger@bam.de
E-mail: wolfgang.kautek@bam.de

Abstract Femtosecond laser micromachining has excited vivid attention in various industrial fields and in medicine owing to the advantages of ultrashort laser pulses compared to long-pulse treatment. These are mainly the reduction of the laser fluence needed to induce ablation and the improvement of the contour sharpness of the laser-generated structures. Recently, special attention was paid to femtosecond laser experiments on nonabsorbing inorganic dielectrics. This is due to the fact that optical damage in dielectric optical elements limits the performance of high-power laser systems. Despite the fact that a large variety of organic polymers can be machined with excimer lasers successfully, the involvement of thermal processes can lead to an unsatisfactory quality of the structures. Ultrashort, fs-laser pulses might be an alternative for the treatment of polymers. Therefore, femtosecond laser machining investigations of dielectrics and polymers are reviewed in this paper. Similarities and differences of the ablation behavior of both material classes are discussed. The influence of the bandgap on the ablation threshold in dependence on the pulse duration, the enhancement of the machining precision with a shortening of the pulse duration, incubation phenomena, and morphological features appearing on the surface after femtosecond laser treatment are mentioned. Possible applications, e.g., in medicine and biosensors, are described.

Keywords Ablation · Dielectrics · Femtosecond laser · Micromachining · Polymers

Abbreviations

a	Avalanche coefficient
α	Linear absorption coefficient
α_{eff}	Effective absorption coefficient
d	Ablation depth per pulse (=ablation rate)
D	Diameter of ablated (modified) area
δ	Thermal diffusivity
Δd	shot-to-shot deviation of *d* from its mean value (99 % confidence interval)
E_0	Maximum energy
E_T	Transmitted energy
E_{th}	Threshold energy
f	Focusing distance
F_0	Maximum fluence
F_{th}	Threshold fluence
I	Intensity
l	Spatial position
λ	Center wavelength
Λ	Ripple period
n	Density of electrons
N	Number of pulses per spot
q	Lateral extension parameter
r	Spatial coordinate
R	Reflectivity
σ_k	*k*-photon absorption cross section
t	Time
τ	Pulse duration (FWHM)
θ	Angle of incidence
w_o	Gaussian beam radius
x	Spatial coordinate
y	Spatial coordinate
ξ	Incubation parameter

1 Introduction

The experimental evidence of light amplification by induced emission of light in a ruby crystal by Maiman in 1960 [1] started up a rapid evolution of laser sources. Additionally, the number of possible applications of these sources has increased dramatically during the last four decades. One major aim of laser and optics design is the qualification of laser systems for materials processing in technology and medicine. For these purposes, high (average or peak) power and a spatial concentration of the light are needed. A crude classification can be made by distinguishing between treatment on a "macro" scale (dimensions $\geq$0.1 mm) and in the "micro" range (structural width <0.1 mm).

Important industrial applications of high-power lasers on a macro scale are laser cutting and welding. Continuous-wave CO_2 and Nd:YAG lasers are employed for these processes. The maximum laser power determines the speed of the process, whereas the spatial beam profile is crucial for the quality of the treatment. This working field triggers demands for lasers emitting even higher power in the multi-kW regime.

1.1 Laser Micromachining

The need for miniaturized structures is not only initiated by the silicon technology in microelectronics, but also by applications in telecommunication, modern measuring systems, traffic, and medicine. Small lateral structural widths and high aspect ratios of cavities, grooves etc. are required.

Laser structuring of materials with powerful pulses shows some advantages compared to other methods, i.e.:

- contactless machining (cf. mechanical methods),
- no expensive vacuum equipment is necessary (cf. X-ray, electron, and ion beams),
- laser pulses can be transmitted through dense material (cf. particle beams), and
- the sample geometry is not restricted to flat substrates (cf. lithographic techniques).

Laser microprocessing allows lateral structures down to the submicrometer range with three different methods [2]:

- direct writing,
- projection patterning,
- patterning by interference of laser beams.

This work will concentrate on the direct writing mechanism and on treatment of materials in the micro range using ultrashort laser pulses.

1.2 Ultrashort Laser Pulses

Starting with the invention of the laser more than 40 years ago, (passive) mode-locking techniques for the generation of very short laser pulses have been developed. During the seventies and eighties, dye lasers played a dominant role in this area (Fig. 1). The "threshold" of 100 fs was reached in 1981 [3]. This dye laser shows a ring configuration that allows two counter-propagating trains of pulses to evolve in the cavity. An organic dye in solution acts as the amplifying medium and an additional one as a saturable absorber. The two pulse trains meet in the absorber, which is the configuration of minimum losses. This loss modulation is the origin of the femtosecond pulse formation. For the dye laser, the culmination was achieved with the generation of 6-fs pulses [4].

The activities for a shortening of the dye laser pulses were paralleled by efforts for the amplification of low-energy pulses to extend the application potentials. Average powers of the order of 10 mW could be extracted. Depending on the basic concept of the amplifier system, either low-energy pulses (~μJ) with high repetition rates (~kHz) [5] or high-energy pulses (~mJ) with low repetition rates (~Hz) were provided [6].

During the last decade, solid-state lasers captured the market and substituted the complex dye systems more and more (Fig. 1). The breakthrough for solid-state femtosecond oscillators was connected with the development of the Kerr lens mode-locking technique for the Ti:sapphire laser [7]. The simple Ti:sapphire cavity contains the active medium (Ti:sapphire rod) and dispersive elements. Kerr lensing in a Ti:sapphire rod develops due to an intensity-dependent refractive index across the spatial beam profile yielding a self-focusing of the laser beam. With an additional aperture in the beam

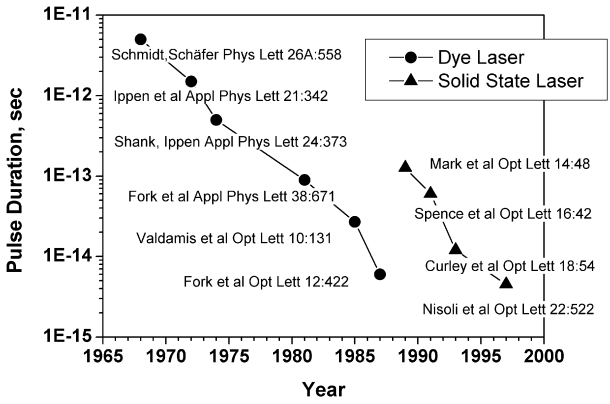

Fig. 1 The "revolution" towards ultrashort light pulses

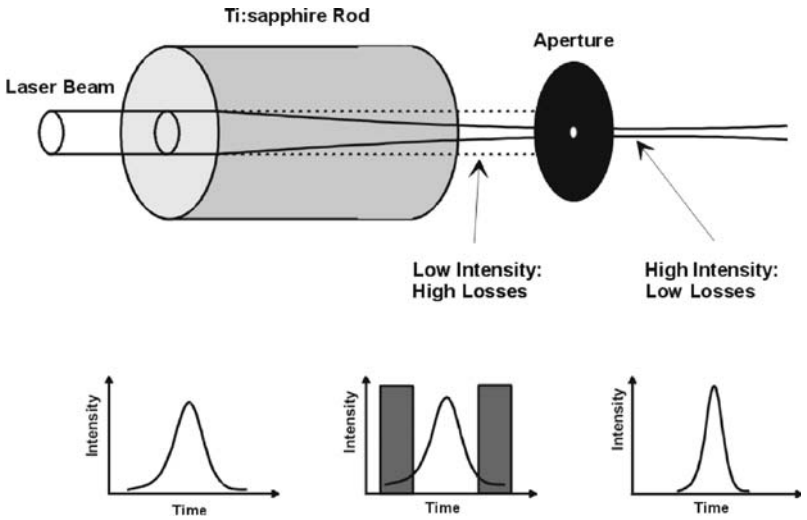

Fig. 2 Kerr lens mode-locking technique for the Ti:sapphire laser

path, higher intensities are enhanced whereas lower intensities are suppressed (Fig. 2). That means a spatial preference of laser rays with high intensities close to the optical axis and additionally a temporal selection of the most intense part of the pulse (bottom of Fig. 2).

Employing the chirped pulse amplification technique [8], typically an increase of the pulse energy from the nJ- to the mJ-level at repetition rates of the order of kHz can be achieved, i.e., average powers of ~W are obtained. A scheme of the chirped pulse amplification technique is depicted in Fig. 3. The basic idea is to stretch the pulses temporally prior to amplification to avoid nonlinear effects or even damage in the amplification crystal. After

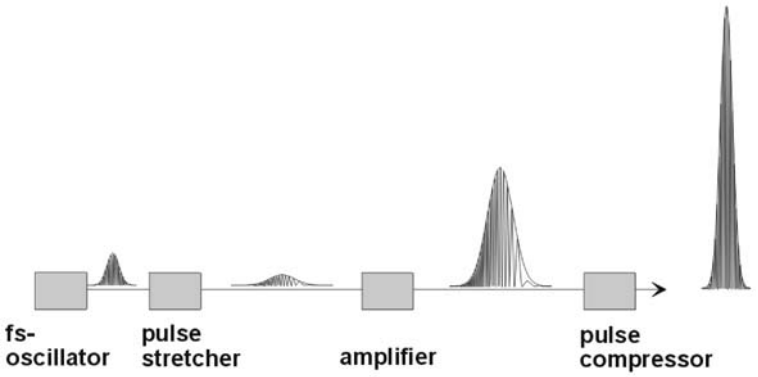

Fig. 3 Chirped pulse amplification (CPA) technique

amplification, the pulses are recompressed using linear optical elements (prisms, gratings).

In 1997, the "old" dye laser record with respect to the shortest pulses was improved by a Ti:sapphire laser. Pulses with a duration of 5 fs could be generated [9]. Despite the many advantages of solid-state femtosecond laser systems compared to dye lasers (power, compactness, no toxic dyes and solvents etc.), one drawback should be noted. The passive mode-locking process is not self-starting in many cases.

An alternative self-starting source may be the upconversion fiber laser which exploits excited-state absorption of rare earth ions in fluoride glasses [10]. In this material, infrared radiation can be efficiently converted into bright visible laser radiation. The setup of an upconversion fiber laser is very simple. It consists of a diode laser as pump source, a coupling optics to launch the diode laser radiation into the active fiber, and the fiber itself. Applications in micromachining require compact, efficient, and powerful lasers with excellent beam quality. The beam characteristics of a diode-pumped fiber laser are determined only by its refractive index profile. To scale the output power beyond a few hundred milliwatts, the double-clad fiber design can be applied. In these fibers, the active fiber core is surrounded by a second fiber core, which acts as a large-diameter waveguide for the pump light. With this concept, fiber lasers with output powers of several watts could be realized. The limit of the output power scaling is determined by the damage threshold of the fiber end faces and the mirrors, and by the threshold for stimulated Raman scattering. So, the scaling of the output power up to 100 W with diffraction-limited beam quality seems to be possible in the near future.

1.3
Femtosecond Laser Applications

Femtosecond laser applications, e.g., in electronic or medical technology require microstructuring on uneven substrates. This cannot be achieved by conventional photolithography which only functions on completely flat supporting materials. Ultraviolet lasers (excimer, fourth harmonic Nd:YAG) have been widely used for such purposes. However, when high precision is required and substrates are extremely fragile and thermally sensitive, the very low heat effect by subpicosecond laser pulses can avoid this micromachining problem.

A couple of micromachining investigations with different types of femtosecond lasers are reviewed in this paper. Special attention will be paid to dielectrics and polymers, and possible applications are discussed.

2 Experimental

2.1 Femtosecond Lasers

For the ablation and machining experiments, different types of femtosecond lasers were employed:

1. Dye laser. Femtosecond pulses were generated and amplified by means of a colliding pulse mode-locked (CPM) dye laser and a dye amplifier (BESTEC), respectively [11, 12]. This generator/amplifier system yielded pulses with a duration of ~300 fs, a center wavelength of ~620 nm, and a single pulse energy of 200 μJ. The repetition rate amounted to 3–4 Hz. Figure 4 depicts the dye laser system. On the lower level, the CPM ring laser (red beam) and the argon ion laser pump radiation (green light) can be seen. At

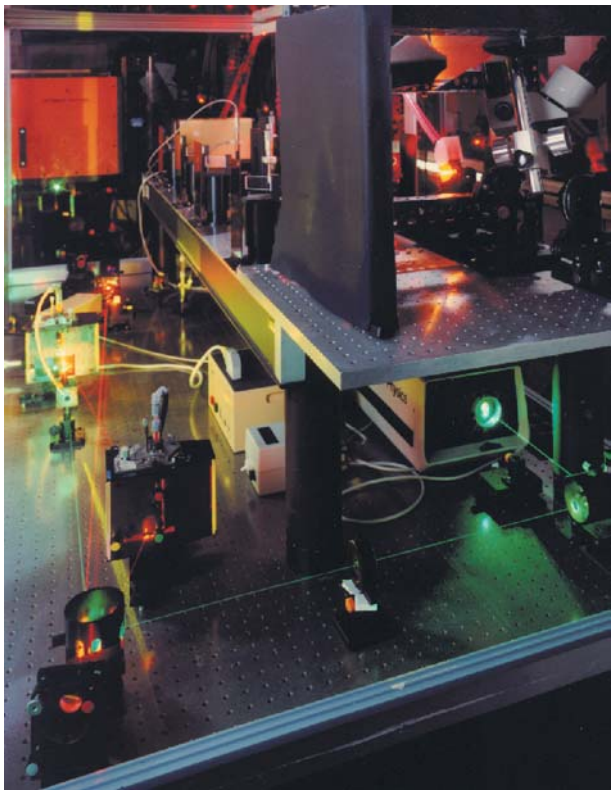

Fig. 4 Femtosecond dye laser consisting of a colliding pulse mode-locked ring laser *(lower level)* and a dye amplifier (*upper level*)

the top, the amplifying part of the system can be viewed. The line focus of a XeCl excimer laser in the final amplification stage is obvious.

2. Ti:sapphire laser. A Ti:sapphire laser system (Spectra Physics, Tsunami and Spitfire) delivering 150-fs pulses of energies up to 800 μJ at 800 nm wavelength was also used for the investigations. The laser provides a spatial TEM_{00} beam profile (M^2<1.5). Repetition rates of 1 kHz are possible, but in many cases the repetition rate of the laser pulses was limited to 2 Hz to avoid cumulative heating of the samples.
3. Ti:sapphire laser. The second Ti:sapphire laser system (Femtopower Compact Pro, Femtolasers) delivered pulses with a duration of τ=25 fs, a central wavelength of λ=800 nm, a spatial TEM_{00} mode (M^2<2), and a repetition rate of 1 kHz. An additional home-built system (Vienna University of Technology, Austria [13]) generates pulses with a duration of 5 fs at a center wavelength of 780 nm in a diffraction-limited beam. Pulse energies up to 500 μJ and repetition rates of 1 kHz are obtained. The key element of the system is a hollow fiber filled with argon gas to broaden the spectrum of the 25-fs pulses from a Ti:sapphire amplifier. Pulses with a duration >25 fs can be achieved by inserting additional dispersive material (e.g., glass) in the beam path.

2.2
Pulse Duration, Pulse Energy, Focusing

The pulse duration could be measured by means of different autocorrelators (e.g., APE, PulseScope). In most cases, the single-pulse energy was changed with a combination of a half-wave plate and a linear polarizer and could be determined with a pyroelectric detector (e.g., BESTEC, PM 200) with an accuracy of ±10%. The laser beam was focused by means of lenses (and for the very short pulses by a silver mirror) on the front side of the samples. Spot sizes (Gaussian beam diameters) of a couple of 10 μm were achieved. The specimens were positioned by a remotely controlled translation stage perpendicular to the direction of laser incidence. All experiments were performed in air (exception 5-fs investigations, soft vacuum ~10^{-3} mbar), that is, relevant for technical micromachining applications. Prior to the laser experiments, specimens were cleaned (nitrogen stream, methanol).

2.3
Gaussian Beam Radius

For the indication of absolute laser fluence values, e.g., for ablation, modification, melting etc. of a material, the determination of the spot size is crucial. Fluence values allow the comparison of laser treatment with different types of lasers showing various spatial beam characteristics like a square (e.g., excimer laser) or a Gaussian beam profile (e.g., Ti:sapphire laser). In the following, the determination of the Gaussian beam radius is described.

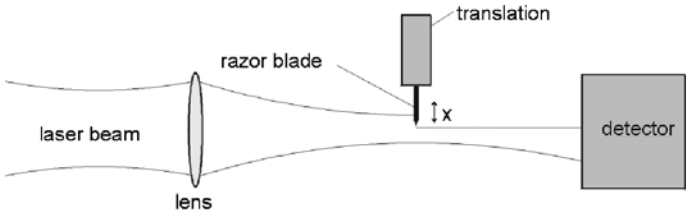

Fig. 5 Scheme of the determination of the focus area by means of the "moving edge" method

The "moving edge" method provides an opportunity widely used. The sample under investigation has to be substituted by an edge, normally a razor blade (Fig. 5). The razor blade is scanned through the focus area in the x-direction and the transmitted energy for a fixed position of the razor blade ($x=l$, one measuring point) is determined with a detector. The coordinate system (x,y) is depicted in Fig. 6.

A two-dimensional Gaussian beam exhibits a fluence distribution $F(x,y)$ according to

$$F(x,y) = F_0 \cdot \exp\left[-\frac{2}{w_0^2}\cdot\left(x^2+y^2\right)\right] \tag{1}$$

with the maximum fluence F_0 and the Gaussian beam radius w_0. At radius w_0, by definition $F(x,y)$ decreases to F_0/e^2. Calculating the transmitted energy E_T for a fixed position of the razor blade $x=l$ (Fig. 6), one obtains

$$E_T(x=l) = F_0 \cdot \int_{-\infty}^{\infty} \exp\left[-2\left(\frac{y}{w_0}\right)^2\right] dy \cdot \int_{l}^{\infty} \exp\left[-2\left(\frac{x}{w_0}\right)^2\right] dx \tag{2}$$

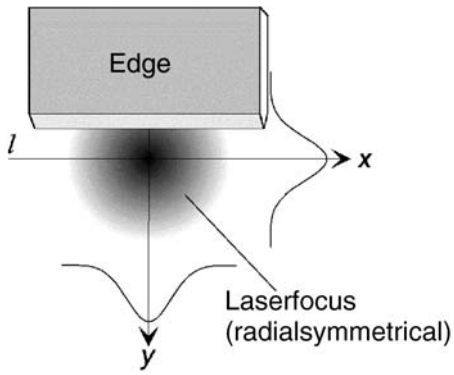

Fig. 6 Coordinate system (x,y) for the "moving edge" measurement

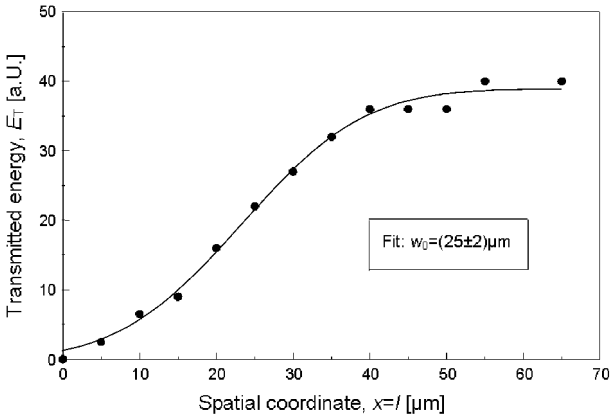

Fig. 7 Plot of transmitted energy E_T vs razor blade ("moving edge") position $x=l$ for the evaluation of the focus area. The *solid line* represents a fit according to Eq. 3 yielding a Gaussian beam radius of w_0=25 µm

Solving the y-integral analytically,

$$E_T(x=l) = F_0 \cdot \sqrt{\frac{\pi}{2}} \cdot w_0 \cdot \int_l^\infty \exp\left[-2\left(\frac{x}{w_0}\right)^2\right] dx \tag{3}$$

can be derived. With Eq. 3 and experimental data $E_T(x=l)$, w_0 and F_0 can be determined by means of a numerical fit. An example can be seen in Fig. 7. Each data point represents an average of N=100 laser pulses.

If a direct determination of w_0 can be performed (e.g., with a CCD camera), the relation between the maximum laser fluence F_0 and the single-pulse energy E_0 for a Gaussian beam can be deduced from Eq. 3 by setting $l=-\infty$. The calculation yields

$$E_0 = F_0 \cdot \frac{\pi}{2} \cdot w_0^2 \tag{4}$$

Therefore, the dependence of the maximum fluence on the single-pulse energy can be written as

$$F_0 = \frac{2\,E_0}{\pi\, w_0^2} \tag{5}$$

It should be noted that a relative error of the w_0 determination of ±10% (see above: error of pulse energy ±10%) results in a fluence accuracy of ±30%.

2.4 Investigation of Laser-Generated Features

For the experiments, only macroscopic front-surface ablation (and if necessary modification) was considered. For an in situ evaluation and the decision if ablation takes place or not, a HeNe laser was focused onto the interaction region between (femtosecond) laser and sample. In the case of ablation, changing Speckle patterns can be observed.

A first ex situ inspection of the laser-generated structures on the different sample surfaces was performed by means of light microscopy (e.g., Reichert-Jung, Polyvar). The microscope featured the opportunity for a vertical and lateral measurement of various patterns with a resolution better than 1 μm. Therefore, absolute ablation depths and ablation depths per pulse d (for multipulse treatment) could be determined. Additionally, lateral cavity diameters D were measured in the case of hole drilling.

It should be noted that the diameter of a laser-produced cavity may differ significantly from the Gaussian beam diameter $2w_0$. Figure 8 illustrates this phenomenon. The distance $2w_0$ is indicated on the x-axis (projection at F_0/e^2 to the x-axis). For ablation, a material- and laser-dependent fluence threshold F_{th} has to be surpassed. On the sample, one can realize a laser-induced hole with a diameter smaller than $2w_0$ (projection at F_{th} to the x-axis) for example. By adjusting F_0 very close to F_{th} (with $F_0 > F_{th}$), the production of tiny structures should be possible.

In addition to the light microscope, morphological changes at the surface of the samples were inspected with a scanning electron microscope (SEM). This SEM (Hitachi, S-4100) was equipped with a cold-field electron emission cathode and was operated at acceleration voltages between 10 and 20 kV. Prior to SEM investigations, nonconducting samples were sputter-deposited on Au films with thicknesses of a few nm (Emscope SC500).

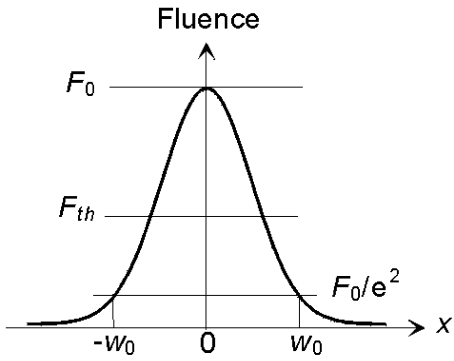

Fig. 8 Scheme of a spatially Gaussian beam profile. F_0 and F_{th} denote the maximum laser fluence and the ablation threshold fluence, respectively. The distance $2w_0$ represents the $1/e^2$-Gaussian beam diameter

If the generated craters exhibited a very low depth, postexperimental evaluation was performed with atomic force microscopes (AFM) in contact mode (Topometrix, Explorer-Scanner) or in tapping mode (Digital Instruments, Dimension 3000 SPM).

2.5 Ablation Threshold Determination

From a physical point of view, but also in the context of the application of laser pulses for micromachining purposes, the determination of ablation rates d (=absolute ablation depth divided by the number of pulses per spot N) and ablation threshold fluences F_{th} is essential.

One option for the quantification of F_{th} is the utilization of a semi-logarithmic plot of d vs maximum fluence F_0. For photochemical as well as for photothermal ablation and many materials, a relation

$$d = \frac{1}{\alpha_{eff}} \ln\left(\frac{F_0}{F_{th}}\right) \tag{6}$$

could be found (e.g., [2]). Equation 6 can easily be understood in terms of Lambert–Beer's law. α_{eff} represents an effective absorption coefficient that includes to a certain extent incubation phenomena (i.e., an increasing absorption due to the generation of defects during repetitive illumination) and nonlinear absorption phenomena. Note that, strictly speaking, nonlinear effects have to be ruled out due to the deduction of Eq. 6 with the assumption of (only) linear absorption (cf., e.g., considerations in [14]). Experimentally, for opaque materials like metals (Ni, Cu, Mo), $\alpha_{eff} \approx \alpha$ was observed with α as the linear absorption coefficient at the laser wavelength [15]. For weaker absorbing samples, normally $\alpha_{eff} > \alpha$ is obtained [16].

The procedure of the F_{th} evaluation according to Eq. 6 is restricted to bulk samples. For deep cavities, the measurement of the absolute crater depth with the help of an optical microscope is difficult. Additionally, w_0 has to be determined, e.g., by means of the "moving edge" method and F_0 has to be calculated employing Eq. 5. This technique requires a substitution of the sample by a razor blade, which might lead to experimental uncertainties.

A solution to these experimental problems can be a method with a self-consistent evaluation of the Gaussian beam diameter w_0 and the ablation threshold F_{th}. The advantages of this procedure are the possibilities of an investigation of thin (film) samples and the avoidance of a substitution of the target by an "edge" for the w_0 determination. The principle is depicted in Fig. 9.

The diameters D of the laser-damaged (ablated) areas are determined with a microscope. The laser fluence sufficient to ablate the material (for a fixed pulse duration τ and number of pulses per spot N) is named threshold fluence F_{th}.

Assuming a Gaussian spatial beam profile, the relation between the crater diameter D and the maximum laser fluence F_0 can be written as [17]

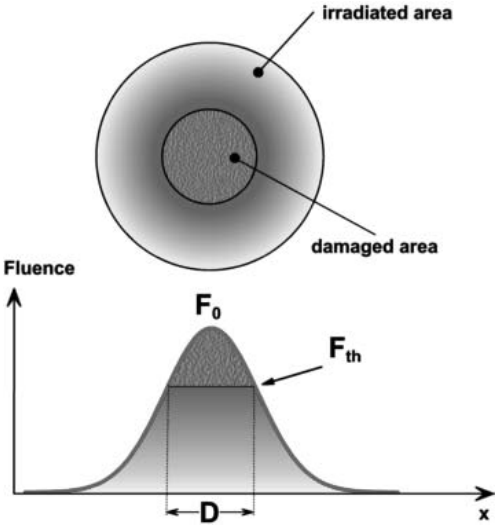

Fig. 9 Diagram of laser-induced ablation on the samples (*top*) and corresponding Gaussian fluence profile along *x*-axis (*bottom*). *D* marks the diameter of the ablated area

$$D^2 = 2w_0^2 \ln\left(\frac{F_0}{F_{\text{th}}}\right) \tag{7}$$

Equation 7 is also valid if the laser fluences F_0 and F_{th} are replaced by the pulse energies E_0 and E_{th}, respectively.

Taking into account Eq. 7 with the energy values, an ablation threshold energy E_{th} is obtained from a semi-logarithmic plot of the squared diameter of the ablated (or modified) area D^2 vs pulse energy E_0. The slope of the straight line yields the Gaussian beam radius w_0. With the known beam radius in the focal plane and Eq. 5, one can calculate the laser fluence values. Figure 10 depicts an example for such a measurement. The squared diameters D^2 (of modified areas) vs laser fluence F_0 for the 150-fs laser treatment of polyimide are shown [18]. Note that the graph represents results for different numbers of pulses per spot (N=1−100) and for various focusing conditions. The dependence on N results in parallel lines representing a fixed slope but different modification thresholds due to incubation phenomena. The extrapolation to D^2=0 delivers the modification threshold fluences. The variation of the focusing conditions (lenses with focusing distances of f=25.4 mm and f=60 mm) yields different slopes of the curves (solid symbols correspond to the right vertical axis and hollow symbols to the left vertical axis) of w_0=8 μm (f=25.4 mm) and w_0=27 μm (f=60 mm), respectively.

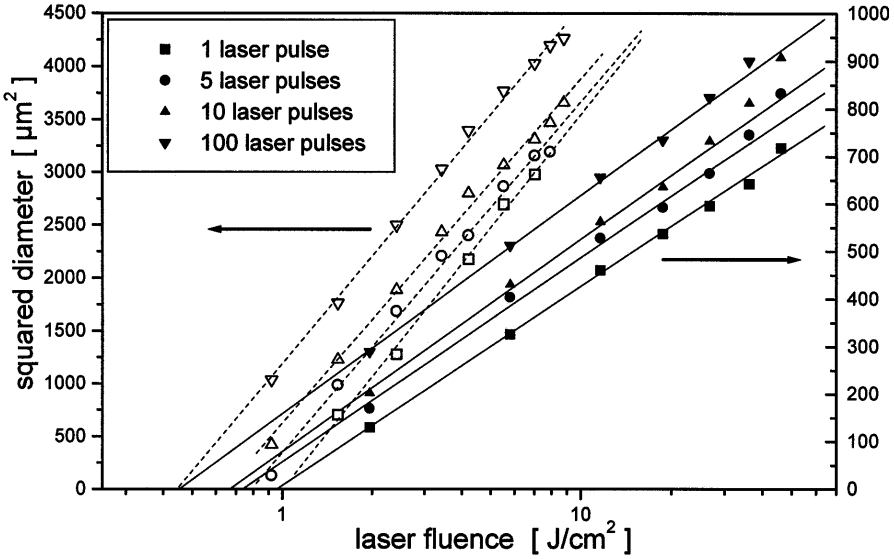

Fig. 10 Femtosecond-pulse laser treatment of polyimide. τ=150 fs, λ=800 nm. Squared diameters of the modified areas of polyimide in dependence on the maximum laser fluence for circularly polarized light. *Solid symbols*: focusing with f=25 mm lens, right axis. *Hollow symbols*: focusing with f=60 mm lens, left axis [18]

3 Femtosecond Laser Ablation

In order to ablate material with a laser, it is necessary to surpass a material-dependent energy volume density [19]. For fixed laser parameters, the ablation behavior of any sample is primarily influenced by its optical (reflectivity R, linear absorption coefficient α) and thermal (thermal diffusivity δ) properties. Therefore, ablation thresholds F_{th} and rates per pulse d vary.

The energy of a laser pulse is absorbed by the electrons of the material. The absorption mechanism is different for opaque and transparent samples. Linear absorption is the main contribution in opaque materials (e.g., metals) whereas absorption has to be realized by nonlinear processes in transparent materials (e.g., dielectrics). These nonlinear processes are avalanche and multiphoton ionization [20–25]. After electronic excitation, the energy is transferred to the lattice and heats it up to boiling and/or to vaporization temperature. Then, electrons and lattice are in thermal equilibrium. The transfer time of the electronic energy to the lattice (electron-phonon-relaxation time) is of the order of picoseconds [26].

For very short pulses, an additional mechanism called Coulomb explosion was reported recently [27]. It could be shown that dielectrics (in contrast to metals and semiconductors) are strongly charged at the surface on a femtosecond time scale and undergo an impulsive explosion.

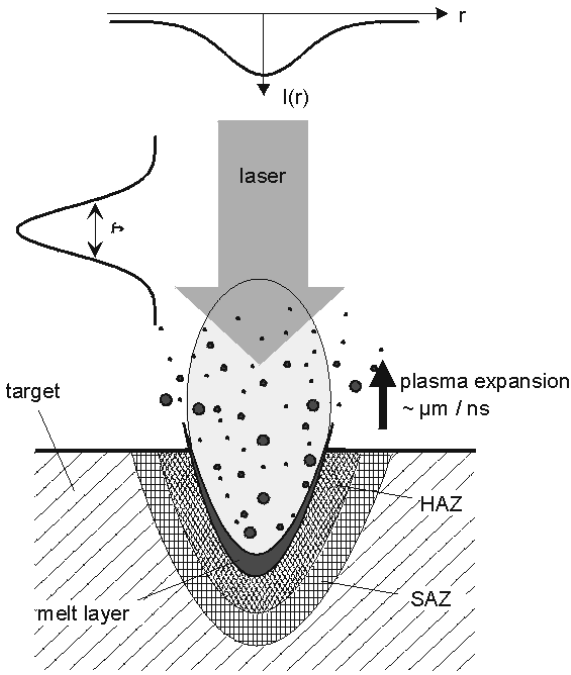

Fig. 11 Scheme of pulse laser ablation. $I(r)$: spatial intensity distribution, r: spatial coordinate, τ: pulse duration, HAZ: heat-affected zone, SAZ: shock-affected zone

A major parameter for the ablation process and the machining result is the pulse duration τ. Two extreme cases may be considered. For long-pulse treatment (nanosecond laser pulses and longer), i.e., pulses that are significantly longer than the electron-phonon-relaxation time of the order of a couple of picoseconds, a local thermal equilibrium between electronic system and lattice can be assumed. Modeling has been done with the simple heat diffusion equation. It could be demonstrated that the ablation threshold F_{th} varies with $\sqrt{\tau}$. The ablation of a sample with a (nanosecond) laser pulse is schematically depicted in Fig. 11. The pulse with duration τ and a spatial intensity distribution $I(r)$ hits the target. The intensity is sufficient to ablate the material. The ablated species leave the target surface with velocities of about µm/ns [28]. That means that the trailing edge of the laser pulse is partly screened by the ablation plume, and the efficiency of the whole ablation process is decreased. Further, a heat-affected zone (HAZ) with an extension of the order of $\sqrt{\delta\tau}$ can be observed [29]. Another disadvantage of long pulse machining is the formation of a relatively thick melt layer in the cavity, which is more or less a part of the HAZ. The expanding plume exerts a recoil pressure on the melt film and droplets are squeezed out of the cavity [11]. Finally, a shock-affected zone (SAZ) may be observed in sensitive (e.g.,

biological) samples [30]. This often leads to unsatisfying surface qualities with structures generated by the influence of heat after ns laser treatment.

For femtosecond laser pulses (which are short compared to the electron-phonon-relaxation time) and a wide variety of materials, the morphologies of laser-generated structures change drastically [2, 11]. At a constant laser wavelength and sample, the ablation threshold decreases compared to the nanosecond treatment [31]. Multipulse ablation of poly(methyl methacrylate) (PMMA) in the 300-fs case could be found at fluences five times lower than the threshold fluence for the 16-ns laser pulses at 248 nm wavelength. The femtosecond ablation spots showed a smoother surface with less signs of thermal degradation. Owing to the high intensities achieved with ultrashort laser pulses, it is possible to make use of nonlinear absorption in samples, such as PMMA, which are transparent for the applied wavelength [32]. The material has a negligible absorption for a wavelength of 308 nm (α<20 cm^{-1} [2]). Therefore, clean etching with 160-fs laser pulses with laser fluences as low as 0.2–0.3 J cm^{-2} can only be achieved by taking advantage of two-photon absorption.

The theoretical description for the ablation with nanosecond laser pulses on the basis of a local thermal equilibrium between electron system and lattice is no longer valid in the femtosecond case. For fs pulses, the electrons are excited instantaneously and thermalize on a time scale of ~100 fs [26]. Due to their low heat capacity, they can reach very high transient temperatures (>10^3 K). During excitation and thermalization of the electronic system, the lattice stays "cold". After the electron-phonon-relaxation time, the lattice is heated up. The modeling of this process is only possible if two different temperatures (electron and lattice temperature) are taken into account. This description is called the two-temperature model (TTM) and is employed mainly for metals and semiconductors. Its basic assumption is that the electrons are in thermal equilibrium [33–36]. Experimentally, the multipulse damage thresholds of copper and molybdenum were found to be constant for pulses in the range 2.5–500 ps (λ=9.3 μm) [34]. These investigations were extended for a gold grating down to the 100-fs limit (λ=1053 nm). A constant threshold fluence F_{th} was reported for pulse durations τ from 100 fs up to 100 ps [23]. The dependence of the threshold fluence on the pulse duration can be well described by the TTM, proving that laser damage in metals is a purely thermal process even for femtosecond laser pulses [37]. For silicon, a variation by a factor of two was observed for the dependence $F_{th}(\tau)$ using pulses ranging from τ=400 fs down to τ=5 fs (λ=780 nm) [38].

Historically, polymers played a decisive role in the understanding of differences between laser treatment with nanosecond laser pulses and the fs domain [31, 32]. Another motivation for the investigation of the basics of laser–material interaction with nonabsorbing samples was the unwanted damage to optical elements (e.g., dielectric mirrors [39]) in the beam path of short-pulse lasers. The destruction of these components limits the performance of short-pulse oscillators and amplifiers. Additionally, frequency con-

version efficiencies and the range of new frequencies accessed by parametric nonlinear optical processes are restricted.

The dependence $F_{th}(\tau)$ for dielectrics has been evaluated by Bloembergen for 1 ps$\leq\tau\leq$10 ns in 1974 [20]. It was claimed that avalanche ionization is the crucial mechanism for electric breakdown in dielectrics, which are free from absorbing inclusions. It was suggested that in real technical samples, damage thresholds are influenced by absorbing inclusions. The avalanche mechanism sets an upper limit for the electrical fields (and laser fluences) applicable to the materials. Thermally excited or trapped electrons provide the seed electrons for the avalanche effect. Therefore, the process has a highly statistical character. The fundamental processes can be summarized as follows: (1) acceleration of the seed electrons in the laser field via inverse bremsstrahlung absorption (=free carrier absorption); (2) generation of secondary electrons by collisional (avalanche) ionization; (3) electron-phonon coupling, i.e., transfer of energy from the electronic system to the lattice; (4) melting, vaporization, plasma formation, and/or ablation. This scenario was related to a critical electron density in the conduction band ($\approx 10^{21}$ cm^{-3} for λ=1053 nm [40]).

Recent measurements have shown that laser ablation (or "negatively" spoken damage) becomes more deterministic when femtosecond laser pulses are applied [22, 23, 40, 41]. This observation is due to the generation of conduction band (seed) electrons by means of multiphoton ionization (MPI). Based on this knowledge, a model for optical breakdown that takes into account avalanche ionization and MPI was developed [40]. The temporal behavior of the free electron density in the conduction band $n(t)$ can be described by a rate equation

$$\frac{\partial n(t)}{\partial t} = aI(t)n(t) + \sigma_k I^k(t) \tag{8}$$

The first term on the right side of Eq. 8 describes the avalanche ionization and the second one the multiphoton ionization. $I(t)$ is the time-dependent intensity of the laser and a the avalanche coefficient. σ_k denotes the k-photon absorption cross section and k is equal to the smallest number of photons needed to overcome the optical bandgap of the material. Equation 8 demonstrates that the bandgap of a dielectric has a major influence on its ablation efficiency. For an increasing bandgap, the relative weight of the avalanche process is greater than that of MPI. Yet, MPI provides a deterministic seed electron production for the subsequent avalanche process. Therefore, for shorter pulses, the statistical character of the ablation is reduced [42, 43].

4 Femtosecond Machining Results

In this chapter, a couple of recent experimental results obtained for the femtosecond laser machining of inorganic dielectrics and organic polymers are

reviewed. Fused silica and barium aluminum borosilicate glass represent the dielectrics. The organic materials polyimide, polycarbonate, poly(ethylene terephthalate), poly(tetrafluoroethylene), and poly(methyl methacrylate) were investigated. The major problem for a successful machining process results from the fact that all samples (with the exception of polyimide) exhibit a negligible linear absorption for the laser wavelengths applied. The dielectrics were treated with λ=780 nm and λ=620 nm, whereas the polymers were evaluated with λ=800 nm. The results for both classes of materials are compared.

4.1
Inorganic Dielectrics

The influence of the bandgap on the ablation threshold F_{th} in dependence on the pulse duration τ will be discussed initially. Then, the enhancement of the machining precision with a shortening of τ, and incubation phenomena will be treated. Finally, morphological features, especially ripples, appearing on the surface of dielectrics after femtosecond laser treatment are mentioned.

Figure 12 displays the F_{th} vs τ dependence for the ablation of fused silica (FS) and barium aluminum borosilicate glass (BBS) down to τ=5 fs. FS (Corning 7940, 0.2 mm thick) exhibits a bandgap of ≈9 eV whereas BBS (Corning 7059, 1 mm thick) shows a bandgap of ≈4 eV. That means that the bandgap is ≈6×photon energy for FS and ≈3×photon energy for BBS, respectively. It can be clearly seen in Fig. 12 that the ablation thresholds of BBS drop faster towards shorter pulses than those of FS employing N=50 and λ=780 nm. The theoretical fits were performed according to Eq. 8 taking into account avalanche and multiphoton ionization. A critical electron density in the conduction band of 10^{21} cm^{-3} was chosen which is close to the plasma critical density for λ=780 nm. Fit parameters were found to be

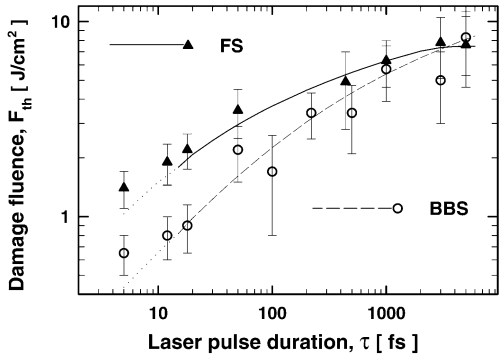

Fig. 12 Threshold fluence F_{th} vs pulse duration τ for the ablation of fused silica (FS) and barium aluminum borosilicate glass (BBS). λ=780 nm, N=50. Theoretical fits (*solid line* for FS, *dashed line* for BBS) were done using Eq. 8 [24]

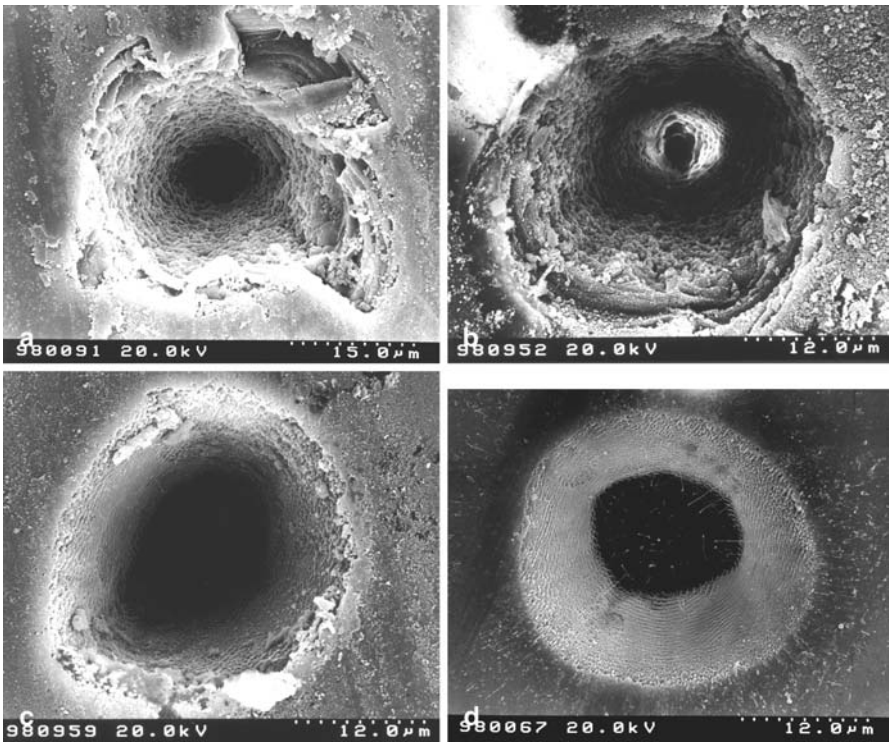

Fig. 13 Scanning electron micrographs of pulse laser-ablated fused silica. λ=780 nm, N=80. (**a**) τ=3 ps, F_0=19.9 J cm^{-2}, (**b**) τ=220 fs, F_0=10.7 J cm^{-2}, (**c**) τ=20 fs, F_0=11.1 J cm^{-2}, (**d**) τ=5 fs, F_0=6.9 J cm^{-2} [42]

a_{FS}=(4±0.6) cm^{2}J^{-1}, σ_6=6×10$^{8\pm0.9}$ cm^{-3}ps^{-1}(cm^2/TW)^6 and a_{BBS}=(1.2±0.4) cm^{2}J^{-1}, σ_3=7×10$^{17\pm0.5}$ cm^{-3}ps^{-1}(cm^2/TW)^3 [24].

A falling ablation threshold down to the shortest pulses of 20 fs was reported for single-shot damage experiments on fused silica [44]. For τ>10 ps, the well known $\sqrt{\tau}$ scaling for shorter pulses, a deviation from the $\sqrt{\tau}$ dependence and the predominance of the avalanche process for the ablation, was confirmed.

The improvement of the machining quality by the application of shorter pulses is shown in Fig. 13. For fused silica, scanning electron microscope (SEM) pictures of ablation craters have been taken. All of them were produced with 80 pulses per spot but with different pulse durations between 3 ps (Fig. 13a) and 5 fs (Fig. 13d). For each hole, the maximum laser fluence F_0 was about (3–5)×F_{th} as can be seen from Fig. 12. It is clearly demonstrated that the crater morphology is much more controlled by the spatial beam profile in the 5-fs case than for pulses with τ>100 fs (Fig. 13a, b). Even compared to the 20-fs pulse treatment (Fig. 13c), the regularity and reproducibility of the ablation is improved for the shortest pulses.

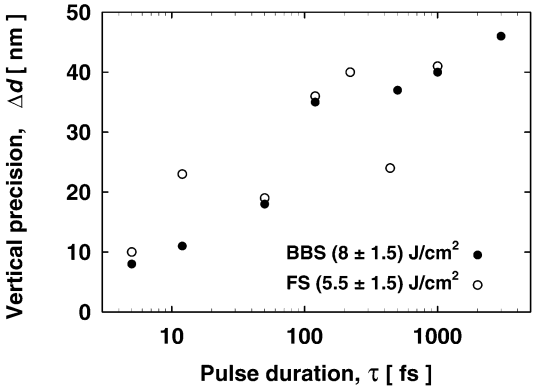

Fig. 14 Absolute vertical precision of ablation Δd for different pulse durations τ, derived from the 99% confidence interval of the slope of ablation curves (ablation depth vs number of pulses) for fused silica (FS) and barium aluminum borosilicate glass (BBS) [45]

Additionally, Fig. 13 suggests a higher vertical and lateral ablation precision when shorter pulses are employed. Figure 14 depicts the absolute vertical ablation precision Δd vs pulse duration τ. Δd describes the shot-to-shot deviation of the ablation depth per pulse d from its mean value for a 99% confidence interval [42]. The d-values were extracted from [24]. For both fused silica (FS) and barium aluminum borosilicate glass (BBS), a tendency of an increasing vertical ablation precision with decreasing pulse duration is clearly evident. This trend is expected to become even more pronounced if data obtained at F_0/F_{th}=const rather than F_0=const could be compared. Figure 14 visualizes that with pulses shorter than 10 fs, an absolute vertical ablation precision of the order of 10 nm can be achieved.

In order to relate the lateral dimensions of the laser-generated cavities to the laser spot size, a lateral extension parameter q can be defined. It is the ratio between the measured cross-sectional area of the ablation crater and the area illuminated by a Gaussian beam defined according to Eq. 1. When ablation is limited to the area with $F(x,y)<F_{th}$, q can be written as

$$q = \frac{1}{2} \ln\left(\frac{F_0}{F_{th}}\right) \tag{9}$$

Figure 15 shows a semi-logarithmic plot of q in dependence on the maximum laser fluence F_0 for the ablation of fused silica with N=50 and λ=780 nm. The solid lines depict the predictions of Eq. 9 with F_{th}(5 fs)=1.4 J cm^{-2} and F_{th}(12 fs)=1.9 J cm^{-2} (cf. Fig. 12). For pulse durations τ>100 fs, the $q(F_0)$ relation strongly deviates from the calculations. For a rising fluence F_0, q increasingly exceeds the values predicted by Eq. 9. This behavior indicates that ablation is not restricted to an area defined by $F(x,y)<F_{th}$. In contrast, for pulses as short as 5 fs and 12 fs, respectively, a good correlation between the measured values and the theoretical predic-

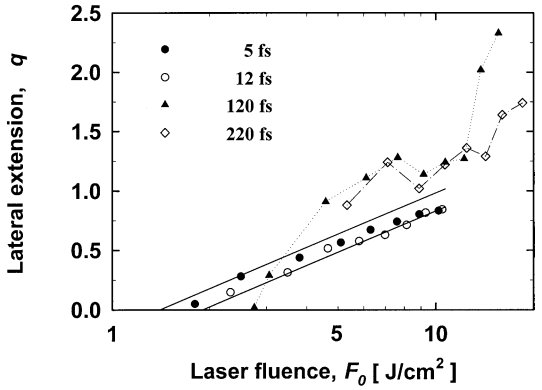

Fig. 15 Lateral extension parameter q in dependence on the maximum laser fluence F_0 for the ablation of fused silica. λ=780 nm, N=50. The *solid lines* are calculated utilizing Eq. 9 with F_{th}(5 fs)=1.4 J cm^{-2} and F_{th}(12 fs)=1.9 J cm^{-2} [45]

tions can be found. The results demonstrate that pulses in the 10-fs domain offer an improved lateral ablation precision in dielectrics compared to longer ones. The shortening of the laser pulses used for machining applications leads to a more deterministic ablation with an enhanced vertical and lateral ablation precision.

A major issue for the structuring of large bandgap dielectrics is the negligible linear light absorption for visible and infrared wavelengths. Therefore, one has to make use of nonlinear absorption effects or modify the material by a number of pulses (incubation), so that a more efficient energy coupling into the sample is possible after these incubation pulses. The incubation phenomenon depends on the material, laser wavelength λ, laser fluence F_0, and pulse duration τ. A significant difference between single- and multishot ablation thresholds implies a preablation modification of the irradiated material. This alteration might be, for instance, the formation of color centers [2]. All the possibilities of material modification result in the generation of electronic states within the forbidden gap that enhance light absorption of the sample. The increased absorption eventually leads to a lower ablation threshold in the case of multipulse treatment of the same spot. Additionally, a lower penetration depth of the laser radiation in the modified material resulting in a lower ablation depth per pulse (and ablated volume per pulse) can be observed. These qualitative considerations are in accordance with experimental results on fused silica down to τ=5 fs [45].

An example for an incubation process is displayed in Fig. 16. The SEM pictures show results of a treatment of barium borosilicate glass at F_0=2.5 Jcm^{-2} with a dye laser (τ=300 fs, λ=620 nm) for different numbers of pulses per spot N [46]. Three pulses generated only darkening at the surface (not shown here). Five pulses caused slight ablation below the depth resolution of the optical microscope (Fig. 16a). For a higher number of pulses per spot (N=20), the crater edges are heavily splintered off (Fig. 16b). Above 60 pulses, circular craters with a satisfying quality are formed (Fig. 16d).

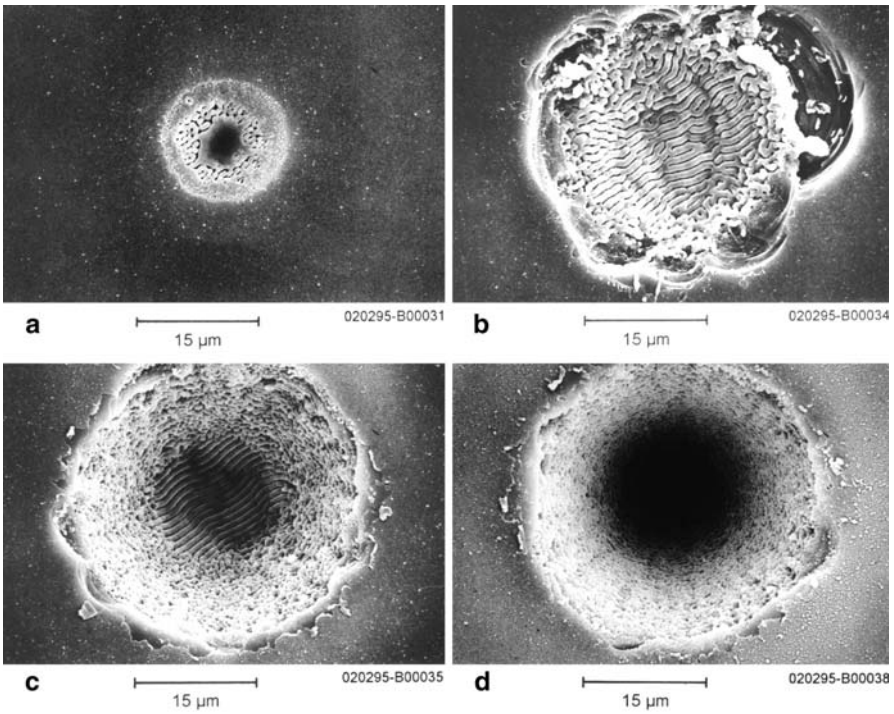

Fig. 16 Scanning electron microscope pictures of pulse laser-ablated barium borosilicate glass. τ=300 fs, λ=620 nm, F_0=2.5 J cm^{-2}. (**a**) N=5, (**b**) N=20, (**c**) N=60, (**d**) N=100 [46]

Figures 16a–c visualize a normally unwanted feature connected with short-pulse laser ablation, the formation of surface corrugations called ripples. In this case, two different kinds of ripple structures are observed. A magnification of an area depicted in Fig. 16a is shown in Fig. 17. In a ring of "intermediate" fluences, a ripple periodicity of ~0.7 µm and another type of ~0.2 µm periodicity in the edge region near the ablation threshold are found. Their orientation does not communicate. At pulse numbers above five, the 0.2-µm ripples disappear, and the 0.7-µm type dominates and grows to a 1.0-µm periodicity at the bottom of the crater (Fig. 16c).

The ripple patterns depicted in Figs. 16 and 17 are far from being understood because they do not comply with "conventional" ripples. A conventional ripple pattern might be found when light is scattered at material imperfections or dust particles. The scattered light interferes with the incident beam and forms a periodical irradiance, which interacts with the material. This illumination results in an energy deposition depending on the spatial coordinate and, therefore, a modulated ablation process. For a linear scatterer (e.g., a scratch), fringes are parallel and exhibit a spacing Λ of [47]

$$\Lambda = \frac{\lambda}{1 \pm \sin\theta} \tag{10}$$

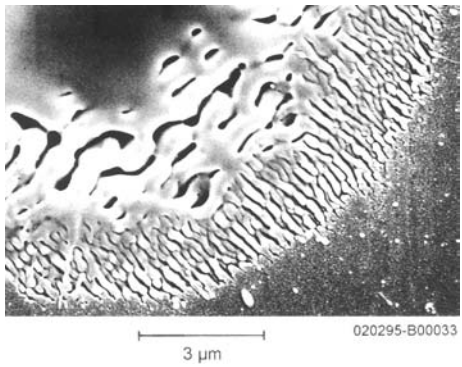

Fig. 17 Scanning electron micrograph of pulse laser-ablated barium borosilicate glass. τ=300 fs, λ=620 nm, F_0=2.5 J cm^{-2}, N=5, detail

θ denotes the angle of incidence of the laser light. The interference efficiency in a certain direction depends on the polarization state of the incident beam. For an illumination perpendicular to the sample surface, θ=0°, ripples with a period of the laser wavelength λ are expected. If the scattered wave propagates inside the material, the fringe spacing scales with the wavelength divided by the refractive index of the sample which was demonstrated for dielectrics, e.g., in [48].

Ripple patterns with periods that differ from the predictions of Eq. 10 cannot be explained with the interference effect. There are first hints that self-organization as a mechanism for the surface relaxation plays a role [49].

4.2 Polymers

The microstructuring of polymers with ultraviolet (nanosecond) laser radiation has reached an advanced status. Originally, it was demonstrated that polymers (PET) can be etched in a controlled manner using an excimer laser (ArF) [50]. The natural advantage of excimer lasers compared to other lasers is the shortness of the wavelength resulting in good focusing of the radiation. Additionally, most polymers absorb significantly in the ultraviolet spectral region [2]. Examples for possible technical applications are the fabrication of a microgear from a PI foil by 248-nm KrF radiation [51], the production of a relief lens array by single-pulse XeCl irradiation of doped PMMA [52], and the generation of wall- and nap-type structures due to internal stress relaxation of PI [53]. Other surface morphologies like dendrites (PET [54]) and cones (PI [55]) as a result of an excimer laser treatment were reported.

Despite the fact that a large variety of polymers can be machined with excimer lasers successfully, the involvement of thermal processes can lead to unwanted deviations from the optimum quality of the structure. Therefore, photopolymers were designed employing photolabile chromophores to

achieve a more or less pure photochemical ablation. With a well-defined decomposition pathway and only gaseous ablation products, a high contour sharpness can be obtained and contamination of the sample surface is avoided [56].

In contrast to dielectrics, only a few papers were concerned with femtosecond laser processing of polymers [18, 31, 32, 57–65]. In the present review, ablation of polymer films with a Ti:sapphire laser system (150 fs, 800 nm) is discussed. The results are presented in the same order as in the previous chapter for the dielectrics: dependence of modification threshold on bandgap, incubation phenomena, morphology after laser illumination.

Bursts of pulses with a predefined number down to N=1 were selected with a pulse picker. The focusing conditions were already described in connection with Fig. 10. Various polymer foils (250 μm thick) like polyimide (PI), polycarbonate (PC), poly(ethylene terephthalate) (PET, amorphous and crystalline), poly(tetrafluoroethylene) (PTFE), and poly(methyl methacrylate) (PMMA) were investigated (all from Goodfellow Cambridge Ltd, Huntington). These are listed together with relevant physicochemical properties in Table 1.

Table 1 specifies the linear absorption coefficient α(308 nm) for the different polymers. From PI to PMMA (i.e., from the left to the right column), an increasing bandgap is noticed (cf. [2]). For λ=800 nm, only PI shows a remarkable absorption coefficient of α(800 nm)=23 cm^{-1}. Therefore, a lower modification threshold is expected for PI as compared to PMMA. Modification means that an irreversible change at the surface of the sample can be detected with a Nomarski light microscope.

Modification thresholds were determined experimentally according to the technique described in the context of Figs. 9 and 10. Figure 10 shows the plot of the squared diameter D^2 of the modified area in dependence on the maximum laser fluence F_0 for the illumination of PI. Different numbers of pulses per spot (N=1–100) were applied and the focusing conditions were varied. A detailed discussion of the curves was presented before.

For PI, a single-pulse modification threshold of $F_{th}(N=1)$=1.0 J cm^{-2} is obtained independently of the focusing conditions (in the range w_0=8–27 μm, Fig. 10). Multipulse modification thresholds of $F_{th}(N=5)$=0.8 J cm^{-2} to $F_{th}(N=100)$=0.5 J cm^{-2} were measured. Again, an influence of the Gaussian beam radius on the threshold values could not be observed (pulse repetition rate 2 Hz).

The determination of threshold fluences was done for PC and PMMA employing the same technique [62]. Single-pulse thresholds of F_{th}=1.8 J cm^{-2} (PC) and F_{th}=2.6 J cm^{-2} (PMMA) were reported, i.e., the single-pulse threshold rose from 1.0 J cm^{-2} for PI to 2.6 J cm^{-2} for PMMA. This behavior is due to an increasing optical bandgap suggesting a multiphoton absorption mechanism. The material with the higher bandgap (PMMA) needs a larger number of photons k to overcome the gap in a one-step multiphoton absorption process. Therefore, the threshold fluence (and threshold intensity) for the machining of PMMA is higher than the threshold of PI. This behavior corresponds to that of the dielectric materials, fused silica and barium

Table 1 Physicochemical polymer properties [66]. Data according to [62] and Goodfellow Cambridge Ltd, Huntington. *Absorption coefficient at λ=308 nm. **Refractive index in the visible spectral region

	Pl	a-PET	c-PET	PC	a-PTFE	PMMA
Melting temperature [°C]	subl.		267			
Glass temperature [°C]	235	67		150	−33	105
Melting enthalpy [10^3 J mol^{-1}]			3.32		3.42	
Vaporization enthalpy [10^3 J mol^{-1}]	133 (degr.)				132	98
Mass density [g cm^{-3}]	1.42	1.33	1.45	1.2	2.15	1.18
Specific heat [J g^{-1} K^{-1}]	1.09	1.2–1.3	2.1	1.2	0.9	1.41
Thermal conductivity [W m^{-1} K^{-1}]	0.1–0.35	0.24–0.40		0.21	0.4	0.18
Absorption coefficient* [cm^{-1}]	10^5	4×10^3		22	<10	<20
Refractive index**	1.66	1.58–1.64		1.56		1.49
Water absorption (>24 h) [%]	0.2–2.9	0.1		0.1		0.2
Oxygen content (23 °C) [%]	53	21		26		20

Table 2 Modification thresholds $F_{th}(N)$ and incubation parameters ξ for the treatment of different polymers with laser pulses of τ=150 fs and λ=800 nm [66]

	$F_{th}(N)$ [Jcm^{-2}]				ξ
	N=1	N=5	N=10	N=100	
PI	1.0	0.8	0.7	0.5	0.9
c-PET	1.8	1.5	1.0	0.3	0.6
a-PET	2.1	1.5	1.0	0.4	0.6
PC	1.8	1.4	1.2	0.5	0.7
PTFE	1.9	1.4	1.2	0.7	0.8
PMMA	2.6	2.3	1.5	0.6	

aluminum borosilicate glass. Fused silica exhibits a greater bandgap and a higher ablation threshold than borosilicate glass for a fixed pulse duration and number of pulses per spot (cf. Fig. 12).

A summary of modification thresholds for N=1−100 for PI, crystalline and amorphous PET, PC, PTFE, and PMMA is presented in Table 2 [66, 67].

In addition to the bandgap-dependence of the threshold, all polymers show incubation effects (Table 2) [66,67]. The modification threshold drops for a higher number of pulses per spot N. A stronger incubation could be found for PC, PET, and PMMA in contrast to the "inert" polymers PI and PTFE due to irreversible chemical alterations. This can be supported by means of a simple phenomenological model. It was established for highly absorbing materials like metals and nanosecond pulse laser structuring. The threshold reduction of laser-induced damage with an increasing number of pulses per spot was correlated with a mechanical-fatigue damage behavior [68]. It could be shown that the applicability of this model can be extended down to the femtosecond time scale for metals [36] and even for polymers [18, 62]. The model describes the relation between the single-pulse (damage) threshold $F_{th}(1)$ and the multipulse threshold $F_{th}(N)$ in the form

$$F_{th}(N) = F_{th}(1)\, N^{\xi-1} \tag{11}$$

with a material-dependent incubation parameter ξ. ξ=1 means that no incubation effect is observable.

Figure 18 depicts two graphs of the accumulated laser fluence $N\times F_{th}(N)$ vs number of pulses N for polycarbonate (PC) and polyimide (PI), respectively. A calculation yields ξ=0.74 (PC) and ξ=0.87 (PI). The ξ-values of all polymers are listed in Table 2. It is obvious that the behavior of the incubation parameters ξ deviates from that of $F_{th}(1)$. As mentioned before, a stronger incubation manifested by a low ξ was observed for PET, PC, and PMMA in contrast to PI and PTFE exhibiting comparatively high ξvalues. The origin of this difference can be related to the fact that the ester bonds in PET, PC, and PMMA show much less stability than, e.g., the CO–N or ether bridges in PI towards repeated laser pulsing. The respective polymer units are displayed in Fig. 19.

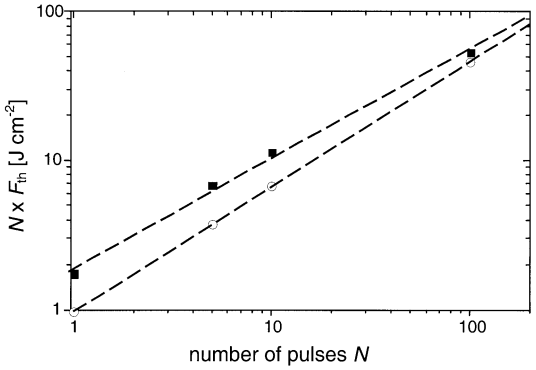

Fig. 18 Multipulse incubation behavior of polycarbonate (■) and polyimide (◯). Accumulated laser fluence $N \times F_{th}(N)$ vs number of laser pulses per spot N. τ=150 fs, λ=800 nm [66]

PI

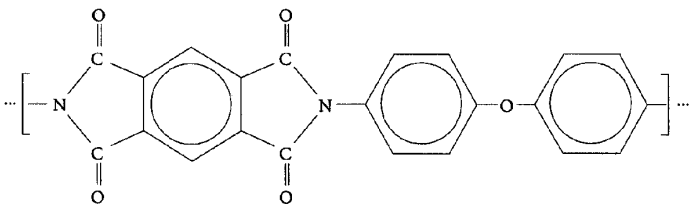

PC

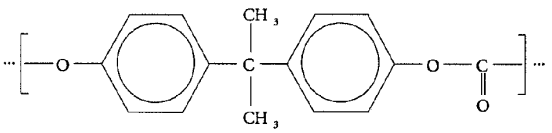

PET

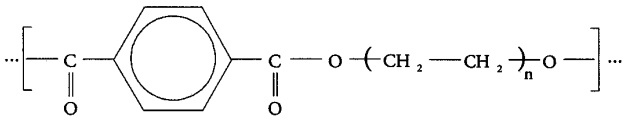

PMMA

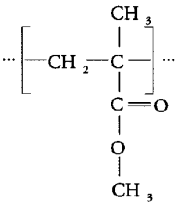

Fig. 19 Polymer units of polyimide (PI), polycarbonate (PC), poly(ethylene terephthalate) (PET), and poly(methyl methacrylate) (PMMA)

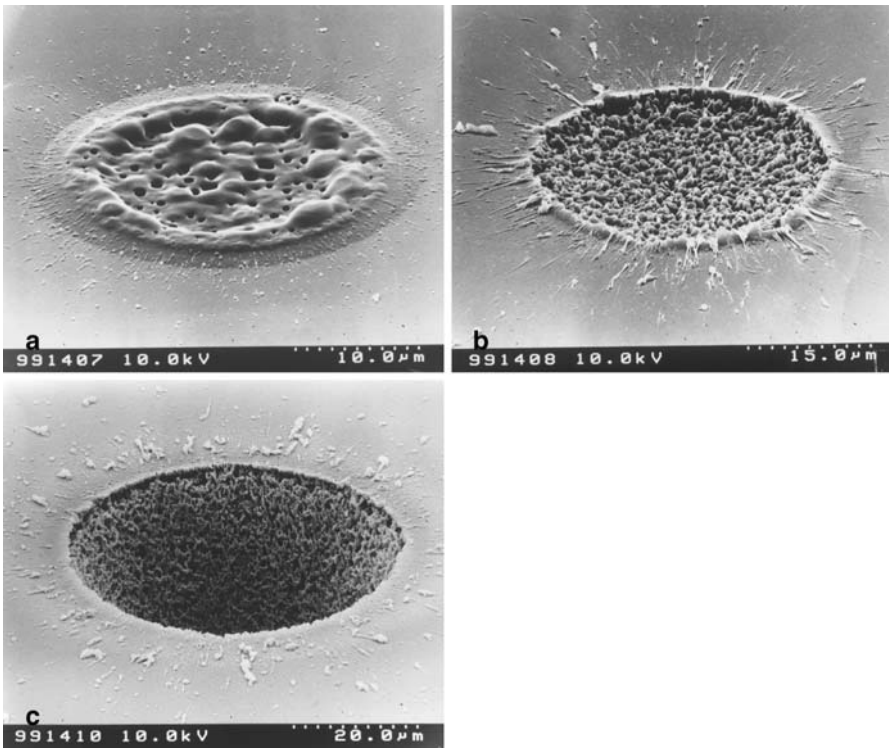

Fig. 20 Scanning electron microscope pictures of fs-pulse laser-ablated polycarbonate. τ=150 fs, λ=800 nm, F_0=3.0 J cm^{-2}, linear polarization. (**a**) N=1, (**b**) N=5, (**c**) N=100 [62]

PC, PMMA, and PTFE exhibit higher optical bandgaps in contrast to PI, and can melt before they vaporize (Table 1). Accordingly, the ablation behavior deviates from that of PI. Both PC (Fig. 20a) and PMMA (Fig. 21 a) show an increase of volume after a single pulse in a fluence range of more than 2 J cm^{-2} above the modification threshold [62]. This is due to the formation of systems consisting of three phases, liquid (melt) and gaseous in addition to solid. Partial gasification led to bubbles in the melt phase, which were frozen after resolidification of the liquid phase. The integrated volume of PMMA increased almost linearly with F_0. A flat top surface profile was reached at 3.3 J cm^{-2} and material removal started in the central spot region at >4.8 J cm^{-2}. Repeated pulses removed the spongy volume and a crater was formed (Fig. 20b,c and Fig. 21b,c). The vaporization may rely on degradation such as bond breaking between oxygen bridges and carbonyl groups in analogy to results for PMMA after nanosecond laser treatment at 308 nm [69].

Cavities could be generated on PI, PC, PET, PTFE, and PMMA with smaller diameters than the Gaussian 1/e^2-diameter of the beam. Diameters D

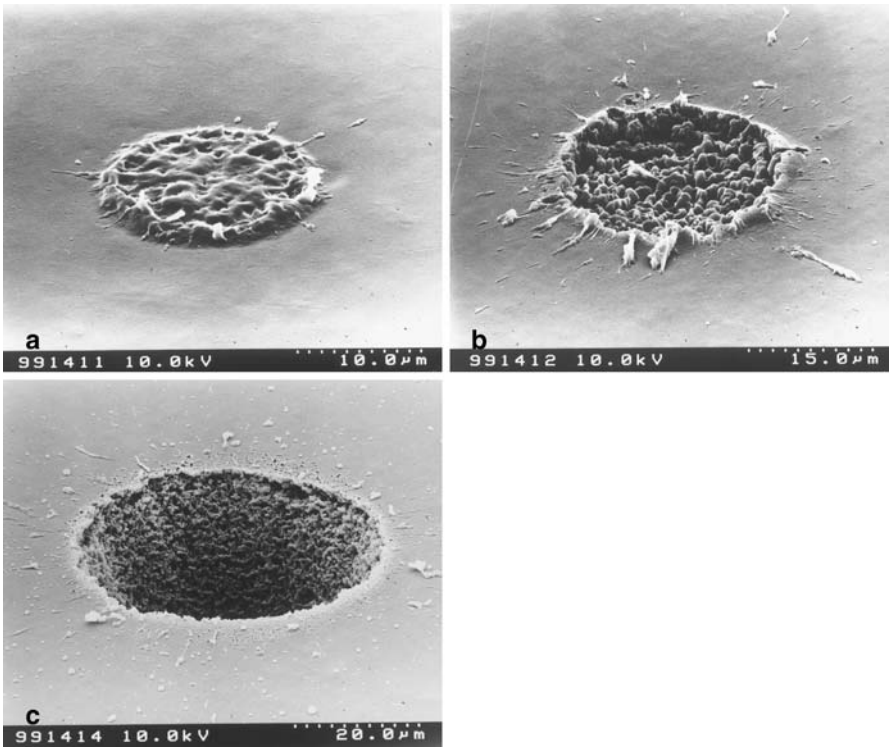

Fig. 21 Scanning electron micrographs of fs-pulse laser-ablated poly(methyl methacrylate). τ=150 fs, λ=800 nm, F_0=3.0 J cm^{-2}, linear polarization. (**a**) N=1, (**b**) N=5, (**c**) N=100 [62]

changed significantly during the first 50–60 pulses. The ablation rates per pulse were of the order of <1 μm.

The polarization state of the laser light with repetitive pulses shows a strong influence on the micro- and nanomorphology of the machining result. This is illustrated for PI in Figs. 22 and 23. Single-pulse illumination or a limited number of pulses per spot (N<5) with different polarization states (linear, circular) result in the same irregular surface pattern as has been described in [18]. For N>5, this behavior changes significantly. For linear polarization, 50 pulses per spot generated an ablation crater (Fig. 22a) with highly oriented ripples on the bottom (Fig. 22b). The ripples exhibited a period comparable to the laser wavelength and their orientation was always parallel to the electric field vector. This was confirmed by a rotation of the sample with respect to the beam axis [67].

Circular light polarization generated by means of a zero-order quarter-wave plate from the linearly polarized output of the femtosecond laser system, on the other hand, caused a radial orientation of the ripples with a period of ~0.8 μm (Fig. 23a). Additionally, the morphology changed to an ar-

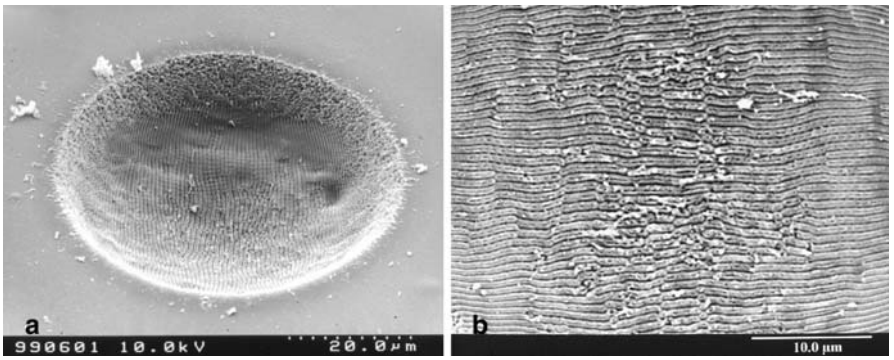

Fig. 22 Scanning electron microscope pictures of femtosecond pulse laser-ablated polyimide. τ=150 fs, λ=800 nm, F_0=1.3 J cm^{-2}, N=50, linear polarization. (**a**) Total aspect, (**b**) detail [18]

ray of cones in the nanometer range (Fig. 23b). For PI, such nanostructures could also be observed for nanosecond pulse laser treatment [70].

Femtosecond laser treatment of all polymers except PI showed melting together with the generation of volatile substances yielding small bubble holes and swelling. PI does not melt and swell because it only sublimates and/or degrades. The remaining material forms periodical surface structures. Linear polarization of repeated laser pulses caused "conventional" ripples parallel to the electric field vector. Circular polarization resulted in cone-like nanostructure arrays exhibiting the periodicity of the ripples for linear polarization.

Coincident with the observations for dielectrics, transparent polymers exhibit an incubation behavior for the multipulse femtosecond laser treatment. The modification (and ablation) thresholds decrease with an increasing

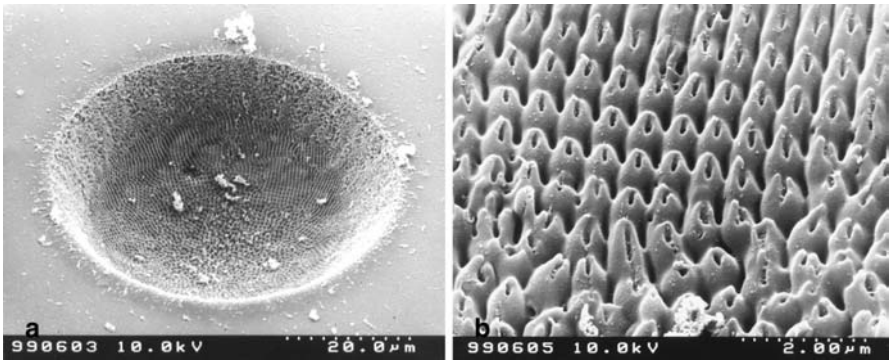

Fig. 23 Scanning electron microscope pictures of femtosecond pulse laser-ablated polyimide. τ=150 fs, λ=800 nm, F_0=1.3 J cm^{-2}, N=50, circular polarization. (**a**) Total aspect, (**b**) detail [18]

number of pulses per spot. Ripples were found for both materials, but for the polymers, primarily wavelength ripples could be seen.

5 Femtosecond Laser Applications

In the previous chapter, it was demonstrated that femtosecond laser pulses can be a powerful tool for the micromachining of large bandgap materials like dielectrics and polymers. These transparent samples can be treated mainly due to self-induced absorption (avalanche ionization, multiphoton processes) and/or incubation effects. By a shortening of the pulse duration, the ablation process gets more deterministic and the lateral and vertical precision of the laser-induced structures is enhanced. The ablation threshold decreases, i.e., the material removal is very localized and requires less energy than in the long-pulse domain. The heat influence onto the laser-generated structures is minimized resulting in negligible collateral damage. The screening of a part of the laser pulse by the escaping ablation products can be ignored for femtosecond laser structuring [2].

Obviously, also a couple of problems of femtosecond laser processing of transparent materials were mentioned in this paper. These are the occurrence of unwanted surface structures (e.g., surface swelling, ripples) and the presence of incubation phenomena (defect generation) that change etching rates. Additionally, self-focusing effects, "gentle" and "strong" ablation phases, and shock-induced microcracking were reported [71].

Nevertheless, during recent years, an increasing number of potential commercial applications of femtosecond laser treatment have been demonstrated, e.g., the fabrication of injection nozzles and medical implants (stents) [72]. Some femtosecond laser systems have already been installed particularly for mask repair in industry [73, 74]. In particular, biological tissue (cornea, tooth, bone) can be treated successfully [11, 75, 76]. Even transparent human chromosomes were laser-cut (170 fs, 800 nm, minimum FWHM cut size ~100 nm) by a multiphoton-mediated process [77]. But, a "killer application" is incalculable.

In the next two paragraphs, three possible femtosecond laser applications are discussed in detail.

5.1 Biosensors

For thermally sensitive or undoped polymers with low linear absorption at the laser wavelength, the use of femtosecond laser pulses can improve the ablation precision in contrast to long-pulse treatment. Further, the thermal load to the samples is minimized. For these reasons, femtosecond laser pulses were chosen to perforate a polyethylene membrane serving as a diffusion-discriminating element on a miniaturized biosensor for the measurement of glucose concentration [78].

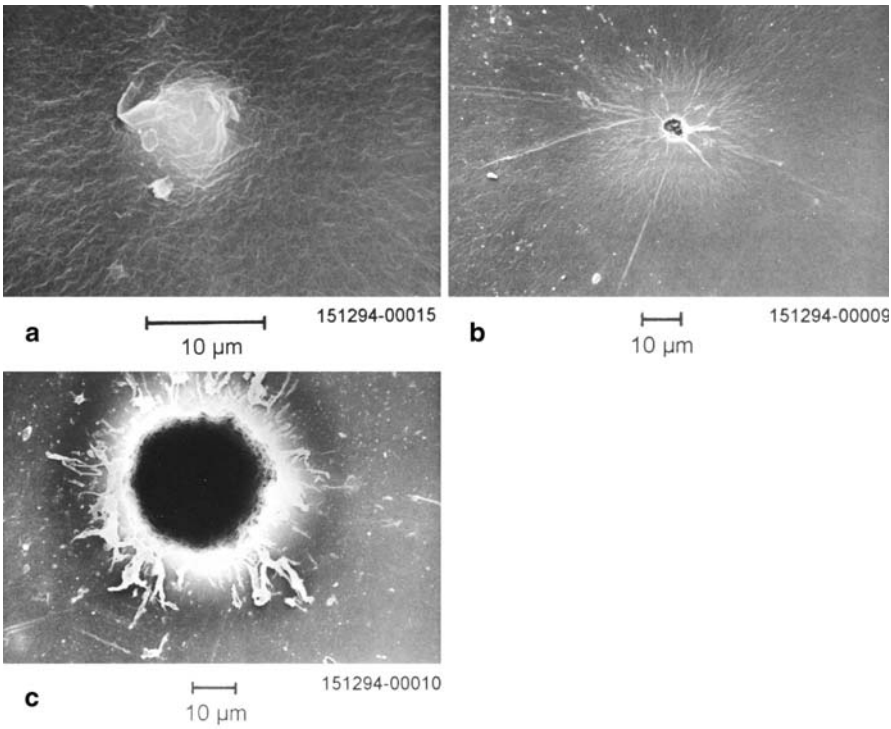

Fig. 24 Scanning electron micrographs of fs-pulse laser-ablated polyethylene. τ=300 fs, λ=620 nm. (**a**) F_0=0.8 J cm^{-2}, N=100, (**b**) F_0=1.0 J cm^{-2}, N=20, (**c**) F_0=1.0 J cm^{-2}, N=100

Polyethylene shows a small linear absorption at the laser wavelength of λ=620 nm (α<10 cm^{-1}). Strong fluence-dependent incubation could be observed for the structuring of polyethylene with 300-fs pulses in the visible spectral range. The application of N=100 pulses at F_0=0.8 J cm^{-2} only leads to a surface modification (Fig. 24a). With N=100 at F_0=1.0 J cm^{-2}, a perforation of the membrane can be achieved (Fig. 24c). For a fluence of 1.0 J cm^{-2}, more than 20 pulses per spot are needed to produce detectable ablation (Fig. 24b).

The polyethylene membrane covered an electrochemical enzymatic biosensor. The construction scheme of the sensor is displayed in Fig. 25. The electrochemical basic electrodes consist of a platinum anode and a silver–silver chloride cathode. A thermally sensitive layer of glucose oxidase was localized directly on the anode surface and was covered by a 30-µm-thick hydrophobic polyethylene membrane. The biosensor for the detection of the glucose concentration is based on an enzyme (glucose oxidase)-catalyzed reaction of the analyte (glucose) and the subsequent electrochemical detection of a reaction product (electron current). A stoichiometric surplus of the coreactant oxygen has to be guaranteed. This is realized by the polyethylene membrane (membrane with “analyte door”) controlling the glu-

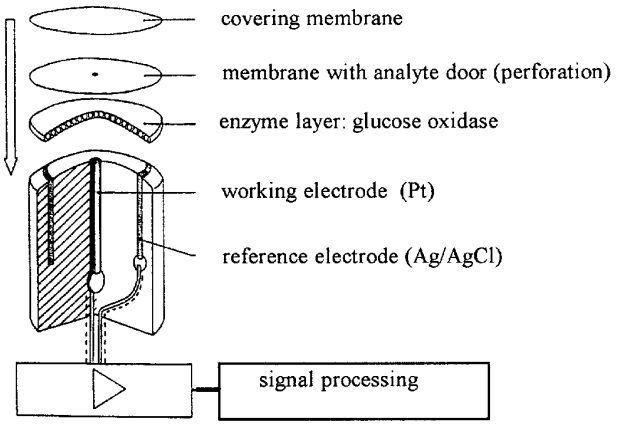

Fig. 25 Construction scheme of an enzymatic amperometric glucose sensor [78]

cose/oxygen diffusion ratio into the enzyme layer of the sensor. The analyte door is created by means of a single laser perforation of an originally analyte-impermeable membrane, restricting the transmembrane analyte transfer quantitatively as well as locally. The diffusion of the coreactant is possible over the whole membrane area. The scheme of the signal generation of the sensor is depicted in Fig. 26.

The delicate task was to perforate the polyethylene membrane with minor damage to the underlying enzyme (degradation temperature 80 °C), which is crucial for the operation of the whole sensor.

Compared to hand-made perforations by means of a specially grinded needle (Fig. 27a,b), the use of a femtosecond pulse laser resulted in well-defined perforations of the polyethylene membrane (Fig. 27c,d). Obviously, the reproducibility of the laser-generated structures is higher (Fig. 27b,d). It was impossible to reach diameters smaller than 50 µm with the mechanical technique (Fig. 27a). The fs-laser structuring yields the opportunity to tune the

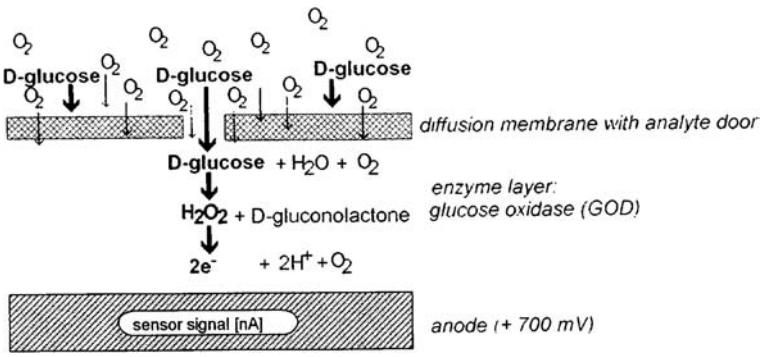

Fig. 26 Scheme of signal generation at an enzymatic amperometric glucose sensor [78]

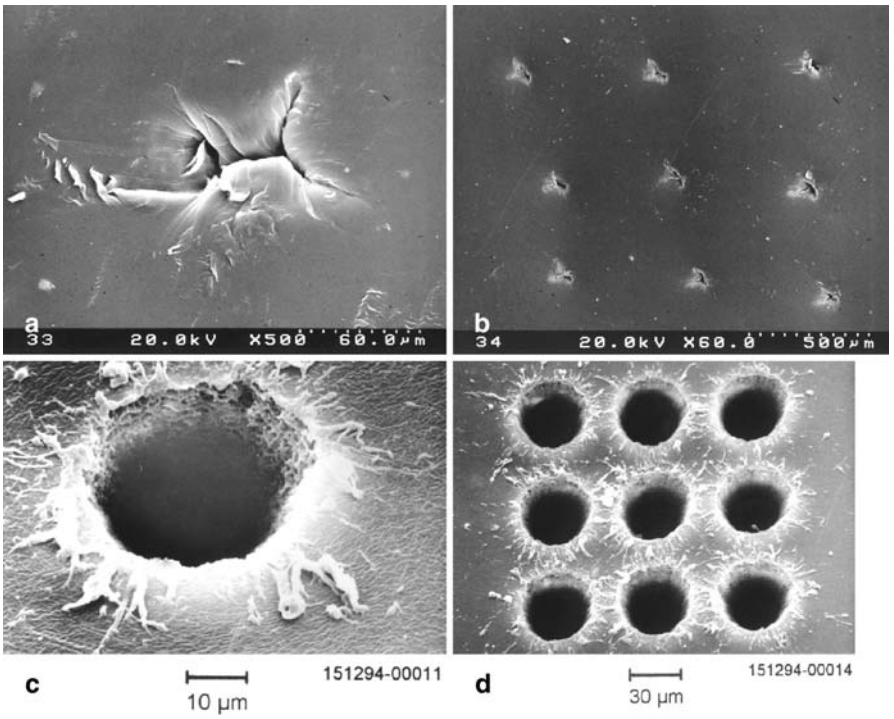

Fig. 27 Scanning electron micrographs of perforations of 30-µm-thick polyethylene membranes. (**a, b**) The perforations were produced mechanically by hand using a special grinded needle, (**a**) single perforation, (**b**) array of perforations. (**c, d**) Laser perforations employing τ=300 fs, λ=620 nm, F_0=1.0 J cm^{-2}, (**c**) N=100, (**d**) N=100 per interleaf [78]

diameters of the perforations by changing the local fluence. As a result, the sensitivity of the sensor and the linearity range of the measurement can be controlled. Additionally, dense multiperforations on a limited area can be achieved (Fig. 27d).

After laser perforation, the whole sensor was covered with cellulose as protection membrane (Fig. 25). With the ready-to-operate sensors, calibration curves were recorded in vitro. The results of four glucose sensors each made with one perforation employing different numbers of pulses are depicted in Fig. 28. The calibration curves show no dependence of the sensor activity on the number of pulses applied to the same spot. That can be taken as a proof of the minimum heat damage to the materials adjacent to the femtosecond pulse laser-excited polyethylene foil volume. A significant "large area" of heat-induced damage of the thermally sensitive enzyme is prevented. The differences in individual calibration curves of the sensors are mainly due to various electrochemical characteristics and variations in available enzyme activities [78]. The microperforations of polyethylene membranes covering a glucose oxidase enzyme layer immobilized directly on the electrode

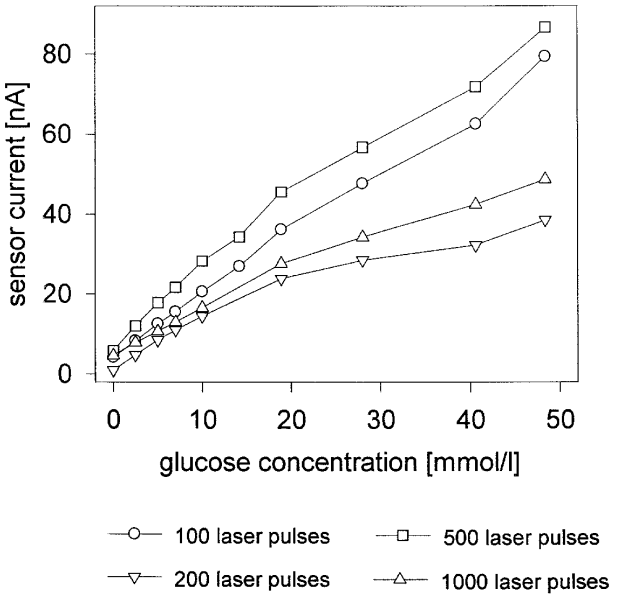

Fig. 28 Calibration lines of four glucose sensors with one perforation each made by a fs-pulse laser utilizing different pulse numbers per spot. τ=300 fs, λ=620 nm, F_0=1.0 J cm^{-2} [78]

resulted in glucose sensors with high sensitivity and an excellent linearity range. For comparison, a healthy person exhibits a glucose concentration in the blood of about 5 mmole/l. The concentration in the case of a diabetic amounts to 10–15 mmole/l. Thus, human glucose concentration data could be acquired in that range.

5.2 Dentistry

The pioneering ablation studies on polymers in the 1980s [31, 32] instilled growing interest in the application of subpicosecond laser pulses for micro-drilling of not only polymeric but also biological materials such as corneas (see below) [75, 76], bone-like material [11], and teeth [11, 79–82]. The reduction of thermal and mechanical tissue destruction, the lowering of the ablation threshold fluences F_{th}, the enhanced control of the vertical (ablation depth per pulse d) and lateral precision of micromachining, and nonlinear absorption phenomena important for the congruent ablation of transparent and composite materials motivated these investigations.

Lasers may replace drilling machines in dentistry to achieve a more controlled material removal. Minimization of pain at the patient's side, usually caused by vibration and friction heat, could be another advantage of this approach. Conventional nanosecond pulse lasers exhibit the problem of ther-

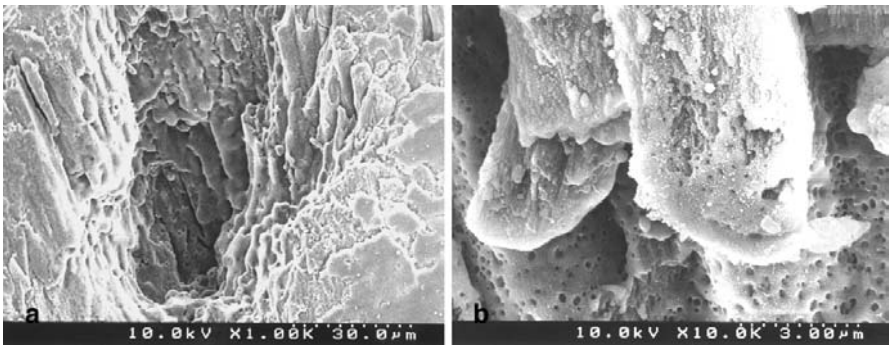

Fig. 29 Scanning electron microscope pictures after nanosecond pulse laser ablation of human dental enamel. τ=7 ns, λ=600 nm, F_0=24.7 J cm^{-2}, N=100. (**a**) Total aspect, (**b**) detail [81]

mal side effects due to finite heat-affected zones of the order of micrometers. This is especially true for Ho:YAG, Er:YAG, and Nd:YLF lasers, both free running and Q-switched, which are very common in medical applications.

In order to visualize the limits of the application of longer laser pulses for the structuring of a nonabsorbent composite material, a result of ablation experiments on human enamel with a 7-ns dye laser (λ=600 nm) is presented in Fig. 29. The lateral ablation precision is unsatisfactory (Fig. 29a). Collagen fiber bundles were disrupted (Fig. 29b). The application of high laser fluences above ~20 J cm^{-2} is necessary to achieve a relatively uncontrolled material removal. The constituents of enamel, water, collagen, and the hydroxyapatite matrix, are practically nonabsorbent for wavelengths in the visible region at λ=600 nm.

The application of femtosecond laser pulses of a comparable wavelength yields machining morphologies as in Fig. 30. The material removal remains

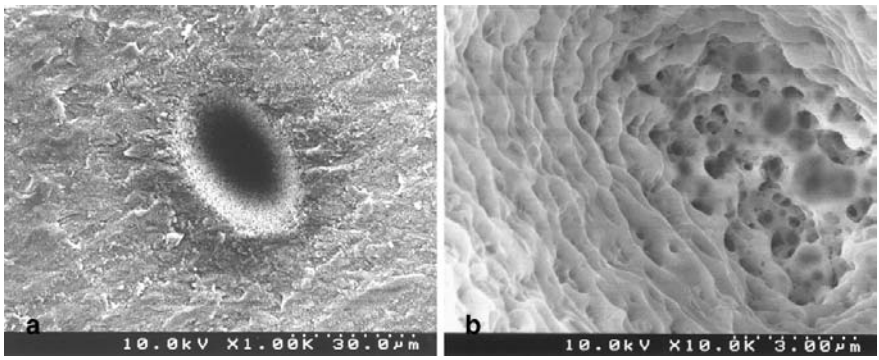

Fig. 30 Scanning electron microscope pictures after femtosecond pulse laser ablation of human dental enamel. τ=300 fs, λ=615 nm, F_0=2.0 J cm^{-2}, N=100. (**a**) Total aspect, (**b**) cavity bottom [81]

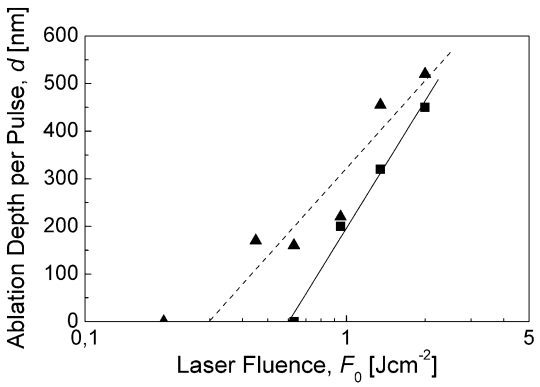

Fig. 31 Ablation depth per pulse d vs laser fluence F_0 for the treatment of human enamel (■) and human dentine (▲).τ=300 fs, λ=615 nm, N=100. The straight lines are fits using a $d \sim \ln(F_0/F_{th})$ dependence. *Solid line*: human enamel; *dashed line*: human dentine [81]

localized on the area of the laser spot (Fig. 30a). Nearly no signs of collateral damage and cracks were observed. The cavity edges are sharply defined. The walls of the crater appear smooth (Fig. 30b) relative to the nanosecond laser result (Fig. 29b with the same magnification).

The ablation depth per pulse d vs laser fluence F_0 at enamel and dentine is depicted in Fig. 31. The data follow a logarithmic law according to Eq. 6. The ablation threshold fluence F_{th} was determined by extrapolating the $d(F_0)$-curve to $F_{th}=F_0(d=0)$. Ablation thresholds of $F_{th}(N=100)=0.6$ J cm^{-2} for healthy human enamel and $F_{th}(N=100)=0.3$ J cm^{-2} for healthy human dentine can be derived. The lower threshold for dentine may be a result of preferential ablation at an increased number of structural defects. Human enamel consists mainly of hydroxyapatite. For comparison, a monocrystalline fluoroapatite was evaluated. The ablation threshold fluence amounts to $F_{th}(N=100)=0.8$ J cm^{-2} [81] which is slightly higher than the F_{th} of human enamel.

The investigation of incubation effects, i.e., that the optical, chemical, and mechanical properties of a (transparent) material can be changed during repetitive illumination of the same spot without ablation, is rather difficult because of the complicated surface structure of a biological composite material. It can be stated that one femtosecond laser pulse at $F_0=2.0$ J cm^{-2} (roughly three times F_{th}) applied to healthy human enamel led to minor ablation (Fig. 32a). Five pulses of the same fluence resulted in a crater with a depth of 2–3 μm (Fig. 32b). The shape of the excision is well defined, and no cracks could be observed.

Human enamel and dentine can be ablated successfully with 300 fs-laser pulses (λ=615 nm) at laser fluences around 1 J cm^{-2}. The application of subpicosecond pulses avoids almost completely thermal damage to neighboring tissue and microcracking. Femtosecond laser fluences necessary for micromachining are one order of magnitude lower than those in the nanosecond

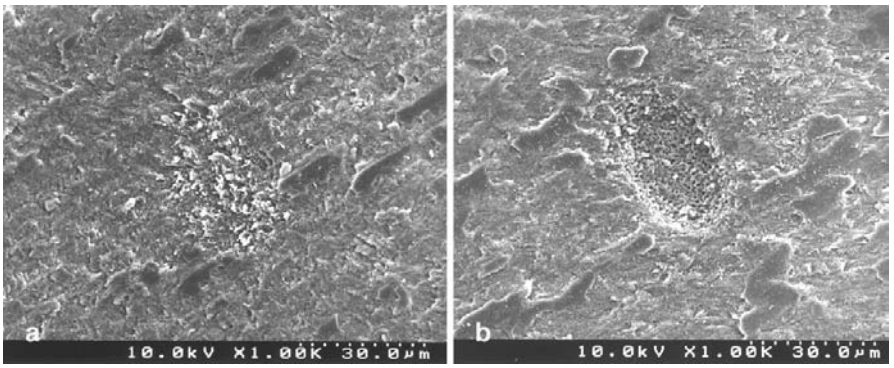

Fig. 32 Scanning electron micrographs after femtosecond pulse laser ablation of human dental enamel. τ=300 fs, λ=615 nm, F_0=2.0 J cm^{-2}. (**a**) N=1, (**b**) N=5 [81]

laser case for equal wavelength and repetition rate. The suppression of microcracks for short pulses is of high importance in dentistry. Microcracks can be the source of new caries.

It can be suggested that the application of short-pulse (femtosecond) lasers as contactless drillers in dentistry can be an alternative to the classical mechanical technique to improve the quality of the tooth treatment. A critical point for the application of the laser in practice is the time a dentist would need for the treatment of a patient. Machining volumes of about 40 mm^3 per minute are necessary for practical applications. Recently, an efficiency of nearly 1 mm^3 per minute was demonstrated with a Ti:sapphire femtosecond laser system at 3 kHz repetition rate [82]. That means that repetition rates of the order of 100 kHz would be needed to reach the conventional drilling productivity.

5.3 Ophthalmology

Surgery to correct refractive errors for the improvement of visual acuity generally aims at changing the corneal curvature. Corneal tissue is mainly constituted of a network of natural collagen polymer with the void volume filled with a special type of aqueous saline solution. A wide variety of laser and nonlaser procedures, such as laser-assisted in situ keratomileusis (LASIK), laser-cut channels for intracorneal ring segment (ICRS) implantation, femtosecond lamellar keratoplasty (FLK), intrastromal vision correction, and corneal transplantation have been developed for refractive surgical correction [83, 84]. They include removal of corneal tissue from the surface, removal of corneal tissue from the interior or stroma, and alteration of the corneal mechanical properties to produce a refractive effect. The most popular by far are procedures based on excimer laser ablation of the corneal surface and/or stroma [85].

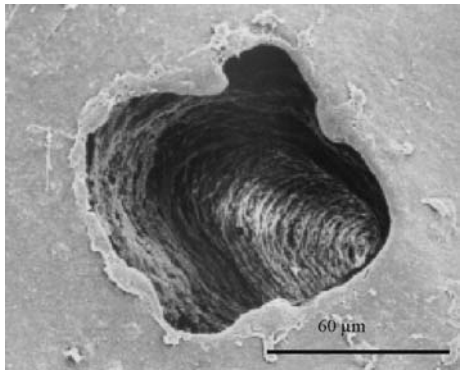

Fig. 33 Scanning electron microscope picture of an excision on an epikeratophakia lenticule after 1.5 h exposure to air. τ=300 fs, λ=615 nm, F_0=3.7 J cm^{-2}, N=4,000 [76]

Excimer laser keratotomy and other cornea-reshaping varieties of refractive eye surgery have already been turned into practical clinical procedures [86–88]. In vivo UV laser corneal surgery, on the other hand, involves considerable mutagenicity danger and cataractogenicity in the anterior chamber of the eye by fluorescence in the range between 250 and 350 nm, besides cavitation problems [89,90]. Ultrashort pulse lasers are, therefore, a potential alternative to excimer lasers in corneal surgery. Ultrahigh-power subpicosecond pulses can ablate practically transparent materials possibly initiated by nonlinear processes [11]. Pioneering femtosecond pulse laser ablation experiments have been conducted on bovine [75] and later on human corneas [76]. Subpicosecond pulse laser microsurgery results in heat-affected zones of <100 nm and absence of any plasma shielding effects.

Self-induced multiphoton absorption limits the laser interaction with the target to a small sharply defined volume. High-quality ablations of the Bowman membrane and the stroma tissue, characterized by damage zones of less than 0.5 μm, were observed at all fluences above the ablation threshold of $F_{th}(N=1{,}000)\approx 1$ J cm^{-2} (Fig. 33). This excision quality compares well with those achieved with far-UV (193 nm) excimer ns-pulse lasers. Ultrashort pulsed lasers allow for nonthermal laser–tissue interaction. Cuts can be made with little collateral damage. A part of the incident energy is absorbed to create a plasma. The initial high pressure in the plasma causes a shock wave to form and propagate. While the heat-affected zone can often be neglected (HAZ<100 nm), a shock-affected zone (SAZ) of several μm occurs in a fresh cornea. Transmission electron microscopy of cross sections indicates damage zones of 2–11 μm [91]. The transplant soaked in nutrient solution, however, appeared more tolerant towards the shock exerted by the recoil thrust of the leaving vapor. Obviously, the soaked tissue exhibits liquid pockets which served to elastically dissipate the shock spreading from the excision. As a result, the SAZ seemed to be considerably smaller than in the fresh tissue.

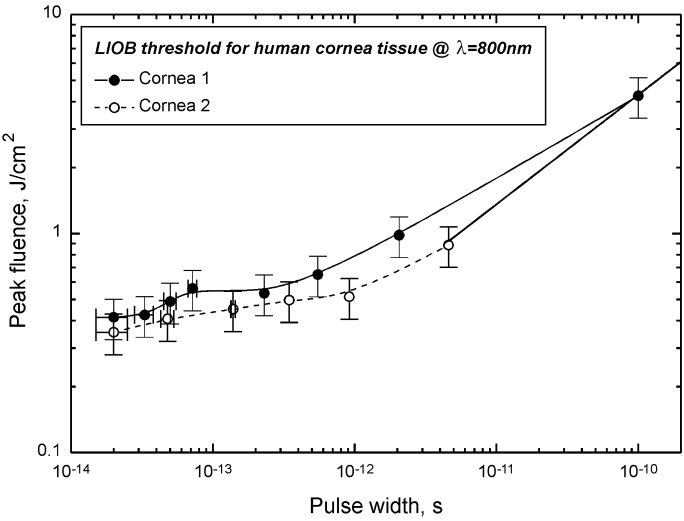

Fig. 34 Laser-induced optical breakdown (LIOB) threshold fluence vs pulse width for the ablation of human corneal tissue. λ=800 nm [93]

As the pulse becomes shorter, the ablation threshold decreases (Fig. 34) [92, 93] in accordance with the observations for inorganic dielectrics (see Fig. 12) and the uncertainty of the threshold value is reduced (cf. Figs. 14 and 15). Thus, femtosecond pulses will produce the most reproducible cuts.

Several procedures to effect a refractive change in the cornea can be performed with ultrafast laser photodisruption. Procedures leading to a direct refractive change are the ultimate goal. Indirect femtosecond methods, recently approved by the US Food and Drug Administration (FDA K993153, 1999; FDA K001211, 2000) are in clinical use today. In these procedures, femtosecond laser cuts or incisions are made for subsequent secondary treatment, which produces the desired refractive change.

6 Summary

High-precision microstructuring of large bandgap dielectrics, polymers, and biological materials with femtosecond laser pulses was reviewed. The processing of such materials with ultrashort laser pulses offers two essential amenities compared to longer pulses of the same wavelength: (1) the reduction of the laser fluence which is necessary to induce ablation and (2) the improvement of the contour sharpness of the laser-generated structures. Additionally, when (biological) substrates are extremely fragile and thermally sensitive, the very low collateral heat effect induced by fs-laser pulses is of outstanding importance. Recently, an increasing number of potential commercial applications of femtosecond lasers was reported, e.g., the production of injection nozzles and medical implants, mask repair techniques, the cut-

ting of human chromosomes, and utilization in dentistry, ophthalmology, and biosensor technology. But, a "killer application" is still incalculable which might be a result of economical considerations.

Femtosecond laser processing of transparent materials shows a couple of (unwanted) effects which are known from long-pulse treatment, like the generation of surface structures (ripples, surface swelling) and the presence of incubation phenomena that change etching rates. Beyond it, self-focusing effects and "gentle" and "strong" ablation phases were observed. A drawback of the use of a Ti:sapphire or a dye femtosecond laser for microstructuring purposes is the wavelength in the infrared or visible spectral region.

A natural advantage of excimer lasers is the shortness of the wavelength resulting in a good ability to focus the radiation and a high linear absorption in most materials. If the involvement of thermal processes in the ablation process can be minimized or even avoided (especially for a possible photochemical bond breaking with 157-nm radiation), controllable material removal at the nanometer level can be achieved [94–100].

Acknowledgements Partial financial funding was provided by the German Ministry for Research and Technology (BMBF, Mikrosystemtechnik, # 16SV 515 and LASER 2000, # 13 N 7048/7) and the European Community (BRITE-EURAM III Project BRPR-CT96–0265). One of us (W.K.) wants to acknowledge support by the "Fonds der Chemischen Industrie im Verband der Chemischen Industrie e.V.", Frankfurt am Main, Germany.

References

1. Maiman TH (1960) Nature 187:493
2. Bäuerle D (2000) Laser processing and chemistry, 3rd edn. Springer, Berlin Heidelberg New York
3. Fork RL, Greene BI, Shank CV (1981) Appl Phys Lett 38:671
4. Fork RL, Brito Cruz CH, Becker PC, Shank CV (1987) Opt Lett 12:422
5. Knox WH, Downer MC, Fork RL, Shank CV (1984) Opt Lett 9:552
6. Rolland C, Corkum PB (1986) Opt Commun 59:64
7. Spence DE, Kean PN, Sibbett W (1991) Opt Lett 16:42
8. Strickland D, Mourou G (1985) Opt Commun 56:219
9. Nisoli M, DeSilvestri S, Svelto O, Szipöcs R, Ferencz K, Spielmann C, Sartania S, Krausz F (1997) Opt Lett 22:522
10. Limpert J, Schreiber T, Clausnitzer T, Zöllner K, Fuchs HJ, Kley EB, Zellmer H, Tünnermann A (2002) Optics Express 10:628
11. Kautek W, Krüger J (1994) SPIE Proc 2207:600
12. Diels J-C, Rudolph W (1996) Ultrashort laser pulse phenomena, Academic, San Diego
13. Sartania S, Cheng Z, Lenzner M, Tempea G, Spielmann C, Krausz F (1997) Opt Lett 22:1562
14. Krüger J, Kautek W (1999) Laser Physics 9:30
15. Preuss S, Demchuk A, Stuke M (1995) Appl Phys A 61:33
16. Kautek W, Krüger J (1995) Materials Science Forum 173–174:17
17. Liu JM (1982) Opt Lett 7:196
18. Baudach S, Bonse J, Kautek W (1999) Appl Phys A 69:S395
19. Preuss S, Späth M, Zhang Y, Stuke M (1993) Appl Phys Lett 62:3049
20. Bloembergen N (1974) IEEE J Quant Electron 10:375
21. Du D, Liu X, Korn G, Squier J, Mourou G (1994) Appl Phys Lett 64:3071
22. Kautek W, Krüger J, Lenzner M, Sartania S, Spielmann C, Krausz F (1996) Appl Phys Lett 69:3146

23. Stuart BC, Feit MD, Herman S, Rubenchik AM, Shore BW, Perry MD (1996) J Opt Soc Am B 13:459
24. Lenzner M, Krüger J, Sartania S, Cheng Z, Spielmann C, Mourou G, Kautek W, Krausz F (1998) Phys Rev Lett 80:4076
25. Stoian R, Boyle M, Thoss A, Rosenfeld A, Korn G, Hertel IV, Campbell EEB (2002) Appl Phys Lett 80:353
26. von der Linde D, Sokolowski-Tinten K, Bialkowski J (1997) Appl Surf Sci 109–110:1
27. Stoian R, Rosenfeld A, Ashkenasi D, Hertel IV, Bulgakova NM, Campbell EEB (2002) Phys Rev Lett 88:097603/1–4
28. Beuermann T, Brinkmann H-J, Damm T, Stuke M (1990) MRS Symp Proc 191:37
29. Matthias E, Reichling M, Siegel J, Käding OW, Petzoldt S, Skurk H, Bizenberger P, Neske E (1994) Appl Phys A 58:129
30. Vogel A, Schweiger P, Frieser A, Asiyo MN, Birngruber R (1990) IEEE J Quant Electron 26:2240
31. Küper S, Stuke M (1987) Appl Phys B 44:199
32. Srinivasan R, Sutcliffe E, Braren B (1987) Appl Phys Lett 51:1285
33. Anisimov SI, Kapeliovich B, Perel'man TL (1974) Sov Phys JETP 39:375
34. Corkum PB, Brunel F, Sherman NK (1988) Phys Rev Lett 61:2886
35. Chichkov BN, Momma C, Nolte S, von Alvensleben F, Tünnermann A (1996) Appl Phys A 63:109
36. Güdde J, Hohlfeld J, Müller JG, Matthias E (1998) Appl Surf Sci 127–129:40
37. Wellershoff S-S, Hohlfeld J, Güdde J, Matthias E (1999) Appl Phys A 69:S99.
38. Bonse J, Baudach S, Krüger J, Kautek W, Lenzner M (2002) Appl Phys A 74:19
39. Bonse J, Baudach S, Kautek W, Welsch E, Krüger J (2002) Thin Solid Films 408:297
40. Stuart BC, Feit MD, Rubenchik AM, Shore BW, Perry MD (1995) Phys Rev Lett 74:2248
41. Varel H, Ashkenasi D, Rosenfeld A, Herrmann R, Noack F, Campbell EEB (1996) Appl Phys A 62:293
42. Lenzner M, Krüger J, Kautek W, Krausz F (1999) Appl Phys A 68:369
43. Lenzner M, Krüger J, Kautek W, Krausz F (2000) Appl Surf Sci 154–155:11.
44. Tien A-C, Backus S, Kapteyn H, Murnane M, Mourou G (1999) Phys Rev Lett 82:3883
45. Lenzner M, Krüger J, Kautek W, Krausz F (1999) Appl Phys A 69:465
46. Krüger J, Kautek W (1996) Appl Surf Sci 96–98:430
47. von Allmen M, Blatter A (1995) Laser beam interaction with materials, 2nd edn. Springer, Berlin Heidelberg New York
48. Lenzner M (1999) J Mod Phys B 13:1559
49. Henyk M, Vogel N, Wolfframm D, Tempel A, Reif J (1999) Appl Phys A 69:S355
50. Srinivasan R, Mayne-Banton V (1982) Appl Phys Lett 41:576
51. Endert H, Pätzel R, Basting D (1995) Opt Quantum Electron 27:1319
52. Beinhorn F, Ihlemann J, Luther K, Troe J (1999) Appl Phys A 68:709
53. Arenholz E, Wagner M, Heitz J, Bäuerle D (1992) Appl Phys A 55:119
54. Arenholz E, Kirchebner A, Klose S, Heitz J, Bäuerle D (1998) Mater Res Soc Symp Proc 526:385
55. Krajnovich DJ, Vazquez JE (1993) J Appl Phys 73:3001
56. Lippert T, Dickinson JT, Langford SC, Furutani H, Fukumura H, Masuhara H, Kunz T, Wokaun A (1998) Appl Surf Sci 127–129:117
57. Kumagai H, Midorikawa K, Toyoda K, Nakamura S, Okamoto T, Obara M (1994) Appl Phys Lett 65:1850
58. Heitz J, Arenholz E, Bäuerle D, Sauerbrey R, Phillips HM (1994) Appl Phys A 59:289
59. Nakamura S, Midorikawa K, Kumagai H, Obara M, Toyoda K (1996) Jpn J Appl Phys 35:101
60. Serafetinidis AA, Skordoulis CD, Makropoulou MI, Kar AK (1998) Appl Surf Sci 135:276
61. Hopp B, Toth Z, Gal K, Mechler A, Bor Z, Moustaizis SD, Georgiou S, Fotakis C (1999) Appl Phys A 69:S191
62. Baudach S, Bonse J, Krüger J, Kautek W (2000) Appl Surf Sci 154–155:555

63. Niino H, Ihlemann J, Ono S, Yabe A (2000) J Photopolym Sci Technol 13:167
64. Niino H, Yabe A (2001) J Photopolym Sci Technol 14:197
65. Zhang Y, Lowe RM, Harvey E, Hannaford P, Endo A (2002) Appl Surf Sci 186:345
66. Baudach S, Krüger J, Kautek W (2001) Review Laser Eng 29:705
67. Baudach S (2001) PhD thesis, University of Technology, Berlin
68. Jee Y, Becker MF, Walser RM (1988) J Opt Soc Am B 5:648
69. Kunz T, Stebani J, Ihlemann J, Wokaun A (1998) Appl Phys A 67:347
70. Himmelbauer M, Arenholz E, Bäuerle D, Schilcher K (1996) Appl Phys A 63:337
71. Herman PR, Marjoribanks RS, Oettl A, Chen K, Konovalov I, Ness S (2000) Appl Surf Sci 154–155:577
72. Korte F, Nolte S, Chichkov BN, Bauer T, Kamlage G, Wagner T, Fallnich C, Welling H (1999) Appl Phys A 69:S7
73. Haight R, Hayden D, Longo P, Neary T, Wagner A (1998) SPIE Proc 3546:477
74. Shani Y, Melnick I, Yoffe S, Sharon Y, Lieberman K, Terkel H (1998) SPIE Proc 3546:112
75. Stern D, Schoenlein RW, Puliafito CA, Dobi ET, Birngruber R, Fujimoto JG (1989) Arch Ophthalmol 107:587
76. Kautek W, Mitterer S, Krüger J, Husinsky W, Grabner G (1994) Appl Phys A 58:513
77. König K, Riemann I, Fritzsche W (2001) Opt Lett 26:819
78. von Woedtke T, Abel P, Krüger J, Kautek W (1997) Sens Actuators B Chem 42:151
79. Neev J, Da Silva LB, Feit MD, Perry MD, Rubenchik AM, Stuart BC (1996) IEEE J Sel Top Quant Electron 2:790
80. Kohns P, Zhou P, Störmann R (1997) J Laser Appl 9:171
81. Krüger J, Kautek W, Newesely H (1999) Appl Phys A 69:S403
82. Serbin J, Bauer T, Fallnich C, Kasenbacher A, Arnold WH (2002) Appl Surf Sci 197–198:737
83. Juhasz T, Loesel FH, Kurtz RM, Horvath C, Bille JF, Mourou G (1999) IEEE J Sel Top Quant Electron 5:902
84. Juhasz T, Djotyan G, Loesel FH, Kurtz RM, Horvath C, Bille JF, Mourou G (2000) Laser Phys 10:495
85. Biowski R, Homolka P, Barisani-Asenbauer T, Baumgartner I, Husinsky W, Kaminski S, Lametschwandtner A, Muss W, Grabner G (2000) J Refract Surg 16:23
86. Husinsky W, Mitterer S, Grabner G, Baumgartner I (1989) Appl Phys B 49:463
87. Altmann J, Grabner G, Husinsky W, Mitterer S, Baumgartner I, Skorpik F, Asenbauer T (1991) J Refract Surg 7:377
88. Husinsky W, Mitterer S, Altmann J, Grabner G, Baumgartner I, Skorpik F, Asenbauer T (1991) J Refract Surg 7:385
89. Müller GJ, Müller-Stolzenburg N (1989) Biotronic 1:55
90. Müller-Stolzenburg N, Müller GJ, Buchwald HJ, Schründer S (1990) Arch Ophthalmol 108:915
91. Gruber D, Husinsky W, Grabner G, Baumgartner I, Scholmann J, Krüger J, Kautek W (1996) In: Waidelich W, Staehler G, Waidelich R (eds) Lasers in medicine. Springer, Berlin Heidelberg New York, p 397
92. Loesel FH, Niemz MH, Bille JF, Juhasz T (1996) IEEE J Quant Electron 32:1717
93. Loesel FH, Tien AC, Backus S, Kapteyn H, Murnane M, Kurtz RM, Sayegh S, Juhasz T (1998) SPIE Proc 3565:116
94. Cefalas AC, Sarantopoulou E, Argitis P, Gogolides E (1999) Appl Phys A 69:S929
95. Zhang J, Sugioka K, Takahashi T, Toyoda K, Midorikawa K (2000) Appl Phys A 71:23
96. Schäfer D, Ihlemann J, Marowsky G, Herman PR (2001) Appl Phys A 72:377
97. Cefalas AC, Sarantopoulou E, Kollia Z (2001) Appl Phys A 73:571
98. Russo RE, Mao XL, Borisov OV, Liu HC (2000) J Anal At Spectrom 15:1115
99. Basting D, Stamm U (2001) Z Phys Chem 215:1575
100. Dyer PE, Maswadi SM, Walton CD, Ersoz M, Fletcher PDI, Paunov VN (2003) Appl Phys A 77:391

Adv Polym Sci (2004) 168:291–340
DOI: 10.1007/b12684

Synchrotron Radiation Direct Photo Etching of Polymers

Y. Zhang

Sumitomo Heavy Industries Ltd., 2-1-1 Yatocho, Nishitokyo, 188-8585 Tokyo, Japan
E-mail: ypz_zhang@shi.co.jp

Abstract In this article, we review studies on the direct photoetching of polymers with synchrotron radiation (SR) in vacuum. The SR etching of poly(tetrafluoroethylene) (also called Teflon) has been applied as a microfabrication process to create high aspect ratio microstructures and to deposit high-quality thin films. This process appears rather similar to x-ray proximity lithography in view of exposure optics and similar to laser ablation in view of photoprocessing; thus, both x-ray lithography and laser ablation will often be mentioned for comparison throughout the review. In order for readers to be familiar with x-ray processing, x-ray lithography will first be introduced before synchrotron radiation is discussed as the light source compared to lasers. Microfabrication, like microstructuring and thin film deposition by using SR etching, will be reviewed and compared with results of deep x-ray lithography and laser ablation deposition. Then the dissociation mechanism involved will be discussed for two photoprocessing procedures, namely SR etching and laser ablation. Finally, as an application example for microfabrication, x-ray refractive single lenses made of Teflon using the SR etching technique will be presented.

This article is dedicated to a late colleague, T. Takayama, who introduced the ingenius idea of injecting high-energy electrons into the world's smallest SR ring, realizing a storage ring without straight sections and without magnetic quadrupoles.

1 Introduction

Photolithography is a printing process for generation of microstructures, which has been applied to industrial fabrication of large-scale integrated circuits, and polymers are used as resists. Since a shorter wavelength can reduce the diffraction effect, being able to generate smaller structures, ultraviolet (UV) light not only from lamps but also from excimer lasers has become the main source for photolithography nowadays. For even shorter wavelengths and even smaller structures, synchrotron radiation (SR), which actually provides x-rays, has been considered to be the next generation source for industrial fabrication. In x-ray lithography using SR [1], proximity exposure replaces projection optics but polymers remain as the resists.

The polymeric resists usually generate the microstructures through developing in a chemical liquid (namely developer), after being exposed to the UV beam through a mask which possesses designed patterns. It was found, however, that polymers like poly(methyl methacrylate) (PMMA) and poly(methyl isopropenyl ketone) (PMIPK) could already generate the structures under UV light without the development. This self-development phenomenon was called *direct etching* [2] and was also observed under the SR beam in PMMA [3] as well as poly(cyclohexylmethylsilane) (PCHMS) [4]. UV excimer laser ablation has been established to directly generate the microstructures in polymers [5], but it was called *self-developing etching* instead of *ablation* in the first report [6]. Except for laser ablation, the self-development process was superficial, namely in the submicron range. We succeeded in applying the SR beam to create deep microstructures on poly(tetrafluoroethylene) (PTFE, also called Teflon) in vacuum [7]. After confirming no threshold in our process, we also called it *direct photoetching*. In our case, *direct* means "no chemicals used upon the irradiation" since the SR etching of inorganic materials such as silicon, amorphous SiO_2, and carbon has been carried out in a chemical atmosphere (such as SF_6 and Cl_2) [8 ,9], whereas it meant "no development process after the irradiation" or "self-developing" in the previous cases [2–4]. No matter what *direct etching* or *ablation* was termed, the polymeric materials were removed from the bulk by photoabsorption, which did not lead to a significant rise in the equilibrium temperature and no chemicals were used for the removal. In fact, *ablation* was first introduced to emphasize the sole role of photons in the removal of polymeric materials in the laser case [10]. So far, some people prefer using *ablation* for the SR case [11]. In this chapter, we will review studies of the interaction between the SR beam and the polymers, emphasizing the SR etching of PTFE and comparing it with laser ablation as well as x-ray lithography.

2 Lithography Using SR

The origins of both the UV excimer laser ablation of polymers [6, 12] and the introduction of the SR source to industry [1, 13] came from photolithography fabrication. The origin of the SR direct etching of polymers was from deep x-ray lithography [7], which is usually called the LIGA (an acronym for the German words *Lithographie, Galvanoformung, Abformung*) process [14]. Though all studies of x-ray lithography will not be reviewed here, we discuss several characteristics of x-ray lithography using SR and compare them with conventional photolithography. This may help those who are not familiar with x-rays to understand what difference exists between the UV range and the x-ray range. The discussion will be useful also in the following sections when SR etching is compared to laser ablation.

X-ray lithography is 1:1 patterning without reduction of the mask patterns, in which the resist and the mask are maintained in close proximity under the SR exposure and the gap between them should be kept as small as possible [1]. Therefore, x-ray lithography is also called *proximity lithography*. In the proximity system, mirrors may be introduced to improve uniformity of the SR beam [15], but one can practically consider no optical system used. Refractive optics is widely used in the wavelength range from infrared to ultraviolet, but can hardly be applied to the x-rays. Both the 1:1 proximity patterning and the introduction of the x-rays have caused difficulty in mask fabrication, since the absorbers in the masks should have their patterns so small as to be printed on the resists, and at the same time have their thickness great enough to keep a certain contrast under highly penetrating x-rays. Especially in the LIGA case, the masks for deep x-ray lithography may have to be fabricated with the LIGA process itself [14]. To create the 800-μm-deep microstructures in PMMA under single exposure of the x-rays, for example, the mask absorbers which are usually made of high-Z metals like Au, W or Ta have to be in the thickness range between 10 and 20 μm, which may need the LIGA process.

The x-ray mask is very different from the optical mask, not due to the proximity optics but due to the photon energy. Glass substrates of the masks for optical lithography are opaque to x-rays and thus cannot be used. To have a high transmission for both x-rays and alignment visible light has let the x-ray mask possess a very thin membrane as the substrate. Thermal distortion of the mask has to be considered seriously even with a small rise in temperature. A typical x-ray mask has 0.4-μm-thick Ta absorbers on a 2-μm-thick SiC membrane, for example. When it is set with a gap of 10 μm to a 0.5-μm-thick PMMA film coated on a silicon wafer and exposed to the SR beam in helium atmosphere, its thermal distortion may be as large as 12.7 nm in the beam-scanning direction for one degree of the temperature rise in the membrane [16]. This can become very serious, especially for the SR etching when powerful white light has been introduced. Furthermore, the mask contrast has never been a problem in the optical range but becomes a serious issue with increasing the photon energy of x-rays. In the optical

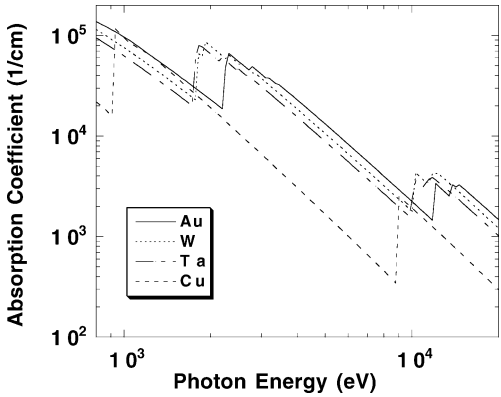

Fig. 1 X-ray absorption spectra calculated for the metals (Au, W, Ta, and Cu) which are mainly used as the absorbers for x-ray masks

range, the metallic absorbers whose thickness is more than a quarter of the wavelength are opaque. For example, the 0.2-μm-thick gold absorber has a contrast large enough for 400-nm light. On the other hand, the mask contrast is equal to the reciprocal of the absorber transmission, i.e., exp (μL) and usually decreases with increasing x-ray energy due to the decrease in the linear absorption coefficient μ (Fig. 1). Therefore, the absorber thickness L has to be increased to keep the contrast. As mentioned above, the absorbers of a LIGA mask may have to be as thick as 20 μm. The thick but fine absorbers have to be formed on the thin membrane of the x-ray masks. Obviously, this practically creates a technical barrier for x-ray lithography.

In the reduction optical system, an increase in the numerical aperture (NA) may not only reduce the feature sizes which are usually decided by the system resolution $\sigma \sim \lambda/\mathrm{NA}$ for a given wavelength λ, but also strongly reduce

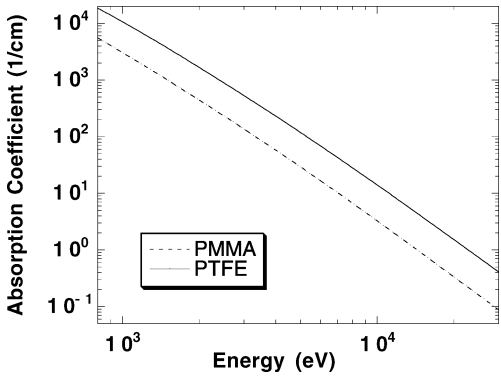

Fig. 2 X-ray absorption spectra calculated for the polymers PMMA and PTFE. PMMA is mainly used in deep x-ray lithography, namely the LIGA process, while PTFE is mainly used in SR direct photoetching, namely the TIEGA process

Fig. 3 SEM picture of the high aspect ratio structure made of PMMA by the LIGA process. Typically, the structural height (depth) is 100–500 μm and the feature size is 2–20 μm; thus, the aspect ratio is between 5 and 100

the depth of focus $DOF \sim \lambda/(\mathrm{NA})^2$, thus limiting the structural depth as well as the aspect ratio, which is defined as the ratio of the maximum depth to the minimum feature size. In KrF laser (248 nm) lithography, by using a laser stepper with NA~0.5 [17], for example, DOF would be 1.6 μm for the 250 nm line-and-space (L&S) pattern on the chemically amplified PMMA resist and the maximum aspect ratio would be limited to 7. In contrast, x-ray lithography is able to reduce the feature sizes thanks to much shorter wavelengths of the x-rays, and meanwhile increase the structural depth, not only due to the very small NA of the proximity system but also due to the large penetration of the x-rays. As shown in Fig. 2 for the polymers PMMA and PTFE, the higher energy in the x-ray range usually leads to less absorption (that is, deeper penetration) in the polymers. For example, the absorption of PTFE at 10 keV is three orders of magnitude less than that at 1 keV. Figure 3 shows the typical structures created in PMMA by the LIGA process at our laboratory, in which the feature size is as small as a few microns and the structural depth more than 100 μm, thus the aspect ratio is of the order of several 10s. In general, the critical wavelength for the LIGA process is ~0.3 nm, while that for standard x-ray lithography is ~0.8 nm, as shown in Fig. 4 for our case. For the given wavelength, the smallest L&S patterns achieved by x-ray lithography are dependent on the proximity gap. The L&S

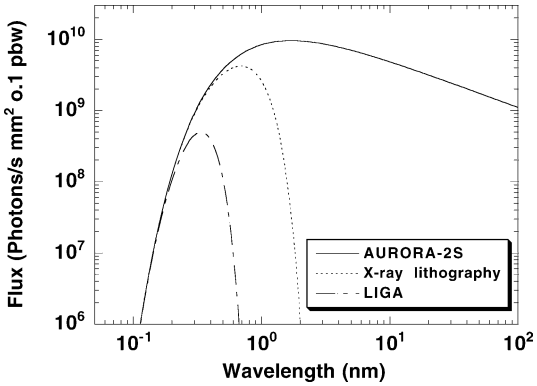

Fig. 4 Synchrotron radiation spectrum of AURORA-2S between 0.1 and 100 nm as well as the typical spectra used for x-ray lithography and the LIGA process

structures down to 70 nm were achieved with a proximity gap of 15 μm under the single exposure at our laboratory [15, 18]. A gap of 10 μm seemed to have the L&S resolution limited to 60 nm [19] and may have to be further reduced for the 50-nm patterns. Since too small a gap (e.g., smaller than 5 μm) may cause problems in the fabrication, application of the shorter wavelengths has been proposed for standard x-ray lithography to print features of 35 nm or smaller [20, 21]. It should be noted that multiple exposure may achieve smaller structures than the single exposure [22].

The SR beam is generated by relativistic electrons (or positrons) which undergo a change of their direction (that is, their acceleration) in a magnetic field. Since their orbits are defined by a storage ring which is built on a horizontal surface, the SR beam directions are also defined on a horizontal surface. It is very difficult either technically to generate the SR beam on a vertical surface or optically to change it to a vertical surface. Therefore, the stages for x-ray lithography have to move on a vertical surface, which creates technical difficulty for making ultrafine stages because of gravity. Figure 5a displays the x-ray stepper developed in our laboratory. By contrast, the optical beam usually comes from top to bottom on the vertical surface, and the stages move on the horizontal surface in optical lithography. We have produced the XY stages in-house (Nanoplane series, Fig. 5b) on the horizontal surface with position precision of ±10 nm and a stroke of 370 mm. The discontinuity between the x-ray stepper and the conventional stepper may also create a large barrier for x-ray lithography to replace optical lithography in industrial fabrication.

The PMMA polymer is the best known resist, due to the fact that it has the best resolution down to at least 5 nm [23]. It has been used exclusively in the LIGA process since the thick resist layer of the order of a few 100 μm could be made readily [14]. Many previous studies, including those on the self-development phenomena [2, 3] and laser ablation [5, 10, 12, 17], have been carried out on this polymer. Therefore, there are relatively more data

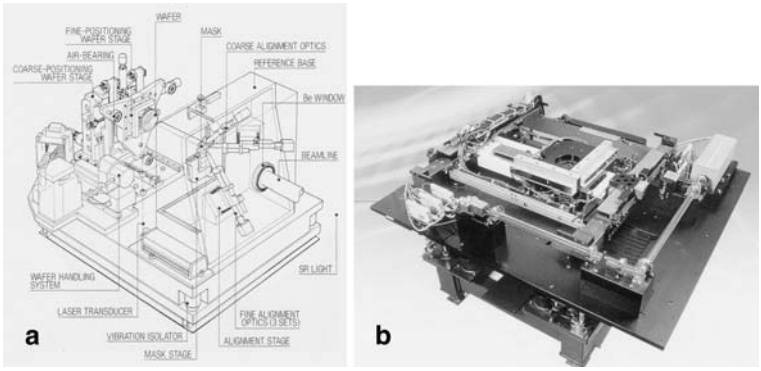

Fig. 5 The x-ray stepper has the stage scanning on the vertical surface (**a**), while the high-precision XY-stage is used to scan on the horizontal surface (**b**). The commercial stage (Nanoplane series) made by Sumitomo can have a position precision of ±10 nm on the horizontal surface. It has a stroke of 370 mm and a maximum scanning speed of 300 mm/s

available for comparison between different light sources (e.g., SR, UV lamps, and lasers at various wavelengths) and between different processes (e.g., UV lithography, laser ablation, and SR etching), though this polymer is of low sensitivity for both UV light and x-rays.

3 Light Sources: SR vs Laser

In the above discussion of x-ray lithography, the optical characteristics of the SR beam have been described, such as much shorter wavelengths (e.g., 0.1–10 nm, see Fig. 4) than laser wavelengths (e.g., 157–1064 nm), different material transmissions between the optical and x-ray ranges, no easy use of optical systems, beams emitted on the horizontal surface and so on. In this section, some physical characteristics of the SR beam and the SR ring will be described. A comparison with pulsed lasers is also given, for we are going to compare the SR direct etching with laser ablation. In fact, Sumitomo Heavy Industries Ltd is one manufacturer, maybe the only one, that offers both SR rings and lasers as commercially available products.

Our first SR ring (AURORA, 575 MeV electron energy) was based on a single superconducting dipole with a circular orbit of 1 m in diameter (Fig. 6). As shown in Fig. 7, it is 3 m in outer diameter, which became the smallest SR ring in the world and the racetrack microtron as its injector is also compact, which can be seen in the right upper corner. It has been installed at Ritsumeikan University since 1996. The SR source in-house now is the second-generation ring (AURORA-2S, 700 MeV electron energy), which has a racetrack orbit based on normal conducting bending magnets (dipole field of 2.7 Tesla). It has up to 20 ports available to installation of beam-lines

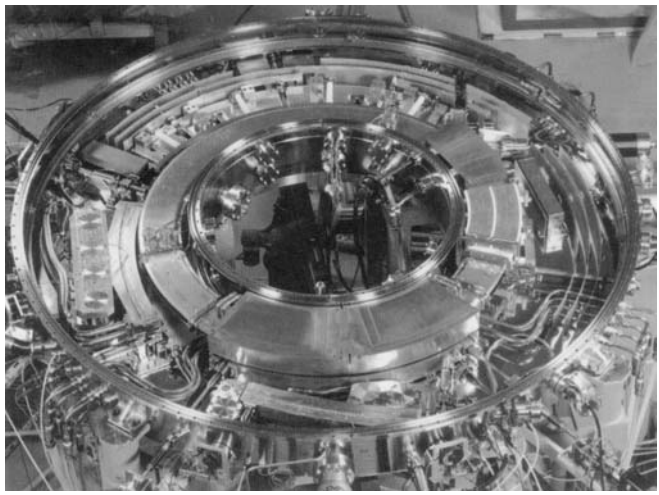

Fig. 6 A photo of the world's smallest storage ring. It has a circular orbit of 1 m in diameter, having no straight section or magnetic quadrupoles

(Fig. 8). As shown in Fig. 9, it is installed with self-radiation shielding, being under routine operation in the beam-current between 300 and 500 mA.

In the beam-lines used for the SR direct etching, there is no mirror or other optical system, but pinholes or slits may be used to select the beam size or to improve the beam uniformity. The SR beam is quasi-continuous, having a pulse duration of 170 ps and a repetition rate of 191 MHz. The pho-

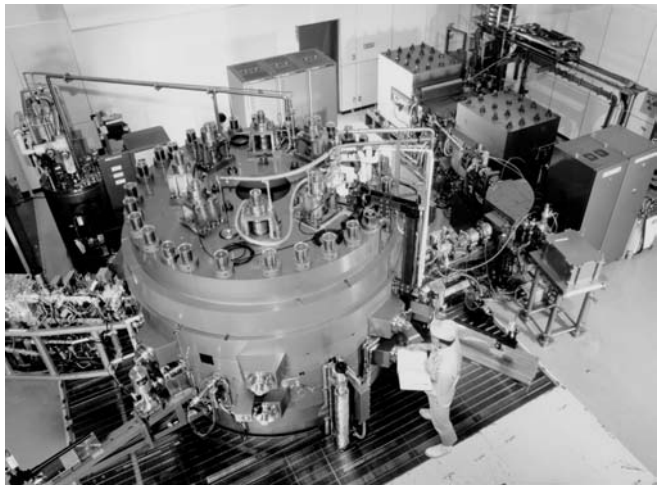

Fig. 7 A bird's eye view of the world's smallest SR machine called AURORA. It has an outer diameter of 3 m. A compact racetrack microtron is used as its injector, which can be seen in the *right upper corner* of the picture

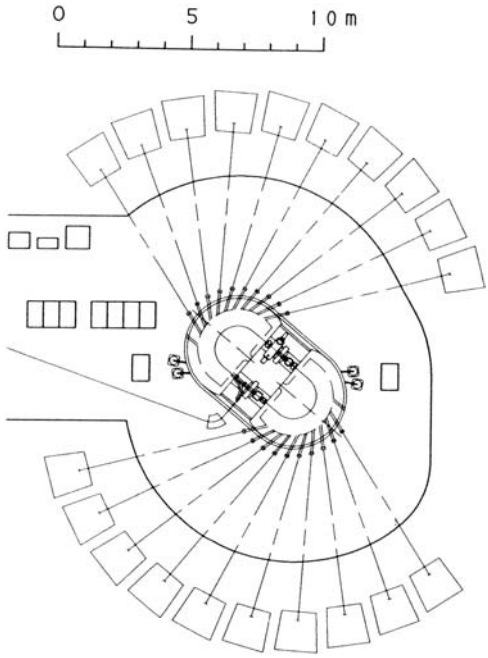

Fig. 8 A layout example of AURORA-2S showing that up to 20 beam-lines can be provided from the ring whose footprint is about 4 m×7 m

Fig. 9 A photo of the commercially available ring AURORA-2S installed with self-radiation shielding

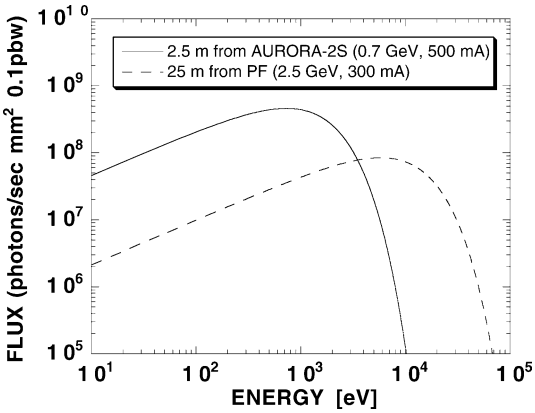

Fig. 10 A comparison between photon flux density at a distance of 2.5 m from the compact ring AURORA-2S with a beam current of 500 mA and that at 25 m from the standard ring (Photon Factory) with 300 mA

ton flux density on the sample surface was 7.3×10^{14} s^{-1} mA^{-1} cm^{-2}. The SR beam has a very broad spectrum from infrared to hard x-rays (Fig. 4), but the spectrum useful for the etching should be in the wavelength range between 0.2 and 200 nm, since polymers like PTFE [24] and PMMA [25] have almost no absorption between 250 and 1000 nm and less in the hard x-ray range (see Fig. 2).

Compared to the standard SR rings whose circumferences are roughly of the order of 100 m, our rings are compact, having the circumference of the order of 10 m. The compact ring has not only advantages like low cost for its construction and facilities, but also appears more friendly to many researchers who have performed their experiments at individual laboratories such as laser researchers. In my own experience, the huge facilities may generate negative feelings that an individual's control would be lost through a centralized arrangement. Furthermore, the beam-lines for the standard ring are normally 10–30 m in length, while they are only 2–4 m for the compact ring. A shorter beam-line not only makes researchers feel closer to the SR source, but also enhances the photon flux density. As shown in Fig. 10, for example, the photon flux density at a distance of 2.5 m from our compact ring AURORA-2S under 500 mA can be more than that at 25 m from the 2.5-GeV ring at Photon Factory under 300 mA in the photon energy range below 3 keV (wavelength >0.4 nm). Obviously, the compact ring generates fewer photons in the hard x-ray range, which has the following merit and demerit. The merit is in the mask contrast. For example, the critical wavelength for the LIGA process is about 0.3 nm using our compact ring (Fig. 4), but may become about 0.1 nm using the 2.5-GeV ring (Fig. 10). Since the Au absorber has a linear absorption coefficient at 0.3 nm about six times larger than at 0.1 nm (see Fig. 1), its thickness can be only one sixth for the same contrast by using our ring. In fact, we have used the 4-μm-thick Au absorbers for the LIGA process instead of 20 μm, which has reduced not only the fabrication

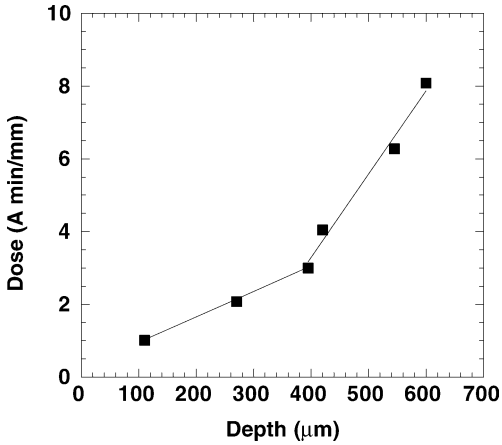

Fig. 11 Dependence of lithography depth on irradiation dose using the compact ring AURORA-2S, showing the significant increase when the depth is more than 400 μm. The dose is given in the unit A min/mm since the exposure is usually carried out by scanning the sample in the vertical

cost but also the technical barrier for the x-ray mask fabrication [26]. On the other hand, the demerit is the limitation in depth of the single exposure. As shown in Fig. 11, the dose for our compact ring significantly increases on increasing the depth to more than 400 μm, due to the lack of high-energy photons. The saturation effect in the depth can be seen in Fig. 12. In the fab-

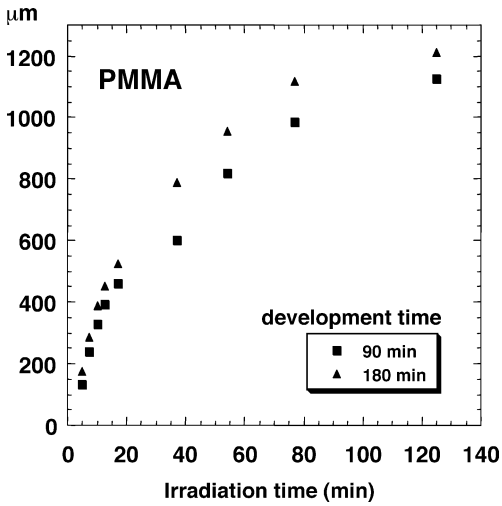

Fig. 12 Dependence of lithography depth on irradiation time using the compact ring AURORA, showing that the irradiation time becomes considerably long when the depth is more than 500 μm. The maximum depth appears to saturate in 1,200 μm due to the lack of high-energy photons from the compact ring (cf. Fig. 10)

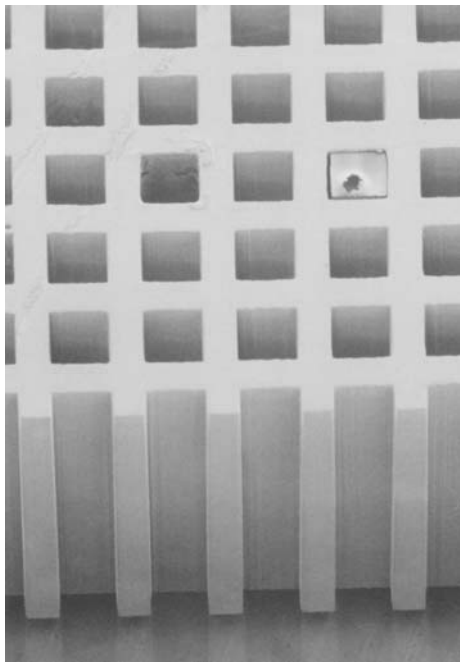

Fig. 13 Lithography achieved on PMMA as deep as 1,000 μm with the compact ring. Thermal damage can be observed due to the long irradiation (cf. Fig. 12)

rication, this means a significant increase in the irradiation time and thus a considerable reduction in the throughput. We achieved lithography as deep as 1,000 μm (see Fig. 13), but the irradiation time was long (see Fig. 12) and some thermal damage was already visible. It should be noted that unreasonably increasing the dose may lead to thermal damage to the resist surface so the development can not be carried out any more, as evident from Fig. 14. Since low-energy photons cannot penetrate deeply into the polymer but are absorbed near its surface, the increase in the dose may increase the temperature on the resist surface leading to thermal damage.

Although our compact ring with a footprint of about 4 m×7 m is about 15 times larger than an industrial laser which normally has a footprint of 1 m×2 m, the ring can provide the SR beams up to 20 at the same time (Fig. 8). To understand the physical characteristics of an SR beam, we compare it with the copper vapor laser which also emits quasi-continuous radiation. The repetition rate is of the order of 10 kHz for the copper laser, while it is of the order of 100 MHz for the SR ring. A laser pulse may have more than 10^{13} photons, while an SR pulse may just have 10^9 photons. Obviously, the SR beam appears more like a continuous beam. In general, the SR beam except from an undulator or a monochromator has a broad spectrum (Fig. 10), whereas the laser beam except from a dye laser has a narrow spectrum. Both the SR beam and the laser beam are highly collimating and have

Fig. 14 Serious thermal damage to the PMMA resist by unreasonably increasing the dose to 52.6 A min, consistent with the saturating phenomenon observed in Fig. 13. The development could not be carried out to create microstructures

a small angular spread. The beam size may be typically 25 mm×20 mm in the case of a gaseous laser, depending on its cavity, while it may be typically 5 mm×50 mm in the SR case, in which the vertical size cannot be expanded but the horizontal one can be, depending on the exit aperture. In general, the SR beam is being scanned in the vertical for the lithography (small depth) case [15], while the stage is vertically scanning for the LIGA or SR etching (large depth) cases [26].

4 Microstructuring with SR Etching

Polymeric microstructures that have the smallest features of the order of a few microns and a structural depth of the order of several hundred microns can be generated by the LIGA process, not only by deep x-ray lithography but also by molding [14]. For polymers like PTFE, however, the LIGA process cannot be applied, since there is no solvent to dissolve it and heating over its melting point does not lead to enough fluidity for the molding. In the laser ablation of polymers, the PTFE case is a well-known example to demonstrate that a vacuum-UV (157 nm) laser [27] or an ultrashort-pulsed (300 fs) laser [28] can create well-defined patterns, whereas the standard laser cannot. We are the first who found that PTFE and its copolymers PFA (perfluoroalkoxy) and FEP (fluorinated ethylene propylene) can be deeply etched by the SR beam in vacuum [7]. The etched depth can be up to 1,500 μm with an etching rate of the order of several 10 μm/min in our case

[29], much deeper and faster than the previous findings on self-development [3, 4]. Recently, similar studies on other fluoropolymers like PVDF [poly(vinylidene fluoride)] and ETFE (ethylene–tetrafluoroethylene copolymer) [11, 30] have turned out to be like the self-development, that is, the etching was limited to a few μm in depth and had the speed of the order of several 10 nm/min, three orders of magnitude less than ours. It should be noted that the SR direct etching is not limited to polymers [31, 32]. In this section, we review the studies on the generation of high aspect ratio microstructures by the SR direct photoetching of polymers. The mechanism involved in the process will be discussed in a latter section.

Commercial sheets of PTFE, PFA, FEP, and PMMA of thickness between 0.2 and 2 mm were used as our etching samples. A sample was cleaned with methanol and set to face the SR beam in an ultrahigh-vacuum chamber where base pressure was 1×10^{-8} mbar. The sample temperature could be increased with a hot plate attached to the sample rear and measured via a thermocouple. Similar to the x-ray lithography, a mask was set in close proximity to the sample but with a relatively large gap between 100 and 500 μm. The mask used was either a metallic stencil or an x-ray mask. The stencil was usually made of Cu or Ni, while the absorber in the x-ray mask was usually made of Au, W, or Ta. The linear absorption coefficients of Cu, Au, W, and Ta are given in Fig. 1 for consideration of the mask contrast. Obviously, the high-Z metals like Au, W, and Ta have more absorption than Cu and Ni (Ni has a similar absorption coefficient to Cu, not shown in the figure), but Ni and Cu can be readily generated by galvanoforming to create the metallic stencil as the mask. For the white light, which is the beam directly from the SR ring without inserting any filter into the beam-line, the etching process was carried out in vacuum and the metallic stencil was better, since both the air and the mask membrane may strongly attenuate the beam. For the filtered light, which was actually x-rays, the process was carried out in a helium atmosphere and the x-ray mask was readily used. The filters used to select the spectral range are usually made of thin films of low-Z materials. For example, the 1-μm-thick Al filter was used to select x-rays mainly in the spectral range between 0.2 and 3 nm, peaked at about 1 nm, and the photon flux density on the sample surface was about one fifth that of the white light [11, 29]. As shown in Fig. 4 for comparison, the 20-μm-thick Be filter was used to select the x-ray peaks at about 0.8 nm for lithography [15, 18], while a 500-μm-thick Be filter was used to select the hard x-ray peaks at about 0.3 nm mainly for the LIGA process [33]. The etched depth was measured with an optical microscope. The etching rate was given by the ratio of the depth to the irradiation time, which was set to be 1 min to prevent any error due to decay of the beam current or due to a temperature rise induced by long irradiation.

Table 1 gives typical results obtained for PTFE, PFA, FEP, and PMMA. The typical high aspect ratio structures generated by the SR etching can be seen in Fig. 15 for the PTFE case. Figure 16 shows the etching rate versus the beam current (i.e., photon flux density) at various sample temperatures, in which the PTFE was etched in vacuum by the 1-μm-thick Al-filtered beam.

Table 1 Synchrotron radiation direct etching of polymers

Polymers	PTFE	PFA	FEP	PMMA
Energy range (keV)	0.4–5.5	0.4–5.5	0.4–5.5	0.9–5.5
Wavelength range (nm)	0.2–3	0.2–3	0.2–3	0.2–1.3
Peak wavelength (nm)	1	1	1	0.3
Etching rate (μm/min)	60	36	17	50
Beam current (mA)[a]	250	330	300	310
Maximum depth (μm)	1,500	250	250	500
Maximum aspect ratio	75	12	12	5
Sample temperature (°C)	200	159	100	70–90

[a] The beam current used for measurement of the etching rate

Although no threshold behavior in the SR etching was observed (Fig. 16), the etching quality appeared to be dependent on the photon flux density. A low flux density (2×10^{17} s^{-1} cm^{-2} for the sample without preheating [7]) resulted in not only a low etching rate but also poor quality of the formed structures. Figure 17 shows a typical case of the low flux density, in which the hole wall had fiber-like structures on its surface to make the hole ill-defined. This has been improved by increasing the flux density to more than 3×10^{17} s^{-1} cm^{-2}. As known from previous studies [2–4], the preheating of the sample could increase the etching rate. For PTFE, whose upper working temperature is about 260 °C, we heated the sample up to 200 °C before irradiation, since the SR irradiation may result in an additional temperature rise of 20–50 °C [34]. The increase in the sample temperature indeed increased

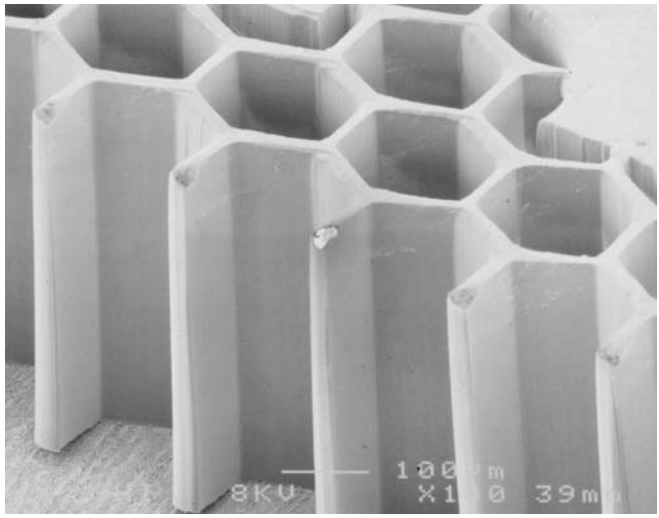

Fig. 15 High aspect ratio structures made of PTFE by SR direct etching in vacuum. Typically, the structural height (depth) is 500 μm and the structural width is 20 μm; thus, the aspect ratio is 25

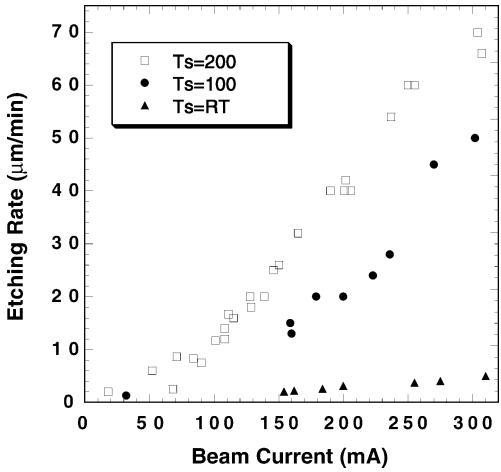

Fig. 16 Etching rate versus beam current when the SR etching was carried out at different temperatures *T*=RT (room temperature), 100, and 200 °C by preheating of PTFE

the etching rate, as is evident in Fig. 16, but, more importantly, smoothed out the fiber-like structured surface which was found at 1.5×10^{17} s^{-1} cm^{-2} or less [34]. Figure 18 shows that not only the wall surface formed by the etching appeared to be smoother than the sample surface, but also the etched

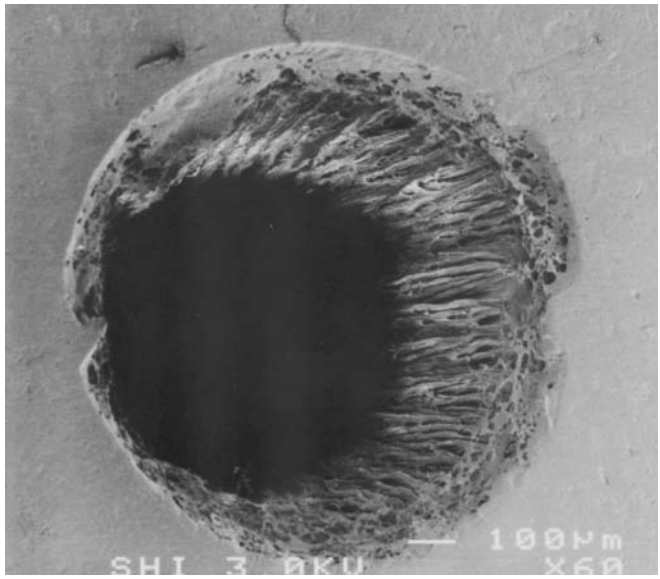

Fig. 17 SEM picture of a hole etched by the SR beam at a low flux density and without preheating of PTFE, showing the fiber-like structures on the etched wall to make the hole ill-defined

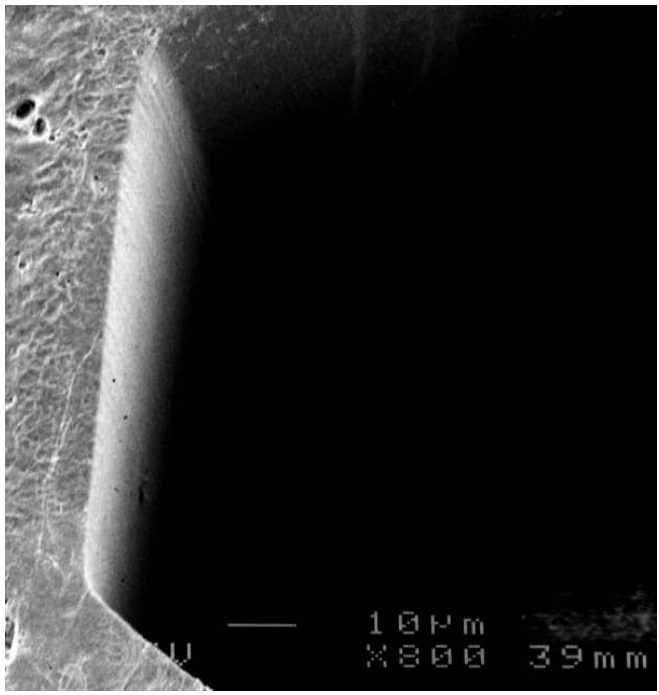

Fig. 18 SEM picture of the edge formed by SR etching of the preheated PTFE, showing the formed surface smoother than the starting surface and well-defined patterns of edge radius less than 1 μm

pattern was so well defined to have the edge radius less than 1 μm. In the case where the hard x-rays peaked at 0.4 nm were used to etch PTFE in the helium atmosphere, increasing the sample temperature from 25 to 200 °C reduced the roughness of the formed surfaces from 3,480 nm to 450 nm and the taper of the formed walls from 4 μm/100 μm to 1.6 μm/100 μm [35]. The surface roughness could be further improved to 110 nm and the taper to 0.6 μm/100 μm when the etching was carried out in vacuum under the higher flux density with preheating. It should be mentioned that the sample temperature may also be increased by the high-flux irradiation, especially in the case using white light. Different from the thermally induced preheating, however, the SR-induced heating is not uniform since the irradiated areas are selected by the mask. Thus, the deformation may occur not only in the polymer but also in the mask. The rise in the sample temperature significantly enhanced the etching rate, but seemed to have little effect on the dissociation, since the in situ mass spectrometric diagnosis using a quadrupole mass spectrometer to detect gaseous species showed no consistent difference. Furthermore, an Arrhenius-like plot for the etching rate [32] gave a slope of 0.1 eV in the PTFE case, much smaller than the activation energy (3.6 eV) for its vacuum pyrolysis [36]. All the data indicate that the thermal-

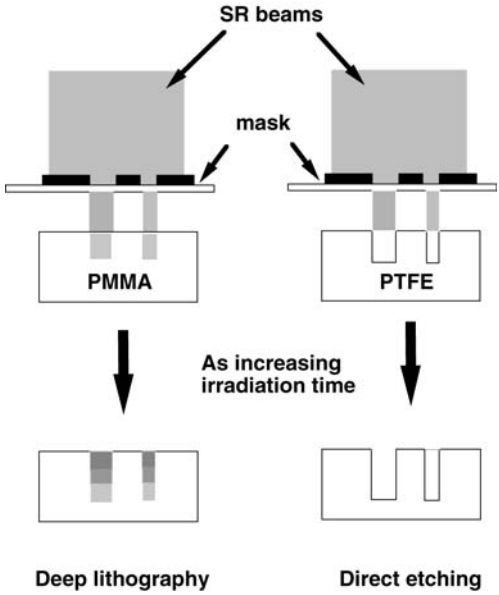

Fig. 19 A comparison between deep lithography and direct etching with increasing irradiation time. The main difference is that the level of the resist surface is falling during the etching, but almost not at all during lithography exposure

ly induced preheating does not take over the role of photons in the dissociation of polymers but may play a considerable role in the desorption of fragments.

As seen in Table 1, in contrast to the previous findings [3, 4, 32], our process is not a surface process but a bulk process like the LIGA process or the bulk dry etching process (such as reactive ion etching, RIE), which is able to create microstructures as deep as 1,500 μm and to achieve aspect ratios of the order of 50. This kind of process has been named high aspect ratio microtechnology [14]. Different from the other high aspect ratio technologies, SR etching does not involve any chemical process such as development or chemical etching. Similar to the LIGA process, the SR etching of PTFE (also named Teflon) which has been bonded to a conducting substrate can be combined with galvanic forming to generate metallic microstructures [29], named the TIEGA (Teflon included etching and galvanoforming) process [37]. For the compact ring, the TIEGA process has two advantages over the LIGA process. The first is that the low-energy (less than 1 keV) photons would not be wasted in the TIEGA process. In the LIGA exposure shown in Fig. 19 (left), since the level of the polymer surface is almost not changed during the irradiation, the larger depth needs the higher energy photons which can penetrate more deeply (see Fig. 2). For the compact ring that has fewer high- energy photons, the necessary dose may increase dramatically with the depth as discussed above (Fig. 11). On increasing the dose, the low-

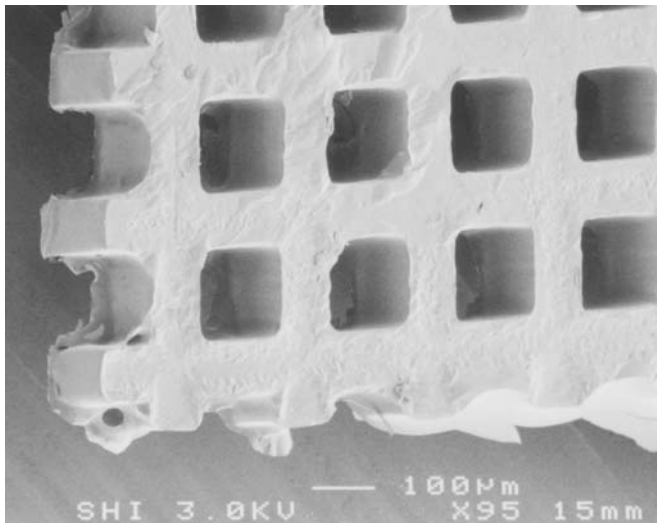

Fig. 20 SEM picture of the typical microstructures made of PMMA by SR direct etching in vacuum. Here, the structural depth is 200 μm, much larger than the 0.6 mm previously observed in the self-development. But the quality is not as good as that of microstructures made by deep x-ray lithography (cf., Fig. 13)

energy photons which may cause thermal damage to the resist surface (Fig. 14) have to be filtered away. On the other hand, since the etched surface is falling during the SR etching as shown in Fig. 19 (right), no higher energy photons are needed for the deeper structures and the surface damage found in the LIGA case (Fig. 14) has not been observed in the TIEGA case (Fig. 20). For our compact ring, the etching depth can be as large as 1,500 μm [34], while the lithography depth can hardly be so large (see Fig. 12). For the same structures as shown in Fig. 13, the TIEGA process may take about 20 min, much shorter than 90 min for the LIGA exposure. The second advantage is the enhancement in the mask contrast. As discussed (cf. Figure 10), the introduction of more low-energy photons means that the peak wavelength in the SR beam becomes longer, leading to enhancement in the mask contrast. Furthermore, it is worth mentioning that, though the etched surface is falling, the highly penetrating hard x-rays still have effects. It has been found [38] that the rate for the hard x-rays became about three times higher when the measuring time increased from 5 to 30 min, in other words, the etching process was accelerating. After the PTFE sample was exposed to the very weak hard x-rays which caused no etching, however, the acceleration effect was eliminated. This suggests that it may be due to chemical modifications which occurred under the etched surface, leading to the higher etching rate. Even though etching did not occur, cross-linking under the SR irradiation was found to occur as deeply as 50 μm under the surface and the etching rate was found to be higher for the cross-linked PTFE [39]. All these results may account for the above acceleration

phenomenon. It should be mentioned that cross-linking under other ionizing radiation like γ-rays or electron beams has been applied to improve the mechanical properties of the PTFE samples [40].

As seen in Table 1, the SR etching rate is of the order of several 10 μm/min, considerably faster than the chemical dry etching process [41]. Among PTFE, PFA, and FEP, since PTFE has the highest working temperature, the highest etching rate has been obtained at the highest sample temperature for PTFE (Table 1), whereas, at the same sample temperature, the highest etching rate has been found in FEP which has the smallest molecular weight and the lowest melting point [42].

For PMMA (Fig. 20), our process has resulted in microstructures much deeper than in the previous study [3], but the quality is not so good as either that given by PTFE (cf. Fig. 15) or that generated by the LIGA process (cf. Fig. 13). On the other hand, the quality for laser ablation of PMMA appears strongly dependent on the absorption. For example, an ArF excimer laser at 193 nm results in better quality than a KrF excimer laser at 248 nm [5, 43]. The poor quality for 248 nm may be improved by using the ultrashort-pulsed laser [43] or by chemical doping to enhance the photoabsorption [44]. It seems that the strong absorption has resulted in better surface roughness in laser ablation. The depth of laser ablation can be several hundred microns, but the formed walls often start to taper with increasing depth, mainly owing to a large NA of the reduction optics. Generally, the achievable aspect ratios are limited. In the KrF excimer laser ablation of PMMA and PET, efforts were made to reduce the taper angle of the hole wall by adjusting the laser fluence [45] and to increase the aspect ratio by reducing the beam divergence (that is, with a small NA) and by improving the beam homogeneity (that is, a non-Gaussian intensity profile) [46]. The aspect ratio was indeed greatly enhanced, but the pattern precision appeared to deteriorate on increasing the aspect ratio. In collaboration with Swinburne University at Melbourne, we carried out the ablation of PMMA using an ultrashort-pulsed (100 fs, 800 nm) laser and achieved high-quality holes with aspect ratios greater than ten (Fig. 21) [47]. This was achieved with an approximately Gaussian beam and large NA (e.g., 0.25) optics, in contrast with the previous methods using the UV excimer laser beam through a homogenizer and a small NA (e.g., 0.035) beam delivery [46]. We suggested the mechanism for this as follows: the hole formed by the ultrashort-pulsed laser ablation may act as a fiber to couple the Gaussian beam of subsequent laser pulses into the bottom of the hole and propagate the drilling deep into the bulk. Furthermore, we also observed that the hole walls started to taper when the aspect ratio was much greater than ten, and the hole axis could bend away from the optical axis as the aspect ratio increased further, which seems to provide additional evidence of a fiber-like coupling of the beam from the surface to the bottom of the hole. A similar phenomenon of bending was also observed in the previous study on the excimer laser ablation of PMMA, and nonuniform self-focusing in the dense plasma formed during ablation was suggested as a cause of this deviation [46], but such an explanation is not applicable for our case as a plasma would not have sufficient

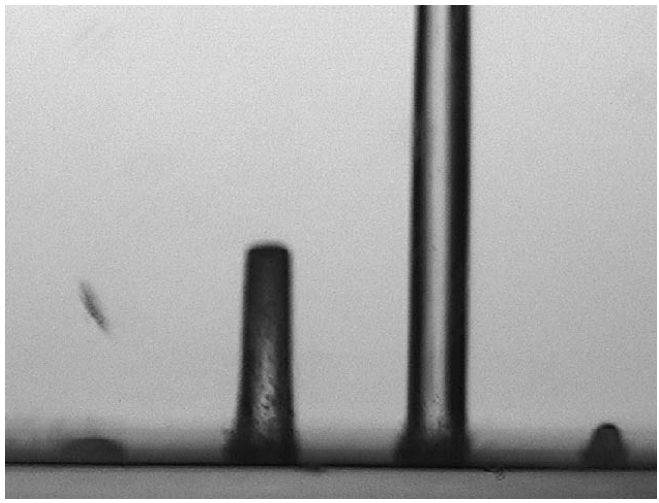

Fig. 21 An optical microscope picture of the holes drilled on PMMA by ultrashort laser pulses (100 fs, 800 nm), showing that the taper angle of the hole wall is very small and the bottom of the holes is relatively flat. The diameter of the holes is about 40 μm

time to develop during the ultrashort pulse [48]. No matter which kind of mechanism has been involved in laser ablation of the polymers, the achievable aspect ratios seem to be limited to ten and the feature sizes to be of the order of 10 μm. Obviously, this achievement by using laser ablation is not competitive with the SR direct etching of PTFE, which can have aspect ratios of the order of 50 and feature sizes of the order of 1 μm. However, laser ablation appears applicable for various kinds of polymers, whereas SR etching seems to be limited to the fluorocarbon polymers like PTFE. In contrast to PTFE, which is highly susceptible to ionizing radiation damage, polyimide (PI, also called Kapton) has good radiation resistance, because the aromatic imide ring has excellent radiation stability due to π-electron delocalization and the aromatic ether is stable under radiation due to lone-pair delocalization [49]. PI is used widely in the beam-lines as the filter material. The SR etching is not applicable to PI, whereas the laser can easily ablate it [5]. This case gives obvious evidence of differences in the dissociation mechanism between the SR etching and laser ablation. As will be discussed later, the PTFE case gives other evidence.

5 Film Deposition with SR Etching

Since the deposition of high-quality PTFE thin films may be important in many applications ranging from material reinforcement to molecular electronics, it has been attempted simply by a mechanical method [50], by vacuum thermal evaporation [51], by ion-beam sputtering [52], and extensively

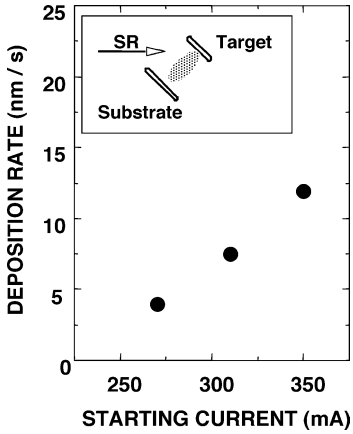

Fig. 22 Deposition rates measured at different starting currents for a given thickness of 500 nm. The *inset* shows the geometry of the PTFE target and silicon substrate with respect to the SR beam in the vacuum chamber

by laser ablation [53–55]. However, there were some problems for the above techniques as follows: the mechanical deposition could not be carried out either on structural surfaces or on the micro scale; the films deposited by thermal evaporation appeared to have numerous fibrous structures [51]; and those deposited by ion-beam sputtering were found to have chemical compositions different from that of the starting material [52]. For laser ablation deposition, lasers from infrared to vacuum ultraviolet have been used. Crystalline PTFE films could be obtained with a UV (266 nm) or a vacuum-UV (157 nm) laser on substrates heated to 100–320 °C in an Ar or CF_4 atmosphere between 50 and 250 mTorr [54, 55]. The unavoidable increase in the substrate temperature reduced the deposition rate and the introduction of the background gas may change the chemical compositions of the films. Thus, it remains a challenge to find a process to deposit thin PTFE films at a low substrate temperature with a high deposition rate and meanwhile to preserve the same chemical compositions, crystalline features, and surface morphologies in the films as the starting materials. In this section, we review our studies on the deposition of thin PTFE films by the SR photoetching technique in vacuum [56–58].

Main components of the setup for film deposition are similar to those used for generating high aspect ratio microstructures. They consisted of a light source and an ultrahigh vacuum chamber with a base pressure of 10^{-8} mbar. As the light source, the white light from the compact ring was used for the SR etching, while the fourth harmonic beam (266 nm, 10 ps, 100 Hz) of a YAG laser (PULRISE) was focused to reach a fluence of more than 1 J/cm^2 for the laser ablation.

A commercial sheet of PTFE between 0.5 and 1.5 mm in thickness was used as the starting material (called target in the following). The insert of Fig. 22 shows the arrangement of the target and the substrate. The target

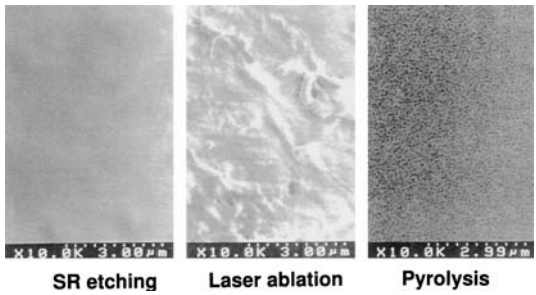

Fig. 23 SEM pictures of the typical surface morphology of the PTFE thin films deposited on Si(100) substrates at T_s=RT (i.e., room temperature) by different processing methods. *Left to right*: SR etching, laser ablation, and thermal evaporation at T_t=550 °C. The surfaces were directly observed without metallic coating. Reproduced with permission from J Phys Chem 2000, B26, 6212–6217. Copyright 1998 Am Chem Soc

was set on a holder which let the light source have an incident angle of about 45°. A Si(100) wafer was cut into many small pieces and used as the deposition substrate. A substrate was set on a sample holder to face the target. Both the target and substrate were cleaned with organic solvent before being set parallel to each other in the chamber. Both of them could be electrically heated by hot plates attached to their rear and their temperatures (T_t=target temperature and T_s=substrate temperature) were measured via thermocouples.

The thickness of the deposited films was monitored with a quartz crystal microbalance and its distribution was measured with ellipsometry at 675 nm. Films of 0.1–1.5 μm thickness were deposited on the Si(100) substrates from gaseous fragments from the SR etching of the PTFE target in vacuum. For comparison, films were also deposited either by laser ablation or by vacuum evaporation with heating of the target to T_t=550 °C. Surface morphology was observed with scanning electron microscopy (SEM). Figure 23 displays three SEM pictures for the typical surface morphology of the PTFE films deposited on the Si(100) substrates at T_s=RT (i.e., room temperature) by SR etching, laser ablation, and vacuum evaporation, respectively (from left to right). The film surface looked smooth in the SR case, but by contrast it showed numerous fibrous structures in the pyrolysis case as observed previously [51]. In the laser case, some rough structures were also observed, but it was reported that they could be smoothed out by increasing the substrate temperature in about 200 mTorr Ar gas atmosphere [55]. In the pyrolysis case, however, the surface structures on the deposited film could not be eliminated by increasing the substrate temperature, as is evident from Fig. 24 where the deposition was carried out at T_s=200 °C. Since the etching rate increases on increasing the beam current or the target temperature (Fig. 16), the deposition rate should have similar behavior. Figure 22 shows the rate increases with the beam current (namely, the photon flux density) at the same substrate temperature T_s=RT, while Fig. 25 shows the deposition rate increases with the target temperature under the same start-

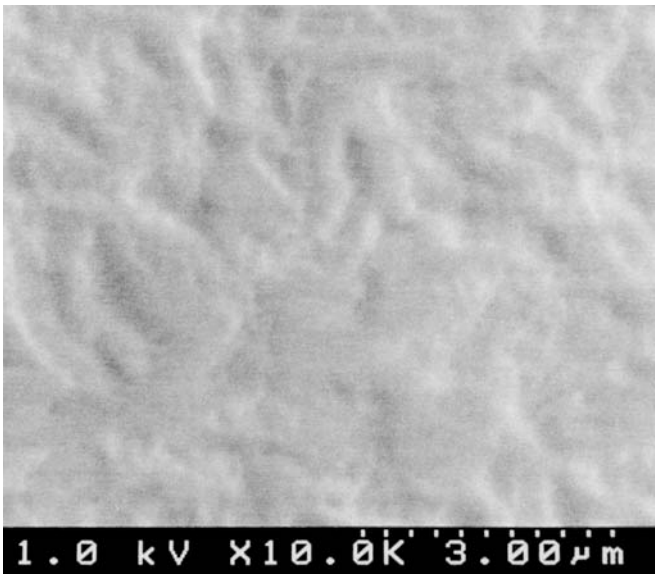

Fig. 24 SEM picture of the typical surface morphology of the PTFE thin films deposited on Si(100) substrates at T_s=200 °C by thermal evaporation with T_t=550 °C

ing current of 310 mA. The maximum deposition rate was about 20 nm/s under the beam starting from 310 mA with the target temperature T_t=200 °C, much higher than 1 nm/s given by the pyrolysis [51] and 0.4 nm/s given by the F_2 laser ablation assuming a repetition rate of 50 Hz [55, 56]. For the insoluble PTFE, to directly evaluate the molecular weight is difficult but the melting temperature T_m may give some information [59]. The measurements with differential scanning calorimetry (DSC) (PERKIN-ELMER, DSC-7) led to T_m=320±10 °C for the PTFE film deposited by SR etching, similar to T_m=323 °C for those deposited by laser ablation [60] but slightly lower than T_m=335±5 °C for the PTFE target. Our data were close to T_m=327 °C for the PTFE powder with a nominal weight of 8,500 [59], but far higher than T_m=262 °C for a nominal weight of 1,500 [59] and T_m=192 °C for $C_{24}F_{50}$ [61]. Therefore, the PTFE deposited by SR etching should have a mean molecular weight of more than 7,500 and the perfluoro-n-alkanes C_nF_{2n+2} ($n \geq 150$) might also be included since they could hardly be distinguished from the polymer [58].

The chemical compositions of both the target and deposited films were analyzed by x-ray photoelectron spectroscopy (XPS) and Fourier-transform infrared (FTIR) spectroscopy. The typical XPS C1 s level spectra for the films deposited at different target temperatures are displayed in Fig. 26, and compared with that of the target (bottom trace) [58]. Besides the CF_2 peak centered at 292 eV, a small shoulder due to CF_3 was detected at 295 eV for the SR-deposited films (top and middle traces) but not for the target (bottom trace). Correspondingly, the ratio of F to C values (measuring errors

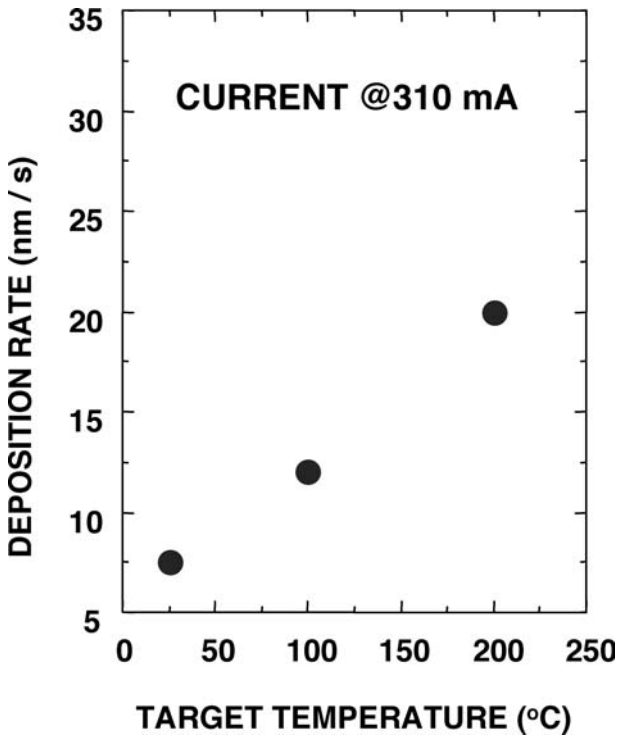

Fig. 25 Deposition rates measured at various target temperatures T_s=RT, 100, and 200 °C for a beam current of 310 mA, showing an increase in the deposition rate with the target temperature, which appears to correspond to the etching rate (cf., Fig. 16)

within ±5%) of the deposited films was between 2.01 and 2.10, slightly larger than 1.95 for the target, indicating that the deposited films were slightly F-rich. This CF_3 component was diminishing with increasing target temperature, but did not change on increasing the substrate temperature. The similar behaviors were also observed in the FTIR spectra. As shown in Fig. 27, besides two strong C–F_2 stretching bands at 1156 and 1211 cm^{-1}, a small C–F_3 stretching band was detected at 980 cm^{-1} in the deposited films but not in the target. The 980 cm^{-1} band due to CF_3 also diminished in the films deposited at the higher target temperature. It should be mentioned that the FTIR spectra in this case may not provide enough evidence of compositional fidelity for the deposited films, since all spectra of the films deposited from PTFE, PFA, and FEP appeared to be too similar to each other with both the C–F_2 and C–F_3 stretching bands [42]. To confirm our process, we have carried out the same deposition with other fluoropolymers such as PVDF and ETFE [57]. The observation that the FTIR spectra of the deposited films were nearly identical to those of their targets but obviously different from each other provided indirect evidence that deposition using SR etching should be able to preserve the chemical composition of the target polymer.

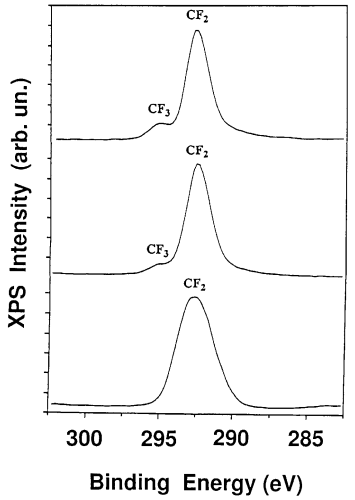

Fig. 26 XPS C1 s level spectra of the thin films deposited on Si(100) substrates at T_s=RT by SR etching of the PTFE target at different target temperatures. T_t=RT (*top*) and T_t=200 °C (*middle*) compared with that of the PTFE target before the irradiation (*bottom*). Reproduced with permission from J Phys Chem 2000, B26, 6212–6217. Copyright 1998 Am Chem Soc

Crystalline features of the target and deposited films were characterized by 2θ x-ray diffraction (XRD) (Cu Kα radiation of 8,040 eV). Both the XRD and DSC data gave evidence that the deposited PTFE films were crystalline [51, 55, 56, 60]. In the XRD spectrum between 2θ=5 and 45 (Fig. 28), five sharp peaks with two broad peaks (centered at 2θ=15 and 39) were observed for the target (top trace). The sharp peaks were due to large-size crystal grains, while the broad peaks were due to small-size grains. A spectrum of the deposited films (bottom trace) showed that they were crystalline but generally had small-size grains. The amount of large-size grains seemed to increase with the target temperature but not with the substrate temperature [56]. The target temperature rather than the substrate temperature had influence on the deposited films not only in their chemical compositions but also in their crystallinity.

The FTIR spectrum of the PTFE film deposited by laser ablation was identical to that of the target [54], but that of the film produced by SR etching showed some visible differences (see Fig. 29). Obviously, the C–F_2 deformation bands at 640 and 513 cm^{-1} appear much smaller in the bottom trace. To understand why these 640 and 513 cm^{-1} bands were so small in the SR case, we measured both normal and oblique transmission of FTIR with an incident angle of 0 and 80° [58]. Two FTIR spectrometers (PERKIN-ELMER and JASCO) were used to measure spectra in the range 400–3000 cm^{-1}. For a cross-check, the film was also deposited on a metallic surface and infrared reflection absorption spectroscopy [62] was carried out to confirm our oblique transmission measurements. Typical changes in the FTIR transmission

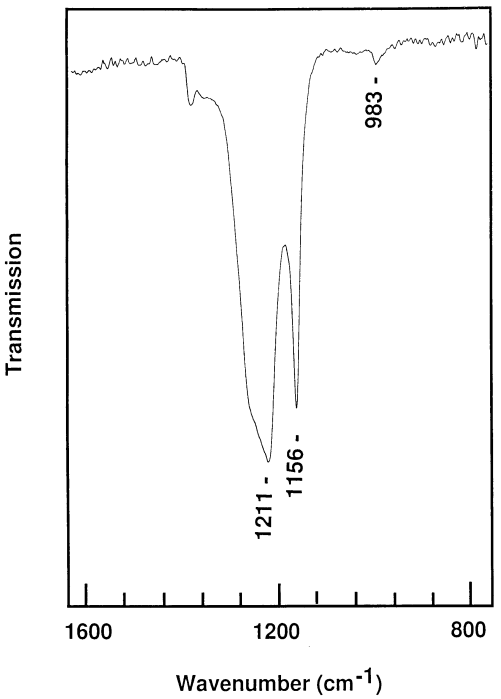

Fig. 27 Oblique transmission FTIR spectrum of the PTFE thin films deposited on Si(100) substrates by SR etching, showing the C–F_3 stretching band detected at 983 cm^{-1} beside two strong C–F_2 stretching bands at 1156 and 1211 cm^{-1}. This CF_3 band diminished on increasing the target temperature. Reproduced with permission from J Phys Chem 2000, B26, 6212–6217. Copyright 1998 Am Chem Soc

spectra are displayed in Figs. 30a and b, where the bottom trace is a spectrum of the normal transmission and the top trace is that of the oblique transmission. For PTFE, fortunately, the infrared bands at 1211, 1156, 640, 556, and 513 cm^{-1} have been well assigned to the modes $E_1(2)$, $E_1(3)$, $A_2(2)$, $E_1(4)$, and $A_2(3)$, respectively [63]. The $E_1(2)$, $E_1(3)$, and $E_1(4)$ bands have the transition moment perpendicular to the chain axis (called perpendicular bands), while the $A_2(2)$ and $A_2(3)$ bands have the transition moment parallel to the chain axis (called parallel bands). Since the light cannot excite the transition moments parallel to the light direction, those bands may diminish when the incident direction of the light changes to the same direction as their transition moments. In this way, the orientation of polymer chains may be understood by changing the incident direction of light. In Fig. 30a for the SR case, when the infrared light changed from the oblique incidence to the normal one, the $A_2(2)$ and $A_2(3)$ parallel bands detected at 644 and 532 cm^{-1} became very small, while the $E_1(2)$, $E_1(3)$, and $E_1(3)$ perpendicular bands detected at 1211, 1156, and 556 cm^{-1} were enhanced, indicating that the chain axes were *perpendicular* to the substrate surface (called perpendicular orien-

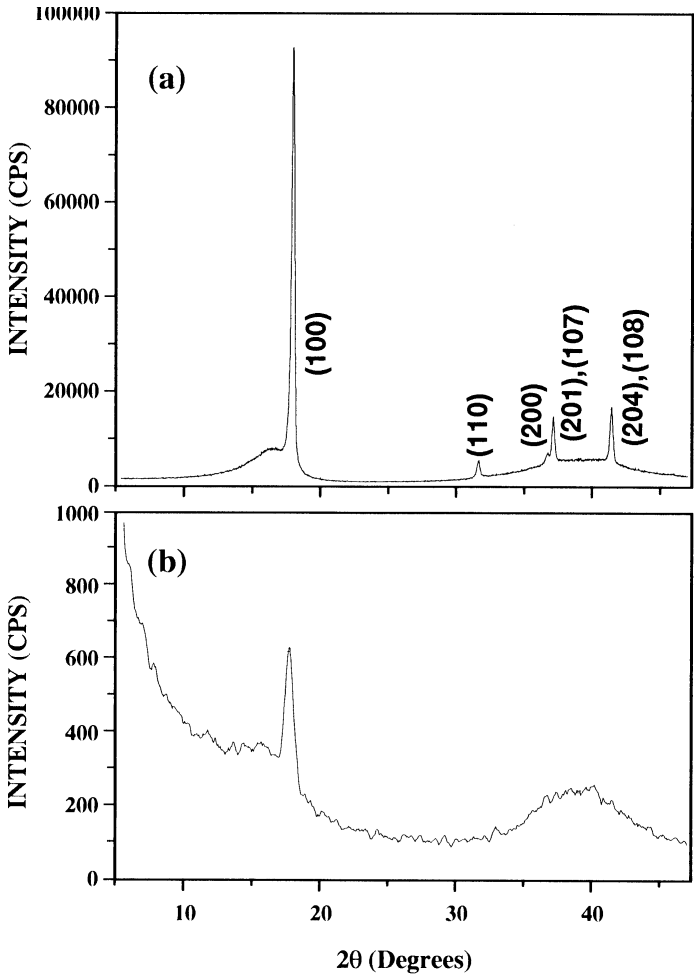

Fig. 28 XRD spectra of the PTFE target (**a**) and films deposited at target temperature T_t=200 °C and substrate temperature T_s=RT (**b**), showing that the deposited films were crystalline but generally had small-size grains

tation for simplicity). On the other hand, in Fig. 30b for the laser case, the $A_2(2)$ and $A_2(3)$ bands detected at 640 and 513 cm^{-1} were enhanced when the oblique incidence turned to the normal, indicating that the chain axes were *parallel* to the substrate surface (called parallel orientation for simplicity), which agrees with the previous report [60]. This suggests that the chain orientation in the films deposited by the two photoprocesses was different, namely the perpendicular orientation in the SR case but the parallel orientation in the laser case. A significant blue shift (~19 cm^{-1}) was observed for the $A_2(3)$ band detected at 532 cm^{-1} in the SR case (Fig. 30a), compared to that detected at 513 cm^{-1} in the laser case (Fig. 30b). Similarly, the $A_2(2)$

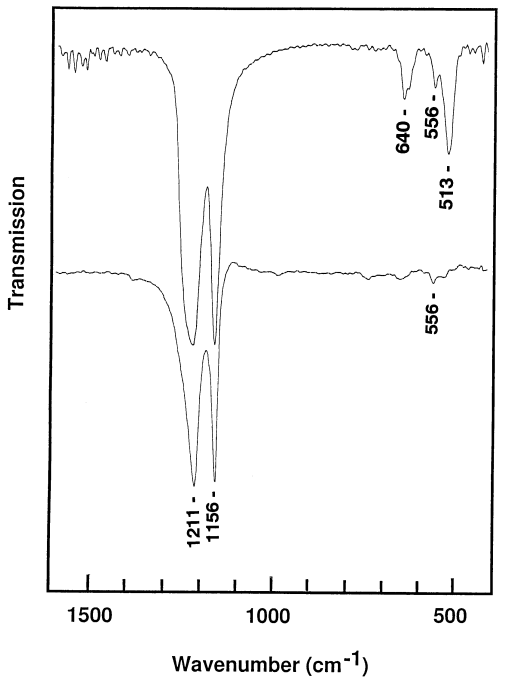

Fig. 29 Typical FTIR transmission spectra of the PTFE films deposited on Si(100) substrates at T_s=RT by SR etching (*bottom trace*) and laser ablation (*top trace*). In the bottom trace, in contrast with the perpendicular bands detected at 556 and 1156 cm^{-1}, the parallel bands at 513 and 640 cm^{-1} appeared very small. Since the intense band at ca. 1210 cm^{-1} with a shoulder at ca. 1250 cm^{-1} could not be uniquely assigned, it is not used for the discussion

band had the blue shift (~4 cm^{-1}) as well. This gives further evidence of the change in crystal morphology of the deposited films [63]. It should be mentioned that the parallel bands have only one direction the same as the polymer chain, but the perpendicular bands can have all directions on the surface normal to the chain, so that the change of the parallel bands appeared more sensitive to the incident angle of light than that of the perpendicular ones, as observed in Fig. 30.

For the thermal deposition, the chain orientation in the PTFE films appeared different when the deposition was carried out at different substrate temperatures. The FTIR spectra of all the films deposited when the substrate was at room temperature showed the same behaviors as observed for the laser case (cf., Fig. 30b), indicating that thermal deposition resulted in the parallel orientation for T_s=RT. When the thermal deposition was carried out at a higher substrate temperature, however, as evident in Fig. 31 for T_s=265 °C, the films showed spectral behaviors similar to the SR case (cf., Fig. 30a). This indicates that the higher substrate temperature resulted in the perpendicular orientation for the thermal deposition. In other words, the chain ori-

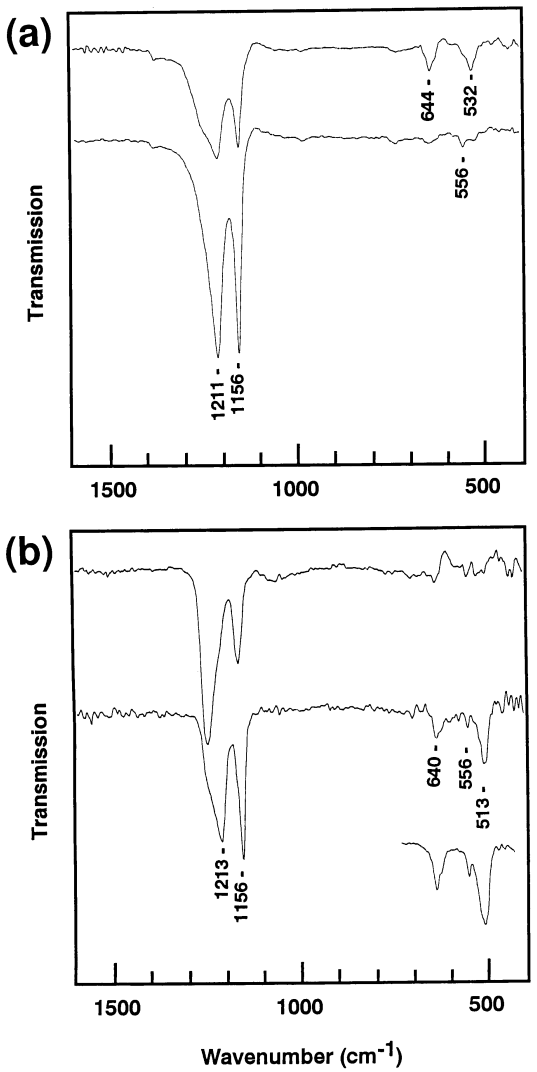

Fig. 30 Typical changes in FTIR transmission spectra of the PTFE films deposited on Si(100) substrates at T_s=RT by SR etching (**a**) and laser ablation (**b**). The *bottom trace* is a spectrum for the normal incidence (incident angle=0°) and the *top trace* is for the oblique incidence (incident angle=80°). Reproduced with permission from J Phys Chem 2000, B26, 6212–6217. Copyright 1998 Am Chem Soc

entation changed from the parallel orientation for T_s=RT to the perpendicular orientation for T_s=265 °C. Figure 32 shows the blue shift of the $A_2(3)$ band as well as the abundance ratio of the $A_2(2)$ band to the $E_1(3)$ band (in the normal transmission) versus T_s to indicate this change starting at T_s>200 °C. The previous study on PTFE films deposited by ionization-assist-

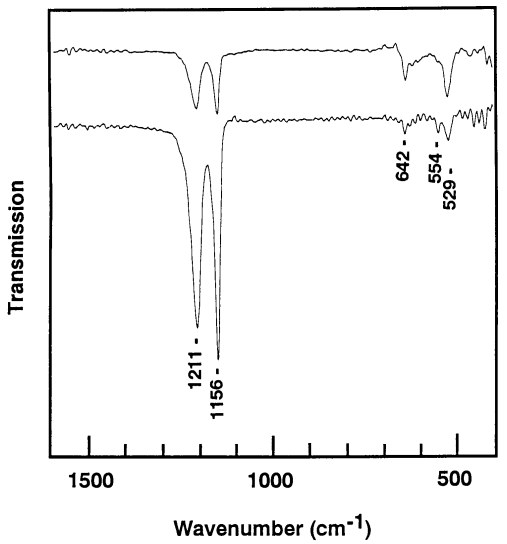

Fig. 31 Typical changes in the FTIR transmission spectra of the PTFE films deposited on Si(100) substrates at a higher substrate temperature T_s=265 °C by thermal evaporation. The *bottom trace* is for the normal incidence and the *top trace* for the oblique incidence. Here, similar behaviors to the SR case (cf., Fig. 30a) can be observed in the spectral change

ed evaporation also reported this change happening at T_s=180–240 °C and suggested that it was due to losing the parallel orientation, but these workers did not know that it changed into the perpendicular orientation [59]. It should be noted that the orientation is not lost but improved, since the perpendicular orientation has only one direction but the parallel orientation can have all directions on the substrate surface. Furthermore, when the film deposited by thermal evaporation at T_s<100 °C was heated to 350 °C for a minute and then cooled back to room temperature, as visible in Fig. 33 its FTIR spectra showed the behavior similar to the case of deposition at T_s=265 °C (cf., Fig. 31), indicating that the parallel orientation was also changed to the perpendicular one by recrystallization from the molten state. This is consistent with a previous study [64].

Why is the chain orientation different in the PTFE thin films deposited by different photoprocesses, namely SR etching and laser ablation? Obviously, it has little to do with the surface morphology (cf., Figs. 23 and 24). In laser ablation, it is known [60] that the fragments are nearly the monomers C_2F_4 like in pyrolysis [36]. The monomer radicals undergo polymerization on the substrate surface and are more likely to form the polymer chains along the surface in the parallel orientation, since simultaneous crystallization has to follow chain-growth reaction kinetics [65]. The surface may play the same role as does the surfactant in granular polymerization of tetrafluoroethylene (TFE) [66]. In SR etching, on the other hand, the saturated fluorocarbons

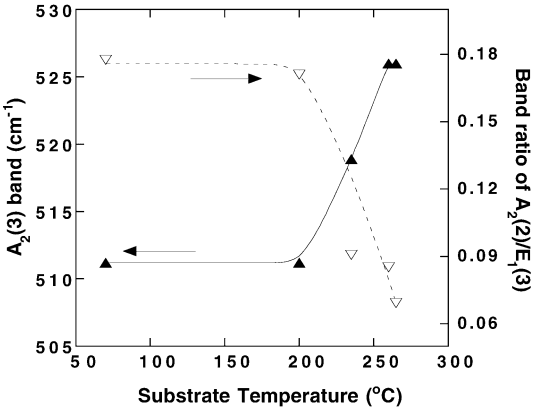

Fig. 32 Dependence of the $A_2(3)$ band position and the ratio of $A_2(2)/E_1(3)$ on the substrate temperature (*lines* drawn to guide eyes), showing the change of crystal morphology starting at T_s>200 °C. Reproduced with permission from J Phys Chem 2000, B26, 6212–6217. Copyright 1998 Am Chem Soc

(perfluoro-n-alkanes C_nF_{2n+2}) may be predominant over the monomer as the main fragments. The crystallization of perfluoro-n-alkane oligomers leads to a lamellar structure with chain axes oriented normal to the basal plane, i.e., the perpendicular orientation [67]. The existence of the saturated fluorocar-

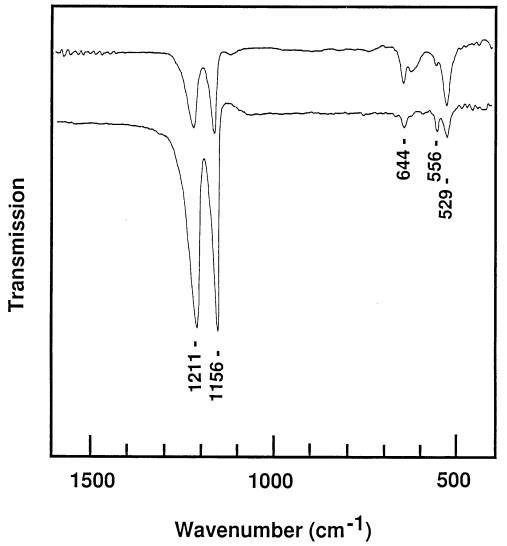

Fig. 33 Typical changes in FTIR spectra of the PTFE films deposited at a lower substrate temperature T_s<100 °C by thermal evaporation and then heated to the melting point for a minute. The *bottom trace* is for the normal incidence and the *top trace* for the oblique incidence. Here, similar behaviors to Fig. 31 can be observed in the spectral change

bons also accounts for the detection of a small amount of CF_3 in the deposited films (see Figs. 26 and 27). The deposited PTFE should have the chains long enough since its melting temperature was found to be close to that of the target. Although the saturated fluorocarbons are not so reactive as the monomer radicals, the growing polymer chains may add to already existing "dead" crystalline particles [65], and further chain growth may still occur to form longer chains in the deposited film. The higher target temperature may make it easier for larger fragments to desorb from the surface and the larger saturated fluorocarbons means less of the CF_3 fraction. This may account for the above observation that the higher target temperature diminished the CF_3 component in the PTFE films deposited by SR etching (see Fig. 26).

Why did the parallel orientation change into the perpendicular orientation when the deposition was carried out at a substrate temperature higher than 200 °C or by recrystallization from the molten state? Since pyrolysis results in almost the monomers, the chain-growth reaction kinetics force the chains to form along the substrate surface in the parallel orientation upon the repolymerization and simultaneous crystallization, as discussed above. The higher substrate temperature during the deposition or heating to the molten state increases the mobility of the forming or formed chains so as to orient the helical axes parallel to each other, and then to pack themselves laterally in a regular manner into a lamellar structure with perpendicular orientation during the crystallization [68]. Since PTFE can undergo chain reorientation by mobile twin-helix reversal defects and the perpendicular orientation possesses lower formation energy than the parallel orientation [68, 69], the change from the parallel orientation to the perpendicular one seems to be feasible. This change may occur without any significant change in crystallinity of the formed film. The temperature for this change seems to be dependent on the size of fragments [59].

6 Comparison Between Two Photoprocesses: SR Etching vs Laser Ablation

Although the SR beam has been used to directly etch PTFE, PFA, and FEP in vacuum, like laser ablation to create microstructures and to deposit thin films, some considerable differences are found. For example, it is not applicable to polymers like PI which has good radiation resistance, and the orientation of the polymer chains in the deposited films is different from that obtained by using the laser. In this section we compare two photoprocesses, namely SR direct etching and laser ablation and discuss the fundamentals for the SR etching of polymers.

First of all, the reason why we do not term our process *SR ablation* is as follows. The laser ablation proceeds layer by layer (here, the layer is defined by Beer's law [43] and is usually more than a molecular layer) and there generally exists a threshold for the onset of the laser ablation, as shown in Fig. 34 for the 266-nm laser ablation of PTFE. Such a process, removing a whole layer from the bulk instead of desorbing individual molecules from the surface, has been described as *explosive desorption* for which a fluence

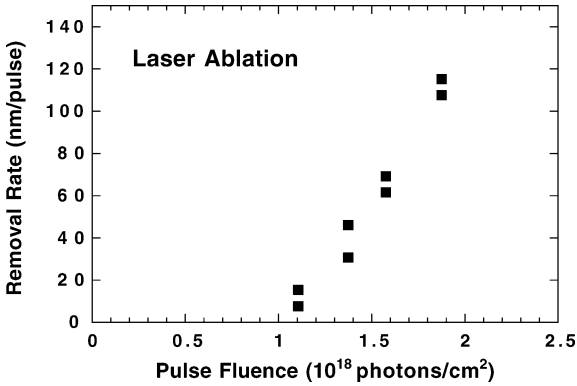

Fig. 34 The removal rate versus pulse fluence for 266-nm laser ablation of PTFE. The fluence threshold can be observed and a single laser pulse can ablate more than a molecular layer (a few Å). Reproduced with permission from J Phys Chem 2000, B26, 6212–6217. Copyright 1998 Am Chem Soc

threshold was observed [70]. For the SR etching of PTFE, however, such a threshold has not been found and to etch a molecular layer (i.e., a few Å) needs 10^5 pulses from the SR beam, as evident from Fig. 16. In the PMMA case, both UV excimer laser ablation [43] and UV direct etching [2] are known, giving another good example to distinguish *ablation* from *direct etching*: The ablation occurs only when a laser pulse reaches a certain fluence threshold [25, 43, 48], whereas direct etching occurs even under continuous UV light [2]. Laser ablation with a rate of 100 nm per pulse usually generates an ablation plume, that is, a dense cloud of ablated material, which may absorb the coming laser pulses to give a shielding effect [44,48], while UV etching proceeds very slowly with a rate of 2 nm per minute [2]. Although the etching rate in our case (Table 1) can be 10^4 times larger than that for the UV light, the SR process with an etching rate of 4×10^{-6} nm per pulse is still essentially different from laser ablation. Thus, the SR etching should not be termed ablation. Our consideration is also in agreement with the molecular dynamics simulations of laser ablation of polymers, where the ablation is referred to as *collective ejection* from the microscopic point of view [71].

Secondly, in order to understand which kind of dissociation may be involved, we performed in situ mass spectrometric analysis of gaseous species evolved upon the SR etching of PTFE. Quadrupole mass spectrometry (QMS) was carried out with a mass spectrometer (INFICON, Quadrex 100) in a mass range between 1 and 100. The typical QMS spectra for the SR etching of PTFE are given in Fig. 35 for different preheating temperatures T_t=RT and 200 °C. Although primary gaseous species evolved upon the SR etching may not be detected directly with QMS due to a large degree of fragmentation from electron-impact ionization, their patterns in the mass spectra can be used to deduce which kinds of photofragments have been generated, based on typical fragmentation patterns of the known species. Figure 36

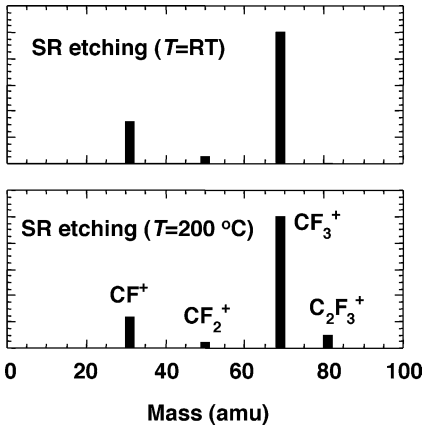

Fig. 35 Typical QMS patterns observed from the gaseous species evolved during the SR etching of PTFE at different temperatures. T=RT (*top*) and 200 °C (*bottom*), showing similarity to those of perfluoro-n-alkanes (cf., Fig. 36)

(from bottom to top) displays the typical fragmentation patterns of the perfluoro-n-alkanes C_3F_8 and C_4F_{10}, as well as the monomer C_2F_4, based on the data given in [72]. For comparison, we also carried out the QMS measurements for KrF or F_2 laser ablation as well as for pyrolysis at T_t=550 °C, and the corresponding spectra are shown in Fig. 37. The home made time-of-

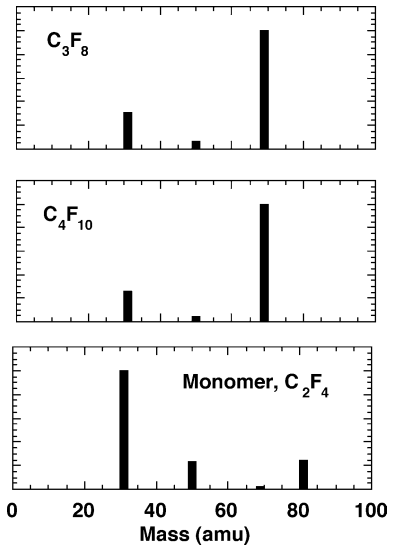

Fig. 36 Typical QMS patterns of perfluoro-n-alkanes. C_3F_8 (*top*), C_4F_{10} (*middle*), and the monomer C_2F_4 (*bottom*), based on the data given in [72]

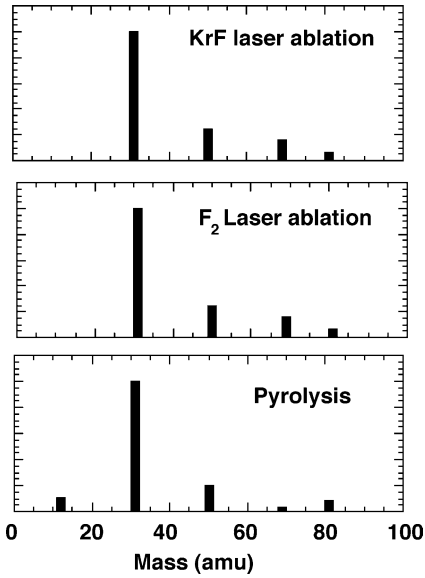

Fig. 37 Typical QMS patterns observed from the gaseous species evolved during laser ablation at 248 nm (*top*) and 157 nm (*middle*), as well as under thermal evaporation (*bottom*), showing similarity to that of the monomer (cf., Fig. 36, bottom trace)

flight detector was also used to detect ionic fragments and the typical spectrum is given in Fig. 38.

In the vacuum pyrolysis of PTFE, the mass spectrum (Fig. 37, bottom trace) appears nearly identical to that of the monomer (Fig. 36, bottom trace) but different from that of the perfluoro-n-alkanes (Fig. 36, top and middle traces). This agrees with the known fact that pyrolysis generates almost the monomer fragments [36].

In laser ablation, nearly the same QMS patterns have been observed for the different wavelengths 248 and 157 nm (Fig. 37, top and middle traces),

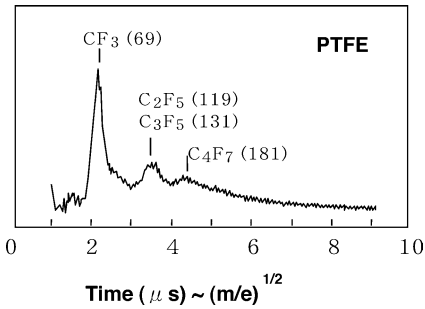

Fig. 38 A typical time-of-flight spectrum observed during the SR etching of PTFE, showing the CF_3^+ ion detected as the dominant peak like in the QMS spectra (cf., Fig. 35)

and the spectra look similar to that given by vacuum pyrolysis (Fig. 37, bottom trace) but different from that given by SR etching (Fig. 35). This indicates that, upon UV laser ablation or even vacuum-UV laser ablation, thermally driven unzipping has occurred at 248 nm or even at 157 nm yielding the monomer radicals as the main fragments, in agreement with the previous study using a 266-nm laser [60].

In the SR direct etching, Fig. 35 shows no consistent difference in the QMS patterns for the different sample temperatures, indicating that preheating has little effect on the dissociation under SR irradiation. The mass spectra obtained on SR etching are similar to that of the degradation under the monochromatic beam (32.6 eV) with a low photon flux density ($\sim 1\times10^{15}$ s^{-1} cm^{-2}) [73], which implies that the dissociation may not change even under the much higher photon flux density (2×10^{17} s^{-1} cm^{-2}) or under much higher photon energies (up to 10 keV) in our case. Furthermore, the QMS patterns for the SR etching (Fig. 35) appear closer to those of the perfluoro-n-alkanes (Fig. 36, top and middle traces) but different from that of the monomer C_2F_4 (Fig. 36, bottom traces). It suggests that the saturated fluorocarbons, namely perfluoro-n-alkanes C_nF_{2n+2}, may be predominant over the monomer as the main fragments evolved upon SR etching. In Fig. 38, the fragment ions detected in the TOF spectrum are again CF_3^+ (69 amu) as the dominant peak with a small amount of $C_2F_5^+$ (119 amu) or $C_3F_5^+$ (131 amu) and $C_4F_7^+$ (181 amu) [73]. It should be noted that nearly no F (19 amu) or F_2 (38 amu) was detected in the mass spectra. The XPS C1 s level spectra have also been measured under the SR irradiation of PTFE with various photon flux densities and compared to those before irradiation, as shown in Fig. 39. Besides CF_2, a large amount of CF_3 and CF were detected at the low photon flux density but they became less at the higher photon flux density. This suggests that CF_3 must have been formed on the surface when the degradation occurred at the low photon flux density, and then maybe as the saturated fluorocarbons desorbed from the surface when the etching started under the higher photon flux density. The existence of the perfluoro-n-alkane fragments in the SR etching of PTFE can easily account for not only the detection of the CF_3 component (see Figs. 26 and 27) but also the perpendicular orientation of polymer chains in the deposited PTFE films. Although no F_2 is found in the evolved gas, the existence of saturated fluorocarbons C_nF_{2n+2} in the evolved gas means a lack of F in the irradiated area. In fact, it has been found that cross-linking has occurred in the SR irradiated area as deeply as 50 μm in the bulk [39]. In conclusion, the SR-induced dissociation of PTFE is completely different from the thermal unzipping dissociation involved in laser ablation, but very similar to the photolysis induced by the ionizing radiation (e.g., 3 keV electron beam [74]). Obviously, our process should also not be termed *evaporation*, which has been introduced to describe the SR direct etching of SiO_2 [32]. Since ionizing radiation chemistry is involved in the SR etching of polymers, not all polymers can be etched. On the other hand, since the laser ablation causes thermal unzipping, almost all polymers can be ablated by the laser as long as they have an absorption large enough at the laser wavelength. The PI case is a good example of this.

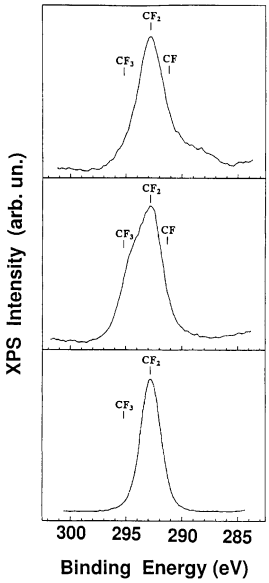

Fig. 39 XPS C1 s level spectra of the PTFE target under exposure to the SR beam with a flux density of 7.5×10^{17} s^{-1} cm^{-2} (*top*) and with a reduced flux density of 2.5×10^{16} s^{-1} cm^{-2} (*middle*), as well as without being irradiated (*bottom*). Reproduced with permission from J Phys Chem 2000, B26, 6212–6217. Copyright 1998 Am Chem Soc

No matter whether the photoprocess is direct etching or ablation, it involves three basic processes, namely absorption, dissociation, and desorption.

Absorption in the x-ray range where core electrons are excited is generally less wavelength-sensitive than that in the optical range where valence electrons are excited. Furthermore, using the broad-band SR is also less wavelength-sensitive than using the narrow-band laser. The PTFE case gives a good example of this: laser ablation can result in well-defined microstructures only in the vacuum-UV range [27, 75], whereas the SR etching carried out in different wavelength ranges shows no strong relationship with the photon energy [7, 29, 37]. In addition, the photoabsorption of polymers seems to be important for the ablation quality, and the PMMA case has given a good example. As mentioned previously, due to the strong absorption the ablation quality such as surface roughness, edge sharpness and so on is better at 193 nm than at 248 nm. In order to enhance the absorption of PMMA in the UV range, various methods have been introduced like chemical doping [44], introducing the incubation effect [25, 43], and using ultrashort laser pulses [28, 43]. On the other hand, in the highly penetrating x-ray range, chemical modification generally occurs far under the irradiated surface upon SR etching [38, 39].

Dissociation has turned out to be very different between SR etching and laser ablation. The PTFE case gives a good example, showing that photolysis

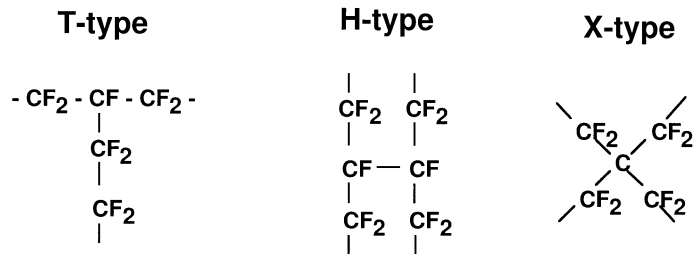

Fig. 40 Typical types of cross-linking suggested for PTFE under the ionizing radiation

occurs in SR etching compared with thermal unzipping in laser ablation. The photolysis of polymers seems to divide into two energy ranges, namely the UV range and the ionizing radiation range. For the UV range, both lasers and lamps have been generally used as the light source and the photolysis results from valence excitation which is strongly dependent on the wavelength. For the ionizing radiation range, not only the SR beam but also the other high-energy beams such as the electron beam, ion beam, and γ-rays have been used as the source and the photolysis (sometime also called radiolysis) results from the core excitation being less sensitive to the energy. The SR-induced degradation of PTFE was studied before we found the SR etching, appearing very similar to that induced by the 3-keV electron beam [72–74]. Recently, the cross-linking in PTFE has been studied for the SR [39] and other accelerator beams like the electron beam or γ-rays [76]. Typical types of cross-linking, called T-type, H-type, and X-type , are displayed in Fig. 40 [40, 72] and the likely formation of T-type cross-linking in the molten state has been reported under the electron beam or γ-rays [76].

Desorption is important for the generation of microstructures and the deposition of thin films. Laser ablation leads to explosive desorption which has little to do with the fragments formed on the surface, but for SR etching the fragments seem to play an important part in desorption. In the SR etching of PTFE, no appreciable amount of F or F_2 has been found in the evolved gas, but mainly the saturated fluorocarbons C_nF_{2n+2} instead. Details of how the active fluoride radical can form saturated fluorocarbon oligomers on the surface after the SR dissociation of PTFE remain unknown, but the saturated oligomers seem to desorb readily from the surface and their formation should interrupt the chain growing on the surface, making the desorption easier. It should be pointed out that the temperature may also play a positive role in the desorption process, even though the SR dissociation is photolytic. A higher temperature may not only help release larger fragments from the surface but may also increase mobility of the fragments on the surface to accelerate the formation of the saturated oligomers, thus leading to a higher etching rate. Either heating PMMA over its glass transition temperature (i.e., Tg=132 °C) [3] or heating PTFE over its α-relaxation temperature (i.e., T_α=130 °C) [39] has shown the significant enhancement of the etching rate. Since either the shorter polymer chain or the lower melting point means a

higher potential for mobility inside the polymer, it should not be surprising that the highest etching rate is obtained for FEP, which has the lowest molecular weight and the lowest melting point among PTFE, PFA, and FEP [42]. When cross-linking occurs, however, the molecular weight may not directly reflect the length of polymer chains and so not the mobility potential either. In fact, the higher etching rate has been observed after cross-linking PTFE [39].

The ionizing radiation chemistry has shown strong similarities between the SR beam and other accelerator beams such as the electron beam, ion beam or γ-rays. By learning it, we are able to understand what may happen with the hydrogenated fluoropolymers such as PVF [poly(vinyl fluoride), $-HCF-CF_2-$], PVDF ($-CH_2-CF_2-$), and ETFE ($-CH_2-CH_2-CF_2-CF_2-$). Obviously, the only difference between these polymers and PTFE is the presence of hydrogen atoms. Under the ionizing radiation [77–80], PVF, PVDF, and ETFE tend to lose the hydrogen and undergo cross-linking, whereas PTFE, PFA, and FEP mainly undergo chain scission to generate saturated and unsaturated fluorocarbons. The ratio of the chain scission to the cross-linking events seems to follow the order PTFE>PVF>PVDF>ETFE [77]. In the PVDF case, for example, this ratio has been found to be about 5:3 [78]. The prompt desorption of H_2 with a slow component of HF has been observed [79], whereas nearly no F_2 has been found in the PTFE case [74]. As we have understood in the above discussion about the desorption of fragments, the atomic ligands on the side chains may play an important part in keeping the fragments readily desorbed and interrupting chain growth and cross-linking. The observation of the desorption of a considerable amount of H_2 and HF [11, 30, 79] means that cross-linking and chain growth of carbon fragments may make desorption difficult. Therefore, it is not surprising that the attempt to generate deep microstructures by the SR etching of PVDF has turned out a failure [30]. Obviously, a similar attempt on the hydrogenated polymer PE (polyethylene, $-CH_2-CH_2-$) should have the same fate. In fact, carbonization under long SR irradiation has been observed for PE, PVDF, and ETFE [11].

7
Application: X-ray Refractive Single Lenses Made by SR Etching

In the x-ray range, the refractive index n in matter is very close to unity and thus the refractive index decrement $\delta=1-n$ is extremely small, typically of the order of 10^{-6}. For example, a refractive lens normally has spherical curvatures of radius R, typically 100 mm in the optical range, and its focal length $F=R/2\delta$ for the x-rays would be 50 km, too long to be useful. The renaissance of refractive optics for x-rays came from an idea of compound refractive lenses (CRL), which consist of a linear array of many concave lenses [81, 82]. The CRL has been made of different kinds of polymers, including PTFE and PMMA, as well as other low-Z materials [83], and is able to focus the x-rays at a reasonable distance, typically of the order of a few meters. However, its thickness leads to absorption so strong that it has not resulted

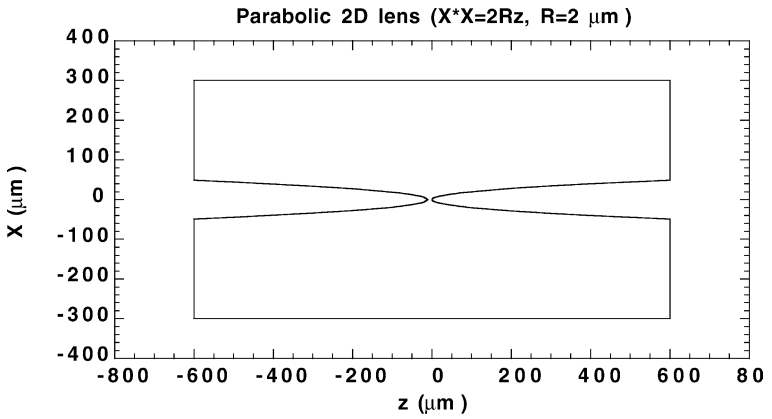

Fig. 41 A typical example of designs for the x-ray refractive concave lenses with parabolic curvatures

in any significant gain yet. For example, the CRL that consists of 134 single lenses of radius R=350 μm and aperture A=200 μm was made of PTFE and focused the hard x-rays (photon energy E=23.4 keV) into a spot of full width at half maximum (FWHM) σ=11 μm at the focal length F=1.78 m [83]. However, the gain G=1.0 was given, which meant no gain in the photon flux density; in other words, this lens actually acted like an 11-μm pinhole. On the other hand, the parabolic single lens is considered to be extremely difficult to achieve, due to the fact that the aspect ratio of the lens thickness z [84] (or the lens aperture A [85]) to the curvature radius R is too large to create. Since the SR etching of PTFE can achieve feature sizes of the order of 1 μm and a structural depth of a few 100 μm, we are able to make the parabolic single lenses by this technique. As an example of the application, the fabrication of the parabolic single x-ray lens is presented in this section.

In contrast with a cylindrical lens [82], a parabolic lens can provide both a reasonably short focal length and an aperture large enough to suit the beam size of hard x-rays from a third-generation SR source. For a beam which is typically 100–200 μm in diameter and has a photon energy between 10 and 30 keV, our single lenses were considered to have two parabolic curvatures with a radius (R=2–20 μm) to keep the focal length reasonably short (F=0.2–2 m) and meanwhile to have large enough apertures (A=50–200 μm). Figure 41 shows a typical design for the lens. Since the refractive index in the x-ray range is slightly smaller in matter than in air, the x-ray lens is concave. It has two parabolic curvatures with the radius R=2 μm, the aperture A=98 μm, and the gap between two curvatures d=10 μm. For 10-keV x-rays, the focal length will be 0.2–0.4 m when it is made of PTFE. As shown in Fig. 42, two curvatures are on the same axis for one-dimensional focus (called 1D for simplicity), while one is in the vertical and another in the horizontal for two-dimensional focus (called 2D for simplicity). The 1D lens needs only a single exposure with a mask which has two curvature patterns

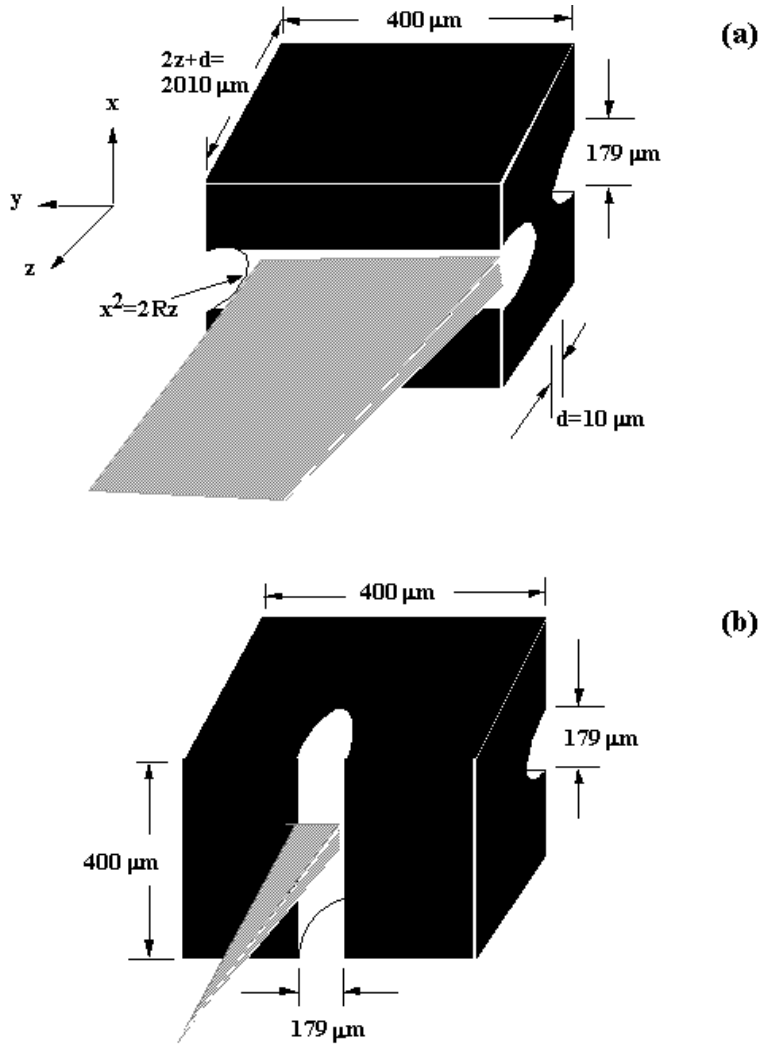

Fig. 42 Typical measurements of x-ray parabolic lenses for the one-dimensional (**a**) and two-dimensional focus (**b**). Reproduced from Microsystem Technologies 2002, 8, 99–101 (Springer)

and the gap between the two curvatures is defined by the mask. To make the 2D lens, on the other hand, the exposure has to be carried out twice in different directions with a mask which has only one curvature, and thus the gap is dependent on the alignment of the second exposure. Furthermore, for the aperture A=100–200 μm, the depth of each exposure should be 200–400 μm and the corresponding aspect ratios of the lens structures would be around 100. Such high aspect ratio microstructures in PTFE are just right to be fabricated by SR etching.

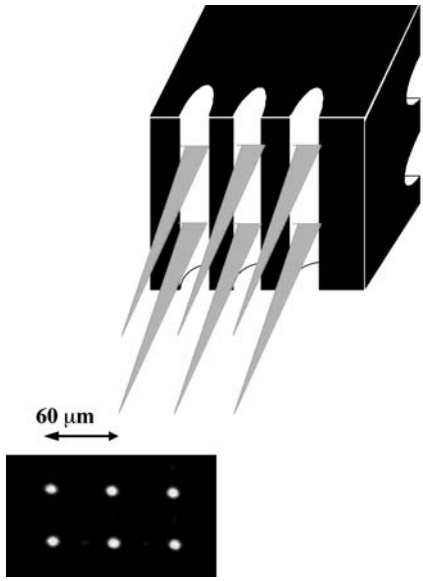

Fig. 43 Lens array for generation of many hard x-ray microbeams. The *insert* shows the microbeams generated from a beam-line

Since the obtainable precision of the mask for SR etching was around 2 μm, the parabolic radius was set to be R=4 μm and the aperture $A=2(2Rz)^{1/2}$=179 μm to match the SR beam size [86]. Figure 42 displays the typical measurements for the 1D and 2D lenses, respectively. The gap between the two curvatures for the 1D lens was d=10 μm defined by the mask, while that for the 2D lens was between 100 and 500 μm achieved by using our exposure setup. Figure 43 displays the lens array, in which the aperture of each lens was designed to be A=40 μm and the spatial period to be 60 μm with regard to the SR beam size. Since the focal depth is of the order of a few tens of millimeters for such a parabolic lens, a deviation in the radius R had to be within 1–2% [26], difficult for all the present microtechniques. In general, this deviation would be compensated for in the mask design, that is, the radius has to be modified in the design in order for the fabrication process to make the final curvatures have R=4 μm within the deviation of 1–2%.

The experimental conditions for generation of the PTFE lenses by SR etching were almost the same as described previously. Figure 44 shows one parabolic curvature created on PTFE by SR etching. It can be seen that the formed surface appeared to be smoother than that of the starting materials.

The performance of our PTFE lenses was checked with a beam of hard x-rays (E=10 keV, $\Delta E/E$~2.4×10^{-4}) from Hyogo beam-line (BL24XU) at SPring-8 [86]. The beam size was varied with two slits in the vertical and with the other two in the horizontal. The focal spot was observed with an x-ray microscope (Hamamatsu-C5333, resolution of 0.5 μm). Two-dimensional intensity mapping is displayed in Fig. 45 for beams focused by the 1D and

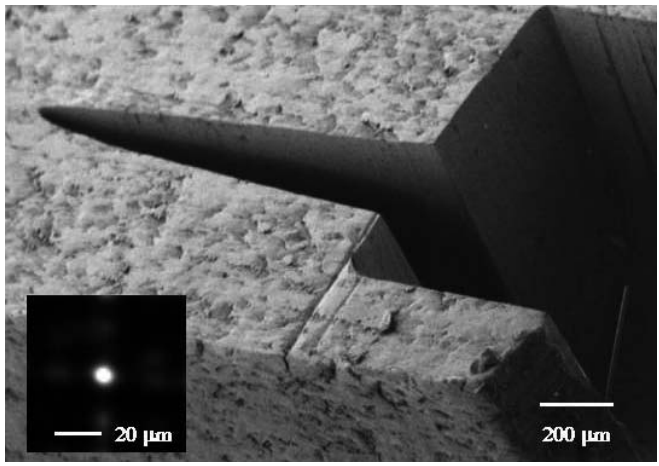

Fig. 44 SEM picture of one parabolic curvature of the 2D lens formed on PTFE by using SR etching. The *insert* shows an x-ray microscopic observation of the 10-keV beam focused by the 2D lens made of PTFE

2D lenses. It can be seen that the beam intensity is enhanced on the focal line in the 1D case, while it is further enhanced on the focal point by collecting photons around it in the 2D case, where the width of the disappeared part of two focal lines corresponds to that of the lens aperture. The insert in Fig. 44 shows the focal spot of the 2D lens, while Fig. 43 shows the focal spots of a lens array with a spatial period of 60 μm. In this way, not only a microbeam but also many microbeams can be generated from a beam-line. It should be mentioned that the generation of the microbeams is a key technology for the application of hard x-rays [87].

The focal width σ_x or σ_y was given as the FWHM, which resulted from a Gaussian fit (line) to the measured intensity distribution (dots) as shown in Fig. 46. The minimum value σ_x=3.4 μm was obtained for the 1D lenses, while σ_x=5.6 μm and σ_y=6.7 μm were obtained for the 2D lenses. Measurements with knife-edge scanning were also carried out for the 1D lenses to cross-check the obtained values of σ_x. Figure 47 shows an example, where the measured points were given in dots with their curve fit in a solid line and the derivation of the fitted curve was in the dashed line, resulting in σ_x=4.3 μm (FWHM). The focal widths σ_x and σ_y actually resulted from a convolution of the demagnified image of the light source and the point spread function of the lens, since we observed the focal spot fluctuating in the range of a few μm due to fluctuation of the SR source. The horizontal values σ_y were slightly larger than the vertical ones σ_x, due to the slightly larger divergence of the SR beam in the horizontal. The focal length F was determined at the position where the minimum value of σ_x was found. The 1D lens resulted in F=0.41 m and the 2D lens resulted in F=0.8 m, twice as long as that of the 1D lens, in agreement with calculations using the refractive index decrement δ.

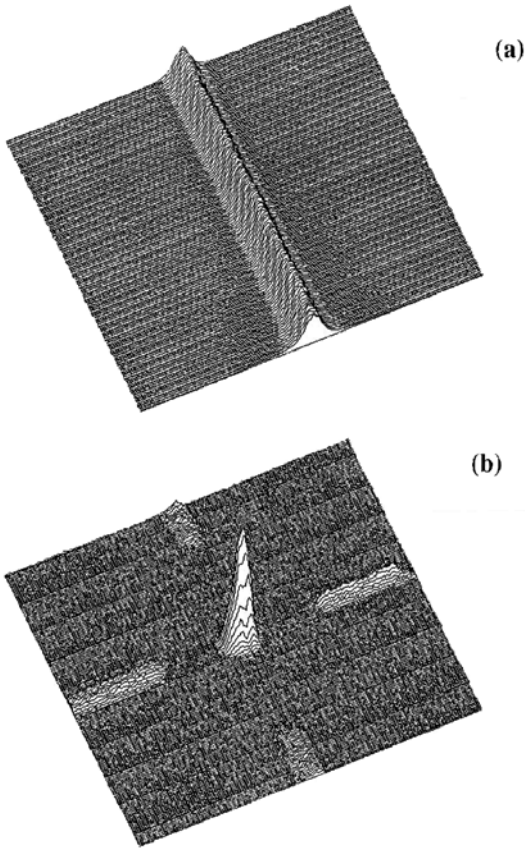

Fig. 45 Two-dimensional intensity mapping for the one-dimensional (**a**) and two-dimensional focus (**b**). Reproduced from Microsystem Technologies 2002, 8, 99–101 (Springer)

The transmission T of a lens was obtained by measuring the x-ray intensity with a PIN photodiode in front of the lens and behind it. The 1D lens had T=54% and the 2D lens had T=40% for the beam of ϕ=100 μm. The transmission of the parabolic lens is a function of the beam size ϕ and for the 1D lens it is

$$T(\phi) = \left(4R/\mu'\phi^2\right)^{1/2} \cdot \exp(-\mu' d) \cdot \mathrm{Erf}\left[\left(\mu'\phi^2/4R\right)^{1/2}\right] \quad (1)$$

where Erf(x) is the error function. In our case, since $\mu' d \ll 1$ and $3\mu'\phi^2/40R \ll 1$, the transmission approximates to

$$T(\phi) = 1 - \mu' d - \mu'\phi^2/12R \quad (2)$$

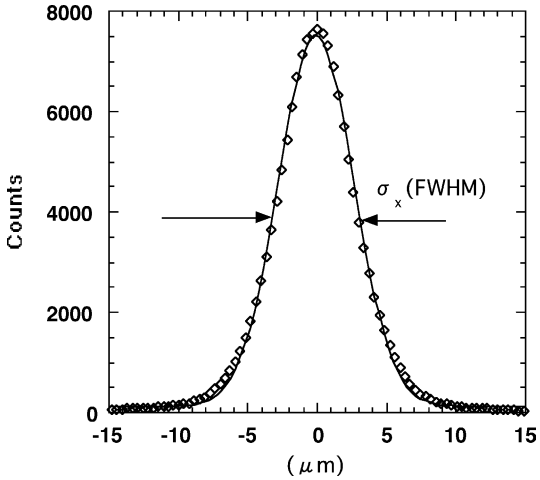

Fig. 46 A Gaussian fit (*line*) to the measured intensity distribution (*dots*), resulting in the focal widths σ_x (FWHM)

Fitting $T(\phi)$ with d=10 μm and ϕ=100 μm to the measured data led to the attenuation parameter μ'=21 cm^{-1}, larger than the linear absorption coefficient of PTFE of μ=14 cm^{-1}. There might be other losses due to surface roughness and small-angle scattering besides the material absorption [83]. For the parabolic lens, the attenuation is mainly due to the curvature part (i.e., $\phi^2/12R \gg d$), strongly dependent on the beam size ϕ. On the other hand, the strong attenuation may lead to an effective aperture of the lens, actually

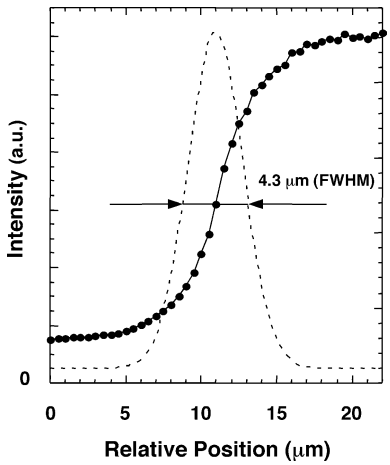

Fig. 47 A typical measurement of knife-edge scanning, showing the curve fit (*solid line*) to the measured points (*solid dots*) and its derivation (*dashed line*) leading to the focal width σ_x=4.3 μm (FWHM)

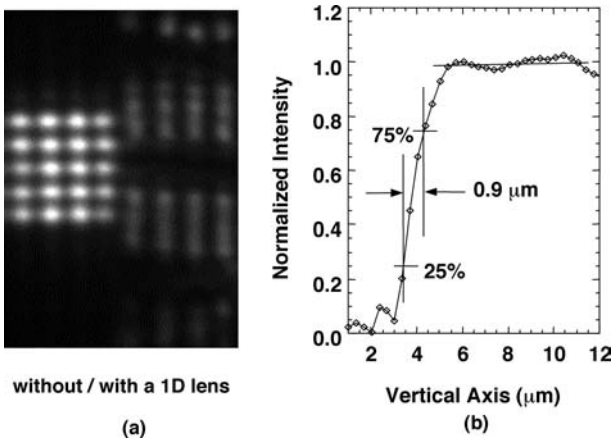

Fig. 48 Two x-ray images of a copper mesh without and with a lens (**a**) and evaluation of the imaging resolution, leading to Δ=0.9 μm (**b**). The image enlarged in the vertical by the 1D lens is visible by comparing two images

limiting the lens aperture. For the PTFE lens at E=10 keV, the effective aperture $A_e=2(2R/\mu')^{1/2}$=123 μm is actually smaller than its aperture A=179 μm. The gain G was $G=T\phi/\sigma_{x=}$16 for the 1D lens and $G=T\phi^2/\sigma_x\sigma_y$=107 for the 2D lens.

The enlarged x-ray image of a copper mesh was taken using the 1D lens. The mesh was set at 0.49 m in front of the lens (F=0.41 m) and the x-ray microscope was set at 2.4 m behind the lens. Figure 48a shows the two images obtained with and without the lens, where a magnification of about 5 (~2.4/0.49) in the vertical is visible by comparing them. Figure 48b shows that the imaging resolution resulting from an evaluation with the criterion of 25–75% of the total contrast was Δ=0.9 μm, poorer than $1.22\lambda F/A_e$=0.5 μm. This seemed to be mainly due to coherency of the beam from an undulator.

Since the PTFE lenses were fabricated with the SR beam, much care was taken about any possible damage caused by the focused hard x-rays. In contrast with the CRL made of PTFE [83], our single lenses did not show any visible damage such as deformation and bubble formation. It should be mentioned that the beam for the fabrication and that for the focusing test were very different in photon flux density and photon energy. For example, the beam used for SR etching peaked at about 1 keV with the flux density ~1.5×10^{17} s^{-1} cm^{-2}, whereas the SR beam used for the focusing test was at 10 keV with 1.1×10^{13} s^{-1} cm^{-2} [86]. For PTFE, its absorption at 10 keV is about three orders of magnitude less than that at 1 keV (see Fig. 1) and the lens absorbs the radiation power from the focusing beam about seven orders of magnitude less than from the etching beam for the same irradiation time. The damage like deformation and bubble formation found in the CRL [83] may be mainly due to heat load rather than photolysis; thus, it was unlikely to cause such damage to the single lens which absorbed 10^6 times less power from the focusing beam.

8 Conclusions

Direct etching of polymers in vacuum with SR which was mainly x-rays between 0.2 and 3 nm has been studied. This is a process involving only photons, like laser ablation, but it is different from laser ablation both in desorption dynamics and dissociation mechanisms.

The studies have focused on the PTFE case. The etching process can progress as deep as 1,000 μm and as fast as 100 μm/min, completely different from the previously reported self-development which was superficial and much slower than chemical etching, and has been applied as a microfabrication process to create high aspect ratio microstructures which may have feature sizes less than 1 μm and a structural depth more than 1,000 μm. X-ray refractive lenses with parabolic curvatures were made of PTFE by using this process and were used to generate hard x-ray microbeams, demonstrating an example of the application. Like the LIGA process, the SR etching of Teflon may be combined with galvanic forming to create metallic microstructures, called the TIEGA process. The dissociation involved in the SR etching is photolytic, in contrast with the thermal unzipping in laser ablation. Thus, limited polymers are applicable to SR direct etching for the generation of high aspect ratio microstructures, whereas almost all polymers can be ablated by laser pulses as long as the polymers have strong enough absorption and the laser pulses can reach the ablation threshold.

SR etching has been carried out to deposit thin films of many polymers such as PTFE, PVDF, ETFE and so on, demonstrating that it may also be a simple and versatile method for fabrication of thin polymeric films, like laser ablation deposition.

References

1. Smith HI (1995) J Vac Sci Technol B12:2323
2. Ueno N, Konishi S, Tanimoto K, Sugita K (1981) Jpn J Appl Phys 20: L709
3. Yamada H, Hori M, Morita S, Hattori S (1988) J Electrochem Soc 135:966
4. Ogawa T, Yamagushi A, Soga T, Tachibana H, Matsumoto M, Oizumi H, Takeda E (1994) Jpn J Appl Phys 33:1577
5. Srinivasan R, Braren B (1989) Chem Rev 89:1303
6. Srinivasan R, Mayne-Banton V (1982) Appl Phys Lett 41:576
7. Zhang Y, Katoh T, Washio M, Yamada H, Hamada S (1995) Appl Phys Lett 67:872
8. Urisu T, Kyuragi H (1987) J Vac Sci Technol B5:1436
9. Kyuragi H, Urisu T (1987) Appl. Phys Lett 50:1254
10. Srinivasan R, Leigh WJ (1982): J Am Chem Soc 104:6784
11. Nakanishi K, Suzuki H, Katoh T, Imai S, Nakayama Y, Miki H (1999) Jpn J Appl Phys 38:863
12. Kawamura Y, Tokyoda K, Namba S (1982) Appl Phys Lett 40:374
13. Levi BG (1991) Phys Today October:17
14. Menz W, Bley W (1993) Mikrosystemtechnik für ingenieure. VCH, Weinheim
15. Hirose S, Miyatake T, Li X, Toyota E, Hirose M, Fujii K, Suzuki K (2000) J Vac Sci Technol B18:2986
16. Yang J, Toyota E, Kawachi S (1998) Jpn J Appl Phys 37:6804

17. Itani T, Yoshino H, Fujimoto M, Kasama K (1995) NEC Report 48:197
18. Miyatake T, Li X, Hirose S, Monzen T, Fujii K, Suzuki K (2001) J Vac Sci Technol B19:2444
19. Deguchi K (1997) PhD thesis, University of Tokyo
20. Khan M, Han G, Tsvid G, Kitayama T, Maldonado J, Cerrina F (2001) J Vac Sci Technol B19:2423
21. Toyoda E, Hori T (2001) J Vac Sci Technol B19:2428
22 Fritze M, Burns J, Wyatt PW, Chen CK, Gouker P, Chen CL, Kease C, Astolfi, D, Yost D, Preble D, Curtis A, Davis P, Cann S, Deneault S, Liu HY (2000) J Vac Sci Technol B18:2886
23. Chen W, Ahmed H (1993) J Vac Sci Technol B11:2519
24. Seki A, Tanaka H, Ohta T (1990) Phys Scr 41:167
25. Küper S, Stuke M (1989) Appl Phys A49:211
26. Zhang Y, Katoh T, Amano D (2002) Microsyst Technol 8:99
27. Basting D, Sowada U, Voß F, Oesterlin P (1991) SPIE 1412:80
28. Küper S, Stuke M (1989) Appl Phys Lett 54:4
29. Katoh T, Zhang Y (1998) J Synchrotron Rad 5:1153
30. Manohara HM, Morikawa E, Choi J, Sprunger PT (1999) J Microelectromech Syst 8:417
31. Katoh T, Zhang Y (1998) Microsyst Technol 4:135
32. Akazawa H, Utsumi Y, Takahashi J, Urisu T (1990) Appl Phys Lett 57:2302
33. Masui S, Amano D, Katoh T, Zhang Y, Yamada H (1995) Rev Sci Instrum 66:2352
34. Zhang Y, Katoh T (1996) Jpn J Appl Phys 35:L186
35. Nishi N, Katoh T, Ueno H, Sugiyama S (2000) Memoirs of the SR Center, Ritsumeikan University 2:29
36. Single JG, Muus LT, Lin, TP, Larsen HA (1964) J Vac Sci Technol A 12:681
37. Zhang Y, Hori T (2000) Synchrotron Radiation News 13:32
38. Nishi N, Katoh T, Ueno H, Sugiyama S (2002) Microsyst Technol 9:1
39. Katoh T, Yamaguchi D, Satoh Y, Ikeda S, Aoki Y, Washio M, Tabata Y (2002) Appl Surf Sci 186:24
40. Oshima A, Tabata Y, Kudoh H, Seguchi T (1995) Radiat Phys Chem 45:269
41. Willians KR, Muller RS (1996) J Microelectromech Syst 5:256
42. Inayoshi M, Ito M, Hori M, Goto T (1999) J Vac Sci Technol B 17:949
43. Küper S (1989) PhD thesis, University of Göttingen
44. Preuß S (1993) PhD thesis, University of Göttingen
45. Harvey E, Rumksy P, Gower M, Remnant J (1995) SPIE 2639:266
46. Lazare S, Lopez J, Weisbuch F (1999) Appl Phys A 69:S1
47. Zhang Y, Lowe RM, Harvey E, Hannaford P, Endo A (2002) Appl Surf Sci 186:345
48. Preuss S, Späth M, Zhang Y, Stuke M (1993) Appl Phys Lett 62:3049
49. Sasuga T, Hayakawa N, Yoshida K, Hagiwara M (1985) Polymer 26:1039
50. Wittmann JC, Smith P (1991) Nature 352:414
51. Nason TC, Moore JA, Lu TM (1992) Appl Phys Lett 60:1866
52. Quaranta F, Valentini A, Favia P, Lamendola R, d'Agostino R (1993) Appl Phys Lett 63:10
53. Hansen SG, Robitaille TE (1988) Appl Phys Lett 52:81
54. Blanchet GB, Shah SI (1993) Appl Phys Lett 62:1026
55. Ueno Y, Fujii T, Kannari F (1994) Appl Phys Lett 65:1370
56. Katoh T, Zhang Y (1996) Appl Phys Lett 68:865
57. Katoh T, Zhang Y (1999) Appl Surf Sci 138–139:165
58. Zhang Y, Katoh T, Endo A (2000) J Phys Chem B 104:6212
59. Usui H, Koshikawa H, Tanaka K (1995) J Vac Sci Technol A 13:2318
60. Blanchet GB, Fincher CRJr, Jackson FL, Shah SI, Gardner KH (1993) Science 262:719
61. Starkweatherm Jr HW (1986) Macromolecules 19:1131
62. Hoffmann FM (1983) Surf Sci Rep 3:107
63. Kobayashi M, Sakashita M, Adachi T, Kobayashi M (1993) Macromolecules 28:316
64. Symons NKJ (1963) J Polymer Sci A 1:2843

65. Wunderlich B (1968) Adv Polymer Sci 5:568
66. Folda T, Hoffmann H, Chanzy H, Smith P (1988) Nature 333:565
67. Schwickert H, Strobl G, Kimmig M (1991) J Chem Phys 95:2800
68. Strobl G (1996) The physics of polymers. Springer, Berlin Heidelberg New York
69. Kimmig M, Strobl G, Stühn B (1994) Macromolecules 27:2481
70. Domen K, Chuang TJ (1987) Phys Rev Lett 59:1484
71. Zhigilei LV, Kodali, PBS, Garrison BJ (1998) J Phys Chem B 102:2845
72. Wheeler DR, Pepper SV (1982) J Vac Sci Technol 20:226
73. Simons JK, Frigo SP, Taylor JW, Rosenberg RA (1994) J Vac Sci Technol A 12:681
74. Wheeler DR, Pepper SV (1990) J Vac Sci Technol A 8:4046
75. Wada S, Tashiro H, Toyoda K, Niino H, Yabe A (1993) Appl Phys Lett 63:211
76. Oshima A, Ikeda S, Katoh E, Tabata Y (2001) Radiat Phys Chem 62:39
77. Katan E, Narikis M, Siegmann A (1998) J Appl Polym Sci 70:1471
78. Rosenberg Y, Siegmann A, Narkis M, Shkolnik S (1991) J Appl Polym Sci 43:535
79. Torrisi L, Ciavola G, Percolla R, Benyaich F (1996) Nucl Instrum Methods Phys Res B 116:473
80. Timmerman R, Greyson W (1962) J Vac Sci Technol 6:456
81. Tomie T (1994) US Patent 5,594,773
82. Snigirev A, Kohn I, Snigireva I, Lengeler B (1996) Nature 384:49
83. Lengeler B, Snigirev A, Snigireva I, Raven C (1998) J Appl Phys 84:5855
84. Yang BX (1993) Nucl Instrum Methods Phys Res A 328:578
85. Snigirev A, Kohn I, Snigireva I, Souvorov A, Lengeler B (1998) Appl Opt 37:653
86. Zhang Y, Katoh T, Kagoshima Y, Matui J, Tsusaka Y (2001) Jpn J Appl Phys 40:L705
87. Dhez P, Chevallier P, Lucatorto TB, Tarrio C (1999) Rev Sci Instrum 70:1907

Author Index Volumes 101–168

Author Index Volumes 1-100 see Volume 100

Subject Index